STUDY OF TAYLOR INSTABILITIES AND TURBULENCE IN LUBRICATING FILMS

MICHAEL GEOFFREY SHORT

Thesis submitted to the
Council for National Academic Awards
for the degree of
Doctor of Philosophy

August, 1977

School of Engineering Science
Plymouth Polytechnic

CONTENTS

ACKNOWLEDGEMENTS

I owe a considerable debt to Mr. J. H. Jackson of the School of Engineering Science, Plymouth Polytechnic, for his supervision of this work, and for his continual support and encouragement. Particular thanks are also due to Mr. G. S. Ritchie of G.E.C. Power Engineering Ltd., Whetstone, for many helpful discussions and suggestions.

I wish to express my appreciation to Mr. D. R. S. Rabley for the use of the facilities of the School of Engineering Science, and to the technicians for the manufacture of components for the test rigs used by the author. Thanks are also extended to Dr. T. E. R. Jones of the School of Mathematical Sciences for his interest in this work.

I am grateful to the Science Research Council for their financial support.

Finally, I wish to thank Miss M. Roberts for typing the thesis.

SUMMARY

The development of the wavy mode of Taylor vortices in the flow between a rotating inner cylinder and a stationary outer cylinder has been investigated by visual observations using a stroboscopic technique and by inner cylinder torque measurements. Radius ratios of 0.874, 0.911, 0.950 and 0.975 have been tested for the concentric and eccentric cylinder cases.

The stability of wavy mode flow has been found to decrease with increasing radius ratio and/or increasing eccentricity. Observations of the flow suggested that the wavy mode can be classified into three regimes called, respectively, the primary, transitional and secondary modes. The three regimes were most easily identified using a radius ratio of 0.911 and concentric cylinders. In this case, the onset of the transitional state (so called because of the tendency for the circumferential wave number to change continually even at particular constant speeds) was found to be particularly violent, completely destroying the well defined nature of the primary wavy mode. Rather surprisingly, this quasi-turbulent regime of wavy mode flow was found to give way to the more regular secondary wavy mode as the speed of the inner cylinder was increased. Non-uniqueness is shown to be an important feature of wavy mode flow.

Results are presented showing that circumferential wave number changes can often be detected by torque measurements. In particular, the onset of the transitional state results in a sudden reduction in the required driving torque, the magnitude of which is considerably influenced by the stability of the primary wavy mode flow. Friction coefficient characteristics derived from the torque measurement results are used to deduce a general relationship incorporating the effects of the eccentricity and radius ratios.

NOTATION

Unless otherwise stated, the following alphabetical list of symbols applies:

γ Sommerfeld substitution angle

δ any small increment

ε eccentricity ratio (= e/c)

η radius ratio (= R_i/R_o)

θ angle measured from wide gap in direction of rotation of inner cylinder

λ axial wavelength of vortices (= $2h_v$)

μ absolute viscosity

μ^* velocity ratio (= ω_o/ω_i)

ν kinematic viscosity

ρ density

τ shear stress

ω angular velocity

ω_i angular velocity of inner cylinder

ω_o angular velocity of outer cylinder

a axial wave number (= $2\pi c/\lambda$)

a_o axial wave number at onset of Taylor vortices for concentric case

C_f friction coefficient (= $M/\pi \rho \omega_i^2 R_i^4 L$)

c radial clearance (= $R_o - R_i$)

e displacement of inner cylinder from concentric position

f stroboscope flashing frequency

g acceleration due to gravity

h local oil film thickness

h_v axial length of vortex cell

K various constants

L axial length of oil column

ℓ slope of friction coefficient characteristics

M inner cylinder torque

N inner cylinder rotational speed

n number of circumferential waves

p pressure

p^* non-dimensional pressure $(= pc^2/\mu R_i^2 \omega_i)$

R_i radius of inner cylinder

R_o radius of outer cylinder

Re Reynolds number $(= R_i \omega_i c/\nu)$

Re_c Reynolds number at onset of Taylor vortices

Re_w Reynolds number at onset of wavy mode

T Taylor number $(= 2\omega_i^2 R_i^2 c^3 /\nu^2\{R_o + R_i\})$

T_c Taylor number at onset of vortices for eccentric case

T_o Taylor number at onset of vortices for concentric case

T_w Taylor number at onset of wavy mode

V circumferential wave velocity

v inner cylinder peripheral velocity

LIST OF TABLES

LIST OF FIGURES

CHAPTER 1

INTRODUCTION

The use of process fluids of low kinematic viscosity as lubricants and the introduction of large diameter bearings running at high rotational speeds in turbo-generating plant has meant that modern plain film-lubricated journal bearings commonly operate under conditions for which the assumption of simple laminar flow is not valid. Except where the clearance / radius ratio is extremely small, the transition to turbulence is preceded by the appearance of Taylor vortices and other even more complicated flows which are described as superlaminar. A great deal of research has been conducted on Taylor vortices since 1923 when Taylor (71)* first predicted and observed their appearance. Taylor's original experiments were concerned with the concentric cylinder case although considerable interest has been recently centred on the formation of Taylor vortices in the flow between a rotating inner cylinder and a stationary outer cylinder when the cylinders are eccentric. The development of superlaminar flow has received rather less attention, however, and this was, therefore, made the primary consideration of the present investigation.

Taylor used the technique of injecting dye into the annular clearance between the inner and outer cylinders to detect the initial onset of the toroidal vortices. Although unable to study the further development of the flow in any detail, because of mixing of the dye with the rest of the fluid in the gap, he described the breakdown of the stable vortex structure into one in which the vortices started to pulsate. More recently, a number of workers have studied flow instabilities over an indefinite period using the alternative technique

* numbers in parenthesis designate references at end of thesis

of suspending very small flakes of aluminium paint pigment in the test fluid. The pulsations observed by Taylor are seen to be due to travelling sinusoidal wave forms superimposed on the basic vortex structure and rotating in the same direction as the inner cylinder. Because of the appearance, this development of Taylor vortex flow is commonly referred to as the "wavy mode" instability.

Coles (16) carried out an extensive study of the formation and subsequent development of the wavy mode for a radius ratio of 0.874 and concentric cylinders. Using the aluminium flake suspension technique, he discovered that the axial and circumferential wave numbers were not unique, being influenced by the past history of the flow.

The first part of the present investigation employs a flow visualisation technique originally developed by Jackson (40) in which wavy mode flow is observed under stroboscopic lighting. The technique is further developed to allow wave numbers to be counted under favourable conditions using radius ratios of 0.874, 0.911 and 0.950 for the concentric and eccentric cylinder cases. In addition, inner cylinder torque measurements are compared with observations from the flow visualisation tests in order that the effect of wave number changes on the torque requirements can be assessed. Torque measurement results are presented for each of the three radius ratios specified above, and also for the reduced clearance given by a radius ratio of 0.975. Eccentricity ratios between zero and 0.9 have been tested in each case. Friction coefficient characteristics are derived from the results and an attempt is made to deduce an empirical relationship incorporating the effects of the eccentricity and radius ratios.

Torque discontinuities are shown to result from circumferential wave number changes for each geometry tested. In particular, as the speed of the inner cylinder is increased, a sudden reduction in the

magnitude of the recorded torque results from the onset of a transitional state of wavy mode flow observed in tests using a radius ratio of 0.911 . Three regimes of wavy mode flow can be identified for this radius ratio, particularly with concentric cylinders, the "transitional state" separating the more regular "primary" and "secondary" wavy modes.

CHAPTER 2

AN INVESTIGATION OF THE WAVY MODE OF TAYLOR VORTEX FLOW USING FLOW VISUALISATION

2.1 REVIEW OF LITERATURE

2.1.1 Flow Visualisation Techniques

Previous authors have used several different techniques to study the development of the flow between rotating cylinders and, of these, the most popular has been to follow the motion of minute particles in suspension in the test fluid. An early investigation by Terada and Hattori (73) used a suspension of fine aluminium powder to study the formation of vortices in their apparatus. This technique has since been employed by Lewis (44), Cole (14), and Kamal (42) although Coles (16) reported that the flake-like particles in aluminium paint pigment resulted in improved visualisation. The investigation carried out by Coles was also the first to use light transmitted through the test fluid from a source in the inner cylinder, the others having used reflected light from an external source. The viscosity of the test fluid is not significantly affected by the addition of the aluminium particles because concentrations of the order of 0.5 gm/l have been found to be sufficient for excellent flow visualisation.

The onset of the Taylor vortex and wavy mode instabilities are clearly evident using this technique and it has been employed by a host of authors too numerous to mention individually for derivations of the critical Taylor numbers T_c and T_w. It has also been used to study the flow beyond the onset of the wavy mode of instability although, in this case, most researchers have found it necessary to enlist the aid of photographic techniques in order

that observed flow changes could be quantified. Unusual techniques were developed by Jackson (40) and Snyder (61), however, to overcome the difficulties in flow visualisation under these circumstances.

Jackson used stroboscopic illumination of the flow to arrest the motion of the aluminium flake particles in the test fluid. He was able to derive circumferential wave numbers from measurements of the flashing frequency and the rotational speed of the inner cylinder. Snyder illuminated an axial plane in the radial direction by a parallel beam of light, defined by a slit in a baffle to be about 2 mm in thickness. This technique permitted study of the vortex cell structure throughout the wavy mode of instability.

Dye injection has been another favourite flow visualisation technique with previous researchers in this field. This method was used by Taylor (71), Cole (14), Donnelly and Fultz (32), Schwarz et al (58) and Castle (8). Castle reported that it was better than the aluminium flake suspension technique for observations of the onset of Taylor vortices between eccentric cylinders. Dye injection is of little use for any finite investigation of Taylor vortex flow, however, because of the eventual mixing of the dyed and undyed fluids.

Hagerty (38) reported that the onset of Taylor vortex flow could be detected using the inherent flow visualisation properties of glycerine-water solutions. This technique was also employed by Brewster and Nissan (5) and Brewster et al (6). Nissan et al (49) followed the motion of small droplets formed by the addition of a mixture of ethyl alcohol and water to their test fluid. They commented that this was inferior to the aluminium flake suspension technique however.

Air was used as the test fluid by Kaye and Elgar (43) and Astill (2), and they found that good flow visualisation could be

achieved, for low Reynolds numbers, by admitting tobacco smoke into the test length. This technique was found to be useful for developed vortices although Cole (15) reported that it was insensitive to incipient vortices.

2.1.2 The Concentric Cylinder Case

In a classical contribution to the study of the stability of the flow between rotating cylinders, Taylor (71) predicted the onset and appearance of a secondary flow and verified these predictions experimentally. The details of his theoretical analysis are not relevant here although these are discussed in Chapter 4.

Taylor investigated the stability problem for the concentric cylinder case using a test rig in which both the inner and outer cylinders could be rotated in either direction. He showed that the flow is unstable at sufficiently high rotational speeds, the criterion for stability being a non-dimensional number that has since become known as the Taylor number. The instability gives rise to a series of toroidal vortices (also named after Taylor), each occupying approximately square cells, and with adjacent vortex pairs contra-rotating. Normally, the radial clearance is completely filled by the width of a single vortex cell although Taylor reported that, for μ^* less than about -0.5 (inner and outer cylinders rotating in opposite directions), the axial spacing of the vortices decreased such that, although the vortex cells remained approximately square, they did not extend to the outer cylinder.

For the purpose of the present investigation, we are primarily interested in Taylor's results using a rotating inner cylinder and a stationary outer cylinder ($\mu^*=0$) and, for this

case, the structure of the Taylor vortices is shown in Fig.1. If the radial clearance is small compared with the inner cylinder radius, the Taylor number may be expressed as

$$T = \omega_i^2 R_i c^3 / \nu^2$$

and Taylor showed that the critical value for the onset of instability (T_o) is 1708.

The onset of Taylor vortex flow has been the subject of many experimental investigations since Taylor's original paper and these have generally confirmed his results. The effect of increasing the radial clearance has been found to be to increase the stability of the flow with the result that the critical Taylor number is higher than that for the narrow gap case.

In his tests, Taylor observed that, when the critical Taylor number had been sufficiently exceeded, the regular vortex flow assumed "some kind of turbulent motion". This development was also observed by Lewis (44) who reported "the vortices becoming irregularly turbulent". More recent research has shown that this is a doubly periodic motion in which a wavy form is superimposed on the vortex structure in the circumferential direction, with a wave velocity in that direction. Because of it's appearance, this type of vortex flow is known as the wavy mode of instability.

The onset of the wavy mode was studied experimentally by Schwarz et al (58) using an apparatus with $\eta = 0.95$. At about $T = 1.03\,T_o$, they observed a transition to a non-axisymmetric mode in which an oscillation developed within the vortex cells without causing any distortion of the cell boundaries. This mode was marked by the appearance of alternating light and dark bands in the vortex pattern resulting from dye injection. As the rotational speed was further increased, waviness of the cell boundaries gradually developed and Schwarz et al reported that the wavy mode

of instability was firmly established by about $T = 1.20\ T_o$.

The non-axisymmetric mode preceding the onset of waviness has also been observed by Donnelly and Fultz (32), Castle et al (10) and Jones (41) and it is generally ascribed to overstable oscillations of the vortex core. Castle et al, using $\eta = 0.899$, reported that waviness first became apparent as a slight rocking of the boundaries between adjacent vortex cells at about $T = 1.08\ T_o$. They referred to this instability as the "weak" wavy mode and suggested that it was probably caused by the presence of a single travelling circumferential wave. When the rotational speed was increased still further, the "weak" wavy mode was replaced by a much stronger type of wavy instability, having three circumferential waves, at about $T = 1.21\ T_o$.

The critical Taylor numbers for the onset of the "strong" wavy mode, T_w, from other workers experimental results, are summarised in Table 1. It is evident that T_w is strongly dependent on the radius ratio η, the range of Taylor number over which regular Taylor vortices remain stable becoming progressively smaller as η tends to unity. Jones (41) reported that the radius ratio was also significant with regard to the form of the strong wavy mode at onset. For the narrow gap case, he observed the expected travelling circumferential waves whereas the onset was quasi-turbulent, with apparently random motion of the sink lines (see Fig.1) for both $\eta = 0.645$ and $\eta = 0.718$. The results indicated a preference for the strong wavy mode to start with three circumferential waves for both the $\eta = 0.85$ and $\eta = 0.90$ cylinders, and four circumferential waves for the $\eta = 0.95$ cylinder. Coles (16), using $\eta = 0.874$ and $\mu^* = 0$, recorded a minimum of four circumferential waves at the onset of the strong wavy mode.

Coles carried out a thorough experimental investigation of

the strong wavy mode, his most important contribution being the discovery that non-uniqueness is a feature of the flow for this instability. Defining a state by the number of vortex cells and the number of circumferential waves present, he showed that it was possible to attain as many as twenty-five different states at a given Taylor number. The results indicated that the state which actually occurred was determined by the whole history of the experiment. When the rotational speed of the inner cylinder was gradually increased, Coles observed a repeatable but irreversible pattern of well-defined transitions to new states. Vortices appeared or disappeared in pairs and waves were added or subtracted in a process which Coles called 'transition by spectral evolution'.

Coles also recorded measurements of the angular velocity of the circumferential waves. These showed that the dimensionless wave velocity V/v is practically constant regardless of the flow state present. When the waves first appeared, their angular velocity was found to be almost half that of the inner cylinder. As the rotational speed was increased, however, V/v rapidly approached a value of 0.34 which was then reasonably constant for the range of Reynolds number from Re = 500 to Re = 2500 ($T = 3.4 \times 10^4$ to $T = 84 \times 10^4$). Results presented by Jackson (40), from an investigation using $\eta = 0.912$, tended to confirm Coles value of $V/v = 0.34$.

The validity of Coles' results concerning non-uniqueness of the wavy mode has been challenged by Segal (59) and Davey et al (20). They suggested that the effect arises because of the end conditions and that in a sufficiently long apparatus the effect would not appear. This hypothesis was tested by Snyder (62), however, and he showed that end effects are not important in the problem of uniqueness if the length to gap ratio is greater than

10. The length to gap ratio for the apparatus used by Coles was 28; those for other workers in this field are summarised in Table 2.

Snyder used a novel side slit illumination technique which permitted study of the vortex cell structure. The two vortices adjacent to the ends of the apparatus were found to be substantially different from those between them and Snyder suggested, therefore, that the axial wavelength is best derived from measurements of the axial length of a number of vortices excluding the boundary cells. In a later paper, Snyder (63) showed that the vortices between the boundary cells do not all have the same wavelength when they are formed. As time progresses, however, a common wavelength is gradually approached. A relaxation time of approximately $L^2/6\nu$ was generally found to be sufficient for the necessary adjustment process to take place. Snyder also reported that non-uniqueness of the axial wave number occurred for the rotationally symmetric case of Taylor vortices as well as for doubly periodic flows.

Snyder (64) observed changes in the structure of the vortex cells for a wide range of μ^* and cylinder radius ratios $\eta = 0.2$, 0.5, 0.8 and 0.959. Five basic cell types were identified; regular Taylor cells, spirals, "puffing" cells and two rotationally asymmetric modes. The spiral and puffing cell types are not relevant to the present investigation because these occurred for negative μ^* only. Snyder referred to the rotationally asymmetric modes as the m-mode and the θ-mode.

The prominent feature of the m-mode is an out-going jet between each pair of vortex cells, whose origin on the inner cylinder does not move vertically and whose outer extremity waves

up and down. This waveform has a node at the inner cylinder and an anti-node near the outer cylinder. The θ-mode differs from the m-mode in that both in-going and out-going jets oscillate. The axial component for this mode appears to have three nodes across the gap at the plane of the cell boundaries and adjacent cell boundaries are out of phase. A feature of the θ-mode is that the ratio of the oscillating amplitude of the out-going jet to that of the in-going jet can vary from 0 to 1 as the Taylor number increases.

When the outer cylinder was stationary ($\mu^* = 0$), Snyder observed the m-mode for $\eta = 0.959$ and the θ-mode for $\eta = 0.8$ and $\eta = 0.959$. Using $\eta = 0.8$, the onset of the θ-mode occurred at about $T/T_o = 1.39$ and Snyder reported that a range of circumferential wave numbers from 2 to 6 was traversed as the rotational speed of the inner cylinder was further increased. Using $\eta = 0.959$, a θ-mode having one circumferential wave was first observed at about $T/T_o = 1.06$. As the rotational speed was further increased, an m-mode with four circumferential waves occurred at about $T/T_o = 1.19$ and this was itself replaced by an m-mode, with more than four circumferential waves, at about $T/T_o = 1.59$.

Snyder suggested that the modes observed by Schwarz et al (58) and Coles (16) were all θ-modes, although he was not able to explain the lack of waviness exhibited by the cell boundaries in the former's initial mode. Observations by Castle et al (10) endorse the view that the strong wavy mode is a θ-mode. They reported that the strong wavy mode is observed as an oscillation of both in-going and out-going jets whereas the weak wavy mode is seen as an oscillation of the out-going jets at the outer cylinder. From these results, it seems reasonable to infer that

the weak wavy mode is an m-mode although this contradicts the observations of Snyder for $\eta = 0.959$. Jones (41) suggested that this confusion can be explained if both the weak and strong wavy modes are θ-modes.

The first non-axisymmetric mode observed by Schwarz et al is believed to be an oscillation of the in-going jets, with a node at the outer cylinder. This would explain why the cell boundaries do not appear wavy when frontal lighting of the apparatus is used. Oscillation of the out-going jets follows after only a very slight increase in Taylor number (the weak wavy mode) and the subsequent stage is the full θ-mode (the strong wavy mode).

Jones reported that the flow became indeterminate soon after the onset of the strong wavy mode in tests using $\eta = 0.85$. The results indicated a complete non-uniqueness of the flow and circumferential wave numbers between three and six were observed. At about $T/T_o = 3.1$, the flow assumed a quasi-turbulent form similar to that observed at the onset of the strong wavy mode for large gaps. Quasi-turbulent flows of this type also occurred in tests using $\eta = 0.90$ and $\eta = 0.95$, at about $T/T_o = 24.4$ and $T/T_o = 10.6$ respectively.

2.1.3 The Eccentric Cylinder Case

Kamal (42) reported that, for eccentricity ratios larger than about $\varepsilon = 0.3$, the flow close to the outer cylinder in the wide gap is in the opposite direction to the rotation of the shaft. This phenomenon was called 'reversed flow'. The extent of the region of reversed flow (Fig.2) was found to increase with increasing ε and it was also influenced by the clearance ratio c/R_i.

The effect of eccentricity on the critical Taylor number T_c has been the subject of several experimental investigations although probably the most important was that of Castle and Mobbs (9). Using an apparatus with a fixed outer cylinder and $\eta = 0.912$, they showed that Taylor vortex flow occurs in two distinct stages between eccentric cylinders. As the rotational speed of the inner cylinder is slowly increased, a weak system of vortices appears which does not extend to the outer cylinder in the vicinity of the widest gap. Following a further increase in speed, these are replaced by a more vigorous system of vortices having a smaller axial wavelength, and which everywhere extend to the outer cylinder.

Castle and Mobbs used a dye injection technique to observe the two systems of vortices described above. They reported that the second of these was also readily detected using a suspension of aluminium flakes together with front lighting, although the first stage was difficult to detect using this technique. Younes (80) found that the aluminium flake suspension technique can be used to view the onset of the first stage, however, if the test fluid is illuminated from within the inner cylinder.

The results presented by Younes were in excellent agreement with those of Castle and Mobbs, the first stage occurring at critical Taylor numbers less than that for the concentric cylinder case if the eccentricity ratio was below about $\varepsilon = 0.4$. Eccentricity had a stabilising influence on the second stage, however, the critical Taylor number for its onset increasing with increasing ε. The results indicated that the Taylor number range over which the first stage remains stable becomes progressively larger as eccentricity increases.

Previous workers observed only one mode and their results for the effect of eccentricity on T_c are rather confusing. There is no doubt that Vohr (76) viewed the onset of the second stage, although it is difficult to decide which of the stages was observed by Cole (14), Kamal (42), and Versteegen and Jankowski (75). Their results plot between those recorded by Castle and Mobbs (9) for the onset of the first and second stages, which suggests that a rather well developed first stage was detected by these authors. In investigations of this type, the criterion for instability is very important; the critical speed for the onset of Taylor vortices usually being defined as the first speed at which vortices are apparent along the entire test length of the apparatus.

Another important consideration is the effect of radius ratio on the critical Taylor number. Vohr (76) and Jones (41) showed that the onset of Taylor vortices between eccentric cylinders is delayed by decreasing η. However, the results of Cole, Kamal and Versteegen and Jankowski were reasonably consistent with each other even though their investigations used $\eta = 0.833$, 0.917 and 0.50 respectively. It is possible that these results were influenced by misalignment of the cylinder axes because Jones reported that the stability boundaries can be considerably affected by even small errors in alignment (see Section 3.1.3).

The effect of eccentricity on the weak and strong wavy modes was investigated by Castle et al (10). For both modes, the normalised Taylor numbers T/T_c remained approximately constant up to an eccentricity ratio of 0.3, after which they decreased progressively to merge at a value of about 1.05 at an eccentricity ratio of 0.7. In the eccentricity range

$\varepsilon = 0.3$ to $\varepsilon = 0.7$, the strong wavy mode became weaker and less distinct, while the weak wavy mode became very weak and difficult to detect. Castle et al suggested that the results were probably influenced by the appearance of a region of reversed flow on the wide gap side of the apparatus, at about $\varepsilon = 0.3$.

Results presented by Jones (41) confirmed that flow reversal is an important effect. Jones investigated the circumferential dependence of the effect of eccentricity on bright band vibration, the weak wavy mode, and the strong wavy mode. Bright band vibration was the name given to the non-axisymmetric mode which Schwarz et al (58) had observed before the weak wavy mode for the concentric cylinder case. It was so called because, when the aluminium flake suspension technique is used with front lighting, the bands on either side of the vortex source appear to be bright, and an oscillation develops within these bands at the onset of the mode.

For each of the three modes, Jones found that the most stable section was the narrow gap and the most unstable section was 90° downstream from the narrow gap. The results for the most unstable section ($\theta = \pi/2$, Fig.2) were in good agreement with those of Castle et al (10). In tests using $\eta = 0.90$ and 0.95, the circumferential variation of the onset of the strong wavy mode was such that, for eccentricity ratios between $\varepsilon = 0.4$ and $\varepsilon = 0.7$, the waves were well developed in the wide gap and hardly more than a slight vibration in the narrow gap. For larger eccentricity ratios, the onset of the strong wavy mode in the wide gap was quasi-turbulent, of the form observed, for any ε, in tests using large gaps.

2.1.4 The Transition to Turbulence

Observations by Coles (16) for the concentric cylinder case indicated that the breakdown of wavy mode flow into turbulence is a gradual process. Using a rotating inner cylinder and a stationary outer cylinder, Coles found that small irregularities became apparent in the flow at sufficiently high speeds. Following further increases in speed, the degree of irregularity increased until finally the flow could only be described as fully turbulent.

Using $\eta = 0.91$ for the eccentric cylinder case, Vohr (76) showed that the transition process originates in the region of the wide gap. The flow in the wide gap was observed to break down into large, apparently irregular eddies at a Reynolds number of about 500 while the flow in the narrow gap was unaffected. As the speed was further increased, however, fully developed turbulence was gradually transferred to the other regions of the flow although vestiges of vortices remained evident up to Reynolds numbers of at least 40,000. Pai (51) similarly reported that the vortex structure persists well into the turbulent regime.

Vohr reported that the vortex pattern was never steady for eccentricity ratios larger than $\varepsilon = 0.8$. He observed that the vortices fluctuated irregularly under these conditions, and the flow appeared to be about to become turbulent in the wide gap region. Similarly, Jones (41) found that the onset of the strong wavy mode was of a random nature when viewed from the wide gap side of the apparatus in tests using $\eta = 0.90$ and 0.95, for eccentricity ratios larger than 0.6.

In his tests using smaller eccentricies, wavy mode flow was gradually destroyed by the appearance of irregularities which Jones suggested were probably the increased effects of harmonics

of the basic waveform. At higher Reynolds numbers, fine high frequency random eddy structures were observed with sink lines remaining evident. Using $\eta = 0.90$ and $\varepsilon = 0$, the irregularities began to have a substantial effect from a Reynolds number of about 650 and the flow appeared to be fully turbulent at about Re = 1300.

2.2 THE FLOW VISUALISATION TEST RIG

The flow visualisation test rig (Fig.3) consisted basically of a vertical shaft enclosed by a transparent outer cylinder. Because of the nature of the proposed investigation, there was no requirement for the outer cylinder to rotate, although it was mounted in such a way that it could be moved laterally to eccentric positions relative to the shaft. The position of the shaft was fixed within the structure of the test rig and it was driven by a variable speed transmission / motor unit.

Glass could have been used for the outer cylinder, although, to reduce the possibility of a breakage, it was decided that perspex would be a more suitable material. The outer cylinder was precision-bored and polished from a perspex tube with a nominal wall thickness of 12.5 mm. On arrival from the manufacturer, the bore was measured across two perpendicular planes, at each of four sections along the axial length of the cylinder, using an internal micrometer. The mean diameter was recorded as 114.45 mm and the eight readings were accurate to within $\pm$0.02 mm. Three shafts were manufactured for use with the flow visualisation test rig. Each of these was turned and polished between centres from a solid block of aluminium in order that out of balance forces would be eliminated A series of measurements similar to those described above for the outer cylinder, indicated mean diameters of 100.05 mm, 104.27 mm and 108.70 mm, the three sets of eight readings again being accurate to within $\pm$0.02 mm.

The three shaft / outer cylinder combinations gave radius ratios of 0.874, 0.911 and 0.950. The ratio of the axial test length to the radial clearance was also important because it has been suggested that the flow in the centre of the test length can be influenced by end effects for (L/c) ratios less than 10. The effective length of this apparatus was 495.30 mm giving (L/c) ratios of 69, 97 and 172 for the three shafts. The geometry ratios for the rigs used by previous researchers are summarised in Table 2.

The weight of the solid aluminium shaft was supported by an angular contact ball bearing which was housed in the lower guide block of the test rig (Fig.3). A deep-groove ball bearing, housed in the upper guide block, constrained the shaft to remain vertical. T-section slide blocks were fitted to the ends of the perspex outer cylinder and these were, in turn, accommodated by accurately machined slideways in the guide blocks. The outer cylinder could be positioned eccentric to the shaft by means of screw couplings between the slide blocks and the guide blocks. The screws at opposite ends of the apparatus were rotated simultaneously to ensure that the perspex cylinder was not subjected to unnecessary strain. The total movement of the outer cylinder was limited by contact with the shaft in one direction (i.e. $\varepsilon = 1.0$) and by contact between the slide blocks and fixed stops in the other direction. The stops were bolted to machined datum surfaces at the ends of the rig, their dimensions being such that the shaft and the outer cylinder were concentric when the slide blocks and the stops were touching. The eccentricity was indicated by a pair of dial indicator gauges mounted adjacent to the screw couplings at the ends of the rig.

The shaft was driven by a Pye Torque and Speed Control (T.A.S.C.) unit type 1K2L. The speed control rheostat in the T.A.S.C. unit gave rather coarse control, the full range of shaft speeds being covered by less than one complete turn of the speed control knob. An equivalent ten-turn rheostat was, therefore, connected in parallel with the original in order that either fine or coarse speed control could be selected by means of a simple switch. In the initial design of the test rig, the drive was transmitted from the motor to a pulley on the lower end of the shaft through a Vee belt. This was later replaced by a toothed timing belt, however, in order that any leakage of test fluid past the lower shaft seal would not result in belt slip. The rotational speed of the shaft was recorded using a steel gear wheel mounted on the upper end of the shaft, and an electromagnetic perception head connected to a digital tachometer (Fig.4). Because of the magnetic linkage between the gear wheel and the perception head, the tachometer was triggered each time a tooth passed in front of the pickup. The number of pulses was counted electronically over a short interval and the corresponding shaft speed was indicated by the tachometer display.

The temperature of the test fluid was not controlled in this test rig and it was, therefore, important that it could be monitored throughout each test run. Two Comark NiCr / NiAl thermocouples were fitted through the guide blocks in such a way that they extended into the test fluid at the ends of the test length, the recorded temperatures being displayed on a Comark Electronic Thermometer type 1601 MLS. The temperature of the test fluid in the centre of the test length was assumed to be equal to the average of the two indicated temperatures. This was

probably a reasonable assumption because heat was mainly generated by the shaft seal at the lower end of the rig, resulting in a negative temperature gradient upwards through the vertical column of test fluid.

The test rig was filled through a length of nylon tubing connected to a hole in the bottom guide block, the air in the apparatus being expelled through vent holes in the upper guide block by the rising column of test fluid. Flow visualisation was effected using aluminium paint pigment suspended in the test fluid. The motion of these aluminium flake particles was arrested using a stroboscopic technique in order that the circumferential wave number could be derived for wavy mode flows. The entire circumference of the outer cylinder was illuminated stroboscopically by means of an aluminium reflector plate mounted opposite a single stroboscope (Fig.6). This technique was found to be most effective when used in a darkened room with the stroboscope inclined at an angle of about 30° to the vertical (Fig.5).

2.3 PRELIMINARY EXPERIMENTS

2.3.1 Calibration of the Instrumentation

2.3.1.1 Test Fluid Temperature

The temperature of the test fluid was measured at the ends of the test length by means of two Comark thermocouples type 1618A connected to a Comark Electronic Thermometer type 1601 MLS. Before being mounted in the test rig, the thermocouples were suspended in a beaker of water next to a calibrated mercury in glass thermometer (no.31553) in order that the accuracy of the

Electronic Thermometer readings could be checked. For the temperature range 18 - 45°C, both of the thermocouples were found to indicate temperatures which were low by constant factors, 0.5°C for one and 0.7°C for the other.

The temperature of the test fluid in the test rig was assumed to be equal to the average of the temperatures indicated by the two thermocouples. A factor of 0.6°C was added to the derived average temperatures to correct for the recorded inaccuracy of the Electronic Thermometer readings.

2.3.1.2 Shaft Speed

The rotational speed of the shaft was measured by means of a steel gear wheel attached to the end of the shaft and an electromagnetic perception head connected to a digital tachometer. The accuracy of the speed measurements was checked against the readings of a second electromagnetic perception head / digital tachometer combination, also triggered by the steel gear wheel. The shaft speeds indicated by the two digital tachometers were found to be within ±1 rev/min over the entire range of the Pye T.A.S.C. drive unit (0 - 1400 rev/min).

2.3.1.3 Stroboscope Flashing Frequency

An Electronic Applications "Flash-Tac" stroboscope was used throughout the flow visualisation investigation. To check the accuracy of the stroboscope's three frequency ranges, a vertical line was marked on the surface of the shaft in the test rig and, for a series of constant shaft speeds, the flashing frequency was adjusted until the mark appeared to remain stationary. The results

of the calibration tests are presented in Fig.7, the recorded flashing frequencies being compared with corresponding readings from the digital tachometer.

The calibration of the scales on the stroboscope was found to be very inaccurate, particularly at the extremes of the frequency ranges. For each of the shafts, however, it was possible to define a useful band of frequencies in which the scale readings were accurate to within ±1% when increased by a constant factor. Consequently, in the flow visualisation tests, the stroboscope was used only within these bands, the scale being dictated by the required flashing frequency. The recorded flashing frequencies were corrected by the addition of the appropriate scale correction factor selected from Table 3.

2.3.1.4 Eccentricity

Movement of the outer cylinder to eccentric positions was indicated by a pair of Mercer dial gauges mounted against the slide blocks at the ends of the test length. The readings of the dial gauges were checked using slip gauges and an external micrometer and were found to be accurate to within ± 0.025 mm over the entire range of outer cylinder movement. The accuracy of the eccentricity ratios derived from the dial gauge readings is discussed further in Section 3.3.1.

2.3.2 The Viscosity Characteristics

Four types of Shell oil were used in the flow visualisation tests in order that the effects of viscosity could be studied. The test fluids were Carnea 15, Tellus 15, Tellus T17 and Tellus 21,

flow visualisation being effected by means of aluminium flake particles suspended in the clear mineral oils. Before the main investigation, tests were carried out to determine the viscosity characteristics of the test fluids and also the effect of the suspension on these characteristics.

Samples of the test fluids were pipetted into suitable British Standard U-tube viscometers which were mounted vertically in holders and immersed in a thermostatically controlled, constant temperature water bath. The kinematic viscosities of the samples were measured at various temperatures in the range $15 - 40^{\circ}C$, the water temperature being indicated by a calibrated thermometer. The tests were carried out using the procedure specified in B.S.188:1957 which requires that, for each test condition, three consecutive flow times must be recorded within an accuracy of 0.2% if the results are to be accepted. The results from these tests are summarised in Table 5 and the viscosity characteristics of the four test fluids are plotted in Fig.8 .

Similar tests were carried out at various stages throughout the main investigation to check that the test fluids had not 'aged'. Typical results are presented in Table 6 and it is evident from Fig.8 that these were in excellent agreement with the original viscosity measurements. This particular series of tests was performed at the end of the main investigation using both U-tube viscometers and Suspended Level viscometers.

Aluminium flake suspensions were formed by mixing aluminium lining powder type 774 (supplied by Johnson and Bloy) with the test fluids. A concentration of 0.5 gm/l resulted in excellent flow visualisation whilst viscometry tests indicated that this was not sufficient to significantly affect the viscosity

characteristics. Typical results are presented in Table 7 and it is evident that, although higher viscosities were generally recorded when particles were suspended in the test fluids, the increases were within the 0.2% specified by B.S.188:1957 .

2.3.3 Evaluation of the Test Rig

A series of preliminary tests was carried out to ensure that the flow visualisation test rig functioned satisfactorily. The effect of eccentricity on the onset of Taylor vortex flow was studied in these tests because this had been the subject of several previous investigations and, therefore, the results were well documented.

Tests were carried out using the shaft radius ratio $\eta = 0.911$ and the results were derived from observations of the flow in the region of the wide gap. Eccentricity was found to have a stabilising influence on the onset of vortex flow and it is evident from Fig.9 that the results were in excellent agreement with those recorded by Castle (8) in a similar series of tests. The results relate to the second stage in the onset of Taylor vortices, the first stage being difficult to detect using the aluminium flake flow visualisation technique and front lighting. For the concentric cylinder case, the critical Taylor number was recorded as $T_o = 1771$. The critical shaft speed was taken to be that for which vortices were first visible along the entire test length.

2.4 EXPERIMENTAL PROCEDURE

The power supply to the test rig was switched on at least one hour before the start of a test run to allow time for the electronics to warm up. The rig was filled with test fluid during this interval. Before the rig was filled, however, the test fluid container was shaken for about one minute in order that the aluminium flake particles, which slowly settle out of suspension when left standing, were redistributed evenly throughout the test fluid. The rig was then filled through a hole in the lower guide block under the action of gravity. As soon as the lower shaft seal was submerged, the shaft was made to rotate slowly because this increased the rate at which trapped air escaped to the top of the column of test fluid. Test fluid was poured into the filler funnel (Fig.3) until it started to rise in vent holes in the upper guide block. This procedure ensured that the test fluid was in contact with fixed boundaries (the guide blocks) at both ends of the test length.

When the rig had been filled, the type of speed control, either coarse or fine, was selected by means of the switch fitted in the T.A.S.C. unit (Section 2.2). The usual sequence for the test runs was to increase the shaft speed in a series of increments up to a maximum, well beyond the onset of the wavy mode, and then to reverse the procedure, results being recorded after each speed change. At the start of a test, the shaft speed was gradually increased from rest until the Taylor vortex cell boundaries became wavy. The stroboscope was then switched on and the room darkened in order that the stroboscopic illumination of the flow was more effective. The shaft speed was further increased until the wavy vortex pattern could be made to appear stationary by adjustment of the stroboscope flashing frequency.

Whenever possible, the author counted the number of circumferential waves by walking around the test rig. This was a simple

procedure for steady flows although it was much more difficult and time-consuming if the flow was at all unsteady. In the cases where counting proved impossible, the circumferential wave number was estimated using the technique described in Section 2.6.1.1. Axial wavelength measurements were also recorded after each speed change, the number of vortex pairs in a 0.2 m gauge length being counted. A central section of the test length was used for these results because previous research had shown that the axial length of the boundary cells can be significantly influenced by end effects.

When the wave number counts had been completed, the temperature of the test fluid at the ends of the test length, the shaft speed and the stroboscope flashing frequency were recorded, in turn, from the instrumentation of the test rig. The shaft speed was then gradually changed and the stroboscope readjusted in order that a second set of results could be recorded. Typically, a shaft speed increment of about 40 r.p.m. was used. This procedure was repeated for a series of shaft speeds, both increasing and decreasing, the maximum being about 1400 r.p.m. Lack of persistence of vision imposed limitations on the stroboscopic technique for small shaft speed settings because low flashing frequencies were required to arrest the motion of the aluminium flake particles under these conditions. The duration of a test run was anything from two to six hours depending on the stability of the flow for the conditions being tested. It will probably come as no surprise to the reader that the author found these tests a most exacting physical strain.

A series of tests was carried out using three shafts, for which $\eta = 0.874$, 0.911 and 0.950. For each of the shafts,

eccentricity was introduced by movement of the outer cylinder in steps of $\varepsilon = 0.05$ and several fluids were tested. The test fluids were the Shell mineral oils Carnea 15, Tellus 15, Tellus T17 and Tellus 21. To clean the rig between tests using different fluids, it was filled with a fresh sample of the fluid to be used in the following tests (without flakes) and the shaft accelerated several times. The rig was then drained and the procedure repeated with a second fresh sample of the test fluid.

2.5 PRESENTATION OF RESULTS

A typical flow visualisation test run incorporated as many as forty shaft speed changes and results were recorded for each speed setting. A total of one hundred and twenty tests were carried out and, therefore, a vast amount of experimental data had to be processed. An IBM 1130 computer was used to calculate the various parameters discussed in Appendix I and the computed results are plotted in Figs.13-69 .

The circumferential wave velocity ratio (V/v) is plotted against Reynolds number in Figs.13-36 for the three radius ratios tested. The results for $\eta = 0.911$ are presented in Figs.13-26, Figs.27-29 show the results for $\eta = 0.950$ and the results for $\eta = 0.874$ are plotted in Figs.30-34. Additional results for $\eta = 0.911$ are plotted in Figs.35-36 which use different symbols to distinguish between the results for increasing and decreasing shaft speeds. The results for $\eta = 0.911$ are summarised in Table 9.

Circumferential (tangential) wave number results are presented in Figs.37-59 . It is evident from Appendix I that, for constant (V/v), the circumferential wave number n defines a

family of equispaced 'radial' lines on a plot of stroboscope flashing frequency against shaft speed. Families of 'radial' lines derived from the concentric cylinder circumferential wave velocity ratio results for each radius ratio are shown in Figs.37-39. Those for $\eta = 0.911$ are compared with raw experimental data in Figs.40-41 and with those derived by Jackson (40) in Fig.42. The 'radial' lines for $\eta = 0.874$ are compared with raw experimental data in Fig.43.

The line diagrams presented in Figs.44-55 show the bands of Reynolds number within which particular circumferential wave numbers were observed in the flow visualisation tests. A non-dimensional parameter based on the mean circumferential wave number, $\bar{n}$, and the radial clearance, c, is plotted against Reynolds number in Figs.56-59 for the eccentricity ratios $\varepsilon = 0$, 0.1, 0.2 and 0.3 respectively. Particular wave number changes observed in typical test runs are summarised in Tables 10-13 and, for $\eta = 0.874$ and $\varepsilon = 0$, a comparison with changes recorded by Coles (16) is presented in Table 14.

Axial wave number results are presented in Figs.60-68. The results for $\eta = 0.911$ are plotted in Figs.60-64 and those for $\eta = 0.874$ are plotted in Figs.65-66. Concentric cylinder results for $\eta = 0.911$ are also presented in Figs. 67 and 68 for increasing and decreasing shaft speeds respectively.

2.6 DISCUSSION OF RESULTS

The results discussed below relate to the strong wavy mode of instability. The stroboscopic illumination technique was unsuitable for observations of the weak wavy mode because of lack of persistence of vision for the low shaft speeds at which it occurred. In the following Sections, the results for $\eta = 0.911$ are discussed before those for $\eta = 0.874$ and $\eta = 0.950$ because the tests using this radius ratio were the most exhaustive.

2.6.1 Visual Observations

2.6.1.1 Concentric Cylinder Tests Using $\eta = 0.911$

Stroboscopic illumination of the flow was found to be an excellent technique for monitoring the number of circumferential waves throughout these tests. Visual observations showed that shaft speed changes were often accompanied by a change in the circumferential wave number, several wave number changes being observed in each test run. In many cases, the wave number change was preceded by oscillation of the entire vortex structure, an effect also reported by Jackson (40). Less common, however, were circumferential wave number changes which occurred suddenly and without oscillation. One particular example of this type of change was that from $n = 10$ to $n = 9$ (marked by h,i) in Fig.40.

The results suggested that the vortex structure was more likely to oscillate before a wave number change if the shaft speed was being increased. The oscillation usually became apparent well before the occurrence of the wave number change and increased in amplitude with successive speed increments. In some of the tests, however, oscillations developed whose amplitudes changed continuously without adjustment of the shaft speed setting. In these cases, a small increase in the magnitude of the

shaft speed was normally sufficient to effect the wave number change.

Following the sequence of events described above, the number of circumferential waves changed, either, along the entire test length at the same time, or, initially at one end of the test length. In the latter case, the change usually occurred at the lower end of the test length and the new mode then replaced the old mode from the entire test length in a finite time. The necessary adjustment process normally lasted about five seconds before the wave number change was complete although sometimes as long as thirty seconds was required. The extended adjustment period was necessary when a situation probably best described as a 'trial of strength' was observed. The 'trial of strength' situation developed between the new mode and the old mode with the new mode assuming the role of the aggressor and gradually expelling the old mode from the entire test length. During the adjustment process, the two modes were both evident in different parts of the test length at the same time.

When the circumferential wave number change was complete, the new mode was generally steady, and free from oscillation, showing no tendency to change again even when left for extended periods. However, in some cases, the new mode was observed to be unsteady and pulsating and, very infrequently, a change back to the previous mode followed shortly after the initial wave number change. Oscillation of the vortex structure soon after a wave number change indicated that another change was imminent.

A maximum Reynolds number of about 800 was used in the early flow visualisation tests because the flow became irregular in nature at about this value. This change generally occurred suddenly with the flow losing the periodic characteristic of the strong wavy mode. The resulting flow was quasi-turbulent rather than turbulent, however, because remnants of the wavy mode could be distinguished from the general disturbance using stroboscopic illumination of the flow. The appearance of this type of flow was described by Kamal (42) as a "violent chaotic motion". It was observed by Jackson (40) using the stroboscopic illumination technique, the onset of quasi-turbulence marking the upper limit of his tests.

Tests performed by the author showed that, although the quasi-turbulent flow was unsteady and disorientated, it was possible for it to be analysed stroboscopically. Visual observations of the flow suggested that, for each shaft speed setting, a series of violent circumferential wave number changes occurred continuously, resulting in continual large scale oscillation of the vortex structure. The particular wavy modes involved were all unsteady and, therefore, the wave number changed repeatedly between the different modes, each mode being evident for very short periods before being replaced. The technique used for observations of this type of flow was to isolate progressively each of the wavy modes, in turn, from the others. A "homing-in" type of procedure was employed for this purpose, the stroboscope flashing frequency being adjusted during the brief appearances of the particular wavy mode until the tangential velocity of

the waves had apparently been reduced to zero. It was not possible for the number of circumferential waves to be counted under these conditions because, apart from the general unsteadiness of the flow, the individual wavy modes were not evident for sufficiently long periods at a time. In these cases, therefore, the circumferential wave numbers were derived from the recorded values of the stroboscope flashing frequency and the shaft speed using Fig.37 (see Appendix II).

The procedure described above was used throughout the present investigation whenever the flow was too unsteady for the number of circumferential waves to be counted. It must be said, however, that it was often very time-consuming and required a great deal of patience on the part of the researcher.

A series of tests was carried out to investigate the development of the quasi-turbulent flow regime as the shaft speed was further increased. Rather surprisingly, the flow did not continue to deteriorate as expected, but gradually became more regular. This change was less well defined than the onset of quasi-turbulence although the process was generally complete by a Reynolds number of about 1100. Wave number changes continued to occur in the new flow regime although these were comparatively infrequent allowing the circumferential wave numbers of the modes involved to be counted. Wavy mode flow was observed up to a maximum Reynolds number of about 2200. The circumferential waves were difficult to detect at higher shaft speeds although the cell boundaries remained clearly evident. Cole (14), using $n = 0.827$,

reported that a vortex pattern persisted at shaft speeds as high as one hundred times the critical and Vohr (76) observed a basic vortex structure up to Reynolds numbers of the order of 40,000 in tests using $\eta = 0.910$.

The wavy flow regimes discussed above were affected in different ways when the shaft speed was progressively increased. For the steady wavy mode observed using low Reynolds numbers, the circumferential wave number gradually increased from $n = 3$ at the start of the tests to $n = 9$ or $n = 10$ at the onset of quasi-turbulence. The general trend was then for the predominant circumferential wave number to gradually decrease, the $n = 4$ and $n = 5$ modes being evident when the flow was again sufficiently regular for the number of waves to be counted. The predominant circumferential wave number for the remainder of the tests (at high Re) was $n = 4$.

The visual observations suggest that, rather than being the first stage in the breakdown of wavy vortex flow into turbulence, the quasi-turbulent flow regime is a region of transition between two well established forms of wavy vortex flow. Consequently, this flow regime is referred to as the "transitional state" in the remainder of this thesis. To distinguish between the form of Castle and Mobbs' (9) strong wavy mode before and after the transitional state, these are designated the "primary" and "secondary" wavy modes respectively.

The change from primary wave mode to transitional state was sudden and violent, and, therefore, easily detected. The Reynolds number at which it occurred varied

considerably between the different test runs, within the range Re = 535 to Re = 855. The corresponding range Re = 610 to Re = 920 was derived from results recorded by Jackson (40) in a series of similar tests. The onset of the secondary wavy mode was observed to occur in the range Re = 900 to Re = 1250 in the present investigation. When the shaft speed was progressively decreased, the transitional state was again traversed although it appeared to be less violent in this case. The flow states which one would observe in a test using positive shaft speed increments are summarised in Table 8.

The visual observations discussed above relate to changes in the number of circumferential waves although the axial length of the vortex cells was also influenced by variation of the shaft speed. This was usually a gradual process and axial wavelength changes often occurred with no change in the total number of vortex cells in the apparatus. Snyder (62) showed that this was made possible by continuous adjustment of the axial lengths of the boundary cells which were substantially different from the remaining cells. In the present investigation, the axial wavelength of the flow was monitored throughout the tests by counting the number of vortex cells in a central section of the apparatus, these results are discussed in Section 2.6.2.3.

A phenomenon frequently observed in the flow visualisation tests was the creation of a pair of vortex cells at particular sections in the test length. This was accompanied by an axial shift of the cells above the section concerned which resulted in a pair of cells being

displaced from the upper end of the test length. This phenomenon was usually repeated several times and ceased after either a short time interval or a change in shaft speed.

2.6.1.2 Eccentric Cylinder Tests Using $\eta = 0.911$

Increasing the eccentricity generally reduced the stability of wavy vortex flow with the result that the stroboscopic technique could not be used satisfactorily for eccentricity ratios greater than about $\varepsilon = 0.2$. Because of the increasing unsteadiness of the flow, it became progressively more difficult to count the circumferential wave numbers as the eccentricity was increased. The wave numbers were, therefore, determined using Fig.37 and the procedure described in Section 2.6.1.1.

Primary wavy mode flow, which had been particularly steady for the concentric cylinder case, displayed a tendency for the number of circumferential waves to change continuously between two values when eccentricity was introduced. This phenomenon was observed only occasionally in tests using $\varepsilon = 0.05$ although it became more common as the eccentricity was further increased. Using $\varepsilon = 0.20$, the circumferential wave number changed continuously for each of the primary wavy mode shaft speed settings. Each change was preceded by oscillation of the vortex structure and one of the two wave numbers involved usually appeared to be more stable than the other.

Transitional state flow was again very irregular although the level of disturbance appeared to be somewhat

less in the tests using $\varepsilon = 0.05$ and $\varepsilon = 0.10$ than for the concentric cylinder case. When the eccentricity was further increased, however, the flow became progressively more irregular. Visual observations also showed that the transitional state generally occurred at lower speeds when the cylinders were eccentric. Using $\varepsilon = 0.20$, for example, the boundaries of the transitional state were observed in the range Re = 370 to Re = 900. It is evident from Figs. 11 and 12 that these results were not particularly affected by the different test fluids used in the investigation.

Secondary wavy mode flow was generally more steady than primary wavy mode flow for the eccentric cylinder case. The circumferential wave number sometimes changed continuously in the secondary wavy mode although these changes occurred much less frequently than those described above for the primary wavy mode. A phenomenon peculiar to the secondary wavy mode was for the vortex structure to have a velocity component in the axial direction; vortex cells disappearing from the upper end of the test length and others appearing at the lower end of the test length. However, this type of flow was not observed very often.

An effect particularly evident for primary wavy mode flow was that the circumferential wavelength was larger in the narrow gap than in the wide gap. This effect was observed in tests using eccentricity ratios as low as $\varepsilon = 0.10$. Under these conditions, the wave form around the entire circumference appeared to be stationary when illuminated using an appropriate stroboscope flashing

frequency. This was made possible by the circumferential variation of the wave velocity. Vohr (76) and Jones (41) also reported that waviness tends to be predominant in the wide gap and strongly damped out in the narrow gap. An important factor in this is the circumferential variation of the local Reynolds number in tests using eccentric cylinders. In Appendix III, an equation is derived which defines the local Reynolds number of a flow in terms of the eccentricity ratio and the radius ratio.

2.6.1.3 Concentric Cylinder Tests Using $\eta = 0.950$

It was immediately obvious in these tests that the test length contained a larger number of vortex cells than was the case for $\eta = 0.911$. This was an expected consequence of reducing the radial clearance because it is well known that the vortices occupy approximately square cells at the onset of vortex flow. The circumferential wave number was also influenced by the change in geometry, the maximum wave number being nineteen in these tests compared to ten for the previous shaft.

Another important effect of decreasing the radial clearance (increasing the radius ratio) was that the stability of the flow was significantly reduced throughout the wavy mode. The flow was observed to be extremely unsteady, even for the concentric cylinder case, with the result that reasonably accurate axial wavelength measurements proved impossible. The circumferential wave number could sometimes be counted soon after the onset of the primary wavy mode although this required a great deal of patience. For the vast

majority of the shaft speed settings used in these tests, however, the circumferential wave numbers had to be derived from the recorded stroboscope flashing frequencies using the procedure described in Appendix II.

The number of circumferential waves generally changed continuously and frequently between two values for each of the shaft speed settings in the primary and secondary wavy modes. The flow was further distorted by the oscillation of the vortex structure which usually accompanied wave number changes. A phenomenon sometimes observed in the primary wavy mode was for the values of the wave numbers observed at a particular speed setting to progressively increase when the rig was left running. This effect can probably be attributed to the time dependence of the test fluid temperature, however, because the wave numbers between $n = 3$ and $n = 16$ each occupied only a very narrow band of Reynolds numbers in the primary wavy mode (Section 2.6.3).

Transitional state flow was again evident as a disturbed version of the primary wavy mode in which the circumferential wave number changed with greater frequency and usually between more than two values. The transitional state was generally observed in the Reynolds number range $Re = 360$ to $Re = 630$. In tests using $\eta = 0.959$, Snyder (61) observed the onset of an unsteady form of flow at a Reynolds number of about $Re = 330$. He reported that unsteady flow gradually developed from an m-mode having more than four circumferential waves.

For high Reynolds numbers, the secondary wavy mode gradually became faint as the shaft speed was increased. Finally, waviness could no longer be detected although the vortex structure remained clearly evident.

2.6.1.4 Eccentric Cylinder Tests Using $\eta = 0.950$

Wavy vortex flow was observed to be even more irregular when eccentricity was introduced for this shaft and, therefore, it became progressively more difficult to detect the boundaries of the transitional state as the eccentricity was increased. Because of the increasing unsteadiness of the flow, the stroboscopic illumination technique could not be used satisfactorily for eccentricity ratios larger than about $\varepsilon = 0.10$. The circumferential wave number again changed continuously throughout both the primary and the secondary wavy modes and, for the latter, waviness was more difficult to detect as the shaft speed was increased. However, the basic vortex structure once again persisted when the waves were no longer evident.

2.6.1.5 Concentric Cylinder Tests Using $\eta = 0.874$

Because of the larger radial clearance for this shaft, fewer vortices were formed in the test length than in the tests using $\eta = 0.911$ or $\eta = 0.950$. The maximum number of circumferential waves was also reduced to six in these tests compared with ten for $\eta = 0.911$ and nineteen for $\eta = 0.950$. Probably the most significant effect of increasing the radial clearance, however, was that wavy mode flow was generally much more stable under these conditions. Consequently, the circumferential

wave number could be counted for most of the shaft speed settings used in these tests.

Wave number changes occurred less frequently than in the previous tests although the mechanisms of wave number change were generally the same as those described in Section 2.6.1.1 . The increased stability of the flow was a feature of the entire range of wavy mode flows observed in these tests and the regime of disturbed flow normally associated with the transitional state was not evident. However, above a Reynolds number of about Re = 980, the steady wavy mode was replaced by a flow regime in which the wave number changed regularly between n = 3 and n = 4. This type of flow lasted until about Re = 1100 after which a single wave number was, once again, evident at each shaft speed setting. The n = 5 mode normally preceded the onset of this flow regime which was followed by the n = 3 mode. The results suggest, therefore, that it was probably a subdued form of transitional state flow.

2.6.1.6 Eccentric Cylinder Tests Using $\eta = 0.874$

Once again, increasing the eccentricity was found to progressively reduce the stability of wavy mode flow. However, using this shaft, the flow remained sufficiently steady for the stroboscopic illumination technique to be used up to an eccentricity ratio of about $\varepsilon = 0.40$. The transitional state could not be positively identified in these tests although, using $\varepsilon = 0.10$ and $\varepsilon = 0.20$, a comparatively unsteady form of wavy mode flow was observed from about Re = 500 to about Re = 900. At higher Reynolds numbers, the flow was influenced by location

within the test length. Using $\varepsilon = 0.10$, for example, the $n = 3$ mode was clearly evident in the flow at the upper end of the test length, above about $Re = 2400$, although there was a tendency for waviness to disappear from the lower end of the test length under these conditions.

A novel mechanism of wave number change was observed in the tests using $\varepsilon = 0.20$. As the shaft speed was increased, a change in the number of circumferential waves first became evident at the upper end of the test length. This phenomenon was not the same as that described in Section 2.6.1.1 because the new mode showed no tendency to expel the old mode from the remainder of the test length until the shaft speed was further increased. The new mode then replaced the old mode in a greater proportion of the test length after each subsequent shaft speed increment until, finally, it occupied the entire test length. In a typical test run, this procedure started at $Re = 1885$ and finished at $Re = 2100$. Consequently, for several shaft speed settings, two different wavy modes were observed in different sections of the test length at the same time. The wave numbers involved in this change were three and seven, the $n = 3$ mode gradually replacing the $n = 7$ mode as the shaft speed was increased. This was also unusual because the wave number changes observed in the tests using $\varepsilon = 0$ and $\varepsilon = 0.10$ were usually of the $n \pm 1$ type.

The circumferential wave number changed continuously throughout the tests using $\varepsilon = 0.30$ and $\varepsilon = 0.40$ although the type of change discussed above was not observed.

The predominant mode evident at the highest Reynolds numbers used in these tests was n = 8 in both cases.

2.6.2 The Circumferential Wave Velocity Ratio

2.6.2.1 Concentric Cylinder Tests Using $\eta = 0.911$

The circumferential wave velocity ratio was found to be reasonably constant at a value of 0.41 for Reynolds numbers above about Re = 500. At the onset of wavy vortex flow, the tangential velocity of the waves was greater than half the peripheral velocity of the shaft, although the ratio gradually decreased as the shaft speed was increased. It is evident from Figs. 13 to 15 that there were no significant differences between the results from the tests using Tellus 21, Tellus T17 and Carnea 15 respectively. The scatter of the results at low Reynolds numbers was caused by a hysteresis type effect which is discussed in Section 2.6.5 .

There is a temptation to correlate the change to a constant wave velocity ratio with the observed onset of transitional state flow. The appearance of wavy mode flow was altered considerably by the onset of the transitional state and it would not, therefore, have been entirely unexpected if the wave velocity had also been affected by this. However, this correlation cannot be justified because the results in Figs. 13 to 15 were recorded in a number of different tests in which transitional state flow was sometimes not observed until Re = 855. The wave velocity ratio was also found to be unaffected by the wave number changes which occurred before Re = 500 in the primary wavy mode. It is evident from the results that this was necessarily the case for the changes observed at higher Reynolds number.

The constant wave velocity ratio for the high Reynolds number results was used to derive the family of 'radial lines' drawn in Fig.37 (see also Appendix II). The appropriate lines are compared with the results of four particular test runs in Figs. 40 and 41, and with results recorded by Jackson (40) in Fig.42 .

Jackson derived circumferential wave numbers from his results by comparing them with a family of 'radial lines' based on a constant wave velocity ratio of 0.34 . However, this value had been derived by Coles (16) using $\eta = 0.874$ (Section 2.6.2.5), whereas the radius ratio used by Jackson was $\eta = 0.911$. It is evident from Fig.42 that there is considerable disagreement between Jackson's results and the 'radial lines' derived from the present investigation. This is not particularly surprising for the results at low shaft speeds, although one would expect better correlation for shaft speeds above about 400 r.p.m., because Re then exceeds 500. What is even more surprising, however, is that the lines drawn through these results do not pass through the origin. This suggests either that the circumferential wave velocity ratio was not constant for the high shaft speeds used by Jackson, or that his shaft speed measurements were inaccurate. The first possibility contradicts the results of the present more-detailed investigation and, therefore, the second seems more likely. In his report, Jackson referred to erratic cylinder speed measurements "particularly in bright sunshine".

2.6.2.2 Eccentric Cylinder Tests Using $\eta = 0.911$

For the eccentric cylinder case, the wavelength of the circumferential waves was observed to depend on the

circumferential viewing point. The results discussed below were derived assuming a constant wavelength and, therefore, these relate to average circumferential wave velocities.

It is evident from Figs. 16 to 26 that the circumferential wave velocity ratio characteristics, for eccentricity ratios up to $\varepsilon = 0.20$, were similar in form to those for the concentric cylinder case. The wave velocity ratio was again found to be reasonably constant at a value of about 0.41, for the results recorded using high shaft speeds, in each of the tests. However, as the eccentricity was increased from $\varepsilon = 0$, there was a tendency for the wave velocity ratio to progressively decrease for results recorded below about Re = 1000. Consequently, the sequence of events, for increasing shaft speed, was for the wave velocity ratio to gradually decrease to a minimum value and then to recover to a value of about 0.41. The results plotted in Figs. 13 to 26 are summarised in Table 9. It is evident that these were not particularly influenced by the choice of test fluid.

Primary wavy mode flow was observed to become progressively more unsteady as the eccentricity was increased (Section 2.6.1.2). The results discussed above indicate that the circumferential wave velocity was reduced under these conditions. Secondary wavy mode flow was relatively unaffected by eccentricity and it follows, therefore, that similar wave velocity ratios should have been recorded for high Reynolds numbers in each of the eccentric cylinder tests. It is evident from Table 9 that the experimental results support this hypothesis.

2.6.2.3 Concentric Cylinder Tests Using $\eta = 0.950$

It is evident from Figs. 27 and 28 that the circumferential wave velocity ratio was, once again, reasonably unaffected by the choice of test fluid. The results for low Reynolds numbers were similar to those recorded using $\eta = 0.911$. However, in this case, the wave velocity ratio gradually decreased from being greater than 0.5 at the onset of wavy vortex flow, to a value of 0.45 at about Re = 400. The ratio remained reasonably constant as the shaft speed was further increased although, above about Re = 650, it was found to progressively increase at the rate of about 0.01 for each Reynolds number increase of 500.

For this shaft, it was difficult to define the boundaries of the transitional state because the flow was extremely unsteady throughout the wavy mode (Section 2.6.1.3). However, the results discussed above suggest that the circumferential wave velocity was significantly affected by the different regimes of wavy mode flow.

2.6.2.4 Eccentric Cylinder Tests Using $\eta = 0.950$

Using $\varepsilon = 0.10$, results could only be recorded for a limited range of Reynolds numbers because of the unsteady nature of the flow under these conditions. It is evident from Fig.29, however, that the circumferential wave velocity was everywhere lower than for the concentric cylinder case. As the shaft speed was increased to Re = 500, the wave velocity ratio gradually decreased to a minimum value; 0.42 in the tests using Tellus 21 and 0.43 in the tests using Carnea 15. The ratio was then reasonably constant up to the maximum Reynolds number, Re = 720. For

higher Reynolds numbers, the results would probably have plotted in the band between a horizontal line and a line having the slope defined by the concentric cylinder results.

2.6.2.5 Concentric Cylinder Tests Using $\eta = 0.874$

Increasing the radial clearance generally reduced the velocity of the circumferential waves. It is evident from Fig.30 that the wave velocity ratio characteristic was similar to that for $\eta = 0.911$, although, in this case, the ratio was reasonably constant, at a value of 0.37, above about Re = 600. At the onset of wavy vortex flow, the velocity of the waves again exceeded half the peripheral velocity of the shaft, a wave velocity ratio of 0.52 being recorded for the mode having three circumferential waves.

These results compare favourably with those recorded by Coles (16) in a series of tests using $\eta = 0.874$ and $\eta = 0.899$. Coles reported that the wave velocity ratio was reasonably constant at a value of 0.34 for high Reynolds numbers, although this was derived assuming the narrow gap approximation whereby

$$(V/v) = \frac{f}{nN}$$

If the radius ratio is not assumed to equal unity then, from Appendix I, the wave velocity is given by

$$(V/v) = \left(\frac{1 + \eta}{2\eta} \right) \frac{f}{nN}$$

and Coles' constant value becomes 0.36.

2.6.2.6 Eccentric Cylinder Tests Using $\eta = 0.874$

In these tests, the wave velocity ratio was found to be significantly affected by some of the observed flow changes. The ratio was again reasonably constant for high Reynolds

numbers although different values were recorded in different ranges of Reynolds number. Using $\varepsilon = 0.10$, for example, it is evident from Fig.31 that wave velocity ratios of 0.37 and 0.36 were recorded in the ranges Re = 900 to Re = 1500, and Re = 1600 to Re = 2300 respectively. Furthermore, the experimental results showed that the wave velocity ratio was constant at a value of 0.37 between Re = 2400 and Re = 2800. The following types of wavy mode flow were observed in these ranges:

Re = 900 to Re = 1500	A mode having three circumferential waves was predominant
Re = 1600 to Re = 2300	The wave number changed continuously between n = 3 and n = 4
Re = 2400 to Re = 2800	A mode having three circumferential waves was evident but only at the upper end of the test length

It is evident from Fig.32 and Table 11 that a similar correlation was valid for the results using $\varepsilon = 0.20$. In this case, the wave velocity ratio remained reasonably constant at values of 0.37, 0.39 and 0.36 in the ranges Re = 500 to Re = 900, Re = 1000 to Re = 1885, and Re = 2100 to Re = 3000 respectively. Between Re = 1885 and Re = 2100, there were two possible wave velocity ratios, (V/v) = 0.39 and (V/v) = 0.36. In this range, a mode with three circumferential waves was observed to gradually displace the n = 7 mode from the entire test length as the shaft speed was progressively increased (Section 2.6.1.6). At intermediate shaft speeds, the flow appeared to be stable with the two systems of wavy vortices occupying different parts of the test length. However, the results indicate that the tangential

velocities of the two wavy modes were different, the n = 7 mode travelling faster than the n = 3 mode by a constant factor of 0.03 times the peripheral velocity of the shaft. It is also interesting to note that the constant wave velocity ratio for the n = 7 mode was greater than that for the concentric cylinder case using $\eta = 0.874$.

The results using $\varepsilon = 0.20$ and low Reynolds numbers were similar in form to those for $\eta = 0.911$ and eccentric cylinders; the wave velocity ratio decreasing to a minimum value and then recovering to a higher value as Reynolds number was increased. It is evident from Fig.33 that increasing the eccentricity ratio to $\varepsilon = 0.30$ further reduced the wave velocity ratios recorded using low Reynolds numbers. In this case, a minimum wave velocity ratio of 0.33 was recorded between Re = 400 and Re = 700. For higher Reynolds numbers, the wave velocity ratio was again found to be reasonably constant at a value of 0.37. However, it is evident from Table 11 that wave numbers between seven and ten were observed under these conditions and not the n = 3 mode which was observed using smaller eccentricity ratios.

Using $\varepsilon = 0.40$ (Fig.34), a minimum wave velocity ratio of 0.34 was recorded at Re = 630. As the Reynolds number was further increased, the wave velocity ratio increased to reach a value of 0.38 at Re = 1150. Only a limited number of results were recorded because of the unsteady nature of the flow under these conditions.

2.6.3 The Circumferential Wave Number

Several circumferential wave number changes were observed in the flow visualisation tests, the mechanisms involved having been described in Section 2.6.1. For the concentric cylinder case, the

changes observed using $\eta = 0.874$ and $\eta = 0.911$ are summarised in Tables 10 and 12. Using $\eta = 0.950$, wavy mode flow was found to be extremely unsteady with the wave number changing frequently between two values. Observations of the flow suggested that the predominant modes for large Reynolds numbers were n = 10, 12 and 14 (Table 13).

The circumferential wave numbers observed in the various tests are summarised by means of line diagrams in Figs. 44 to 55. With the exception of the results using $\eta = 0.874$, and eccentricity ratios above $\varepsilon = 0.10$, the line diagrams displayed similar trends. As the shaft speed was increased, the number of waves increased to reach a maximum value at about Re = 250, then decreased to a value which was constant within $n \pm 1$ above about Re = 1000. The maximum wave number was influenced by the radial clearance, n = 7, 10 and 19 being recorded using $\eta = 0.874$, 0.911 and 0.950 respectively. In each case, three circumferential waves were usually observed shortly after the appearance of waviness. However, in one particular test, using $\eta = 0.911$ and $\varepsilon = 0.10$, the n = 3 mode was observed to be preceded by a mode having two circumferential waves. The weak wavy mode (n = 1), reported by Castle et al (10), was not recorded in any of the tests because of a lack of persistence of vision when the stroboscopic illumination technique was used for low shaft speeds.

It is evident from Table 14 that typical wave number changes observed using $\eta = 0.874$ and $\varepsilon = 0$ were in reasonable agreement with those recorded by Coles (16). The non-unique nature of wavy mode transitions was also endorsed by the present investigation (Section 2.6.6). Coles derived mean values of the circumferential wave number from his results, n = 6 and n = 4 being the expected modes at Re = 450 and 1500 respectively. In tests using $\eta = 0.950$ and $\varepsilon = 0$, Snyder (61) recorded a single wave mode between Re = 225 and Re = 240,

the n = 4 mode between Re = 240 and Re = 275, and a mode having more than four waves up to Re = 330. For higher Reynolds numbers, he described the flow as unsteady. Wavy mode flow was observed to be unsteady in the present tests using $\eta = 0.950$, although it is evident from Fig.49 that wave numbers between three and nineteen were recorded.

The effect of radius ratio was virtually eliminated from the results for $\varepsilon = 0$ and $\varepsilon = 0.10$ by multiplying the mean circumferential wave number, $\bar{n}$, by the clearance ratio (Figs. 56 and 57). The non-dimensional parameter $(\bar{n}\, c / R_i)$ was not particularly successful for higher eccentricity ratios (Figs. 58 and 59), however, because of the unusually high wave numbers which were observed in the tests using $\eta = 0.874$. It is evident from Fig.53 that, for $\varepsilon = 0.20$, a mode with three or four waves changed to a mode with seven or eight waves at about Re = 900. This was followed by a gradual transition from n = 7 to n = 3 (Section 2.6.1.6) which started after about Re = 1900 and finished by about Re = 2200. For $\varepsilon = 0.30$ and $\varepsilon = 0.40$ (Figs. 54 and 55), the lowest wave numbers recorded at high Reynolds numbers were seven and eight respectively.

2.6.4 The Axial Wave Number

Axial wave numbers were derived from measurements of the number of vortex cells in a central section of the test length (Appendix I). Using $\eta = 0.950$, the flow was too unsteady for these measurements to be recorded and, therefore, no results are presented for this radius ratio.

Using $\eta = 0.911$, the axial wave number varied considerably throughout the wavy mode. The axial length of the vortex cells was observed to become progressively larger as the shaft speed was increased through the primary wavy mode, the axial wave number ratio

(a/a_o) decreasing from a value of unity shortly after the appearance of waviness to a value of about 0.6 at the onset of transitional state flow (Figs. 60 to 64). Results could not be recorded in the transitional state because of the unsteady nature of this flow regime. However, above about Re = 1100 (secondary wavy mode flow), there was a tendency for the axial wavelength to gradually decrease as the shaft speed was increased. Maximum axial wave number ratios of 0.66, 0.77, 0.75, 0.74 and 0.82 were recorded using high Reynolds numbers for $\varepsilon = 0$, 0.05, 0.10, 0.15 and 0.20 respectively. It is evident from Figs. 60 to 64 that the results were not particularly influenced by these eccentricity ratios. The scatter of the results recorded using low Reynolds numbers, for the concentric cylinder case, is discussed in Section 2.6.5.

Using $\eta = 0.874$, the recorded variation of the axial wave number was somewhat different from that discussed above. For the concentric cylinder case, the axial wavelength was again increased by increasing the shaft speed through the primary wavy mode, although at a lower rate than for $\eta = 0.911$. It is evident from Fig.65 that the axial wave number ratio decreased from a value of 0.81 at Re = 255 to a value of 0.73 at Re = 975. As the shaft speed was further increased, the stable n = 5 mode was observed to be replaced by a mode in which the circumferential wave number changed frequently between three and four (Section 2.6.1.5). Axial wavelength measurements could not be recorded under these conditions, although results recorded at higher Reynolds numbers indicated that the axial wave number ratio was signficantly reduced by this form of transitional state flow. The onset of secondary wavy mode flow occurred at about Re = 1100 with the appearance of the stable n = 3 mode. The corresponding axial wave number ratio was 0.58 although this value increased as the shaft speed was increased through the secondary wavy mode. The scatter of the results recorded in the primary wavy mode is

discussed in Section 2.6.5 .

It is evident from Fig.66 that comparatively few axial wavelength measurements were recorded using $\eta = 0.874$ and eccentric cylinders. However, an unusual feature of the results for $\varepsilon = 0.20$ was that the axial wave number ratio approached a value of unity at about Re = 1500. The high axial wave numbers recorded above Re = 930 in these tests coincided with a change from a mode with three or four circumferential waves to a mode with seven or eight circumferential waves (Section 2.6.3).

2.6.5 Hysteresis Effects

Circumferential wave velocity ratios recorded at low Reynolds numbers showed considerable scatter. This is particularly evident in Figs. 13 to 15, the concentric cylinder results for $\eta = 0.911$. The scatter is shown to be a hysteresis effect in Figs. 35 and 36 because the ratios recorded when the shaft speed was decreasing were generally lower than those recorded when the shaft speed was increasing. Results recorded above about Re = 500 were not affected.

Axial wave numbers recorded at low Reynolds numbers were also significantly influenced by hysteresis effects. Using $\eta = 0.911$ and $\varepsilon = 0$, it is evident from Figs. 60, 67 and 68 that, whereas the axial wave number generally decreased as the shaft speed was increased, there was a tendency for it to remain reasonably constant as the shaft speed was decreased. Consequently, the results recorded for decreasing shaft speeds were generally lower than those recorded for increasing shaft speeds. Once again, the results recorded at high Reynolds numbers (secondary wavy mode) were not affected. It is evident from Fig.65 that similar trends were recorded using $\eta = 0.874$ and $\varepsilon = 0$. The axial wave number appeared to be less influenced by hysteresis effects in tests using eccentric cylinders.

Hysteresis was also a feature of circumferential wave number changes, the Reynolds number for a particular change being lower when the shaft speed was decreasing than when the shaft speed was increasing. This effect is evident from the results of typical tests, using $\eta = 0.874$ and $\varepsilon = 0$, in Fig.43 and Table 14. These are in reasonable agreement with results presented by Coles (16). One would not expect exact agreement because of the non-unique nature of wavy mode flow.

2.6.6 Non-Uniqueness

Non-uniqueness was found to be a feature of wavy vortex flow. This is a necessary conclusion of Section 2.6.5 because both the number of circumferential waves and the axial length of the vortex cells were shown to be influenced by hysteresis effects. Furthermore, the results indicated that another important factor was the manner in which the final shaft speed was approached. In general, circumferential wave number changes were found to be reasonably predictable if tests were carried out under the same experimental conditions and using similar procedures. It is evident from Fig.41, for example, that the same sequence of wave number changes was observed in three particular tests using $\eta = 0.911$ and $\varepsilon = 0$. However, the change from $n = 10$ to $n = 9$ occurred at a higher shaft speed in Test 36, presumably because larger shaft speed increments were used in this test.

The non-unique nature of wavy vortex flow was also reported by Coles (16). Defining a state by the number of circumferential waves and the total number of vortex cells between the ends of his apparatus, Coles recorded as many as twenty different states at particular shaft speeds. However, rotation of the outer cylinder was frequently required as part of the build-up procedure for many of these states. In the present investigation, the outer cylinder of the

test rig could not be rotated. Coles suggested that a knowledge of the previous history of operation would normally be sufficient for a skilled operator to set up particular states. The results of the present work tend to endorse this statement as far as circumferential wave number changes are concerned. Coles' axial wave number results cannot be correlated with the author's because he included the boundary cells in his results. Snyder (62) reported that the boundary cells are substantially different from the vortex cells between them. He showed that changes in the axial length of the latter are usually accommodated by adjustment of the boundary cells and only infrequently by a change in the number of cells in the apparatus.

It is evident from Figs. 44 to 55 that the circumferential wave number was generally non-unique. However, it must be remembered that, under some conditions, more than one wave number was observed at particular speed settings. In tests using eccentric cylinders, for example, the wave number was often observed to change continuously between two particular values. In these cases, non-uniqueness was a feature of the range of wave numbers observed rather than one particular wave number. This also applied to transitional state flow for which a range of different modes each appeared briefly before being replaced (Section 2.6.1). It is evident from Figs. 11 and 12 that, as well as the circumferential wave numbers involved, the boundaries of the transitional state were found to be non-unique.

2.7 CONCLUSIONS CONCERNING THE FLOW VISUALISATION TESTS

The stroboscopic illumination technique is excellent for observations of the development of wavy mode flow in large radial clearances between concentric cylinders. However, the stability of

the flow is significantly reduced by either the introduction of even small eccentricity settings or by decreasing the radial clearance and, therefore, the technique would not be suitable for investigations of realistic journal bearing configurations.

Visual observations suggested that wavy mode flow can be sub-divided into three regimes, a quasi-turbulent flow regime separating two well defined wavy mode configurations. The quasi-turbulent flow regime was named the 'transitional state' because the circumferential wave number appeared to be in a state of transition between a high value and a low value. Wavy mode flow preceding the transitional state was named the 'primary wavy mode' and that following the transitional state was named the 'secondary wavy mode'.

The three wavy mode flow regimes were most easily identified using $\eta = 0.911$ and $\varepsilon = 0$. In this case, the onset of the transitional state was particularly violent, completely destroying the well defined nature of primary wavy mode flow. Using eccentric cylinders, the appearance of transitional state flow was less well defined because the primary wavy mode was itself less stable. The secondary wavy mode usually appeared fairly gradually, transitional state flow becoming less disturbed as the shaft speed was increased. Using eccentric cylinders, the secondary wavy mode was generally more stable than the primary wavy mode.

The geometry of wavy mode flow followed different trends in each of the three regimes. As the shaft speed was increased through the primary wavy mode, the number of circumferential waves increased fairly rapidly to a maximum value and the vortex cells became progressively wider. The circumferential wave number decreased through the transitional state although the axial wavelength appeared to be reasonably unaffected (except using $\eta = 0.874$ and $\varepsilon = 0$). In the secondary wavy mode, the number of circumferential waves generally

remained reasonably constant whereas there was a tendency for the axial length of the vortex cells to decrease. However, using $\eta = 0.874$ and eccentric cylinders, the maximum number of circumferential waves often occurred in the secondary, rather than the primary, wavy mode. In these cases, the axial wavelength approached a value equal to the diametral clearance (as at the onset of Taylor vortex flow).

Using small eccentricity settings, the velocity of the circumferential waves usually exceeded half the peripheral velocity of the shaft at the onset of wavy vortex flow. The wave velocity ratio decreased as the shaft speed was increased although for $\eta = 0.911$ and $\eta = 0.874$, it remained reasonably constant throughout the secondary wavy mode at values of 0.41 and 0.37 respectively. Using $\eta = 0.950$, the ratio increased as the shaft speed was increased through the secondary wavy mode.

Several different mechanisms of circumferential wave number change were observed in the flow visualisation tests; most of which were accompanied by oscillation of the vortex structure. In tests using $\eta = 0.874$ and $\varepsilon = 0.20$, it was found to be possible for wavy mode flow to be stable with different wave numbers in different parts of the test length. In this case, the $n = 3$ mode appeared at the upper end of the test length and gradually replaced the $n = 7$ mode from the entire test length as the shaft speed was increased.

Hysteresis and non-uniqueness were both features of wavy vortex flow, although hysteresis effects particularly influenced results recorded in the primary wavy mode. Non-uniqueness was a feature, not only of the circumferential wave number and the axial wavelength, but also of the boundaries of the transitional state. The results indicated that the previous history of operation was an important factor in the appearance of the wavy mode under particular conditions.

CHAPTER 3

AN INVESTIGATION OF THE WAVY MODE OF TAYLOR VORTEX FLOW USING TORQUE MEASUREMENTS

3.1 REVIEW OF LITERATURE

3.1.1 Torque Measurement Techniques

Since the early experiments on fluid viscosity by Couette (18) and Mallock (46), torque measurement techniques have been frequently used for investigations of the flow between a rotating shaft and a fixed outer cylinder. Most previous researchers have measured the torque transmitted through the test fluid to the outer cylinder, a typical test arrangement being that used by Donnelly (30) whose outer cylinder was suspended on a calibrated torsion wire, or that used by Taylor (72) who applied known forces to the end of a lever arm mounted on the outer cylinder.

Inner cylinder torque measurements were recorded by Cole (15) whose shaft was driven by a torsion mounted motor. More recently, Younes (80) and Jones (41) have used an inductive torque measuring system to monitor directly the torque input to the shaft in their test rigs.

3.1.2 The Concentric Cylinder Case

Donnelly (30) reported that the onset of Taylor vortices was marked by a sudden increase in the slope of the torque-speed characteristic. This has since been confirmed by the results of numerous researchers and the onset of wavy vortex flow has also been shown to influence torque measurements.

Debler et al (21), using narrow gaps ($\eta \geq 0.85$), found that the appearance of the wavy mode resulted in the torque being reduced below that which would have been recorded had the regular Taylor cells remained stable. The wavy mode was observed to manifest itself in two well defined stages by Castle et al (10), both of which resulted in a decrease in the slope of their outer cylinder torque measurements. The first stage to occur with increasing shaft speed was named the "weak" wavy mode because the corresponding torque reduction was less than that for the second stage, the "strong" wavy mode. These results were endorsed by the inner cylinder torque measurements of Jones (41).

For the large gap case, Jones observed a quasi-turbulent flow regime at, or soon after, the onset of the wavy mode which resulted in an increase in the slope of the torque-speed characteristic. He also observed a region of quasi-turbulence using $\eta = 0.85$ although, in this case, it did not occur until well after the onset of wavy mode flow. However, it was again found to be marked by an increase in the slope of the torque measurement results. Jones' torque measurements recorded within the quasi-turbulent flow regime showed a complete non-uniqueness whereas, using $\eta = 0.90$ (narrow gap), he was able to correlate observed circumferential wave number changes with discontinuities in the torque-speed characteristics. Circumferential wave numbers between three and seven were studied and the results were found to show reasonable agreement with discontinuities in the outer cylinder torque measurements of Markho (47).

Previous researchers have often presented their torque measurement results in the non-dimensional form of a logarithmic plot of a function such as the friction coefficient, C_f, against Reynolds number. This type of characteristic has been found to

be particularly useful because, for a given geometry, the results embracing simple laminar flow coalesce on to a single line independent of viscosity. Furthermore, for turbulent flow, C_f has been shown to be related to Re by the formula

$$C_f = \frac{K}{Re^{\ell}} \qquad 0 < \ell < 1$$

Outer cylinder torque measurements covering a large range of Reynolds numbers were recorded by Wendt (79) using $\eta = 0.680$, 0.850, and 0.935. These were found to be well defined by the empirical formula

$$C_f = K \left(\frac{(R_o - R_i)R_o}{R_i^2} \right)^{0.25} \frac{1}{Re^{\ell}}$$

if the constants K and ℓ were given values of 0.46 and 0.5 respectively between Re = 400 and Re = 10^4 and values of 0.07 and 0.3 respectively between Re = 10^4 and Re = 10^5. The values of K and ℓ derived from the results of other previous researchers are summarised in Table 41.

Taylor (72) recorded outer cylinder torque measurements using a range of shafts between $\eta = 0.790$ and $\eta = 0.973$ and seven different test fluids. The results gave reasonable agreement with Wendt's empirical formula although the slope ℓ was always numerically less than 0.30 for high Re. Typical values of K = 0.02 and $\ell = 0.16$ were derived, in excellent agreement with the results presented by Vohr (76). Table 41 suggests disagreement for low Re between the results of Wendt and those of Donnelly (30) and Debler et al (21). In the latter cases, the results showed negative slopes with magnitudes in excess of $\ell = 0.50$ whereas Wendt's conclusions did not mention this possibility. However, slope changes derived from his results at about Re = 700 are summarised in Table 44. Similarly, Vohr's torque measurement results also plotted above the basic slope of -0.48 for Reynolds numbers below about 725.

Debler et al reported that their logarithmic plots were composed of segments between which there were jump discontinuities in magnitude but no change in slope. The present author derived a change in the basic slope from -0.48 to -0.59 from their results for $\eta = 0.850$ (Table 41) although these could also have been interpreted as four segments each with a slope of -0.54. Debler et al's results for $\eta = 0.875$ and $\eta = 0.935$ showed segments with similar slopes and there were clearly three segments each having a slope of about -0.58 between Re = 200 and Re = 400 in the friction coefficient characteristics presented by Castle and Mobbs (9) for $\eta = 0.899$.

It should be pointed out at this stage that, although there was some disagreement between the constants derived from the results of previous authors for low Reynolds numbers, their friction coefficient characteristics were generally found to give reasonable agreement overall. The magnitude of the constant K is considerably influenced by small variations in the magnitude of the basic slope ℓ.

The low Reynolds number results of Wendt, Taylor and Donnelly were analysed by Donnelly and Simon (33) who reported that, between the onset of vortex flow and up to ten times the critical velocity, the recorded torque was given by the formula

$$M = a\omega_i^{-l} + b\omega_i^{m}$$

The constants a and b were dependent on the geometry of the test rig and the viscosity of the test fluid and m typically took a value of 1.36. For shaft speeds well beyond the critical and up to about Re = 1000, Donnelly and Simon suggested that the influence of test rig geometry on the results could be

eliminated by means of the formula

$$C_f \propto \left(\frac{(R_o - R_i)}{R_i} \right)^{0.31} \frac{1}{Re^{0.50}}$$

They commented that Wendt's geometry factor did not result in any significant improvement compared with that above. In an appendix to their paper, Batchelor derived a similar relationship using an inviscid core surrounded by a boundary layer as the theoretical model of the flow.

3.1.3 The Eccentric Cylinder Case

The onset of Taylor vortices in the flow between eccentric cylinders was investigated by Cole (15) and Vohr (76) who reported that the corresponding increase in slope of the torque-speed characteristic became progressively less well defined for eccentricity ratios above about $\varepsilon = 0.5$. Flow visualisation tests carried out by Castle and Mobbs (9) showed that the onset actually occurs in two stages between eccentric cylinders. The first stage, consisting of vortices which did not extend to the outer cylinder in the region of the wide gap, was found to be replaced by a system of vortex cells with a smaller axial wavelength, but which everywhere extended to the outer cylinder, at a slightly higher shaft speed. Castle and Mobbs were able to detect the onset of the second stage from their outer cylinder torque measurements but not that of the first stage. Conversely, Younes (80) reported that the onset of the first stage resulted in an increase in the slope of his inner cylinder torque measurements whereas the onset of the second stage had no effect. The situation was further complicated by Jones (41) who detected the onset of both stages from his inner cylinder torque measurements. However, tests carried out by Mobbs and Zarti (unpublished) at

Leeds University suggested that the detection of the first stage by Younes and Jones was probably the result of misalignment. Mobbs and Zarti showed that, for eccentric aligned operation, only the onset of the second stage should be detected by inner cylinder torque measurements.

Jones reported that the onset of the first stage was destablised by small eccentricity ratios whereas the onset of the second stage was everywhere stabilised by increasing eccentricity. However, for a given eccentricity ratio, the critcal Taylor number for the onset of the second stage was found to be decreased by increasing the misalignment between the cylinders and/or by increasing the radius ratio. Misalignment and rig geometry have probably been important factors in the existing confusion between the results of the numerous previous researchers who have studied the variation of T_c with eccentricity.

Castle et al (10) used outer cylinder torque measurements to investigate the effect of eccentricity on the onset of wavy mode flow. The weak and the strong wavy modes were both delayed by increasing eccentricity and for large eccentricity ratios, there was a tendency for the modes to merge. Changes in the magnitude of the corresponding torque discontinuities indicated that the modes both became progressively weaker as the eccentricity ratio was increased above about $\varepsilon = 0.3$, an effect attributed to the appearance of a region of reversed flow in the wide gap under these conditions. Castle et al's results were confirmed by Jones who also reported that misalignment lowered the critical shaft speeds at which the weak and strong wavy modes were detected from his inner cylinder torque measurements.

Jones recorded torque inflexions beyond the onset of the strong wavy mode using $\varepsilon \leq 0.7$ and those for $\eta = 0.90$ were

correlated with observed circumferential wave number changes. Changes in the predominant wave number were detected as well defined torque inflexions whereas smaller torque inflexions were found to correspond with non-unique $n \pm 1$ type changes. The well defined inflexions gave reasonable agreement with the outer cylinder torque measurements of Markho (47) which indicated unique torque inflexions at points where regions of $n+2$ waves became accessible (i.e. where a change from n to $n+2$ could occur).

Jones' torque measurements beyond the onset of the strong wavy mode for $\eta = 0.85$ were ill defined with large inflexions at random points. He suggested that this was due to non-uniqueness of the circumferential wave number under these conditions. However, for eccentricity ratios up to $\varepsilon = 0.6$, an upward torque inflexion was found to correspond with the onset of a quasi-turbulent flow regime which followed the onset of vortex flow more closely as the eccentricity was increased. A similar effect was recorded by Frêne and Godet (36) from torque measurements on the sleeve of a model bearing for which $\eta = 0.995$. An upward torque inflexion was clearly indicated by their results at a point where the flow was described as becoming irregular in nature. Using figures presented by Frêne (35), it can be shown that these inflexions were recorded at about Re = 800 and Re = 950 in tests using $\varepsilon = 0.25$ and $\varepsilon = 0.59$ respectively.

Friction coefficient characteristics covering the transition from simple laminar flow to wavy mode flow were presented by Castle and Mobbs (9) for $\eta = 0.899$. Results recorded up to about Re = 500 indicated that the magnitude of the negative slope of the wavy mode characteristic was increased by increasing eccentricity. Slopes of -0.58 and -0.70 were derived from the results for $\varepsilon = 0$

and $\varepsilon = 0.80$ respectively. Characteristics covering a larger range of Reynolds number were presented by Vohr (76) for $\eta = 0.910$ and $\eta = 0.990$. The results for large ε and high Re defined a basic slope of about -0.25, in excellent agreement with that predicted by the turbulent theories of Ng and Pan (50) and Burton (7), and with the results of various experimental investigations using real journal bearings. Table 45 shows that this basic slope was derived from the results of Duffin and Johnson (34), Ramsden (53) and Booser et al (4) who used different bearing types. The range of Reynolds number covered in these investigations was typically from Re = 1000 to Re = 10,000. A basic slope of -0.43 was indicated by the torque measurements recorded by Smith and Fuller (60) using an unloaded bearing giving $\eta = 0.997$. This compared favourably with Wendt's empirical formula (for $Re < 10^4$) and the long bearing theory of Constantinescu (17).

3.2 THE TORQUE MEASUREMENT TEST RIG

The flow visualisation test rig had generally performed satisfactorily and, therefore, rather than automatically designing a new rig for the proposed torque measurement investigation, the possibility of modifying the existing rig was considered. This decision could not be made, however, until the method of torque measurement had been selected. Several previous researchers had employed techniques which allowed measurement of the viscous torque experienced by the stationary outer cylinder whereas, more recently, equipment capable of monitoring the torque input to the rotating shaft had become commercially available. The latter technique was preferred by the author and equipment consisting of a Vibrometer torque transducer type TG/02B and a matched Vibrometer digital torque

meter type 8-CT-1/AD was selected. A successful application was made to the Science Research Council for a grant to cover the cost of this equipment.

This type of torque transducer uses an inductive measuring system to monitor the twist in a section of the tempered, high quality, steel shaft through which the torque is transmitted. The shaft is supported in two precision ball bearings and two flanges, fixed on both sides of the measuring section, hold the inductive coil and core arrangement. The torsional twist of the flanges is a direct measurement of the torque transmitted and, due to the high sensitivity of the sensing system, only a very small torsional angle (about 0.25^{o}) is required. Rotary transmitters are used for the power supply to the inductive coil system mounted on the shaft and the output signal is recovered in the same way. When torque is transmitted through the transducer shaft, the output signal causes unbalance in a bridge circuit in the torque meter. The bridge voltage is amplified and fed to a digital voltmeter which is calibrated to give average torque readings.

To monitor the torque input to the shaft in the test rig, the transducer had to be mounted between the drive motor and one end of the shaft. Ideally, the axes of the drive motor, transducer and test rig shafts had to be aligned to ensure that the transducer shaft was not exposed to unnecessary bending moments which would have influenced the accuracy of the torque measurements. In the flow visualisation test rig, the drive was transmitted to the lower end of the vertical shaft by means of a timing belt. This arrangement would clearly have been unacceptable for the torque measurement test rig and there was insufficient clearance between the lower end of the shaft and the floor to accommodate

the transducer and drive motor mounted in line. This difficulty could have been overcome but it was decided to design a new test rig for the torque measurement investigation rather than attempt to modify the existing rig for the purpose.

The torque measurement test rig (Figs. 69 and 70) was designed to be much more rigid than the flow visualisation test rig had been. The drive motor was mounted on a substantial frame and bolted to the laboratory wall above the test rig. The torque transducer was mounted between the drive motor and the shaft in the test rig on a bracket bolted to the drive motor support frame at one end and to the top of the test rig at the other. The top of the test rig was also connected to the laboratory wall by means of a tie bar. Two short lengths of rubber tubing were used to transmit the drive from the output shaft of the motor to the input shaft of the torque transducer and from the output shaft of the torque transducer to the upper end of the shaft in the test rig. Jubilee clips were used to hold the tubing in place on each of the four shafts. This arrangement was used in preference to the more sophisticated flexible couplings commercially available because it was important that the consequences of misalignment should not be catastrophic. The rubber tubing was capable of accommodating fairly large misalignments without introducing significant bending forces to the transducer shafts and was sufficiently strong to transmit the drive.

Positioned as it was, the transducer would have monitored not only the torque required to drive the shaft against viscous forces within the test fluid, but also that required to overcome

friction in the bearings and seals supporting the shaft. It was desirable to eliminate as much of this latter torque component as possible and, therefore, the rig was designed in such a way that shaft seals were not necessary. The lower shaft seal was made redundant by closing the bottom of the test rig. This was possible in this case because the drive was transmitted to the upper end of the shaft and there was no longer any need for the lower end of the shaft to extend beyond the bottom block. A clearance of about one inch was allowed between the meniscus of the test fluid and the top of the test rig in order that an upper shaft seal would not be necessary. This was originally tried for the previous rig and was found to be sufficient to prevent the test fluid from being pumped out of the rig through the top block at high shaft speeds.

The shaft was supported vertically by an angular contact ball bearing at the lower end and by a deep groove ball bearing at the upper end. The weight of the shaft was supported by the lower bearing whereas the upper bearing was little more than a guide for the upper end of the shaft. A housing plate was machined for the lower bearing to facilitate the removal of the shaft from the rig. (This had sometimes proved to be rather difficult in the flow visualisation test rig.) The plate was accurately located on dowel pins and bolted to the lower surface of the bottom block with an "O" ring seal between the mating faces. This arrangement allowed the shaft to be withdrawn from the rig through the bottom block without disturbing the alignment between the drive motor and the torque transducer.

Four shafts were turned between centres from solid blocks of aluminium. Their diameters were measured in perpendicular planes at four equispaced axial sections. The mean diameters of the four

shafts were recorded as 99.83 mm, 104.10 mm, 108.55 mm and 111.41 mm, the deviation from the mean being ± 0.02 mm in each case. The outer cylinder was a precision-bored, perspex tube whose mean bore was found to be 114.27 mm with a maximum deviation of 0.07 mm throughout the axial length. The tube was 500.51 mm long giving the L/c ratios shown in Table 15. The radius ratios for the shafts numbered 1, 2 and 3 corresponded with those used in the flow visualisation tests whereas shaft number 4 gave a reduced radial clearance.

The outer cylinder was mounted between a pair of aluminium blocks located in slideways in the upper and lower guide blocks (Fig.69). The aluminium blocks were moved by means of a simple screw thread arrangement which allowed the outer cylinder to be positioned eccentric relative to the shaft. The positions of the slide blocks, relative to fixed stops marking the concentric setting, were indicated by dial gauges. A hole was drilled through each of the slide blocks to accommodate a Comark NiCr/NiAl thermocouple. The thermocouples were mounted flush with the central bore through the blocks (same diameter as the outer cylinder bore) and cemented in place using 'Araldite'. They were connected to a Comark Electronic Thermometer type 1601 MLS for indication of the temperature of the test fluid at the ends of the rig.

A ferrous wheel having sixty uniform teeth machined on its periphery was attached to the upper end of the shaft. Rotation of the shaft caused the teeth to pass in front of an electro-magnetic perception head (Fig.70), mounted on top of the rig, which sent one impulse per tooth to a Smith's digital tachometer. This instrument counted the number of impulses in a fixed sampling

time and converted this information into the speed of rotation of the shaft which was displayed digitally.

The author had been rather disappointed with the general performance of the speed control system used in the flow visualisation tests. Having encountered similar difficulties, researchers at Leeds University had carried out a series of tests to evaluate some of the systems commercially available at the time. Their results showed that the Fenner Speedranger system was particularly suited to this type of application and it was, therefore, specified for the torque measurement test rig. The selected speed control system consisted of a 0.75 h.p. Fenner drive motor type 55000000 and a Hainsworth controller type 50000041. This combination gave a speed range from zero to 2000 r.p.m. although this required less than one complete turn of their standard speed adjustment knob. As an alternative to this coarse speed control, an equivalent ten-turn potentiometer was connected in parallel with the existing speed control rheostat in such a way that either could be selected by means of a simple switch.

3.3 PRELIMINARY EXPERIMENTS

3.3.1 Calibration of the Instrumentation

3.3.1.1 The Temperature of the Test Fluid

Before being cemented into the slide blocks of the test rig, the two thermocouples were immersed in a beaker of water and the readings of the Comark Electronic Thermometer were compared with those of a calibrated mercury in glass thermometer for temperatures within the range 18 - 35°C. The temperatures sensed by the thermocouples were consistently found to be 0.1°C below those

indicated by the thermometer. A correction factor of $0.1^{\circ}C$ was, therefore, incorporated in the computer programme used to process the experimental data from the torque measurement tests.

3.3.1.2 The Rotational Speed of the Shaft

The speed monitoring equipment was calibrated against a similar system arranged such that it was also activated by the ferrous wheel attached to the upper end of the shaft. The readings of the two digital tachometers were found to give excellent agreement throughout the range of shaft speed available from the drive motor. The selected electromagnetic perception head / digital tachometer combination was, therefore, taken to give an accurate indication of the rotational shaft speed.

3.3.1.3 Eccentricity

The fixed stops bolted to the frame of the rig at the ends of the test length (Fig.69) were used as a positive location of the concentric position. Eccentricity was introduced by simultaneously moving each of the slide blocks, housing the ends of the outer cylinder, the same distance away from the stops. These distances were measured by means of a pair of dial indicator gauges mounted on the front of the rig, thereby allowing particular eccentricity ratios to be selected. The dial gauges were calibrated using slip gauges and their readings were found to be accurate to within ± 0.01 mm throughout the travel of the outer cylinder. Table 16 shows that this level of inaccuracy would not significantly influence the derived eccentricity ratios.

Tests were carried out for each of the shafts at eccentricity ratios from zero to $\varepsilon = 0.90$ in steps of 0.10 . The dial gauge readings corresponding with these eccentricity ratios were calculated assuming that the concentric position was indicated by the fixed stops, as intended in the original design. However, a check on the validity of the concentric setting showed that the assumed eccentricity ratios were slightly inaccurate, presumably due to tolerance accumulation in the manufacture of components for the test rig.

The ends of the perspex cylinder were located in close-tolerance bores in the slide blocks and, therefore, the check on the validity of the concentric setting was carried out in the following two stages. The test rig was assembled without the perspex cylinder and the concentricity of first the cylinder, and then the shaft and the slide block bores was investigated.

A datum mark was drawn on the perspex cylinder to indicate the end which had been at the front and upper end of the test rig. The cylinder was rested horizontally between a pair of Vee blocks on a flat surface (Fig.71) and rotated until the datum was at its highest point. A long-armed dial gauge was then entered into the bore and adjusted on a magnetic base to ensure that the stem was in contact with the lowest part of the bore. Having adjusted the dial gauge to read zero, the cylinder was carefully indexed through ninety degrees and the new reading noted. When the cylinder had been indexed four times, the procedure was repeated at a section further inside the bore (No.2, Fig.71) and then twice more with the dial gauge entered from the opposite end of the cylinder

(Nos. 3 and 4, Fig.71). The final set of measurements is shown in Fig.72. At the first section, for example, the front wall of the cylinder was found to be 0.16 mm thinner than the rear wall. The side walls were also found to be thinner than the rear wall, by 0.05 mm and 0.10 mm for the right-hand and left-hand sides of the rig respectively. Average results derived for the upper and lower ends of the cylinder indicated that, for a central section, the centre of the bore was offset by 0.03 mm towards the left-hand side of the rig and 0.09 mm towards the front. Furthermore, the average results for the upper and lower ends of the cylinder were identical showing that, although eccentric, the axis of the bore was aligned with that of the outer periphery (see Section 3.3.1.4).

Having established the position of the bore in the outer cylinder, the next stage was to determine the position of the shaft relative to the bores in the slide blocks which had housed the ends of the cylinder. The slide blocks were adjusted until they were in contact with the fixed stops and then the variation of the gap between the shaft and the housing bores was measured using slip gauges and a calibrated prism of the type used for screw thread measurements (Fig.73). Gap measurements were carried out at four perpendicular stations using each of the shafts in turn. The results are summarised in Table 17 using the gap at the front of the upper slide block as the standard. The four sets of measurements were expected to be reasonably consistent because the shafts had been turned between centres from solid blocks of aluminium. These were averaged, for accuracy, and the resulting relative clearance data are presented in Fig.74. It is evident that, for the "concentric

setting", the axes of the shaft and the bore housing the ends of the outer cylinder were both eccentric and misaligned. The centre of the upper end of the shaft was found to be 0.040 mm in front of, and 0.240 mm to the right of, the centre of the housing bore whereas the centre of the lower end of the shaft was 0.125 mm in front of the latter.

Having, in effect, established the positions of the shaft and the bore of the outer cylinder relative to the same datum, their own relative positions could be determined. Fig.75 shows that, for the "concentric setting", the centre of the upper end of the shaft was 0.050 mm in front of, and 0.270 mm to the right of, the centre of the outer cylinder bore whereas the centre of the lower end of the shaft was 0.035 mm in front of, and 0.30 mm to the right of, the latter. The axes of the shaft and the outer cylinder bore were, therefore, eccentric and misaligned under these conditions. The misalignment is considered in Section 3.3.1.4.

Eccentricity ratios corresponding with the outer cylinder displacements (x) used in the torque measurement tests were derived using the formula

$$e = \left[(0.005 + x)^2 + (0.150)^2 \right]^{\frac{1}{2}}$$

These are compared with the ratios based on the "concentric setting" in Table 18. The nominal eccentricity ratios were generally found to be insignificantly affected by the eccentricity inherent in the test rig, the notable exceptions being for tests using the larger diameter shafts and small eccentricity ratios.

The basic designs of the flow visualisation and torque measurement test rigs were rather similar and, therefore,

the above procedure was repeated for the former rig. The results of these measurements are summarised in Table 20.

3.3.1.4 Misalignment

In the previous Section, misalignment was shown to be a feature of the torque measurement test rig. The magnitude of the misalignment was derived from the results in Fig.75 using the method indicated in Fig.76 . In this case, the procedure was simplified by the fact that the bore of the outer cylinder was found to be aligned with the peripheral surface and, therefore, the centres C_U and C_L plotted as one on the plan view of the rig. The same basic method would have been used had the axes of the outer cylinder been misaligned although the positions of the shaft centres S_U and S_L would then have been corrected so as to be based on the axis of the outer cylinder bore rather than that of the peripheral surface.

The ends of the shaft were found to be misaligned by 0.255 mm as indicated by the dimension S_US_L in Fig.76 . The corresponding percentage misalignments for each of the shafts are given in Table 19 and it is evident from Table 21 that the flow visualisation test rig was less misaligned than the torque measurement test rig. The derived values were independent of eccentricity because the ends of the outer cylinder were always moved by equal amounts.

3.3.1.5 Torque Measurement

Before being dispatched, the torque transducer and digital torque meter were calibrated as a matched pair in the Vibrometer laboratories. The calibration was checked statically when the equipment was received by the author

and, after a slight adjustment of the zero setting, the accuracy was found to be excellent.

The torque meter incorporated a test circuit which was used periodically during the investigation to check the stability of the unit.

3.3.2 Physical Properties of the Test Fluids

3.3.2.1 The Kinematic Viscosity

Of those test fluids used in the flow visualisation investigation, Carnea 15 and Tellus 21 were also used in the torque measurement investigation. The viscosity characteristics of these test fluids had previously been determined (Fig.8). However, torque measurement tests using a fluid less viscous than Carnea 15 and a fluid more viscous than Tellus 21 were also planned. The low viscosity fluid was required in order that high speed tests using the largest shaft ($\eta = 0.975$) would not exceed the maximum torque of the transducer and the high viscosity fluid was to be used in tests to detect the onset of vortex flow for $\eta = 0.874$ and $\eta = 0.911$. Shell Macron A was selected for the high speed tests and the other test fluid was blended by the author using appropriate measures of Tellus 21 and Shell Talpa 20.

Samples of Macron A and the blended test fluid, named "Mixture A", were pipetted into suitable British Standard 'Suspended Level' viscometers and the viscosity characteristics derived using the procedure in B.S.188:1957. The viscometers were mounted vertically in a holder which was then lowered into a thermostatically controlled constant temperature water bath. A calibrated thermometer was immersed

in the water adjacent to the viscometers and viscosity measurements recorded at temperatures between 15°C and 35°C. Before a reading was accepted, three consecutive tests carried out at the same temperature were required to give a maximum variation of 0.2% in the derived kinematic viscosities. The results of the viscometry tests are summarised in Table 22 and the derived viscosity characteristics are plotted in Fig.77 .

3.3.2.2 The Specific Gravity

A hydrometer was used to measure the variation with temperature of the specific gravities of Macron A, Carnea 15, Tellus 21 and "Mixture A". A measuring cylinder containing a sample of the test fluid was lowered into a thermostatically controlled constant temperature water bath and clamped vertically with the test fluid completely immersed. A calibrated thermometer was mounted adjacent to the measuring cylinder and the hydrometer lowered gently into the test fluid. Results recorded at temperatures between 15°C and 35°C are summarised in Table 23 and the density characteristics are plotted in Fig.78 .

3.4 EXPERIMENTAL PROCEDURE

The power supply to the test rig instrumentation was switched on at least one hour before the start of a test run, this being the recommended minimum warm-up period for the torque measuring system. The rig was normally filled with test fluid during this period. The shaft was rotated slowly whilst the rig was being filled because this was found to aid the release of entrained air pockets.

The shaft speed was either gradually increased or decreased in increments of about 30 r.p.m. in the test runs. Following a speed change, the readings of the various instruments (Fig.70) were allowed time to settle and then the shaft speed, the average driving torque and the upper and lower thermocouple temperatures were recorded. A maximum shaft speed of 1800 r.p.m. was used overall although that for particular test runs was dictated by the viscosity of the test fluid.

Shafts giving radius ratios of 0.874, 0.911, 0.950 and 0.975 (Table 15) were tested for nominal eccentricity ratios between zero and $\varepsilon = 0.9$ in steps of 0.1 (Table 18). The fluids Macron A, Carnea 15, Tellus 21 and "Mixture A" were used. A typical test run lasted about one hour, much shorter than a comparable flow visualisation test because the time consuming adjustment of the stroboscope was no longer necessary.

3.5 PRESENTATION OF RESULTS

The results of the torque measurement tests are presented both as raw data and in the form of friction coefficient characteristics. To simplify computation of the friction coefficient, linear relationships between the density and temperature of the test fluids were derived. The density characteristics of the four fluids used in these tests are plotted in Fig.78 and constants derived from them, based on a reference temperature of $20^{\circ}C$, are summarised in Table 4. Constants for the Walther equation (Appendix I), derived from the recorded viscosity characteristics plotted in Fig.77, are also summarised in Table 4.

The results of a series of tests carried out to detect the onset of instability are presented in Figs. 79 - 84 and Tables 24 - 26 . Raw torque-speed results for wavy vortex flow between eccentric cylinders are plotted in Figs. 87 - 92 for $\eta = 0.911$, Figs. 93 - 97 for $\eta = 0.874$, Figs. 98 - 100 for $\eta = 0.950$, and Figs. 101 - 106 for $\eta = 0.975$. The Reynolds numbers and normalised Taylor numbers at which torque discontinuities were detected in these tests are summarised in Tables 27 - 35 and Figs. 107 - 118.

Friction coefficient characteristics derived from the torque measurement data, using the procedure discussed in Section 3.8, are presented in Figs. 119 - 139. Values for Wendt's empirical constants K and ℓ (Section 3.1.2) derived from Figs. 119 - 132, the results for increasing shafts speeds, are summarised in Tables 37 - 40. Cavitation of the flow occurred in the tests using $\eta = 0.975$ for high eccentricity ratios as shown by the photographs in Figs. 140 - 141. The friction coefficient characteristics derived for these conditions are plotted in Fig.142 . A simple theory for cavitating laminar flow is developed in Appendix VI and predicted friction coefficient characteristics are compared with those for non-cavitating flow in Fig.143 .

Figs. 144 - 155 and Tables 49 - 53 form the basis of an attempt to eliminate the effects of eccentricity and radius ratio from the derived friction coefficient characteristics (Section 3.9.4).

3.6 DISCUSSION OF RAW TORQUE-SPEED RESULTS

3.6.1 Low Reynolds Numbers

The test fluids used in this series of torque measurement tests were "Mixture A" for $\eta = 0.874$ and $\eta = 0.911$, Tellus 21 for $\eta = 0.950$ and Carnea 15 for $\eta = 0.975$. These were selected in order that the critical shaft speed for the appearance of Taylor vortices would be sufficiently high for the corresponding torque discontinuity to be detected accurately in each case. Typical torque-speed data are presented in Fig.79 and it is evident that, for each radius ratio tested, a sudden increase in the slope of the results was followed by a sudden decrease in slope with increasing shaft speed. Visual observation of the flow showed these discontinuities to be caused by the onset of the Taylor vortex and wavy modes of instability respectively. Slope discontinuities were also detected at speeds beyond the onset of the wavy mode and these are discussed in Section 3.6.2.

The results for simple laminar flow (before the first slope discontinuity) gave linear relationships between torque and speed as one would expect from Appendix IV. However, it might, at first, seem strange that the lines do not pass through the origin. The reason for this is simply that the recorded torque was made up of not only that due to viscous drag on the surface of the shaft but also that required to overcome friction in the bearings supporting the shaft. This is discussed further in Section 3.8.

The onset of vortex flow in the torque measurement test rig was found to be considerably influenced by the temperature of the test fluid. It is evident from Figs. 80 to 83 that the critical Reynolds number decreased with increasing temperature for each

radius ratio tested whereas the spacing between the onset of vortex flow and the appearance of waviness was reasonably unaffected by temperature. A summary of these results is presented in Table 24 and the derived critical Taylor numbers are compared with the theoretical predictions of Walowit et al (77) in Table 25. The derived values of T_c were generally found to be less than those predicted theoretically by an amount which increased with increasing temperature. However, the normalised critical Taylor numbers for the onset of wavy vortex flow (T_w/T_c) were in reasonable agreement with the results of previous researchers (Table 1) in spite of the premature appearance of Taylor vortices. Castle et al (10) also reported that the critical Taylor number was temperature dependent although, in their tests, T_c increased with increasing temperature up to about 25°C and was constant for higher temperatures. They suggested that this effect could be attributed to the test fluid in their rig being out of equilibrium. The design of their rig was substantially different from that used by the author and it seems likely that this was an important factor in the respective trends of the results.

Before continuing with the intended programme of research, the possibility that the temperature effects discussed above could have been accounted for by shortcomings in the author's technique was considered.

One possible explanation was that the temperatures sensed by the thermocouples in the test rig were lagging behind the actual temperature of the test fluid. The thermocouples were mounted flush with the bore in the slider blocks at the ends of the outer cylinder (Fig.69) and it was thought possible that the temperature readings might have been influenced by the proximity

of these aluminium blocks. A similar concern was expressed by Debler et al (21) with regard to the results from their test rig. The errors in test fluid temperature measurement which would have accounted for the differences between the maximum and minimum values of T_c in Table 24 are summarised in Table 26 . However, the temperature of the test fluid usually increased by less than $1^{\circ}C$ during each of these test runs and, therefore, the necessary errors in excess of $3^{\circ}C$ were not possible.

The temperature indicated by the lower thermocouple was generally higher than that indicated by the upper thermocouple because of the amount of heat generated in the lower bearing. Consequently, the average of the two thermocouple readings was used to derive the magnitude of the test fluid viscosity for the calculation of the critical Taylor number. The results of Castle (8) suggested that the higher of these readings would have given more realistic results because he also derived low values of T_c when using an average temperature. However, Younes (80) used the average of the temperatures indicated by the thermcouples in his test rig to derive critical Taylor numbers in excellent agreement with those predicted by Walowit et al. The critical values in Table 24 would have been increased somewhat if the higher of the thermocouple readings had been used in each case although the largest difference between any pair of thermocouple readings in this series of tests was only $0.6^{\circ}C$ and, therefore, once again, insufficient to have accounted for the recorded discrepancies.

Becker and Kaye (3) have shown that the onset of Taylor vortices can be significantly influenced by radial temperature gradients. Heating of the inner rotating cylinder was found to stabilise the flow whereas heating of the outer stationary

cylinder destabilised the flow. The substitution of data for Shell Tellus oils into their equation 37 suggested that, for T_c to be reduced to 75% of that predicted theoretically (for isothermal flow), the temperature at the outer cylinder would have to be about 3.5°C above that at the inner cylinder. The outer cylinder in the test rig was perspex (poor conductor) whereas the inner cylinder was solid aluminium (good conductor) and, therefore, the heat generated by viscous shearing of the test fluid could have given rise to a temperature gradient across the radial clearance in this direction.

The effect of eccentricity on T_c was also relevant to the author's concentric cylinder results discussed above because it was shown in Section 3.3.1.3 that the "concentric setting " actually represented eccentricity ratios of 0.02, 0.03, 0.05 and 0.11 for $\eta = 0.874$, 0.911, 0.950 and 0.975 respectively. Castle observed that the onset of Taylor vortices between eccentric cylinders occurred in two distinct stages with increasing shaft speed, firstly the appearance of a system of vortices which did not extend to the outer cylinder in the vicinity of the wide gap and then the sudden radial growth of the vortices to completely fill the radial clearance. The critical Taylor number for the appearance of the first stage was found to be reduced by small eccentricity settings (compared with T_o) whereas that for the second stage was everywhere increased by increasing eccentricity. Castle was only able to detect the onset of the second stage from his outer cylinder torque measurements. However, Younes reported that the onset of the first stage was indicated by a discontinuity in his inner cylinder torque measurements. Hence, it was not entirely unreasonable that the author's inner cylinder torque measurements for the "concentric setting" should have resulted in

values of T_c somewhat below those predicted theoretically for $\varepsilon = 0$. The normalised Taylor numbers (T_c/T_o) derived from the low temperature results (Table 25) were of the same order of magnitude as Younes' eccentric cylinder results although it might be considered significant that he quoted a typical test fluid temperature of 20°C. The high temperature results gave values of (T_c/T_o) which were considerably lower, however, suggesting that the temperature effect could not be attributed to the eccentricity inherent in the test rig.

The effect of higher eccentricity settings on the value of T_c was determined from the results of a series of torque measurement tests using $\eta = 0.911$ and $\eta = 0.975$. It is evident from Figs. 84 and 86 that the derived results generally plotted within Di Prima's(25) stability boundaries for $\theta = 0$ and $\theta = \pi/2$ and were, therefore, reasonably in agreement with the theoretical predictions of Ritchie (56). The results of Jones (41) and Younes (80) in Fig.85 suggested that their rig was initially more misaligned than that used in the present investigation (Section 3.3.1.4). Jones did not specify the actual misalignment in their test rig although he reported that the effect of increasing the misalignment was to progressively reduce the amount by which the onset of vortex flow was stabilised for increasing eccentricity. The author's results for $\eta = 0.975$ (Fig.84), for example, would have plotted below Jones' aligned cylinder results for $\eta = 0.970$ (Fig.85) and above the misaligned cylinder results of Younes for $\eta = 0.950$.

It was decided that tests to further investigate the recorded temperature dependence of the critical Taylor number were not justified since time was already at something of a premium. Furthermore, the main purpose of the torque measurement

tests was to investigate the effects of flow changes beyond the onset of the wavy mode of instability.

3.6.2 High Reynolds Numbers

The aim of this part of the investigation was to determine whether the torque measurement results were significantly affected by the transition processes observed within the wavy mode during the flow visualisation tests. Two test fluids were used with three of the four shafts tested (the exception being that giving $\eta = 0.950$) so that a large range of Reynolds number was investigated overall. These test fluids were generally less viscous than those discussed in Section 3.6.1 and, therefore, the onset of vortex flow was often observed at shaft speeds which were too low for the corresponding torque discontinuity to be detected accurately. Because of the stabilising effect of eccentricity, however, detection was sometimes possible for eccentric shaft settings and normalised critical Taylor numbers derived from tests using $\eta = 0.911$ and $\eta = 0.975$ are presented in Fig.84 .

It is evident from Fig.79 that torque discontinuities were recorded beyond the onset of the wavy mode in the tests discussed in Section 3.6.1. The significance of these discontinuities is discussed below by reference to the raw torque-speed results from typical test runs using the less-viscous test fluids. Results from tests in which the shaft speed was progressively increased from rest are plotted in Figs. 87 - 106 . The results for $\eta = 0.911$ are discussed before those for $\eta = 0.874$ because of the large number of flow visualisation tests which had been performed using the former geometry.

3.6.2.1 Tests Using $\eta = 0.911$

The test fluids used with this shaft were Tellus 21 and Carnea 15 and the raw torque-speed data are presented in Figs. 87 - 92 . For Tellus 21 and $\varepsilon = 0.03$, Fig.87 shows that the most striking phenomenon, with increasing shaft speed, was a large reduction in the magnitude of the recorded torque (labelled d) at a shaft speed of 765 r.p.m. A sudden, large torque reduction was recorded in each of several similar tests carried out to investigate this phenomenon although the Reynolds number at which it occurred was not unique. In the particular test shown in Fig.87, a second, smaller torque reduction (e) was recorded after the shaft speed had been increased to 1245 r.p.m. and an increase in the recorded torque (f) was detected at N = 1605 r.p.m. Three slope discontinuities (a, b, c) were also detected at shaft speeds of 245, 325 and 465 r.p.m. respectively. These magnitude and slope discontinuities were also found to be reproducible although, once again, non-uniqueness was a feature of the Reynolds number at which they occurred. This was also the case for each of the geometries tested, typical examples being given in Table 34 for $\eta = 0.874$ and $\eta = 0.975$.

The large torque reduction (d) was recorded at a Reynolds number of 590 in the test plotted in Fig.87 . It is evident from the flow visualisation results in Fig.11 that this was within the range in which the onset of transitional state flow would have been expected to occur. This flow change was observed to be both sudden and violent and, therefore, one might reasonably expect that the torque measurement results would be significantly affected by it. Consequently, it seems more than likely that the large

torque reduction was caused by the onset of transitional state flow. Similarly, the onset of secondary wavy mode flow was observed to occur between Reynolds numbers of 900 and 1050 in the flow visualisation tests for $\varepsilon = 0.02$ and this compared favourably with the position of the smaller torque reduction (e) in Fig.87. This discontinuity was recorded at Re = 1035 and one might reasonably expect it to be less dramatic than that associated with the onset of transitional state flow because the change to the secondary wavy mode was observed during the stroboscopic tests to be gradual and not at all violent. The results suggested, therefore, that both the onset of transitional state flow and that of the secondary wavy mode can be detected by discontinuities in the torque-speed characteristics.

The first slope discontinuity (a) was detected at a Reynolds number of 180 and Table 24 shows that this was beyond the onset of the wavy mode. The three slope discontinuities (a, b, c) were recorded before the onset of transitional state flow (marked by discontinuity d) and they were, therefore, within the primary wavy mode. The discontinuity recorded near the end of this particular test run (f) was within the secondary wavy mode. The primary wavy mode torque discontinuities (a, b, c) were detected at Reynolds numbers of 180, 250 and 355 respectively. It is evident from Fig.79 that slope increases were also recorded as the shaft speed was increased beyond the onset of the wavy mode in the tests using the higher viscosity test fluids. Using $\eta = 0.911$ and "Mixture A", for example, slope discontinuities were detected at Reynolds numbers of 210 and 290 in the test shown.

Markho (47) also recorded torque discontinuities after the onset of the wavy mode and Jones (41) reported that these were the result of circumferential wave number changes. This is consistent with the author's observations using the flow visualisation test rig. Using $\eta = 0.911$ and the concentric setting, for example, wavy mode flow was observed to be generally steady except when the wave number was about to change in which case oscillation of the wave structure usually occurred. It is not unreasonable to expect that this type of change would have significantly affected the torque measurement results.

Jones, using $\eta = 0.90$, investigated the circumferential wave number changes between $n = 3$ and $n = 7$ and reported that there were two types; non-unique $n \pm 1$ changes and unique $n+2$ changes. Both types of wave number change resulted in torque discontinuities although those for the $n+2$ type changes were more severe. This range of circumferential wave numbers was not investigated in the same detail by the author because of the unsuitability of the stroboscopic technique for low shaft speeds. It is evident from Fig.44 that wave numbers less than nine were recorded in narrow bands of Reynolds number within the primary wavy mode and, therefore, because of the speed increments used, the wave number often changed to modes greater than $n+2$ when the shaft speed was increased. Consequently, in any particular test run, all of the wave numbers between $n = 3$ and $n = 9$ were not observed and it follows that the number of torque discontinuities would have been less than the number of possible wave number changes.

A summary of the circumferential wave number changes observed within the primary wavy mode in the flow visualisation tests using the "concentric setting" is presented in Table 12. It is evident from Table 27 that the primary wavy mode torque discontinuities (a, b, c) from Fig.87 were in reasonable agreement with observed changes from n = 3 to n = 4, n = 6 to n = 7 and n = 8 to n = 9 respectively. The secondary wavy mode torque discontinuity (f) was detected at a Reynolds number of 1435 and this was within the range in which a change from n = 5 to n = 4 was observed in the flow visualisation tests (Fig.44).

Using $\varepsilon = 0.11$ and Tellus 21, only three torque discontinuities could be identified although others could have been obscured by the considerable experimental scatter for this test run in Fig.87. The three discontinuities detected were slope increases (labelled j and k) at shaft speeds of 245 and 735 r.p.m. and a reduction in the magnitude of the recorded torque (ℓ) at N = 800 r.p.m. The magnitude of this torque reduction was much less than that recorded using $\varepsilon = 0.03$, although this might have been expected from the flow visualisation tests. Increasing the eccentricity was observed to reduce the stability of wavy mode flow in general and that of the primary wavy mode in particular. Consequently, the onset of transitional state flow appeared to be less violent and was more difficult to detect visually. It seems reasonable to suggest, therefore, that it would have had much less influence on the torque measurement results.

A single torque reduction, much smaller in magnitude than that for the "concentric setting", was recorded in

each of the tests using $\varepsilon \geq 0.11$. The inference from this is that a form of transitional state flow occurred for each eccentricity setting even though wavy mode flow had deteriorated to such an extent for $\varepsilon > 0.20$ that it could not be investigated stroboscopically. A summary of the torque discontinuities detected in the test runs plotted in Figs. 87 - 89 is presented in Table 27 and the boundaries defined by these results are plotted in Fig.107.

The transitional state boundaries derived from the torque measurement results gave reasonable agreement with those recorded in the flow visualisation tests (Fig.11), although the range of eccentricity covered by the latter was rather limited. Using $\eta = 0.90$ and Tellus 13, Jones detected the onset of a quasi-turbulent flow regime by an increase in the slope of the torque-speed characteristic (for increasing shaft speed) and, for small eccentricity settings, this was in excellent agreement with the author's onset of transitional state flow. He reported that the effect of eccentricity was stabilising, however, although this seems to contradict his visual results for this geometry which indicated that the onset of the strong wavy mode was quasi-turbulent for large eccentricity settings.

As well as the transitional state boundaries in Fig.107, the torque discontinuities also apparently defined two wave number boundaries. This is not necessarily the case, however, because of the effect of eccentricity on the stability of wave numbers within the primary wavy mode. For the "concentric setting", the flow was generally observed to be steady unless the wave number was about to change whereas, as the eccentricity was increased, the bands of

steady wave numbers were gradually replaced by bands in which the wave number changed frequently, usually between two adjacent values.

Predominant wave number boundaries were derived by Jones from photographs of the flow taken at $\theta = 0$, $\pi/2$, π and $3\pi/2$. His upper and lower bound results are compared with the torque discontinuities discussed above in Figs. 108 and 109 respectively. The discontinuities detected at low Reynolds numbers gave excellent agreement with the $n=4$, $n=5$ and $n=6$ boundaries and it is evident from Fig.108 that the discontinuities detected at high Reynolds numbers defined boundaries for which predominant wave numbers of seven and eight were consistent with the trends of Jones' results. For the "concentric setting", the results suggested that the primary wavy mode discontinuities (a, b, c) in Fig.87 were probably the result of wave number changes from $n=4$ to $n=5$, $n=6$ to $n=7$ and $n=7$ to $n=8$ respectively. Two of these changes involved higher wave numbers than would have been inferred from the flow visualisation results in Table 12, although this could possibly be accounted for by non-uniqueness of the wave number boundaries and differences between the critical Taylor numbers recorded in each of the author's rigs.

In Section 3.6.1, the normalised Taylor number for the onset of the wavy mode was found to give reasonable agreement with the results of previous authors even though the onset of vortex flow had occurred earlier than would normally have been expected. It follows that the onset of the wavy mode was also premature and, therefore, it seems reasonable to suggest that the wave number boundaries would have been affected in the same way. However, these effects

would probably not have significantly influenced the correlation between the normalised results of the author and Jones in Figs. 108 and 109. A summary of the normalised Taylor numbers derived for the torque discontinuities from Figs. 87 - 89 is presented in Table 28 and the corresponding transitional state boundaries are plotted in Fig.110 .

The torque discontinuity detected shortly before the onset of transitional state flow using $\varepsilon = 0.11$ (Fig.107) was beyond the range of Fig.108. However, analysis of the results from particular flow visualisation tests showed that it was in reasonable agreement with a change from a mode in which the number of circumferential waves fluctuated between nine and ten to a mode in which the wave number fluctuated between eight and nine. This suggests that the discontinuity was probably the result of a change from the predominantly $n = 10$ mode to the predominantly $n = 9$ mode. The $n = 10$ mode was not indicated by a discontinuity in the torque measurement results for the "concentric setting" although it was often observed in the flow visualisation tests for nominal eccentricity settings less than $\varepsilon = 0.2$. It is evident from Table 12 that the usual sequence with increasing shaft speed was for changes from $n = 9$ to $n = 10$ and then from $n = 10$ to $n = 9$ to be observed before the onset of transitional state flow.

Secondary wavy mode torque discontinuities were not recorded in any of the torque measurement tests using $\varepsilon > 0.03$ and Tellus 21. In these tests, the maximum shaft speed was reduced, however, to avoid the possibility of test fluid being pumped from the rig through the upper bearing under these conditions. A series of tests using

Carnea 15 was carried out to investigate the secondary wavy mode in more detail. The maximum Reynolds number for these tests was typically twice that for those using Tellus 21. Because of the lower viscosity of Carnea 15, the onset of transitional state flow occurred at a much lower shaft speed in these tests and only one primary wavy mode torque discontinuity was recorded. The torque discontinuities detected from the typical series of results in Figs. 90 - 92 are summarised in Tables 29 and 30.

For the "concentric setting", a sudden reduction in the magnitude of the recorded torque was detected at a shaft speed of 375 r.p.m. (Re = 705) and this again compared favourably with the range in which the onset of transitional state flow was observed in the flow visualisation tests (Fig.12). It is evident from Fig.90 that the magnitude of this torque reduction was less than that recorded using Tellus 21 for the "concentric setting" (Fig.87) although this was probably influenced by the lower viscosity of Carnea 15. Torque reductions could not be detected from the results of tests using eccentric cylinders. From the results discussed above, for Tellus 21, one would have expected smaller torque reductions to mark the onset of transitional state flow under these conditions. However, because of the small torque reduction recorded for the "concentric setting", these were presumably indistinguishable from slope discontinuities.

Using $\varepsilon = 0.03$ (Fig.90), slope discontinuities were recorded at Reynolds numbers of 545, 1050 and 1440. The second of these compared favourably with the observed onset of secondary wavy mode flow (Fig.12) and it follows, therefore, that the first discontinuity was within the primary wavy mode and the third was within the secondary wavy mode. Table 12 suggests that the primary

wavy mode discontinuity was probably the result of a circumferential wave number change from n = 10 to n = 9. The secondary wavy mode discontinuity was in excellent agreement with that recorded using Tellus 21 for the "concentric setting" (f, Fig.87) and this was correlated with an observed change from n = 5 to n = 4 in the above discussion.

The Reynolds numbers at which torque discontinuities were recorded in the tests using $\varepsilon \leqslant 0.90$ (Figs. 90 - 92) are plotted in Fig.111 and the corresponding normalised Taylor numbers are plotted in Fig.112. Four boundaries were indicated by the results and it is evident from Figs. 107 and 110 that two of these were in reasonable agreement with the transitional state boundaries derived using Tellus 21. The two remaining boundaries were within the secondary wavy mode. The first of the secondary wavy mode boundaries compared favourably with changes observed from the predominantly n = 5 mode to the predominantly n = 4 mode for $\varepsilon \leqslant 0.17$. Fig.48 shows that the n = 4 mode was not recorded in the flow visualisation tests for $\varepsilon = 0.22$, although it would have been expected according to the torque measurement tests. However, using stroboscopic illumination, the n = 5 mode was observed to change infrequently to a mode which could not be positively identified. This was probably the n = 4 mode. The second of the secondary wavy mode boundaries was assumed to mark a change to the predominantly n = 3 mode. The Reynolds numbers at which this change was detected from the torque measurement results was near to the maximum used in the flow visualisation tests and it is not surprising, therefore, that the n = 3 mode was rarely observed. A change from n = 4 to n = 3 was

observed only once, in fact, in a test using the "concentric setting" and in which the shaft speed was increased fairly rapidly using large increments. This change occurred at a Reynolds number of 2085.

The wave number boundaries shown in Fig.112 could not be correlated with observed circumferential wave number changes for nominal eccentricity settings above $\varepsilon = 0.2$ because the stroboscopic technique was found to be of little use under these conditions. However, it is evident from Figs. 108 and 110 that these boundaries were consistent with the trends of those derived from the tests using Tellus 21.

3.6.2.2 Tests Using $\eta = 0.874$

Tests were carried out for this geometry using either Tellus 21 or Carnea 15. The results of typical test runs are plotted in Figs. 93 - 97 and the torque discontinuities derived from these are summarised in Table 31. The discontinuities generally occurred as increases in the slope of the torque-speed results (for increasing shaft speed) although some slope decreases and torque reductions were also recorded. The latter were, in each case, smaller than that recorded using Tellus 21 and the "concentric setting" (Fig.93) and they could not be correlated with the onset of any particular regime of wavy mode flow.

Tables 10 and 31 show that, with the exception of the torque reduction recorded at Re = 1540, the torque discontinuities for the "concentric setting" were in reasonable agreement with circumferential wave number changes observed in the flow visualisation tests. The slope increase detected at N = 230 r.p.m. (Re = 240) in the test using Tellus 21, for example, could possibly have been the

result of a wave number change from n = 3 to n = 5. These modes could not be investigated thoroughly in the flow visualisation tests because of limitations in the stroboscopic technique for low shaft speeds. However, a change from n = 3 to n = 5 was observed to occur between Reynolds numbers of 205 and 250 in one of the tests. (Results presented by Jones also suggested that there were usually three circumferential waves at the onset of the strong wavy mode for this geometry.) The last change observed as the shaft speed was increased towards its maximum value in the flow visualisation tests was from n = 3 to n = 2 (Table 10). However, the torque measurement results for the test using Carnea 15 (Fig.96) showed a discontinuity at Re = 2965 suggesting that a change from the n = 2 mode occurred at a shaft speed beyond that used in the flow visualisation tests.

Using $\eta = 0.874$, wavy mode flow was observed to be more regular than that for smaller radial clearances (higher η) and the violent onset and disturbed nature of transitional state flow (Section 2.6.1.1) were not observed. In Section 2.6.1.5, it was suggested that the n = 4/3 mode (Table 10) was probably a form of transitional state flow subdued by the general increase in stability of the flow under these conditions. The circumferential wave number changed frequently between n = 3 and n = 4 in this mode (n = 4/3) which was only observed within a narrow band of Reynolds numbers between the steady n = 5 and n = 3 modes. The torque measurement results showed a single discontinuity corresponding with the n = 4/3 mode, presumably because of the magnitude of the speed increments used in these tests.

Six slope decreases were derived (for increasing shaft speed) from the results plotted in Figs. 93 - 97 and it would appear that five of these were the result of changes from the n = 3 mode. For the "concentric setting", slope decreases were recorded at Re = 755 and Re = 1840 in the test using Tellus 21 and it is evident from Table 10 that these compared favourably with observed wave number changes from n = 6 to n = 5 and from n = 3 to n = 2 respectively. This type of torque discontinuity was also recorded at Re = 1695 in the test using Tellus 21 for $\varepsilon = 0.10$ and at Re = 2855 and Re = 2730 in the tests using Carnea 15 for $\varepsilon = 0.10$ and $\varepsilon = 0.20$ respectively. Each of these discontinuities occurred near the upper end of one of the three bands in which the n = 3 mode was observed in the corresponding flow visualisation tests.

Wavy mode flow for this geometry was observed to be considerably influenced by eccentricity (Section 2.6.1.6). Unique flow configurations were observed for each of the eccentric conditions investigated stroboscopically and these are summarised in Table 11. It is evident from Fig.113 that the recorded torque discontinuities (Table 31) showed reasonable agreement with the observed changes between the various flow regimes. Using $\varepsilon = 0.10$, for example, the discontinuity at Re = 215 compared favourably with an observed wave number change from n = 3 to n = 6. The intermediate n = 4 and n = 5 modes were not recorded although it is possible that these would have occurred if small shaft speed increments had been used in the tests. Furthermore, the torque measurement results suggest that a change from the n = 3 mode would have been observed if the

flow visualisation tests had been continued beyond Re = 2800. The slope decrease at Re = 2855 was the final discontinuity recorded in the test shown in Fig.96 and, therefore, the new mode would presumably have been observed up to about Re = 4000. However, using $\varepsilon = 0.20$, the slope decrease marking the end of the n = 3 mode was followed by a slope increase at Re = 3025 suggesting that two different modes would have been observed beyond the n = 3 mode in this case.

The range of circumferential wave numbers recorded in the tests using the various eccentricity settings showed considerable variation. Using $\varepsilon = 0.20$, wave numbers of seven and eight were regularly recorded and a flow regime in which the n = 7 mode was progressively expelled from the test length by the n = 3 mode (labelled n=7,3) was observed. Wave numbers of nine and ten were observed in the tests using $\varepsilon = 0.30$ and $\varepsilon = 0.40$. These wave number variations meant that the boundaries defined by the recorded torque discontinuities in Fig.113 could not be interpreted as predominant wave number boundaries. The flow visualisation and torque measurement results were, therefore, rationalised and a phase diagram (Fig.114) derived for the various flow regimes. Boundaries could not be derived for $\varepsilon > 0.40$ because the flow was found to be too unsteady under these conditions for the satisfactory operation of the stroboscopic flow visualisation technique.

The normalised Taylor numbers for the torque discontinuities discussed above are used to define a phase diagram in Figs. 115 and 116. (The values of T_c for eccentricity ratios between $\varepsilon = 0.10$ and $\varepsilon = 0.70$ were assumed from those recorded in the torque measurement tests using "Mixture A" for the "concentric setting" and using Tellus 21 for $\varepsilon = 0.80$ and $\varepsilon = 0.90$.)

Jones, using $\eta = 0.85$, recorded torque measurement results which were ill defined with large inflexions at random points. However, he correlated one particular slope increase with the onset of a quasi-turbulent flow regime which occurred at a normalised Taylor number decreasing from $(T/T_c) = 3.1$ for $\varepsilon = 0$ to $(T/T_c) = 2.3$ for $\varepsilon = 0.6$. Using $\eta = 0.874$, the author observed several different flow regimes for $(T/T_c) > 3$ (Figs. 115 and 116) although these would not have been described as quasi-turbulent. As reported in Section 2.6.1, wavy mode flow for $\eta = 0.874$ was everywhere more regular than that for $\eta = 0.911$ and using the "concentric setting", in particular, the observed modes were very well defined.

3.6.2.3 Tests Using $\eta = 0.950$

The results of a series of typical tests using Carnea 15 are plotted in Figs. 98 - 100 and the torque discontinuities recorded in these tests are summarised in Table 32. The discontinuities were usually detected as increases in the slope of the torque-speed characteristics (for increasing shaft speed) although some small torque reductions were also recorded.

For the "concentric setting" ($\varepsilon = 0.05$), the first discontinuity occurred at Re = 575 and was probably caused by the onset of the secondary wavy mode. Transitional state flow was observed in the flow visualisation tests for this geometry (Section 2.6.1.3) although it did not normally persist beyond about Re = 630. In the primary wavy mode (low Re), wave numbers between three and nineteen were recorded within narrow bands of Reynolds number (Fig.49). The detection of torque discontinuities corresponding with

these wave number changes would have required tests using a fluid more viscous than Carnea 15. However, there proved to be insufficient time for these tests to be carried out.

In the secondary wavy mode, the wave number was everywhere observed to change frequently between two or more values although the flow visualisation test results suggested that n = 10, 12 and 14 were the predominant wave numbers. Table 13 shows the range of Reynolds number in which each of these modes was observed and it is evident from Fig.117 that the recorded torque discontinuities ($\varepsilon = 0.05$) were in reasonable agreement with the predominant wave number changes. The results suggest, therefore, that the torque discontinuities in the secondary wavy mode were probably caused by n - 2 type predominant wave number changes. Wave number changes of the $n \pm 1$ type were observed within each of the predominant wave number bands, although these could not be correlated with torque discontinuities. The usual sequence with increasing shaft speed was for the n and n + 1 modes to be observed (alternately) at the lower end of the band whereas the n and n - 1 modes were observed at the upper end of the band. In the case of the n = 14 mode, for example, the wave number frequently changed between n = 14 and n = 15 initially although the n = 15 mode was replaced by the n = 13 mode as the shaft speed was increased.

Wavy mode flow for $\eta = 0.950$ was found to be generally unsteady with frequent wave number changes and continual oscillation of the wave structure. Consequently, the stroboscopic flow visualisation technique was not suitable for nominal eccentricity settings larger than $\varepsilon = 0.1$ and,

even for this setting, only up to a maximum Reynolds number of 720. However, observations of the predominantly n = 14 mode in these tests suggested that its boundaries were probably marked by the first and second torque discontinuities recorded using $\varepsilon = 0.12$ (Table 32). In Fig.117, boundaries were inferred from the torque discontinuities derived from Figs. 98 - 100, although it cannot be assumed that these relate to n = 10, 12 and 14 modes for the entire range of eccentricity tested. Five torque reductions were recorded in these tests whilst the remaining discontinuities were detected as increases in the slope of the torque-speed results. The author could attach no significance to this. However, the torque reductions were recorded at Re = 1300, 1190, 1255, 920 and 635 in the tests using $\varepsilon = 0.05$, 0.12, 0.21, 0.80 and 0.90 respectively.

Jones derived a boundary for the onset of a quasi-turbulent flow regime from his torque measurements for this geometry. He reported that it was everywhere marked by a slope increase (for increasing shaft speed) which was progressively delayed as the eccentricity was increased. Typically, the torque discontinuity was recorded at Re = 600 for $\varepsilon = 0$, and at Re = 1050 for $\varepsilon = 0.8$.

3.6.2.4 Tests Using $\eta = 0.975$

Tests were carried out for this geometry using either Carnea 15 or Macron A. The results of typical test runs are plotted in Figs. 101 - 106 and the torque discontinuities derived from these are summarised in Table 33. The discontinuities generally occurred as increases in the slope of the torque-speed characteristics, although some slope

decreases and torque reductions were also recorded (Table 35). A single sudden torque increase was also recorded (for increasing shaft speed) at Re = 2475 in the test using $\varepsilon = 0.91$ and Macron A.

Flow visualisation tests were not carried out for this geometry because wavy mode flow was found to be extremely unsteady even for the "concentric setting". Consequently, the torque measurement results could not be correlated with observed wave number changes in this case. However, several boundaries were inferred from the recorded torque discontinuities (Fig.118) suggesting that changes were occurring within the wavy mode even though the general appearance of the flow under these conditions could only be described as quasi-turbulent.

For the "concentric setting" ($\varepsilon = 0.11$), a slope increase at Re = 240 was followed by a slope decrease at Re = 260 in the test using Carnea 15 (Table 33). These discontinuities marked the onset of vortex flow and the wavy mode respectively. The onset of vortex flow was recorded for each eccentricity setting tested, and the discontinuities form the first boundary in Fig.118 . The second boundary possibly represents the onset of the wavy mode although this could not be detected from the torque measurement results for some of the tests because of an insufficient number of experimental points in the critical region. Furthermore, the discontinuities recorded in the tests using $\varepsilon = 0.32$, 0.61, 0.81 and 0.91 were not slope decreases.

Rather surprisingly, a torque discontinuity was recorded before the onset of vortex flow in each of the tests using

$\varepsilon \geqslant 0.61$ and Carnea 15. Table 33 shows that torque reductions were recorded at Re = 145 and Re = 155 using $\varepsilon = 0.61$ and $\varepsilon = 0.71$ respectively, whilst slope decreases were recorded at Re = 290 and Re = 305 using $\varepsilon = 0.81$ and $\varepsilon = 0.91$ respectively. Cavitation was observed to occur when this low clearance shaft ($\eta = 0.975$) was used at large eccentricity settings (Section 3.9.3) and it is probable, therefore, that these discontinuities were in some way influenced by this phenomenon. A slope decrease might reasonably be expected when one considers the growth of a region of cavitating flow with increasing shaft speed (i.e. viscous drag reduced by progressive development of air pockets) although sudden torque reductions cannot be explained in this manner. Torque reductions were also recorded at low shaft speeds in the tests using Macron A and large eccentricity settings (Fig.106).

3.7 DERIVATION OF NON-DIMENSIONAL TORQUE CHARACTERISTICS

3.7.1 The Non-Dimensional Parameter

Four different fluids were used in the various torque measurement tests discussed in Section 3.6. The manner in which compatible characteristics were derived from the results of tests using different fluids for a given rig geometry (η and ε) is discussed below.

The raw torque-speed data were converted into a non-dimensional form using the friction coefficient, C_f, and Reynolds number, Re. Several previous researchers have presented their torque measurement results in terms of non-dimensional parameters based on the friction coefficient because, when C_f is plotted against Re, all of the data

recorded in the simple laminar flow regime for a given geometry coalesces on to a curve that is independent of viscosity (Appendix IV). Friction coefficient characteristics are usually plotted on logarithmic axes because of the large ranges of C_f and Re that can be effectively compressed into these axes.

3.7.2 Elimination of Unwanted Components from the Recorded Torque

Friction coefficient characteristics derived from the results of typical tests using the "concentric setting" are presented in Figs. 119 - 122. For each radius ratio, the characteristic derived for the most viscous test fluid was found to be everywhere above that predicted by simple laminar flow theory (Appendix IV) even though laminar flow had been observed using low shaft speeds in each case. Furthermore, these characteristics were incompatible with those derived for the less viscous test fluids. The explanation of these effects was that the torque transducer had monitored, not only, the torque driving the shaft against the viscous drag of the test fluid, but also, that required to overcome friction in the bearings supporting the shaft.

The bearing torque was estimated from the results of a series of tests carried out with the rig drained of test fluid except for that surrounding the lower bearing. The results showed that the bearing torque remained reasonably constant throughout each of the tests at values between 0.04 Nm and 0.08 Nm depending on which shaft was used. It seemed reasonable to assume, therefore, that the subtraction of a suitable constant torque correction factor from each of the results for a particular test run would eliminate the effect of the bearing torque and allow compatible friction coefficient characteristics to be derived. Fig.121 shows that, after 0.06 Nm had been

subtracted from each torque measurement recorded in a test using $\eta = 0.950$ and Tellus 21, the derived friction coefficient characteristic was in excellent agreement with the theoretical relationship for simple laminar flow at low Re. The results of other tests embracing simple laminar flow were corrected in the same way and, in each case (Figs. 119, 120, 122), the necessary torque correction factor compared favourably with the estimated bearing torque.

It was established, therefore, that the theoretical relationship for simple laminar flow could be used as a datum to which the results of suitable tests could be adjusted by the subtraction of a torque correction factor whose magnitude was determined by trial and error. However, this datum was of little use for the results from those tests not embracing simple laminar flow. It is evident from Figs. 119 - 122 that, for any particular test run, the results least affected by the subtraction of a constant torque correction factor were those recorded using high shaft speeds. The reason for this was simply that, in comparison with the magnitude of the recorded torque, the correction factor became less significant as the shaft speed was increased. The correction procedure was, therefore, most accurate for the high-speed results and these were used as the datum to which the results from tests using lower viscosity fluids were corrected.

Consequently, the procedure used to eliminate the effects of bearing torque from the friction coefficient characteristics for a given geometry was as follows:

(i) a constant torque correction factor was subtracted from the torque data recorded using the higher

viscosity test fluid such that results from the simple laminar flow regime were in reasonable agreement with the theoretical relationship given in Appendix IV;

(ii) suitable constant torque correction factors were then subtracted from the torque data recorded using each of the lower viscosity test fluids such that the corrected results gave reasonable agreement wherever they overlapped.

It is evident from Figs. 119 - 122 that the above procedure was successfully applied to the results of typical test runs using each of the shafts. In each case, the corrected friction coefficient characteristics (for the various test fluids) merged to give a single characteristic and the required torque correction factors compared favourably with the estimated bearing torque. Fig.122 shows that correlation between the corrected characteristics using Carnea 15 and Macron A for $\eta = 0.975$ was limited to a small range of Reynolds number. However, this was probably due to the comparatively low viscosity of Macron A because the corrected results for Carnea 15 gave excellent agreement with the theoretical relationship for simple laminar flow at low Re. Consequently, the author felt justified in neglecting the incompatible results recorded at low shaft speeds using Macron A.

The procedure described above was used to eliminate the effect of bearing torque from the results discussed in Section 3.6. The derived friction coefficient characteristics are plotted in Figs. 123 - 139 and these are discussed in Section 3.8.

3.8 DISCUSSION OF THE FRICTION COEFFICIENT CHARACTERISTICS

3.8.1 For Increasing Shaft Speed

The friction coefficient characteristics derived using the procedure described in Section 3.7 generally consisted of a number of linear segments. The Reynolds numbers at which discontinuities were detected in the characteristics for typical tests using the "concentric setting" (Fig.123) are summarised in Table 36 and, as one might expect, these were in reasonable agreement with those derived from the corresponding raw torque-speed plots (Tables 27, 29 and 31 - 33).

It is evident from the derived characteristics that the Reynolds numbers at which particular discontinuities were detected for a given geometry were not unique. Using $\eta = 0.911$ and the "concentric setting", for example, a sudden reduction in the magnitude of the friction coefficient was followed by a slope increase and then a slope decrease for both Tellus 21 and Carnea 15, although these discontinuities occurred at Re = 605, 1000 and 1385 respectively in the test using Tellus 21, and at Re = 735, 1075 and 1515 respectively in the test using Carnea 15. In Section 3.6.2, the corresponding torque-speed discontinuities were correlated with the onset of transitional state flow, the onset of the secondary wavy mode, and a wave number change from $n=5$ to $n=4$ respectively. Non-uniqueness was reported to be a feature of each of the wavy mode flow changes observed in the flow visualisation tests.

Because of this non-uniqueness and rather than duplicating the results discussed in Section 3.6, a series of basic slopes were derived from the friction coefficient characteristics for each geometry tested. Using $\eta = 0.874$ and the "concentric setting", for example, the characteristics for both Tellus 21 and Carnea 15 were

reasonably represented by basic slopes of -0.43, -0.81 and -0.51 with slope discontinuities at Re = 760 and Re = 1035. Similarly, using $\eta = 0.911$ and the "concentric setting", a basic slope of -0.50 everywhere gave a good approximation to the characteristics for both Tellus 21 and Carnea 15. Eccentricity generally reduced the amount by which the characteristics were influenced by individual discontinuities with the result that there was usually less scatter about the derived basic slopes in these cases. Using $\eta = 0.874$ and $\varepsilon = 0.10$, however, it is evident from Fig.124 that, although the characteristics for both Tellus 21 and Carnea 15 were reasonably represented by a basic slope of -0.55, the results at high Reynolds numbers were somewhat different. This effect is discussed in Section 3.8.2. Results using $\eta = 0.975$ and Carnea 15 for $\varepsilon = 0.91$ are not plotted in Fig.132 because they were found to be incompatible with those from tests using Macron A. This was attributed to the occurrence of cavitation when these test conditions were used (section 3.9.3).

The basic slopes (ℓ) derived from the friction coefficient characteristics plotted in Figs. 123 - 132 are summarised in Tables 37 - 40. It is evident from the results discussed in Section 3.6.2 that, for any given geometry, there was reasonable agreement between the Reynolds numbers at which basic slope changes occurred and those at which particular discontinuities were detected in the raw torque-speed data. The implication of this was that the flow changes which caused the basic slope changes were probably more fundamental than those which brought about the remaining torque discontinuities.

Using $\eta = 0.911$ and small eccentricity ratios, the fundamental flow change was shown to be the onset of transitional state flow. This was not entirely unexpected because it was observed to be both sudden and violent in the flow visualisation tests for these

conditions. However, Figs. 123 and 124 show that, whereas this onset resulted in a sudden reduction in the magnitude of the friction coefficient for $\varepsilon = 0.03$, a well defined decrease in the magnitude of the basic slope was detected for $\varepsilon = 0.11$. The results indicated that the transitional state was less significant for larger eccentricity settings which was also consistent with observations in the flow visualisation tests. It was reported in Section 2.6.1 that the onset of transitional state flow became more difficult to detect with increasing ε because of the general degradation of wavy mode flow under these conditions.

Using $\eta = 0.874$ and the "concentric setting", the two basic slope changes (Table 37) were in excellent agreement with observed wave number changes from $n = 6$ to $n = 5$, and from $n = 5$ to $n = 3$ respectively. A variety of unusual flow regimes were observed in the flow visualisation tests using eccentric shaft settings although it is evident from Figs. 124 - 126 that the characteristics for $\varepsilon = 0.10$, 0.20 and 0.30 could each be reasonably defined by single basic slopes.

Using $\eta = 0.950$ and the "concentric setting", the results suggested that the fundamental flow change was from the predominantly $n = 14$ mode to the predominantly $n = 12$ mode. The two basic slope changes derived for $\varepsilon = 0.12$ compared favourably with observed changes to the predominantly $n = 14$ mode and from the predominantly $n = 10$ mode to what was assumed to be the predominantly $n = 8$ mode.

It is evident from Tables 37 - 40 that basic slope changes were derived from the characteristics for each of the shafts in the range of ε for which wavy mode flow was found to be too unsteady for the stroboscopic technique to be used (Section 2.6.1). Although the corresponding fundamental flow changes could not

normally be identified in these cases, the results suggested that some of the changes occurred outside the wavy mode. Basic slopes with magnitudes close to unity were derived and it is evident from Appendix IV that these probably indicated results recorded in the simple laminar flow regime. In these cases, therefore, the first fundamental flow change would have been the onset of vortex flow. Basic slopes of this magnitude were derived from the results for large eccentricity settings because, as discussed in Section 3.6.1, the critical Reynolds number was generally delayed by increasing eccentricity. The discrepancies between these basic slopes and unity could probably be attributed to the author's correction procedure (Section 3.7.2) being least accurate for low shaft speeds when the level of the recorded torque was comparatively small.

The derived friction coefficient characteristics were generally in excellent agreement with the results of previous authors. Typical of this agreement was the correlation between the results for $\eta = 0.950$ and the "concentric setting" shown in Table 43. These results compare values for the torque at various Reynolds numbers in the wavy mode with those which would have been recorded had the flow remained laminar.

The magnitude of the constant K in Wendt's empirical formula (Section 3.1.2) was derived for each of the basic slopes (ℓ) discussed above. It is evident from Tables 37 - 40 that the results for high Re using the "concentric settings" were in excellent agreement with those recorded by Wendt ($K = 0.46$, $\ell = 0.5$). The basic slope changes derived from the results for low Re were not reported by Wendt although his increments between successive test points were much larger than those used by the author. However, Tables 37 and 41 show that the results for

$\eta = 0.874$ compared favourably with those presented by Debler et al. The author recorded a well defined basic slope change to -0.81 at Re = 760 whereas Debler et al recorded a sudden torque reduction at about Re = 850. Furthermore, the value of K derived from their results above Re = 1070 was larger than would have been expected although this is not particularly significant because K was found to be considerably influenced by small changes in the magnitude of the basic slope.

Debler et al did not present results for $\eta = 0.911$ although their results for $\eta = 0.935$ were in reasonable agreement with those in Table 38. They also recorded a sudden torque reduction in these tests and this was in excellent agreement with that recorded by the author using $\eta = 0.911$. Their tests using $\eta = 0.950$ were somewhat limited although no sudden torque reductions were recorded in this case. The author's results suggested that this type of discontinuity was replaced by a basic slope change from -0.59 to -0.50 for this geometry (Table 39). This was endorsed by results recorded by Donnelly (Table 41) which also showed the tendency towards a small negative slope at low Re.

Rather surprisingly, the results recorded by Wendt for $\eta = 0.680$, 0.850 and 0.935 each indicated a decrease in the magnitude of the basic slope at a Reynolds number of about 700 (Table 44). This compared favourably with trends shown by the results of Vohr, although basic slope changes of this type were not recorded by the author or Debler et al for geometries other than $\eta = 0.950$. However, it is evident from Table 38 that a basic slope change from -0.65 to -0.47 was recorded at Re = 710 in the test using $\eta = 0.911$ and $\varepsilon = 0.11$. One might infer from this that the basic slope changes recorded at about Re = 700 by Wendt, Donnelly and Vohr resulted from there being eccentricity inherent

in their test rigs. This was supported to some extent by the author's results for $\eta = 0.950$ because this "concentric setting" was actually equivalent to $\varepsilon = 0.05$ (Section 3.3.1.3) and a basic slope change from -0.63 to -0.43 was recorded using $\varepsilon = 0.12$ (Table 39).

Predictably, the eccentric cylinder case has attracted much less attention than the concentric cylinder case and, therefore, the results with which those of the author could be compared were somewhat limited. Results were presented by Castle and Mobbs for $\eta = 0.899$ and eccentricity ratios up to $\varepsilon = 0.80$ although their maximum Reynolds number was rather low because of the small shaft speed increments used. However, the basic slopes derived from their results are summarised in Table 46 and it is evident from Table 38 that these were in excellent agreement with the author's results for $\eta = 0.911$. The eccentric cylinder case was also investigated by Vohr and his results for $\eta = 0.910$ and $\eta = 0.990$ were found to give excellent agreement with those recorded by the author using $\eta = 0.911$ and $\eta = 0.975$ respectively (Tables 38, 40 and 42).

In Section 3.8.4, an attempt is made to eliminate the effects of both radius ratio and eccentricity ratio from the friction coefficient characteristics in Figs. 123 to 132 in order that an empirical formula similar to that derived by Wendt for the concentric cylinder case might be established. This did not prove to be entirely successful because of the general non-conformity of the eccentric cylinder results for the various rig geometries. An important factor in this was the effect of eccentricity on a basic slope whose magnitude was about 0.25. It is evident from Table 40 that basic slopes of this magnitude were recorded for most of the eccentricity settings using $\eta = 0.975$, although their occurrence

was generally delayed by increasing eccentricity. In the test using $\varepsilon = 0.11$, for example, a basic slope of -0.24 was detected between Re = 250 and Re = 425 whereas, using $\varepsilon = 0.81$, a basic slope of -0.27 was not detected below Re = 1995. This trend was also reflected in Vohr's results for $\eta = 0.990$ (Table 42) although not generally by the author's results for $\eta = 0.874$, 0.911 and 0.950 . However, slopes of this magnitude were recorded in the tests using $\eta = 0.950$ and eccentricity ratios between $\varepsilon = 0.51$ and $\varepsilon = 0.70$ (Table 39) and the results of Donnelly, using the concentric setting for this geometry (Table 41), also indicated a basic slope of -0.20 for low Re.

Basic slopes of about -0.25 were recorded by Vohr for $\eta = 0.910$ although, in this case, eccentricity had the opposite effect to that discussed above for the smaller radial clearances. The Reynolds numbers at which these basic slope changes occurred, decreased for increasing eccentricity. Using $\varepsilon = 0$, for example, Vohr recorded a basic slope of -0.17 for Reynolds numbers larger than 1.3×10^4 (Table 41) whereas, for $\varepsilon = 0.89$, a basic slope of -0.27 was recorded for Reynolds numbers larger than 2400. These results suggest that basic slopes of this type would probably have been recorded in the author's tests using large eccentricity settings for this geometry if the maximum Reynolds number had been increased somewhat.

It is evident from Table 45 that a basic slope of -0.25 was in excellent agreement with the results from the actual bearing tests of Duffin and Johnson (34), Ramsden (53) and Booser et al (4), and also with the predictions of the turbulent flow theories of Burton (7) and Ng and Pan (50).

3.8.2 For Increasing and Decreasing Shaft Speed

Whilst it was not the intention of the author to duplicate the results discussed in Section 3.8.1, this is sometimes necessary in order that particular points may be clarified in the following discussion.

3.8.2.1 Tests Using $n = 0.874$

For each test fluid using the "concentric setting", there were several well defined discontinuities in the results for both increasing and decreasing shaft speed (Figs. 133 and 134) and the characteristics were clearly non-unique. The discontinuities derived from these results are summarised in Table 47.

Using 'Mixture A' (Fig.133(a)), sudden changes in the magnitude of the friction coefficient were recorded for both increasing and decreasing shaft speed although the slope of the characteristics was reasonably unaffected by these discontinuities. Slope changes were detected in the results for $Re \geqslant 700$, however, and under these conditions, the characteristics for increasing and decreasing shaft speed showed excellent agreement. A single, well defined magnitude discontinuity was recorded using Tellus 21 and increasing shaft speed (Fig.133(b)) although this did not occur until about $Re = 1550$. A slope change from -0.42 to -0.86, recorded at $Re = 715$ in this test (Table 47), gave excellent agreement with a similar discontinuity recorded using 'Mixture A'. In the flow visualisation tests for this geometry, the circumferential wave number decreased from $n = 6$ to $n = 3$ as the shaft speed was gradually increased from $Re = 765$ to $Re = 1100$. Fig.133 shows this range of Re to be in excellent agreement with that for which the increased slope was recorded in the tests using 'Mixture A' and Tellus 21. Furthermore, it is interesting to

note that the results from the test using Tellus 21 might have been interpreted as a series of sudden reductions in the magnitude of C_f at Re = 760, 870 and 990. These discontinuities compared favourably with wave number changes observed in the flow visualisation tests (Table 10).

In Fig.133, the characteristics for decreasing shaft speed generally plotted below those for increasing shaft speed. This effect was also recorded by Debler et al who suggested that it could be attributed to the non-unique nature of wavy mode flow. Non-uniqueness of the wavy mode was investigated by Coles who reported that the flow state present at any particular shaft speed was considerably influenced by the previous history of operation of the test rig. A large number of flow states (defined by the circumferential and axial wave numbers) were found to be admissable at any particular shaft speed. Consequently, the differences between the friction coefficient characteristics for increasing and decreasing shaft speed might reasonably be attributed to different flow states having been present in the two cases.

The results discussed above showed that a decrease in the number of circumferential waves generally resulted in the friction coefficient being reduced below that which would have been expected had the change not occurred. It follows, therefore, that the characteristics for decreasing shaft speed probably plotted below those for increasing shaft speed because there were more circumferential waves in the latter case. This was endorsed, to some extent, by results from the flow visualisation tests using $\eta = 0.874$ and the "concentric setting". For example, the n = 6 mode was observed up to about Re = 800 when the shaft speed was increasing whereas the change from n = 5 to n = 6

sometimes did not occur before Re = 300 when the shaft speed was decreasing. Consequently, there was generally a large range of Re in which the n = 6 mode was observed for increasing shaft speed and the n = 5 mode was observed for decreasing shaft speed.

Relating the above hypothesis to the results plotted in Fig.133(a) suggests that, in this particular test, the wave number changed at Re = 365 when the shaft speed was increasing to a mode which was also present at this Reynolds number for decreasing shaft speed. This change was probably followed by an increase and then a decrease in the number of circumferential waves at Re = 415 and Re = 595 respectively.

It is evident from Fig.134(a) that the friction coefficient characteristics for decreasing shaft speed did not always plot below those for increasing shaft speed. In this particular test, the shaft speed was rapidly increased to a high value and results were then recorded as the shaft speed was progressively decreased and increased. The rapid initial increase in shaft speed raised the magnitude of the friction coefficient above that recorded when the shaft speed was gradually increased with the result that the characteristic for decreasing shaft speed plotted above that for increasing shaft speed in this case. According to the above discussion, this would occur if the wave number was generally higher for decreasing shaft speed than for increasing shaft speed. The characteristic for increasing shaft speed was found to give reasonable agreement with those from tests using 'Mixture A' and Tellus 21 (Fig.133) and also with that from a test using Carnea 15 in which the shaft speed was progressively increased and then decreased in the usual manner (Fig.134(b)). In the

latter case, the characteristic for decreasing shaft speed again generally plotted below that for increasing shaft speed.

The characteristics derived from the results of typical tests using Carnea 15, for eccentricity ratios up to $\varepsilon = 0.40$, are plotted in Fig.135. Using $\varepsilon = 0.10$, 0.20 and 0.30 for increasing shaft speed, a discontinuity was recorded between Re = 2000 and Re = 2250 which resulted in the friction coefficient being increased above that which would otherwise have been recorded. Corresponding reductions in the magnitude of the friction coefficient were recorded using $\varepsilon = 0.10$ and 0.30 for decreasing shaft speed at Re = 1750 and Re = 1450 respectively. Using $\varepsilon = 0.20$ (Fig.135(b)), a slope reduction at Re = 2250 was followed by a reduction in the magnitude of C_f at Re = 2750 although neither of these was recorded for decreasing shaft speed.

3.8.2.2 Tests Using $\eta = 0.911$

The friction coefficient characteristics derived from the results of typical tests using 'Mixture A', Tellus 21 and Carnea 15 and the "concentric setting" are presented in Figs. 136(a), 136(b) and 137(a) respectively. A sudden reduction in the magnitude of C_f was recorded for increasing shaft speed in each of the tests and, as discussed in Section 3.8.1, these were within the range of Re in which the onset of transitional state flow was observed in the flow visualisation tests for this geometry. A sudden reduction in the magnitude of C_f recorded before the onset of transitional state flow in the test using Tellus 21 was found to be in reasonable agreement with an observed wave number change from n = 10 to n = 9.

There was a tendency for the slope of the characteristics to increase across these magnitude discontinuities (for increasing shaft speed). Larger slope changes were recorded at Re = 990 and Re = 1080 in the tests using Tellus 21 and Carnea 15 respectively and these compared favourably with the range of Re in which the onset of secondary wavy mode flow was observed in the flow visualisation tests. Using Carnea 15 (Fig.137(a)), a slope decrease at Re = 1500 was followed by a slope increase at Re = 1950 and results from the flow visualisation tests suggested that these were probably caused by changes from n = 5 to n = 4, and n = 4 to n = 3 respectively.

The characteristics for decreasing shaft speed again generally plotted below those for increasing shaft speed at low Re. The reason for this was that the change from the transitional state to the primary wavy mode did not result in an increase in the magnitude of the friction coefficient, and, therefore, the results recorded within the primary wavy mode for decreasing shaft speed plotted below those for increasing shaft speed. This is consistent with observations of wavy mode flow because it was reported in Section 2.6.1 that, whereas the onset of the transitional state was both sudden and violent for increasing shaft speed, the onset of the primary wavy mode was difficult to detect for decreasing shaft speed.

The characteristics derived from the results of typical tests using Carnea 15 and eccentricity ratios up to $\varepsilon = 0.50$ are plotted in Figs. 137(b) to 137 (f). Hysteresis-type effects were recorded in each case although these were particularly evident at high Re. A single reduction in the magnitude of C_f, corresponding with the onset of transitional state flow, was recorded for each eccentricity ratio although, as discussed in

Section 3.8.1, these were smaller than those for the "concentric setting".

3.8.2.3 Tests Using $\eta = 0.950$

In the test using the "concentric setting" shown in Fig.138(a), a slope decrease at Re = 650 was followed by a reduction in the magnitude of C_f at Re = 1300. These discontinuities were in reasonable agreement with the observed predominant wave number changes from n = 14 to n = 12 and n = 10 to n = 8 respectively (Section 3.6.2.3). The change from n = 12 to n = 10 for increasing shaft speed was not detected from the friction coefficient characteristic although it was marked by a discontinuity in the raw torque-speed results.

A sudden increase in the magnitude of C_f was recorded at Re = 1000 for decreasing shaft speed and the results were then in excellent agreement with those for increasing shaft speed. This magnitude discontinuity was in reasonable agreement with the Reynolds number at which the predominant wave number change from n = 12 to n = 10 was observed in the flow visualisation tests for increasing shaft speed. However, it probably resulted from a different change, perhaps that from n = 8 to n = 10, because particular wave number changes generally occurred at lower Re for decreasing shaft speed than for increasing shaft speed.

The characteristics derived from the results of typical tests using eccentricity ratios up to $\varepsilon = 0.31$ are plotted in Figs. 138(b) to 138(d). In each case, a sudden increase in the magnitude of C_f was recorded at a lower Re for decreasing shaft speed than that at which a sudden decrease in the magnitude of C_f was recorded for increasing shaft speed. The characteristics

were particularly non-unique at high Re.

3.8.2.4 Tests Using $\eta = 0.975$

Wavy mode flow for this geometry was observed to be extremely unsteady even for the "concentric setting" and, therefore, the stroboscopic flow visualisation technique could not be used. However, the friction coefficient characteristics (Figs. 139(a) to 139(j)) showed several well defined discontinuities suggesting that significant flow changes had occurred during the various tests. Sudden changes in the magnitude of C_f were recorded for both increasing and decreasing shaft speed and non-uniqueness was clearly a feature of the results for each eccentricity ratio. The results from tests using large eccentricity ratios were also considerably influenced by cavitation of the flow downstream of the narrow gap. This phenomenon is discussed further in Section 3.8.3 .

3.8.3 Air Cavitation

Cavitation of the flow was observed in the tests using large eccentricity settings and $\eta = 0.975$. Air pockets formed initially in the centre of the test length at a section downstream of the narrow gap and these increased in size as the shaft speed was increased whilst others were formed above and below, along a vertical line. For large Reynolds numbers (tests using Macron A), the flow around the entire circumference of a central section of the test length was contaminated by aerated fluid which had been washed downstream. Photographs of this sequence of events in tests using Carnea 15 and Macron A are presented in Figs. 140 and

141. The onset of vortex flow cannot be detected from the photographs because the aluminium flake particles used to effect flow visualisation were not used in these particular tests.

Oil normally contains between 8 and 12% by volume of dissolved air, and if the pressure to which it is subjected falls below the saturation pressure, air comes out of solution to maintain the saturation pressure locally. The full Sommerfeld solution of Reynolds equation for a long journal bearing predicts that the minimum pressure occurs at a section ($\theta = \bar{\theta}$) in the diverging clearance beyond the narrow gap ($\theta = \pi$). It is shown in Appendix V that, according to this analysis, sub-atmospheric pressures would have been generated in the tests using Carnea 15 for Reynolds numbers greater than 172, 99 and 36 using $\varepsilon = 0.71$, 0.81 and 0.91 respectively. The saturation pressure of air in oil is near to atmospheric and, therefore, these Reynolds numbers also represent the predicted onset of air cavitation for the specified conditions.

As one would expect, the torque measurement results were considerably affected by the formation of air pockets. It is evident from Fig.142 that, of the derived friction coefficient characteristics from the tests using Carnea 15, those for $\varepsilon = 0.81$ and $\varepsilon = 0.91$ plotted below the corresponding lines predicted by simple long journal bearing theory, whereas the results recorded before the onset of vortex flow for $\varepsilon = 0.71$ were in excellent agreement with the theoretical predictions. This is consistent with the development of cavitation in these tests because the Reynolds number at which the air pockets began to form decreased with increasing eccentricity. It is evident from Figs. 140 and 141

that, for $\varepsilon = 0.91$, the air pockets had reached a more advanced stage in their development by Re = 170 than those for $\varepsilon = 0.71$ had reached by Re = 495. (It is interesting to note that the corresponding maximum sub-atmospheric pressures predicted by the full Sommerfeld solution for these two cases are 7906 N/m^2 and 3958 N/m^2 respectively.) In tests using Macron A and $\varepsilon = 0.91$, it was necessary for the Reynolds number to approach a value of 1000 before the air pocket formation resembled that observed at Re = 170 in tests using Carnea 15 and $\varepsilon = 0.91$. It is not surprising, therefore, that the corresponding friction coefficient characteristics for this geometry were found to be incompatible, (Section 3.8.1). For lower eccentricity ratios, the derived characteristics from tests using Carnea 15 and Macron A were compatible.

In Appendix VI, an expression for the friction torque on the journal of a long cavitating bearing is derived. The analysis uses boundary conditions first suggested by Swift (70) and Stieber (67), whereby simple laminar flow is assumed between $\theta = 0$ and a section $\theta = \bar{\theta}$ ($> \pi$) where the pressure gradient is assumed to be zero and the pressure is atmospheric. The cavitating region of the flow is assumed to extend from $\theta = \bar{\theta}$ to $\theta = 2\pi$ taking the form of streamers between circumferential air pockets. Predicted friction coefficient characteristics for $\varepsilon = 0.71$, 0.81 and 0.91 assuming cavitating and non-cavitating laminar flow are compared in Fig.143. It is evident from Fig.142 that the results from the test using Carnea 15 and $\varepsilon = 0.91$ would plot between the 'non-cavitating' and 'cavitating' lines in Fig.143. However, before the onset of

vortex flow (indicated by a decrease in the slope of the characteristic), the experimental results tend to plot away from the 'non-cavitating' line and towards the 'cavitating' line as the Reynolds number increases. This is consistent with the progressive development of the air pocket formation. Limitations on the accuracy of the simple theory derived in Appendix VI include the assumption that the cavitating region always extends to $\theta = 2\pi$ and the exclusion of sub-cavity pressures from the analysis. Many experimentalists have recorded the presence of a sub-cavity pressure loop immediately upstream of the cavitating region although this normally occupies a very narrow zone. The pressure in the cavitating region has been shown to remain nearly constant and slightly below atmospheric.

3.8.4 An Empirical Relationship for Superlaminar Flows

Wendt (79) reported that his outer cylinder torque measurements for the concentric cylinder case could be defined by the empirical formula

$$C_f = K \left[\frac{(R_o - R_i) R_o}{R_i^2} \right]^{0.25} \frac{1}{Re^{\ell}}$$

in which K and ℓ were constants taking values of 0.46 and 0.5 respectively for Reynolds numbers between 400 and 10^4, and 0.07 and 0.3 respectively for larger Reynolds numbers. In this Section, it is proposed to investigate the extent to which the effects of both the eccentricity and radius ratios can be eliminated from the friction coefficient characteristics in Figs. 123 to 132. The reader will, no doubt, appreciate that, because of the range of slopes previously

discussed in Section 3.9.1, it will not be possible for a unique relationship to be derived. However, this type of analysis is, nevertheless, considered useful.

Considering the radius ratios $\eta = 0.874$, 0.911, 0.950 and 0.975 in turn, a suitable value of a variable log F was subtracted from the results for each of the eccentric settings such that they were then in reasonable agreement with those for the "concentric setting" (Section 3.3.1.3) for as large a range of Reynolds number as possible. The modified friction coefficient characteristics are plotted in Figs. 144 to 147 and the corresponding values of F are summarised in Table 48. It is evident from Fig.148 that the variation of F with eccentricity ratio was reasonably independent of radius ratio and that, of the five trial relationships shown, the best approximation to the results was given by

$$F_1 = 1 + \varepsilon^3$$

A mean curve was derived from the values of F in Table 48 and the results are summarised in Table 49, where they are compared with those for the five curves shown in Fig.148. The method of least squares was used to fit a curve of the form

$$F_2 = 1 + a\,\varepsilon^b$$

to the derived values of F for $\varepsilon = 0.1$, 0.3, 0.5, 0.7 and 0.9. Re-writing the equation as

$$\log (F_2 - 1) = \log a + b \log \varepsilon$$

gives the following

$$-1.921 = \log a - b$$

$$-1.222 = \log a - 0.523\,b$$

$$-0.854 = \log a - 0.301\,b$$

$$-0.530 = \log a - 0.155\, b$$

$$-0.125 = \log a - 0.046\, b$$

Two unknowns cannot normally be made to satisfy more than two conditions and, therefore, it was necessary to determine values of a and b which fitted the above five equations as nearly as possible. To set up the pair of normal equations required by the method of least squares, each of the equations of condition were multiplied by the coefficient of a in that equation and then added together, and then the procedure was repeated multiplying by the coefficient of b in each equation. Hence, the normal equations were found to be

$$-4.652 = 5 \log a - 2.025\, b$$

$$-2.905 = 2.025 \log a - 1.390\, b$$

and therefore

$$a = 0.62 \qquad b = 1.79$$

or

$$F_2 = 1 + 0.62\, \varepsilon^{1.79}$$

It is evident from Table 50 that the sum of the squares of the deviations (E) of F_2 from the mean curve for F was found to be 0.0589 whereas a corresponding value of E = 0.0042 was derived for F_1 (Table 51). The inaccuracy of the solution for F_2 was brought about because the error in the function $\log (F_2 - 1)$ was minimised, thereby giving undue weight to the values of F near to 1. However, taking F_1 to be a reasonable approximation to a solution, an approximate linearization of the problem was achieved by expanding each of the equations of condition in a generalized Taylor series about the point ($a_o = 1$, $b_o = 3$) according to

$$f_i(a,b) = f_i(a_o,b_o) + \frac{\partial f_i}{\partial a}\bigg|_{a_o,b_o}(a-a_o) + \frac{\partial f_i}{\partial b}\bigg|_{a_o,b_o}(b-b_o)$$

in which $f_i = a\,\varepsilon^b + 1 - F = 0$ in this case, and therefore

$$\frac{\partial f_i}{\partial a} = \varepsilon^b$$

$$\frac{\partial f_i}{\partial b} = a\,\varepsilon^b \ln \varepsilon$$

Using the five equations of condition

$$a\,0.1^b - 0.012 = 0$$
$$a\,0.3^b - 0.060 = 0$$
$$a\,0.5^b - 0.140 = 0$$
$$a\,0.7^b - 0.295 = 0$$
$$a\,0.9^b - 0.750 = 0$$

it followed that for the point $(a_o = 1,\ b_o = 3)$

$$-0.011 + 0.001\,(a-1) + 0.001\,(b-3)\ln 0.1 = 0$$
$$-0.033 + 0.027\,(a-1) + 0.027\,(b-3)\ln 0.3 = 0$$
$$-0.015 + 0.125\,(a-1) + 0.125\,(b-3)\ln 0.5 = 0$$
$$0.048 + 0.343\,(a-1) + 0.343\,(b-3)\ln 0.7 = 0$$
$$-0.021 + 0.729\,(a-1) + 0.729\,(b-3)\ln 0.9 = 0$$

or re-writing $(a-1)$ as u and $(b-3)$ as v

$$0.001\,u - 0.0023\,v = 0.011$$
$$0.027\,u - 0.0325\,v = 0.033$$
$$0.125\,u - 0.0866\,v = 0.015$$
$$0.343\,u - 0.1223\,v = -0.048$$
$$0.729\,u - 0.0768\,v = 0.021$$

The normal equations were constructed in the manner described above and were solved to give values of 0.03 and 0.19 for u and v respectively from which it followed that a = 1.03 and b = 3.19. Hence

$$F_3 = 1 + 1.03\,\varepsilon^{3.19}$$

which has a least squares error of E = 0.0037 compared with 0.0042 for F_1. One further application of the generalized Taylor series to expand the equations of condition about the point ($a_o = 1.03$, $b_o = 3.19$) gave the solution

$$F_4 = 1 + 1.04\,\varepsilon^{3.23}$$

although the improvement in the error term E was not evident until the sixth decimal place.

It is evident from Fig.148 that, of the five trial solutions

$$F = \frac{2(1 + 2\varepsilon^2)}{(2 + \varepsilon^2)(1 - \varepsilon^2)^{\frac{1}{2}}}$$

was the most inaccurate. However, when the derived values of F from Table 49 were plotted against this function (Fig.149), they were found to give excellent agreement with the solution

$$F_5 = 0.22\left[\frac{2(1 + 2\varepsilon^2)}{(2 + \varepsilon^2)(1 - \varepsilon^2)^{\frac{1}{2}}}\right] + 0.80$$

giving an error term of E = 0.0003 for the five eccentricity values used above. A disadvantage of this solution was that it gave F a value of 1.02 for zero eccentricity and, therefore, the correction factor to be applied to the friction coefficient characteristics in this case would not have been zero. To overcome this, the solution

$$F_6 = 0.23 \left[\frac{2(1 + 2\varepsilon^2)}{(2 + \varepsilon^2)(1 - \varepsilon^2)^{\frac{1}{2}}} \right] + 0.77$$

was used. This solution was slightly less accurate than that for F_5 giving an error term of $E = 0.0008$. However, this was evidently a significant improvement on the previous solutions. F_6 is plotted against eccentricity ratio in Fig.150 and again in Fig.151 for comparison with results derived from the eccentric cylinder torque measurements of Vohr (76) and Castle and Mobbs (9).

Values of F were derived from their results in the manner described above using the magnitude of the difference between the friction coefficient characteristic for each eccentricity setting and that for the concentric setting at a Reynolds number of 1000. Vohr did not present concentric cylinder results for $\eta = 0.990$ and, therefore, in this case, the eccentric cylinder results were based on those for $\varepsilon = 0.08$, the derived values of log F then being adjusted in order that F for $\varepsilon = 0.08$ plotted on the curve for F_6. The friction coefficient characteristics presented by Castle and Mobbs were based directly on their outer cylinder torque measurements and, therefore, the values of F derived from their results were multiplied by the factor $\left[(1 + 2\varepsilon^2)/(1 - \varepsilon^2)\right]$, the ratio journal/bearing torque according to simple long journal bearing theory for a 2π oil film (full Sommerfeld).

The effect of radius ratio was eliminated from the results in Figs. 144 to 147 in much the same way as the effect of eccentricity was eliminated from the original friction coefficient characteristics. Suitable values of a variable log K' were subtracted from the results for $\eta = 0.874$, 0.911 and 0.950 such that they were then in reasonable agreement with those for $\eta = 0.975$ for as large a range of Reynolds number as possible. The values of log K' and the corresponding values of K' are summarised in Table 52. Following Wendt's empirical

formula K' was plotted against $\left[(R_o - R_i)R_o/R_i^2\right]^{0.25}$ and it is evident from Fig.152 that the results could be expressed with reasonable accuracy by the formula

$$K' = 2.52 \left[\frac{(R_o - R_i)R_o}{R_i^2}\right]^{\frac{1}{4}}$$

Ideally, the friction coefficient characteristics for the various geometries would have been related to the condition $\eta = 1$ rather than $\eta = 0.975$. However, the above formula gave $K' = 0$ for $\eta = 1$ whereas log K' was required to be zero for the datum condition. This difficulty was overcome by using $\eta = 0.999$ as the datum condition and defining a variable K'' equal to K' times a constant (thereby ensuring the same differences between the values of both log K'' and log K' for any given pair of radius ratios). Now letting $K'' = 1$ for $\eta = 0.999$, then

$$\log K'' = \log K' + \log C$$

$$0 = -0.348 + \log C$$

and, therefore, $C = 2.23$. The values of K'' for the other four radius ratios are summarised in Table 52 and it follows that

$$K'' = 5.62 \left[\frac{(R_o - R_i)R_o}{R_i^2}\right]^{\frac{1}{4}}$$

This relationship for K'' is plotted against radius ratio in Fig.153 and again in Fig.154 for comparison with values derived from the results of various authors (again using Re = 1000).

The "corrected" friction coefficient characteristic is plotted in Fig.155 and considerable scatter is evident particularly for low Reynolds numbers. However, for $Re \geqslant 1000$, the results were found to be bounded by the relationships

$$(C_f/FK'') = 0.073/Re^{0.50}$$

and $$(C_f/FK'') = 0.013/Re^{0.25}$$

It is evident from Figs. 144 to 147 that this scatter was mainly due to the inability of the present method to entirely eliminate the effects of eccentricity from the results for $\eta = 0.950$ and $\eta = 0.975$. For the concentric cylinder case, $F = 1$ and using the first of the two expressions above and substituting for K'' gives

$$C_f = 0.41 \left[\frac{(R_o - R_i)R_o}{R_i^2} \right]^{\frac{1}{4}} \frac{1}{Re^{0.5}}$$

in excellent agreement with Wendt's empirical formula. For the eccentric cylinder case

$$C_f = K_3 \left[\frac{(R_o - R_i)R_o}{R_i^2} \right]^{\frac{1}{4}} \left[\frac{2(1 + 2\varepsilon^2)}{(2+\varepsilon^2)(1-\varepsilon^2)^{\frac{1}{2}}} + 3.35 \right] \frac{1}{Re^{\ell}}$$

where $0.017 \leq K_3 \leq 0.094$

and $0.25 \leq \ell \leq 0.50$

3.9 CONCLUSIONS CONCERNING THE TORQUE MEASUREMENT TESTS

Inner cylinder torque measurements can be used to detect both the onset of Taylor vortex flow and the appearance of waviness at the cell boundaries. The onset of Taylor vortices is marked by an increase in the slope of the torque-speed data whereas the onset of the wavy mode of instability is marked by a decrease in the slope. Eccentricity generally increases the critical Taylor number T_c although the amount by which the flow is stabilised against the onset of vortex flow decreases as the radius ratio increases.

For wavy mode flow, the boundaries between predominant circumferential wave number regimes are marked by discontinuities in the torque-speed data. These discontinuities often take the form of increases in the slope of the torque-speed characteristics. Using $\eta = 0.911$, the onset of transitional state flow results in a sudden reduction in the magnitude of the recorded torque for increasing shaft speed and the magnitude of the reduction is significantly affected by the stability of primary wavy mode flow. This discontinuity is particularly evident for the concentric cylinder case. Using $\eta = 0.874$, a change from the $n = 3$ mode is marked by a decrease in the slope of the torque-speed characteristic for increasing shaft speed. Using $\eta = 0.950$, discontinuities in the secondary wavy mode are generally caused by changes of the $n - 2$ type. Using $\eta = 0.975$ and large eccentricity ratios, the appearance of cavitation downstream of the narrow gap results in a decrease in the slope of the torque-speed characteristics.

For the test rig used, friction coefficient characteristics relating to the viscous drag on the shaft can be derived by the subtraction of a constant torque correction factor from the torque

measurements. Basic slopes defined by the derived friction coefficient characteristics suggest that the various observed regimes of wavy mode flow are not equally important with regard to their effect on the power requirements to drive the shaft. Significant flow changes are indicated by the results for $\eta = 0.975$ even though wavy mode flow is everywhere extremely unstable in this case.

Differences between the derived characteristics for increasing and decreasing shaft speed can be accounted for by the non-unique nature of circumferential wave number changes.

Wendt's empirical formula is confirmed for the concentric cylinder case although the influence of test rig geometry cannot be entirely eliminated from the eccentric cylinder results. However, for $Re \geq 1000$, the results suggest that the magnitude of the friction coefficient can be expressed as

$$C_f = K_3 \left[\frac{(1-\eta)}{\eta^2}\right]^{\frac{1}{4}} \left[\frac{2(1+2\varepsilon^2)}{(2+\varepsilon^2)(1-\varepsilon^2)^{\frac{1}{2}}} + 3.35\right] \frac{1}{Re^{\ell}}$$

where $0.017 \leq K_3 \leq 0.094$

$0.25 \leq \ell \leq 0.50$

CHAPTER 4

REVIEW OF THEORETICAL LITERATURE CONCERNING TAYLOR VORTEX FLOW

4.1 THE CONCENTRIC CYLINDER CASE

In 1916, Rayleigh (54) derived a simple criterion for the inertial instability of curved flows. He considered an element of ideal fluid moving along a circular path of radius r_1 with a circumferential velocity v_1. The criterion was based on the balance between the centrifugal and pressure forces acting on the element when it is displaced to a radius r_2 where the velocity of other fluid elements is v_2. Angular momentum is conserved for an inviscid fluid and, therefore, it was shown that the pressure force would restore equilibrium if

$$\left| v_2 r_2 \right| > \left| v_1 r_1 \right|$$

Applied to the flow between concentric, rotating cylinders, Rayleigh's criterion predicts stability if the modulus of the circulation increases in passing from the inner to the outer cylinder, or

$$\left(\frac{\omega_o}{\omega_i} \right) > \left(\frac{R_i}{R_o} \right)^2 \qquad \text{for stability.}$$

According to Rayleigh's criterion, therefore, the flow between a fixed, outer cylinder and a rotating, inner cylinder cannot be stable. However, in a brilliant contribution to the literature, Taylor (71) showed that the presence of viscosity acts as a damper to delay the onset of instability until a critical condition is reached. Taylor predicted the onset of instability,

verified his calculations experimentally, and described the appearance of the resulting secondary flow. A general account of Taylor's theory is presented below because of its classical nature.

Taylor considered the basic Couette flow of an incompressible, viscous fluid between two, infinitely long, concentric, rotating cylinders and superimposed a small disturbance velocity in each of the axial, radial and circumferential directions. The disturbance velocities were assumed to be periodic in the axial direction and functions of the radius only. The stability of the disturbance was determined by the value of an exponential time constant, σ, a positive value indicating a disturbance whose amplitude increased with time and which was, therefore, unstable. A stable disturbance was satisfied by a negative value of σ and $\sigma = 0$ corresponded with marginal stability.

Taylor substituted his assumed form of the disturbance velocities in the equations of motion and the continuity equation. Terms containing products or squares of the disturbance velocities were neglected thereby restricting the theory to infinitessimal disturbances (linear stability theory). Bessel type solutions were derived which resulted in an equation in the form of an infinite determinant equated to zero. The terms in the determinant were simplified by neglecting powers of the radial clearance to inner cylinder radius ratio (the narrow gap approximation). Substituting $\sigma = 0$, Taylor found that the resulting determinant could be expressed in terms of the non-dimensional number

$$\frac{2\,\omega_i^{\,2}\,d^3\,(R_i^{\,2} - \mu^* R_o^{\,2})(1 - \mu^*)}{\nu^2\,(R_i + R_o)}$$

This has since become known as the Taylor number, T. For the case of a rotating inner cylinder and a fixed outer cylinder ($\mu^* = 0$), the Taylor number reduces to the form

$$T = \frac{2\,\omega_i^2\, d^3\, R_i^2}{\nu^2 (R_i + R_o)}$$

which can be further reduced, using the narrow gap approximation, to

$$T = \frac{\omega_i^2\, R_i\, d^3}{\nu^2}$$

Taylor showed that, as the speed of the inner cylinder is increased, a new steady secondary motion appears at a critical value of T. This secondary flow takes the form of a series of contra-rotating, toroidal vortices (Taylor vortices) spaced regularly along the axis of the cylinder. To a good approximation, instability is confined to the part of the fluid indicated by Rayleigh's criterion. Consequently, for $\mu^* = 0$, the vortices occupy approximately square cells which completely fill the radial clearance between the cylinders (Fig.1). If the radial clearance is small compared with the inner cylinder radius, Taylor vortices first become apparent at a critical Taylor number of about 1708.

Linear stability theories determine an eigenvalue problem for T as a function of η, μ^* and the non-dimensional axial wave number of the disturbance, a. The critical Taylor number is taken to be the minimum value on a marginal stability curve of T against a, derived for fixed values of η and μ^*. Recent theoretical work has been concerned with the development of alternative techniques for solving the eigenvalue problem, often using a wider range of parameters than originally considered by Taylor. One particular area of interest has been the derivation of critical Taylor numbers

for the wide gap case, for example, Taylor's original theory having been considerably simplified by the narrow gap approximation. Chandrasekhar (11) solved the eigenvalue problem for $\eta = 0.5$ using a linear combination of Bessel functions which ultimately lead to the condition that an infinite order determinant was equal to zero. One of the difficulties of this technique was the need to resort to numerical integration to evaluate several of the integrals. This was avoided by Chandrasekhar and Elbert (13), however, who considered the adjoint boundary value problem, again for $\eta = 0.5$. Sparrow et al (66) used direct numerical integration procedures to derive solutions of the eigenvalue problem for radius ratios between 0.10 and 0.95. Similar procedures were also employed by Harris and Reid (39) and Roberts (57). For the case $0 \leqslant \mu^* < \eta^2$, Walowit et al (77) showed that the stability problem can be conveniently solved using the Galerkin method (see Di Prima (22)) in conjunction with simple polynominal expansion functions for the disturbance velocities. The results were found to be in excellent agreement with those derived by Chandrasekhar and Elbert. The wide gap stability problem and other aspects of linear stability theory are reviewed in considerable detail by Chandrasekhar (11) and Di Prima (26).

Linear stability theory correctly predicts both the critical speed for the appearance of Taylor vortices and the axial spacing of the vortices. However, this type of analysis is rather limited for speeds greater than the critical. According to linear theory, the amplitude of an unstable disturbance increases exponentially with time, whereas experiments have shown that a finite amplitude equilibrium flow is established. To understand the nature of the finite amplitude motions, it is necessary for non-linear effects to be included in the analysis.

An important exploration of the non-linear stability problem was carried out by Stuart (68) for the narrow gap case and $\mu^* = 0$. Non-linear effects were shown to change the rate at which kinetic energy is transferred from the mean motion to the disturbance until, eventually, an equilibrium state is reached. Stuart computed the equilibrium mean flow and the corresponding torque by assuming that, at speeds above the critical, the disturbance velocities and vorticity distributions have the form predicted by linear stability theory, but are multiplied by an unknown time-dependent amplitude. This is the so-called 'shape assumption'. A more rigorous analysis of the non-linear growth of Taylor vortices was carried out by Davey (19) for arbitrary gap width and any μ^*. The analysis included the effects of the generation of harmonics of the fundamental mode, both ignored by Stuart, and was solved using a perturbation expansion procedure. Assuming that the axial wave number of the secondary flow remains constant at the value a_o predicted by linear stability theory, Davey computed the amplitude of the disturbance and the additional torque required to maintain the motion at $T > T_o$. For $\mu^* = 0$, the results were found to give good agreement with Stuart's theoretical predictions and Donnelly's (30) torque measurements, up to about $T = 4.0\, T_o$ for $\eta = 0.5$, and $T = 1.4\, T_o$ for $\eta \to 1$.

Non-axisymmetric disturbances have been shown to play an important role in the instability of Taylor vortices. For $\mu^* = 0$, the regular vortices assume a wavy form in the circumferential direction, and a wave velocity in that direction, when the speed of the inner cylinder reaches a second critical value. These doubly-periodic motions were first observed by Taylor (71) and have since become known as the wavy mode of instability. This "higher-order" instability of the steady motion, consisting of the

distorted original velocity distributions plus Taylor vortices, clearly represents a formidable mathematical problem. Consequently, Di Prima (24) considered the stability of Couette flow to non-rotationally symmetric disturbances. Using the Galerkin method, he solved the resulting eigenvalue problem for the case of a narrow gap. The results for $\mu^* = 0$ showed that the critical speed increases with increasing wave number in the circumferential direction, the minimum corresponding to axisymmetric disturbances. The critical Taylor numbers for n = 1 and 2 were only slightly greater than T_o whereas that for n = 4 was qualitatively in agreement with the observations of Coles (16). Di Prima suggested that the fact that wavy motions do not occur immediately after the onset of Taylor vortices can only be explained by considering the full non-linear equations. However, referring to the work of Stuart and Davey, he conjectured that, in the interaction processes between the possible modes at $T > T_o$, the n = 1, 2 and 3 modes die out whilst the n = 4 mode grows and eventually dominates the vortex motion at a sufficiently high value of T (about $1.2\, T_o$). Di Prima's results were confirmed by the direct numerical calculations of Roberts (57) who considered the case $\mu^* = 0$ without making the narrow gap assumption. Results were derived for $\eta = 0.75$, 0.85, 0.90 and 0.95 and, in each case, the critical Taylor number was found to increase with the number of circumferential waves. At the onset of the wavy mode, the angular velocity of the waves was shown to be close to half the angular velocity of the inner cylinder, as previously reported by Coles.

The interaction between a motion which is periodic in the axial direction (Taylor vortices) and one which is periodic in the axial and circumferential directions (the wavy mode) was first considered by Di Prima and Stuart (28). The analysis was based on

the full non-linear equations which were reduced to a system of ordinary differential equations and then solved in succession, using a method suggested by Stuart (69) and Watson (78). Taylor vortices were shown to remain stable for Taylor numbers above that at which, according to linear theory, wavy modes are possible. However, the number of circumferential waves at the onset of the wavy mode was not predicted by the theory. The stability of Taylor vortices against doubly-periodic perturbations was also treated by Davey et al (20). The regular vortices were found to be stable with respect to perturbations of the same axial wavelength and phase, but unstable with respect to perturbations of the same axial wavelength and axial phase shift of $\pi/2$. The results indicated that, for $\eta = 0.95$, the wavy mode would appear at about $T = 1.08\ T_o$ with a slight preference for one circumferential wave. The analysis did not predict a stable flow corresponding to the non-axisymmetric mode with plane boundaries observed by Schwarz et al (58).

Meyer (48) used a combination of Fourier analysis and finite difference techniques to study the onset of the wavy mode. Calculations were carried out for $\eta = 0.83$ and a range of Reynolds numbers up to $Re = 2000$. The results confirmed the axial phase shift between the regular and wavy vortex motions, reported by Davey et al, and wave velocities were found to be in good agreement with those predicted by linear stability theory. Furthermore, variation of the axial wavelength was suggested to be the predominant mechanism for affecting the torque in the wavy mode.

4.2 THE ECCENTRIC CYLINDER CASE

A popular approach to the eccentric cylinder stability problem has been to consider the stability of the flow at a number of circumferential sections taken in isolation. Local stability theories have been derived by Di Prima (25), Ritchie (56), and Urban and Krueger (74). Di Prima's theory was based on the linear stability theory of Di Prima (23) which considered the flow between concentric cylinders with the inner cylinder rotating and a circumferential pressure gradient. An analysis of the stability of the local velocity profiles for a range of eccentricity ratios showed that the widest gap ($\theta = 0$, Fig.2) is the most unstable section (lowest values of T_c) and the narrowest gap ($\theta = \pi$) is the most stable section. Consequently, the critical Taylor numbers for these sections are normally referred to as the lower and upper bounds of stability. Di Prima's curves for $\theta = 0$ (lower bound), $\theta = \pi/2$, and $\theta = \pi$ (upper bound) are included in Fig.86. The curve derived by Ritchie is the upper bound of the stability boundary for a simplified eigenvalue problem. However, he suggested that it could also be regarded as the upper bound for the exact narrow gap problem ($\eta \to 1$). Ritchie used the same cylindrical, bipolar system of co-ordinates as had been used by Kamal (42). The resulting complicated eigenvalue problem was simplified using results from concentric cylinder theory and approximate solutions were derived using a modified Galerkin technique. Urban and Krueger derived an approximate solution of the eccentric cylinder eigenvalue problem by assuming that the disturbance amplitudes and the Taylor number could be expanded by perturbation series. The predicted circumferential variation of T_c was found to be in qualitative agreement with the results of Di Prima.

A non-local solution for the eccentric cylinder stability problem is complicated by the fact that the basic flow has components in the radial and circumferential directions and is dependent on both of these co-ordinates. Consequently, the linear stability equations are partial differential equations rather than ordinary differential equations. A non-local solution was obtained by Di Prima and Stuart (29), however, by letting the clearance ratio and the eccentricity ratio tend to zero in such a way that $(c/R_i)^{\frac{1}{2}}$ is proportional to ε. The critical Taylor number was found to increase with increasing ε, rather than initially decreasing as predicted by local stability theory for the case of maximum local instability. However, this apparent disagreement can be explained by the experimental results of Castle and Mobbs (9). They observed that the onset of Taylor vortices occurs in two stages when the cylinders are eccentric (Section 2.1.3). The first stage becomes evident close to Di Prima's lower bound whereas, for low values of ε, the predictions of Di Prima and Stuart give good agreement with the onset of the second stage. It was suggested by Di Prima and Stuart that the first stage may be a manifestation of local instabilities. Their non-local theory predicted that the amplitude of the Taylor vortices is largest at about 90° downstream of the widest gap. A corresponding angle of about 50° was suggested by the experimental observations of Vohr (76) using $\eta = 0.9$ and $\varepsilon = 0.475$.

4.3 THE TRANSITION TO TURBULENCE

The ultimate breakdown of wavy vortex flow into turbulence is not particularly well documented although it would appear to be a very gradual process. In an important contribution to the problem, Pai (51) found that the vortex structure persisted well into the turbulent regime. Considering the important role played by large

eddy structures in turbulent flow, one might reasonably expect that the presence of a well organised vortex system would significantly influence the structure of turbulence. However, Pan and Vohr (56) presented evidence to the contrary. They recorded the pressure distributions in the flow between eccentric rotating cylinders under conditions where both Taylor vortices and turbulence were expected to be present and found good agreement with the theoretical predictions of Ng and Pan (50), which did not consider the possibility of Taylor vortices. Ng and Pan suggested that, for realistic clearances, vortex flow and turbulence become important simultaneously.

The question of whether turbulence in journal bearings may be preceded by a secondary vortex flow regime was first considered by Di Prima (25). Assuming that turbulence occurs at a Reynolds number of approximately 2000 and that Taylor vortices appear at a Taylor number of approximately 1700, he considered that Taylor vortices will precede turbulence provided that $c/R_i > 4 \times 10^{-4}$. Pan and Vohr (52) concluded that vortices will occur first if $c/R_i > 10^{-3}$ and suggested that, since typical process fluid bearings are designed with values of c/R_i between 10^{-3} and 3×10^{-3}, a marginal secondary flow regime will often exist.

Turbulent lubrication theories have drawn upon mixing length theory and laws developed for fully developed pipe flow to predict the characteristics of bearings operating within the turbulent flow regime. These analyses have proved to be surprisingly accurate, although Macken and Saibel (45) attributed this to the fact that they contain adjustable constants which can be made to fit existing experimental data. Their review of turbulence and inertia effects in bearings suggested that inertia effects should be included in turbulent lubrication theories. They concluded that a new model is required, which takes into account the vortex nature of the flow and three-dimensional effects.

REFERENCES

(1) ARWAS, E. B., STERNLIGHT, B., WERNICK, R. J. - "Analysis of Plain Cylindrical Journal Bearings in Turbulent Regime", J.B.E., 86, 1964, pp.387 - 395

(2) ASTILL, K. N. - "Studies of the Developing Flow Between Concentric Cylinders with the Inner Cylinder Rotating", T.A.S.M.E., 63-HT-15, 1963, pp.1 - 9

(3) BECKER, K. M., KAYE, J. - "The Influence of a Radial Temperature Gradient on the Instability of Fluid Flow in an Annulus with an Inner Rotating Cylinder", A.S.M.E. Paper No. 61-SA-20, 1961, pp.1 - 5

(4) BOOSER, E. R., MISSANA, A., RYAN, F.D. - "Performance of Large Steam Turbine Journal Bearings", T.A.S.L.E., 13, 4, 1970, pp.262 - 268

(5) BREWSTER, D. B., NISSAN, A. H. - "The Hydrodynamics of Flow Between Horizontal Concentric Cylinders", Chem. Eng. Sci., 7, 1958, pp.215 - 221

(6) BREWSTER, D. B., GROSBERG, P., NISSAN, A. H. - "The Stability of Viscous Flow Between Horizontal Concentric Cylinders", P.R.S., A251, 1959, pp.76 - 91

(7) BURTON, R. A. - "Turbulent Film Bearings Under Small Displacements", T.A.S.L.E., 7, 1964, pp.322 - 332

(8) CASTLE, P. - "Hydrodynamic Stability of the Flow Between Eccentric Rotating Cylinders", Ph.D. Thesis, University of Leeds, 1968

(9) CASTLE, P., MOBBS, F. R. - "Experiments on the Hydrodynamic Stability of the Flow Between Eccentric Rotating Cylinders", Proc.I.M.E., 181, 3B, 1967, pp.134 - 137

(10) CASTLE, P., MOBBS, F. R., MARKHO, P. H. - "Visual Observations and Torque Measurements in the Taylor Vortex Regime Between Eccentric Rotating Cylinders", T.A.S.M.E., 70-Lub-13, 1970, pp.1 - 9

(11) CHANDRASEKHAR, S. - "The Stability of Viscous Flow Between Rotating Cylinders", P.R.S., 246, 1958, pp.301 - 311

(12) CHANDRASEKHAR, S. - "Hydrodynamic and Hydromagnetic Stability", Oxford University Press, 1961

(13) CHANDRASEKHAR, S., ELBERT, D. D. - "The Stability of Viscous Flow Between Rotating Cylinders", P.R.S., A263, 1962, pp.145 - 152

(14) COLE, J. A. - "Experiments on the Flow in Rotating Annular Clearances", Proc. Conf. on Lub. and Wear, I.M.E., Paper 15, 1957, pp.16 - 19

(15) COLE, J. A. - "Experiments on Taylor Vortices Between Eccentric Rotating Cylinders", Second Australian Conf. on Hydraulics and Fluid Mechanics, B, 1965, pp.313 - 320

(16) COLES, D. - "Transition in Circular Couette Flow", J.F.M., 21, 1965, pp.385-425

(17) CONSTANTINESCU, V. N. - "On Turbulent Lubrication", Proc.I.M.E., 173, 38, 1959, pp.881-900

(18) COUETTE, M. M. - "Etudes sur le frottement des liquides", Ann.Chim.Phys., 1890 , 21, 6, pp.433-510

(19) DAVEY, A. - "The Growth of Taylor Vortices in Flow Between Rotating Cylinders", J.F.M., 14, 1962, pp.336-368

(20) DAVEY, A., DI PRIMA, R. C., STUART, J. T. - "On the Instability of Taylor Vortices", J.F.M., 31, 1968, pp.17-52

(21) DEBLER, W., FÜNER, E., SCHAAF, B. - "Torque and Flow Patterns in Supercritical Circular Couette Flow", Proc. of the Twelfth Int. Congr. of App. Mechanics, Stanford University, 1968

(22) DI PRIMA, R. C. - "Application of the Galerkin Method to Problems in Hydrodynamic Stability", Quarterly of Applied Mathematics, 13, 1955, pp.55-62

(23) DI PRIMA, R. C. - "The Stability of Viscous Flow Between Rotating Concentric Cylinders with a Pressure Gradient Acting Round the Cylinders", J.F.M., 6, 1959, pp.462-468

(24) DI PRIMA, R. C. - "Stability of Non-Rotationally Symmetric Disturbances for Viscous Flow Between Rotating Cylinders", Phys. Fluids, 4, 1961, pp.751-775

(25) DI PRIMA, R. C. - "A Note on the Stability of Flow in Loaded Journal Bearings", T.A.S.L.E., 6, 1963, pp.249 - 253

(26) DI PRIMA, R. C. - "Stability of Curved Flows", T.A.S.M.E., E, 85, 4, 1963, pp.486 - 493

(27) DI PRIMA, R. C. - "Viscous Flow Between Rotating Concentric Cylinders with a Circumferential Pressure Gradient at Speeds Above Critical", T.A.S.L.E., 7, 1964, pp.333 - 341

(28) DI PRIMA, R. C., STUART, J. T. - "Non-Linear Aspects of Instability of Flow Between Rotating Cylinders", Proc. of the Eleventh Int. Congr. of App. Mechanics, Munich, 1964, pp.1037 - 1044

(29) DI PRIMA, R. C., STUART, J. T. - "Non-Local Effects in the Stability of Flow Between Eccentric Rotating Cylinders", J.F.M., 54, 3, 1972, pp.393 - 415

(30) DONNELLY, R. J. - "Experiments on the Stability of Viscous Flow Between Rotating Cylinders. I, Torque Measurements", P.R.S., A246, 1958, pp.312 - 325

(31) DONNELLY, R. J. - "Experiments on the Stability of Viscous Flow Between Rotating Cylinders. IV, The Ion Technique", P.R.S., A283, 1965, pp.509 - 519

(32) DONNELLY, R. J., FULTZ, D. - "Experiments on the Stability of Viscous Flow Between Rotating Cylinders. II, Visual Observations", P.R.S., A258, 1960, pp.101 - 123

(33) DONNELLY, R. J., SIMON, N. J. - "An Empirical Torque Relation for Supercritical Flow Between Rotating Cylinders", J.F.M., 7, 1960, pp.401 - 418

(34) DUFFIN, S., JOHNSON, B. T. - "Some Experimental and Theoretical Studies of Journal Bearings for Large Turbine Generator Sets", Proc.I.M.E., 181, 3B, Paper 4, 1966

(35) FRÊNE, J. - "Contribution a L'Etude des Regimes de Transition dans les Paliers Lisses", Ph.D. Thesis, University of Lyon, 1970

(36) FRÊNE, J., GODET, M. - "Transition from Laminar to Taylor Vortex Flow in Journal Bearings", Tribology, 4, 4, 1971, pp.216 - 217

(37) GUMBEL, L. - Monatsblatter Berlin Bezirksver, V.D.I., 1914, 5

(38) HAGERTY, W. W. - "Use of an Optical Property of Glycerine-Water Solutions to Study Viscous Fluid Flow Problems", J.A.M., 17, 1950, pp.54 - 58

(39) HARRIS, D. L., REID, W. H. - "On the Stability of Viscous Flow Between Rotating Cylinders; Part 2, Numerical Analysis", J.F.M., 20, 1964, pp.95 - 101

(40) JACKSON, J. H. - "A Visual Study of the Wavy Mode Instability in the Flow Between Rotating Cylinders", M.Sc.(Tribology), Exp. Project Report, University of Leeds, 1969

(41) JONES, C. D. - "A Study of Secondary Flow and Turbulence Between Eccentric Rotating Cylinders", Ph.D. Thesis, University of Leeds, 1973

(42) KAMAL, M. M. - "Separation in the Flow Between Eccentric Rotating Cylinders", T.A.S.M.E., 66-FE-2, 1966, pp.1 - 8

(43) KAYE, J., ELGAR, E. - "Modes of Adiabatic and Diabatic Fluid Flow in an Annulus with an Inner Rotating Cylinder", T.A.S.M.E., 80, 1958, pp.753 - 765

(44) LEWIS, J. W. - "An Experimental Study of the Motion of a Viscous Liquid Contained Between Two Coaxial Cylinders", P.R.S., A117, 1927, pp.388 - 407

(45) MACKEN, N. A., SAIBEL, E. A. - "Turbulence and Inertia Effects in Bearings", Tribology, 5, 4, 1972, pp.154 - 160

(46) MALLOCK, A. - "Experiments on Fluid Viscosity", Phil. Trans. Roy. Soc., A187, 1896, pp.41 - 56

(47) MARKHO, P. H. - "Torque Investigation of Wavy Mode Instability", M.Sc.(Tribology), Exp. Project Report, University of Leeds, 1969

(48) MEYER, K. A. - "Three-Dimensional Study of Flow Between Concentric Rotating Cylinders", Phys. Fluids Supplement, II, 1969, pp.165 - 170

(49) NISSAN, A. H., NARDACCI, J. L., HO, C. Y. - "The Onset of Different Modes of Instability in Flow Between Rotating Cylinders", A.I.Ch.E.J., 9, 1963, pp.620 - 624

(50) NG, C. W., PAN, C. H. T. - "A Linearized Turbulent Lubrication Theory", J.B.E., T.A.S.M.E., D, 87, 3, 1965, pp.675 - 688

(51) PAI, S. I. - "Turbulent Flow Between Rotating Cylinders", N.A.C.A., T.N.892, 1943

(52) PAN, C. H. T., VOHR, J. H. - "Superlaminar Flow in Bearings and Seals", Proc. of Symposium on Lubrication in Nuclear Applications, Miami, 1967

(53) RAMSDEN, P. - "Review of Published Data and Their Application to the Design of Large Bearings for Steam Turbines", Proc.I.M.E., 182, 3A, 1967 - 68, pp.75 - 81

(54) RAYLEIGH, Lord - "On the Dynamics of Revolving Fluids", P.R.S., London, A, 93, 1916, pp.148 - 154

(55) REYNOLDS, O. - "On the Theory of Lubrication and its Application to Mr. Beauchamp Tower's Experiments, Including an Experimental Determination of the Viscosity of Olive Oil", Phil.Trans.Roy.Soc., A177, 1886, pp.157 - 234

(56) RITCHIE, G. S. - "On the Stability of Viscous Flow Between Eccentric Rotating Cylinders", J.F.M., 32, 1, 1968, pp.131 - 144

(57) ROBERTS, P. H. - P.R.S., A, 283, 1965, pp.550 - 556

(58) SCHWARZ, K. W., SPRINGETT, B. E., DONNELLY, R. J. - "Modes of Instability in Spiral Flow Between Rotating Cylinders", J.F.M., 20, 1964, pp.281 - 289

(59) SEGEL, L. A. - "Non-Linear Hydrodynamic Stability Theory and its Application to Thermal Convection and Curved Flows", Non-Equilibrium Thermodynamics, Variational Techniques and Stability; Edited by R. J. Donnelly, R. Herman and I. Prigogine; University of Chicago Press, 1966

(60) SMITH, M. I., FULLER, D. D. - "Journal Bearing Operation at Superlaminar Speeds", T.A.S.M.E., 78, 1956, pp.469 - 474

(61) SNYDER, H. A. - "Stability of Rotating Couette Flow.I. Asymmetric Waveforms", Phys. Fluids, 11, 1968, pp.728 - 734

(62) SNYDER, H. A. - "Change in Wave-form and Mean Flow Associated with Wavelength Variations in Rotating Couette Flow. Part 1", J.F.M., 35, 1969, pp.337 - 352

(63) SNYDER, H. A. - "Wave Number Selection at Finite Amplitude in Rotating Couette Flow", J.F.M., 35, 1969, pp.273 - 298

(64) SNYDER, H. A. - "Waveforms in Rotating Couette Flow", Int. Journal of Non-Linear Mechanics, 5, 1970, pp.659 - 685

(65) SOMMERFELD, A - Zeit. Math. Phys., 1904, 150

(66) SPARROW, E. M., MUNRO, W. D., JONSSON, V. K. - "Instability of the Flow Between Rotating Cylinders: The Wide Gap Problem", J.F.M., 20, 1964, pp.35 - 46

(67) STIEBER, W. - "Das Schwimmlager", V.D.I., Berlin, 1933

(68) STUART, J. T. - "On the Non-Linear Mechanics of Hydrodynamic Stability", J.F.M., 4, 1958, pp.1 - 21

(69) STUART, J. T. - "On the Non-Linear Mechanics of Wave Disturbances in Stable and Unstable Parallel Flows. Part 1. The Basic Behaviour in Plane Poiseville Flow", J.F.M., 9, 1960, pp.353 - 370

(70) SWIFT, H. W. - "The Stability of Lubricating Films in Journal Bearings", J.Inst.Engrs., 233, 1, 1931, 267

(71) TAYLOR, G. I. - "Stability of a Viscous Liquid Contained Between Two Rotating Cylinders", Phil.Trans.Roy.Soc., London, A223, 1923, pp.289 - 343

(72) TAYLOR, G. I. - "Fluid Friction Between Rotating Cylinders", P.R.S., A157, 1936, pp.546 - 578

(73) TERADA, T., HATTORI, K. - "Some Experiments on Motions of Fluids", Report of the Aeronautical Research Institute, Tokyo Imperial University, 11, 1926, pp.287 - 326

(74) URBAN, R. L., KRUEGER, E. R. - "On the Stability of Viscous Flow Between Two Rotating Nonconcentric Cylinders", Journal of the Franklin Institute, 293, 3, 1972, pp.153 - 172

(75) VERSTEEGEN, P. L., JANKOWSKI, D. F. - "Experiments on the Stability of Viscous Flow Between Eccentric Rotating Cylinders", Phys. Fluids, 12, 6, 1969, pp.1138 - 1143

(76) VOHR, J. H. - "An Experimental Study of Taylor Vortices and Turbulence in the Flow Between Eccentric Rotating Cylinders", J.L.T., 90, F, 1968, pp.285 - 296

(77) WALOWIT, J., TSAO, S., DI PRIMA, R. C. - "Stability of the Flow Between Arbitrarily Spaced Concentric Cylindrical Surfaces Including the Effect of a Radial Temperature Gradient", J.A.M., 86, E, 1964, pp.585 - 593

(78) WATSON, J. - "On the Non-Linear Mechanics of Wave Disturbances in Stable and Unstable Parallel Flows. Part 2. The Development of a Solution for Plane Poiseville Flow and for Plane Couette Flow", J.F.M., 9, 1960, pp.371 - 389

(79) WENDT, F. - "Turbulente Strömungen zwischen Zwei Rotierenden Konaxialen", Ingenieur Archiv., 4, 1933, pp.577 - 595

(80) YOUNES, M. A. M. A. - "Stability of Spiral Flow Between Eccentric Rotating Cylinders", Ph.D. Thesis, University of Leeds, 1972

APPENDIX I

PARAMETERS DERIVED FROM THE FLOW VISUALISATION TEST RESULTS

In the flow visualisation tests, the following results were recorded after each shaft speed change; the number of circumferential waves, the number of cell pairs in an axial length of 0.20 m, the temperature of the test fluid, the shaft speed, and the stroboscope flashing frequency. Various parameters were derived from the results using the equations presented below.

THE CIRCUMFERENTIAL WAVE VELOCITY RATIO (V/v)

The number of circumferential waves is given by

$$n = \frac{2\pi}{x} \left[\frac{R_i + R_o}{2} \right]$$

where x is the wavelength. If the waves appear to be stationary when the stroboscope flashing frequency is f, then the tangential velocity of the waves is given by

$$V = x f$$

or,
$$V = \frac{\pi (R_i + R_o) f}{n}$$

The peripheral velocity of the shaft is given by

$$v = 2\pi R_i N$$

and therefore

$$\frac{V}{v} = \left[1 + \frac{R_o}{R_i} \right] \frac{f}{2 n N}$$

THE AXIAL WAVE NUMBER RATIO (a/a_o)

The axial wave number, a, is defined as

$$a = \frac{2\pi (R_o - R_i)}{\lambda}$$

where λ is the axial wavelength (the axial length of a pair of vortex cells). For the concentric cylinder case, the vortices normally occupy approximately square cells at the onset of Taylor vortex flow, and, therefore

$$\lambda_o = 2 (R_o - R_i)$$

and the critical axial wave number $a_o = \pi$

Thus

$$\frac{a}{a_o} = \frac{2 (R_o - R_i)}{\lambda}$$

THE TAYLOR NUMBER

The Taylor number can be defined as

$$T = \frac{2 \omega_i^2 R_i^2 (R_o - R_i)^3}{\nu^2 (R_o + R_i)}$$

and when Reynolds number is based on the radial clearance and the shaft peripheral velocity

$$Re = \frac{\omega_i R_i (R_o - R_i)}{\nu}$$

and

$$T = \frac{2(1 - \eta)}{(1 + \eta)} Re^2$$

The above equation has been plotted in Fig.10 for the radius ratios used in the flow visualisation investigation (η = 0.874, 0.911 and 0.950).

THE WALTHER EQUATION

Before Reynolds numbers could be derived from the results, the recorded test fluid temperatures had to be converted into equivalent kinematic viscosities. This could have been accomplished by direct interpolation of the viscosity characteristics presented in Fig.8 although, because of the vast amount of recorded data, this was impractical. The viscosity measurements were, therefore, used to define the constants A and B in the Walther equation

$$\log_{10} \log_{10} (\nu + 0.8) = A - B \log_{10} T^*$$

which was incorporated in a computer programme for computation of the parameters discussed above (T^* being the absolute temperature). The values of the constants derived for the test fluids used in the flow visualisation and torque measurement investigations are presented in Table 4 (also summarised are relevant values of test fluid densities at 20°C, ρ_{20}, and the slopes of the corresponding density/temperature characteristics).

APPENDIX II

DERIVATION OF CIRCUMFERENTIAL WAVE NUMBERS

Circumferential wave numbers could not be counted in many of the flow visualisation tests because of the unsteady nature of the flow. In these cases, the modes present were isolated using the procedure described in Section 2.6.1.1 and the corresponding wave numbers were derived from the recorded values of the stroboscope flashing frequency, f, and the shaft speed, N, as follows:

from Appendix I

$$f = \left(\frac{V}{v}\right) \frac{2\,n\,R_i}{(R_o + R_i)} \quad N$$

Coles (16), using $\eta = 0.874$, had shown that the circumferential wave velocity ratio was reasonably constant for Reynolds numbers above about Re = 500 which suggests that, for a particular radius ratio,

$$f = K_1\,n\,N$$

This equation defines a family of equispaced lines on a graph of f against N, each line representing a particular number of circumferential waves. The value of the constant K_1 was derived, for each of the shafts, from results recorded when the flow was sufficiently steady for the circumferential wave number to be counted, and the resulting families of lines for $\eta = 0.911$, 0.950 and 0.874 are presented in Figs. 57, 58 and 59 respectively. Whenever the number of circumferential waves could not be counted, it was deduced by plotting the recorded values of f and N on the appropriate graph.

APPENDIX III

CIRCUMFERENTIAL VARIATION OF REYNOLDS NUMBER

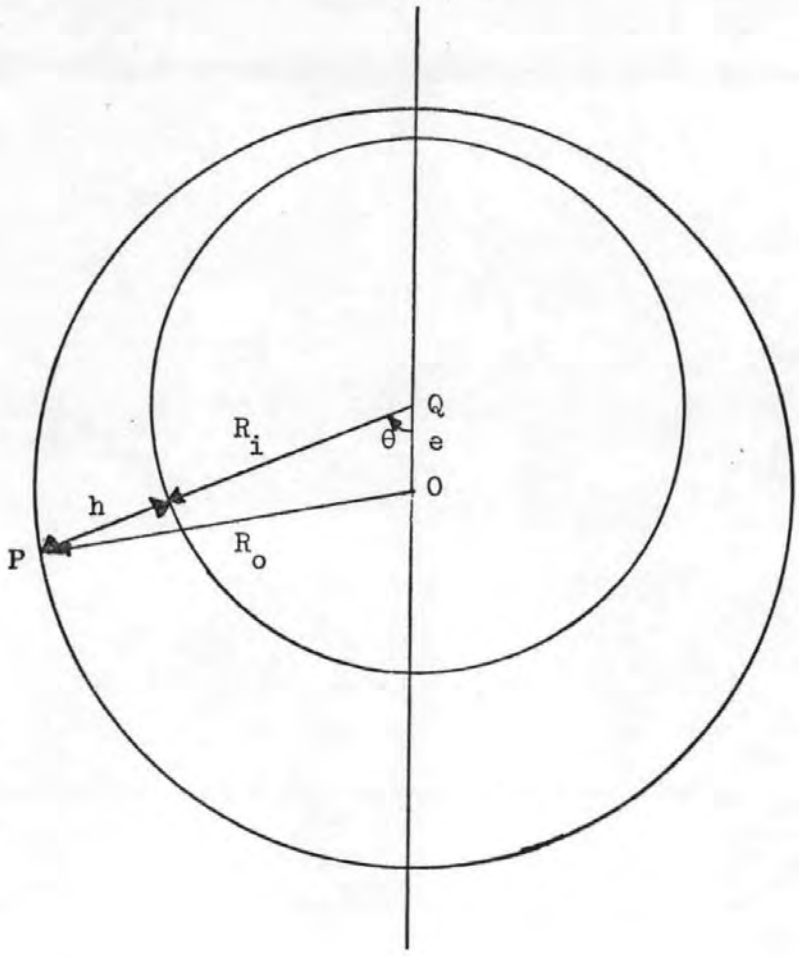

For the triangle OPQ in the figure above

$$R_o^2 = (h + R_i)^2 + e^2 - 2(h + R_i)\, e \,.\, \cos\theta$$

and re-arranging

$$h^2 + 2h\,(R_i - e\cos\theta) + e^2 + R_i^2 - R_o^2 - 2R_i\, e\cos\theta = 0$$

h, the local clearance, is given by

$$h = (e\cos\theta - R_i) \pm (R_o^2 - e^2\sin^2\theta)^{\frac{1}{2}}$$

or, neglecting the trivial solution and substituting for e,

$$h = (\varepsilon c \cos\theta - R_i) + (R_o^2 - \varepsilon^2 c^2 \sin^2\theta)^{\frac{1}{2}}$$

$$h = c\left[\varepsilon\cos\theta - \left[\frac{\eta}{1-\eta}\right] + \left[\frac{1}{(1-\eta)^2} - \varepsilon^2\sin^2\theta\right]^{\frac{1}{2}}\right]$$

The local Reynolds number Re^* is based on the shaft peripheral velocity and the local clearance h whereas the Reynolds number Re is based on the shaft peripheral velocity and the radial clearance, c. Consequently, it follows that

$$Re^* = Re\left[\varepsilon\cos\theta - \left[\frac{\eta}{1-\eta}\right] + \left[\frac{1}{(1-\eta)^2} - \varepsilon^2\sin^2\theta\right]^{\frac{1}{2}}\right]$$

and Re^* is equal to $Re(1-\varepsilon)$ and $Re(1+\varepsilon)$ for the narrow gap and wide gap cases respectively.

APPENDIX IV

THE FRICTION COEFFICIENT RELATIONSHIP FOR SIMPLE LAMINAR FLOW

For simple laminar flow, the torque exerted by the viscous drag of the test fluid on the shaft can be expressed as

$$M = \frac{8\pi\mu L\omega_i R_i^2 R_o^2 (1 + 2\varepsilon^2)}{(R_o^2 - R_i^2)(2+\varepsilon^2)(1-\varepsilon^2)^{\frac{1}{2}}}$$

The friction coefficient, C_f, is defined as

$$C_f = \frac{M}{\pi\rho\omega_i^2 R_i^4 L}$$

Substituting for M and re-arranging gives

$$C_f = \left[\frac{4}{\eta(1+\eta)}\right] \frac{1}{Re} \left[\frac{2(1+2\varepsilon^2)}{(2+\varepsilon^2)(1-\varepsilon^2)^{\frac{1}{2}}}\right]$$

and

$$\log C_f = K_2 - \log Re$$

where

$$K_2 = \log\left[\frac{4}{\eta(1+\eta)}\right]\left[\frac{2(1+2\varepsilon^2)}{(2+\varepsilon^2)(1-\varepsilon^2)^{\frac{1}{2}}}\right]$$

The values of K_2 used in the present investigation are summarised in Table 53.

APPENDIX V

MINIMUM PRESSURES ACCORDING TO THE FULL SOMMERFELD ANALYSIS

The equation governing pressure distribution in the regions of a fluid film bearing not affected by cavitation was derived by Reynolds (55). It can be written as

$$\frac{\partial}{\partial x}\left(\frac{\rho h^3}{12\mu}\frac{\partial p}{\partial x}\right) + \frac{\partial}{\partial y}\left(\frac{\rho h^3}{12\mu}\frac{\partial p}{\partial y}\right) = \frac{\partial}{\partial x}\left(\frac{\rho (u_1 + u_2)\, h}{2}\right) + \frac{\partial}{\partial y}\left(\frac{\rho(v_1 + v_2)h}{2}\right) + \frac{\partial}{\partial t}(\rho h)$$

The equation represents a combination of the equations of motion for a Newtonian fluid and the continuity equation. The above equation can be simplified by selecting co-ordinate directions to eliminate all velocity terms involving y ($v_1 = v_2 = 0$), whilst for steady-state conditions, the last term becomes zero. If the fluid is assumed to be incompressible, density vanishes from the equation and if only one of the boundaries moves with a constant surface speed, U, the reduced equation becomes

$$\frac{\partial}{\partial x}\left(\frac{h^3}{\mu}\frac{\partial p}{\partial x}\right) + \frac{\partial}{\partial y}\left(\frac{h^3}{\mu}\frac{\partial p}{\partial y}\right) = 6U\frac{\partial h}{\partial x}$$

Now, for a bearing infinitely long in the y direction, the flow in this direction will be zero which requires that the pressure gradient $\partial p/\partial y$ must also be zero. Hence,

$$\frac{\partial}{\partial x}\left(\frac{h^3}{\mu}\frac{\partial p}{\partial x}\right) = 6U\frac{\partial h}{\partial x}$$

and integrating once gives

$$\frac{dp}{dx} = 6U\mu\left(\frac{h-\bar{h}}{h^3}\right)$$

where $\bar{h}$ is defined as the oil film thickness where the pressure gradient $\partial p/dx$ is zero. This is Reynolds equation in one dimension.

The variation of oil film thickness around a journal bearing can be expressed as

$$h = c\,(1+\varepsilon\cos\theta)$$

and substituting this and $x = R_i\theta$ into the above equation gives

$$\frac{dp}{d\theta} = \frac{6U\mu R_i}{c^2}\left(\frac{(1+\varepsilon\cos\theta)-(1+\varepsilon\cos\bar{\theta})}{(1+\varepsilon\cos\theta)^3}\right)$$

where

$$\bar{h} = c\,(1+\varepsilon\cos\bar{\theta})$$

Integration of the above equation gives the pressure p as a function of θ. To perform this integration, Sommerfeld (65) defined an angle γ such that

$$1+\varepsilon\cos\theta = \frac{(1-\varepsilon^2)}{(1-\varepsilon\cos\gamma)}$$

Using this substitution, it can be shown that

$$\int\frac{d\theta}{(1+\varepsilon\cos\theta)^2} = \frac{\gamma-\varepsilon\sin\gamma}{(1-\varepsilon^2)^{\frac{3}{2}}}$$

and

$$\int \frac{d\theta}{(1 + \varepsilon \cos\theta)^3} = \frac{1}{(1 - \varepsilon^2)^{\frac{5}{2}}} \left[\gamma \left(\frac{2 + \varepsilon^2}{2} \right) - 2\varepsilon \sin\gamma + \frac{\varepsilon^2}{4} \sin 2\gamma \right]$$

and it follows that

$$p = \frac{6 R_i^2 \mu \omega}{c^2} \left[\frac{(\gamma - \varepsilon \sin\gamma)}{(1 - \varepsilon^2)^{\frac{3}{2}}} - \frac{1}{(1 - \varepsilon^2)^{\frac{3}{2}}(1 - \varepsilon \cos\bar{\gamma})} \left(\frac{(2 + \varepsilon^2)\gamma}{2} - 2\varepsilon \sin\gamma + \frac{\varepsilon^2}{4} \sin 2\gamma \right) \right]$$

$$+ \text{Constant}$$

and the non-dimensional pressure p^* is given by

$$p^* = \frac{p c^2}{\mu R_i^2 \omega} = \frac{6}{(1 - \varepsilon^2)^{\frac{3}{2}}} \left[(\gamma - \varepsilon \sin\gamma) - \left(\frac{(2 + \varepsilon^2)2\gamma - 8\varepsilon \sin\gamma + \varepsilon^2 \sin 2\gamma}{4(1 - \varepsilon \cos\bar{\gamma})} \right) \right] + C$$

Two boundary conditions are required to evaluate $\bar{\gamma}$ and the constant of integration C. Sommerfeld assumed that the clearance space was full of lubricant at all times and that $p = 0$ at $\theta = 0$ and 2π. Using these boundary conditions (noting that the Sommerfeld substitution angle γ has the property that for $\theta = 0$, π and 2π, γ is also 0, π and 2π), C is found to be zero and it follows that

$$\cos\bar{\gamma} = -\frac{\varepsilon}{2}$$

and therefore

$$\cos\bar{\theta} = -\frac{3\varepsilon}{2 + \varepsilon^2}$$

Substituting for C and $\cos\bar{\gamma}$ in the above equation for p^* gives

$$p^* = \frac{6\varepsilon \sin\gamma (2 - \varepsilon^2 - \varepsilon\cos\gamma)}{(1 - \varepsilon^2)^{\frac{3}{2}} (2 + \varepsilon^2)}$$

or, in terms of θ

$$p^* = \frac{6\varepsilon \sin\theta (2 + \varepsilon \cos\theta)}{(2 + \varepsilon^2)(1 + \varepsilon \cos\theta)^2}$$

According to this equation, the pressure will be zero not only at $\theta = 0$ and 2π but also at $\theta = \pi$. The pressure will be antisymmetric about $\theta = \pi$ which implies the existence of sub-atmospheric and even sub-zero pressures for the divergent section of the lubricating film ($\pi < \theta < 2\pi$). The maximum pressure p_m occurs when $dp/d\theta = 0$, i.e. at $\theta_m = \bar{\theta}$, and it, therefore, follows that

$$p^*_m = \frac{3\varepsilon}{2(2 + \varepsilon^2)} \left[\frac{(4 - \varepsilon^2)}{(1 - \varepsilon^2)}\right]^{\frac{3}{2}}$$

The variation of p^*_m and θ_m with eccentricity is shown in Fig.156 . p_m also defines the magnitude of the minimum negative pressure which, according to the above analysis, occurs at $\theta = 2\pi - \theta_m$. The derived values for the magnitude of p^*_m and the angles θ_{max} and θ_{min} at which the maximum and minimum pressures are predicted to occur for $\varepsilon = 0.71$, 0.81 and 0.91 are summarised in Table 54.

ε	p^*_m	θ_{max}	θ_{min}
0.71	7.96	148.3	211.7
0.81	13.87	156.2	203.8
0.91	38.26	164.9	195.1

TABLE 54

Now, by definition

$$p = \frac{p^* \mu \omega R_i^2}{c^2} = \frac{p^* \mu^2 \eta Re}{\rho(1-\eta)^3 R_o^2}$$

For the torque measurement test rig $R_o = 114.27$ mm and cavitation was encountered in the tests using $\eta = 0.975$. Assuming a test fluid temperature of 20°C, it follows from Figs. 77 and 78 that, for the tests using Carnea 15,

$$p = 1.54\ p^*\ Re \qquad (N/m^2)$$

and for those using Macron A

$$p = 0.14\ p^*\ Re \qquad (N/m^2)$$

In the above analysis, p was assumed to be zero at $\theta = 0$ (i.e. p_o). However, because of the vertical axis of the shaft in the test rig, p_o is actually given by the sum of the atmospheric pressure, p_a, and $\rho g d$ (where d is the vertical distance between the upper end of the test fluid column and the horizontal section under consideration). For a non-zero inlet pressure, it follows that, for Carnea 15,

$$p - p_o = 1.54\ p^*\ Re \qquad (N/m^2)$$

and for Macron A

$$p - p_o = 0.14\ p^*\ Re \qquad (N/m^2)$$

For the central section of the test rig, $d = 0.25$ m and, therefore, for Carnea 15 (again assuming a test fluid temperature of 20°C)

$$p - p_a = 1.54\ p^*\ Re + 2110 \qquad (N/m^2)$$

and for Macron A

$$p - p_a = 0.14\, p^* Re + 2040 \qquad (N/m^2)$$

Considering a test using $\varepsilon = 0.91$ and Carnea 15, for example, the minimum non-dimensional pressure is given by $p^*_{min} = -38.26$ and, therefore,

$$p - p_a = -58.9\, Re + 2110 \qquad (N/m^2)$$

such that sub-atmospheric pressures would be expected for Reynolds numbers above about 36. The corresponding Reynolds numbers for $\varepsilon = 0.71$ and 0.81 are 172 and 99 respectively.

APPENDIX VI

THEORETICAL TORQUE RELATIONSHIP FOR CAVITATING FLOW

In a journal bearing with the shaft rotating at a constant angular velocity ω, the Couette and Poiseuille flow components combine to give a total flow in the circumferential direction of

$$q = \frac{R_i \omega h}{2} - \frac{h^3}{12\mu} \frac{\partial p}{\partial \theta}$$

Assuming that the viscosity is constant through the thickness of any given part of the fluid film, the viscous shear stress on the surface of the shaft is given by

$$\tau = \frac{\mu R_i \omega}{h} + \frac{h}{2R_i} \frac{\partial p}{\partial \theta}$$

The variation of film thickness around the bearing can be expressed as

$$h = c\ (1 + \varepsilon \cos \theta)$$

The drag on the shaft, F_s, can be found by integrating the shear stress such that for a continuous film

$$F_s = L R_i \int_0^{2\pi} \left[\frac{\mu R_i \omega}{c\ (1 + \varepsilon \cos \theta)} + \frac{c\ (1 + \varepsilon \cos \theta)}{2R_i} \frac{\partial p}{\partial \theta} \right] d\theta$$

Substituting the expression for the circumferential pressure gradient from Appendix V and again using the Sommerfeld substitution

$$1 + \varepsilon \cos \theta = \frac{1 - \varepsilon^2}{1 - \varepsilon \cos \gamma}$$

it is a relatively simple matter to show that the torque due to the shear force F_s acting on the shaft is given by

$$M = \frac{4\pi L R_i^3 \mu\omega(1 + 2\varepsilon^2)}{(2 + \varepsilon^2)(1 - \varepsilon^2)^{\frac{1}{2}}}$$

However, in the case of a cavitating oil film, the frictional torque comprises two parts, that due to the solid film extending over the extent of the pressure curve, say from θ_1 to θ_2, and that due to the cavitating zone from θ_2 to $2\pi + \theta_1$. The start of the pressure curve is usually taken to occur at $\theta = 0$ whereas the boundary conditions at the lubricant-cavity interface (θ_2) has been the subject of much discussion. The first attempt to adapt hydrodynamic lubrication theory to take account of film rupture is attributed to Gumbel (37) although the approach is often referred to as the half-Sommerfeld solution. In this solution, the sub-atmospheric pressures predicted by Sommerfeld to occur in the divergent clearance space (Appendix V) are neglected giving $\theta_2 = \pi$. This form of solution is widely used although it is basically unsatisfactory because of the implied flow discontinuity at the end of the pressure curve. A more acceptable boundary condition was suggested independently by Swift (70) and Stieber (67). From consideration of journal stability, Swift showed that the oil film should rupture at a position beyond $\theta = \pi$ where

$$\frac{dp}{d\theta} = 0 , \qquad p = p_{cavity}$$

The same boundary condition was arrived at by Stieber by consideration of flow continuity. The cavity pressure often differs little from atmospheric and is usually taken as such. The above represents the generally accepted cavitation boundary condition and will be used in the present analysis. It follows that $\theta_2 = \bar{\theta}$ (minimum pressure condition, see Appendix V).

Beyond θ_2, the pressure gradient is assumed to be zero and, therefore, the flow required if the gap is to remain full is $(R_i \omega h/2)$. However, because there is only $(R_i \omega \bar{h}/2)$ available, the flow breaks into streamers of fractional width $(\bar{h}/h)$. Hence, assuming that the air or vapour between the streamers is inviscid, the frictional torque on the shaft is given by

$$M = \int_{\theta_1}^{\theta_2} L R_i^2 \left[\frac{\mu R_i \omega}{h} + \frac{h}{2R_i} \frac{\partial p}{\partial \theta} \right] d\theta \quad +$$

$$\int_{\theta_2}^{2\pi+\theta_1} L R_i^2 \left[\frac{\mu R_i \omega \bar{h}}{h^2} \right] d\theta$$

Substituting for $\partial p/\partial \theta$ (from Appendix V) and h, and re-arranging

$$M = \frac{L R_i^3 \mu \omega}{c} \left[4 \int_{\theta_1}^{\theta_2} \frac{d\theta}{(1 + \varepsilon \cos \theta)} - \frac{3\bar{h}}{c} \int_{\theta_1}^{\theta_2} \frac{d\theta}{(1+\varepsilon \cos \theta)^2} + \right.$$

$$\left. \frac{\bar{h}}{c} \int_{\theta_2}^{2\pi+\theta_1} \frac{d\theta}{(1 + \varepsilon \cos \theta)^2} \right]$$

Using the Sommerfeld substitution, it can be shown that

$$\int \frac{d\theta}{(1 + \varepsilon \cos \theta)} = \frac{\gamma}{(1 - \varepsilon^2)^{\frac{1}{2}}}$$

and

$$\int \frac{d\theta}{(1 + \varepsilon \cos \theta)^2} = \frac{\gamma - \varepsilon \sin \gamma}{(1 - \varepsilon^2)^{\frac{3}{2}}}$$

Then, if γ_1, γ_2 and γ_3 are equivalent to θ_1, θ_2 and $2\pi + \theta_1$ respectively, it follows that

$$M = \frac{L R_i^3 \mu \omega}{c} \left[4 \left(\frac{\gamma_2 - \gamma_1}{(1-\varepsilon^2)^{\frac{1}{2}}} \right) - \frac{3\bar{h}}{c} \left(\frac{\gamma_2 - \gamma_1 - \varepsilon(\sin\gamma_2 - \sin\gamma_1)}{(1-\varepsilon^2)^{\frac{3}{2}}} \right) + \frac{\bar{h}}{c} \left(\frac{\gamma_3 - \gamma_2 - \varepsilon(\sin\gamma_3 - \sin\gamma_2)}{(1-\varepsilon^2)^{\frac{3}{2}}} \right) \right]$$

For the boundary conditions specified above, i.e. $\theta_1 = 0$ and $\theta_2 = \bar{\theta}$ (the angle beyond $\theta = \pi$ for which $\partial p / \partial \theta = 0$), it follows that $\gamma_1 = 0$, $\gamma_2 = \bar{\gamma}$ and $\gamma_3 = 2\pi$. Hence the above expression becomes

$$M = \frac{L R_i^3 \mu \omega}{c} \left(\frac{4\bar{\gamma}}{(1-\varepsilon^2)^{\frac{1}{2}}} - \frac{3\bar{h}}{c} \left[\frac{\bar{\gamma} - \varepsilon \sin\bar{\gamma}}{(1-\varepsilon^2)^{\frac{3}{2}}} \right] + \frac{\bar{h}}{c} \left[\frac{2\pi - \bar{\gamma} + \varepsilon \sin\bar{\gamma}}{(1-\varepsilon^2)^{\frac{3}{2}}} \right] \right)$$

Substituting for $\frac{\bar{h}}{c} = 1 + \varepsilon \cos\bar{\theta} = \frac{1-\varepsilon^2}{1 - \varepsilon\cos\bar{\gamma}}$

$$M = \frac{L R_i^3 \mu \omega}{c} \left(\frac{4\bar{\gamma}}{(1-\varepsilon^2)^{\frac{1}{2}}} - (1-\varepsilon^2) \left[\frac{3(\bar{\gamma} - \varepsilon\sin\bar{\gamma}) - (2\pi - \bar{\gamma} + \varepsilon\sin\bar{\gamma})}{(1-\varepsilon^2)^{\frac{3}{2}} (1 - \varepsilon\cos\bar{\gamma})} \right] \right)$$

$$M = \frac{L R_i^3 \mu \omega}{c(1-\varepsilon^2)^{\frac{1}{2}}} \left(4\bar{\gamma} - \left[\frac{3\bar{\gamma} - 3\varepsilon\sin\bar{\gamma} - 2\pi + \bar{\gamma} - \varepsilon\sin\bar{\gamma}}{(1 - \varepsilon\cos\bar{\gamma})} \right] \right)$$

$$M = \frac{L R_i^3 \mu \omega}{c(1-\varepsilon^2)^{\frac{1}{2}}} \left[\frac{2\pi - 4\varepsilon(\bar{\gamma}\cos\bar{\gamma} - \sin\bar{\gamma})}{(1 - \varepsilon\cos\bar{\gamma})} \right]$$

or

$$M = \frac{4\pi L R_i^3 \mu \omega (1 + 2\varepsilon^2)}{c(1 - \varepsilon^2)^{\frac{1}{2}} (2 + \varepsilon^2)} \left[I \right]$$

where

$$I = \frac{(2+\varepsilon^2)}{(1 + 2\varepsilon^2)} \left[\frac{\pi - 2\varepsilon (\bar{\gamma} \cos \bar{\gamma} - \sin \bar{\gamma})}{2\pi (1 - \varepsilon \cos \bar{\gamma})} \right]$$

In the above analysis, $\bar{\theta}$ and $\bar{\gamma}$ have been used to define the position of the end of the pressure curve where $\partial p / \partial \theta = 0$ and $p = 0$. Now it follows from substitution of these boundary conditions (together with $p = 0$ at $\gamma = 0$) in the expression for p in Appendix V that

$$\varepsilon = \frac{4 (\bar{\gamma} \cos \bar{\gamma} - \sin \bar{\gamma})}{(\sin 2\bar{\gamma} - 2\bar{\gamma})}$$

Hence ε can be derived for given values of $\bar{\gamma}$, and $\bar{\theta}$ can be derived in turn using

$$1 + \varepsilon \cos \bar{\theta} = \frac{1 - \varepsilon^2}{1 - \varepsilon \cos \bar{\gamma}}$$

$\bar{\gamma}$ and $\bar{\theta}$ are plotted against ε in Fig.157 and the corresponding curve for I against ε is plotted in Fig.158.

$$C_f = \frac{M}{\pi \rho \omega^2 R_i^4 L}$$

and therefore in this case

$$C_f = \frac{4\ (1 + 2\varepsilon^2)\quad [I]}{(1 - \varepsilon^2)^{\frac{1}{2}}\ (2 + \varepsilon^2)\ Re}$$

The predicted friction characteristics for cavitating laminar flow for $\varepsilon = 0.71$, 0.81 and 0.91 are compared with those for the full Sommerfeld solution ($I = 1$) in Fig.143 .

AUTHOR	η	T_w/T_o
JONES, C. D.	0.97	1.15
	0.95	1.20
DEBLER, W. et al	0.95	1.21
DONNELLY, R. J. et al	0.95	1.15
SCHWARZ, K. W. et al	0.95	1.20
YOUNES, M. A. M. A.	0.95	1.20
DEBLER, W. et al	0.935	1.21
	0.925	1.26
CASTLE, P. et al	0.912	1.21
JONES, C. D.	0.912	1.23
VOHR, J. H.	0.91	1.15
YOUNES, M. A. M. A.	0.90	1.29
COLES, D.	0.874	1.55
DEBLER, W. et al	0.875	1.80
NISSAN, A. H. et al	0.86	1.40
DEBLER, W. et al	0.85	1.64
JONES, C. D.	0.85	1.30
YOUNES, M. A. M. A.	0.85	1.40
JONES, C. D.	0.80	1.53
	0.718	28
	0.645	45
SNYDER, H. R.	0.50	>100

TABLE 1 NORMALISED TAYLOR NUMBERS FOR THE ONSET OF WAVY MODE FLOW

AUTHOR	η	L/c
TAYLOR, G. I.	0.743	87
	0.880	187
	0.942	382
DONNELLY, R. J. ; FULTZ, D.	0.500	29
NISSAN, A. H. et al	0.821	40
	0.846	110
DONNELLY, R. J.	0.850	33
	0.900	50
	0.950	100
COLES, D.	0.874	28
COLE, J. A.	0.827	18
CASTLE, P.	0.899	100
	0.912	110
SNYDER, H. R.	0.200	18
	0.500	29
	0.800	72
	0.959	360
VOHR, J. H.	0.910	120
	0.990	1110
DEBLER, W. et al	0.5 - 0.950	8 - 80
JACKSON, J. H.	0.912	110
MARKHO, P. H.	0.899	100
VERSTEEGEN, P. L. ; JANKOWSKI, D. F.	0.500	22
YOUNES, M. A. M. A.	0.846	98
	0.900	151
	0.949	295
JONES, C. D.	0.64 - 0.97	27 - 500

TABLE 2 RIG GEOMETRIES USED BY PREVIOUS AUTHORS

STROBOSCOPE SCALE	USEFUL RANGE	SCALE CORRECTION FACTOR
	(c/min)	(c/min)
1	300 - 800	+15
2	800 - 2500	+20
3	2500 - 7000	+190

TABLE 3 STROBOSCOPE CORRECTION FACTORS

TEST FLUID	VISCOSITY CONSTANTS		DENSITY CONSTANTS	
	A	B	ρ_{20}	NEGATIVE SLOPE
			(kg/m^3)	($kg/m^3.K$)
CARNEA 15	9.8073	3.9288	861.25	0.677
TELLUS 15	10.3705	4.1451	-	-
TELLUS T17	9.1588	3.6449	-	-
TELLUS 21	9.8441	3.8996	869.00	0.650
MACRON A	9.8078	4.0090	830.85	0.630
"MIXTURE A"	10.2495	4.0338	881.00	0.650

TABLE 4 VISCOSITY AND DENSITY CONSTANTS FOR THE TEST FLUIDS

TEST FLUID	VISCOMETER TYPE	TEMPERATURE	VISCOMETER CONSTANT	AVERAGE FLOW TIME	KINEMATIC VISCOSITY
		°C	cs/sec	secs	cs
CARNEA 15	B.S.'U'No.4518	17.98	0.03095	684.85	21.20
		23.78		535.55	16.58
		29.67		428.20	13.25
		32.17		391.75	12.12
		37.06		329.65	10.20
		40.46		298.85	9.25
TELLUS 15	B.S.'U'No.3525	18.38	0.02846	914.85	26.04
		23.78		713.55	20.31
		29.67		552.00	15.71
		32.17		501.80	14.28
		37.16		419.70	11.95
		40.46		371.55	10.57
TELLUS T17	B.S.'U'No.4910	17.98	0.09120	344.90	31.46
		23.78		267.65	24.41
		32.17		193.70	17.66
	B.S.'U'No.65	29.67	0.02718	711.55	19.34
		37.06		550.70	14.97
		40.36		493.20	13.40
TELLUS 21	B.S.'U'No.4910	16.63	0.09120	612.25	55.84
		22.78		442.25	40.33
		33.11		276.20	25.19

TABLE 5 RESULTS OF VISCOMETRY TESTS USING FRESH OIL SAMPLES

TEST FLUID	VISCOMETER TYPE	TEMPERATURE	VISCOMETER CONSTANT	AVERAGE FLOW TIME	KINEMATIC VISCOSITY
		°C	cs/sec	secs	cs
CARNEA 15	B.S.'S.L.' No.7460	21.38	0.03132	586.80	18.38
		25.88		488.45	15.30
		33.87		368.60	11.54
TELLUS 15	B.S.'U' Nos.4910&4518	21.68	0.09120	241.60	22.03
		25.88	0.03095	587.40	18.18
		33.87		428.05	13.25
TELLUS T17	B.S.'S.L.' No.7460	21.68	0.03132	858.20	26.88
		25.88		711.05	22.27
		33.87		531.15	16.64
TELLUS 21	B.S.'S.L.' No.3313	21.68	0.11390	375.10	42.72
		25.88		303.20	34.53
		33.87		213.30	24.30

TABLE 6 RESULTS OF VISCOMETRY TESTS FOR USED OIL SAMPLES

TEST FLUID	ALUMINIUM PARTICLES	TEMPERATURE	VISCOMETER CONSTANT	AVERAGE FLOW TIME	KINEMATIC VISCOSITY
		°C	cs/sec	secs	cs
CARNEA 15		22.20	0.09120	195.05	17.79
	✓	22.20	0.03095	575.00	17.80
		30.00	0.02718	485.50	13.20
	✓	30.00	0.03095	426.45	13.20
TELLUS T17		19.80	0.09120	318.95	29.09
	✓	19.80	0.09120	319.05	29.10
		30.00	0.02718	706.15	19.19
	✓	30.00	0.09120	210.65	19.21

TABLE 7 RESULTS OF VISCOMETRY TESTS USING ALUMINIUM FLAKE PARTICLES IN SUSPENSION (0.5 gm/l)

DESCRIPTION OF FLOW	n	(T/T_o) AT ONSET
COUETTE FLOW	0	-
TAYLOR VORTICES	0	1
BRIGHT BAND VIBRATION	0	1.03
WEAK WAVY MODE	1	1.08
PRIMARY WAVY MODE	3 - 10	1.20
TRANSITIONAL STATE	5 ÷ 9	15 - 40
SECONDARY WAVY MODE	4 - 5	45 - 85
TURBULENCE	0	-

TABLE 8 TYPICAL SEQUENCE OF FLOW CHANGES WITH INCREASING SHAFT SPEED USING $\eta = 0.911$ AND CONCENTRIC CYLINDERS

ε	TEST FLUID	RANGE OF Re FOR $(V/v)_{min}$	(V/v)	
			$(V/v)_{min}$	RECOVERY VALUE
0	TELLUS T17, 21	-	-	0.41
	CARNEA 15	-	-	0.41
0.05	TELLUS T17, 21	500 - 1000	0.39	0.41
	CARNEA 15	550 - 950	0.40	0.41
0.10	TELLUS T17, 21	400 - 1000	0.38	0.40
	CARNEA 15	475 - 900	0.38	0.41
0.15	TELLUS T17, 21	350 - 1000	0.38	0.40
	CARNEA 15	400 - 1050	0.38	0.41
0.20	TELLUS T17, 21	350 - 850	0.36	0.39
	CARNEA 15	350 - 1200	0.37	0.40

TABLE 9 CIRCUMFERENTIAL WAVE VELOCITY RATIO RESULTS FOR $\eta = 0.911$

WAVE NUMBER CHANGE		Re
FROM	TO	
5	6	380 - 425
6	5	800, 765, 785
5	4/3	980, 995
4/3	3	985 - 1100
3	2	1655 - 1790
		1705 - 1815
		1785 - 1918

TABLE 10 OBSERVED CIRCUMFERENTIAL WAVE NUMBER CHANGES USING $\eta = 0.874$ AND CONCENTRIC CYLINDERS

ε	Re	n	COMMENTS
0.10	250 - 500	6	Predominant mode
	530 - 900	4	Predominant mode
	900 - 1500	3	Predominant mode
	1600 - 2300	3/4	Continual oscillation between n = 3 and n = 4
	2400 - 2800	3	Visible at upper end of test length only
0.20	235 - 430	6	Predominant mode
	500 - 900	5/4, 4/3	Changing infrequently between two wave numbers which decrease with increasing shaft speed
	945 - 1885	7/8	Changing infrequently between n = 7 and n = 8
	1885 - 2100	7,3	With increasing shaft speed, the n = 3 mode progressively replaced the n = 7 mode from the upper end of the test length downwards.
	2100 - 3000	3	Predominant mode
0.30	300 - 450	5/6	Continual oscillation between n = 5 and n = 6
	500 - 675	4	Predominant mode
	700 - 1260	10/9, 9/8	Changing between two wave numbers which decrease with increasing shaft speed
	1260 - 1625	7/8	Frequent changes between n = 7 and n = 8
	1625 - 2250	8	Predominant mode

TABLE 11 OBSERVED REGIMES OF WAVY MODE FLOW USING $\eta = 0.874$

WAVE NUMBER CHANGE		Re
FROM	TO	
3	4	181 - 204
6	7	239
7	8	278
8	9	320, 305, 312, 300
9	10	402, 429, 431, 415
10	9	563, 544, 583, 562, 575, 565

TABLE 12 OBSERVED CIRCUMFERENTIAL WAVE NUMBER CHANGES USING $\eta = 0.911$ AND CONCENTRIC CYLINDERS

n	Re	
	min	max
14	570	640
12	645	980
10	940	1720

TABLE 13 OBSERVED PREDOMINANT WAVE NUMBER BANDS USING $\eta = 0.950$ AND CONCENTRIC CYLINDERS

SHAFT SPEED	WAVE NUMBER CHANGE	Re	
		SHORT	COLES
INCREASING	3 - 5	250	-
	4 - 5	-	201
	5 - 6	400	407
	6 - 5	785	759
	5 - 4	990	969
	4 - 3	1040	-
	3 - 2	1800	-
DECREASING	2 - 3	1410	-
	3 - 4	845	-
	4 - 5	700	679
	5 - 6	510	482

TABLE 14 CIRCUMFERENTIAL WAVE NUMBER CHANGES IN TYPICAL TESTS USING $\eta = 0.874$ AND CONCENTRIC CYLINDERS

SHAFT No.	R_i/R_o	L/c
1	0.874	69.5
2	0.911	98.4
3	0.950	175.2
4	0.975	350.4

TABLE 15 GEOMETRY RATIOS FOR THE TORQUE MEASUREMENT TEST RIG

SHAFT No.	R_i/R_o	ERROR (%)
1	0.874	0.14
2	0.911	0.20
3	0.950	0.35
4	0.975	0.70

TABLE 16 MAXIMUM ERRORS IN ε DUE TO DIAL GAUGE INACCURACY

TEST SECTION DETAILS		GAP MEASUREMENTS (mm)			
		AS RECORDED		RELATIVE TO DATUM ($\theta = 0$, UPPER BLOCK)	
R_i/R_o	θ	UPPER BLOCK	LOWER BLOCK	UPPER BLOCK	LOWER BLOCK
0.874	0	19.975	19.825	0	-0.150
	$\pi/2$	20.255	19.995	+0.280	+0.020
	π	20.055	20.065	+0.080	+0.090
	$3\pi/2$	19.775	19.940	-0.200	-0.035
0.911	0	17.830	17.690	0	-0.140
	$\pi/2$	18.125	17.830	+0.295	0
	π	17.920	17.920	+0.090	+0.090
	$3\pi/2$	17.615	17.870	-0.215	+0.040
0.950	0	15.610	15.455	0	-0.155
	$\pi/2$	15.890	15.620	+0.280	+0.010
	π	15.685	15.735	+0.075	+0.125
	$3\pi/2$	15.430	15.635	-0.180	+0.025
0.975	0	14.200	14.020	0	-0.180
	$\pi/2$	14.465	14.210	+0.265	+0.010
	π	14.275	14.300	+0.075	+0.100
	$3\pi/2$	13.985	14.200	-0.215	0

TABLE 17 "CONCENTRIC SETTING" MEASUREMENTS OF THE CLEARANCE BETWEEN THE OUTER CYLINDER HOUSINGS AND THE SHAFT IN THE TORQUE MEASUREMENT TEST RIG

ε_{nom}	R_i / R_o			
	0.874	0.911	0.950	0.975
0	0.02	0.03	0.05	0.11
0.10	0.10	0.11	0.12	0.15
0.20	0.20	0.20	0.21	0.23
0.30	0.30	0.30	0.31	0.32
0.40	0.40	0.40	0.41	0.42
0.50	0.50	0.50	0.51	0.51
0.60	0.60	0.60	0.60	0.61
0.70	0.70	0.70	0.70	0.71
0.80	0.80	0.80	0.80	0.81
0.90	0.90	0.90	0.90	0.91

TABLE 18 ECCENTRICITY RATIOS USED IN THE TORQUE MEASUREMENT TESTS

R_i / R_o	MISALIGNMENT (%)
0.874	3.6
0.911	5.0
0.950	9.0
0.975	17.9

TABLE 19 INHERENT MISALIGNMENT IN THE TORQUE MEASUREMENT TEST RIG

ϵ_{nom}	R_i / R_o		
	0.874	0.911	0.950
0	0.01	0.02	0.03
0.05	0.06	0.07	0.08
0.10	0.11	0.12	0.13
0.15	0.16	0.17	0.18
0.20	0.21	0.22	0.23
0.25	0.26	0.27	-
0.30	0.31	0.32	0.33
0.40	0.41	0.42	0.43
0.50	0.51	0.52	0.53

TABLE 20 ECCENTRICITY RATIOS USED IN THE FLOW VISUALISATION TESTS

R_i / R_o	MISALIGNMENT (%)
0.874	1.1
0.911	1.5
0.950	2.8

TABLE 21 INHERENT MISALIGNMENT IN THE FLOW VISUALISATION TEST RIG

TEST FLUID	VISCOMETER No.	TEMPERATURE	VISCOMETER CONSTANT	AVERAGE FLOW TIME	KINEMATIC VISCOSITY
		°C	cs/sec	secs	cs
MACRON A	1541	18.88	0.01096	555.50	6.088
		19.18		553.80	6.070
		24.73		472.65	5.180
		29.22		422.45	4.630
		33.32		376.80	4.130
"MIXTURE A"	8668	17.39	0.31140	365.00	113.661
		22.38		267.70	83.362
		26.92		204.90	63.806
	3313	29.42	0.11390	490.15	55.828

TABLE 22 RESULTS OF VISCOMETRY TESTS USING MACRON A AND "MIXTURE A"

TEST FLUID	TEMPERATURE	DENSITY
	^{o}C	kg/m^3
MACRON A	20.58	830.5
	29.27	825.0
	33.22	822.5
CARNEA 15	15.08	864.5
	17.18	863.0
	21.18	860.5
	29.72	854.5
TELLUS 21	19.63	869.0
	21.48	868.0
	24.88	866.0
	28.87	863.0
"MIXTURE A"	21.78	880.0
	25.13	877.5
	29.37	875.0
	33.57	873.0

TABLE 23 RESULTS OF HYDROMETRY TESTS

R_i / R_o	TEMP (^{o}C)		Re_c		T_c		Re_w		T_w	
	min	max	min	max	min	max	min	max	min	max
0.874	19.75	29.75	101	112	1372	1687	118	129	1873	2238
0.911	20.90	30.35	120	137	1341	1735	127	148	1502	2039
0.950	19.90	31.40	159	183	1292	1711	168	194	1442	1923
0.975	18.95	32.95	222	262	1241	1737	243	277	1494	1941

TABLE 24 TEMPERATURE DEPENDENCE OF RECORDED CRITICAL REYNOLDS AND TAYLOR NUMBERS

R_i / R_o	ε	T_o	(T_c / T_o)	(T_w / T_c)
0.874	0.02	1858	0.74, 0.91	1.37, 1.33
0.911	0.03	1804	0.74, 0.96	1.12, 1.18
0.950	0.05	1756	0.74, 0.97	1.12, 1.12
0.975	0.11	1723	0.72, 1.01	1.20, 1.12

TABLE 25 DERIVED NORMALISED TAYLOR NUMBER VARIATION (USING T_o PREDICTED BY WALOWIT ET AL)

R_i / R_o	TEMPERATURE (^oC)		ERROR (^oC)
	RECORDED	NECESSARY	
0.874	29.75	33.50	-3.75
0.911	30.35	35.35	-5.00
0.950	31.40	34.50	-3.10
0.975	32.95	38.10	-5.15

TABLE 26 NECESSARY TEMPERATURE MEASUREMENT ERRORS TO ACCOUNT FOR RECORDED VARIATION OF CRITICAL TAYLOR NUMBER

ε	MAGNITUDE DISCONTINUITIES		SLOPE DISCONTINUITIES	
	N	Re	N	Re
	(r.p.m.)		(r.p.m.)	
0.03	765 1245 1605	590 1035 1435	245 325 465	180 250 355
0.11	800	660	245 735	190 590
0.20	685	580	235 470 1135	185 390 1005
0.30	665	545	280 410 1000	220 330 860
0.40	670	550	200 275 515 1030	150 210 405 875
0.50	665	560	230 295 485 970	180 235 395 835
0.60	645	525	240 370 555 900	190 300 450 745
0.70	640	520	305 380 570 915	240 300 460 760
0.80	580	440	355 530 840	265 400 660
0.90	425	325	385 700	295 560

TABLE 27 DISCONTINUITIES FROM TYPICAL TORQUE MEASUREMENT TESTS USING TELLUS 21 AND $\eta = 0.911$

ε	T_1/T_c	T_2/T_c	T_3/T_c	T_4/T_c	T_5/T_c	T_6/T_c
0.03	1.9	3.7	7.5	20.6	63.4	121.8
0.11	2.3	22.3	27.9	-	-	-
0.20	2.2	9.7	21.5	64.6	-	-
0.30	2.7	6.0	16.3	40.6	-	-
0.40	1.0	2.0	7.3	13.4	34.0	-
0.50	1.0	1.7	4.8	9.7	21.5	-
0.60	1.0	2.5	5.6	7.6	15.4	-
0.70	1.0	1.6	3.7	4.7	10.0	-
0.80	1.0	2.3	2.8	6.2	-	-
0.90	1.0	1.2	4.5	-	-	-

TABLE 28 NORMALISED TAYLOR NUMBERS FOR TYPICAL TORQUE DISCONTINUITIES USING TELLUS 21 AND $\eta = 0.911$

ε	MAGNITUDE DISCONTINUITIES		SLOPE DISCONTINUITIES	
	N	Re	N	Re
	(r.p.m.)		(r.p.m.)	
0.03	375	705	290 560 785	545 1050 1440
0.11			345 560 840 1285	690 1000 1595 2485
0.20			330 575 800 1170	700 1055 1460 2160
0.30			330 460 755 1050	630 870 1435 2000
0.40			325 525 810 1105	625 1000 1545 2125
0.50			320 505 755 1060	615 950 1435 2030
0.60			315 475 760 1025	575 855 1380 1880
0.70			365 635 940	680 1175 1770
0.80			360 630 935	660 1155 1730
0.90			370 590 860 1250	695 1100 1630 2460

TABLE 29 DISCONTINUITIES FROM TYPICAL TORQUE MEASUREMENT TESTS USING CARNEA 15 AND $\eta = 0.911$

ε	T_1/T_c	T_2/T_c	T_3/T_c	T_4/T_c
0.03	17.6	29.4	65.2	122.7
0.11	30.5	64.0	162.8	395.2
0.20	31.4	71.2	136.4	298.6
0.30	21.8	41.5	113.0	219.5
0.40	17.4	44.4	106.1	200.7
0.50	11.7	27.9	63.6	127.2
0.60	9.2	20.3	52.8	97.9
0.70	8.0	24.0	54.4	-
0.80	6.2	19.0	42.6	-
0.90	5.6	13.9	30.5	69.5

TABLE 30 NORMALISED TAYLOR NUMBERS FOR TYPICAL TORQUE DISCONTINUITIES USING CARNEA 15 AND $\eta = 0.911$

ε	TELLUS 21		CARNEA 15	
	N	Re	N	Re
	(r.p.m.)		(r.p.m.)	
0.02	230	240	400	990
	465	505	665	1705
	715	755	1145	2965
	960	1016		
	1330	1540		
	1510	1840		
0.10	205	215	325	815
	465	480	490	1190
	910	955	730	1755
	1465	1695	900	2185
			1155	2855
0.20	385	405	365	890
	830	905	630	1575
	1355	1570	850	2125
			1085	2730
			1190	3025
0.30	290	305	365	870
	440	455	650	1605
	805	845	1165	2980
	1125	1235		
0.40	240	250	290	720
	320	335	410	1020
	545	570	620	1545
	765	810	775	1930
0.50	215	225	335	845
	350	365	535	1350
	600	630	800	2040
	730	775		
0.60	225	235	240	595
	375	390	345	855
	590	620	570	1410
	740	775	760	1900
0.70	255	265	235	585
	470	495	335	845
	785	835	520	1295
	1010	1105	715	1795
			925	2370
0.80	225	235	215	535
	300	315	370	940
	465	465	540	1375
	715	725	755	1930
	985	1030		
0.90	225	235	235	585
	470	490	320	800
	730	790	545	1325
	1135	1300	795	1985
			1055	2700

TABLE 31 DISCONTINUITIES FROM TYPICAL TORQUE MEASUREMENT TESTS USING $\eta = 0.874$

ε	N	Re	ε	N	Re
	(r.p.m.)			(r.p.m.)	
0.05	495	575	0.60	380	460
	585	675		505	605
	775	895		645	770
	1095	1300		900	1085
0.12	460	525		1130	1390
	580	660	0.70	370	480
	705	805		495	645
	1035	1190		680	815
0.21	370	465		890	1075
	485	600		1105	1370
	695	860	0.80	365	470
	1010	1255		520	665
0.31	370	465		730	920
	455	560		940	1180
	635	775		1055	1340
	1055	1305	0.90	355	430
0.41	300	375		530	635
	500	625		760	920
	675	840		920	1130
	1050	1325			
0.51	370	465			
	490	615			
	655	820			
	1015	1275			
	1280	1650			

TABLE 32 DISCONTINUITIES FROM TYPICAL TORQUE MEASUREMENT TESTS USING CARNEA 15 AND $\eta = 0.950$

ε	CARNEA 15		MACRON A	
	N	Re	N	Re
	(r.p.m.)		(r.p.m.)	
0.11	445 480 610 775 1120	240 260 335 435 650	385 455 650 810 1105	665 780 1120 1395 1930
0.15	455 540 780 1090 1385	235 285 415 600 785	440 595 835 1280	775 1045 1465 2320
0.23	460 670 915 1170	250 365 505 665	475 645 855 1225	840 1145 1510 2220
0.32	420 505 705 950 1250	225 270 385 530 730	375 495 650 845 990 1190 1365	650 845 1110 1445 1705 2110 2475
0.42	455 690 815 1080 1250	245 370 445 605 715	400 595 775 1125 1395	720 1050 1365 2025 2600
0.51	555 895 1015 1210	295 490 565 690	445 610 790 1120 1330	805 1100 1425 2045 2475
0.61	275 565 685 930 1315	145 305 375 515 770	400 460 615 810 1040 1270	695 795 1065 1400 1835 2330

cont'd/.....

TABLE 33 DISCONTINUITIES FROM TYPICAL TORQUE MEASUREMENT TESTS USING $\eta = 0.975$

ε	CARNEA 15		MACRON A	
	N	Re	N	Re
	(r.p.m.)		(r.p.m.)	
0.71	295 690 1170	155 375 675	345 480 585 740 890 1085 1265	605 840 1020 1295 1565 1940 2330
0.81	530 690 790 1125	290 380 445 665	355 495 675 805 1050 1390	625 865 1190 1420 1910 2640
0.91	570 730 835	305 400 455	230 420 485 715 1125 1295	415 750 860 1285 2100 2475

TABLE 33 DISCONTINUITIES FROM TYPICAL TORQUE MEASUREMENT TESTS USING $\eta = 0.975$

TEST NUMBER						
T44	T54	T70	T71	T73	T74	T87
990	1150	240	245	665		630
1705	1635	335	340	780	735	740
2965	2750	435	455	1120	1050	915
		650	785	1395	1490	1350
				1930	2140	2195
CARNEA 15		CARNEA 15		MACRON A		
$\eta = 0.874$, $\varepsilon = 0.02$		$\eta = 0.975$, $\varepsilon = 0.11$				

TABLE 34 NON-UNIQUENESS OF REYNOLDS NUMBERS FOR TYPICAL TORQUE DISCONTINUITIES

ε	SLOPE DECREASE		TORQUE REDUCTION	
	CARNEA 15	MACRON A	CARNEA 15	MACRON A
0.11	260	-	435	1930
0.15	-	-	415	-
0.23	-	-	-	-
0.32	-	1705	-	2475
0.42	-	-	245	-
0.51	-	-	565	-
0.61	-	-	145, 375	-
0.71	-	-	155	1020
0.81	290	-	665	625, 1420
0.91	305	750	-	415

TABLE 35 REYNOLDS NUMBERS FOR PARTICULAR TORQUE DISCONTINUITIES RECORDED IN TYPICAL TESTS USING $\eta = 0.975$

η	ε	TEST FLUID	Re	$\log_{10} Re$
0.874	0.02	TELLUS 21	490	2.69
			760	2.88
			1035	3.01
			1550	3.19
			2020	3.31
		CARNEA 15	1245	3.10
			1495	3.17
			1780	3.25
			2115	3.33
			2820	3.45
			3430	3.54
0.911	0.03	TELLUS 21	605	2.78
			1000	3.00
			1385	3.14
		CARNEA 15	735	2.87
			1075	3.03
			1515	3.18
			1950	
0.950	0.05	TELLUS 21	320	
			480	
			615	
		CARNEA 15	650	
			1300	
0.975	0.11	CARNEA 15	440	
		MACRON A	1215	
			1820	
			2370	

TABLE 36 DISCONTINUITIES FROM CORRECTED FRICTION COEFFICIENT CHARACTERISTICS FOR THE "CONCENTRIC" SETTING

ε	Re	ℓ	K
0.02	250 - 760	0.43	0.30
	760 - 1035	0.81	3.63
	1035 - 4000	0.51	0.46
0.10	250 - 4000	0.55	0.64
0.20	250 - 4000	0.54	0.61
0.30	250 - 4000	0.52	0.54
0.40	200 - 500	0.43	0.32
	500 - 3150	0.51	0.52
0.50	200 - 575	0.43	0.32
	575 - 3150	0.50	0.50
0.60	200 - 3150	0.47	0.43
0.70	200 - 535	0.52	0.60
	535 - 3150	0.44	0.37
0.80	200 - 300	1.00	11.24
	300 - 470	0.84	2.90
	470 - 715	0.44	0.39
	715 - 3150	0.40	0.29
0.90	200 - 370	0.97	13.70
	370 - 725	0.67	2.52
	725 - 1860	0.53	0.84
	1860 - 3150	0.40	0.32

TABLE 37 CONSTANTS DERIVED FROM THE FRICTION COEFFICIENT CHARACTERISTICS FOR $\eta = 0.874$ USING THE FORMULA

$$C_f = K \left(\frac{(R_o - R_i)R_o}{R_i^2} \right)^{\frac{1}{4}} \frac{1}{Re^{\ell}}$$

ε	Re	ℓ	K
0.03	360 - 605	0.50	0.47
	605 - 3250	0.50	0.43
0.11	360 - 710	0.65	1.13
	710 - 3250	0.47	0.35
0.20	250 - 3250	0.51	0.48
0.30	250 - 380	0.39	0.24
	380 - 3150	0.50	0.45
0.40	200 - 310	0.23	0.10
	310 - 935	0.45	0.34
	935 - 3150	0.50	0.48
0.50	200 - 1290	0.42	0.29
	1290 - 3150	0.54	0.66
0.60	230 - 405	0.52	0.55
	405 - 945	0.40	0.26
	945 - 3150	0.49	0.48
0.70	200 - 315	0.88	4.67
	315 - 640	0.54	0.66
	640 - 1160	0.37	0.22
	1160 - 3000	0.44	0.36
0.80	200 - 365	0.95	8.81
	365 - 570	0.70	2.03
	570 - 1120	0.45	0.41
	1120 - 2600	0.38	0.25
0.90	200 - 415	0.98	15.45
	415 - 820	0.73	3.40
	820 - 1515	0.57	1.16
	1515 - 3000	0.46	0.52

TABLE 38 CONSTANTS DERIVED FROM THE FRICTION COEFFICIENT CHARACTERISTICS FOR $\eta = 0.911$ USING THE FORMULA

$$C_f = K \left(\frac{(R_o - R_i)R_o}{R_i^2} \right)^{\frac{1}{4}} \frac{1}{Re^{\ell}}$$

ε	Re	ℓ	K
0.05	300 – 690	0.59	0.73
	690 – 2500	0.50	0.39
0.12	300 – 525	0.63	0.89
	525 – 1110	0.43	0.26
	1110 – 2650	0.54	0.56
0.21	400 – 1230	0.44	0.28
	1230 – 2500	0.52	0.49
0.31	400 – 945	0.40	0.22
	945 – 2500	0.48	0.38
0.41	300 – 975	0.34	0.15
	975 – 2500	0.46	0.35
0.51	250 – 400	0.82	2.66
	400 – 900	0.27	0.10
	900 – 2500	0.40	0.24
0.60	250 – 400	0.89	4.48
	400 – 550	0.57	0.66
	550 – 910	0.24	0.08
	910 – 2500	0.38	0.21
0.70	250 – 425	0.94	7.26
	425 – 740	0.61	0.99
	740 – 2500	0.30	0.13
0.80	250 – 435	0.95	9.64
	435 – 685	0.68	1.87
	685 – 2000	0.44	0.39
0.90	250 – 650	1.01	21.33
	650 – 975	0.67	2.37
	975 – 2100	0.43	0.46

TABLE 39 CONSTANTS DERIVED FROM THE FRICTION COEFFICIENT CHARACTERISTICS FOR $\eta = 0.950$ USING THE FORMULA

$$C_f = K \left(\frac{(R_o - R_i) R_o}{R_i^2} \right)^{\frac{1}{4}} \frac{1}{Re^{\ell}}$$

ε	Re	ℓ	K
0.11	250 - 425	0.24	0.08
	425 - 3150	0.48	0.36
0.15	250 - 350	0.23	0.08
	350 - 3150	0.46	0.32
0.23	250 - 675	0.35	0.16
	675 - 3150	0.45	0.30
0.32	250 - 390	0.66	0.95
	390 - 840	0.26	0.09
	840 - 3150	0.43	0.27
0.42	200 - 270	1.08	10.81
	270 - 425	0.82	2.49
	425 - 830	0.21	0.07
	830 - 3150	0.37	0.19
0.51	200 - 375	0.89	4.07
	375 - 500	0.71	1.48
	500 - 830	0.25	0.08
	830 - 3150	0.32	0.14
0.61	200 - 475	0.93	6.44
	475 - 1035	0.48	0.41
	1035 - 1680	0.17	0.05
	1680 - 3150	0.23	0.07
0.71	200 - 400	0.99	11.08
	400 - 710	0.71	2.06
	710 - 1620	0.43	0.33
	1620 - 3150	0.18	0.05
0.81	200 - 425	1.06	20.80
	425 - 805	0.57	1.04
	805 - 1995	0.45	0.47
	1995 - 3150	0.27	0.12
0.91	530 - 1010	0.85	9.28
	1010 - 3150	0.49	0.77

TABLE 40 CONSTANTS DERIVED FROM THE FRICTION COEFFICIENT CHARACTERISTICS FOR $\eta = 0.975$ USING THE FORMULA

$$C_f = K \left(\frac{(R_o - R_i)R_o}{R_i^2} \right)^{\frac{1}{4}} \frac{1}{Re^{\ell}}$$

AUTHOR	η	Re	ℓ	K
WENDT, 1933	0.680 0.850 0.935	400 - 10^4	0.50	0.46
	0.680	10^4 - 10^5		
	0.850	10^4 - 4.6 x 10^4	0.30	0.07
	0.935	10^4 - 4.6 x 10^4		
TAYLOR, 1936	0.790	980 - 2 x 10^4	0.52	0.54
	0.886	695 - 2 x 10^4	0.52	0.54
	0.909	2700 - 1.6 x 10^4	0.52	0.55
	0.960	785 - 8000	0.50	0.43
	0.973	150 - 4950	0.52	0.49
	0.790	2 x 10^4 - 9.5 x 10^4	0.19	0.02
	0.886	2 x 10^4 - 8.5 x 10^4	0.08	0.01
	0.909	1.6x10^4 - 5.9x10^4	0.16	0.02
	0.960	8000 - 3.1 x 10^4	0.14	0.02
	0.973	4950 - 3 x 10^4	0.14	0.02
DONNELLY, 1958	0.500	100 - 2000	0.62	1.02
	0.950	240 - 400	0.20	0.07
		400 - 670	0.69	1.36
		670 - 1200	0.52	0.43
VOHR, 1968	0.910	725 - 1.3 x 10^4	0.48	0.38
		1.3x10^4 - 4.2x10^4	0.17	0.02
DEBLER ET AL, 1969	0.500	150 - 350	0.57	0.77
	0.650	250 - 680	0.57	0.91
	0.675	250 - 680	0.57	0.88
	0.850	290 - 450	0.49	0.49
		500 - 630	0.48	0.44
		690 - 1300	0.59	0.82
		1300 - 1585	0.59	0.86
	0.875	315 - 850	0.47	0.37
		1070 - 1585	0.57	0.71
	0.925	315 - 690	0.46	0.36
	0.935	400 - 630	0.50	0.47
		675 - 1000	0.57	0.65
	0.950	400 - 630	0.70	1.39

TABLE 41 CONSTANTS DERIVED FROM PREVIOUS AUTHORS' FRICTION COEFFICIENT CHARACTERISTICS FOR THE CONCENTRIC CYLINDER CASE USING THE FORMULA

$$C_f = K \left(\frac{(R_o - R_i)R_o}{R_i^2} \right)^{\frac{1}{4}} \frac{1}{Re^{\ell}}$$

η	ε	Re	ℓ	K
0.910	0.45	500 - 7000	0.50	0.51
		7000 - 40000	0.25	0.05
	0.71	600 - 3200	0.41	0.30
		3200 - 34000	0.31	0.14
	0.89	500 - 2400	0.60	1.49
		2400 - 35000	0.27	0.11
0.990	0.08	500 - 900	0.12	0.04
		900 - 4145	0.50	0.48
	0.35	525 - 1400	0.20	0.06
		1400 - 3800	0.38	0.21
	0.51	650 - 4100	0.22	0.07
	0.68	900 - 1450	0.34	0.17
		1450 - 3300	0.09	0.03
	0.83	900 - 1900	0.39	0.31
		1900 - 4200	0.24	0.10

TABLE 42 CONSTANTS DERIVED FROM VOHR'S FRICTION COEFFICIENT CHARACTERISTICS FOR THE ECCENTRIC CYLINDER CASE USING THE FORMULA

$$C_f = K \left(\frac{(R_o - R_i)R_o}{R_i^2} \right)^{\frac{1}{4}} \frac{1}{Re^{\ell}}$$

AUTHOR	Re		
	300	500	850
TAYLOR, 1936	1.90	2.34	2.58
DONNELLY, 1958	1.70	2.22	2.30
DEBLER ET AL, 1969	1.66	2.18	2.42
THE PRESENT WORK	1.66	2.07	2.61

TABLE 43 THE EFFECT OF REYNOLDS NUMBER ON THE RATIO M/M_{lam} FOR $\eta = 0.950$ AND $\varepsilon = 0$

η	Re	ℓ	K
0.680	135 - 700	0.72	1.88
0.850	200 - 700	0.61	0.99
0.935	265 - 780	0.61	0.96

TABLE 44 CONSTANTS DERIVED FROM WENDT'S FRICTION COEFFICIENT CHARACTERISTICS ($\varepsilon = 0$) USING THE FORMULA

$$C_f = K \left(\frac{(R_o - R_i)R_o}{R_i^2} \right)^{\frac{1}{4}} \frac{1}{Re^{\ell}}$$

AUTHOR	K	ℓ	BEARING TYPE
SMITH AND FULLER, 1956	0.078	0.43	PLAIN CYLINDRICAL, SINGLE OIL FEED ON UNLOADED SIDE
DUFFIN AND JOHNSON, 1966	0.019	0.25	ELLIPTICAL, ONE OIL FEED EACH SIDE OF HORIZONTAL DIAMETER
RAMSDEN, 1967	0.017	0.25	CYLINDRICAL, TWO OIL FEEDS ON HORIZONTAL DIAMETER WITH RECESSES
BOOSER ET AL, 1970	0.012 0.020	0.25 0.25	ELLIPTICAL WITH HORIZONTAL CLEARANCE PAD (FLOODED DESIGN)

TABLE 45 CONSTANTS DERIVED FROM THE RESULTS OF REAL BEARING TESTS USING THE FORMULA

$$C_f = \frac{K}{Re^{\ell}}$$

ϵ	Re	ℓ
0.20	170 - 270	0.07
	270 - 425	0.57
0.40	185 - 325	0.07
	325 - 415	0.48
0.60	245 - 485	0.55
0.80	305 - 460	0.70

TABLE 46 BASIC SLOPES DERIVED FROM CASTLE AND MOBBS' FRICTION COEFFICIENT CHARACTERISTICS FOR $\eta = 0.899$

Re	NEGATIVE SLOPE AFTER DISCONTINUITY	COMMENTS	SHAFT SPEED
		TEST No.T140, "MIXTURE A", FIG.133(a)	DECREASING INCREASING
	0.48		
865	0.49	TORQUE REDUCTION	
415	0.44	TORQUE INCREASE	
595	0.49	TORQUE REDUCTION	
700	0.85		
925	0.50		
1230	0.50	TORQUE INCREASE	
925	0.85		
765	0.50		
445	0.50	TORQUE INCREASE	
		TEST No.T130, TELLUS 21, FIG.133(b)	DECREASING INCREASING
	0.42		
715	0.86		
1050	0.44		
1550	0.57	TORQUE REDUCTION	
1820	0.38		
1680	0.50	BRIEF TORQUE REDUCTION AT Re = 1365	
925	0.47	TORQUE INCREASE	
		TEST No.T44, CARNEA 15, FIG.134(a)	INCREASING DECREASING
	0.59		
2820	0.50	TORQUE INCREASE	
2165	0.50	SERIES OF STEPS REDUCING TORQUE AT Re = 1905 AND 1460; SLOPE AFTER EACH STEP IS -0.50	
990	0.65		
1260	0.37		
1515	0.68		
1800	0.37		
2140	0.59		
3550	0.37		
		TEST No.T54, CARNEA 15, FIG.134(b)	DECREASING INCREASING
	0.43		
765	0.75		
1125	0.44		
1660	0.35	TORQUE REDUCTION	
2090	0.54		
3390	0.44		
3390	0.54		
1930	0.54	TORQUE REDUCTION	
1190	0.44	TORQUE REDUCTION	
1000	0.54		

TABLE 47 DISCONTINUITIES FROM THE FRICTION COEFFICIENT CHARACTERISTICS OF TYPICAL TESTS USING $\eta = 0.874$ AND $\varepsilon = 0.02$

ε	η			
	0.874	0.911	0.950	0.975
0.02	1.000	-	-	-
0.03	-	1.000	-	-
0.05	-	-	1.000	-
0.10	1.028	-	-	-
0.11	-	1.012	-	1.000
0.12	-	-	1.007	-
0.15	-	-	-	1.017
0.20	1.048	1.005	-	-
0.21	-	-	1.026	-
0.23	-	-	-	1.041
0.30	1.096	1.041	-	-
0.31	-	-	1.064	-
0.32	-	-	-	1.064
0.40	1.135	1.086	-	-
0.41	-	-	1.102	-
0.42	-	-	-	1.100
0.50	1.176	1.126	-	-
0.51	-	-	1.155	1.141
0.60	1.205	1.195	1.184	-
0.61	-	-	-	1.151
0.70	1.296	1.314	1.222	-
0.71	-	-	-	1.303
0.80	1.400	1.409	1.424	-
0.81	-	-	-	1.598
0.90	1.585	1.642	1.824	-
0.91	-	-	-	1.950

TABLE 48 VALUES OF F DERIVED FROM FRICTION COEFFICIENT CHARACTERISTICS

ε	F	$(1+\varepsilon^2)$	$(1+\varepsilon^3)$	$\frac{(1+2\varepsilon^2)}{(1+\varepsilon^2)}$	$\frac{2(1+2\varepsilon^2)}{(2+\varepsilon^2)}$	$\frac{2(1+2\varepsilon^2)}{(2+\varepsilon^2)(1-\varepsilon^2)^{\frac{1}{2}}}$
0	1	1	1	1	1	1
0.1	1.012	1.010	1.001	1.010	1.015	1.020
0.2	1.035	1.040	1.008	1.038	1.059	1.081
0.3	1.060	1.090	1.027	1.083	1.129	1.184
0.4	1.095	1.160	1.064	1.138	1.222	1.333
0.5	1.140	1.250	1.125	1.200	1.333	1.540
0.6	1.200	1.360	1.216	1.265	1.458	1.823
0.7	1.295	1.490	1.343	1.329	1.590	2.226
0.8	1.445	1.640	1.512	1.390	1.727	2.879
0.9	1.750	1.810	1.729	1.448	1.865	4.279

TABLE 49 COMPARISON OF DERIVED MEAN VALUES OF F WITH THOSE GIVEN BY PARTICULAR TRIAL SOLUTIONS

ε	F	F (given)	ERROR	$(\text{ERROR})^2$
0.1	1.010	1.012	-0.002	0.400×10^{-5}
0.3	1.072	1.060	0.012	0.144×10^{-3}
0.5	1.179	1.140	0.039	0.152×10^{-2}
0.7	1.327	1.295	0.032	0.102×10^{-2}
0.9	1.513	1.750	-0.237	0.562×10^{-1}
			E = 0.0589	

TABLE 50 ERROR TABLE FOR $F = 1 + 0.62\,\varepsilon^{1.79}$

	E
$(1+\varepsilon^2)$	0.0546
$(1+\varepsilon^3)$	0.0042
$\frac{(1+2\varepsilon^2)}{(1+\varepsilon^2)}$	0.0965
$\frac{2(1+2\varepsilon^2)}{(2+\varepsilon^2)}$	0.1423
$\frac{2(1+2\varepsilon^2)}{(2+\varepsilon^2)(1-\varepsilon^2)^{\frac{1}{2}}}$	7.4380

TABLE 51 ERROR VALUES GIVEN BY PARTICULAR TRIAL SOLUTIONS FOR F

η	LOG K'	K'	K''
0.874	0.2125	1.631	3.637
0.911	0.1650	1.462	3.260
0.950	0.0800	1.202	2.680
0.975	0	1.000	2.230
0.999	-	-	1.000

TABLE 52 VALUES OF K' AND K'' DERIVED FROM FRICTION COEFFICIENT CHARACTERISTICS

ε \ η	0.874	0.911	0.950	0.975
0.02	2.444	-	-	-
0.03	-	2.302	-	-
0.05	-	-	2.170	-
0.10	2.491	-	-	-
0.11	-	2.368	-	2.141
0.12	-	-	2.222	-
0.15	-	-	-	2.171
0.20	2.639	2.483	-	-
0.21	-	-	2.351	-
0.23	-	-	-	2.299
0.30	2.891	2.720	-	-
0.31	-	-	2.584	-
0.32	-	-	-	2.513
0.40	3.257	3.064	-	-
0.41	-	-	2.918	-
0.42	-	-	-	2.845
0.50	3.760	3.537	-	-
0.51	-	-	3.377	3.249
0.60	4.450	4.186	3.934	-
0.61	-	-	-	3.855
0.70	5.439	5.117	4.809	-
0.71	-	-	-	4.731
0.80	7.031	6.614	6.216	-
0.81	-	-	-	6.167
0.90	10.448	9.829	9.237	-
0.91	-	-	-	9.411

TABLE 53 VALUES OF K_2 FOR THE TORQUE MEASUREMENT TEST RIG

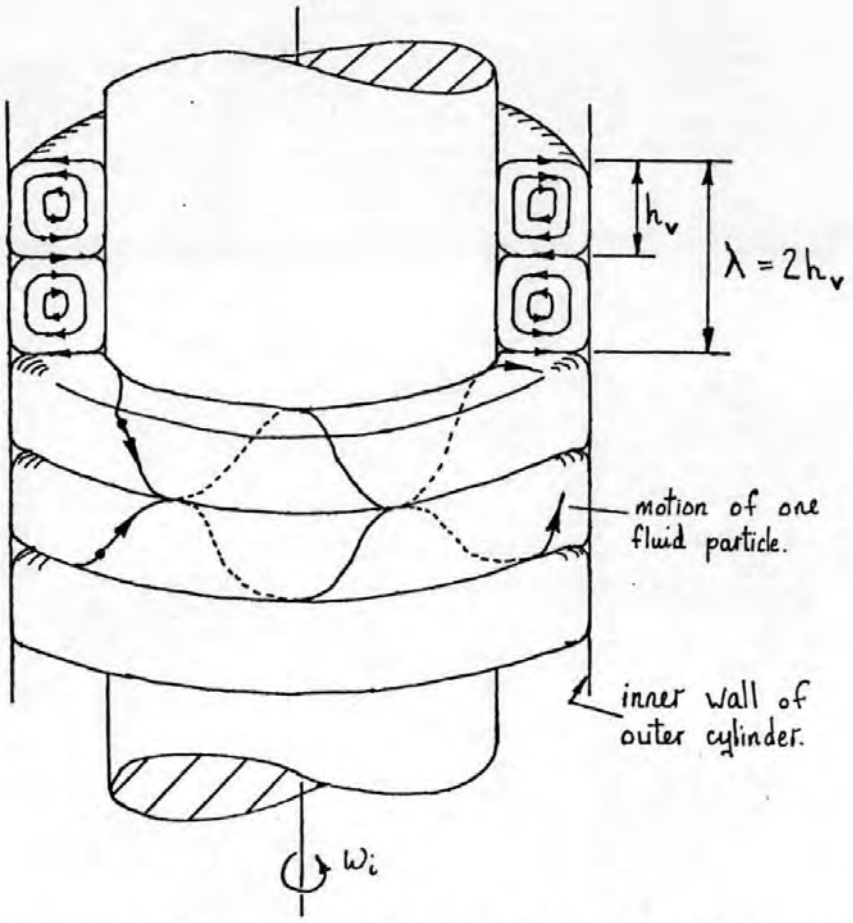

FIG. 1 SCHEMATIC VIEW OF THE TAYLOR VORTEX MODE. ($\varepsilon = 0$, $\mu^* = 0$)

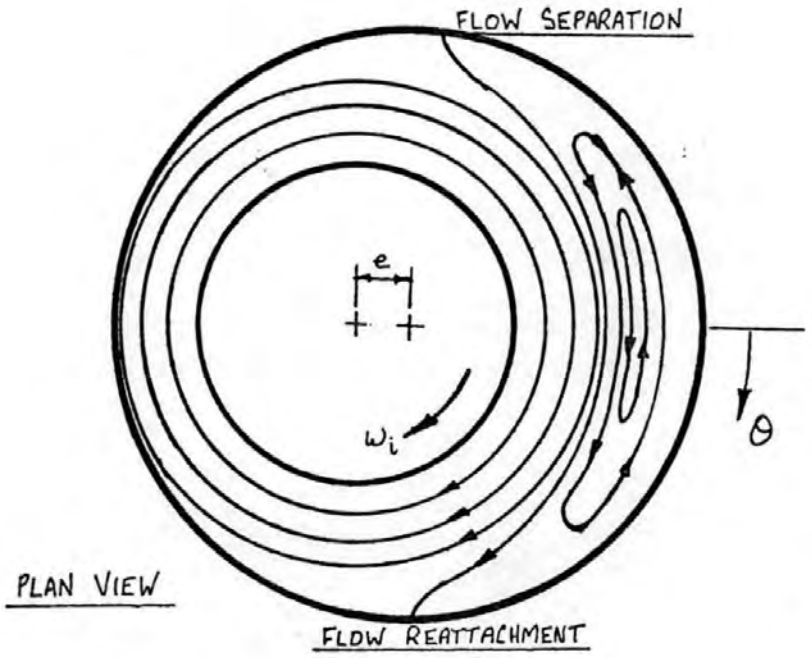

FIG. 2 'REVERSED FLOW' WITH ECCENTRIC CYLINDERS.

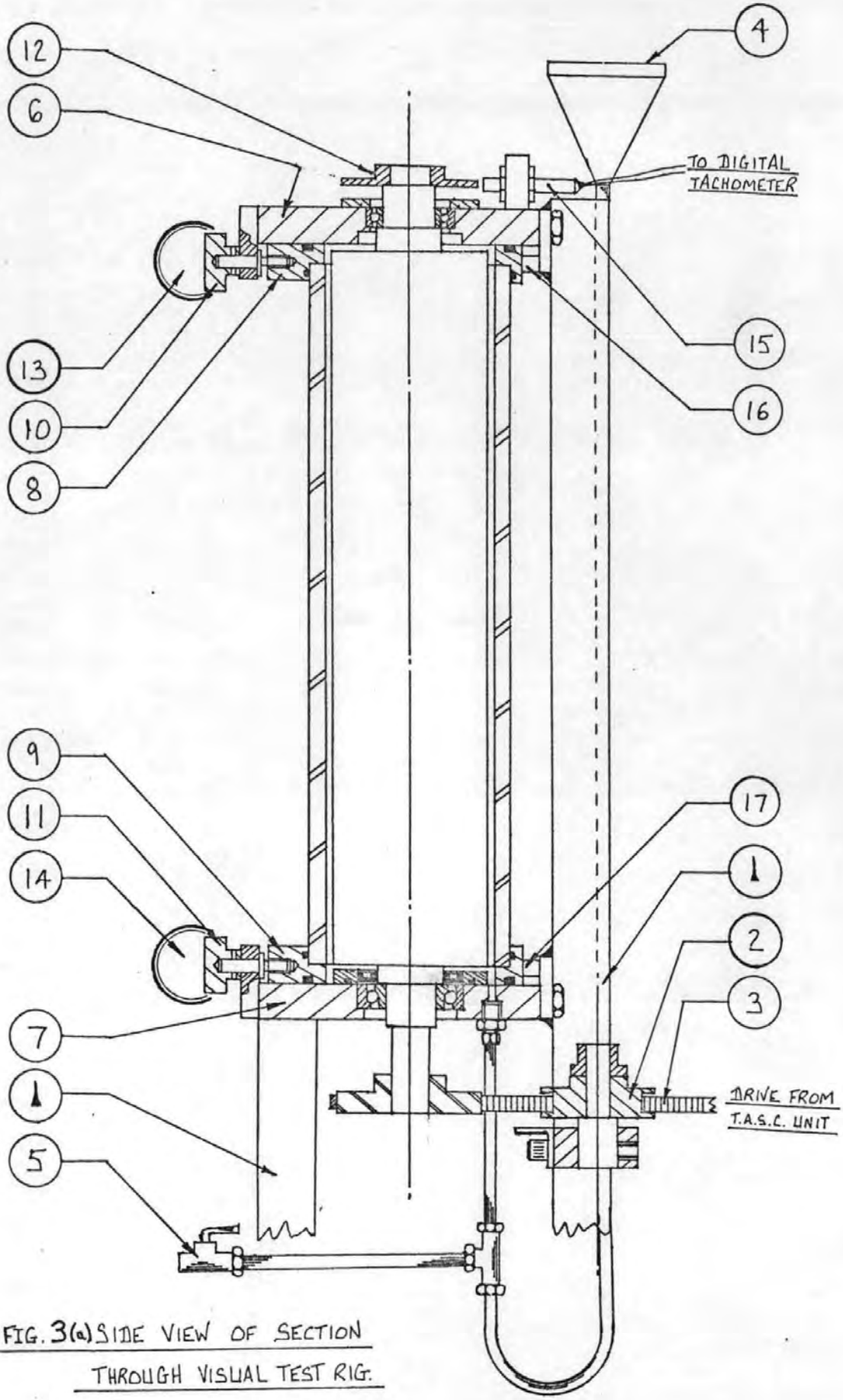

FIG. 3(a) SIDE VIEW OF SECTION THROUGH VISUAL TEST RIG.

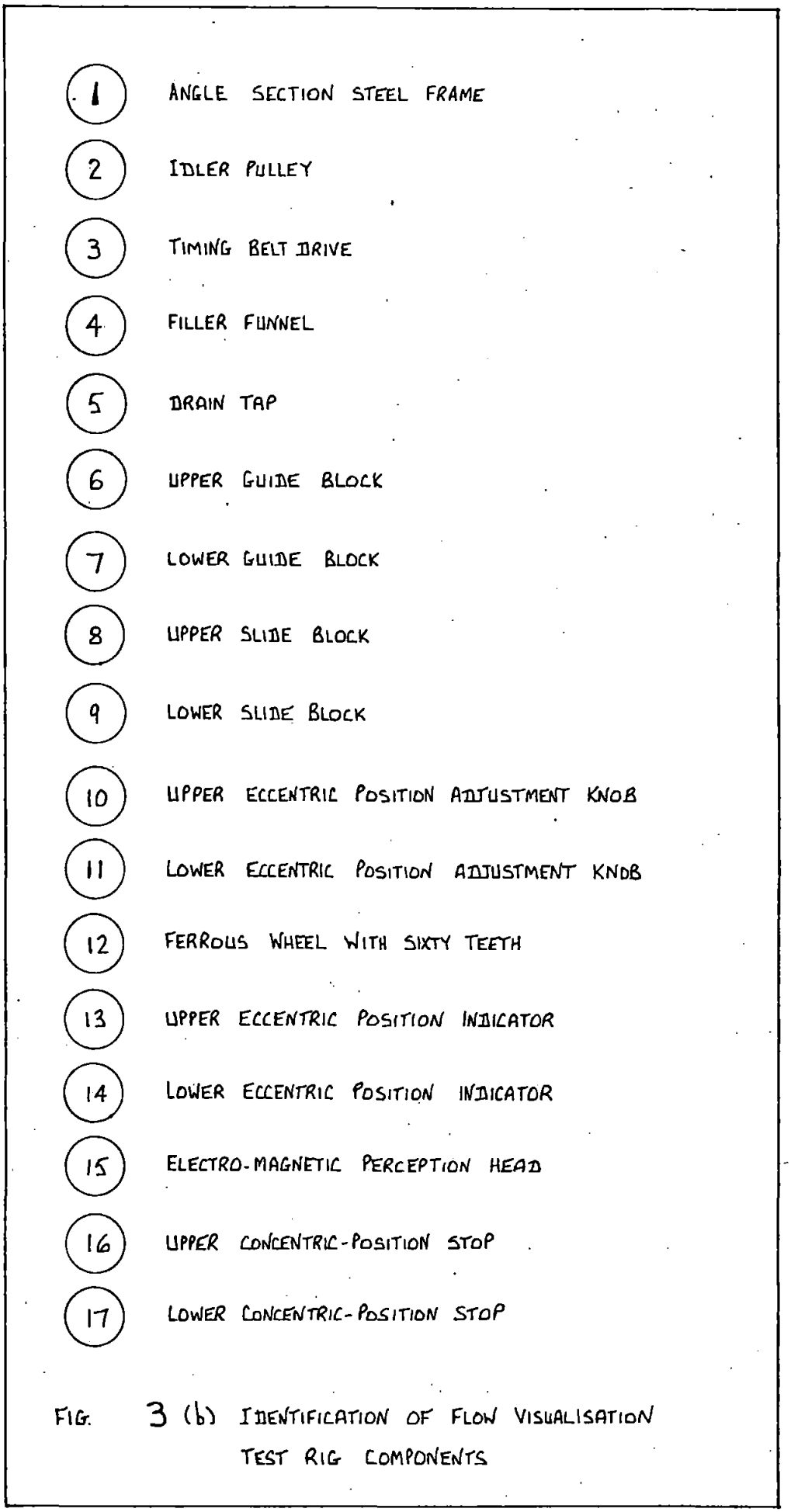

FIG. 3 (b) IDENTIFICATION OF FLOW VISUALISATION TEST RIG COMPONENTS

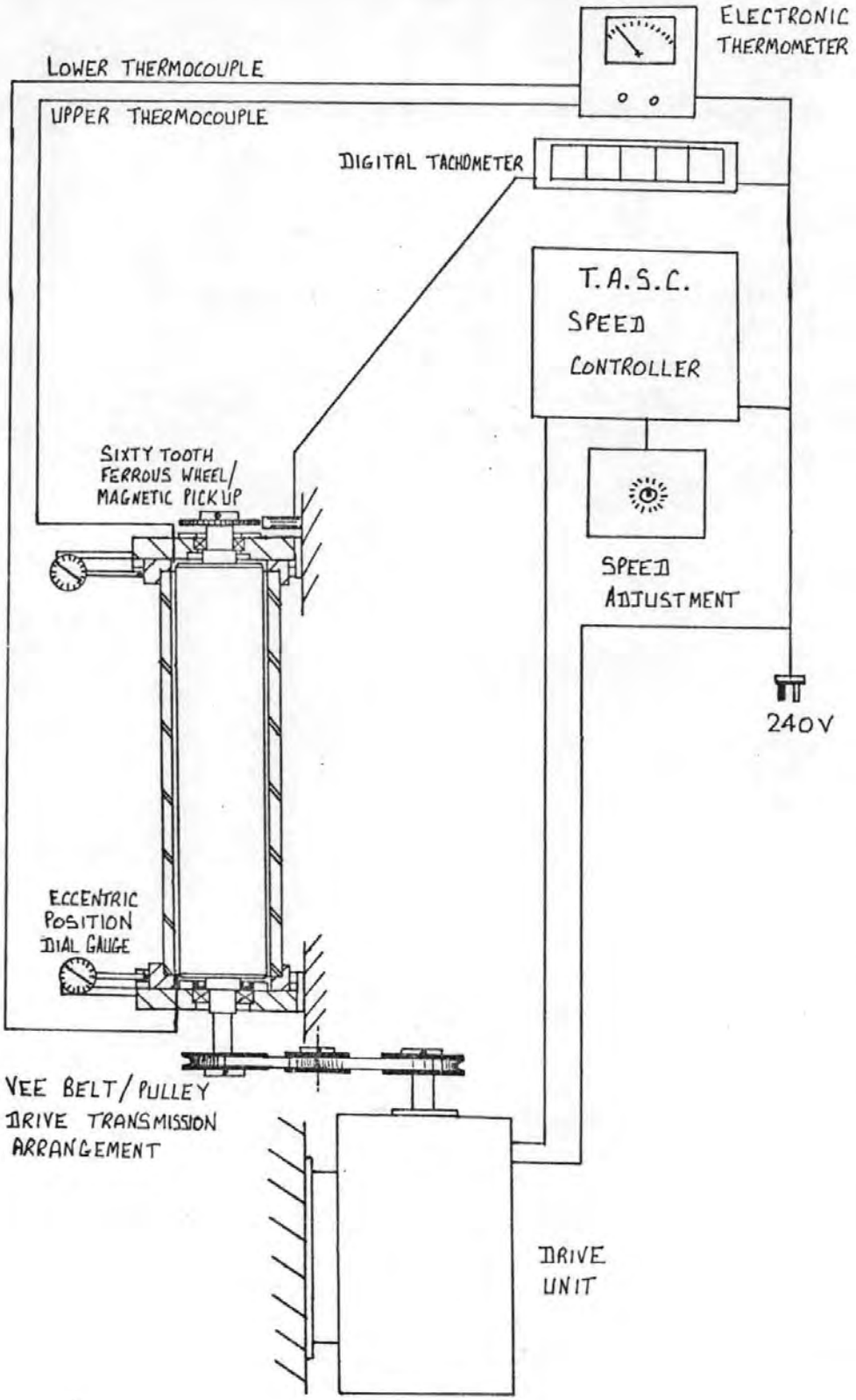

FIG. 4 GENERAL ARRANGEMENT OF FLOW VISUALIZATION TEST RIG AND INSTRUMENTATION.

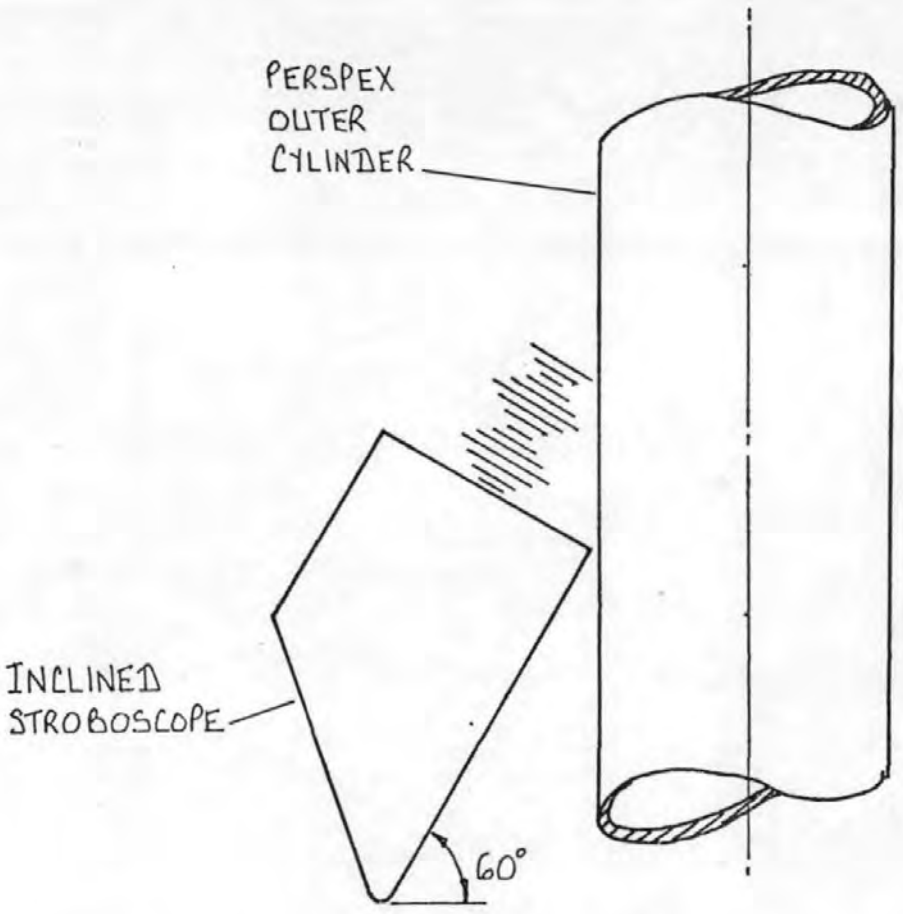

FIG. 5 SCHEMATIC REPRESENTATION OF OPTIMUM STROBOSCOPE INCLINATION.

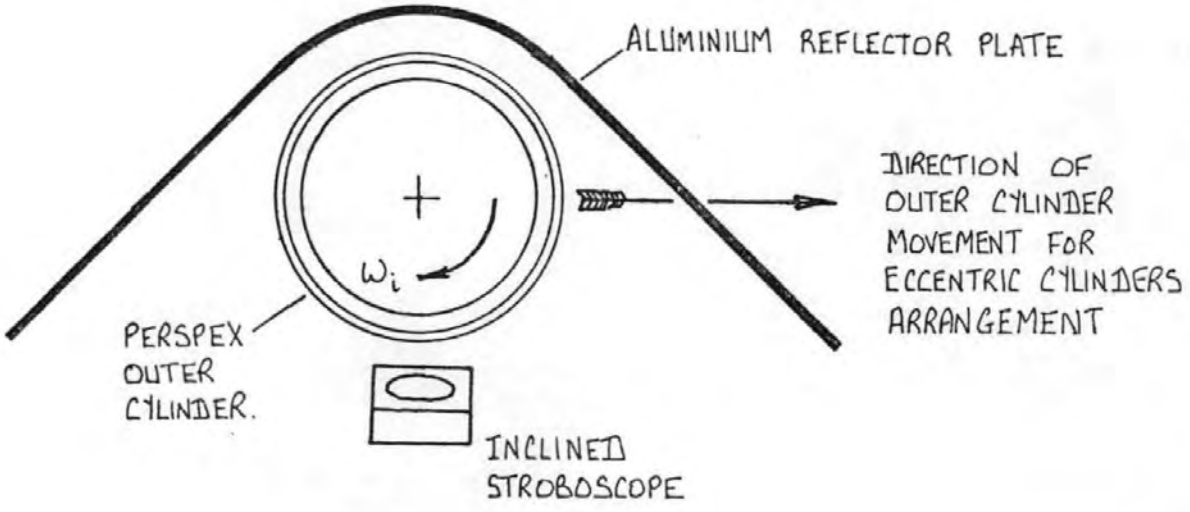

FIG. 6 SCHEMATIC PLAN VIEW SHOWING RELATIVE POSITIONS OF ILLUMINATION EQUIPMENT.

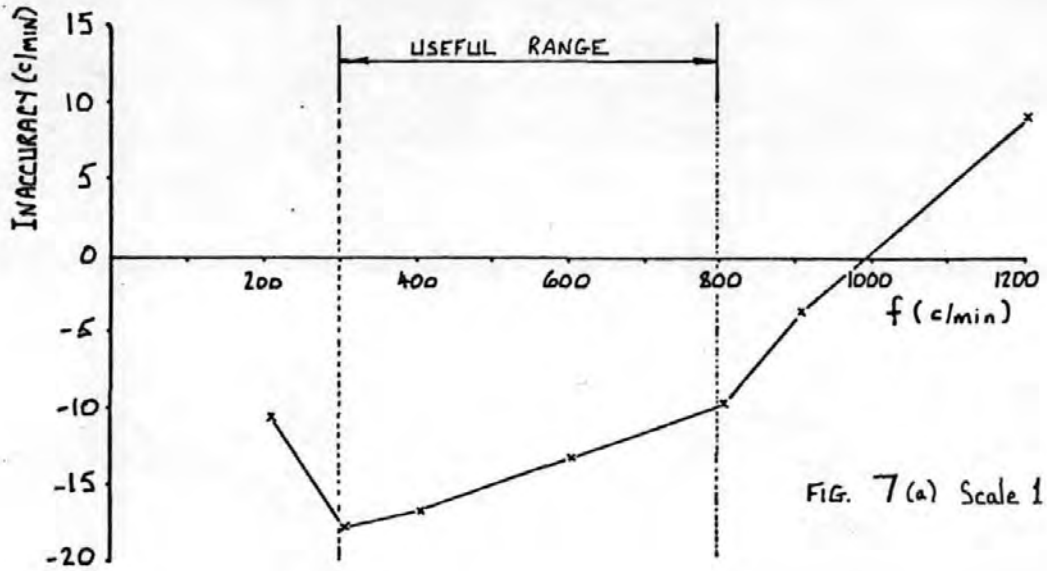

FIG. 7 (a) Scale 1

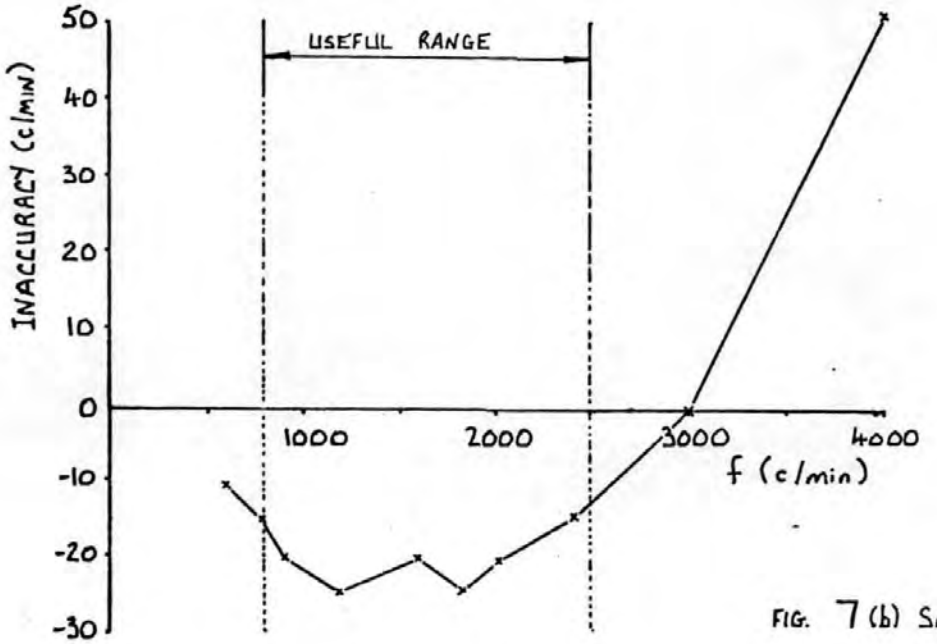

FIG. 7 (b) Scale 2

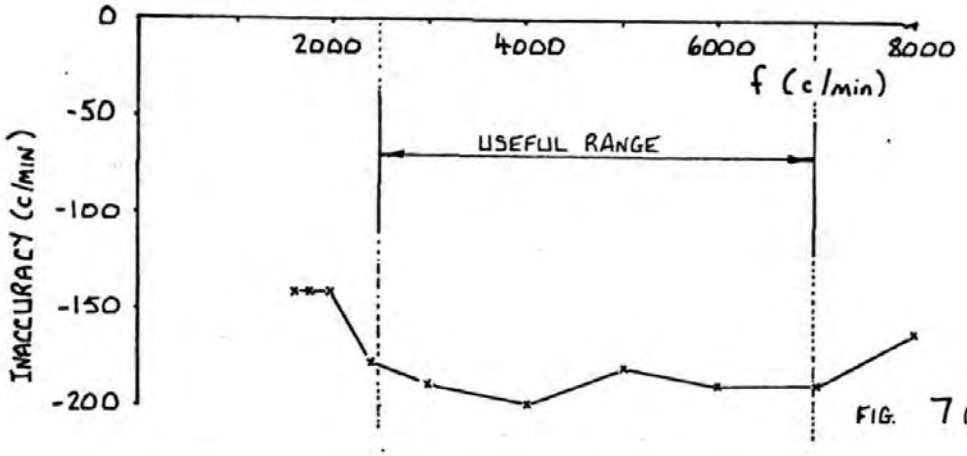

FIG. 7 (c) Scale 3

FIG. 7 STROBOSCOPE CALIBRATION CURVES

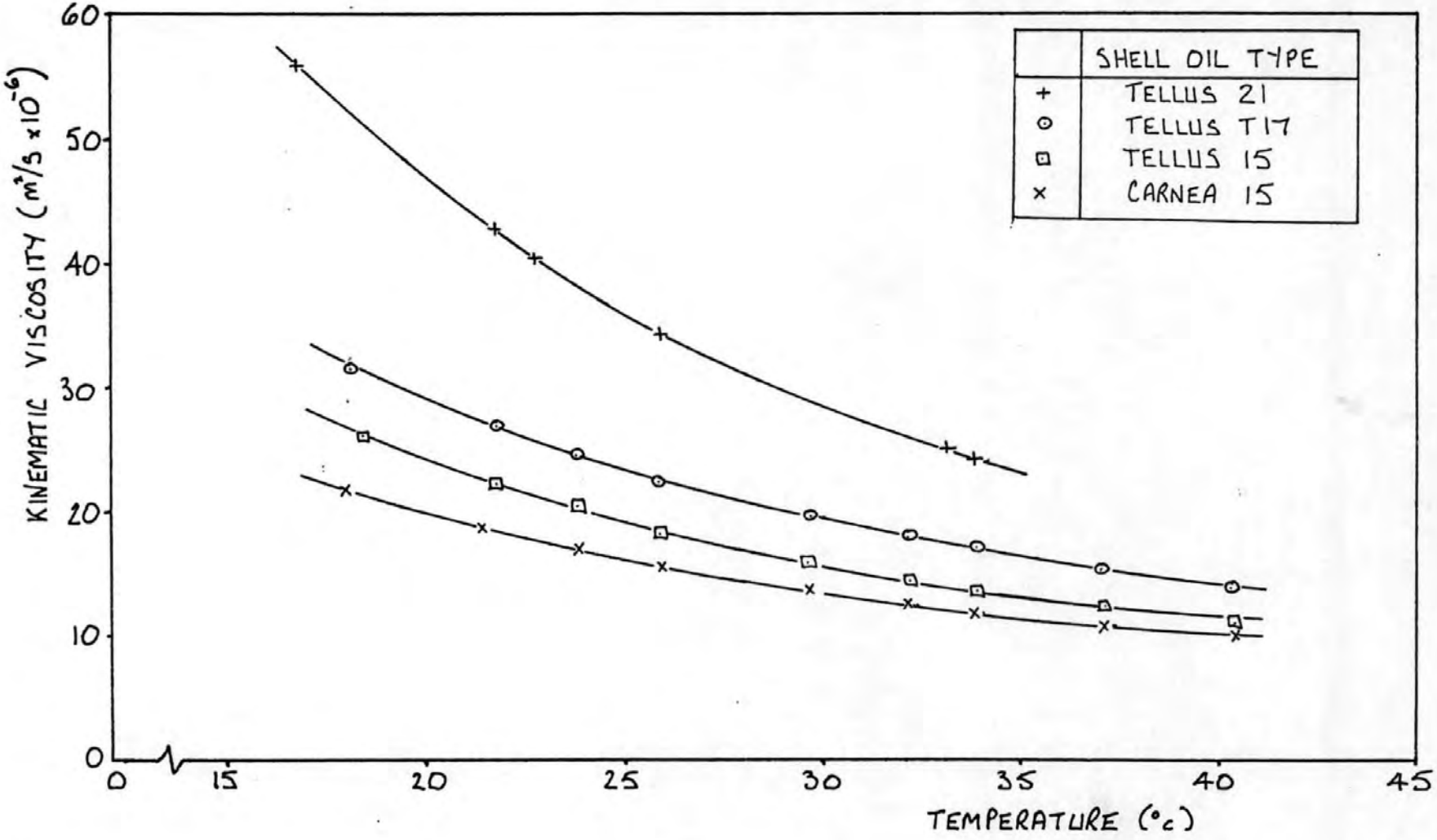

FIG. 8 VISCOSITY CHARACTERISTICS OF TEST FLUIDS.

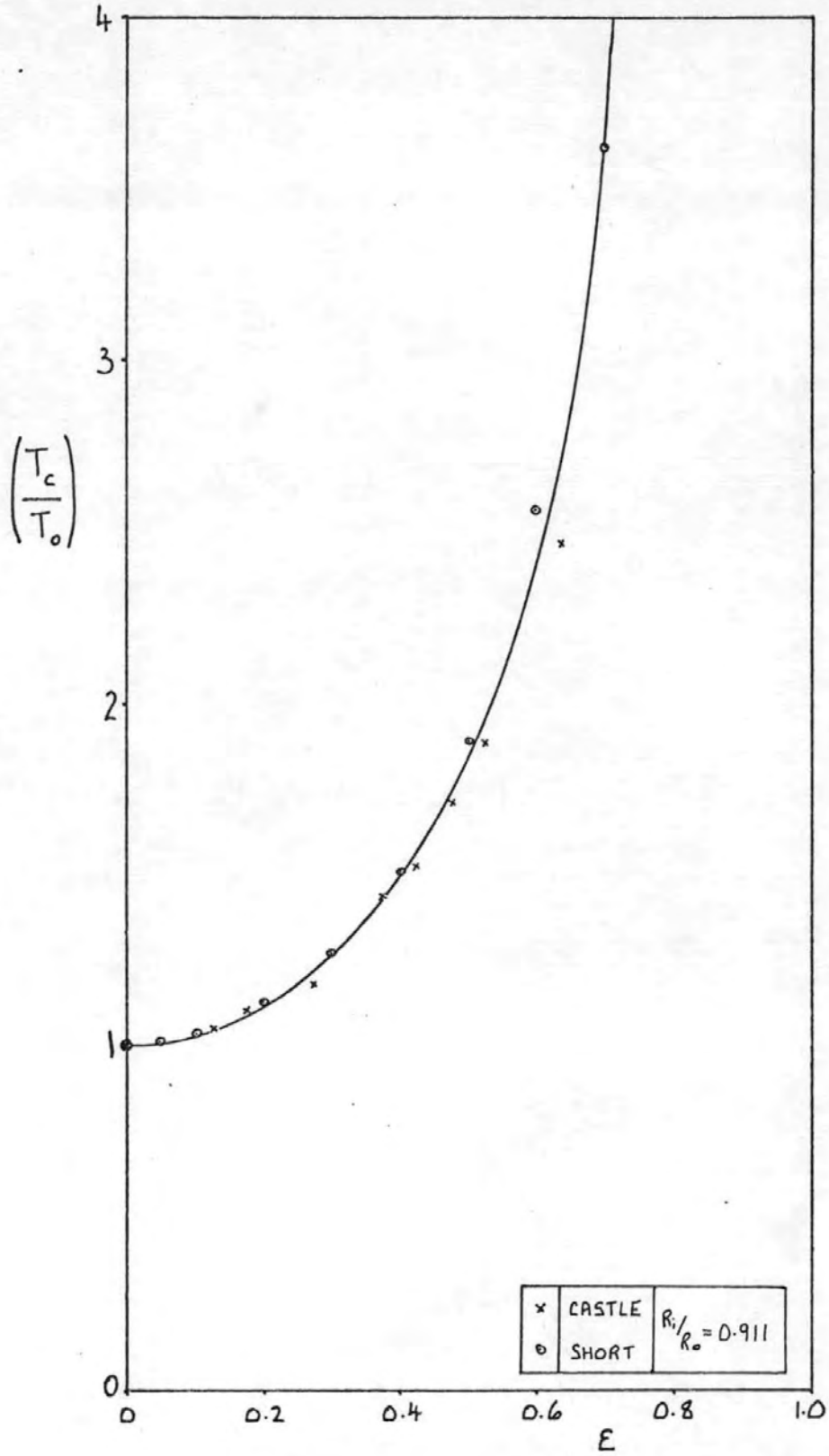

FIG. 9 THE EFFECT OF ECCENTRICITY ON THE ONSET OF TAYLOR VORTEX FLOW

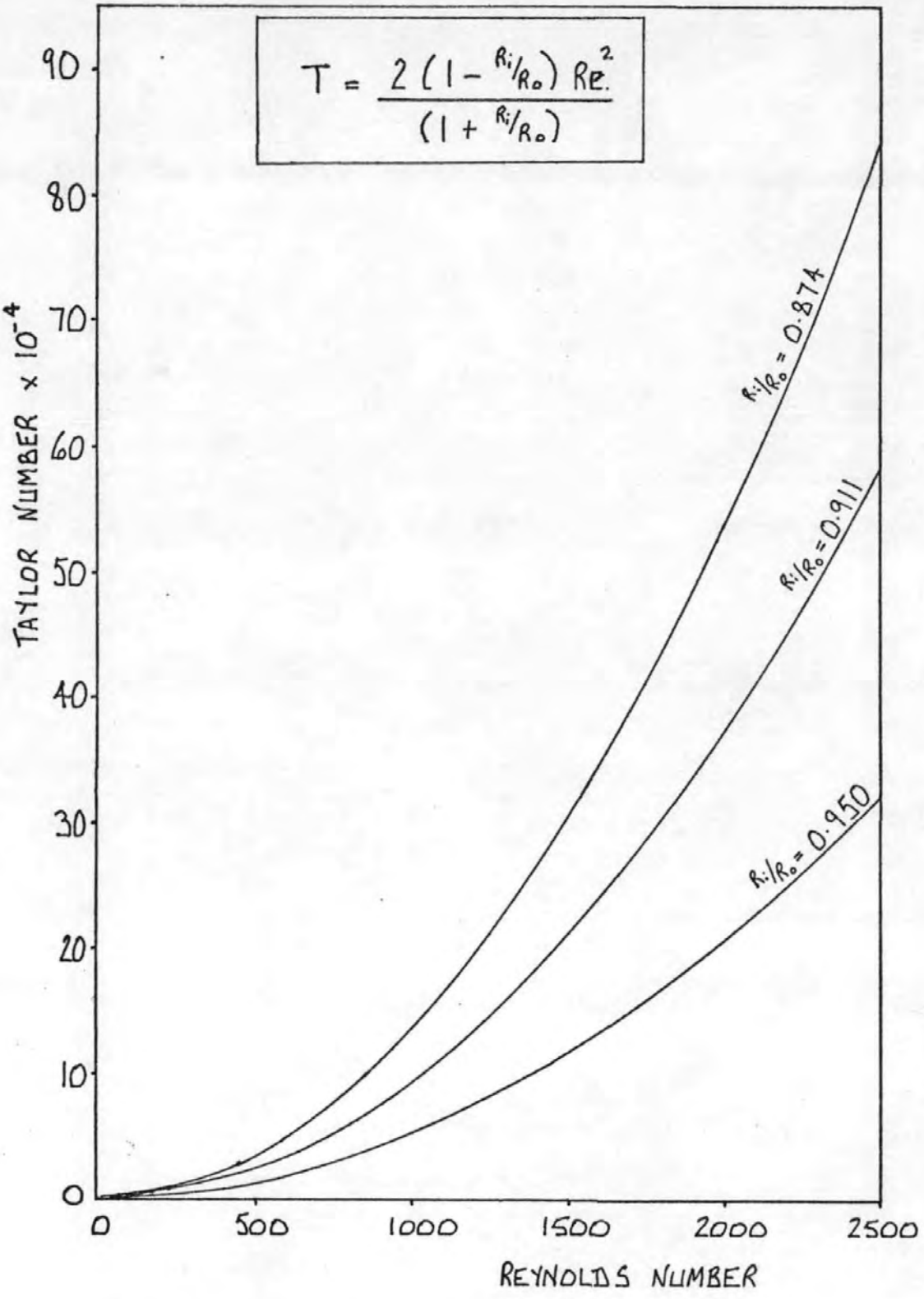

FIG. 10 COMPARISON BETWEEN REYNOLDS NUMBER AND THE TAYLOR NUMBER.

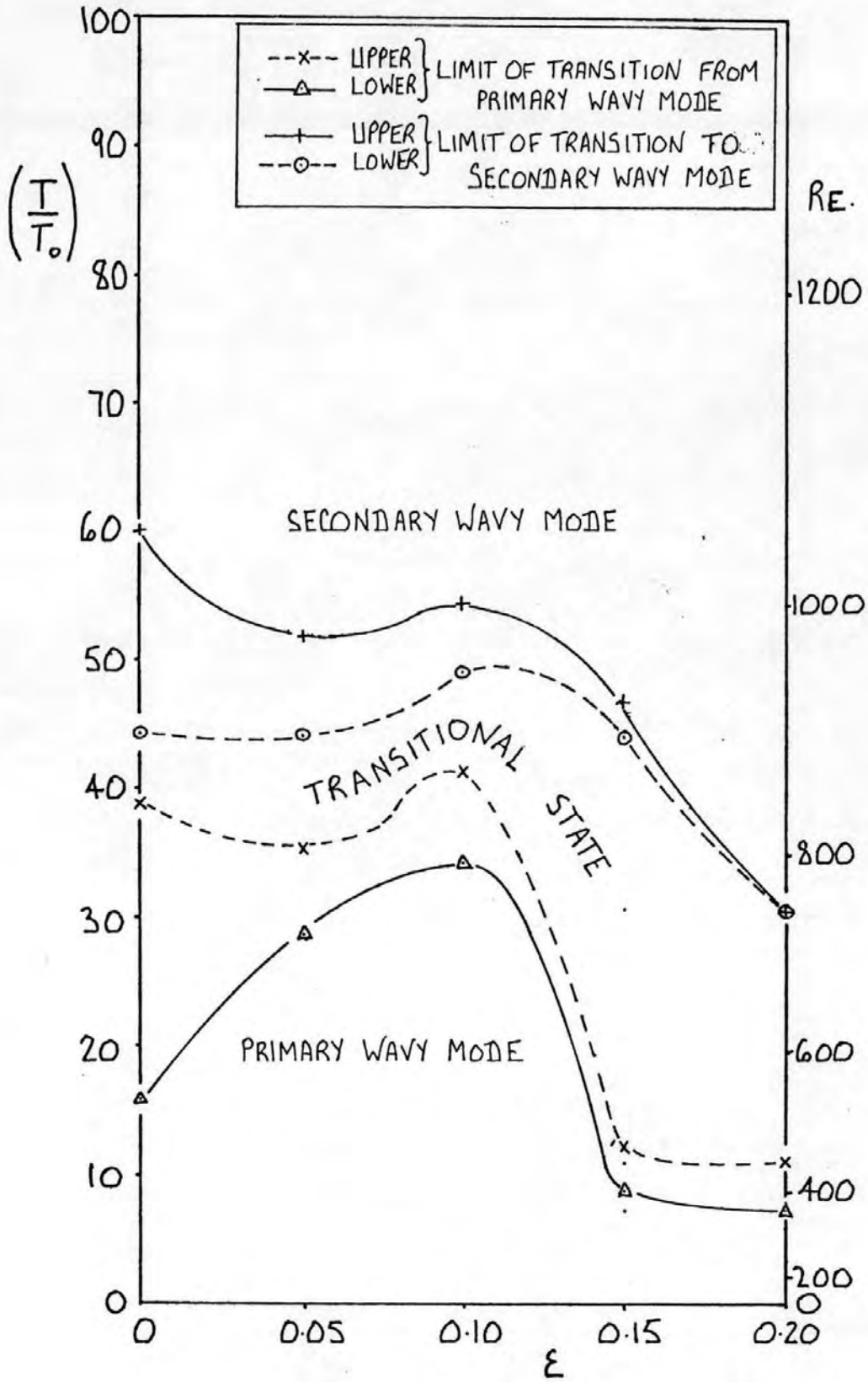

FIG. 11 LIMITS OF THE TRANSITIONAL STATE
$R_i/R_\infty = 0.911$ (TELLUS T17, 21)

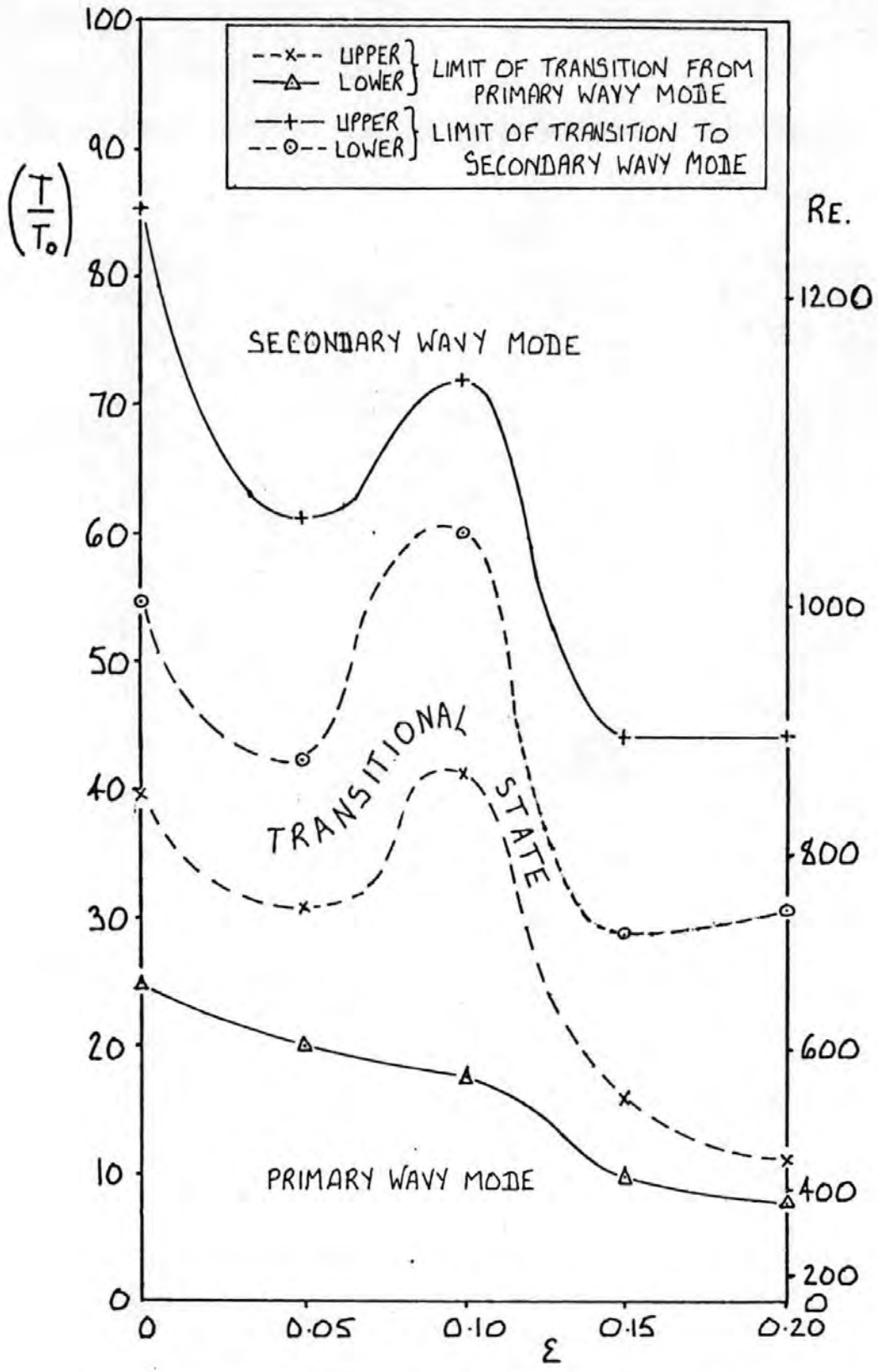

FIG. 12 LIMITS OF THE TRANSITIONAL STATE
$R_i/R_o = 0.911$ (CARNEA 15)

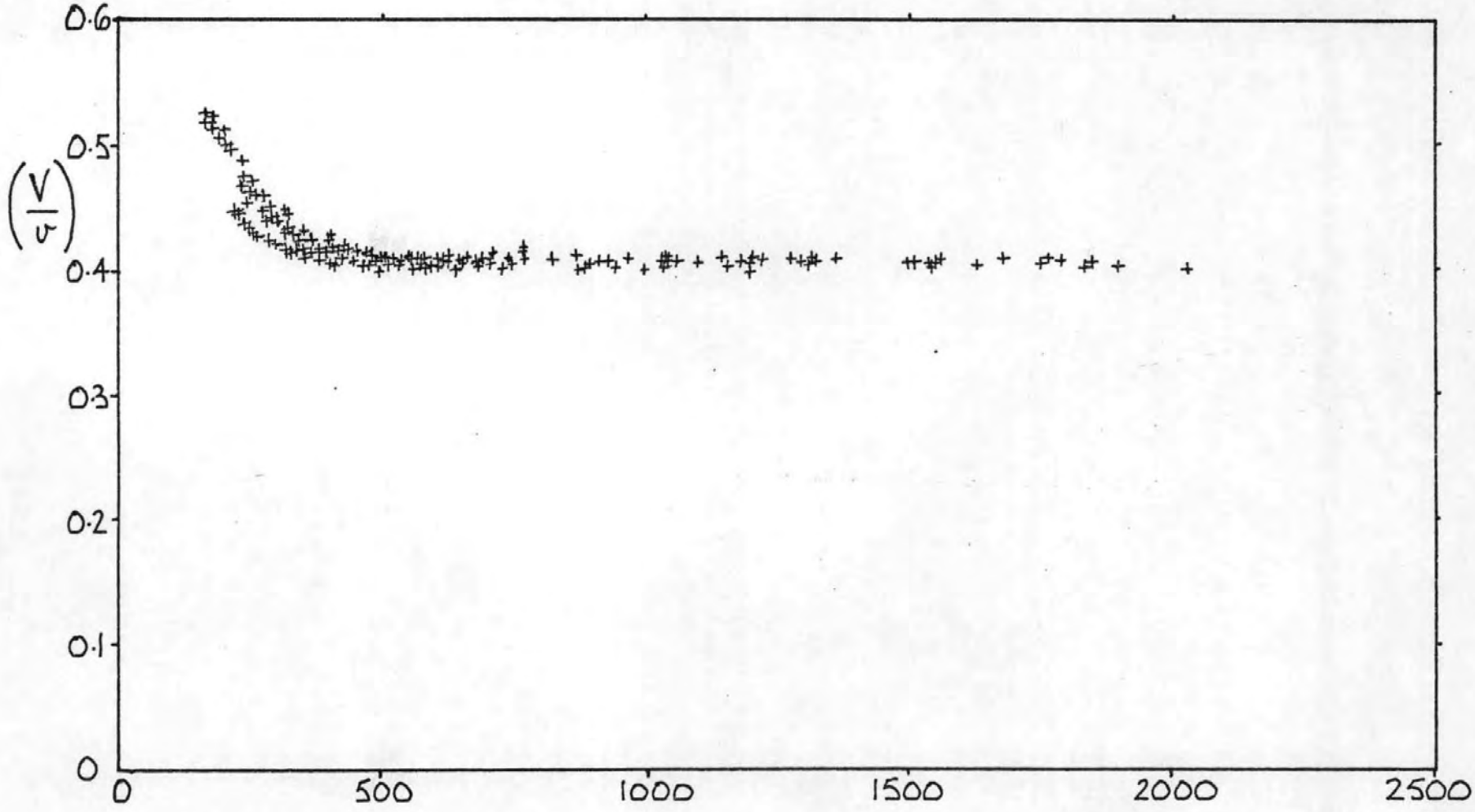

FIG. 13 $R_i/R_o = 0.911$, $\mathcal{E} = 0$, TELLUS 21

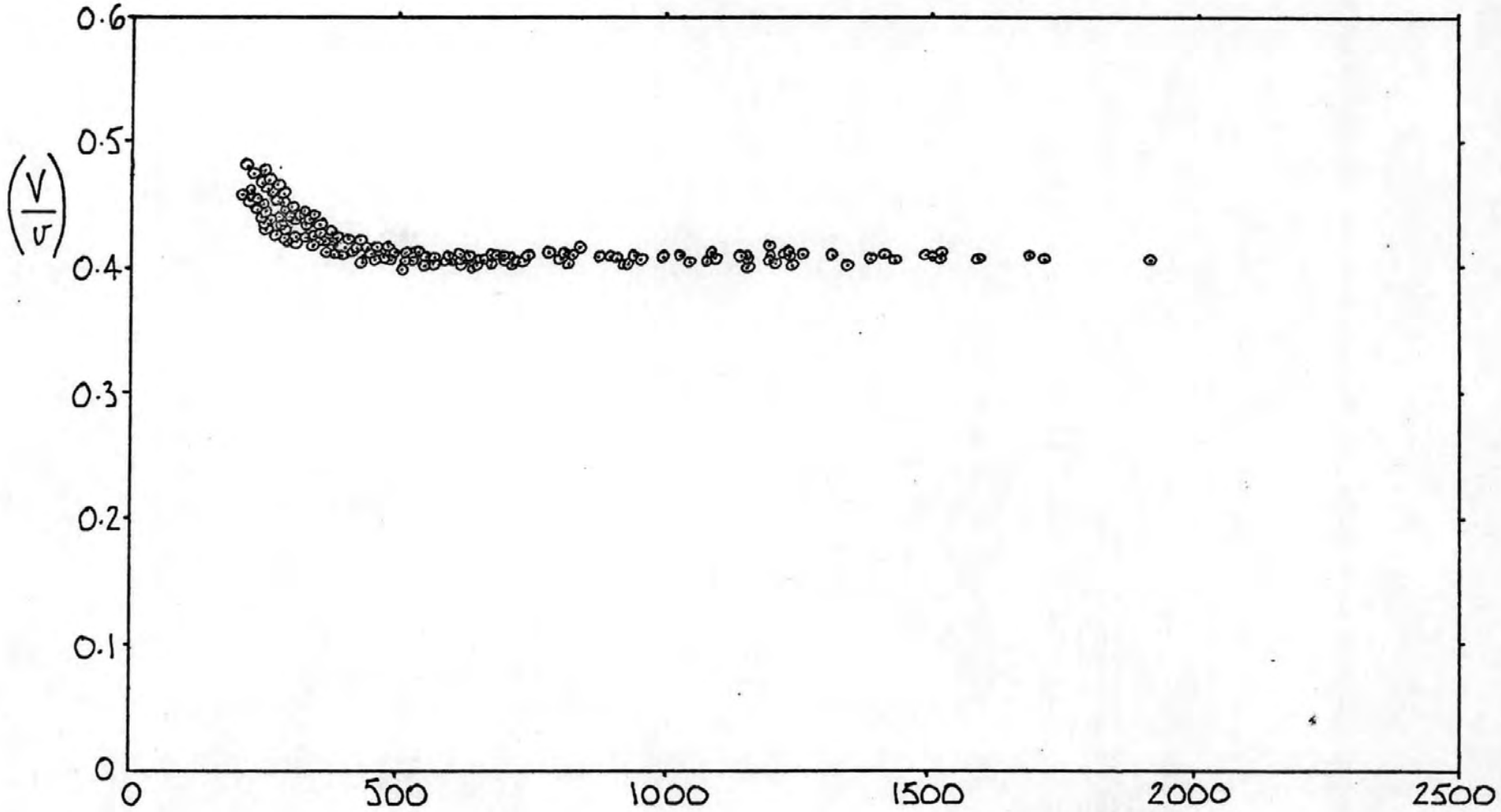

FIG. 14 $R_i/R_D = 0.911$, $\varepsilon = 0$, TELLUS T17

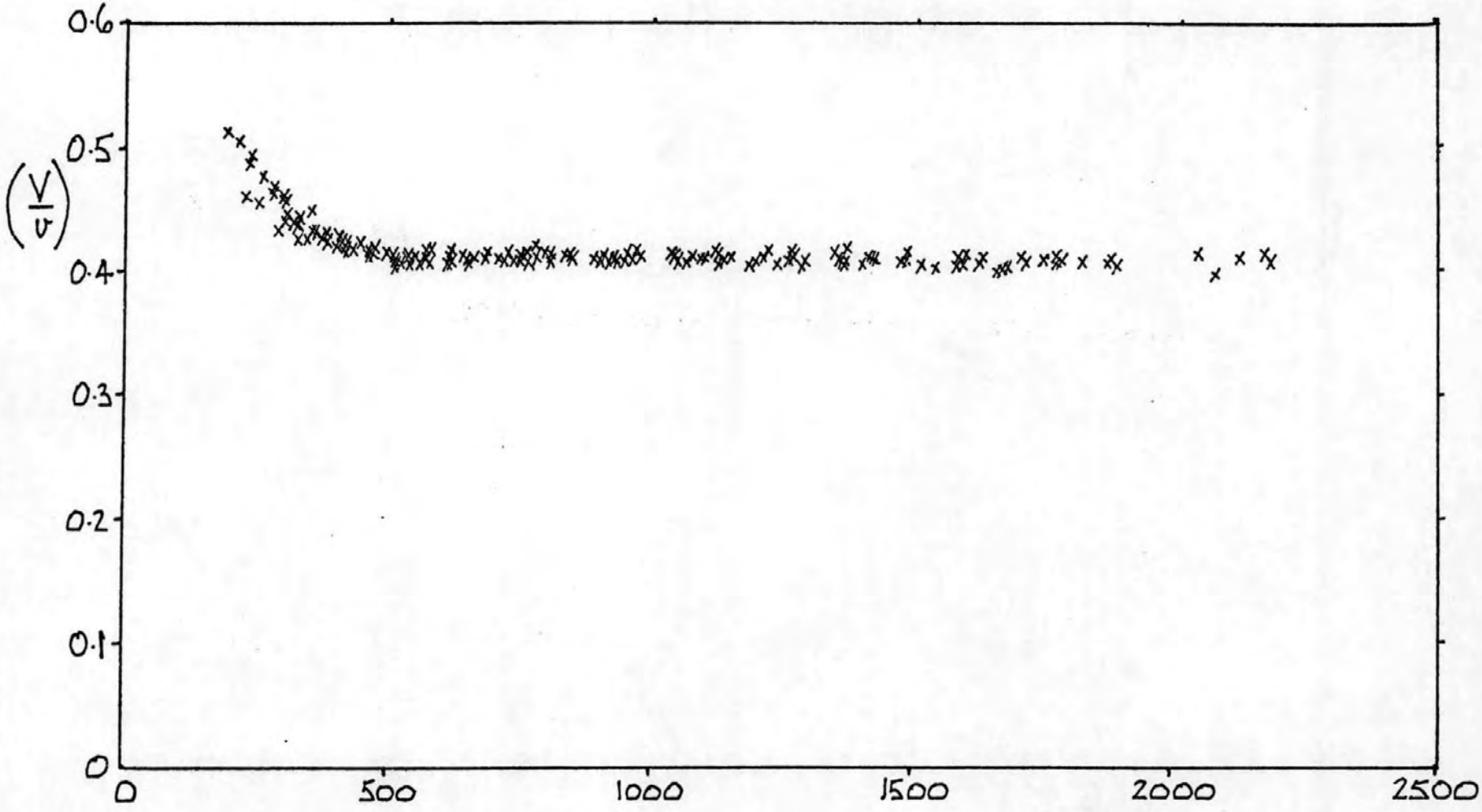

FIG. 15 $R_i/R_o = 0.911$, $\varepsilon = 0$, CARNEA 15

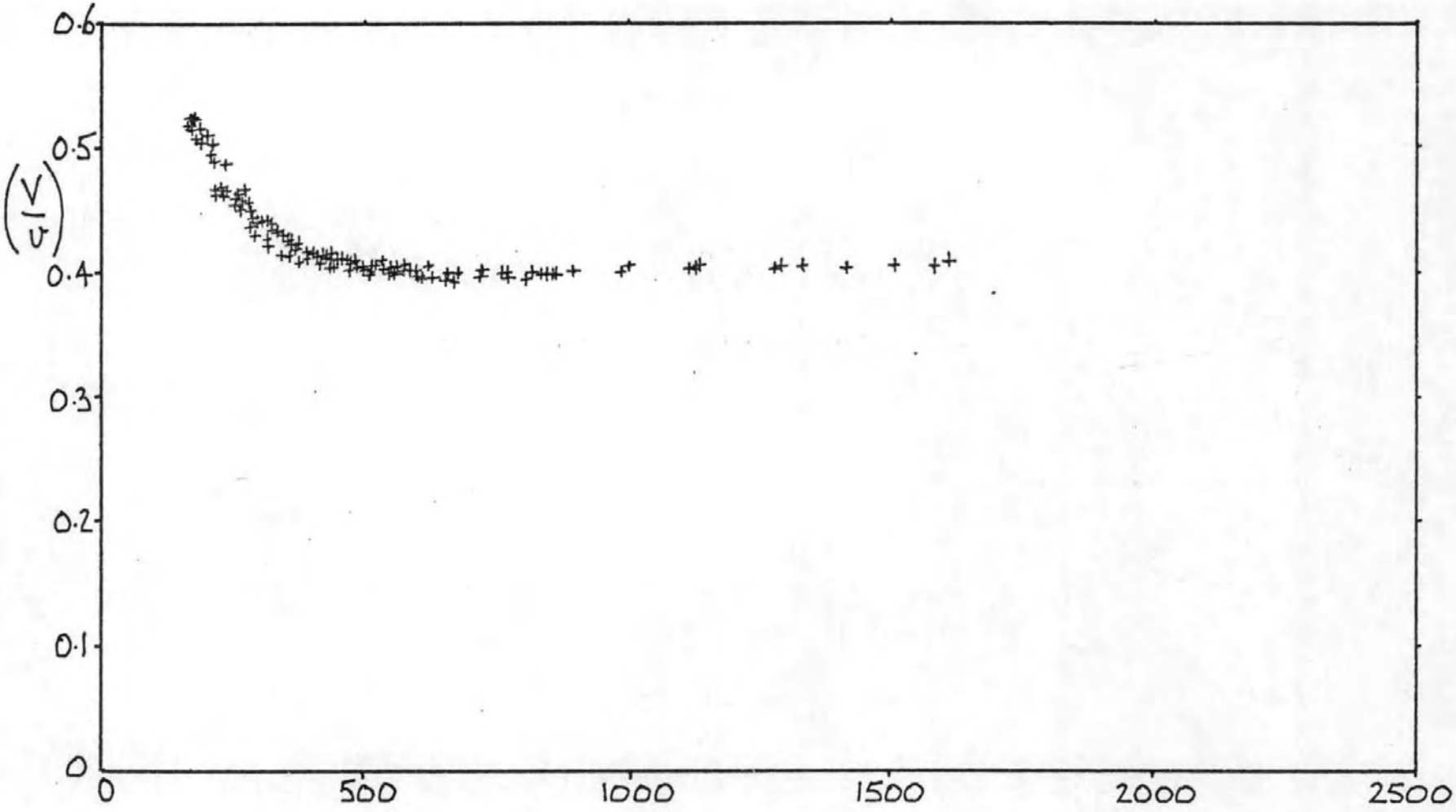

FIG. 16 $R_i/R_o = 0.911$, $\varepsilon = 0.05$, TELLUS 21

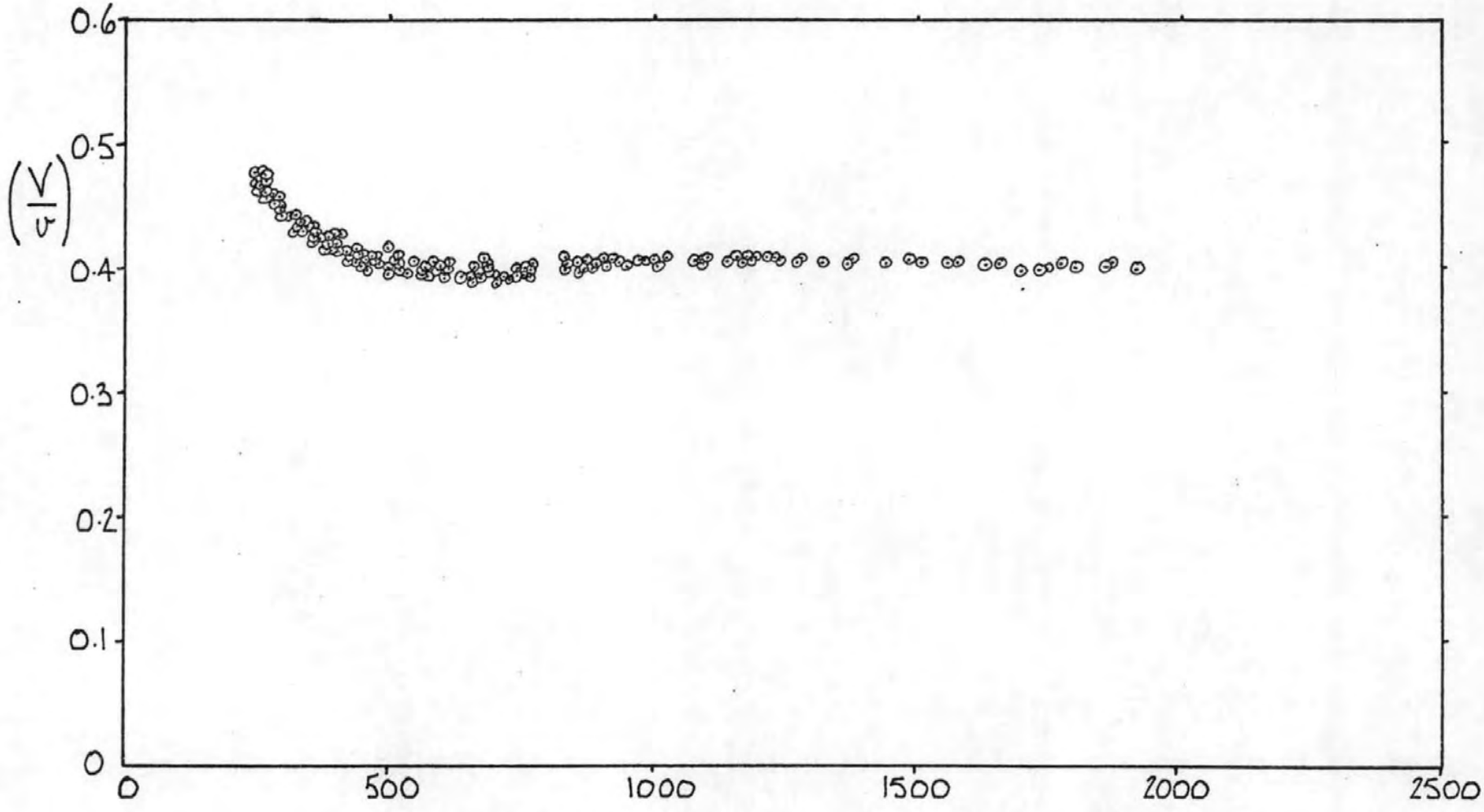

FIG. 17 $R_i/R_o = 0.911$, $\varepsilon = 0.05$, TELLUS T17

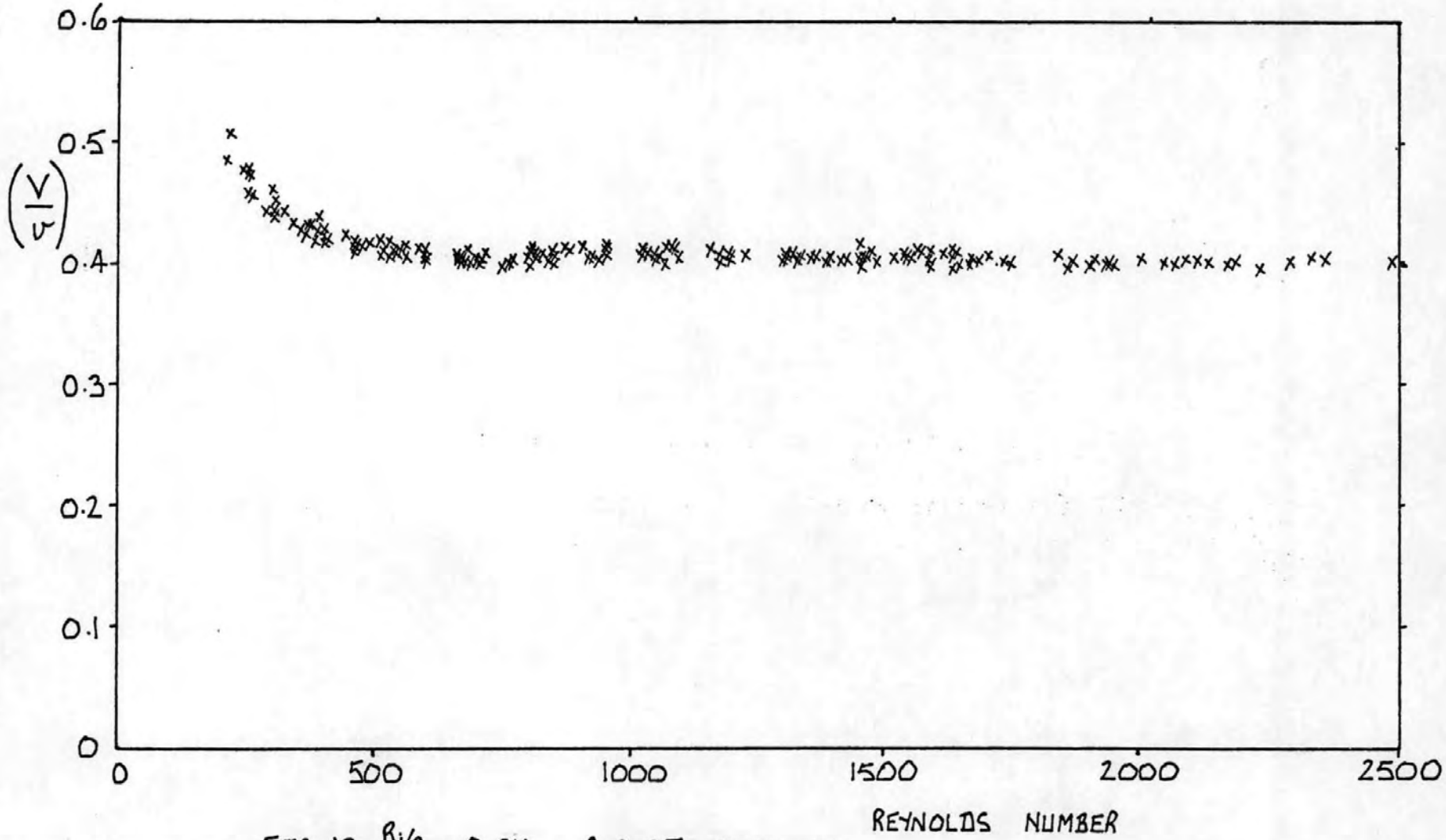

FIG. 18 $R_i/R_o = 0.911$, $\varepsilon = 0.05$, CARNEA 15

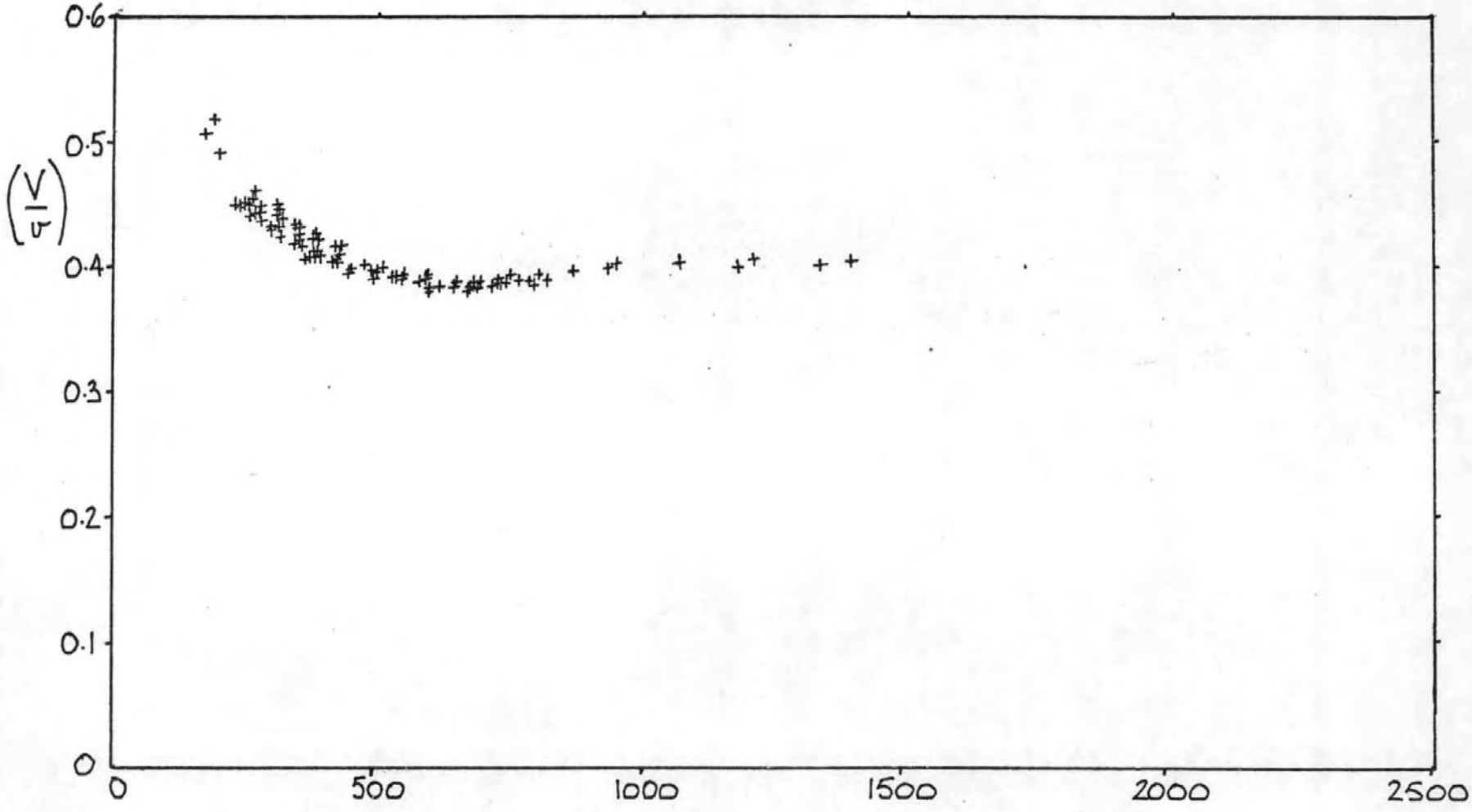

FIG. 19 $R_i/R_o = 0.911$, $\varepsilon = 0.10$, TELLUS 21

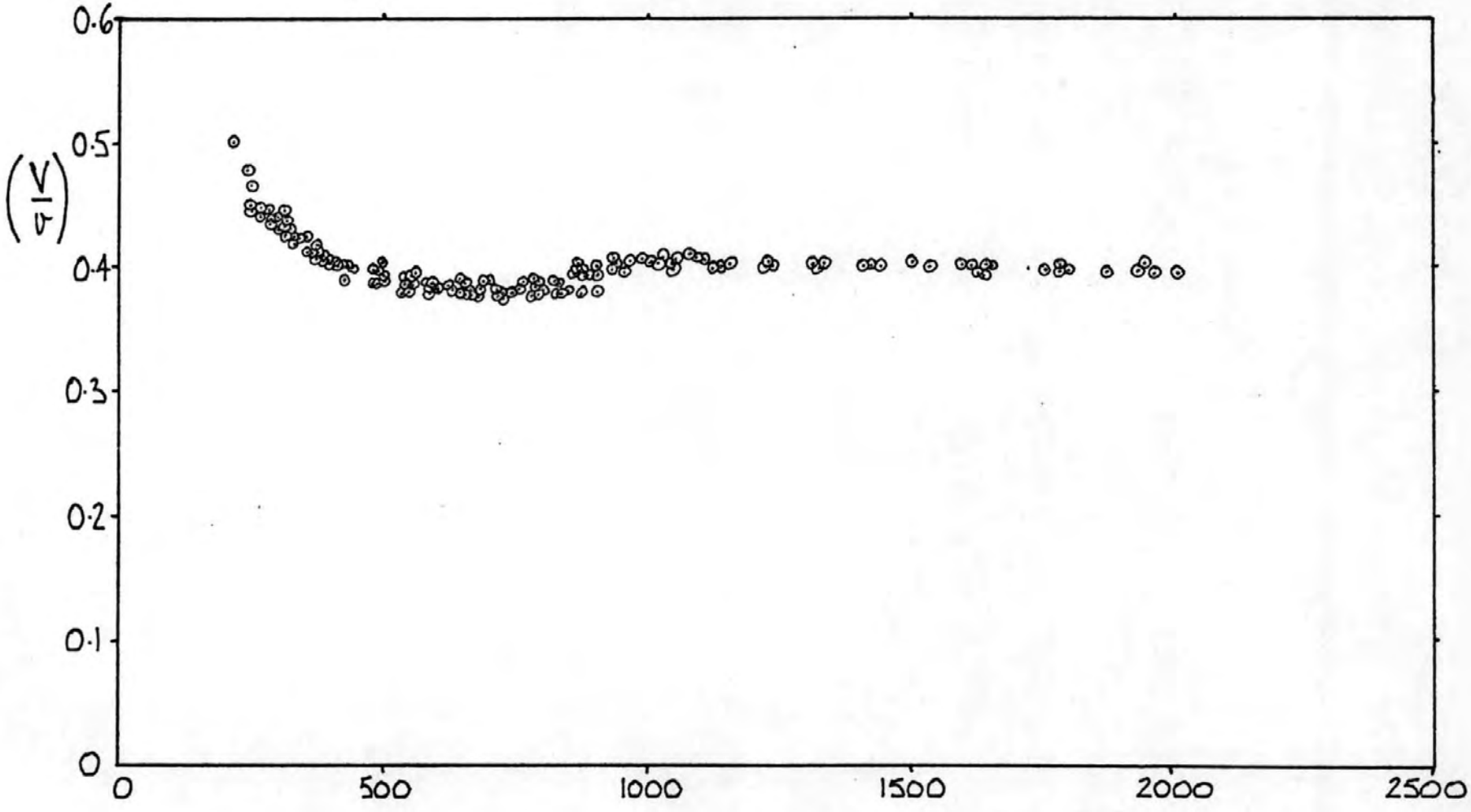

FIG. 20 $R_i/R_o = 0.911$, $\varepsilon = 0.10$, TELLUS T17

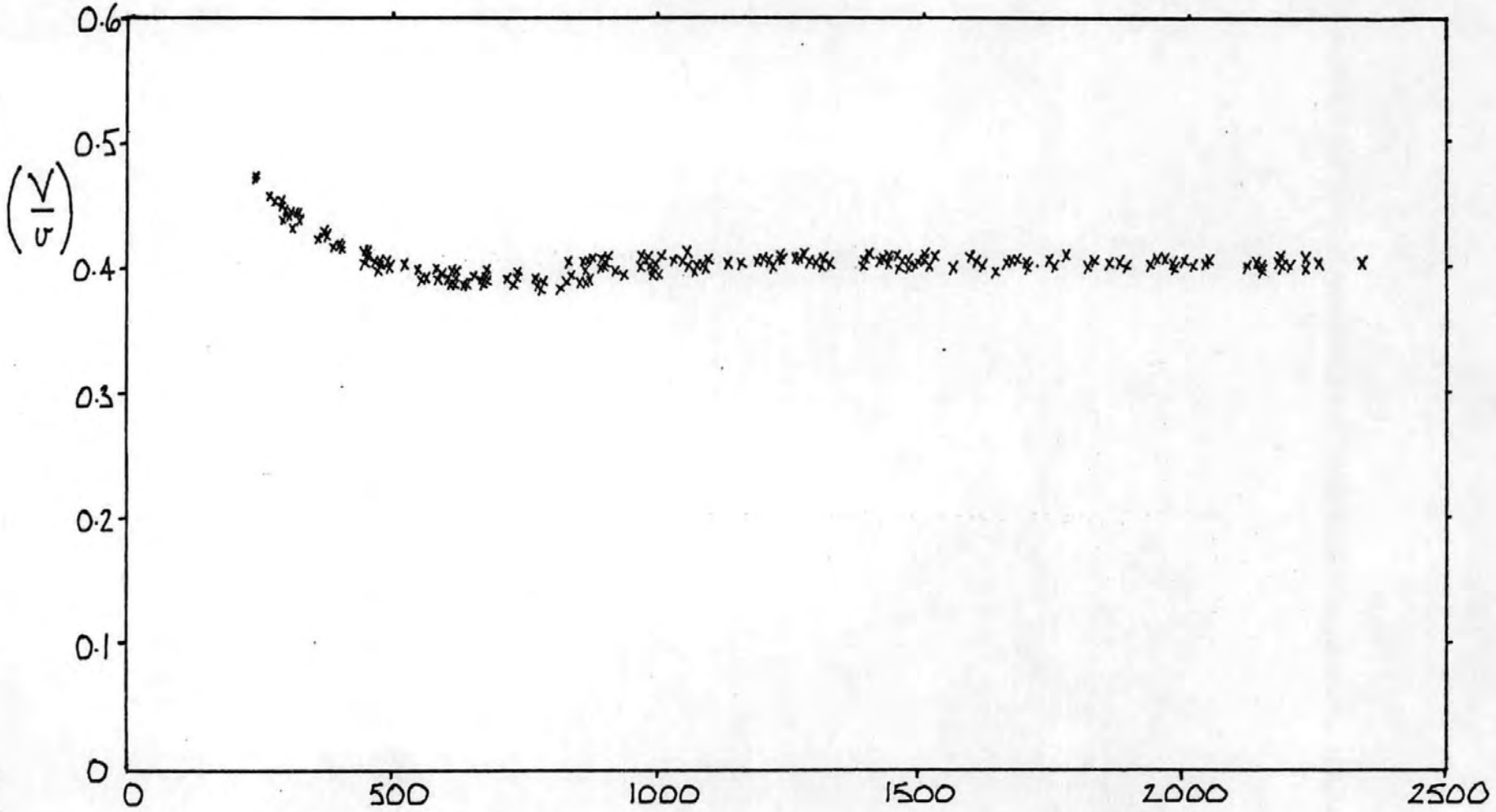

FIG. 21 $R_i/R_o = 0.911$, $\varepsilon = 0.10$, CARNEA 15

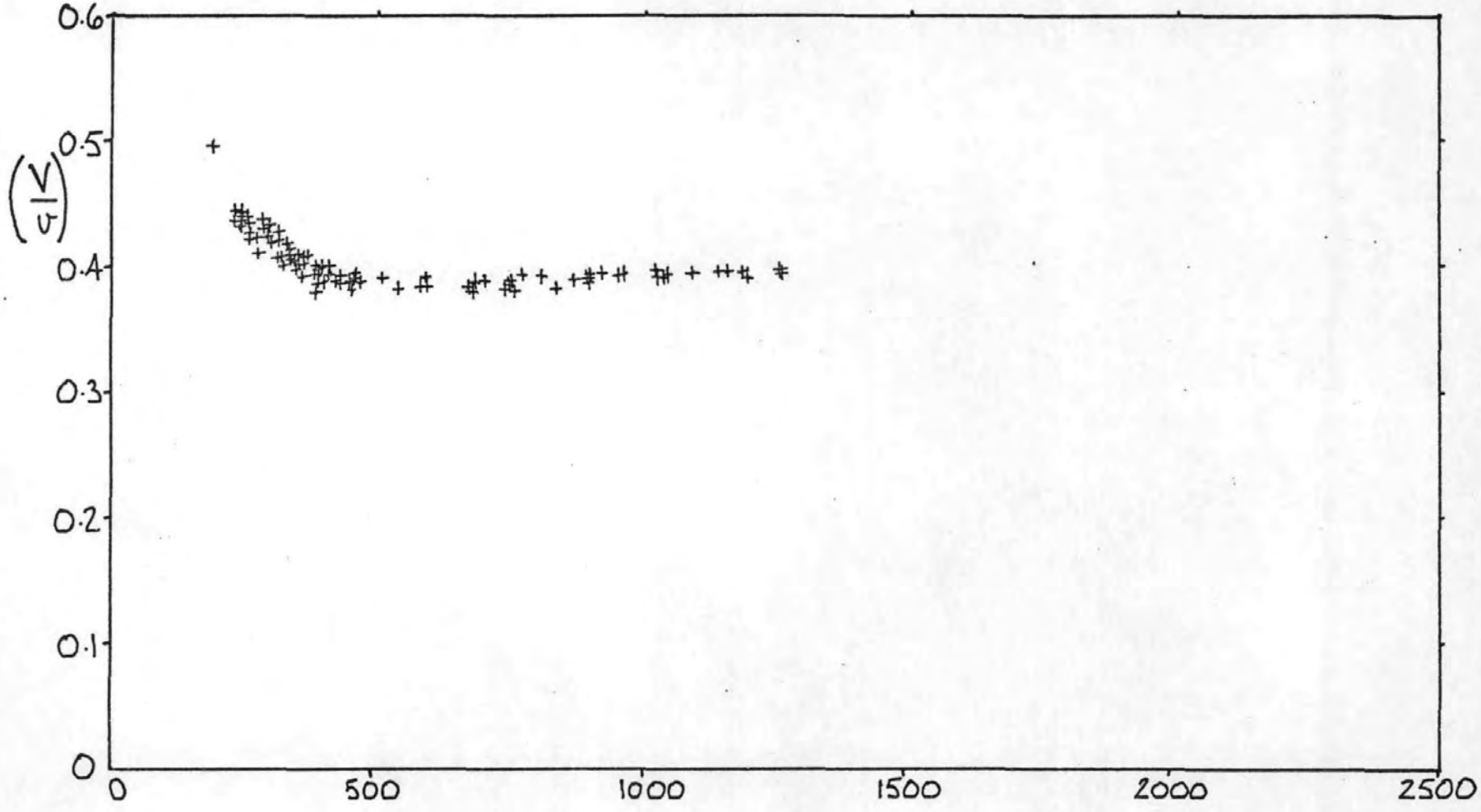

FIG. 22 $R_i/R_o = 0.911$, $\varepsilon = 0.15$, TELLUS 21

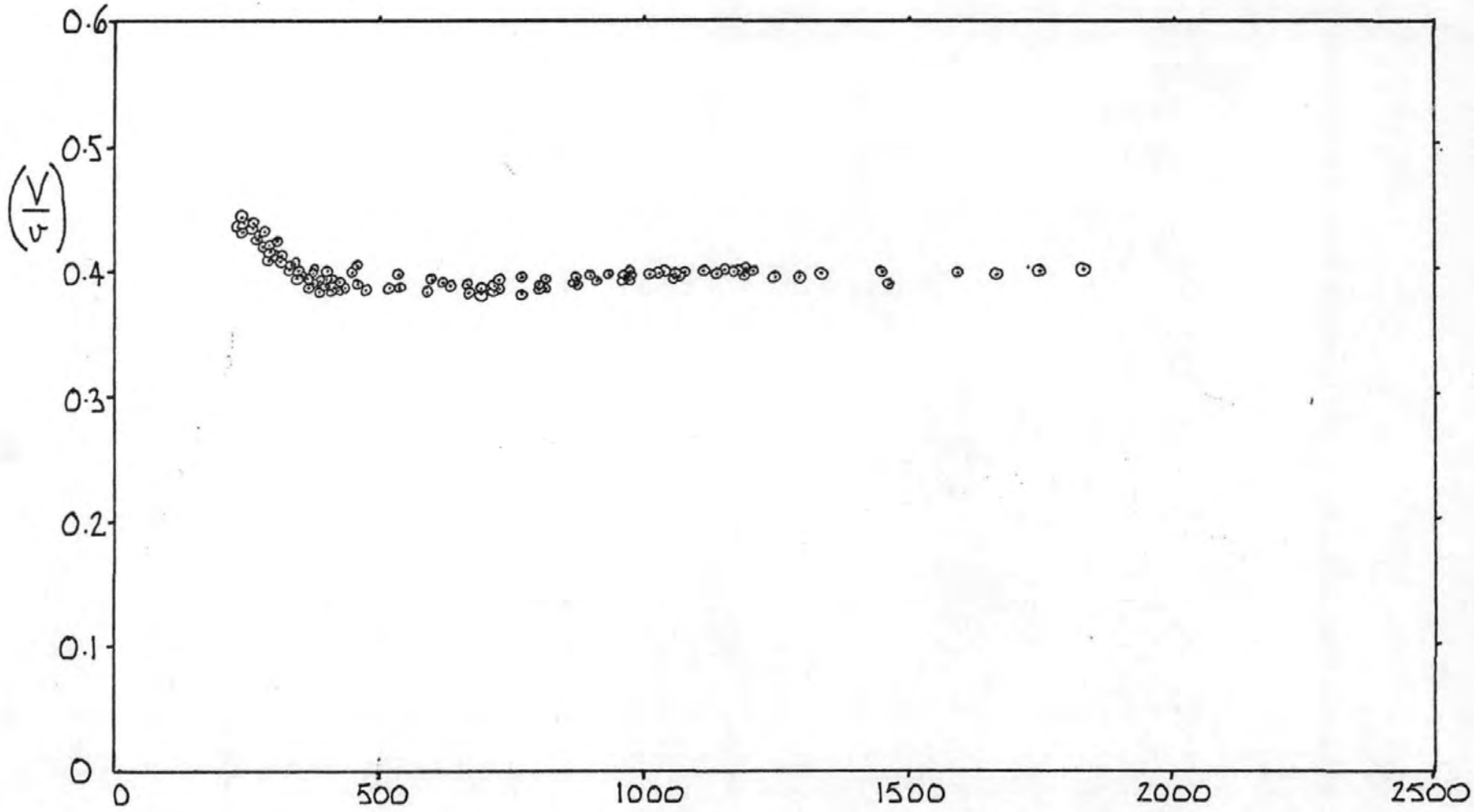

FIG. 23 $R_i/R_o = 0.911$, $\varepsilon = 0.15$, TELLUS T17

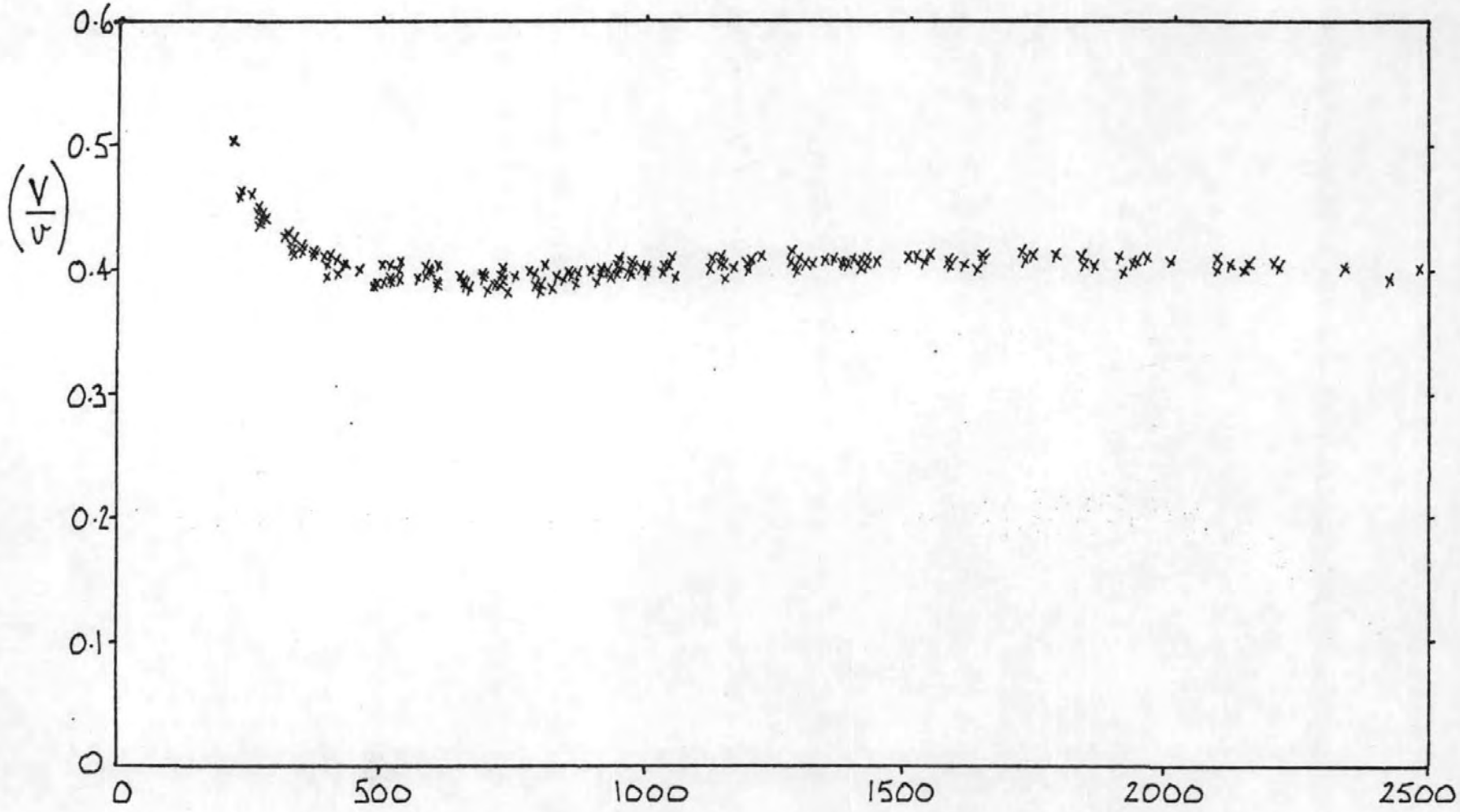

FIG. 24 $R_i/R_o = 0.911$, $\varepsilon = 0.15$, CARNEA 15

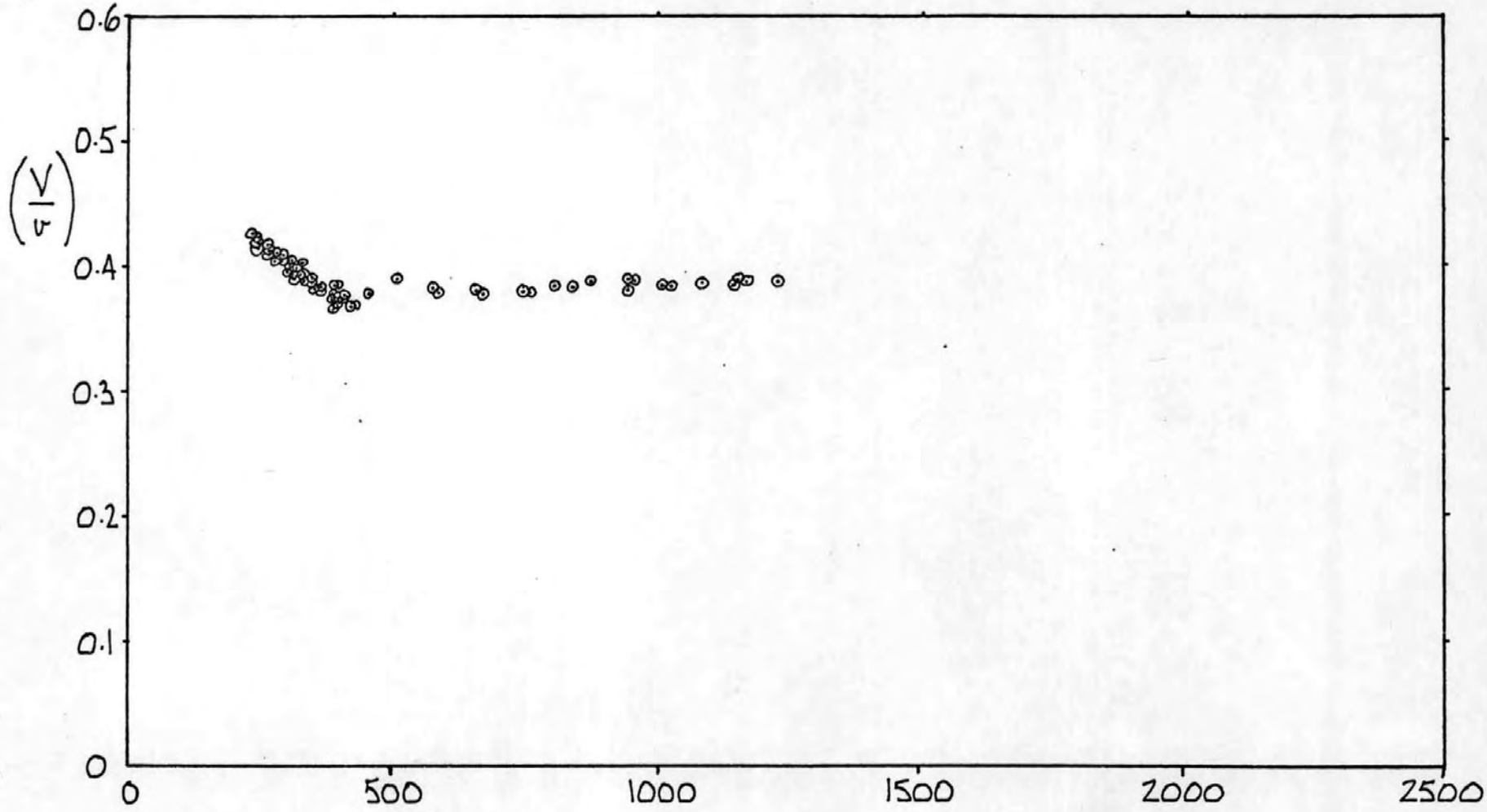

FIG. 25 $R_i/R_o = 0.911$, $\mathcal{E} = 0.20$, TELLUS T17

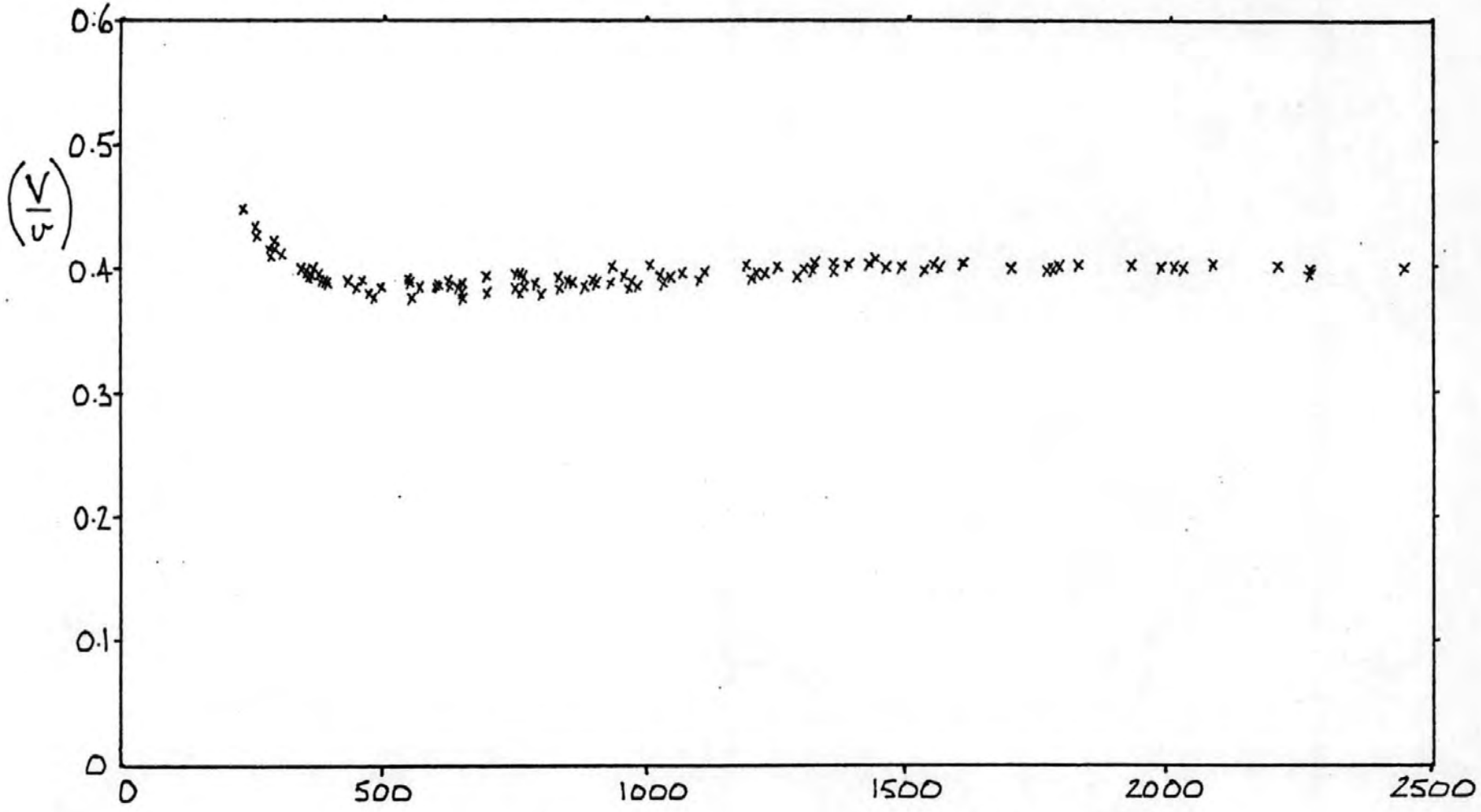

FIG. 26 $R_i/R_o = 0.911$, $\varepsilon = 0.20$, CARNEA 15

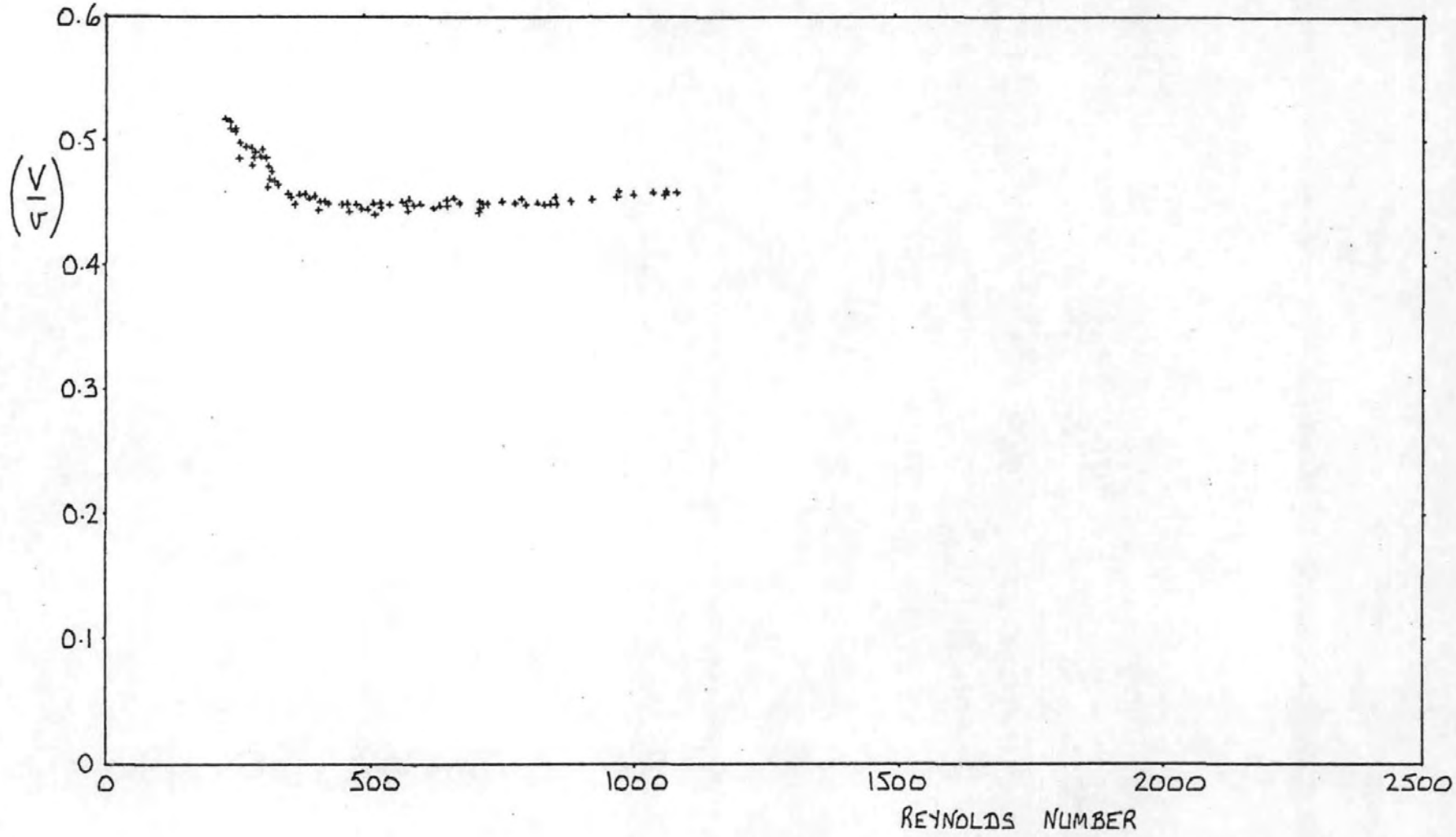

FIG. 27 $R_i/R_o = 0.950$, $\varepsilon = 0$, TELLUS 21

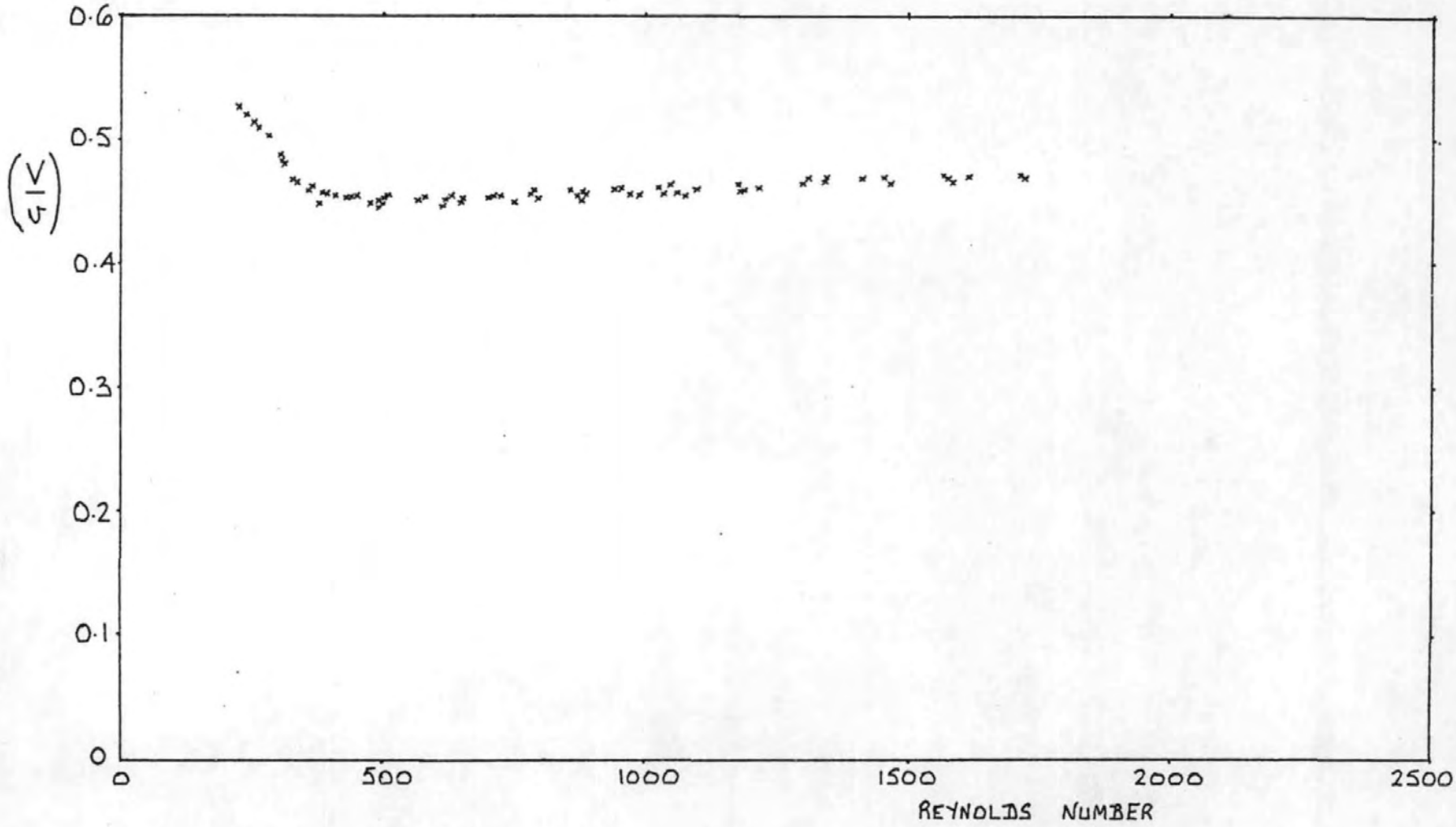

FIG. 28 $R_i/R_o = 0.950$, $\varepsilon = 0$, CARNEA 15

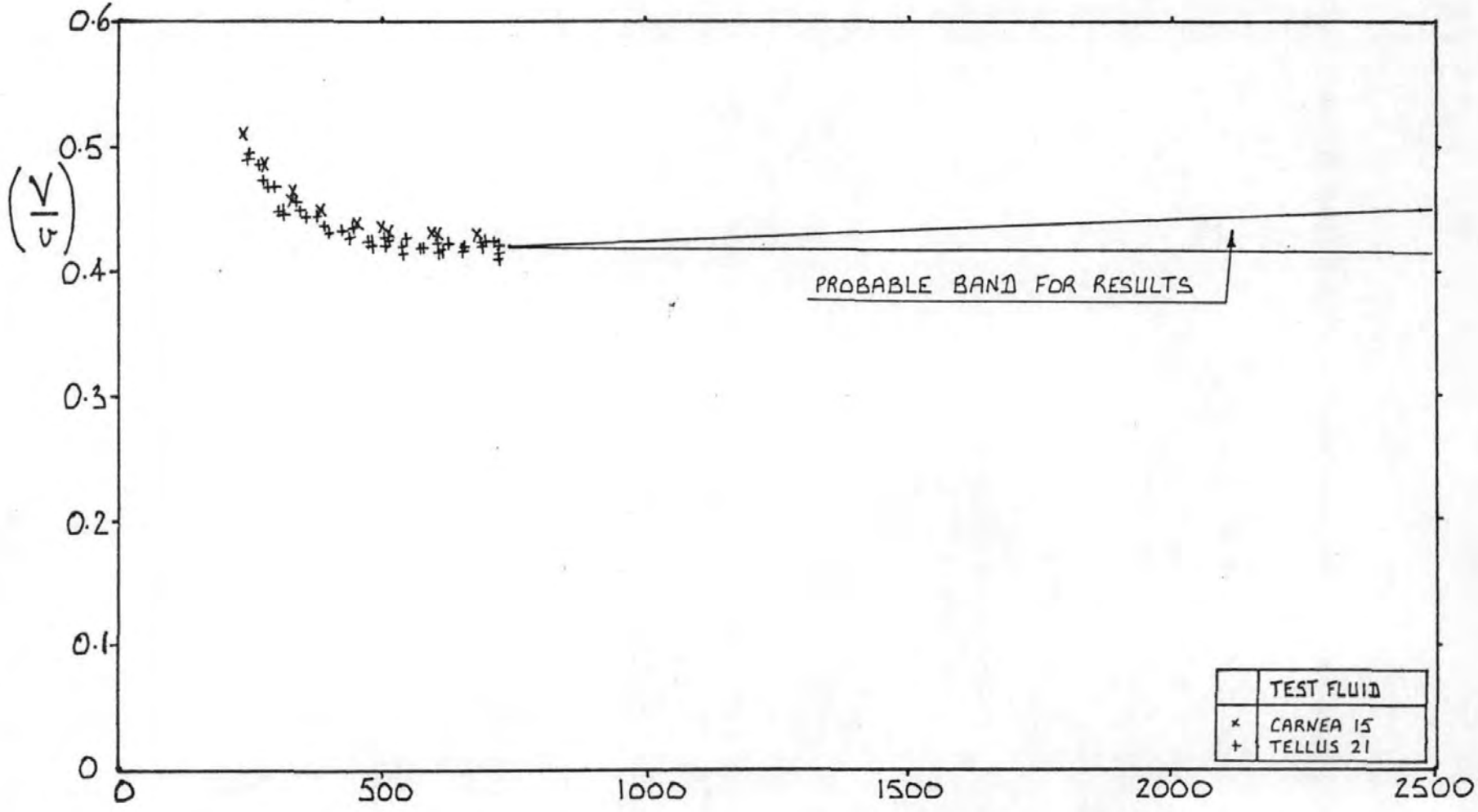

FIG. 29 $R_i/R_o = 0.950, \varepsilon = 0.10$

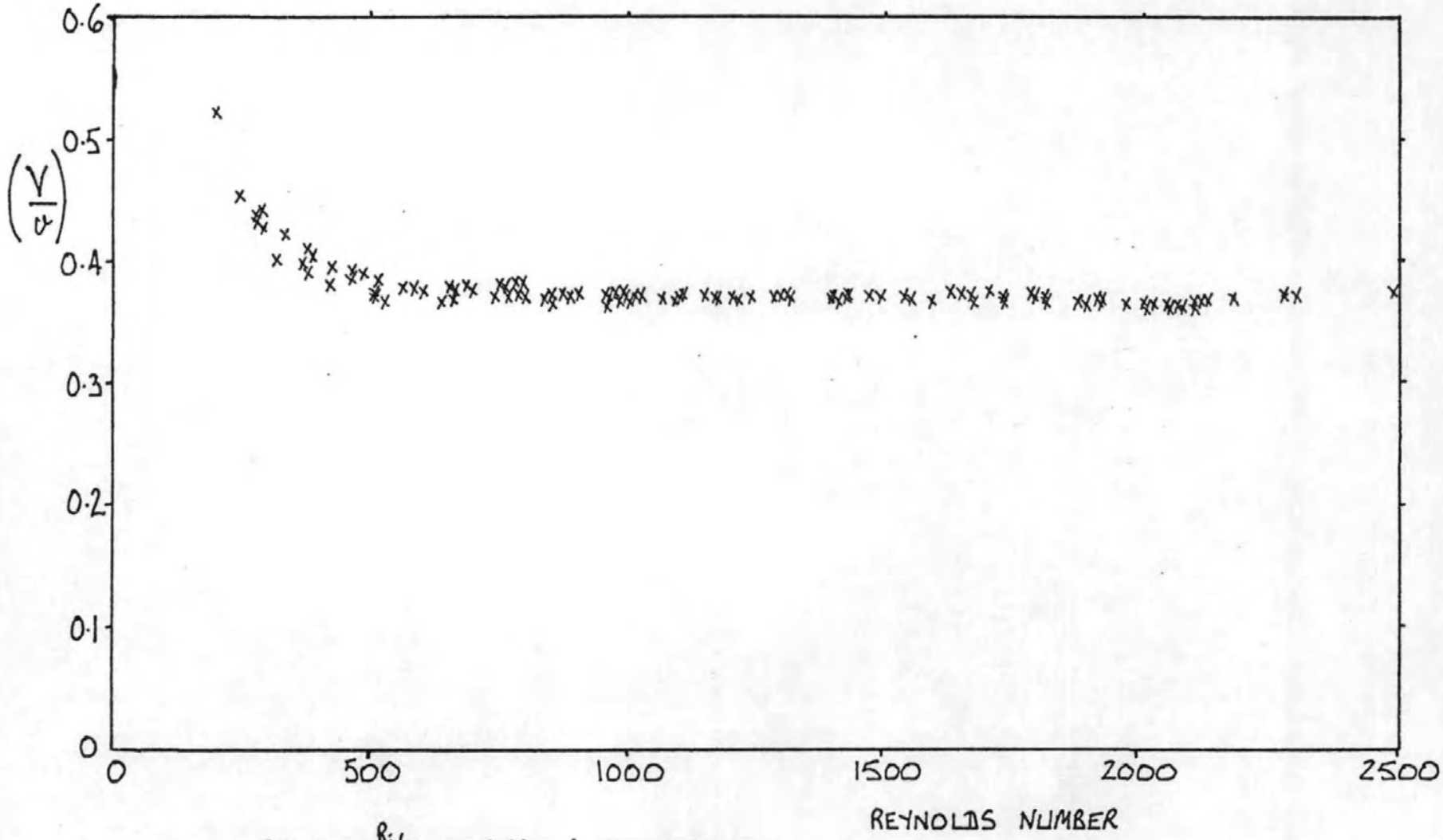

FIG. 30 $R_i/R_o = 0.874$, $\varepsilon = 0$, CARNEA 15

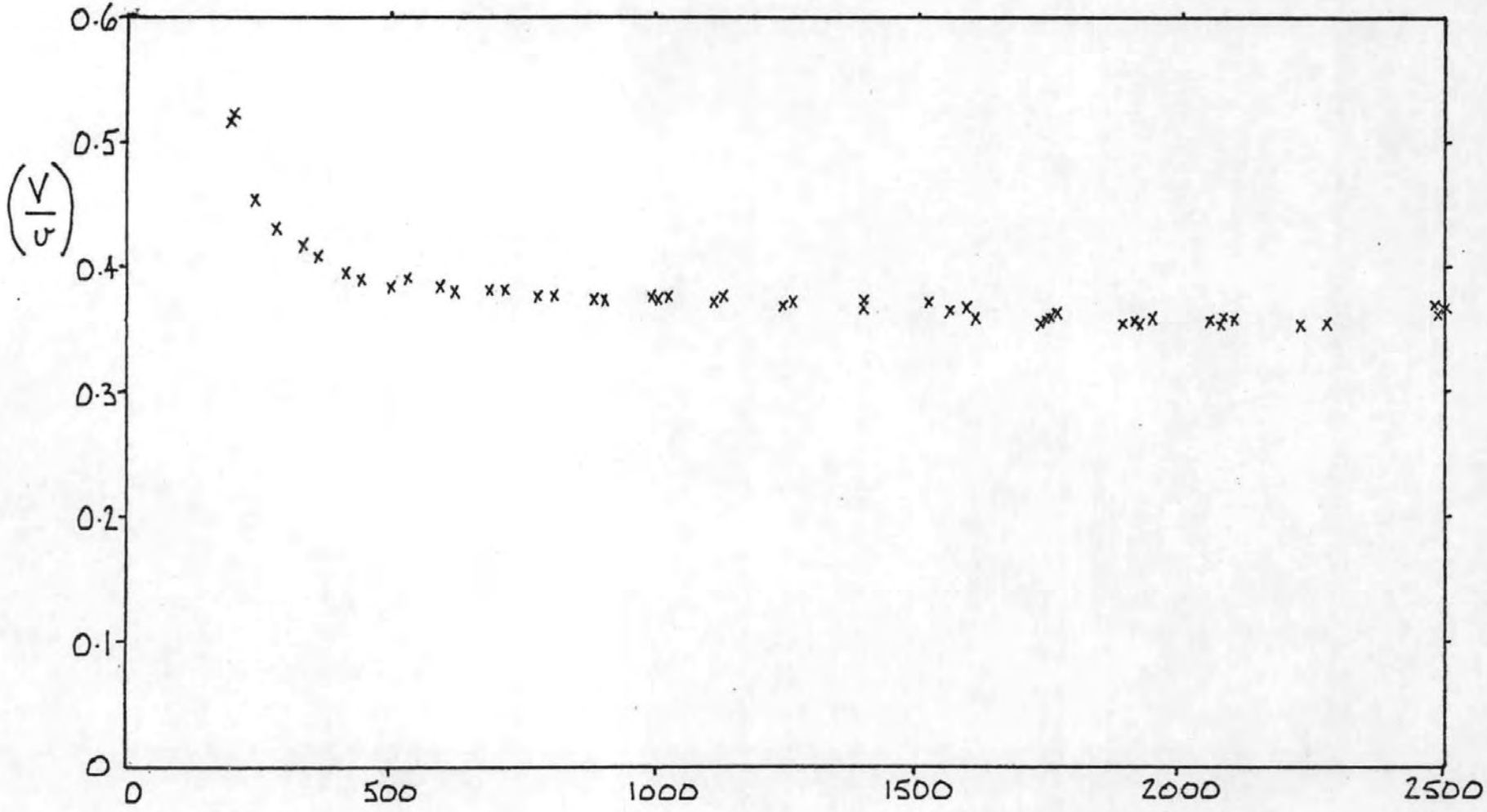

FIG. 31 $R_i/R_o = 0.874$, $\varepsilon = 0.10$, CARNEA 15

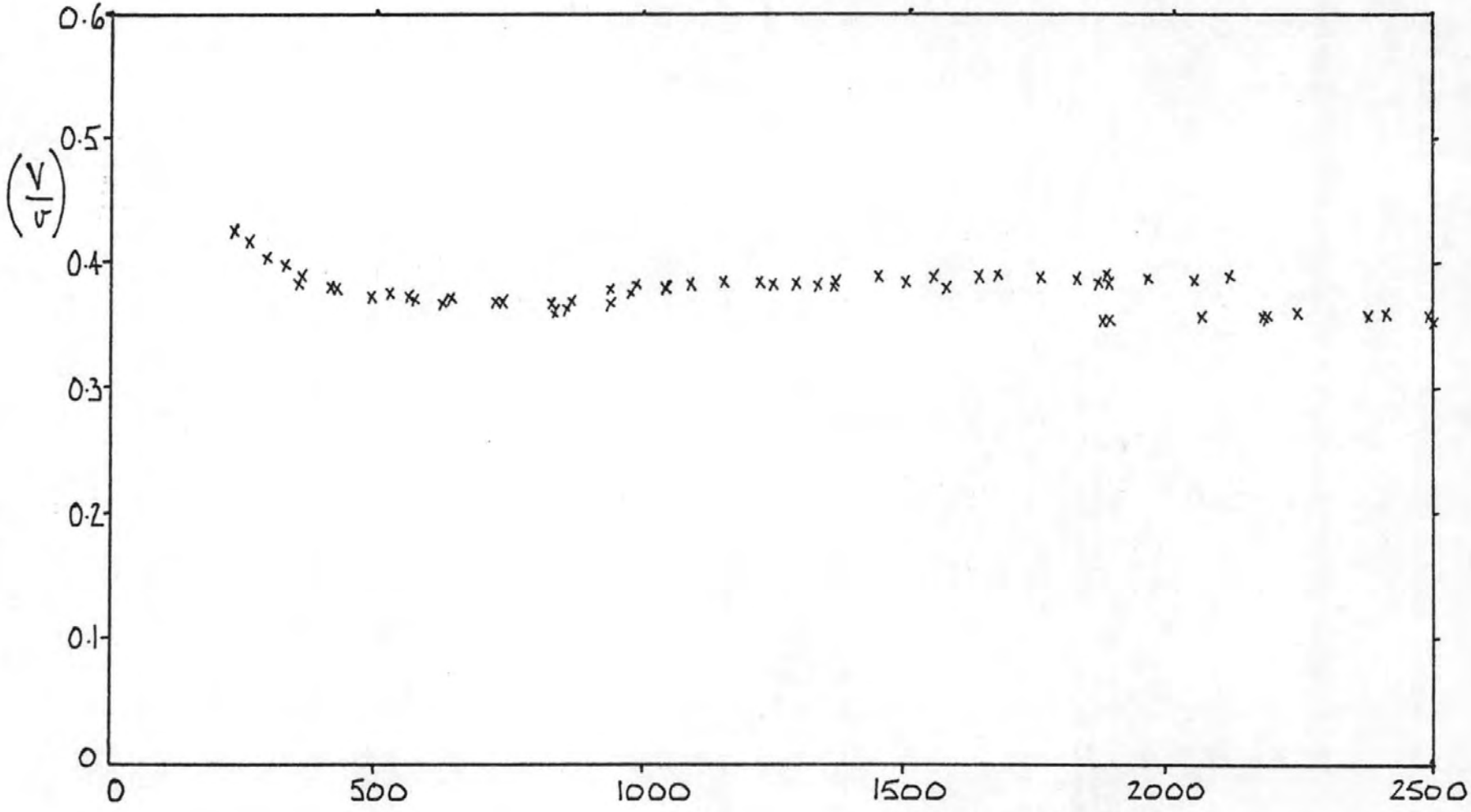

FIG. 32 $R_i/R_o = 0.874$, $\varepsilon = 0.20$, CARNEA 15

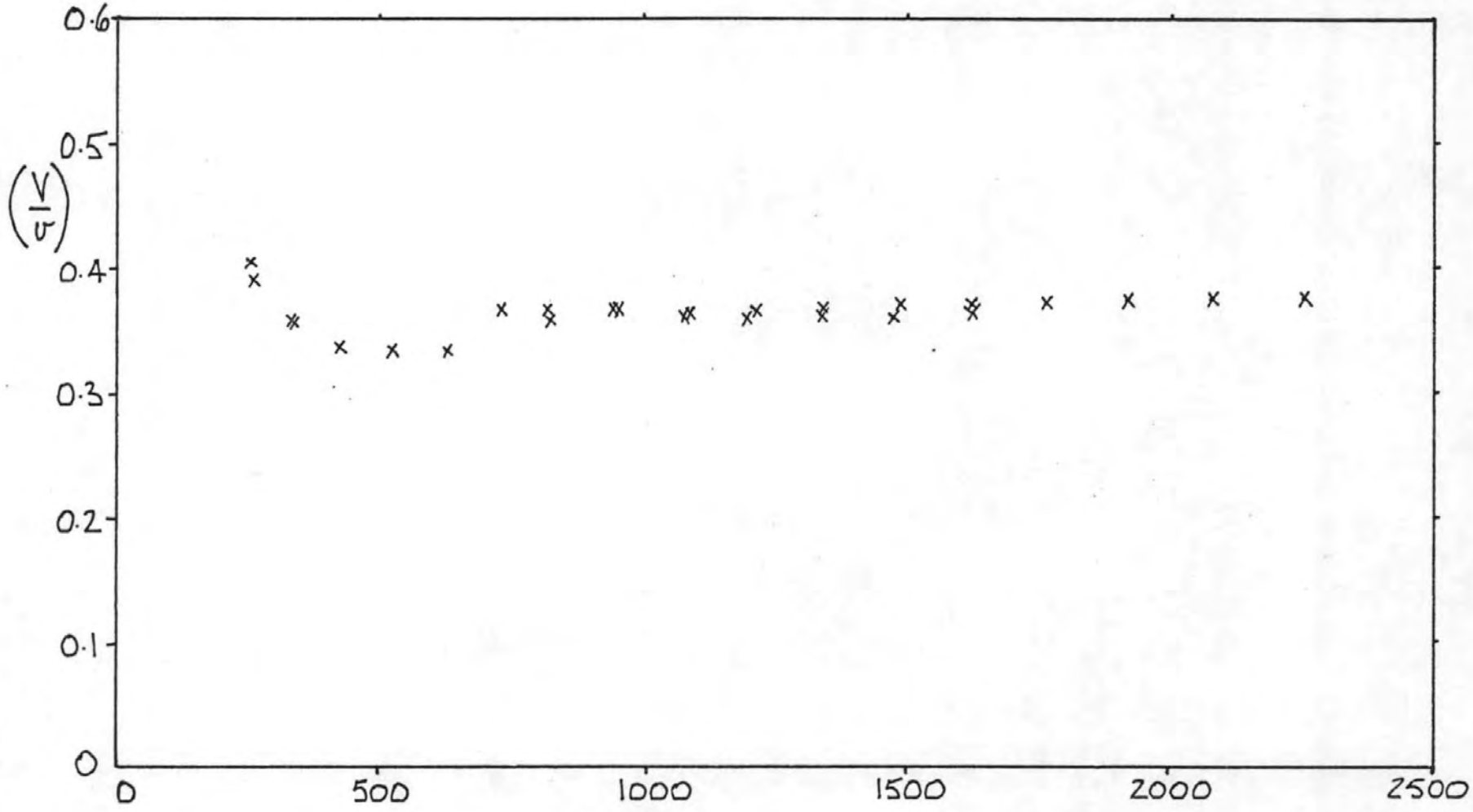

FIG. 33 $R_1/R_0 = 0.874$, $\varepsilon = 0.30$, CARNEA 15

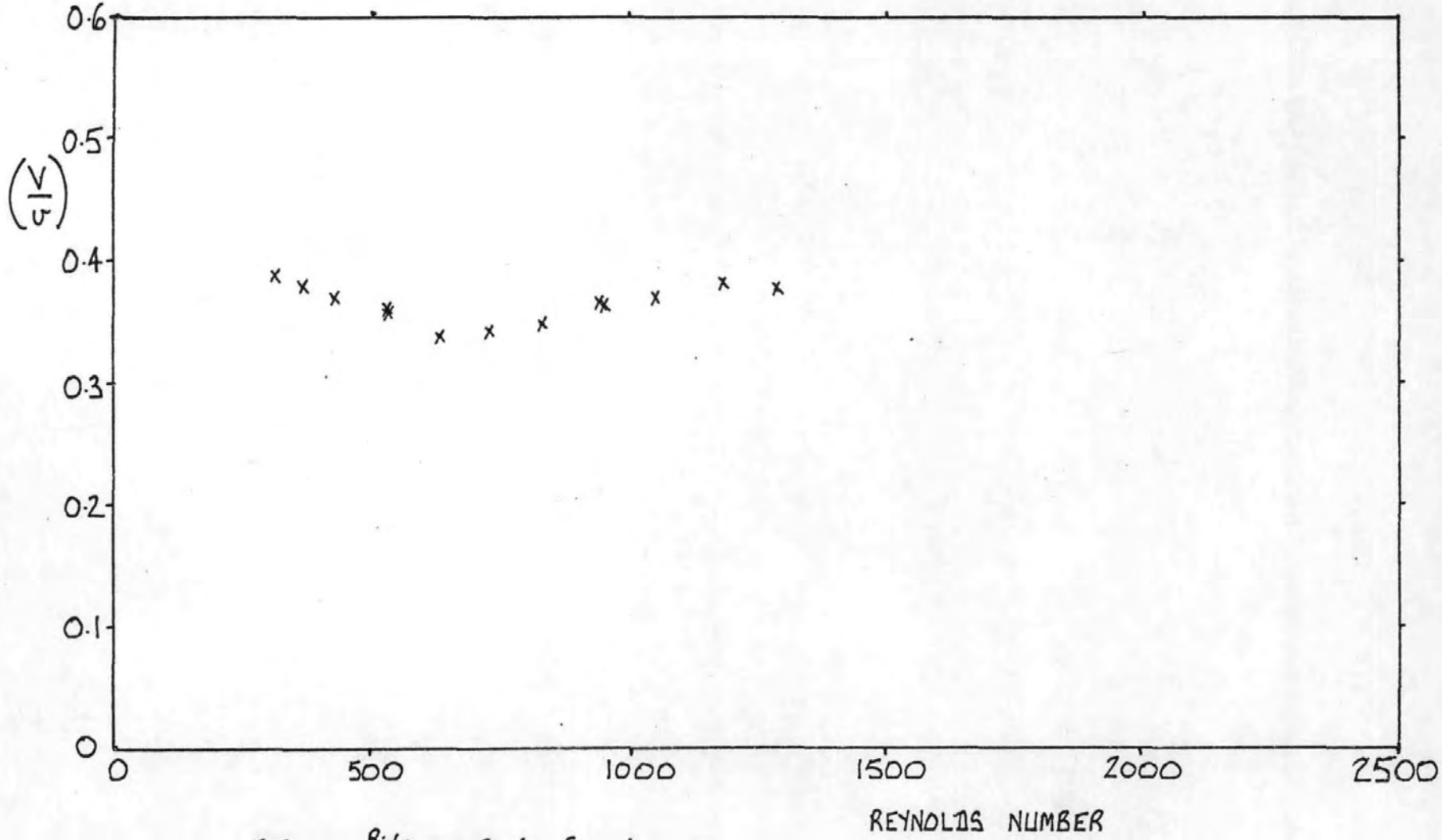

FIG. 34 $R_i/R_o = 0.874$, $\varepsilon = 0.40$, CARNEA 15

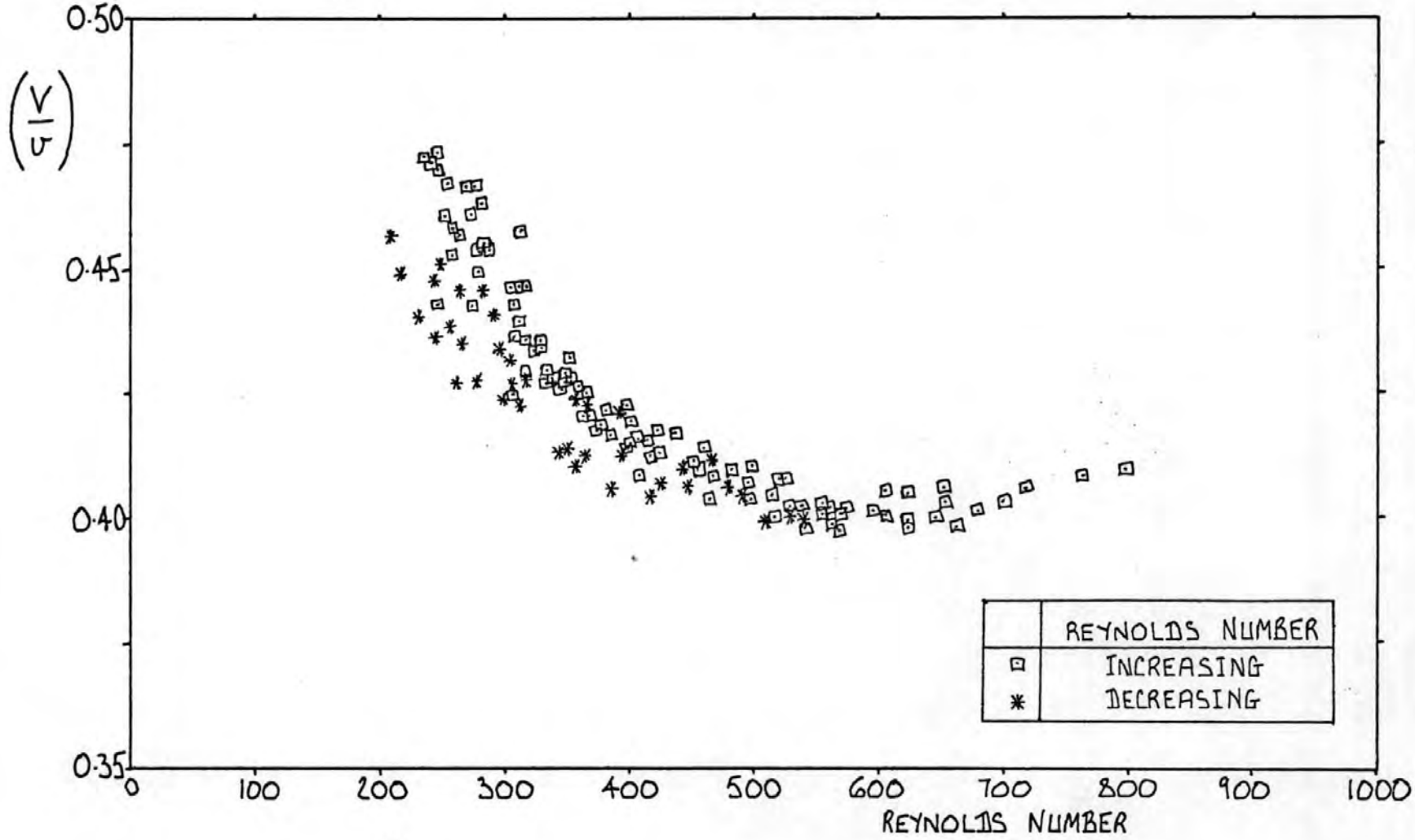

FIG. 35 $R_i/R_o = 0.911$, $\varepsilon \cdot 0$, (TELLUS 15)

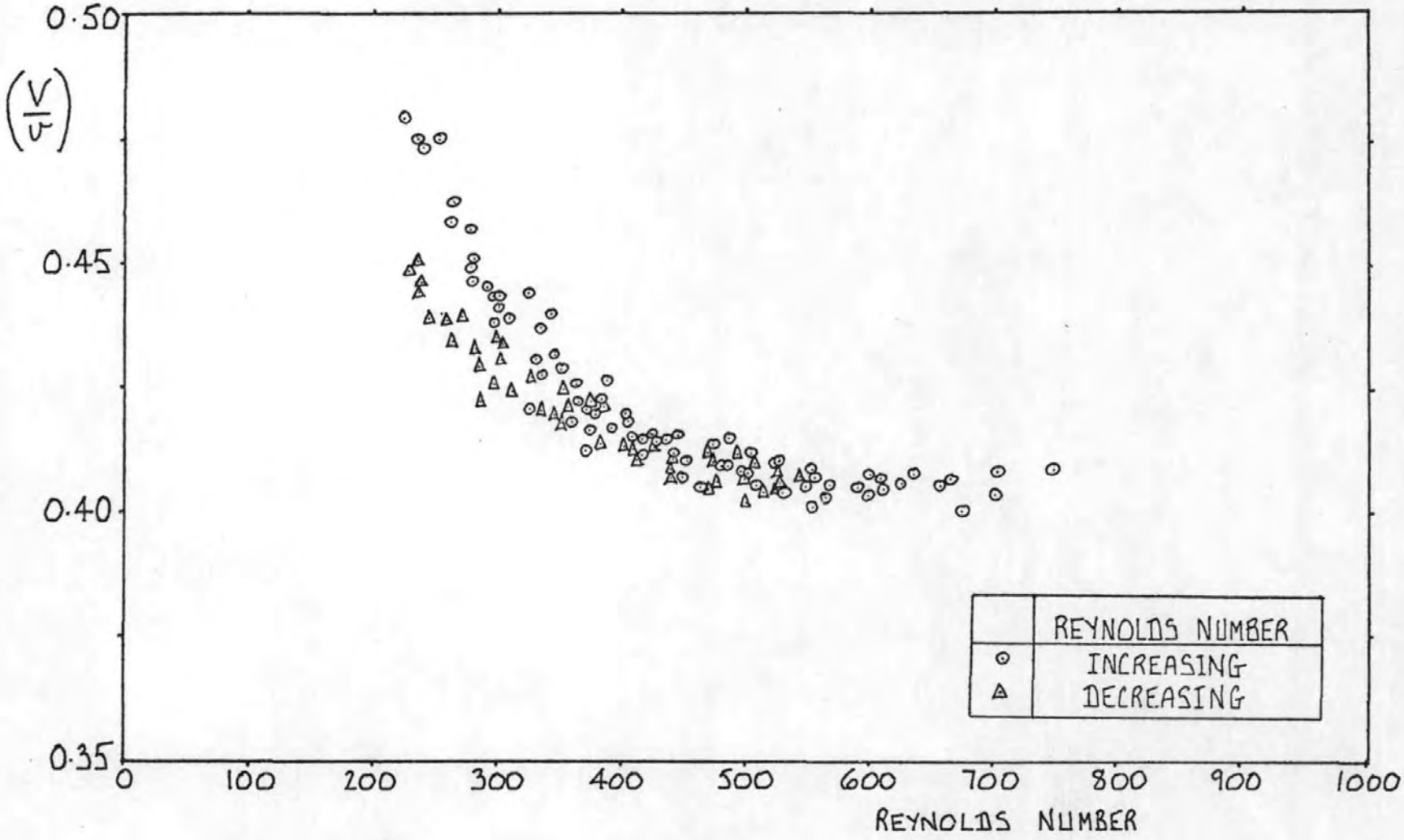

FIG. 36 $R_i/R_o = 0.911$, $\varepsilon = 0$, (TELLUS T17)

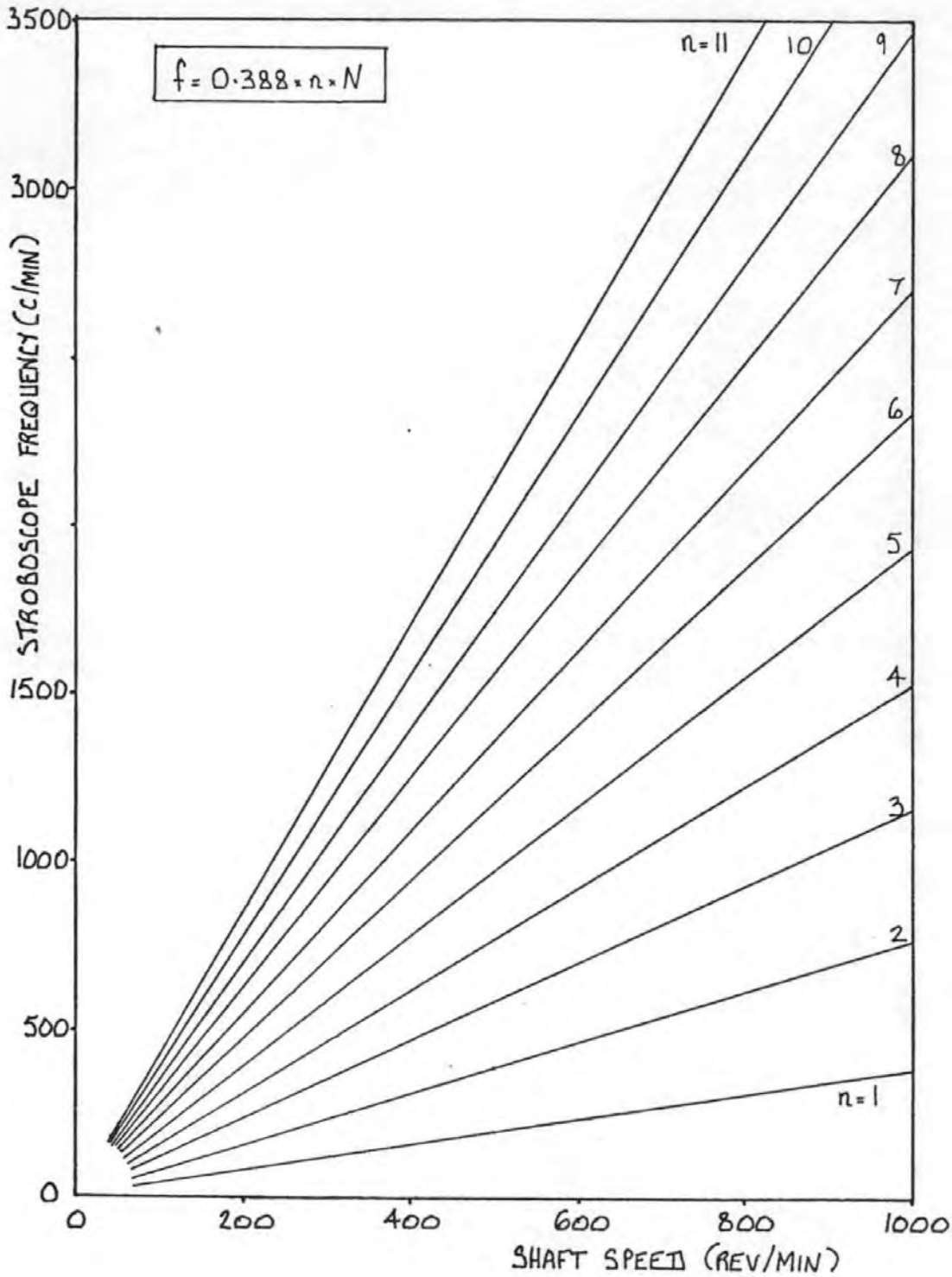

FIG. 37 'RADIAL LINES' DEFINED BY TANGENTIAL WAVE NUMBERS WITH $R_i/R_o = 0.911$, $\varepsilon = 0$.

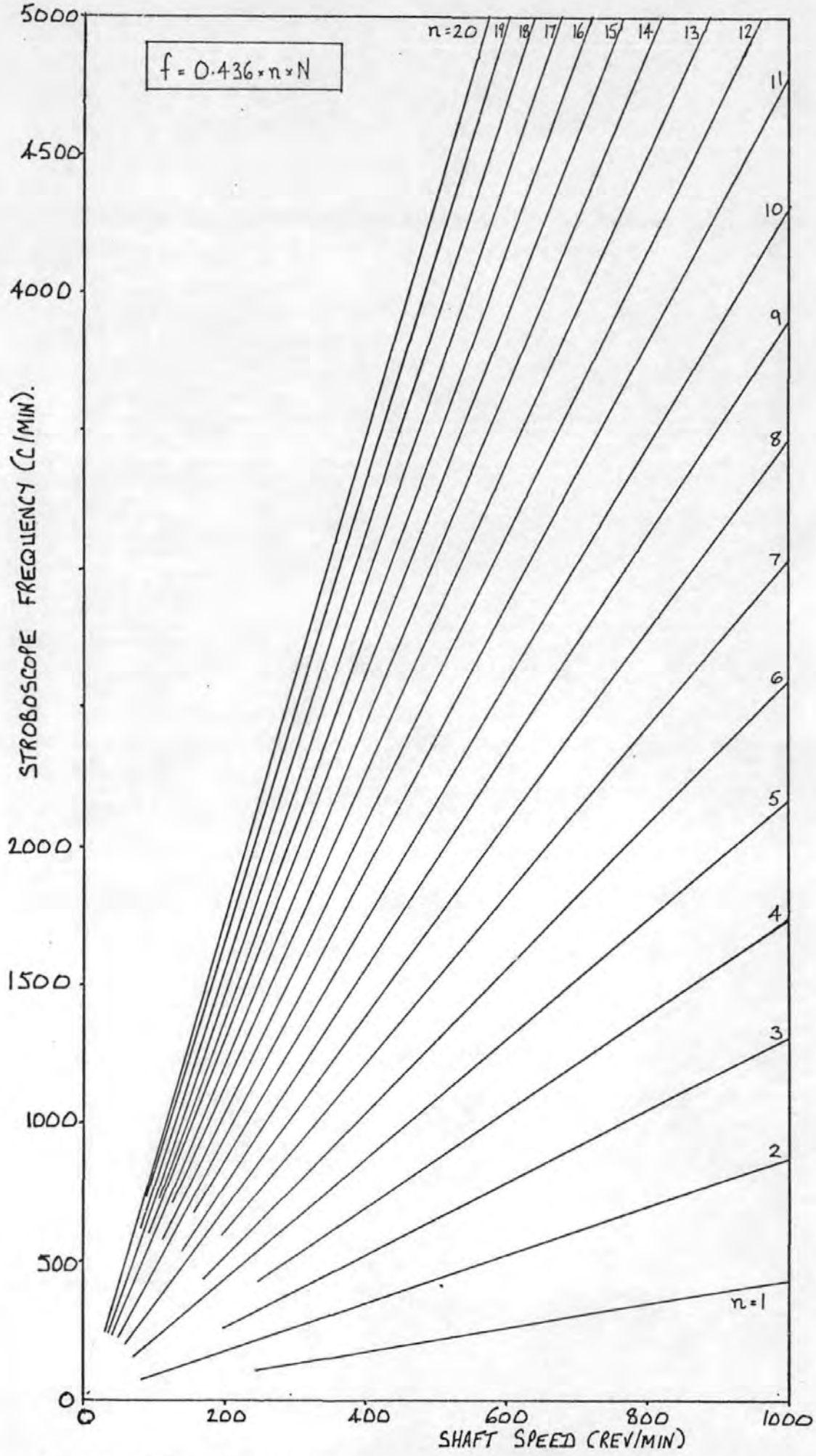

FIG. 38 'RADIAL LINES' DEFINED BY TANGENTIAL WAVE NUMBERS WITH $R_i/R_o = 0.950$, $\varepsilon = 0$

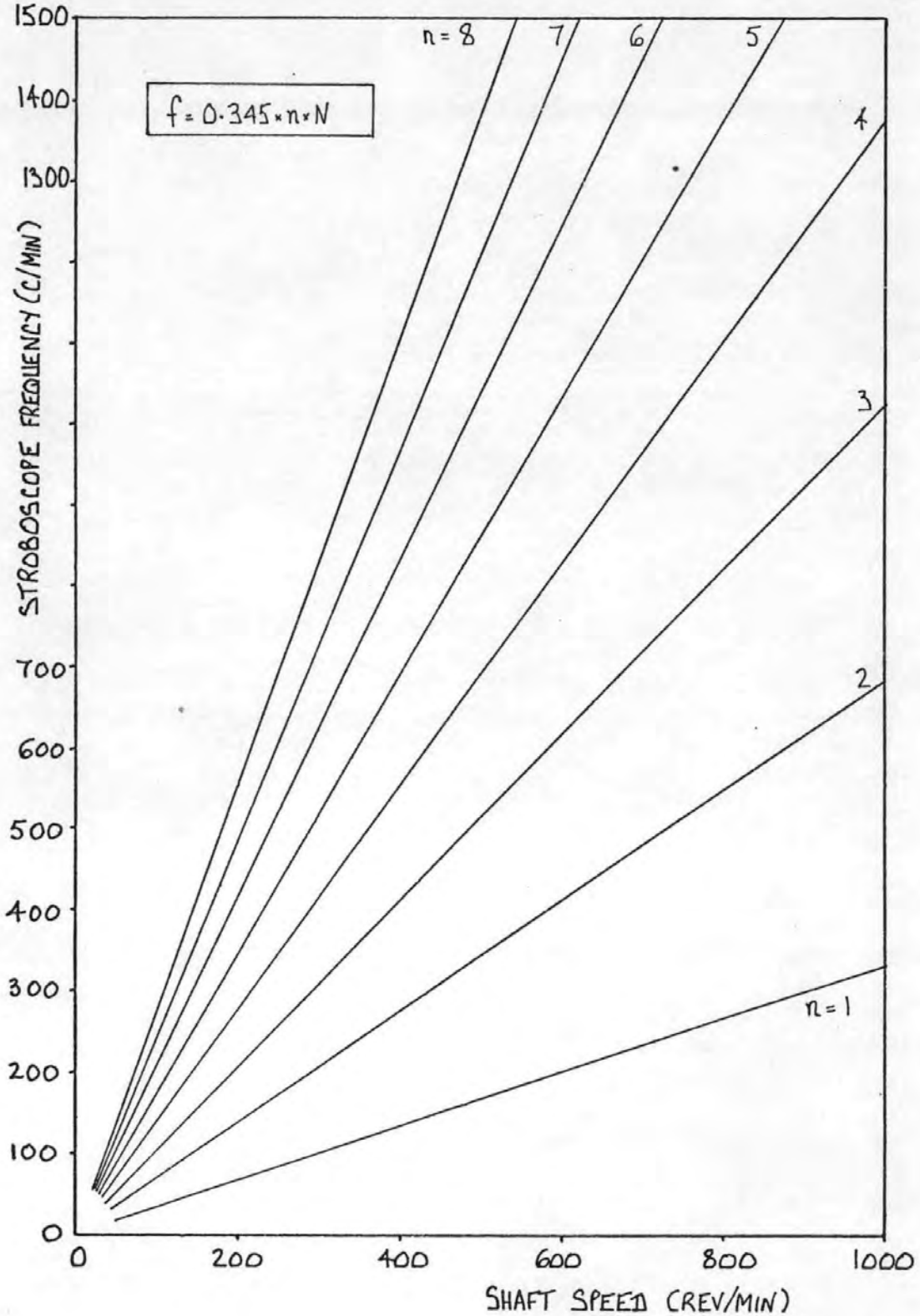

FIG. 39 'RADIAL LINES' DEFINED BY TANGENTIAL WAVE NUMBERS WITH $R_i/R_o = 0.874$, $\varepsilon = 0$.

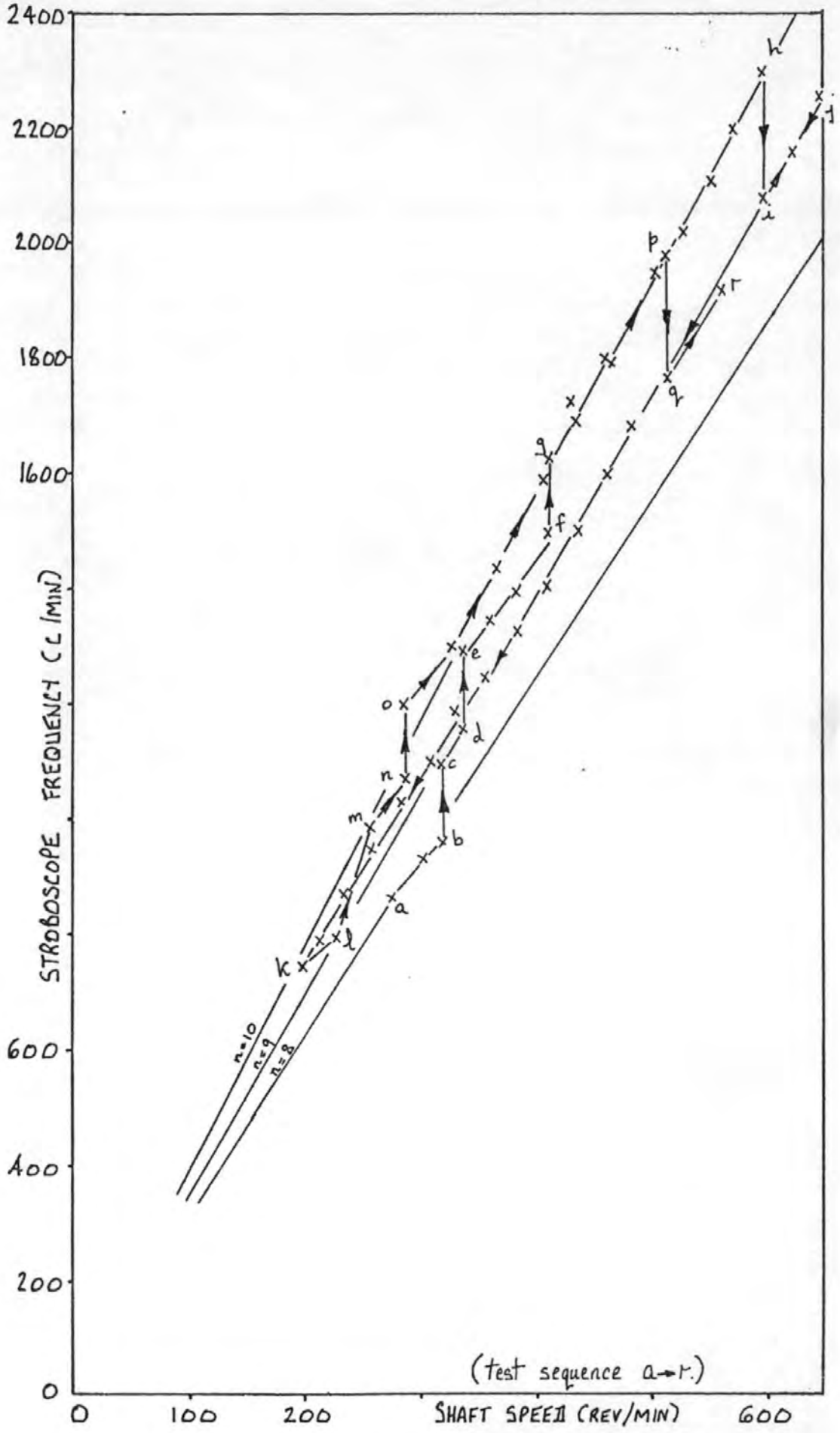

FIG. 40 SEQUENCE OF TANGENTIAL WAVE NUMBER TRANSITIONS IN A PARTICULAR TEST. $R_i/R_o = 0.911$, $\varepsilon = 0$.

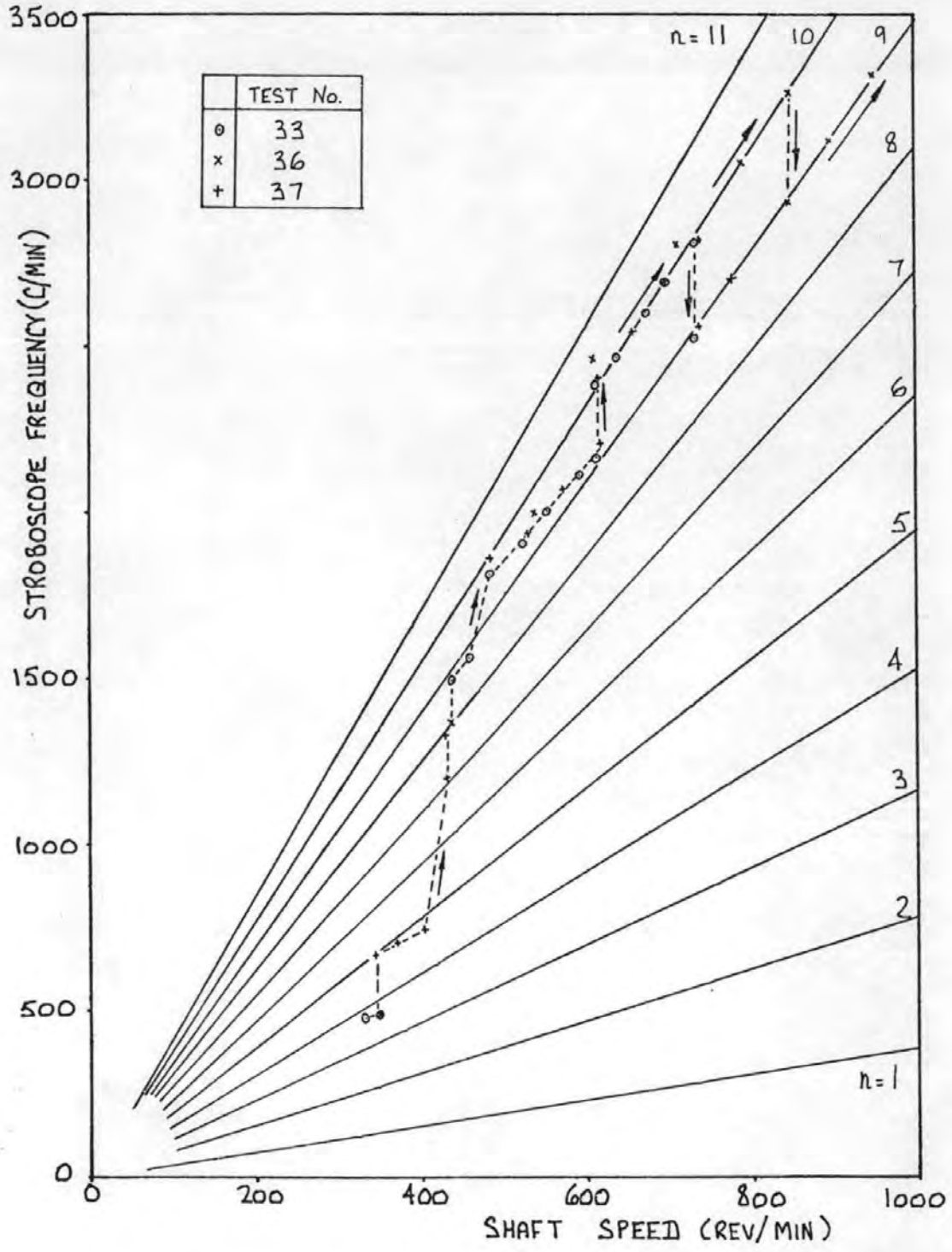

FIG. 41 TYPICAL PRIMARY WAVY MODE TANGENTIAL WAVE NUMBER TRANSITIONS WITH INCREASING SHAFT SPEED.
$R_i/R_o = 0.911$, $\varepsilon = 0$

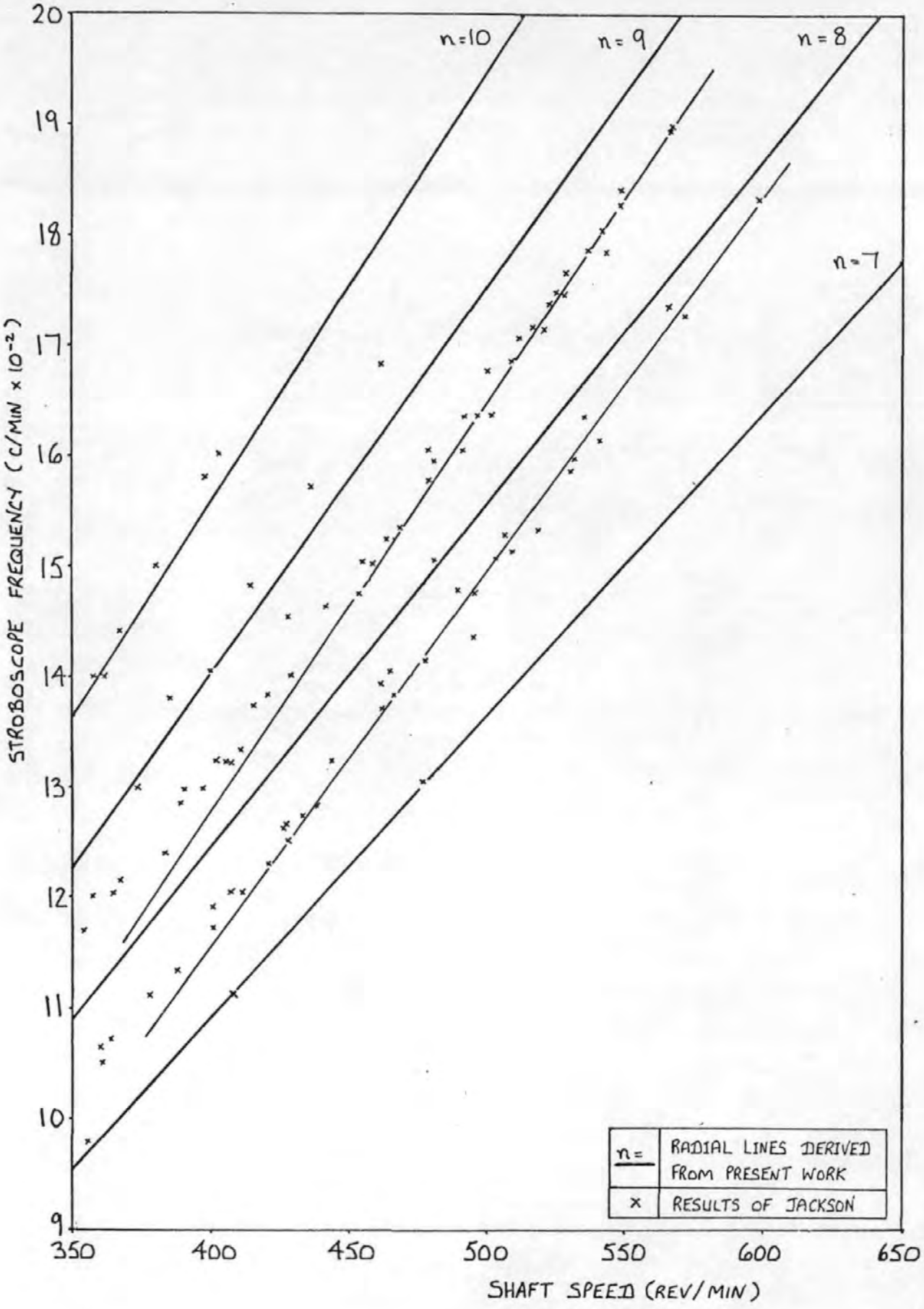

FIG. 42 COMPARISON BETWEEN DERIVED RADIAL LINES AND RESULTS OF JACKSON (η=0·911, ε=0)

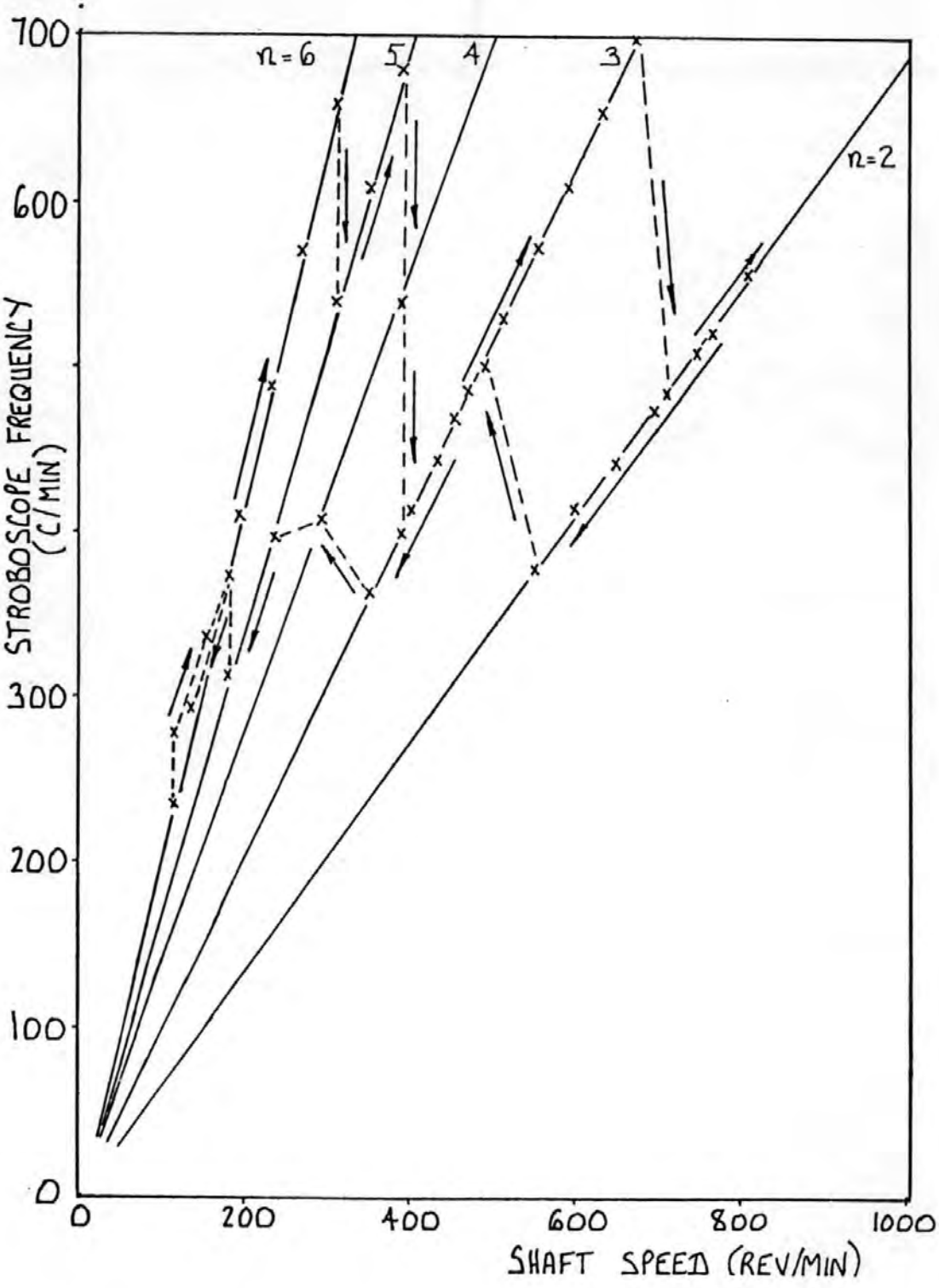

FIG. 43 HYSTERESIS EFFECT TYPICAL OF TANGENTIAL WAVE NUMBER TRANSITIONS.
$R_i/R_- = 0.874, \quad \varepsilon = 0.$

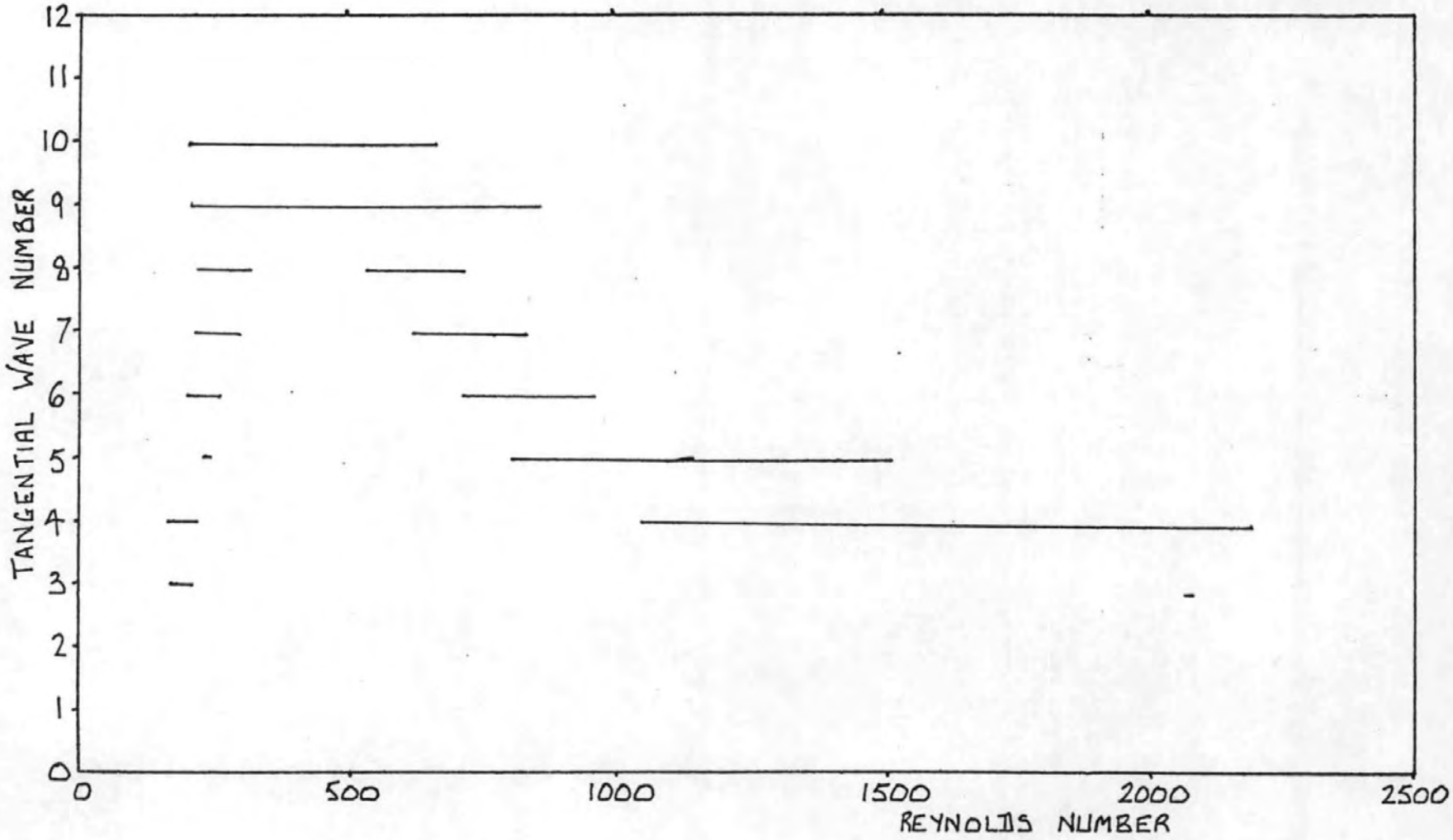

FIG. 44 $R_i/R_o = 0.911$, $\varepsilon = 0$

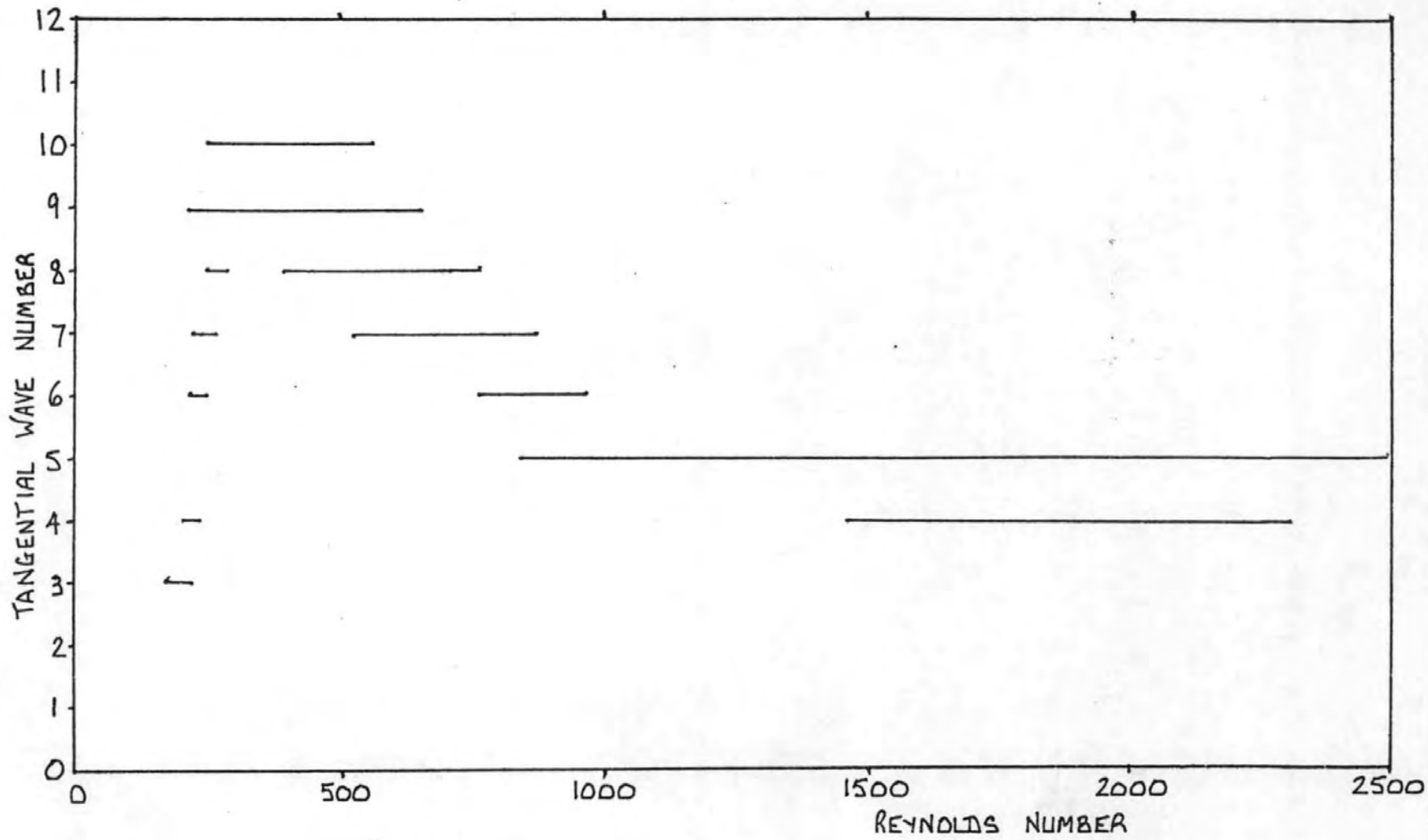

FIG. 45 $R_i/R_o = 0.911$, $\varepsilon = 0.05$

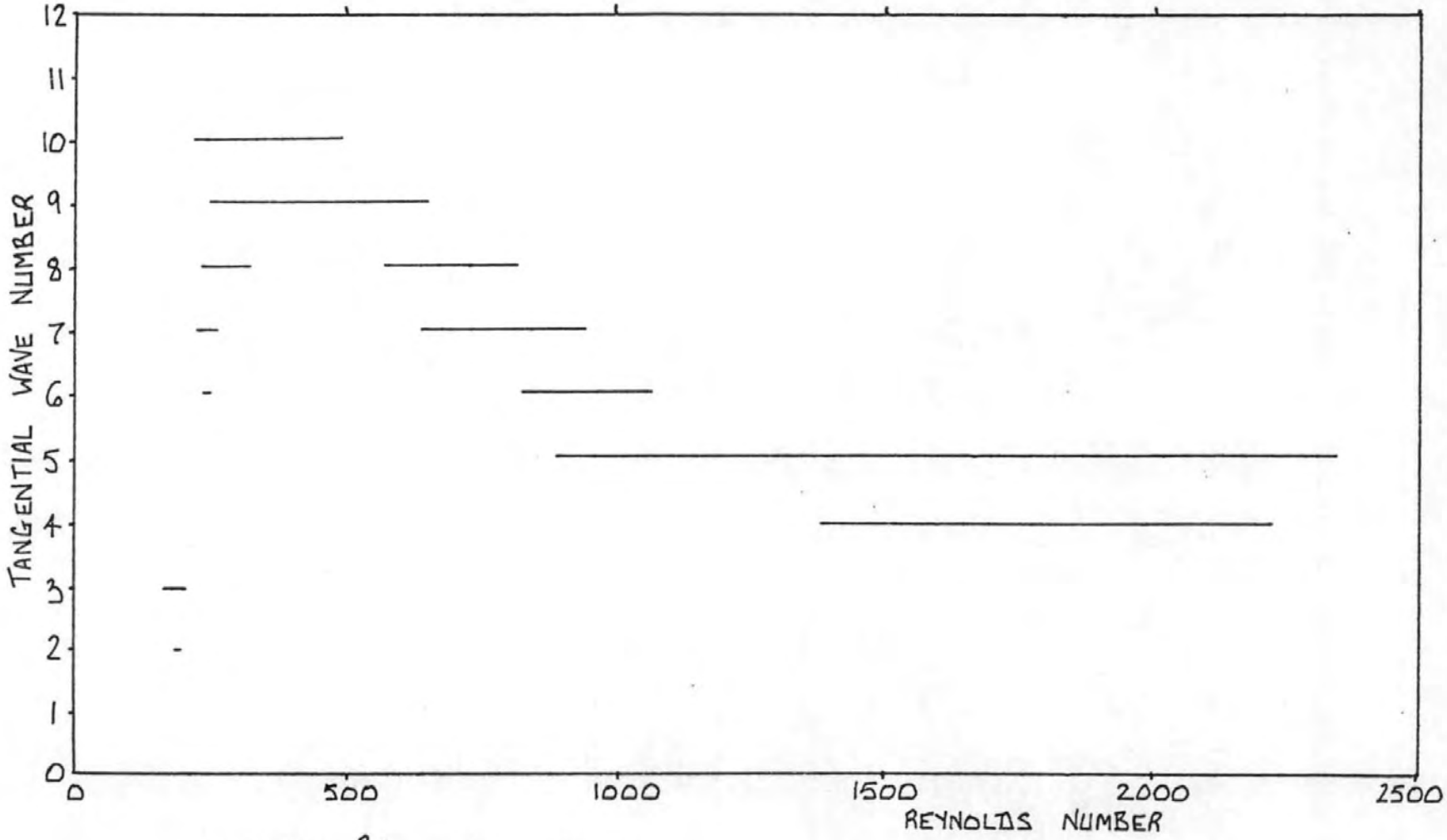

FIG. 46 $R_i/R_o = 0.911$, $\varepsilon = 0.10$

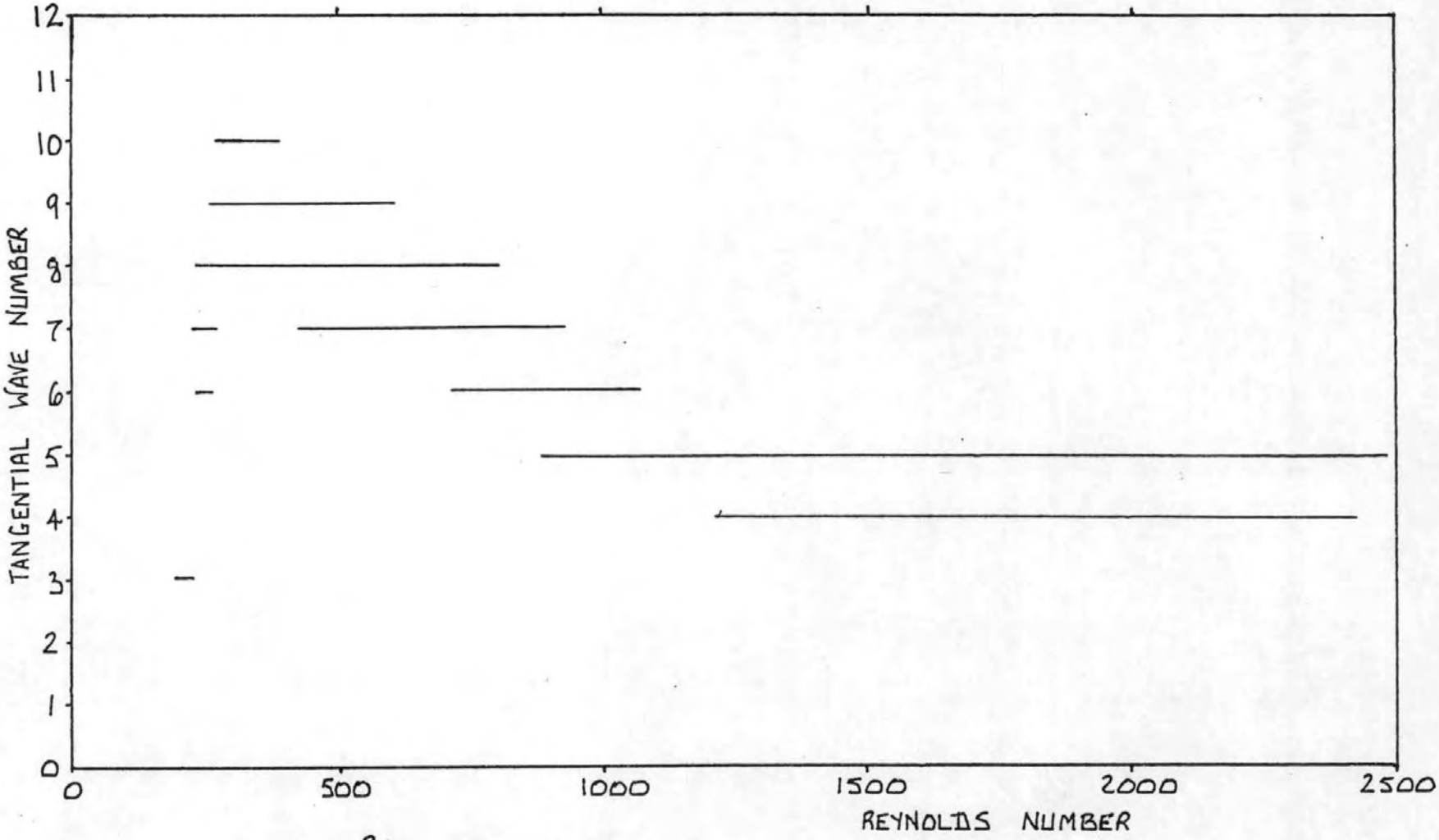

FIG. 47 $R_i/R_o = 0.911$, $\xi = 0.15$

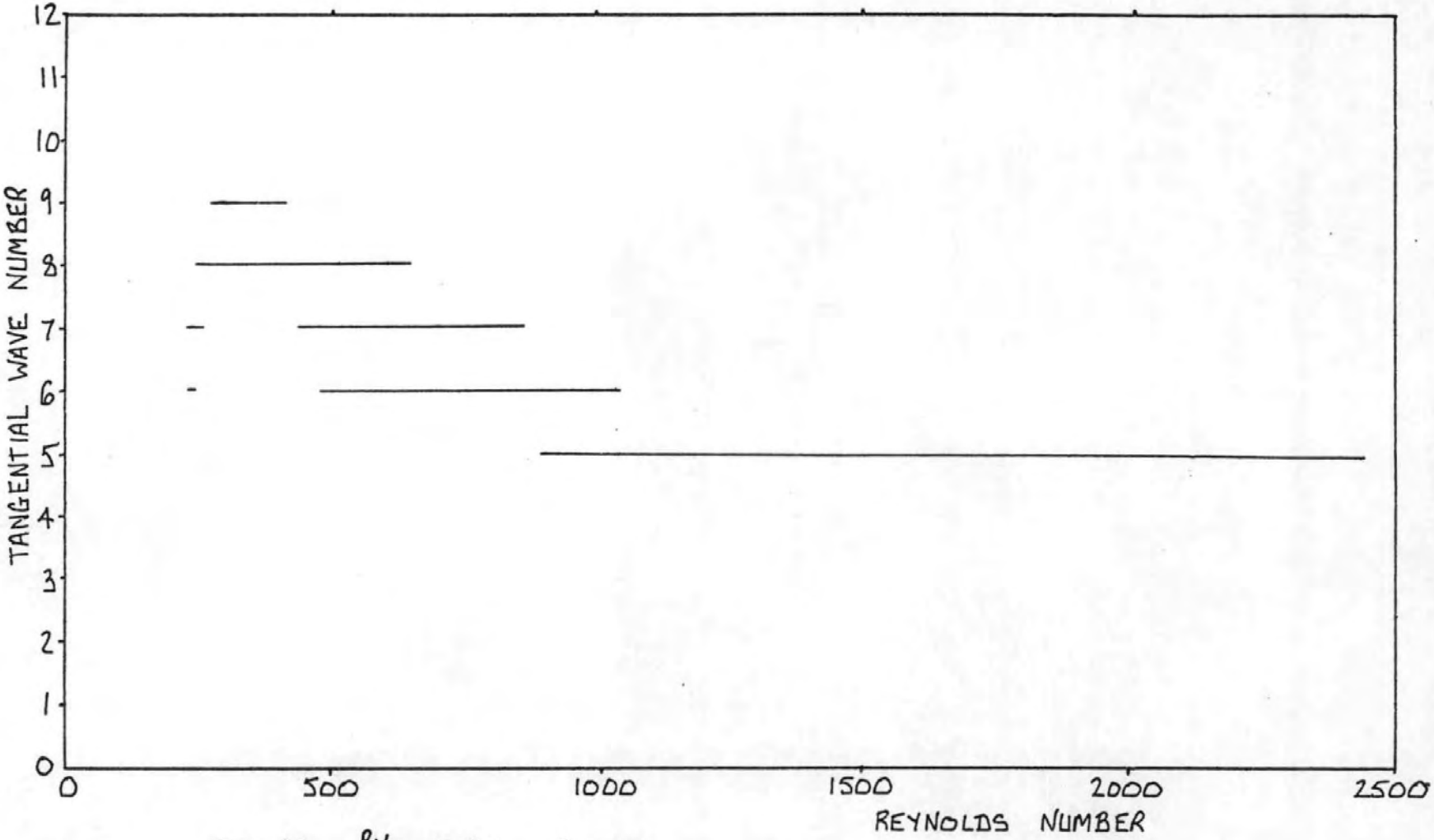

FIG. 48 $R_i/R_o = 0.911$, $\varepsilon = 0.20$

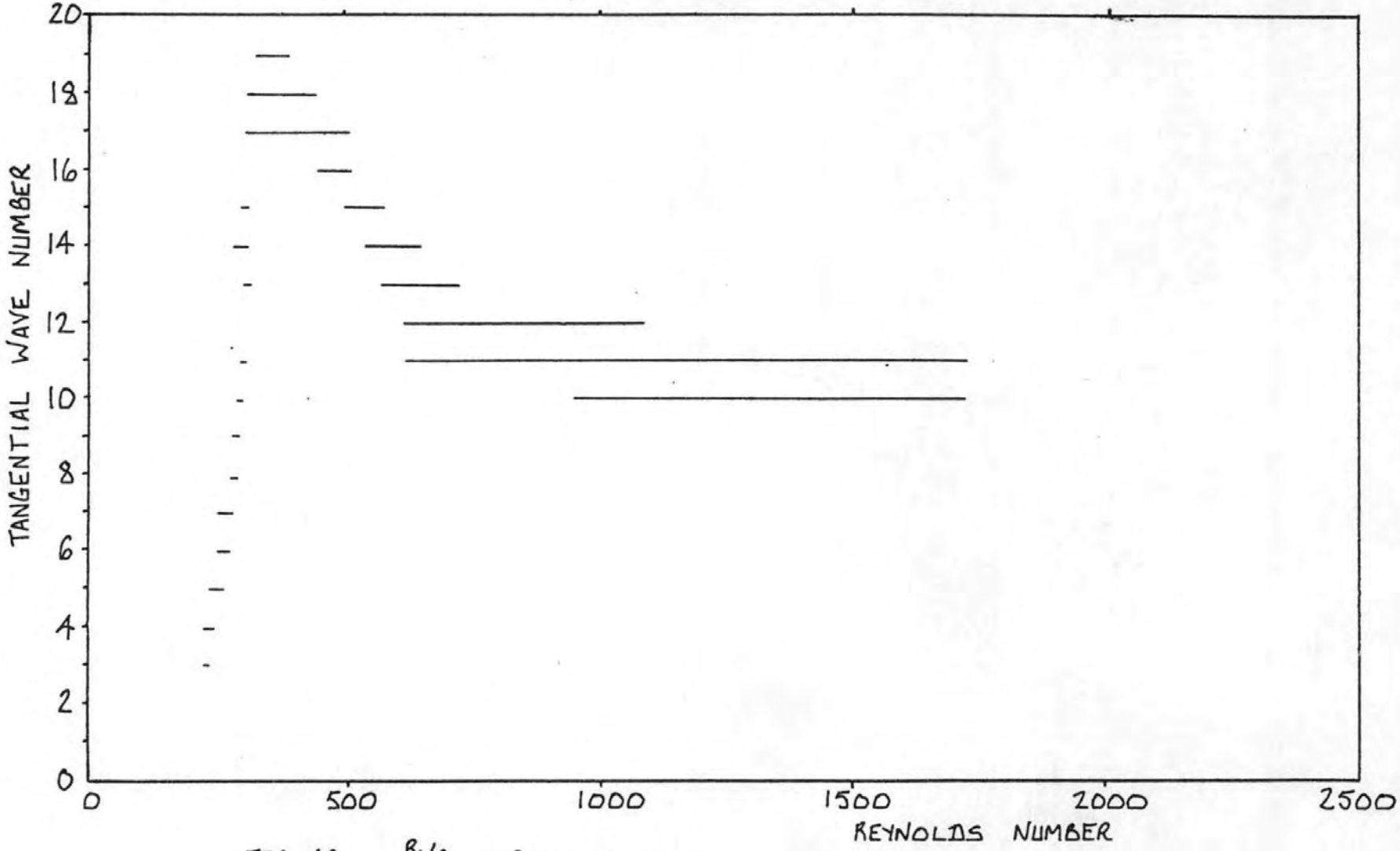

FIG. 49 $R_i/R_o = 0.95$, $\varepsilon = 0$

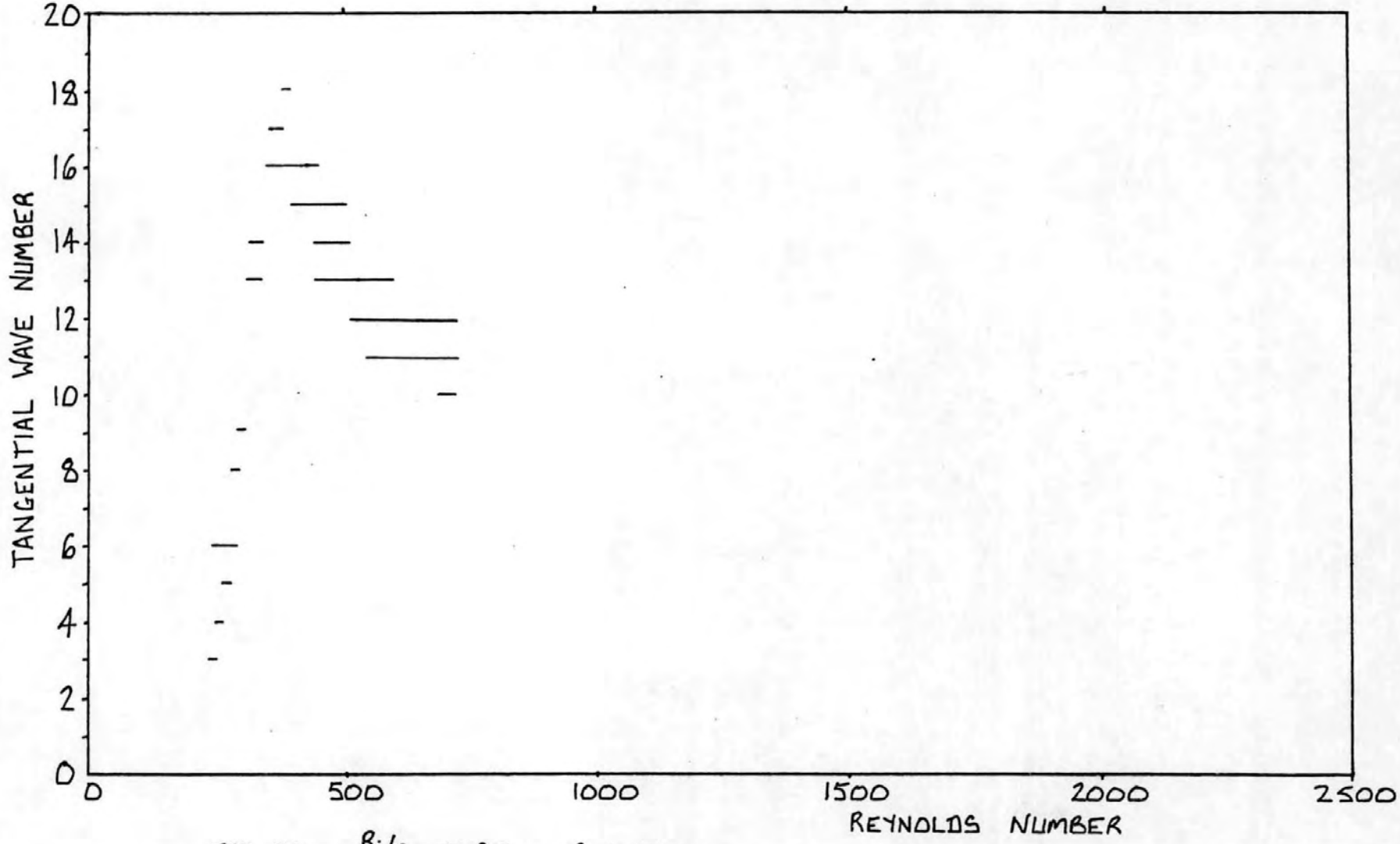

FIG. 50 $R_i/R_o = 0.95$, $\mathcal{E} = 0.10$

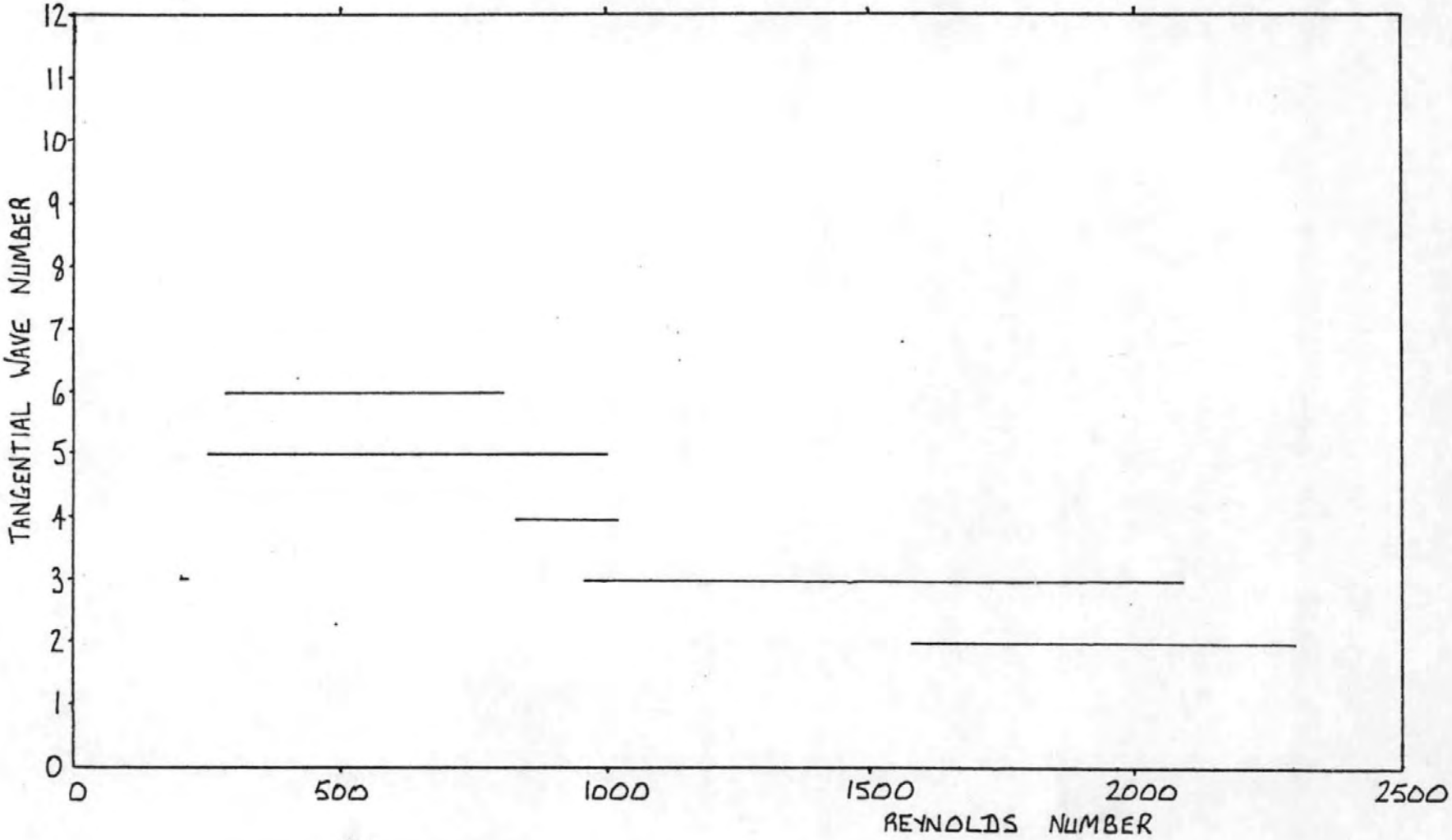

FIG. 51 $R_i/R_o = 0.874$, $\varepsilon = 0$

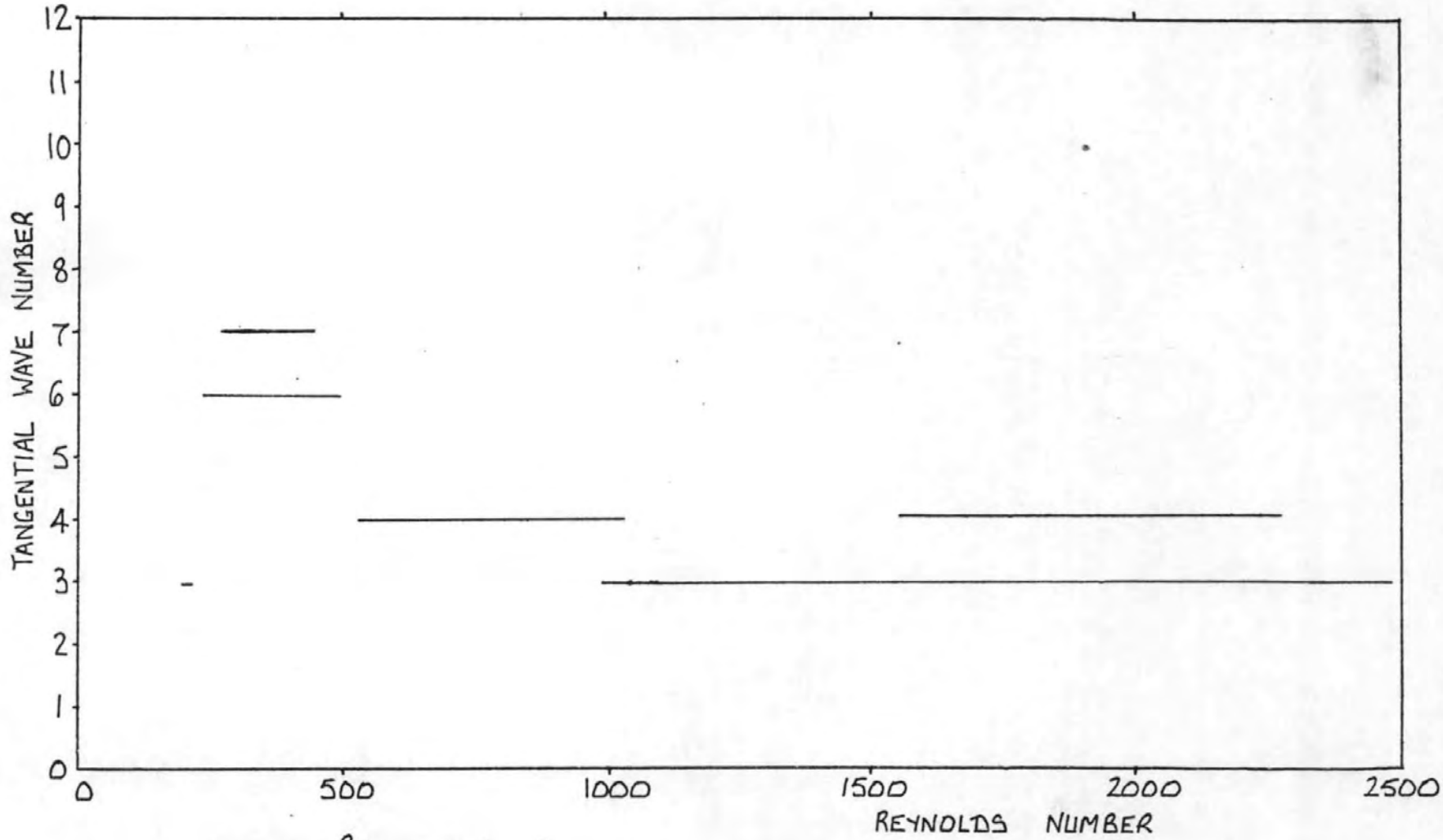

FIG. 52 $R_i/R_o = 0.874$, $\varepsilon = 0.10$

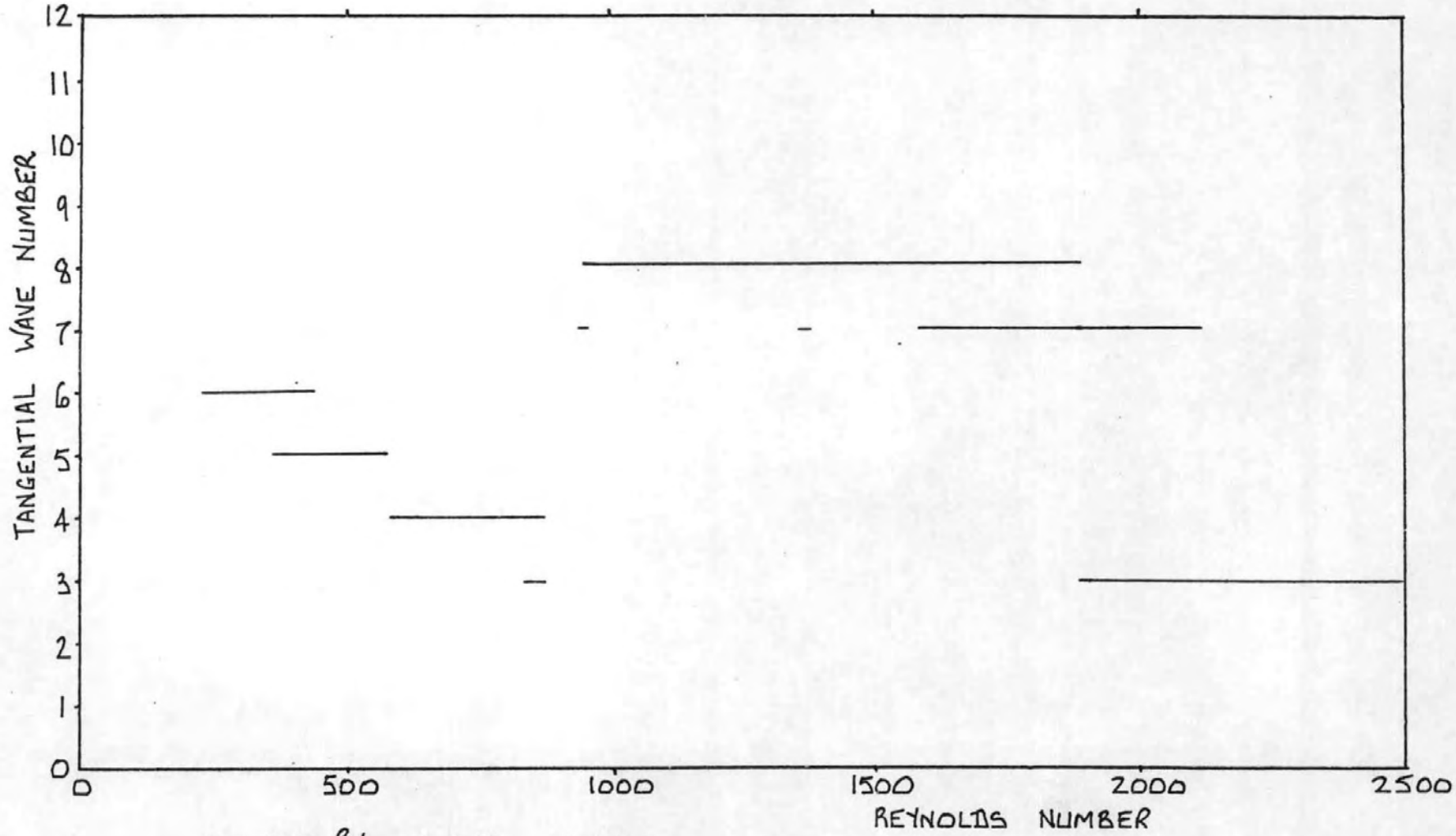

FIG. 53 $R_i/R_o = 0.874$, $\varepsilon = 0.20$

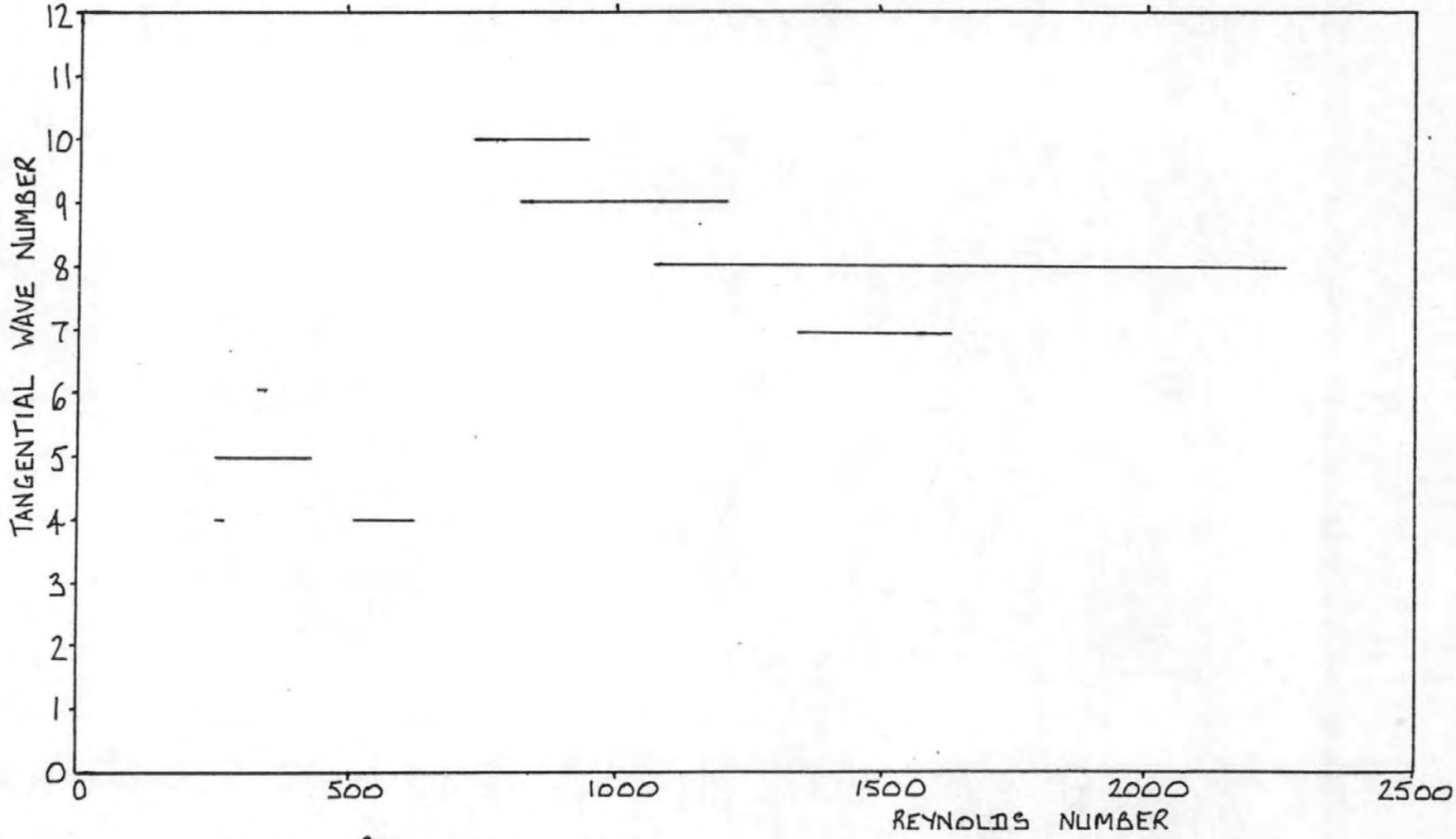

FIG. 54 $R_i/R_o = 0.874$, $\varepsilon = 0.30$

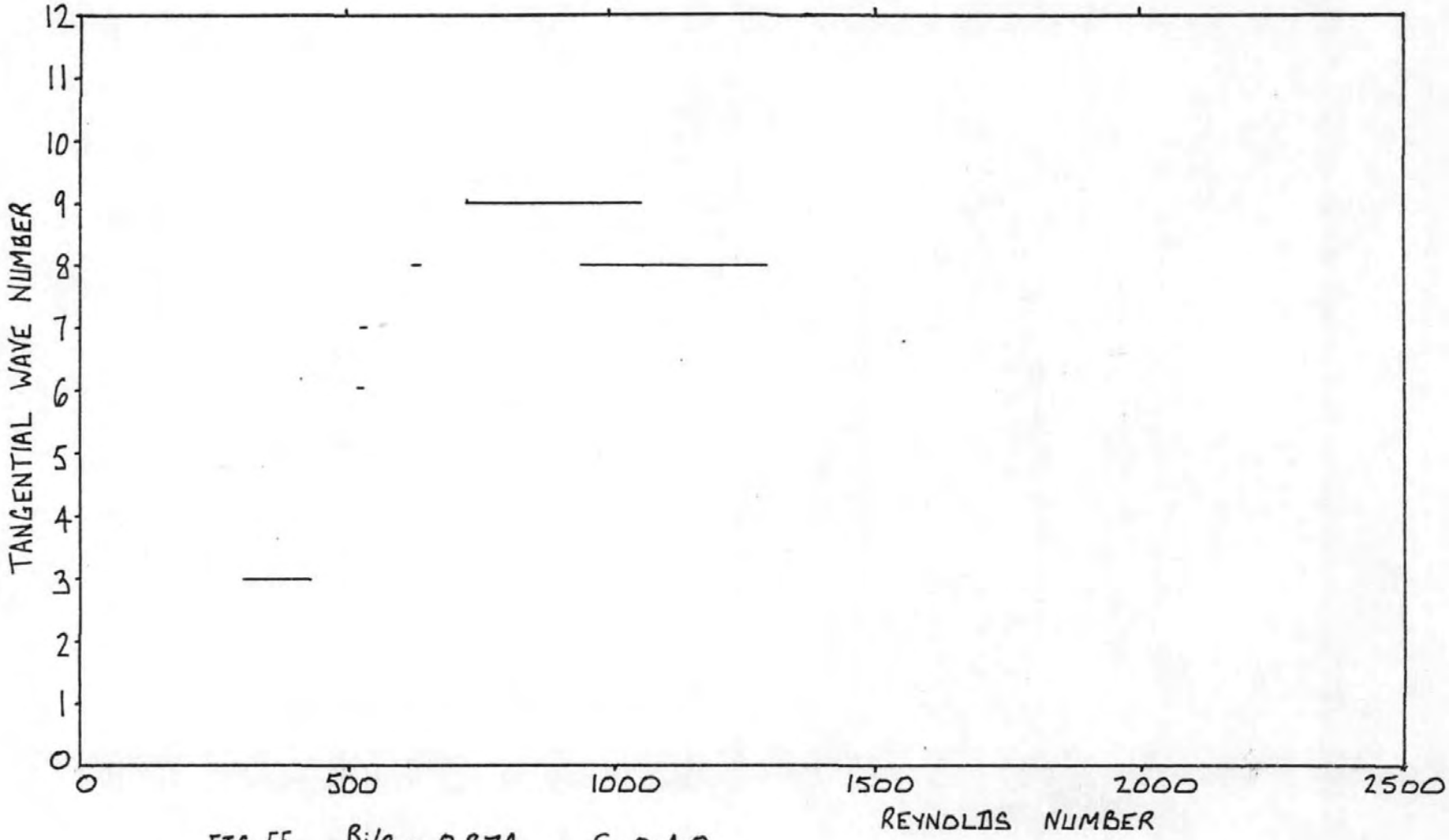

FIG. 55 $R_i/R_o = 0.874$, $\varepsilon = 0.40$

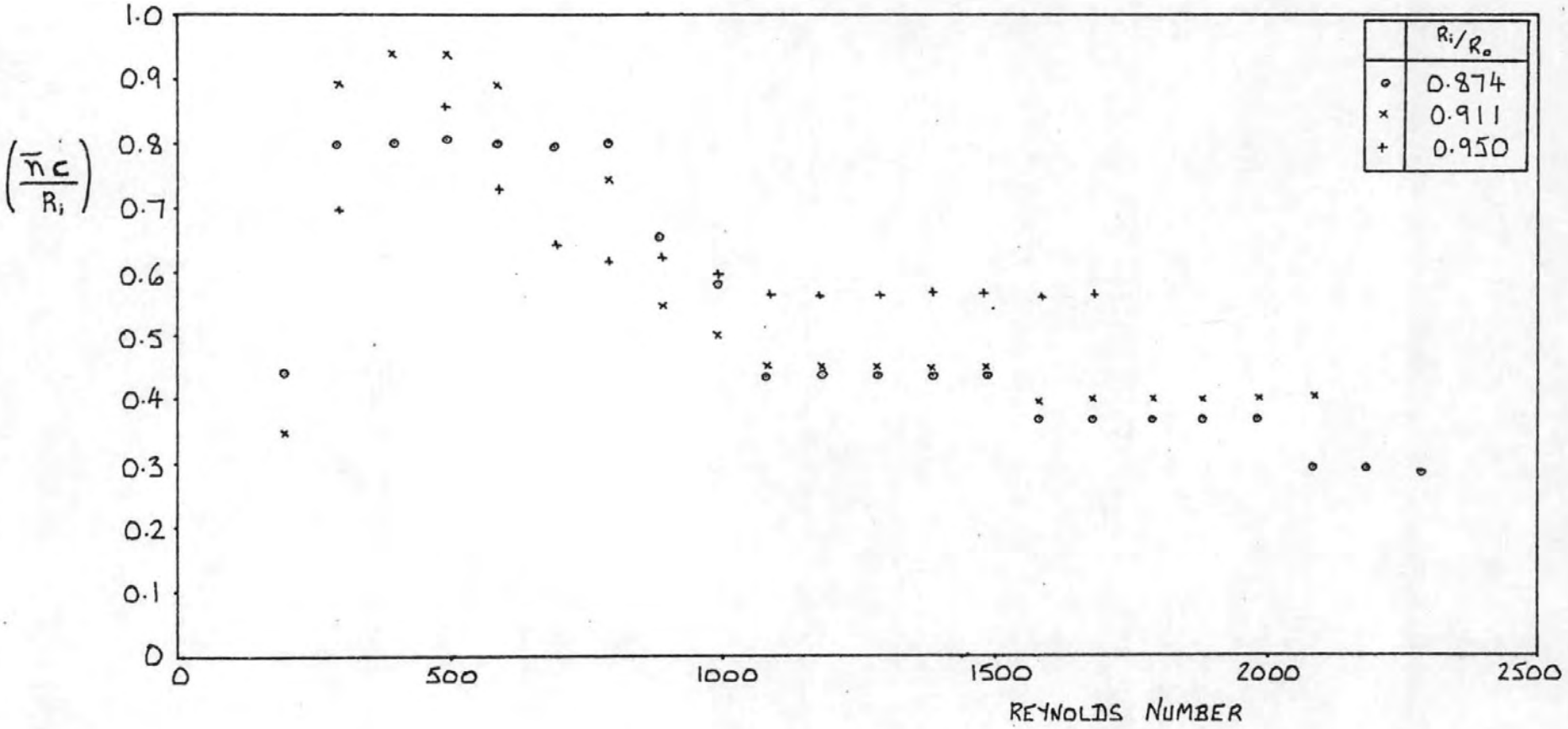

FIG. 56 VARIATION OF NON-DIMENSIONAL WAVE NUMBER PARAMETER, $\varepsilon = 0$

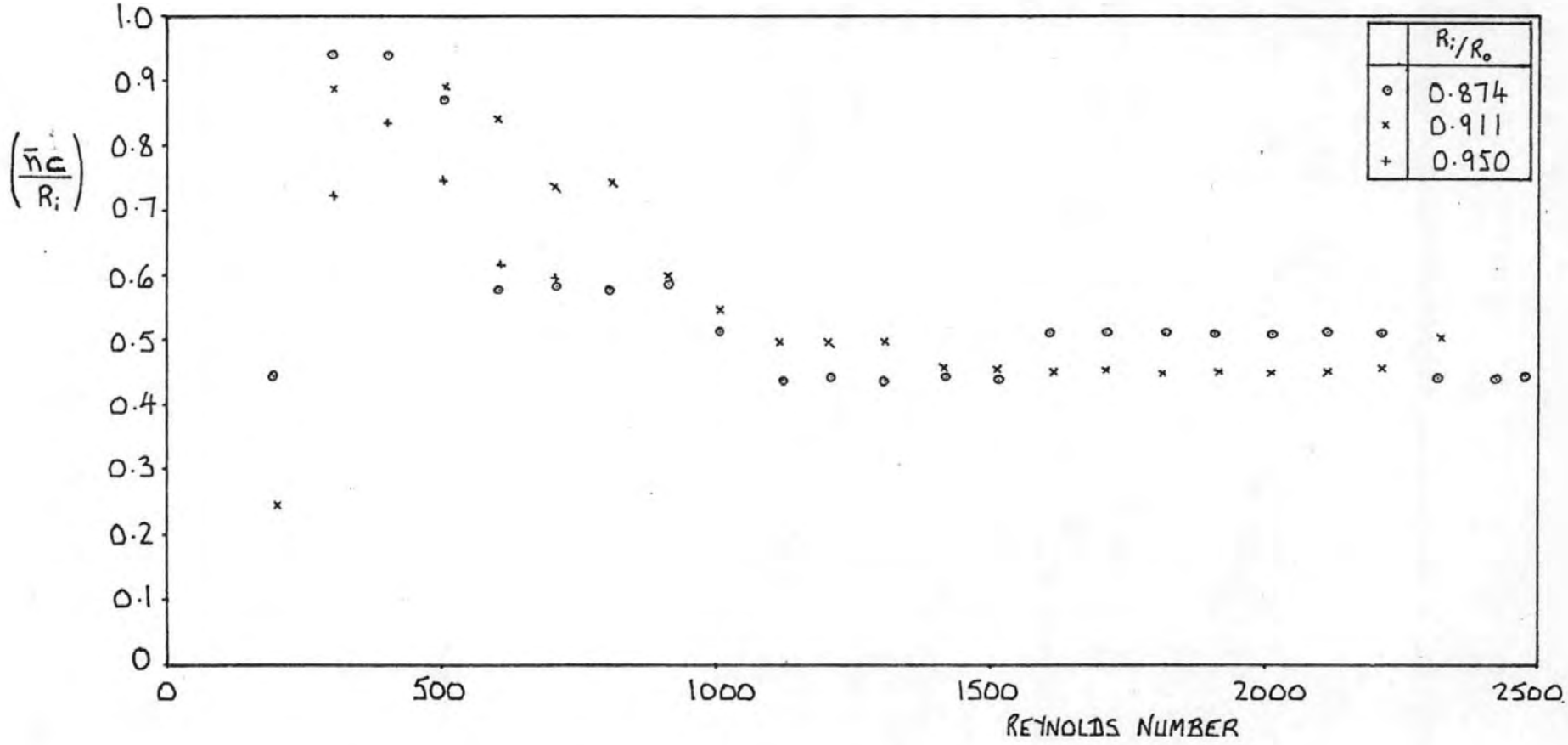

FIG. 57 VARIATION OF NON-DIMENSIONAL WAVE NUMBER PARAMETER, $\varepsilon = 0{\cdot}10$

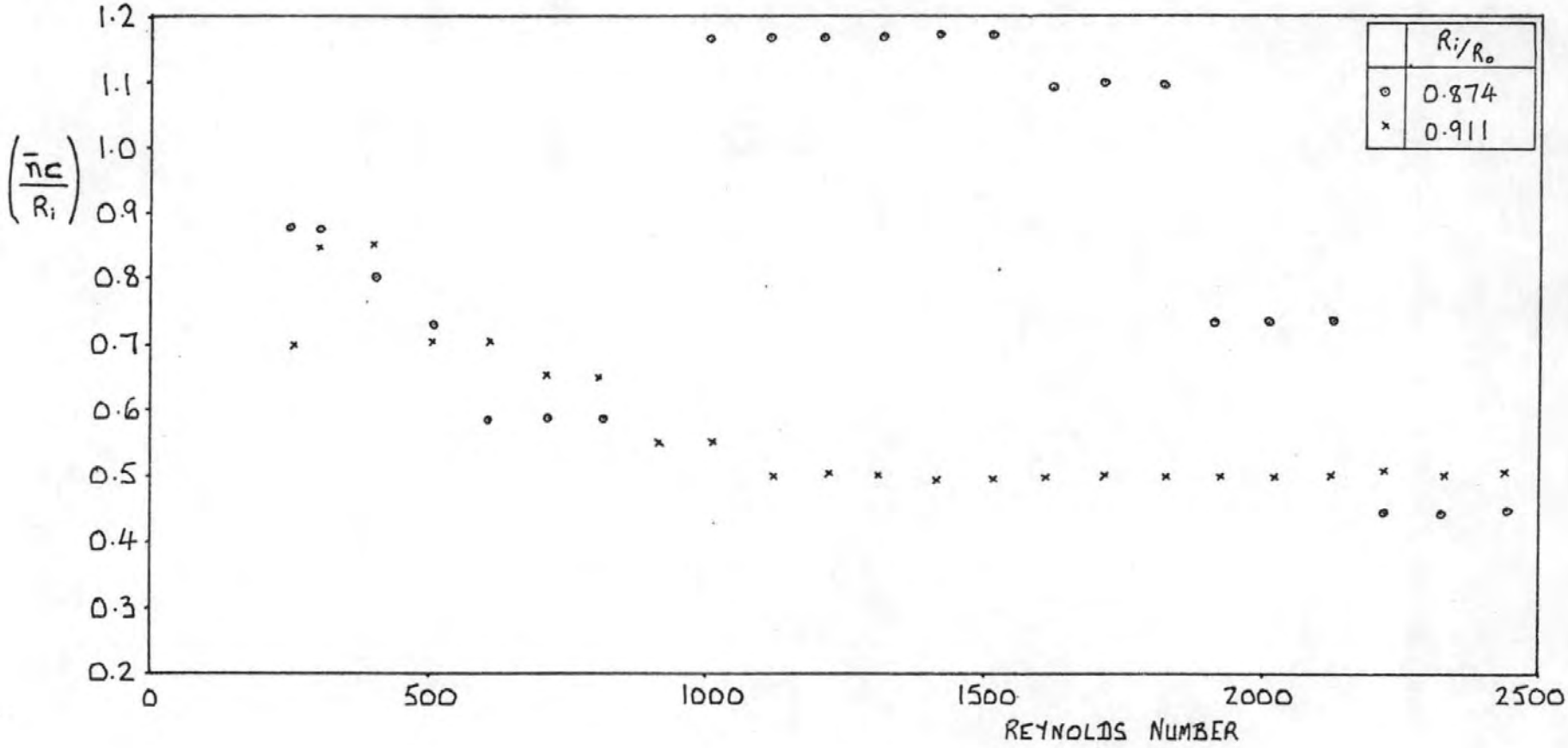

FIG. 58 VARIATION OF NON-DIMENSIONAL WAVE NUMBER PARAMETER, $\varepsilon = 0.20$

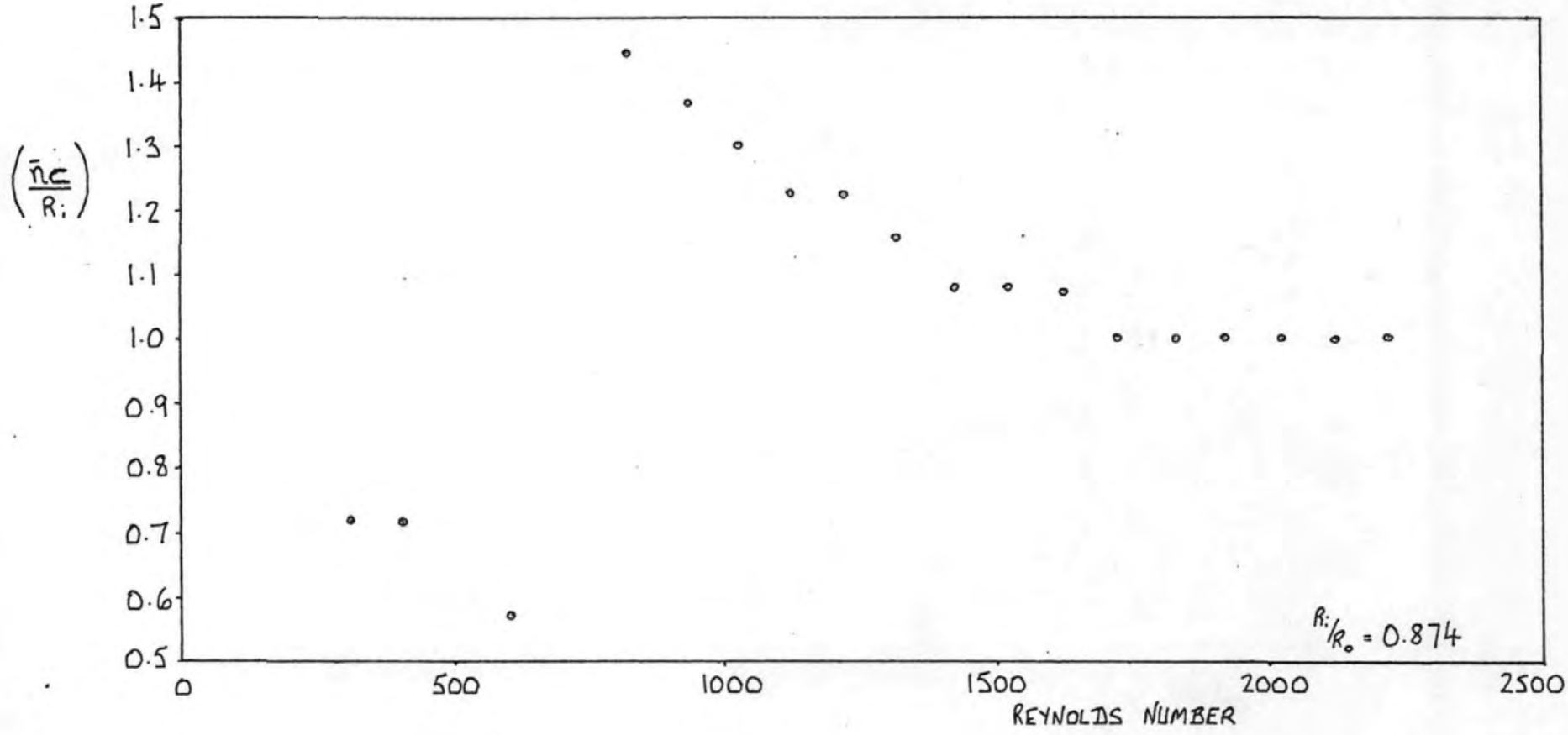

FIG. 59 VARIATION OF NON-DIMENSIONAL WAVE NUMBER PARAMETER, $\varepsilon = 0.30$

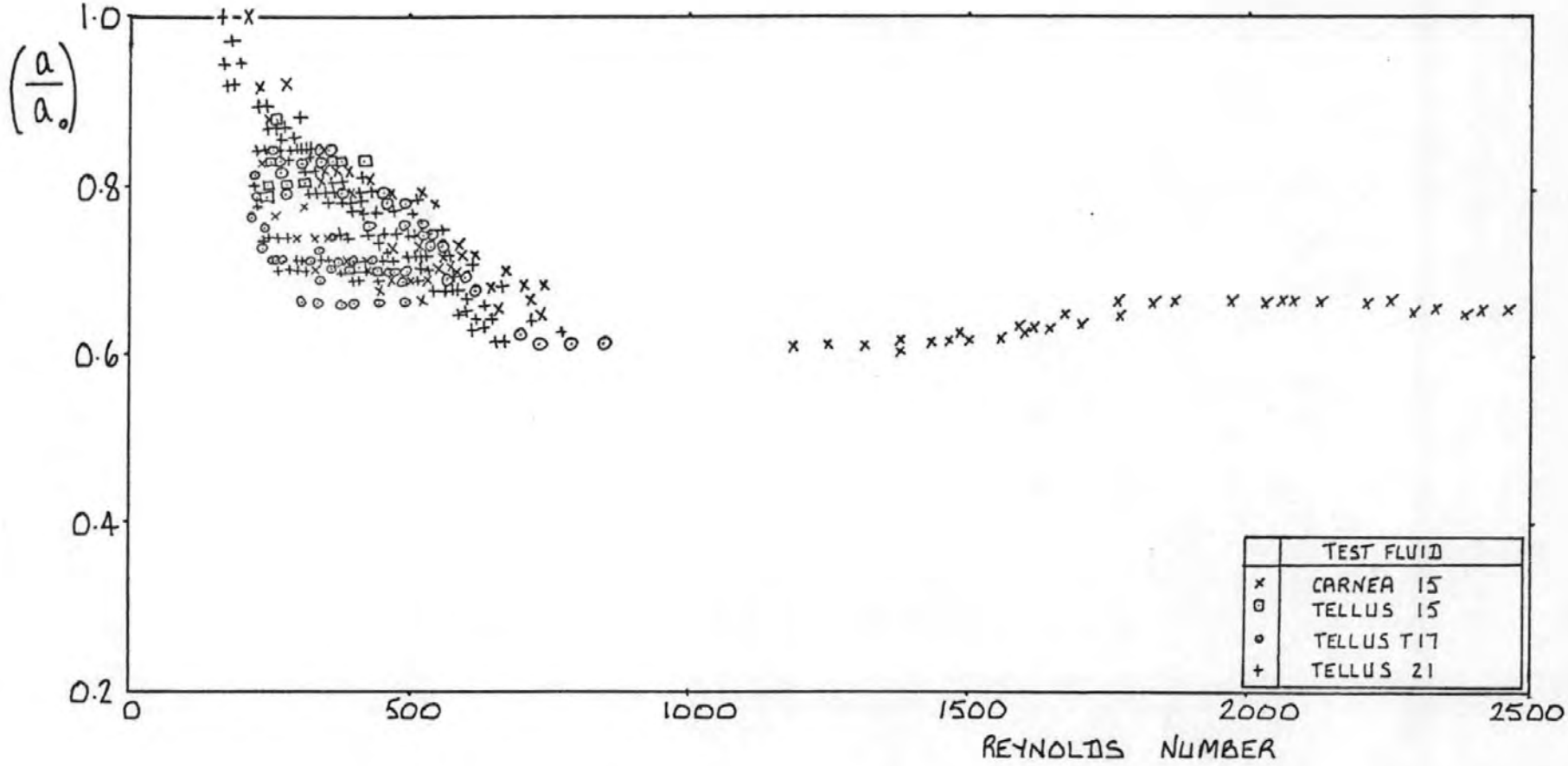

FIG. 60 $R_i/R_o = 0.911$, $\varepsilon = 0$

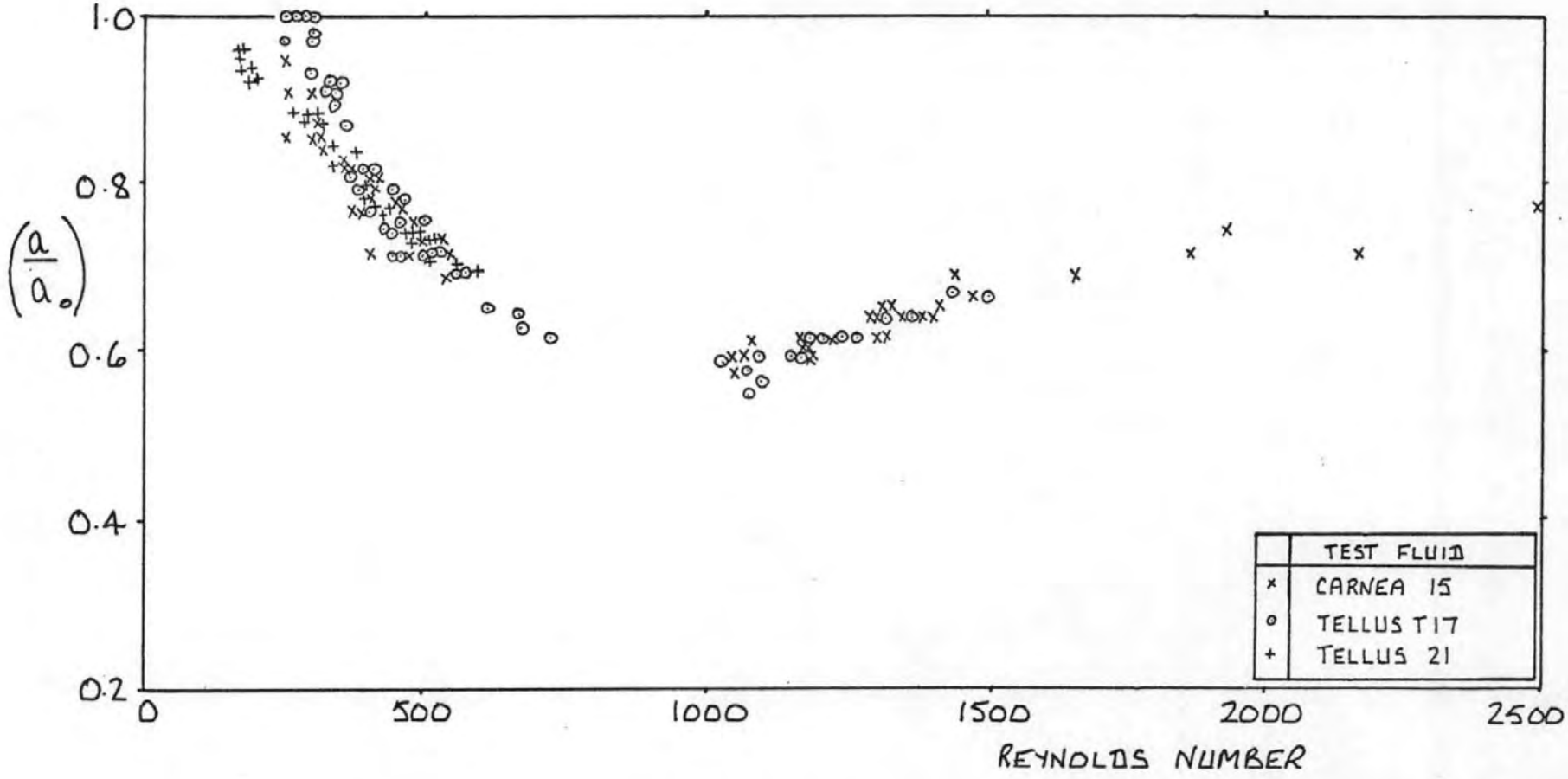

FIG. 61 $R_i/R_o = 0.911$, $\varepsilon = 0.05$

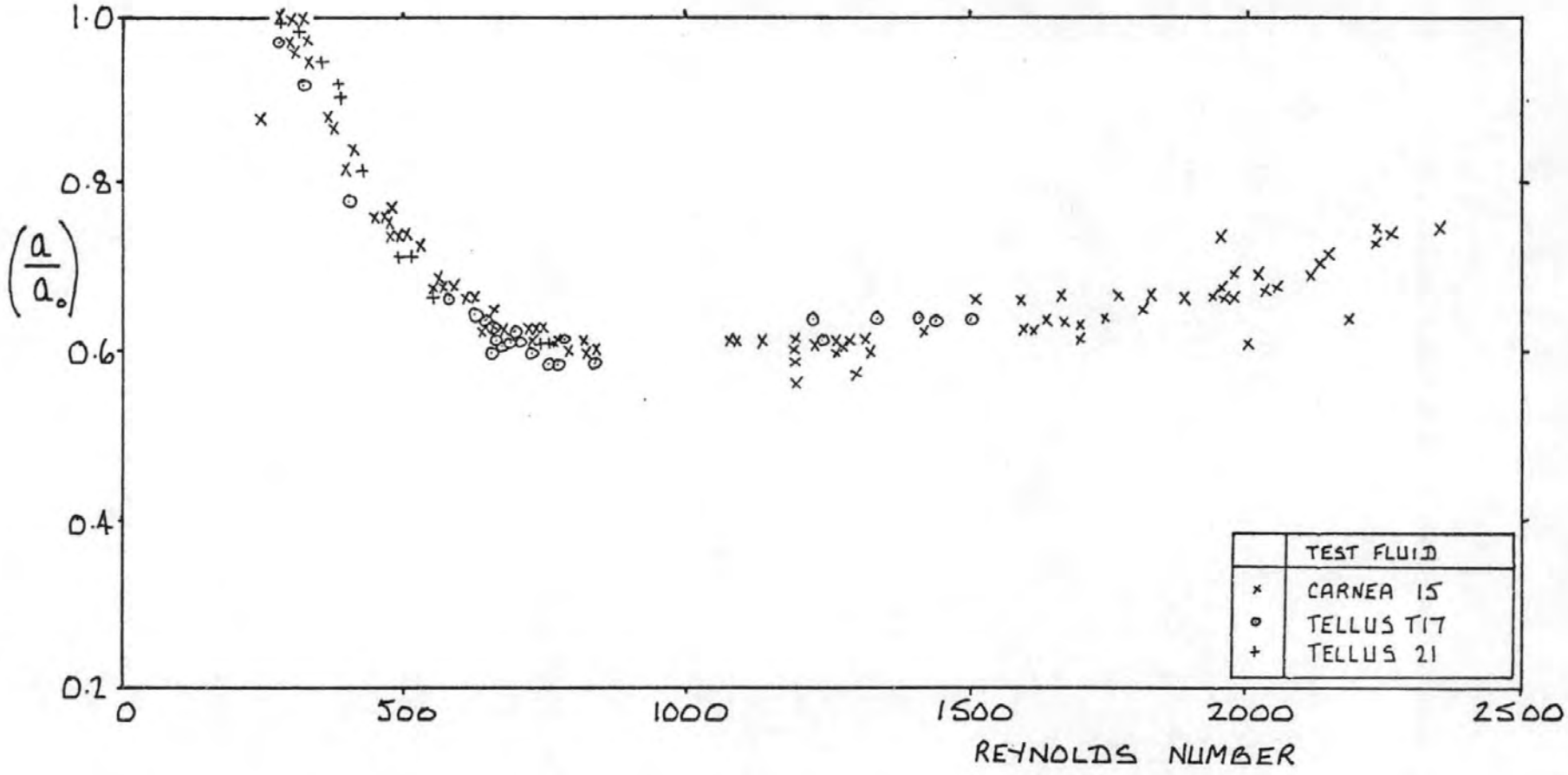

FIG. 62 $R_i/R_o = 0.911$, $\mathcal{E} = 0.10$

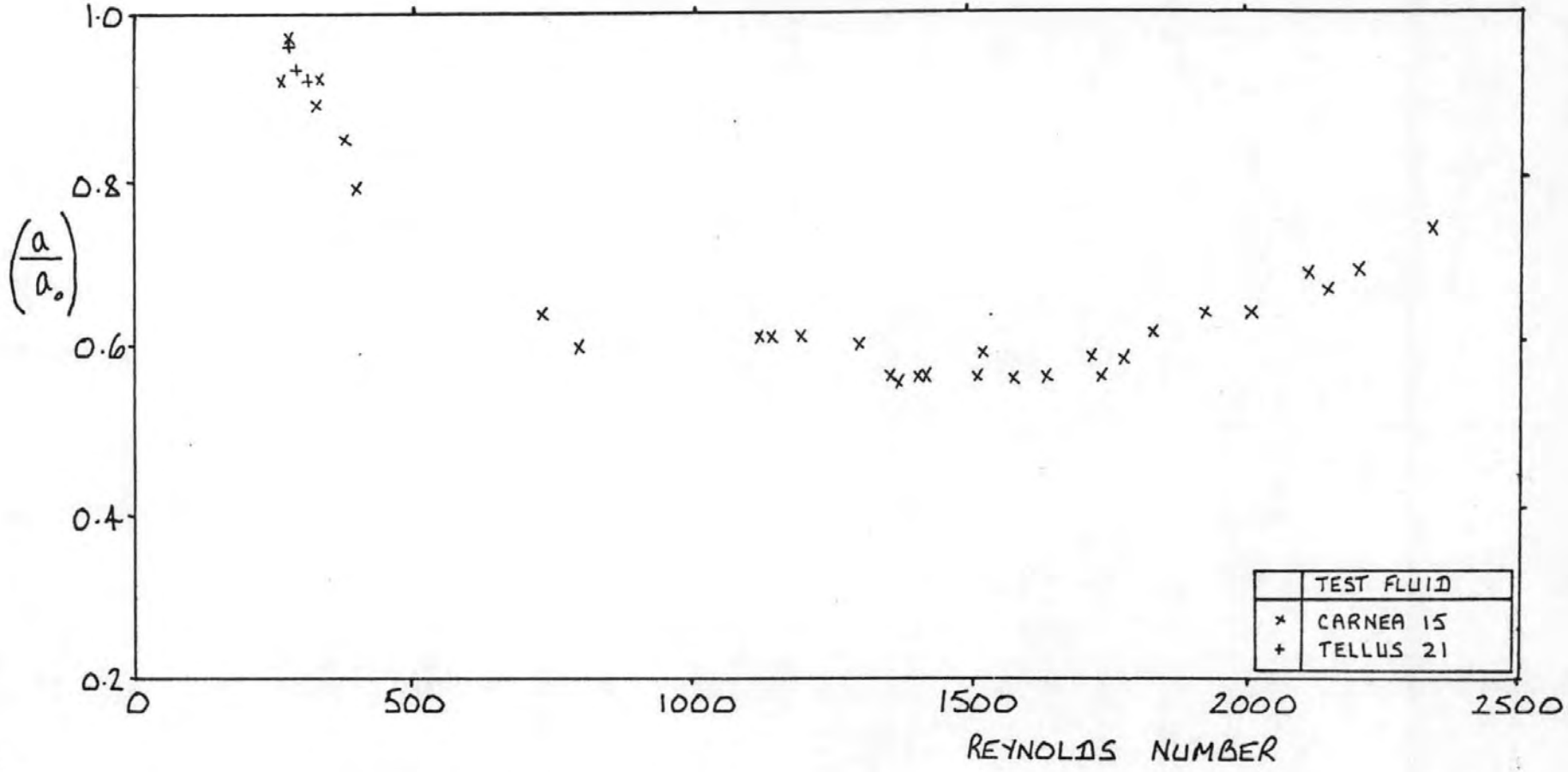

FIG. 63 $R_i/R_o = 0.911$, $\varepsilon = 0.15$

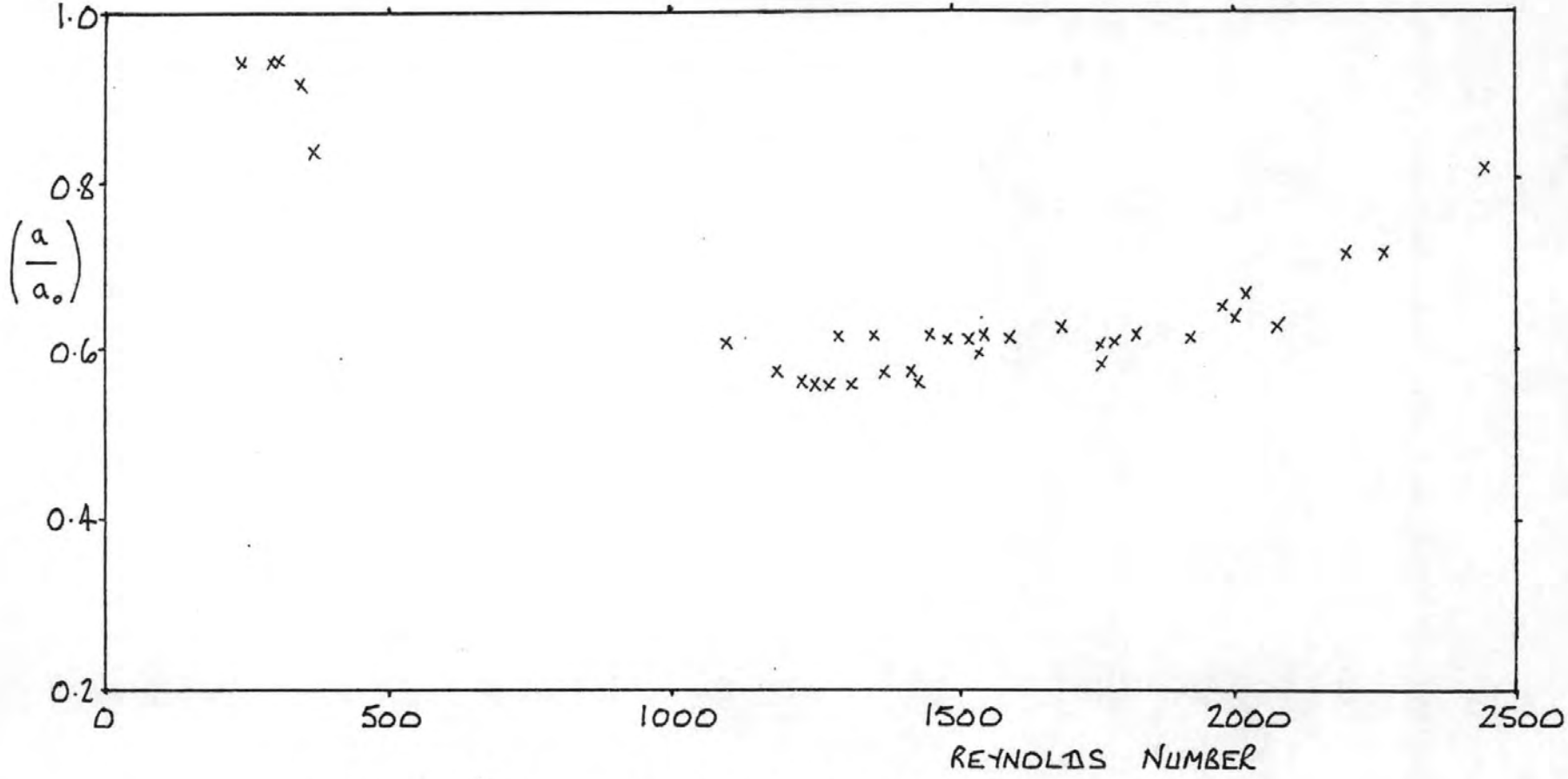

FIG. 64 $R_i/R_o = 0.911$, $\varepsilon = 0.20$, CARNEA 15

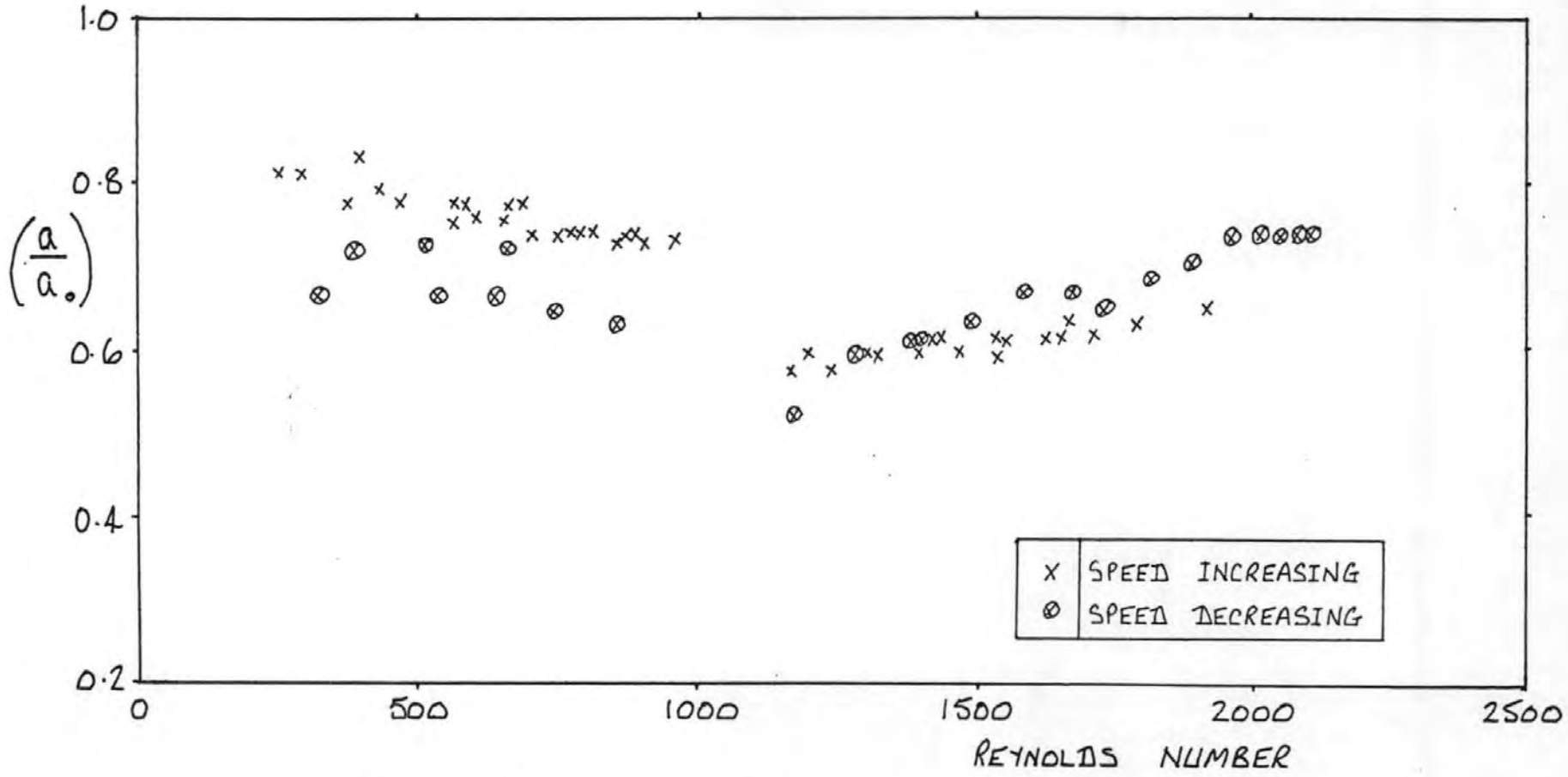

FIG. 65 $R_i/R_o = 0.874$, $\varepsilon = 0$, CARNEA 15

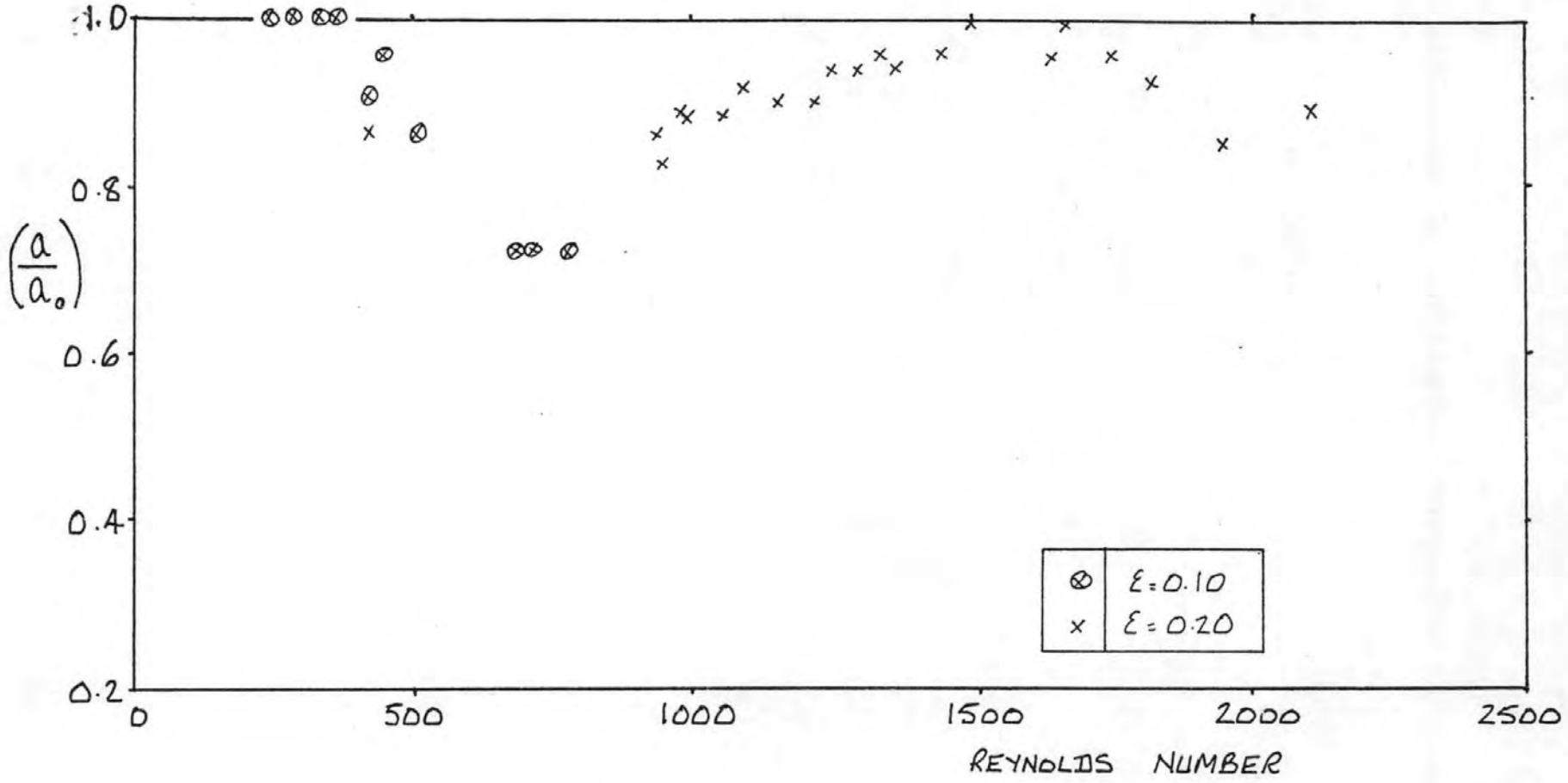

FIG. 66 $R_i/R_o = 0.874$; $\varepsilon = 0.10, 0.20$; CARNEA 15

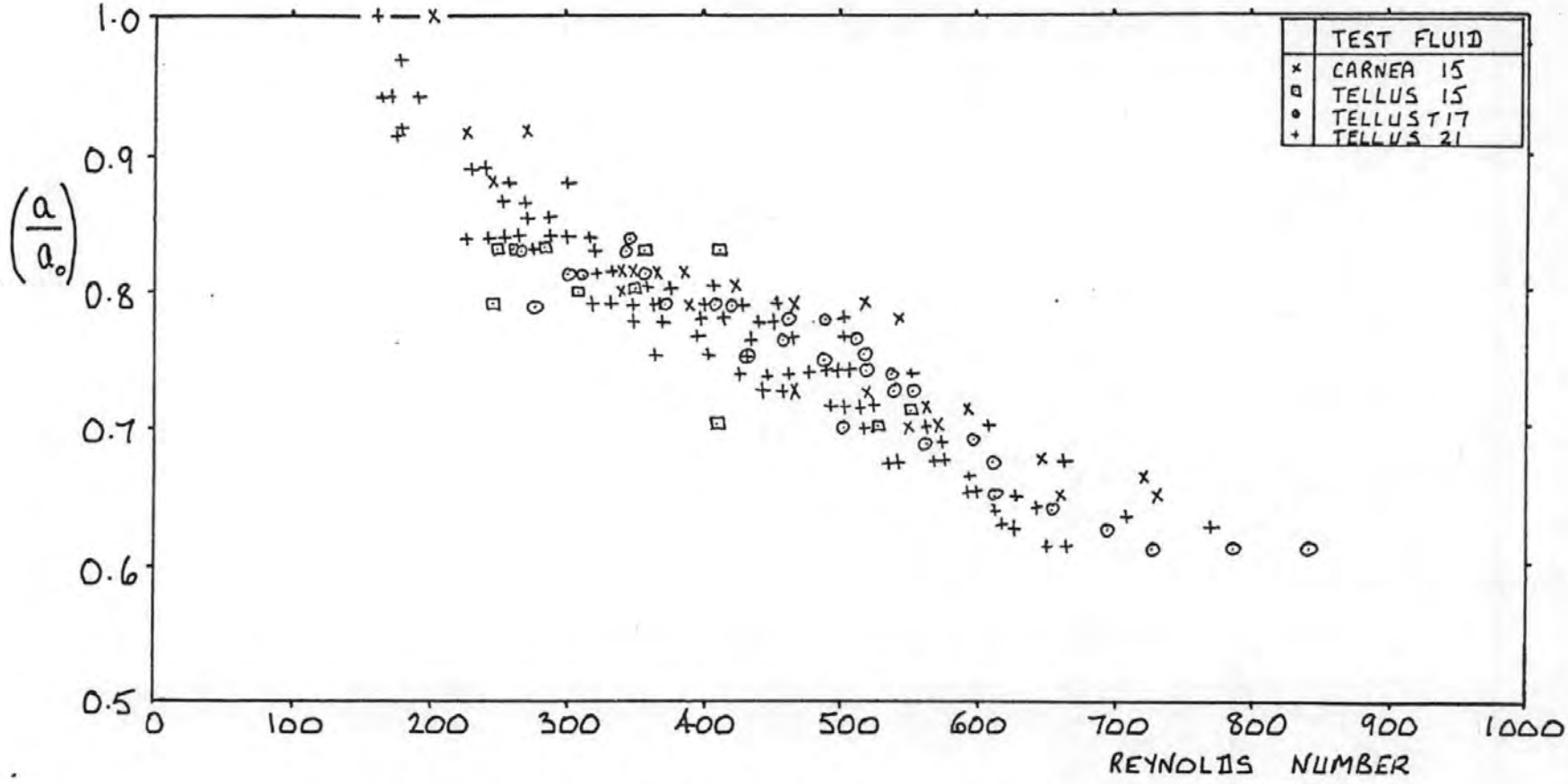

FIG. 67 $R_i/R_o = 0.911$, $\varepsilon = 0$, SPEED INCREASING

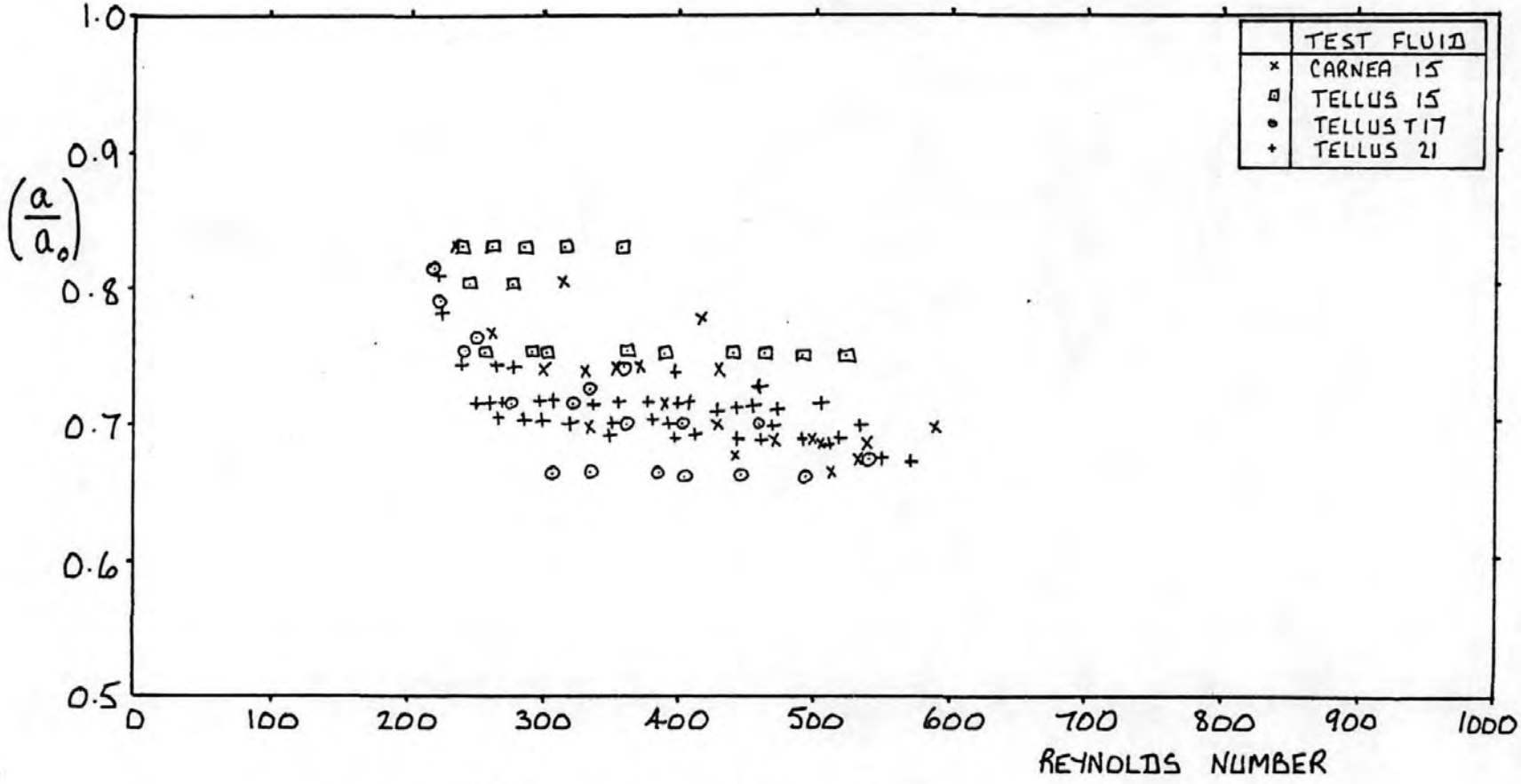

FIG. 68 $R_i/R_o = 0.911$, $\varepsilon = 0$, SPEED DECREASING.

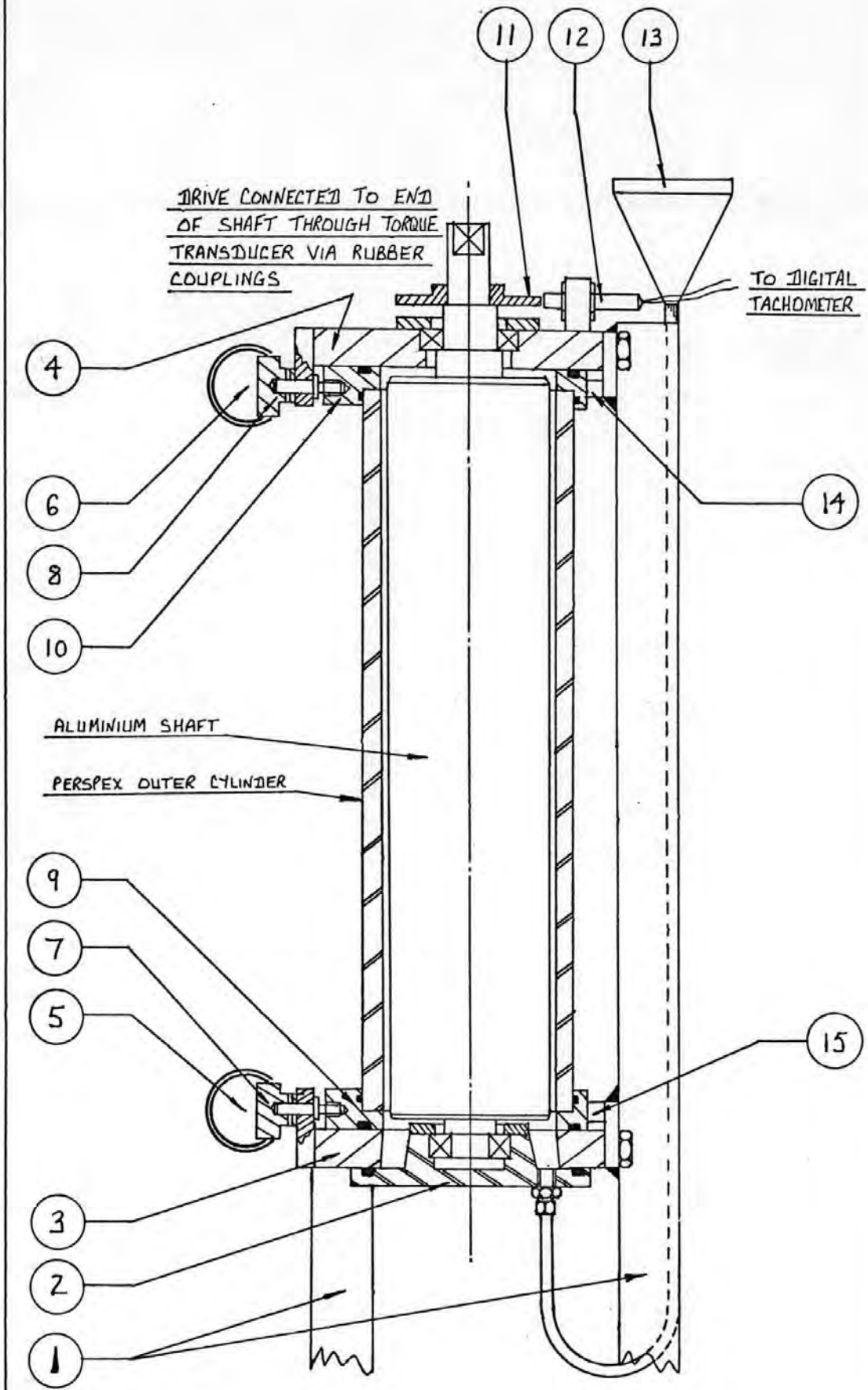

FIG.69 (a) GENERAL ARRANGEMENT OF THE TORQUE MEASUREMENT. TEST RIG.

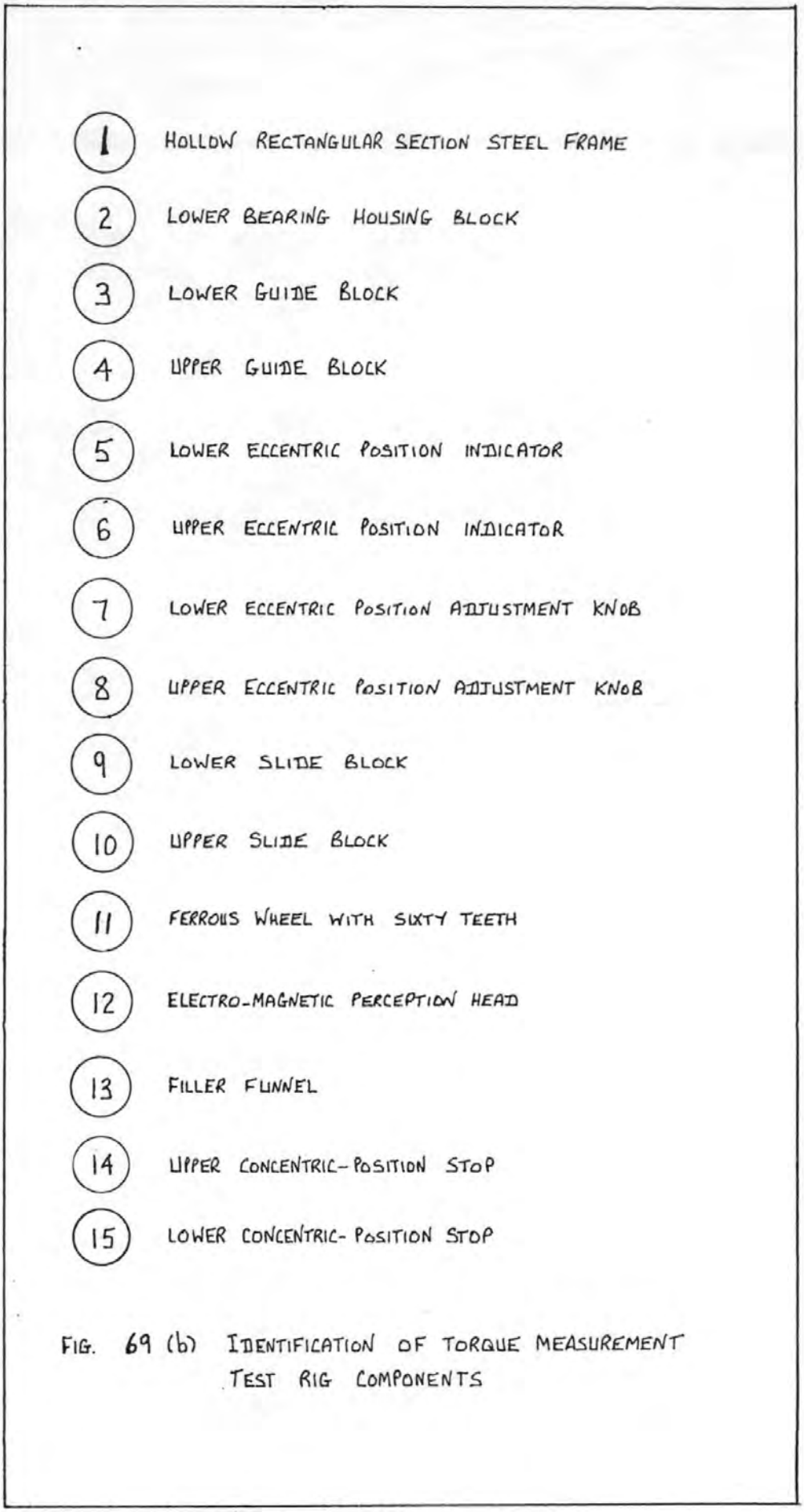

FIG. 69 (b) IDENTIFICATION OF TORQUE MEASUREMENT TEST RIG COMPONENTS

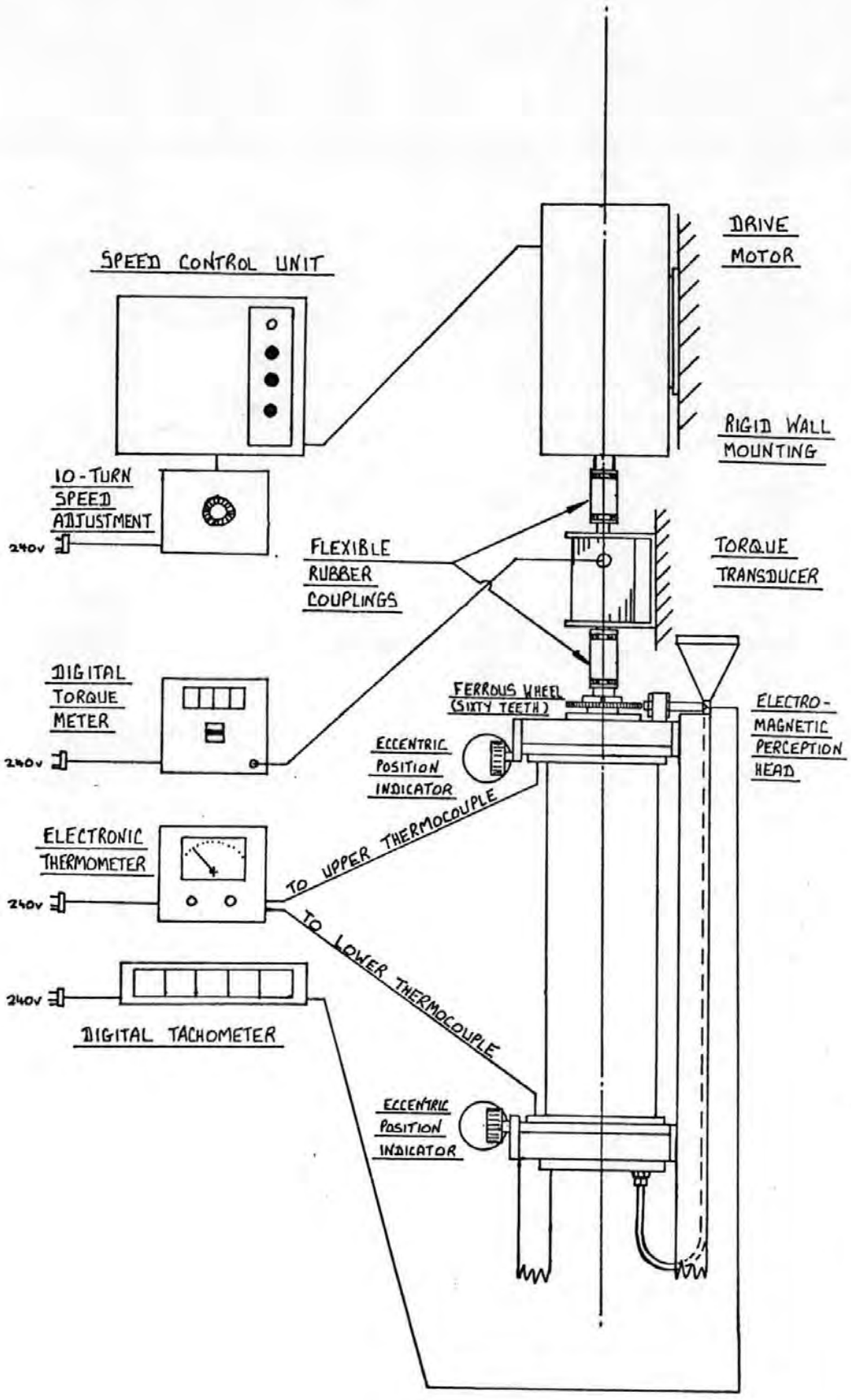

FIG. 70 INSTRUMENTATION OF THE TORQUE MEASUREMENT TEST RIG

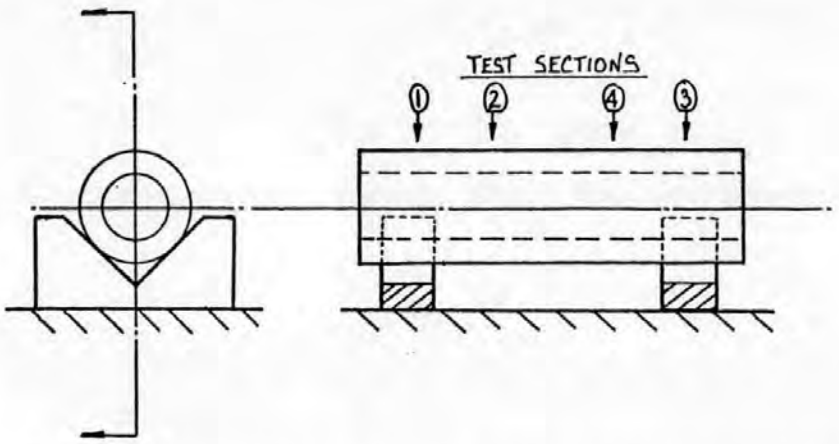

FIG. 71 ARRANGEMENT FOR THE PERSPEX CYLINDER CONCENTRICITY MEASUREMENTS.

[Plan views of test sections 1-4 showing dial gauge readings (m.m.) relative to that on surface of bore at back of test rig.]

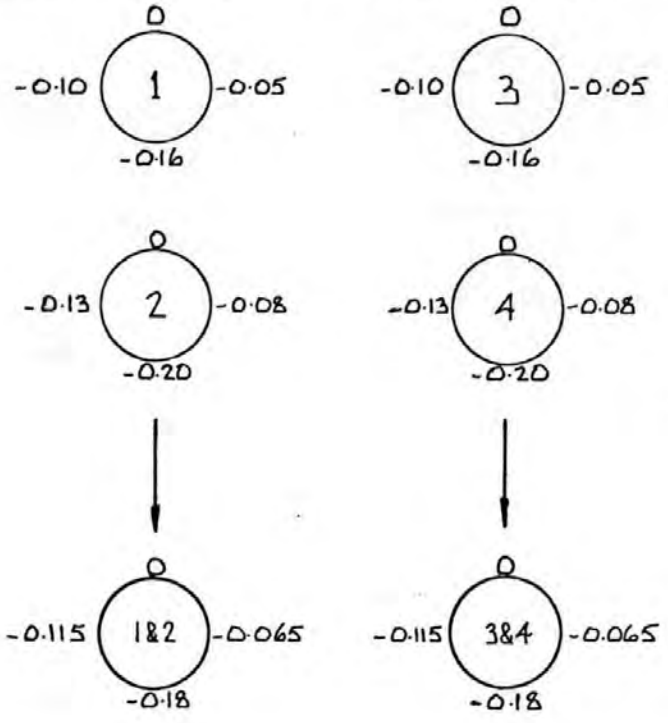

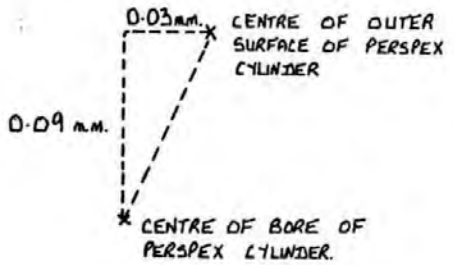

FIG. 72 DERIVATION OF THE POSITION OF THE CENTRE OF THE BORE OF THE PERSPEX CYLINDER RELATIVE TO THAT OF THE OUTSIDE SURFACE

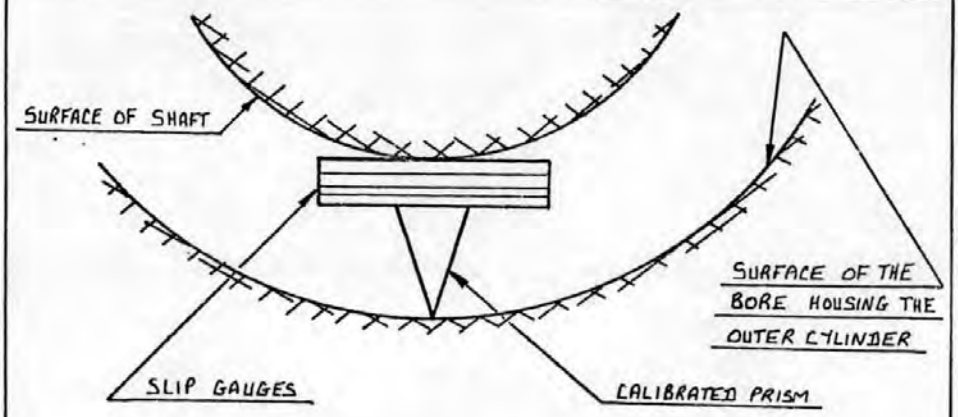

FIG. 73 MEASUREMENT OF THE CLEARANCE BETWEEN THE OUTER CYLINDER HOUSING AND THE SHAFT.

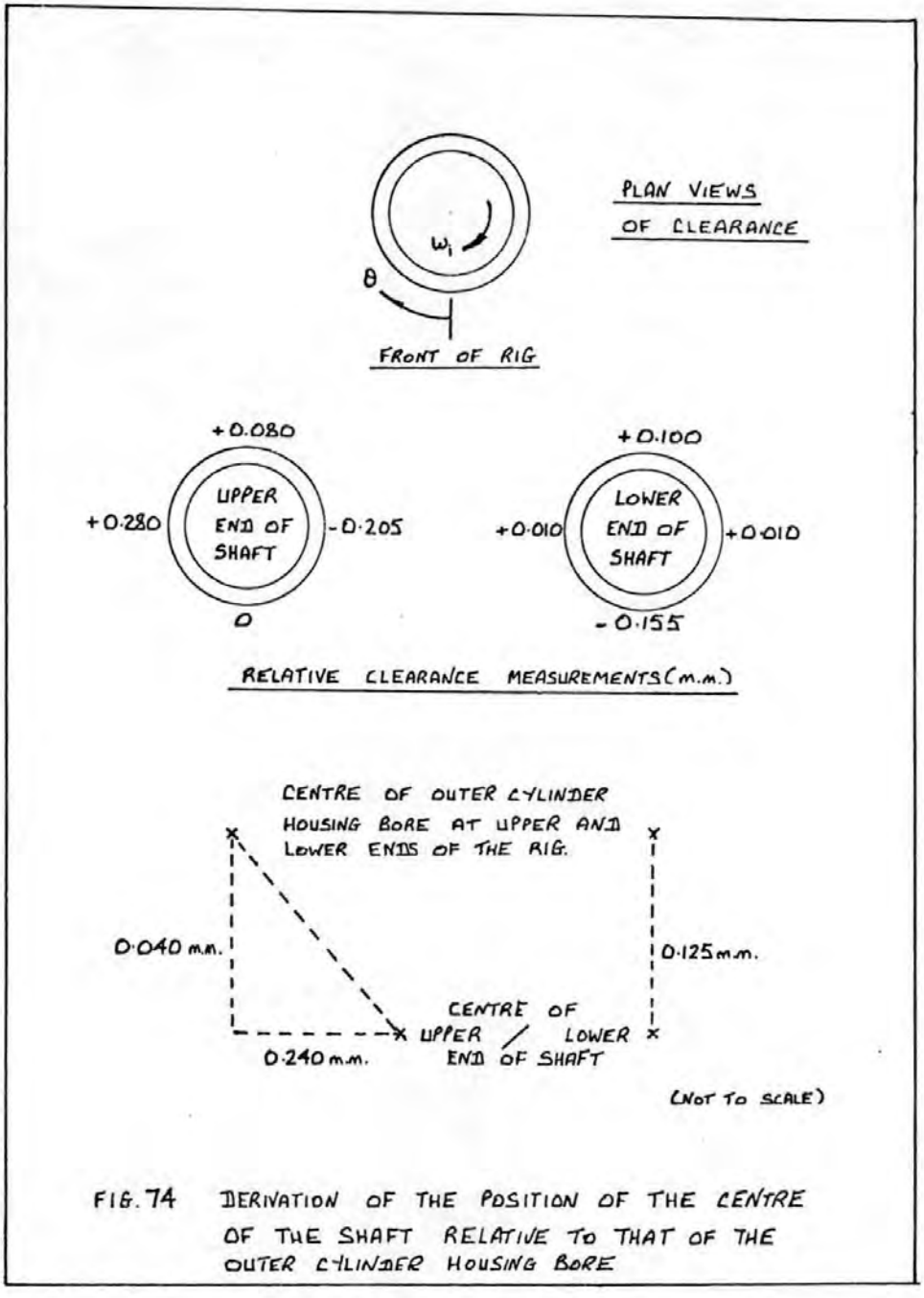

FIG. 74 DERIVATION OF THE POSITION OF THE CENTRE OF THE SHAFT RELATIVE TO THAT OF THE OUTER CYLINDER HOUSING BORE

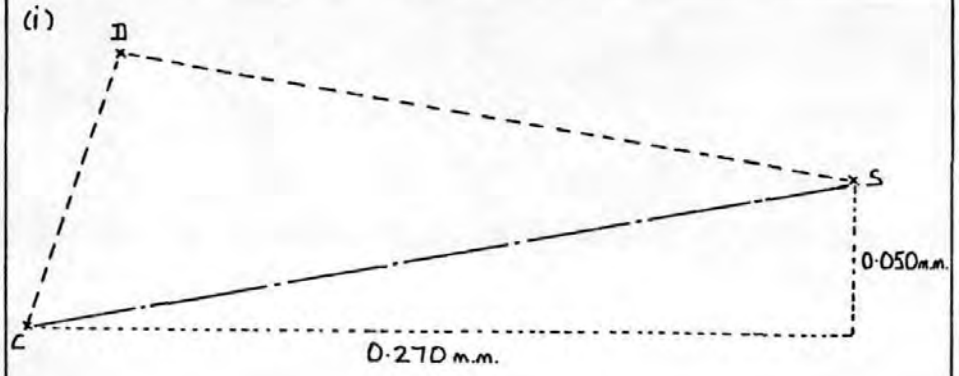

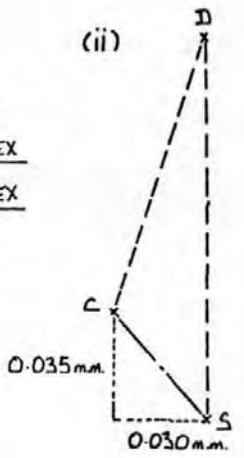

RELATIVE POSITIONS OF THE CENTRES OF THE OUTSIDE SURFACE OF THE PERSPEX CYLINDER (D), THE BORE OF THE PERSPEX CYLINDER (C) AND THE SHAFT (S) AT

(i) THE UPPER END OF THE TEST RIG

(ii) THE LOWER END OF THE TEST RIG

(iii) THE MIDDLE OF THE TEST LENGTH

PLAN VIEWS SCALE 1cm. = 0·025m.m.

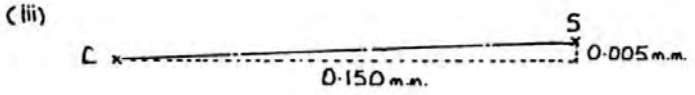

From (iii)

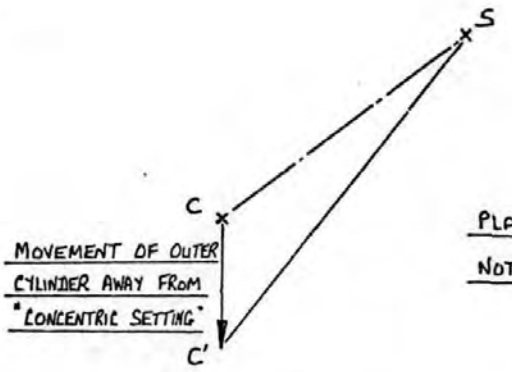

PLAN VIEW

NOT TO SCALE

FRONT OF RIG

$$SC' = e = \left[(0.005 + CC')^2 + (0.150)^2\right]^{1/2}$$

$$\varepsilon = e / (R_o - R_i)$$

FIG. 75 DERIVATION OF THE MEAN ECCENTRICITY RATIO FROM THE RECORDED MOVEMENT OF THE OUTER CYLINDER.

NOT TO SCALE

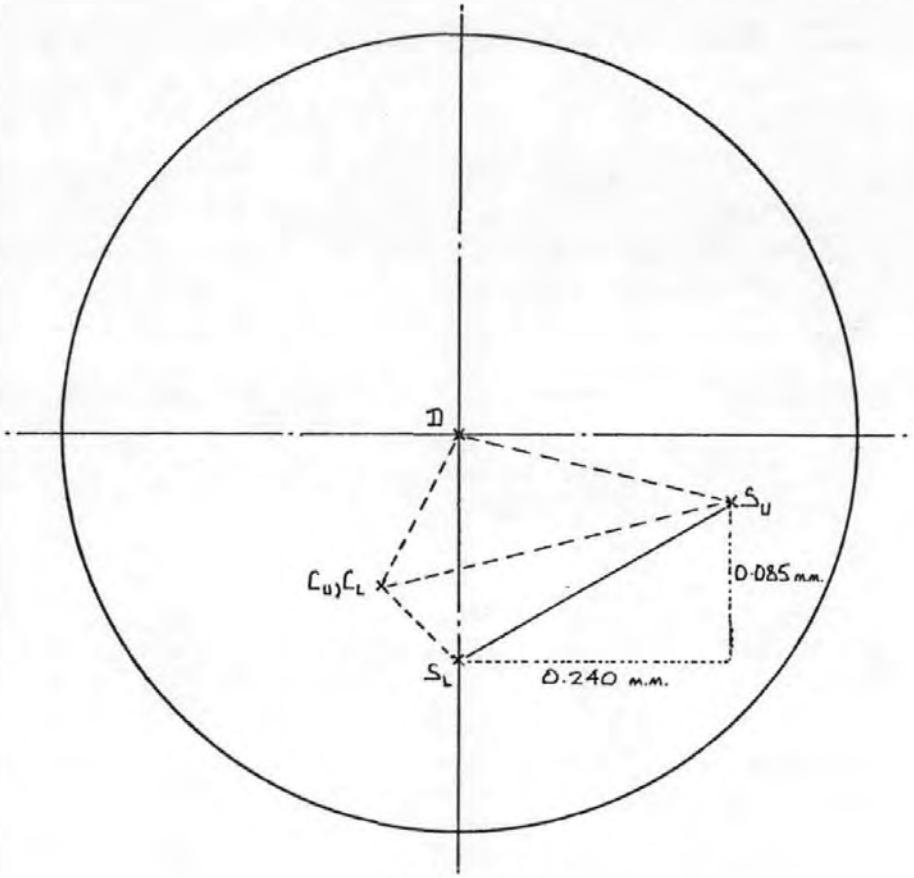

(The symbols U and L denote the upper and lower end of the test rig respectively)

$$\% \text{ MISALIGNMENT} = \frac{(S_L S_U) \times 100}{(R_o - R_i)}$$

FIG. 76 SCHEMATIC PLAN VIEW OF TEST RIG SHOWING MISALIGNMENT BETWEEN THE AXES OF THE OUTER CYLINDER BORE AND THE SHAFT

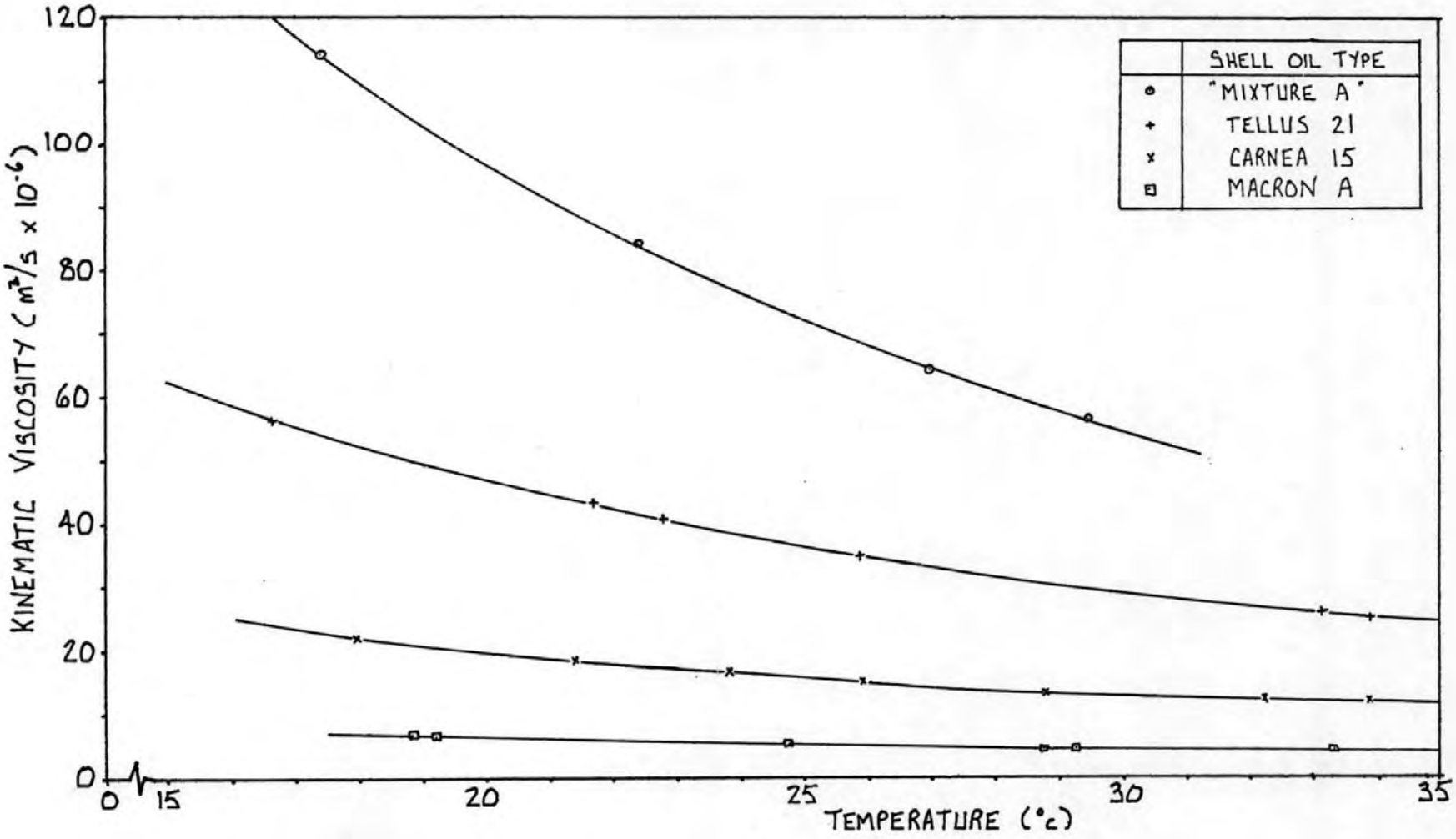

FIG. 77 VISCOSITY CHARACTERISTICS FOR THE TEST FLUIDS

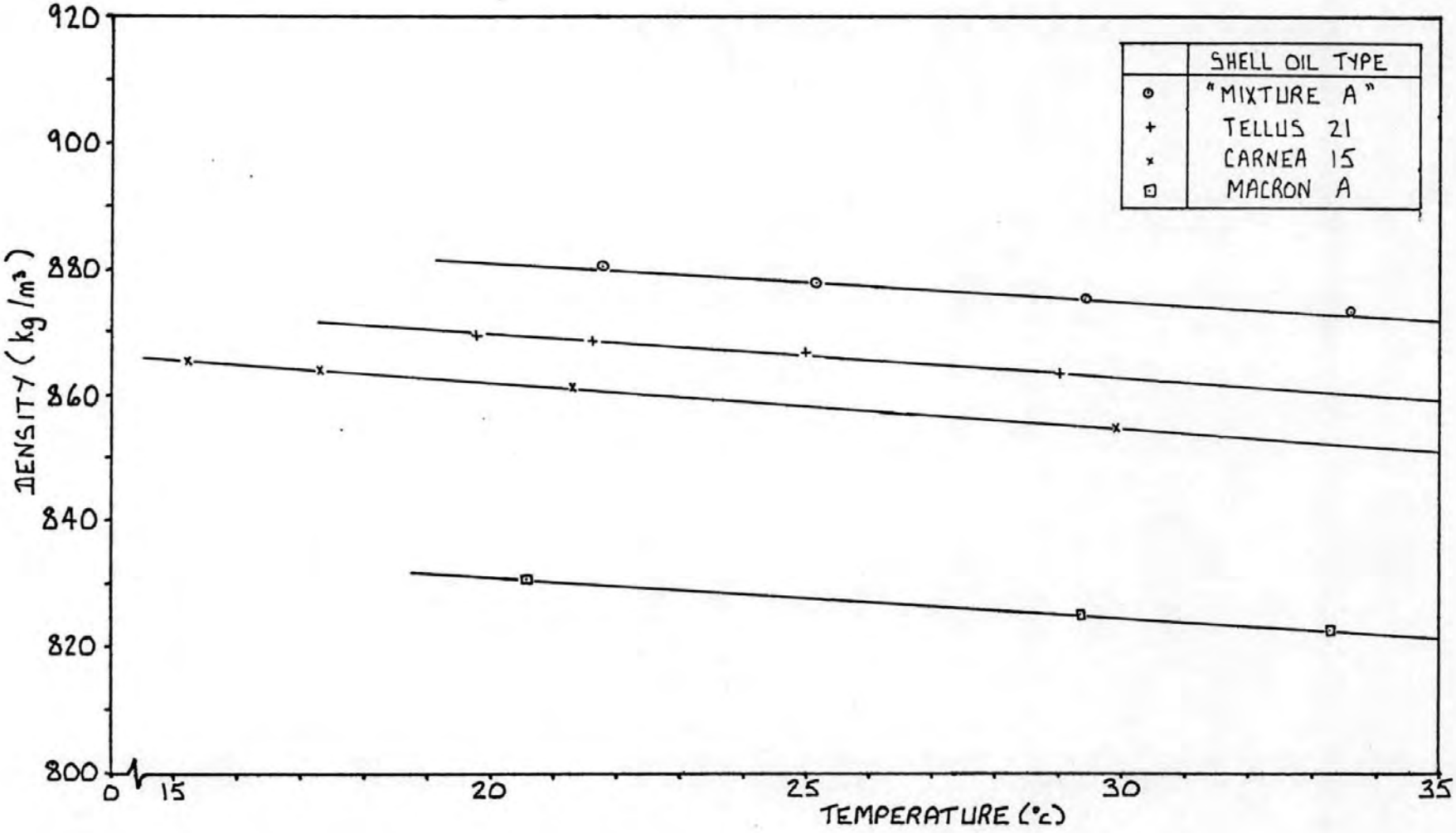

FIG. 78 DENSITY CHARACTERISTICS FOR THE TEST FLUIDS

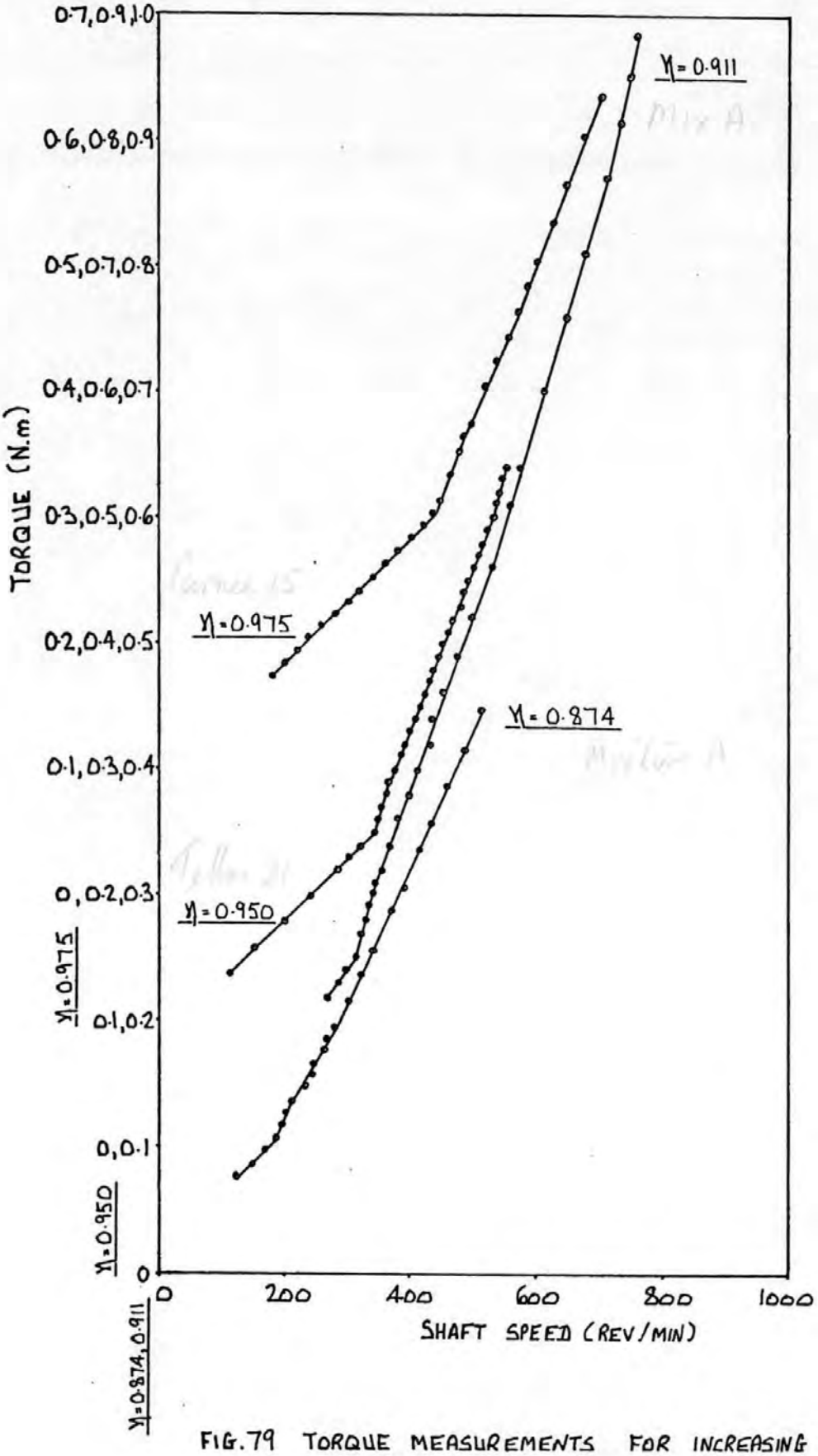

FIG. 79 TORQUE MEASUREMENTS FOR INCREASING SHAFT SPEED FROM SIMPLE LAMINAR FLOW INTO WAVY VORTEX REGIME USING THE CONCENTRIC CYLINDERS SETTING

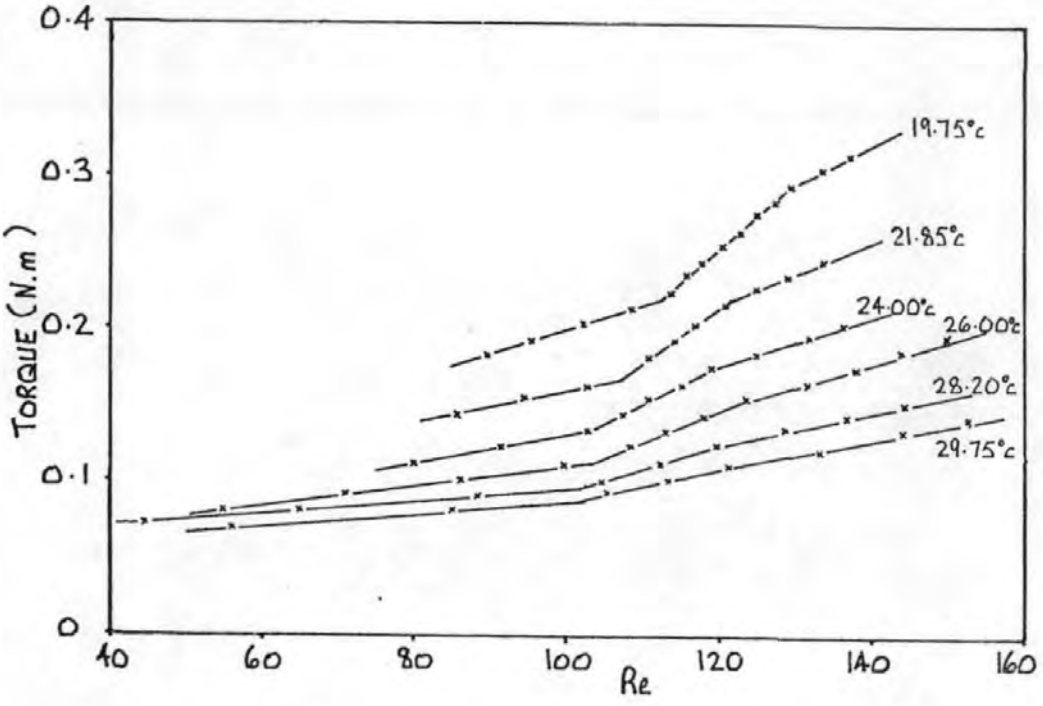

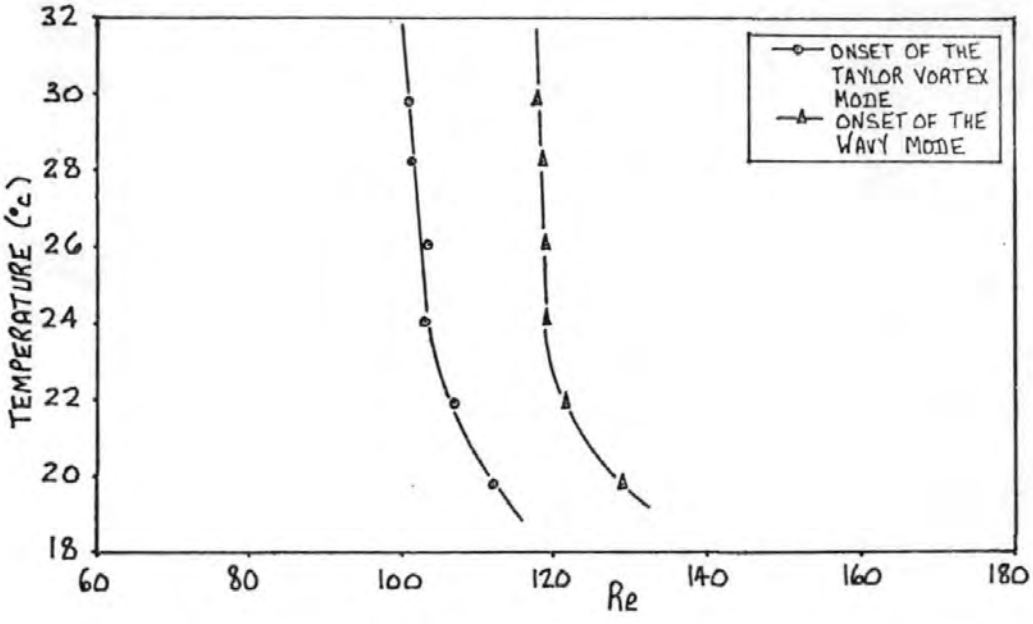

FIG. 80 THE EFFECT OF TEMPERATURE ON THE ONSET OF INSTABILITY FOR THE CONCENTRIC CYLINDERS SETTING: $R_i/R_o = 0.874$, "MIXTURE A"

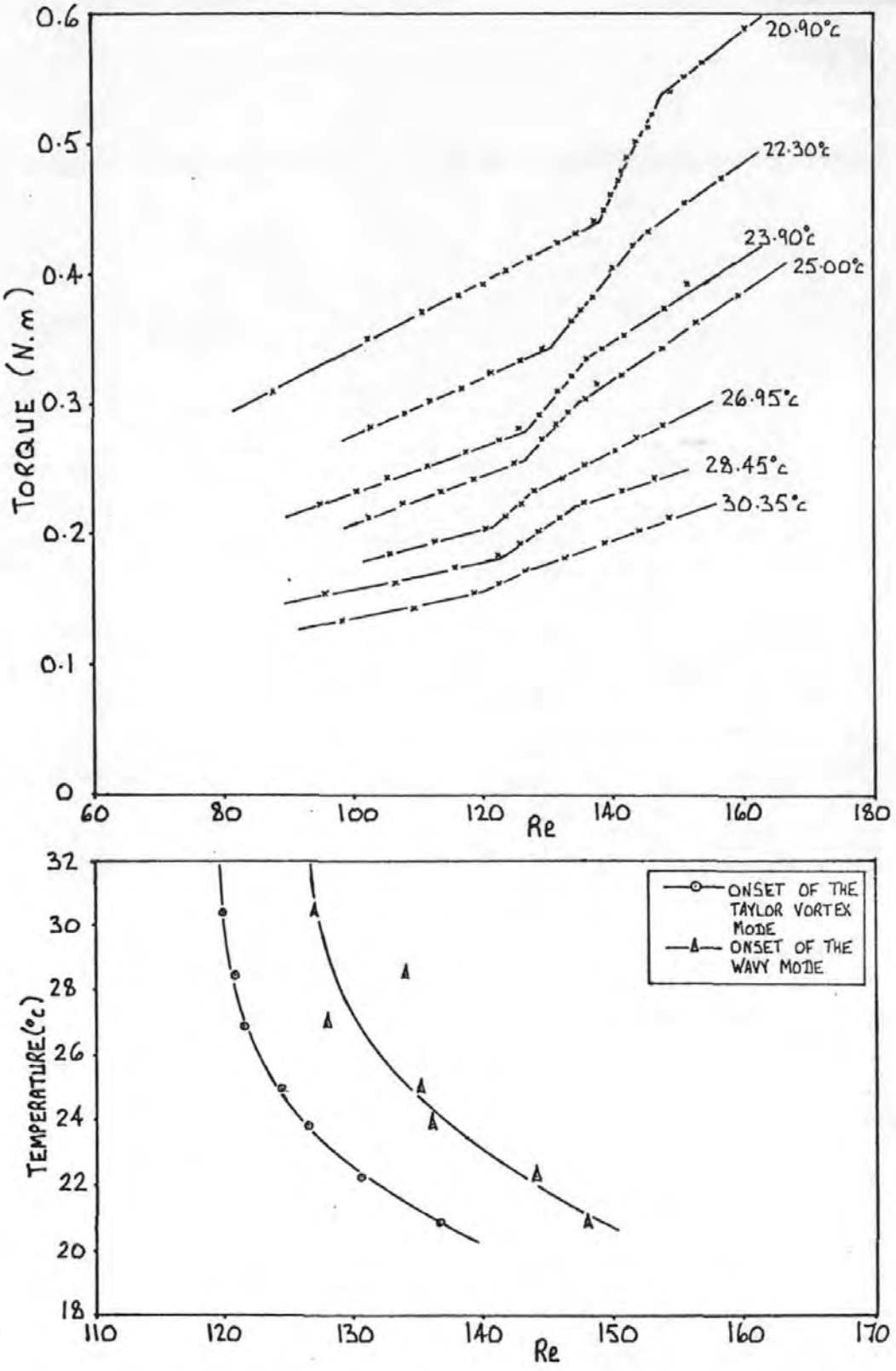

FIG. 81 THE EFFECT OF TEMPERATURE ON THE ONSET OF INSTABILITY FOR THE CONCENTRIC CYLINDERS SETTING: $R_i/R_o = 0.911$, "MIXTURE A"

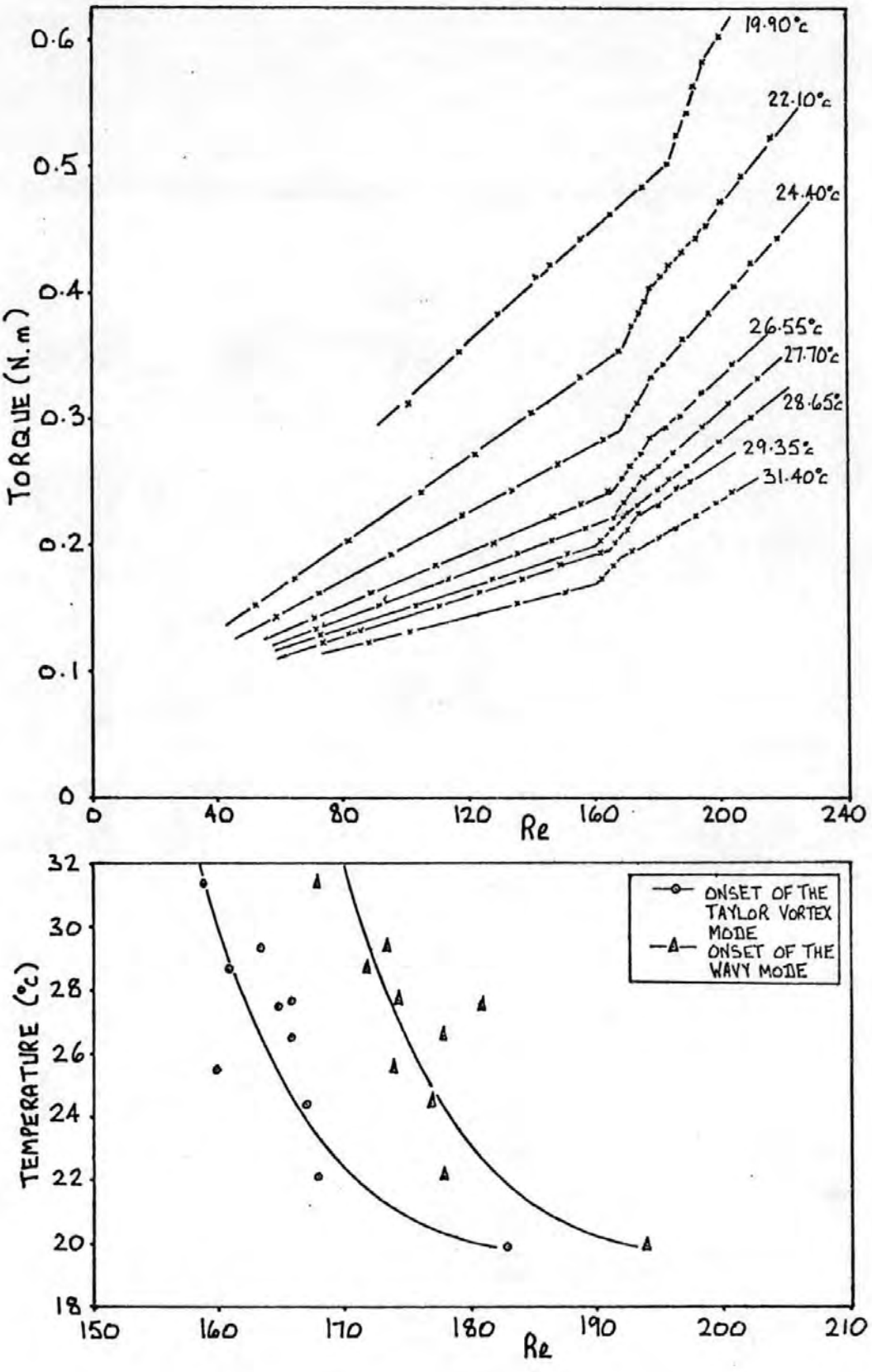

FIG. 82 THE EFFECT OF TEMPERATURE ON THE ONSET OF INSTABILITY FOR THE CONCENTRIC CYLINDERS SETTING: $R_i/R_o = 0.950$, TELLUS 21

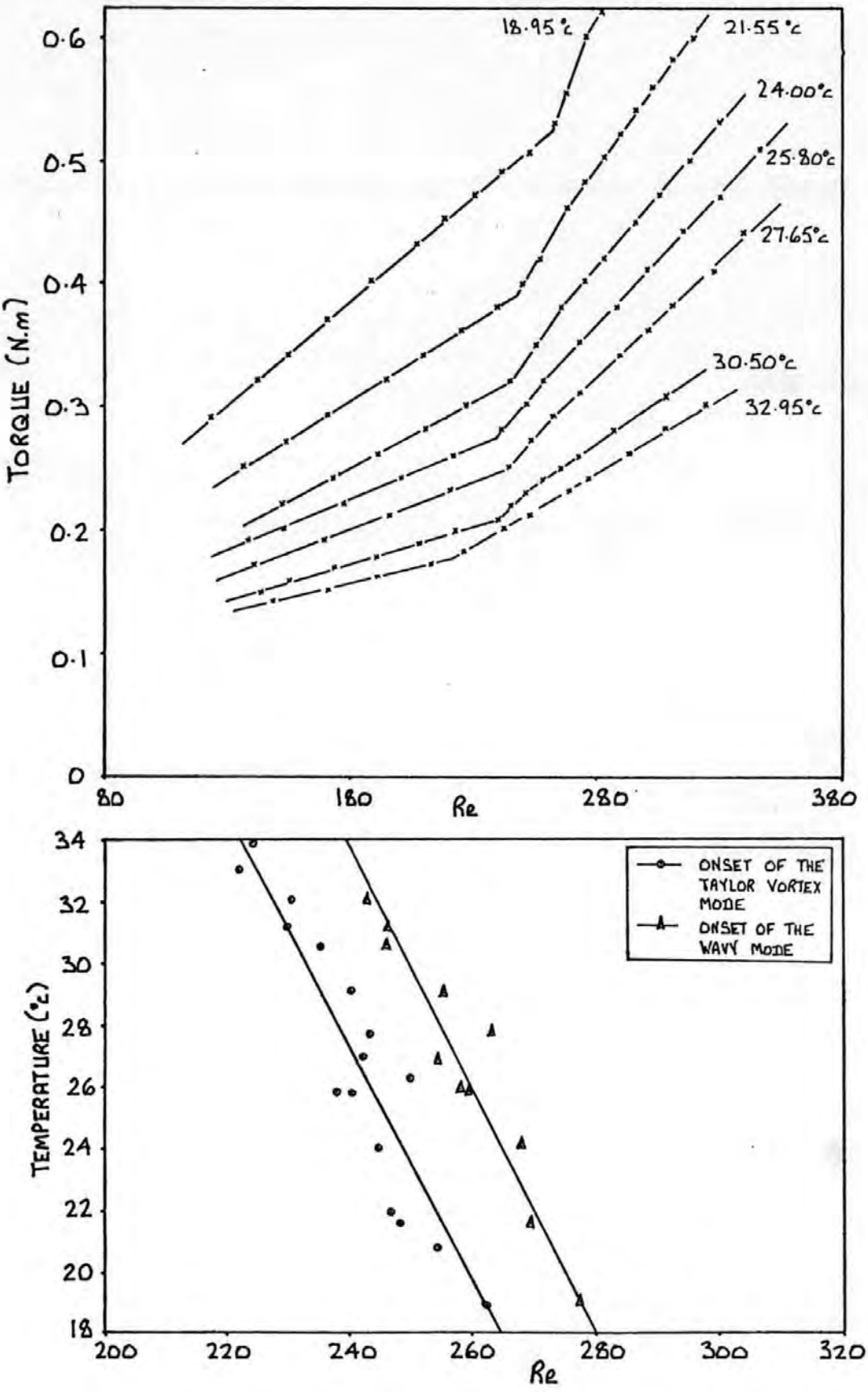

FIG. 83 THE EFFECT OF TEMPERATURE ON THE ONSET OF INSTABILITY FOR THE CONCENTRIC CYLINDERS SETTING: $R_i/R_o = 0.975$, CARNEA 15

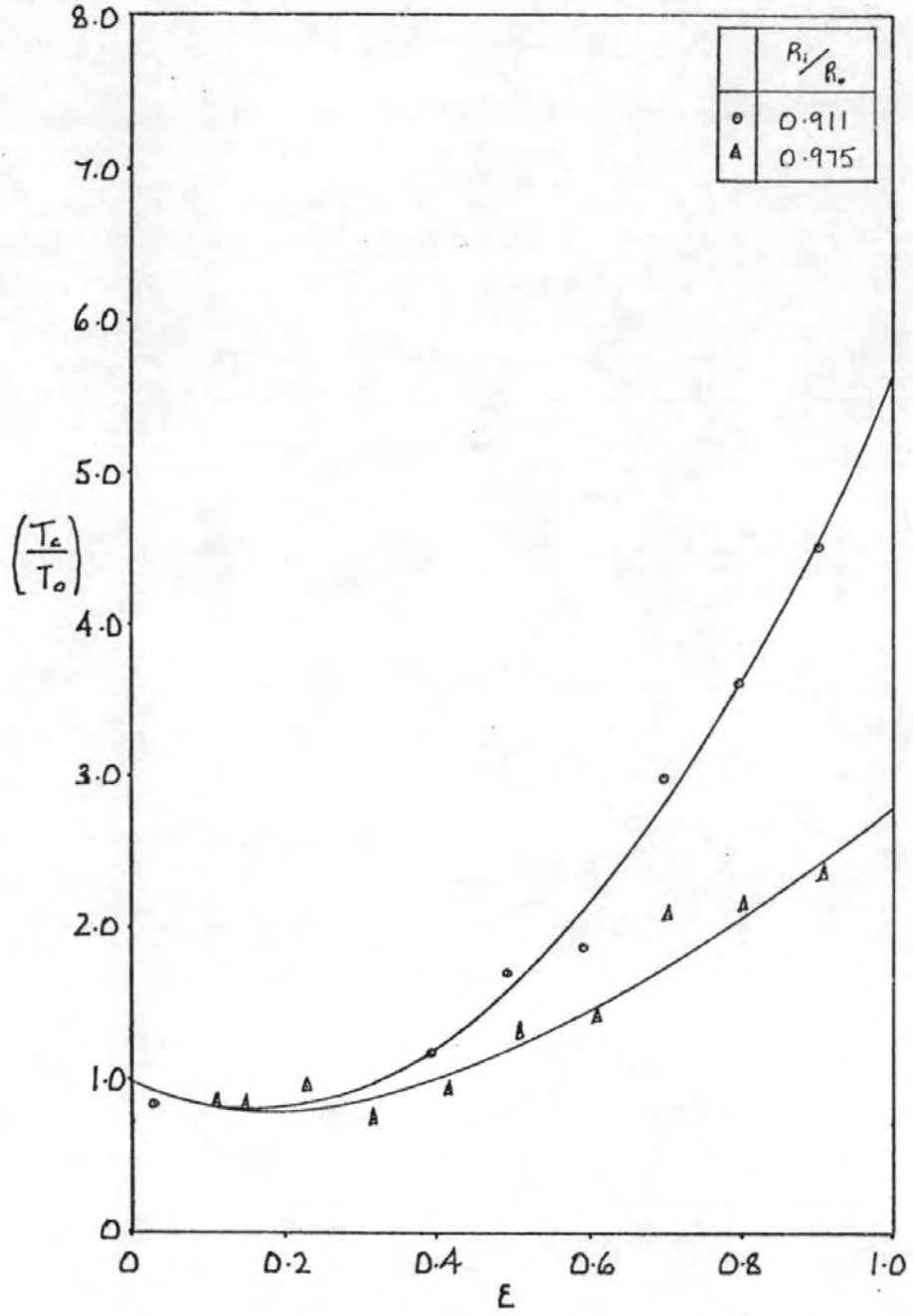

FIG. 84 VARIATION OF THE CRITICAL TAYLOR NUMBER WITH ECCENTRICITY RATIO FROM TORQUE MEASUREMENT RESULTS

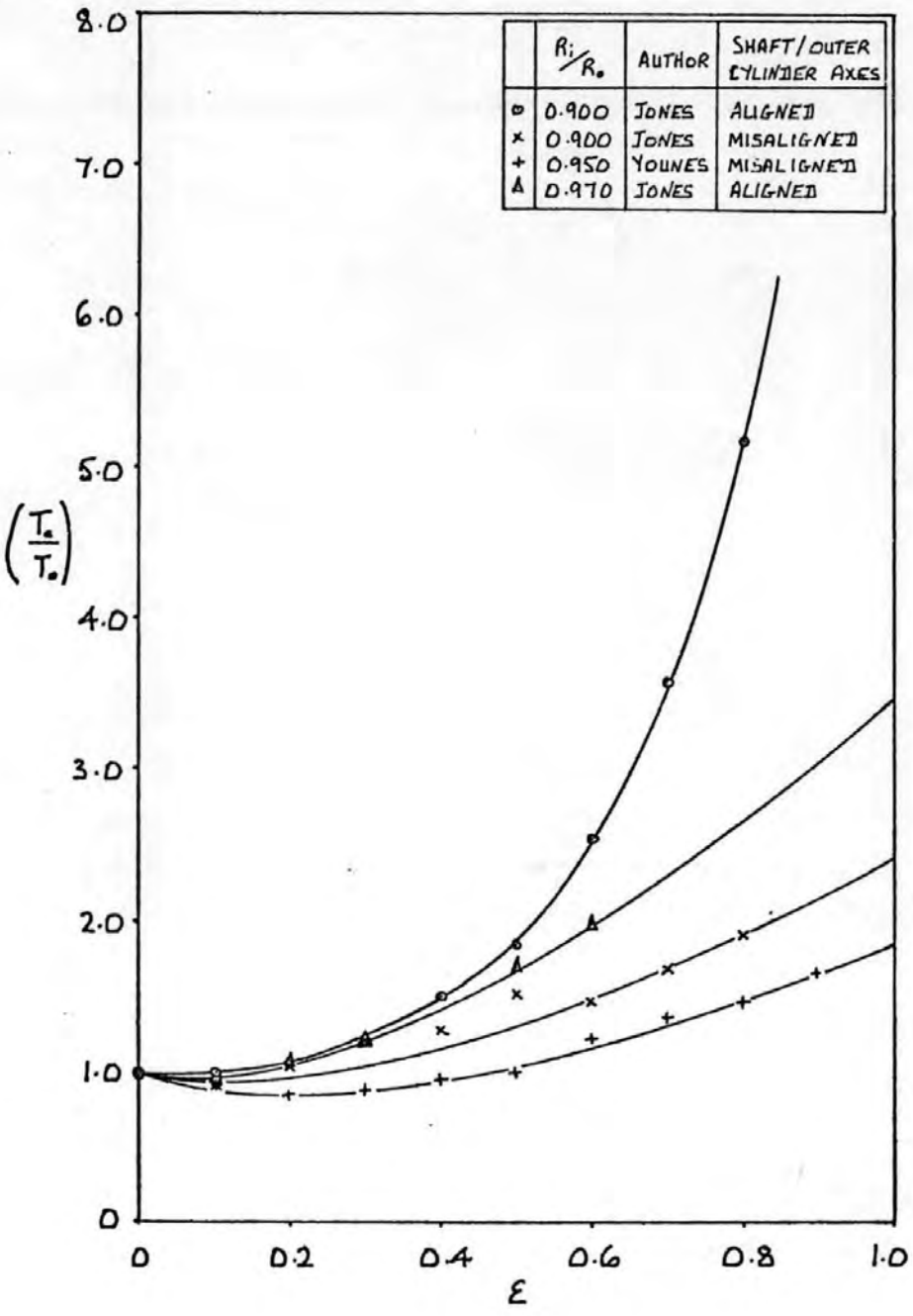

FIG. 85 VARIATION OF THE CRITICAL TAYLOR NUMBER WITH ECCENTRICITY RATIO FROM THE TORQUE MEASUREMENT RESULTS OF PREVIOUS AUTHORS

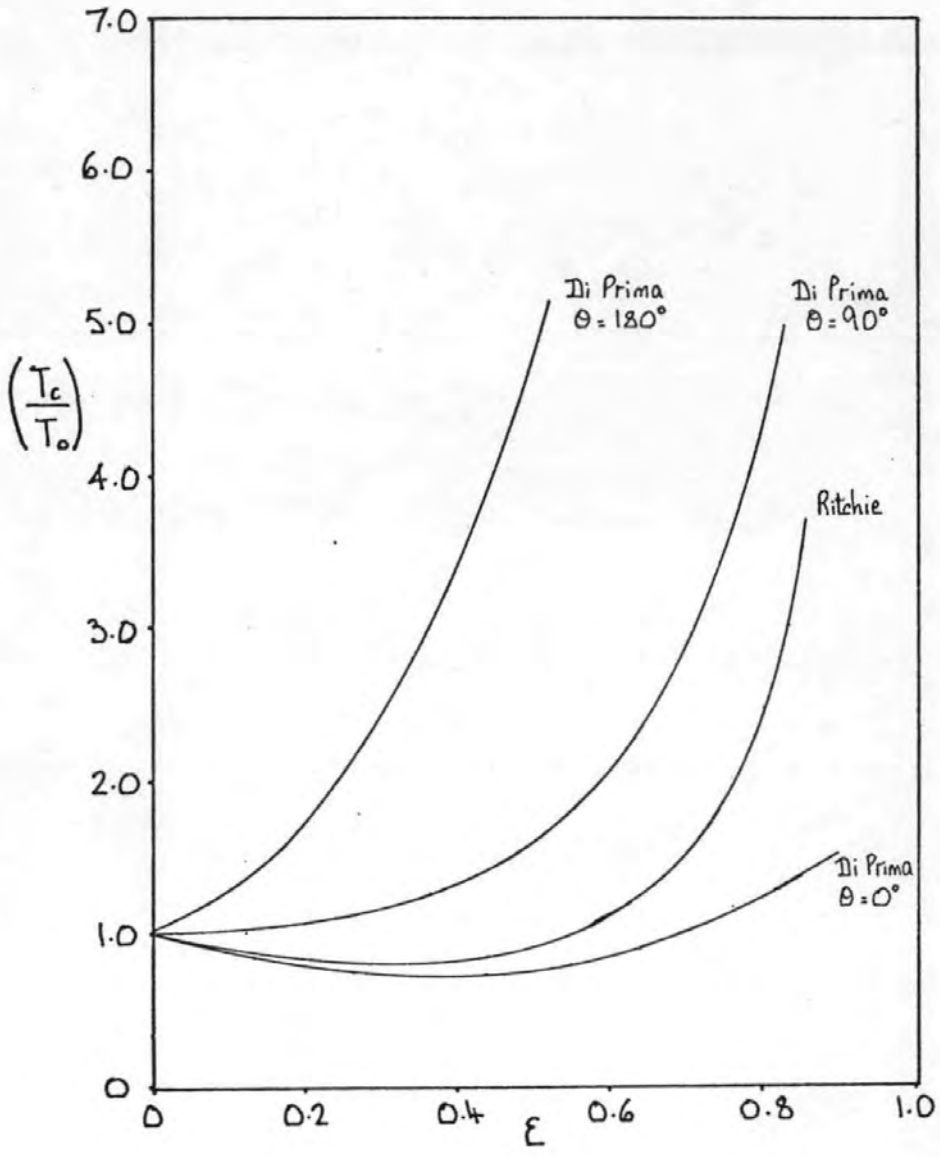

FIG. 86 THEORETICAL PREDICTIONS OF THE VARIATION OF THE CRITICAL TAYLOR NUMBER WITH ECCENTRICITY RATIO

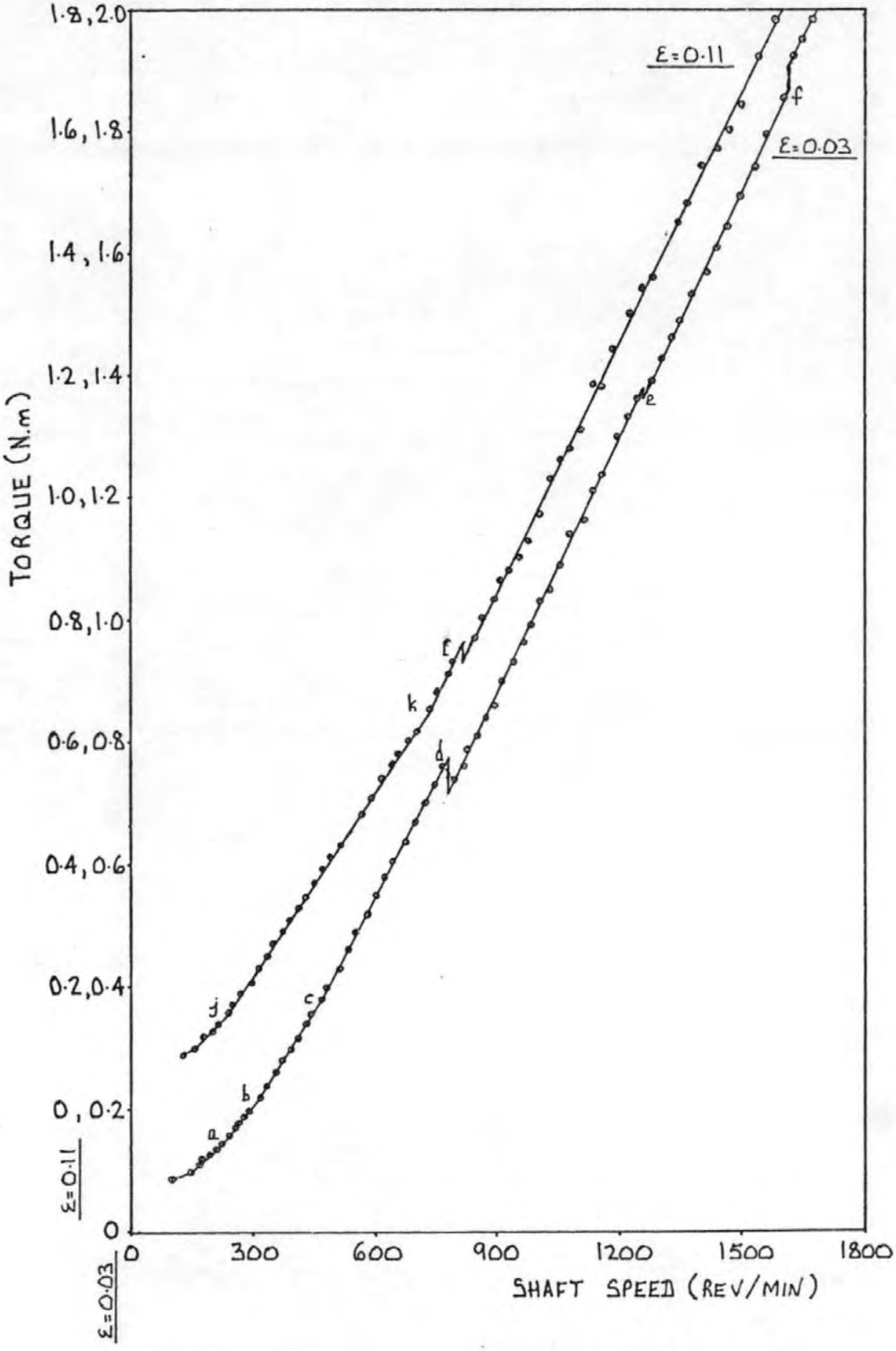

FIG. 87 TORQUE MEASUREMENTS FOR INCREASING SHAFT SPEED: $R_i/R_o = 0.911$, TELLUS 21

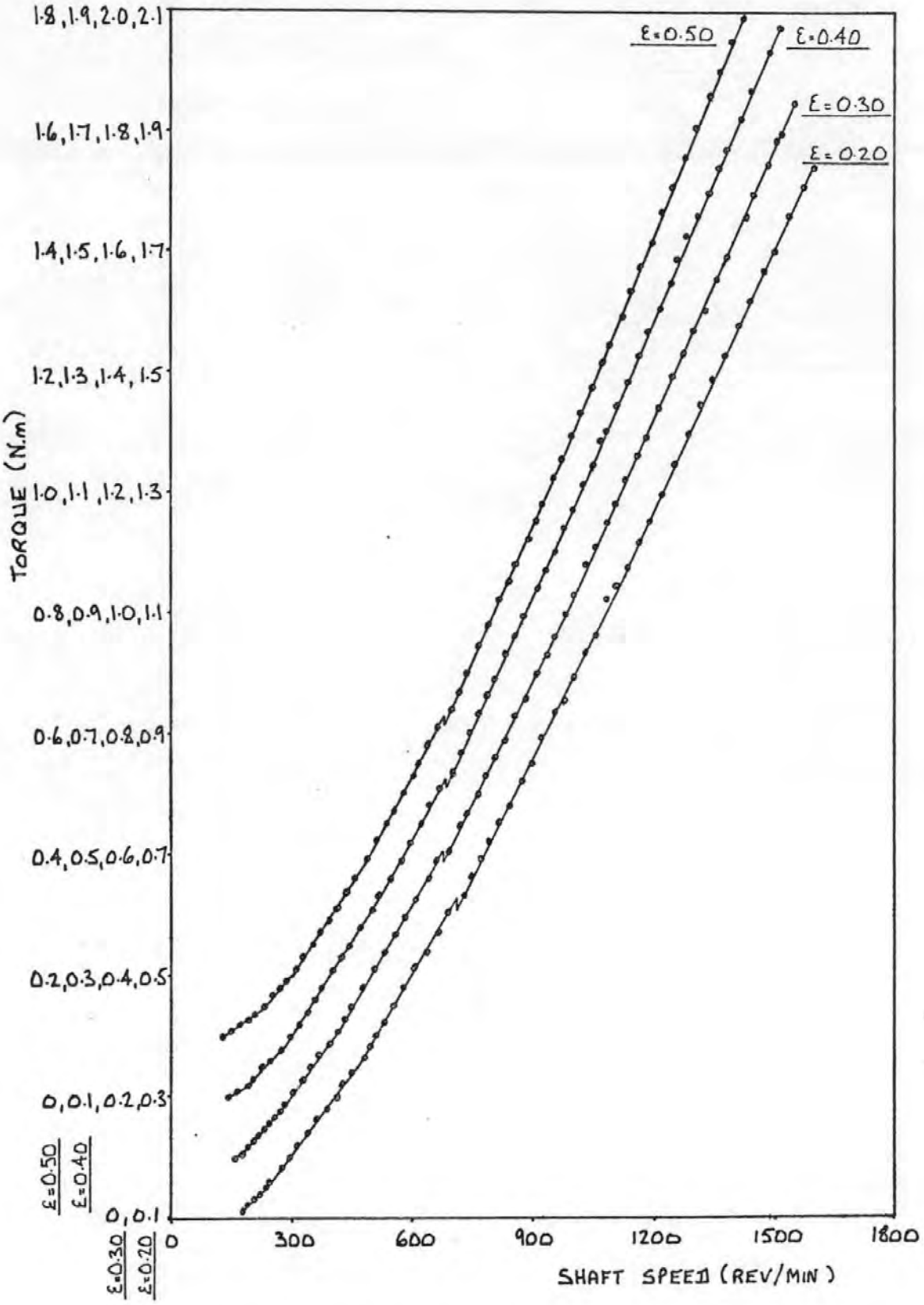

FIG. 88 TORQUE MEASUREMENTS FOR INCREASING SHAFT SPEED: $R_i/R_o = 0.911$, TELLUS 21

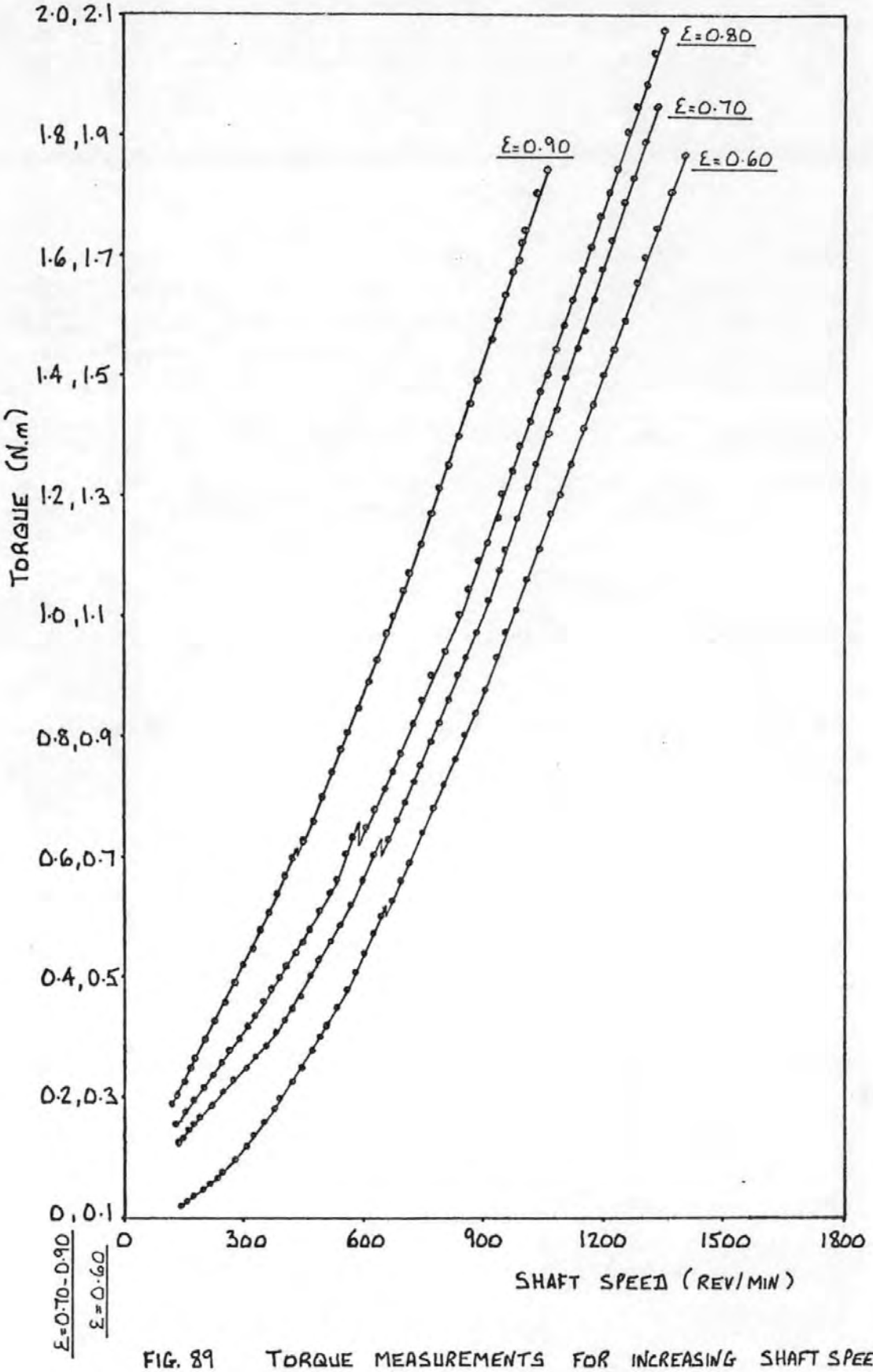

FIG. 89 TORQUE MEASUREMENTS FOR INCREASING SHAFT SPEED: $R_i/R_o = 0.911$, TELLUS 21

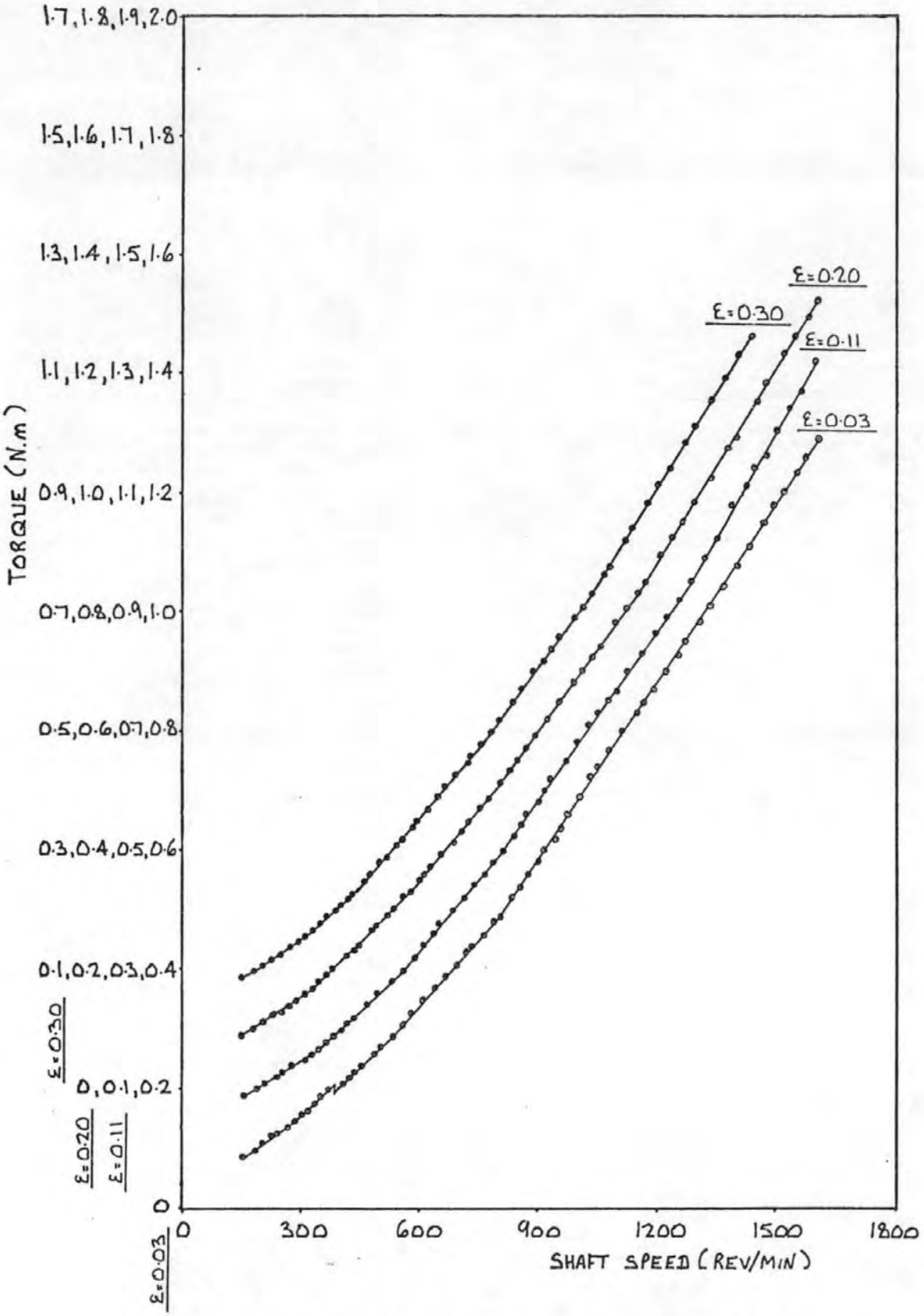

FIG. 90 TORQUE MEASUREMENTS FOR INCREASING SHAFT SPEED: $R_i/R_o = 0.911$, CARNEA 15

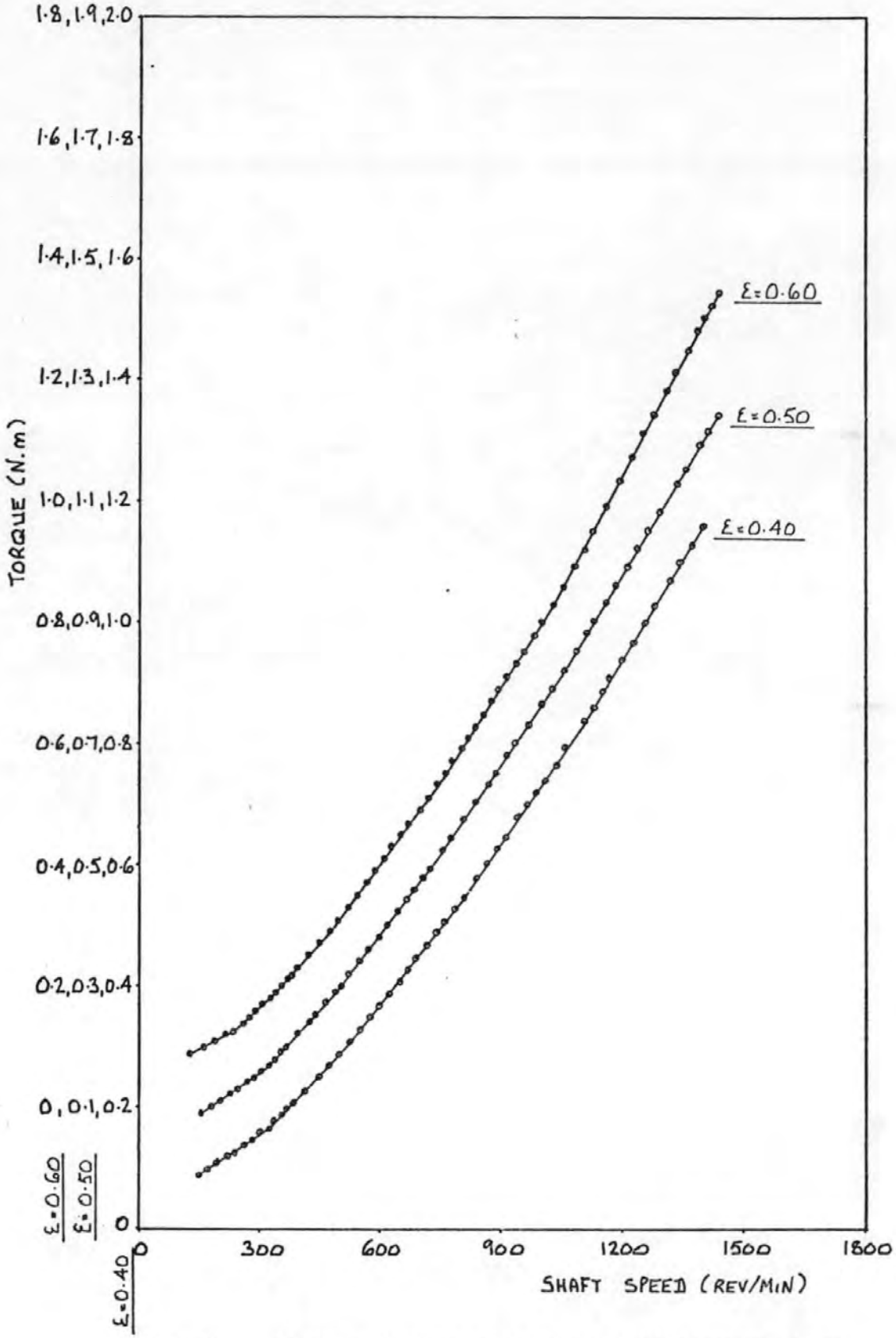

FIG. 91 TORQUE MEASUREMENTS FOR INCREASING SHAFT SPEED: $R_i/R_o = 0.911$, CARNEA 15

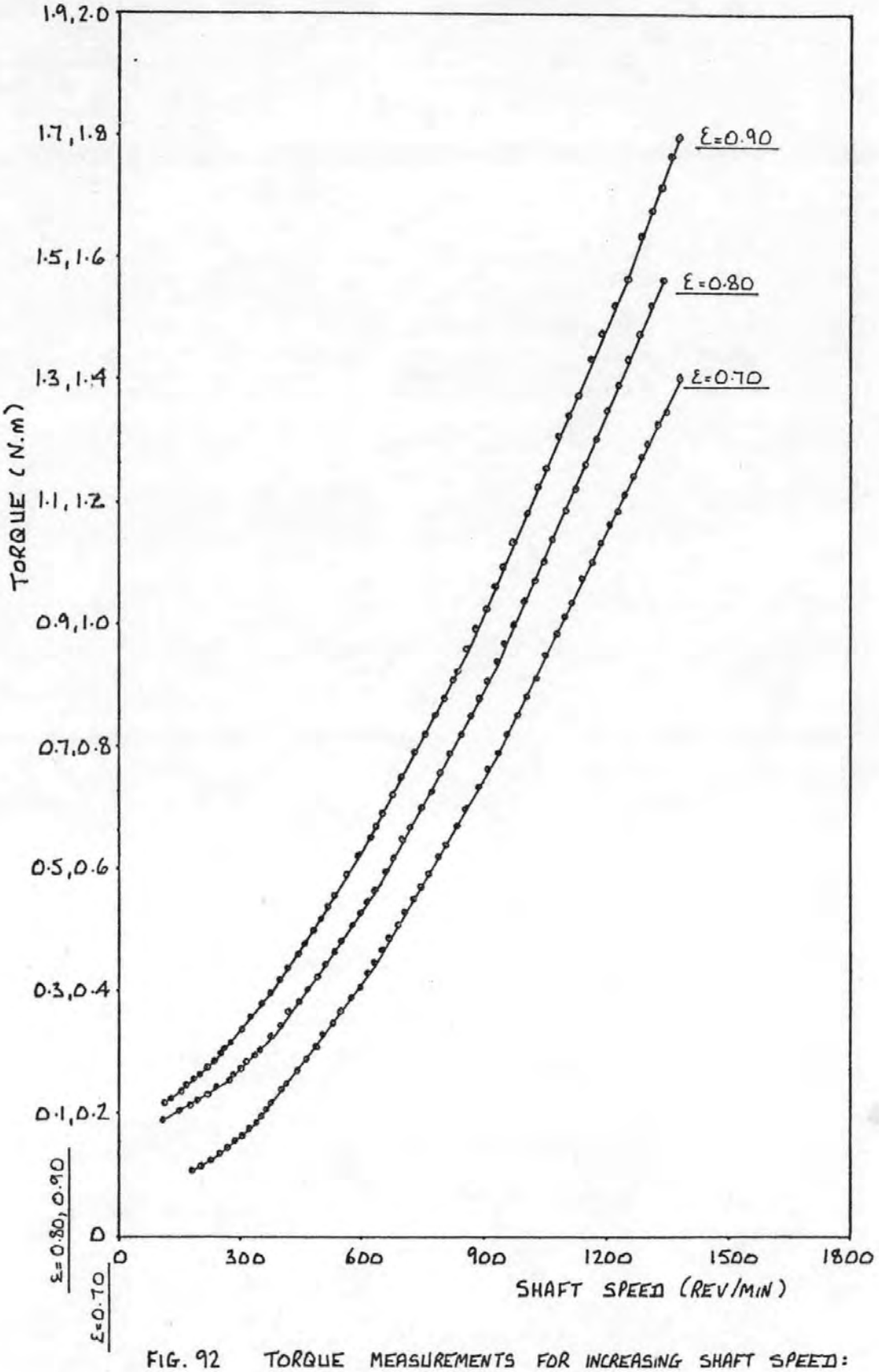

FIG. 92 TORQUE MEASUREMENTS FOR INCREASING SHAFT SPEED: $R_i/R_o = 0.911$, CARNEA 15

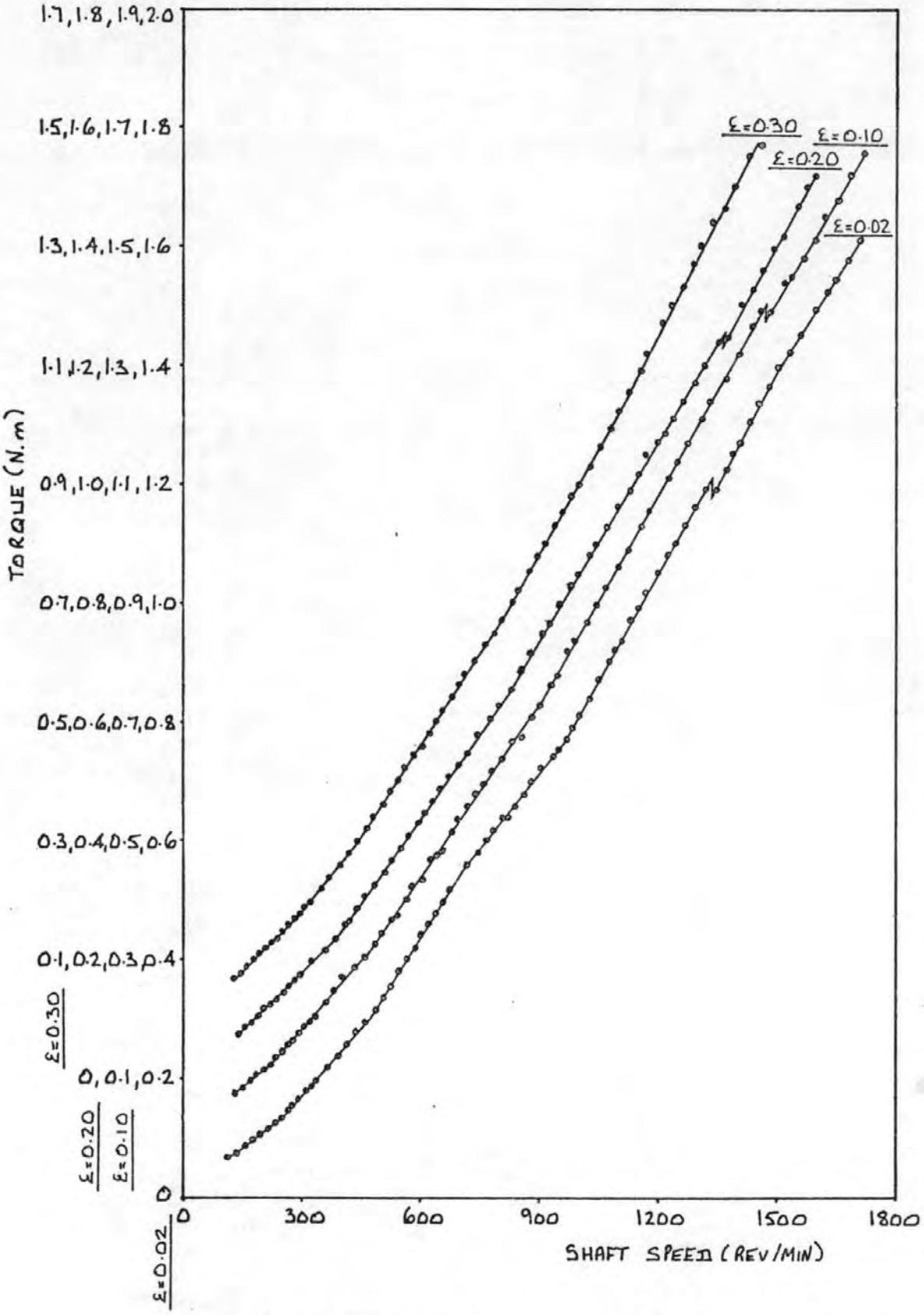

FIG. 93 TORQUE MEASUREMENTS FOR INCREASING SHAFT SPEED:
$R_i/R_o = 0.874$, TELLUS 21

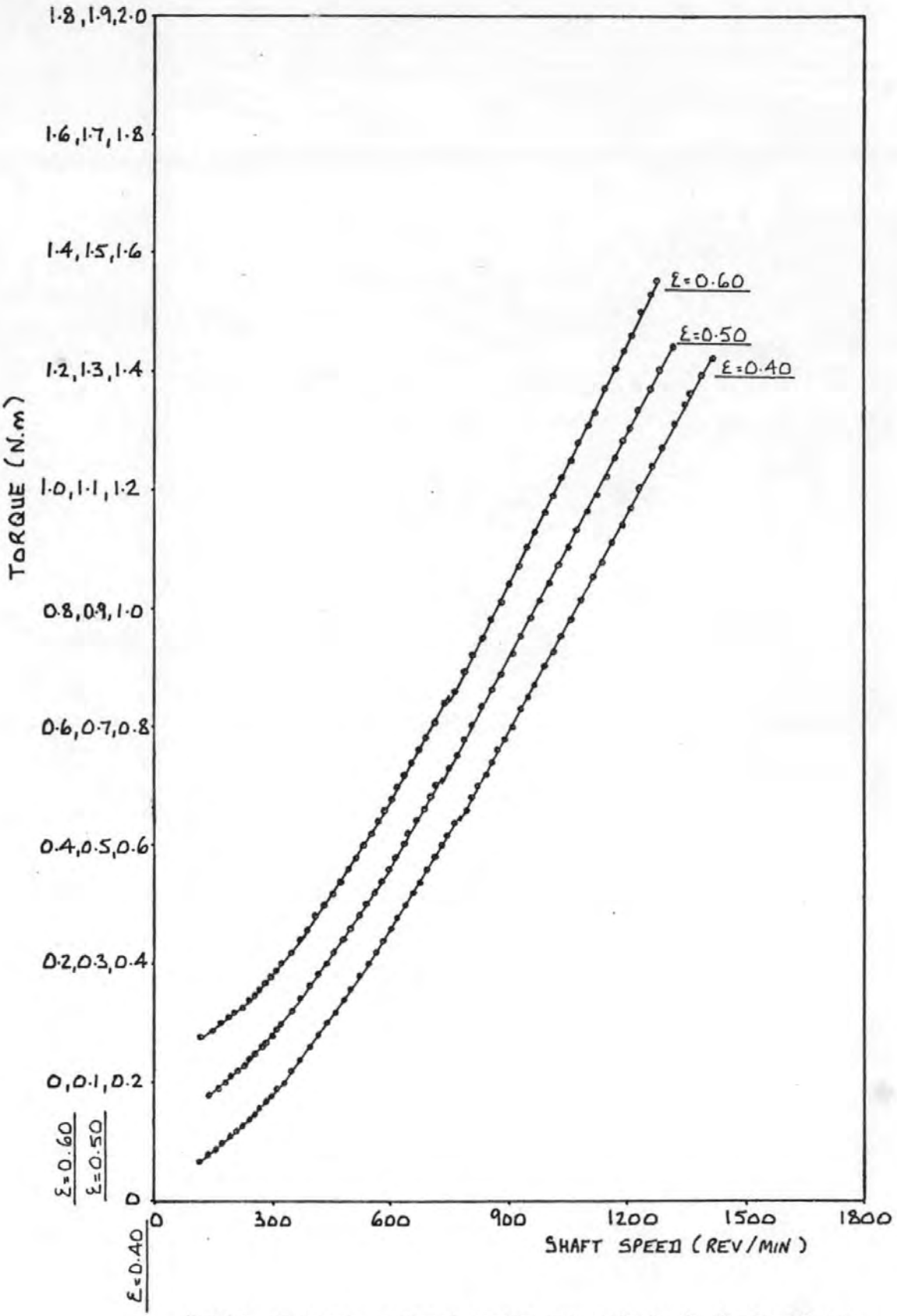

FIG. 94 TORQUE MEASUREMENTS FOR INCREASING SHAFT SPEED:
$R_i/R_o = 0.874$, TELLUS 21

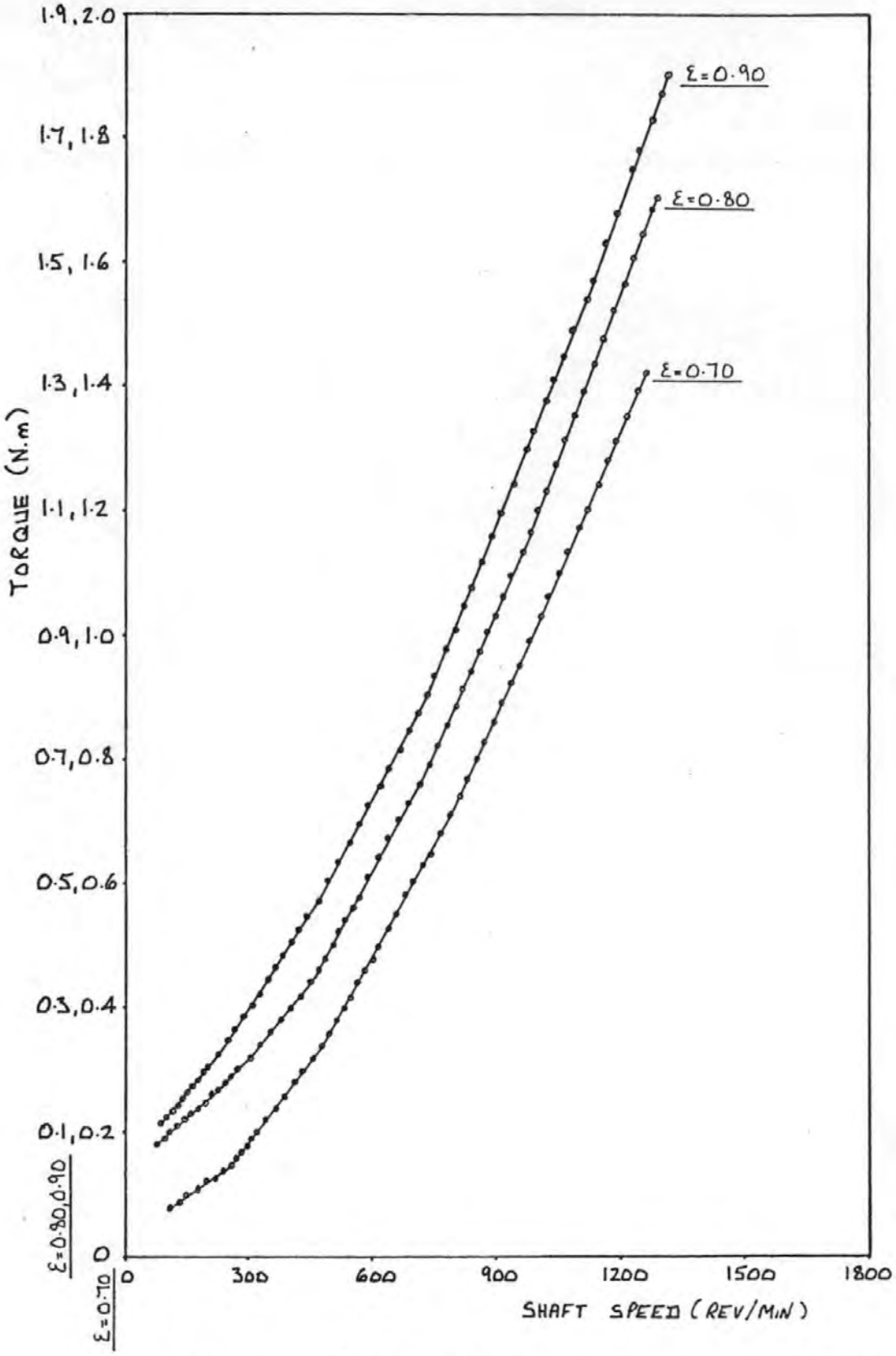

FIG. 95 TORQUE MEASUREMENTS FOR INCREASING SHAFT SPEED: $R_i/R_o = 0.874$, TELLUS 21

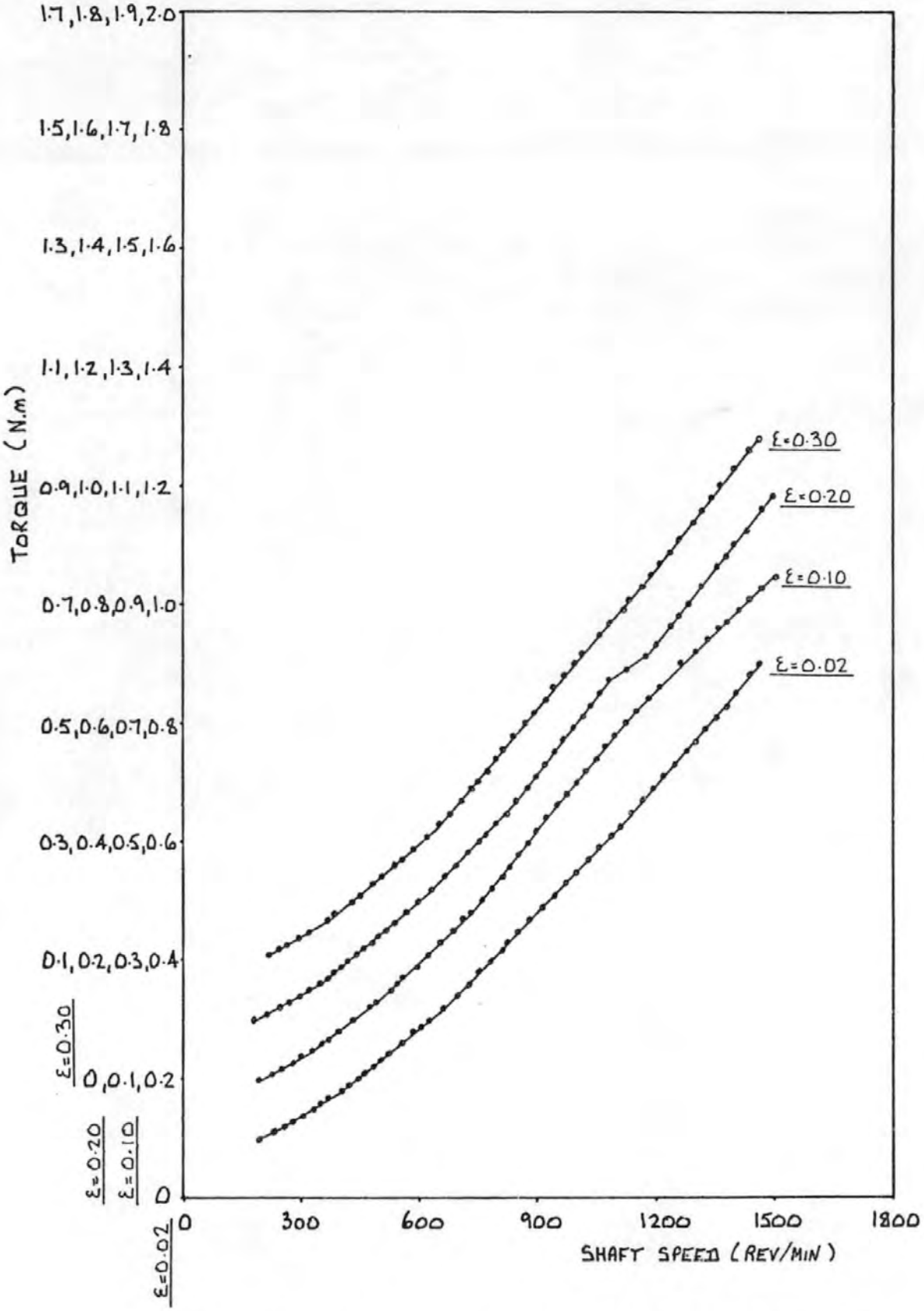

FIG. 96 TORQUE MEASUREMENTS FOR INCREASING SHAFT SPEED: $R_i/R_o = 0.874$, LARNEA 15

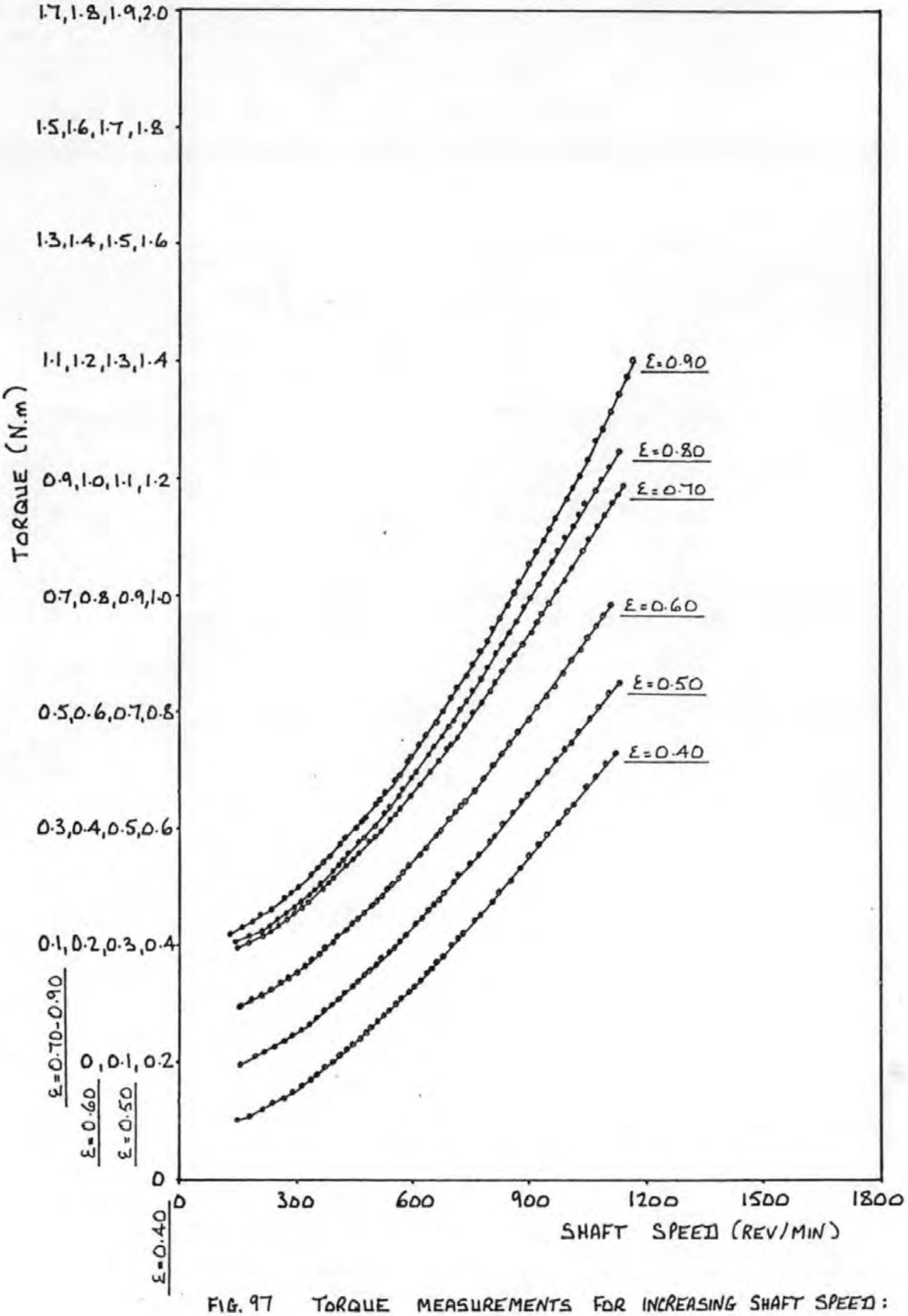

FIG. 97 TORQUE MEASUREMENTS FOR INCREASING SHAFT SPEED: $R_i/R_o = 0.874$, LARNEA 15

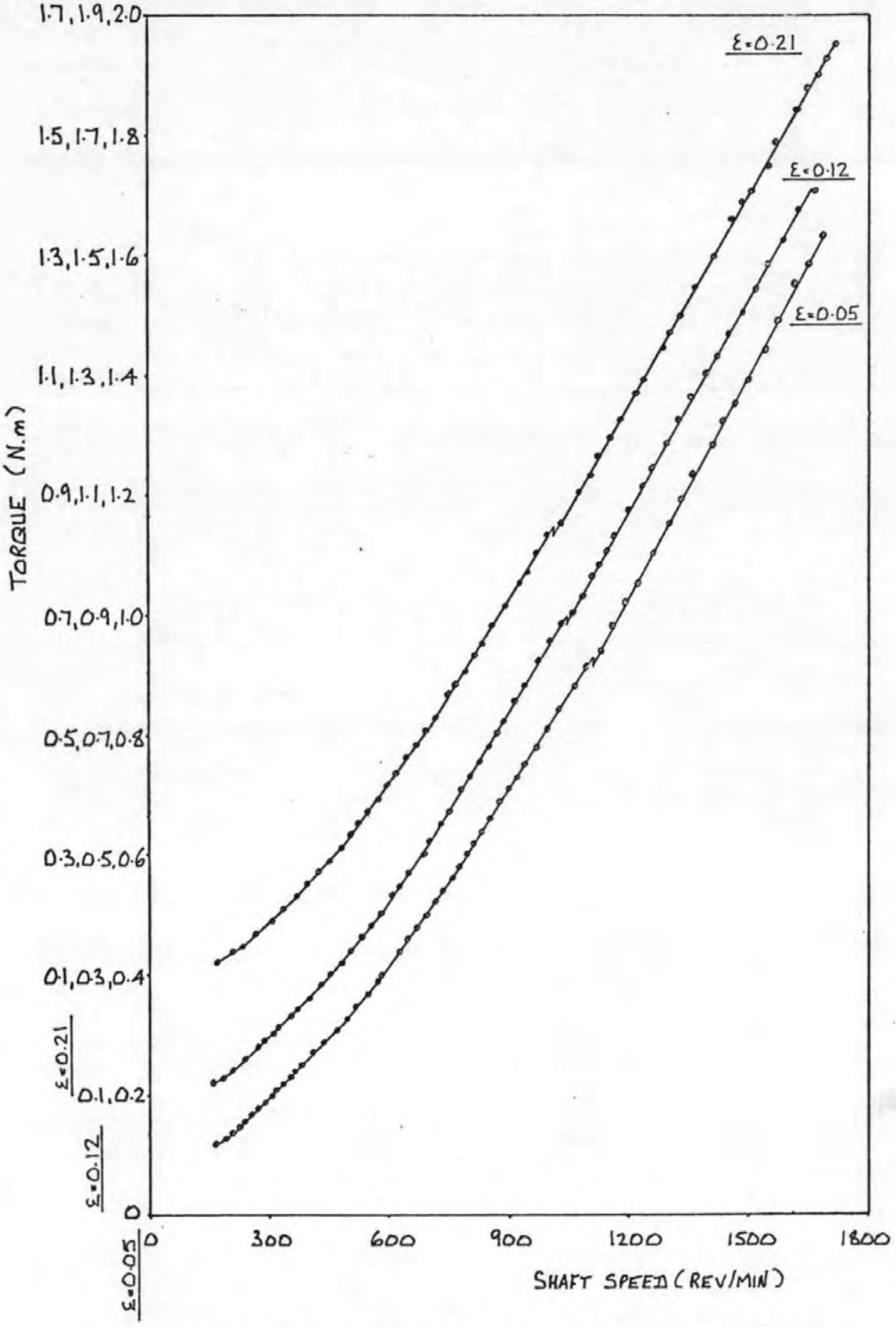

FIG. 98 TORQUE MEASUREMENTS FOR INCREASING SHAFT SPEED: $R_i/R_o = 0.950$, CARNEA 15

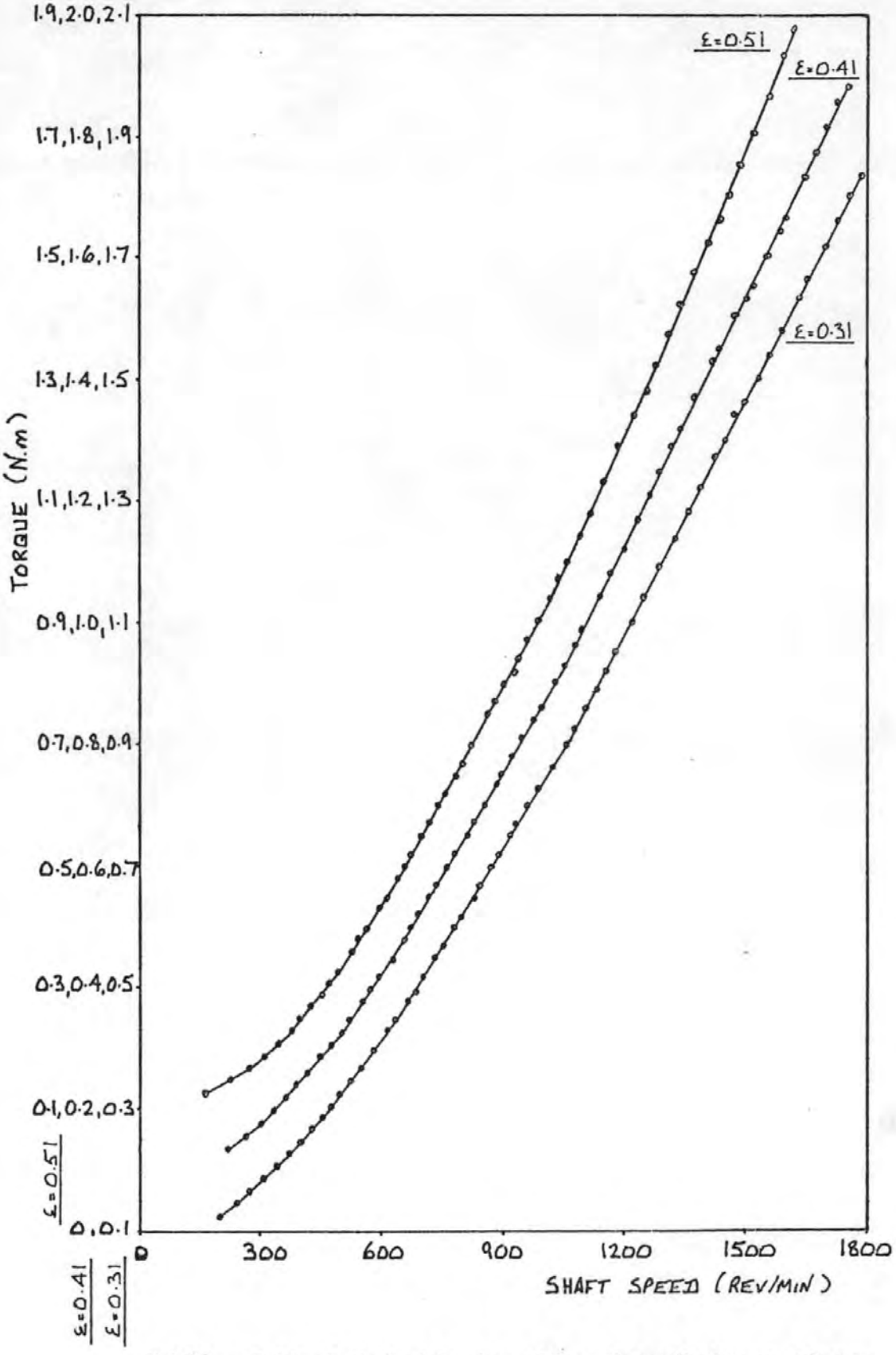

FIG. 99 TORQUE MEASUREMENTS FOR INCREASING SHAFT SPEED: $R_i/R_o = 0.950$, CARNEA 15

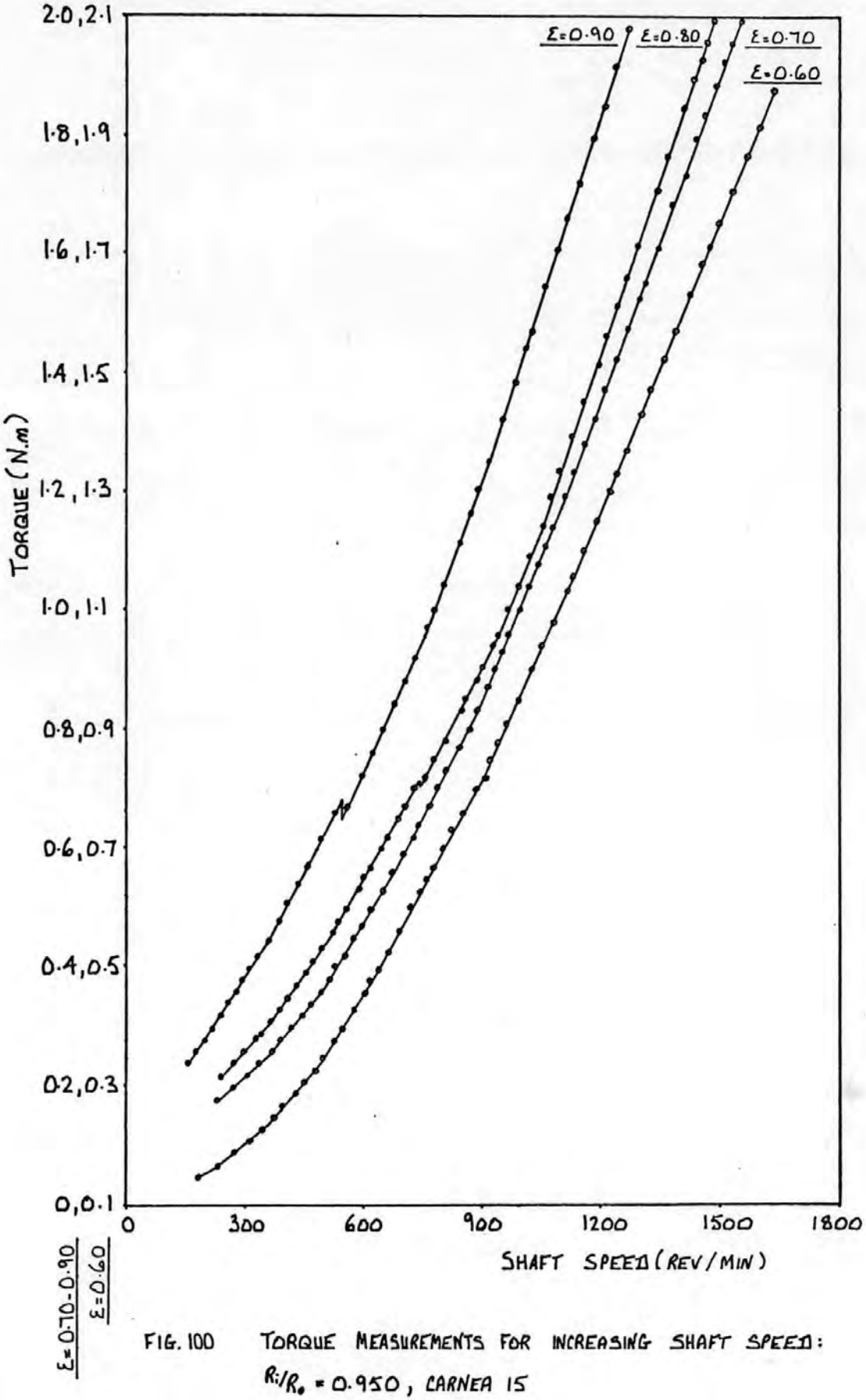

FIG. 100 TORQUE MEASUREMENTS FOR INCREASING SHAFT SPEED: $R_i/R_o = 0.950$, CARNEA 15

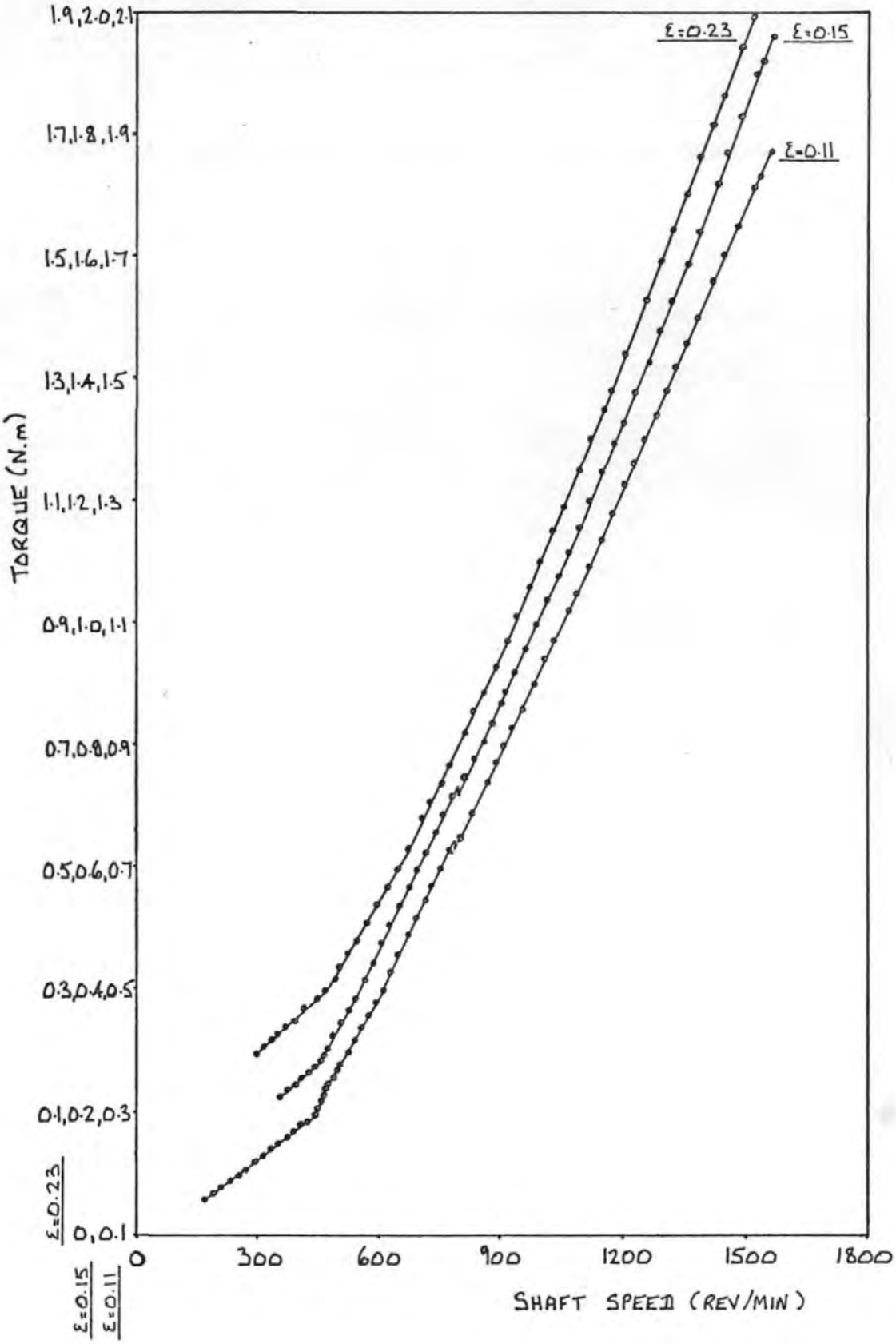

FIG. 101 TORQUE MEASUREMENTS FOR INCREASING SHAFT SPEED: $R_i/R_o < 0.975$, CARNEA 15

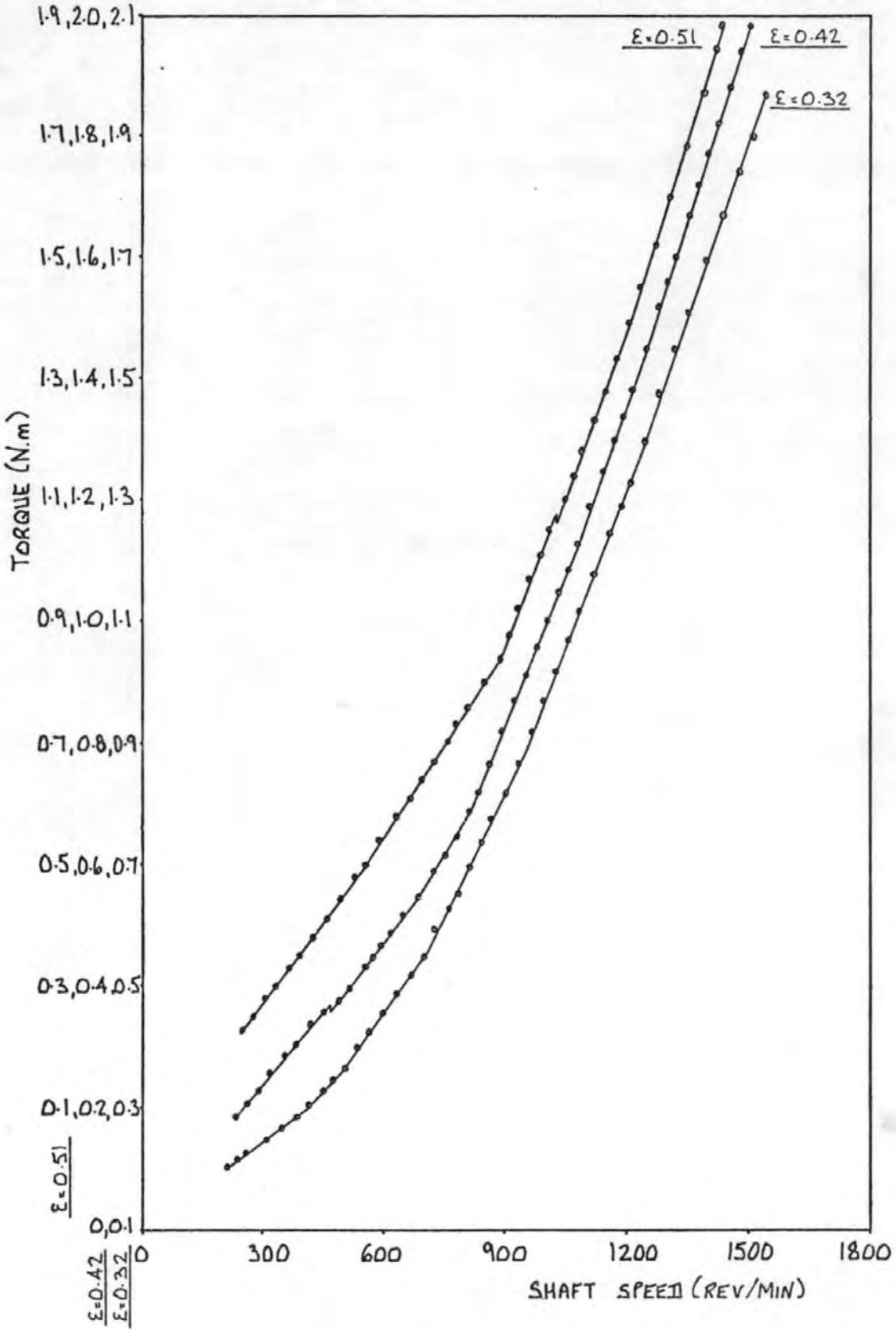

FIG. 102 TORQUE MEASUREMENTS FOR INCREASING SHAFT SPEED: $R_i/R_o = 0.975$, CARNEA 15

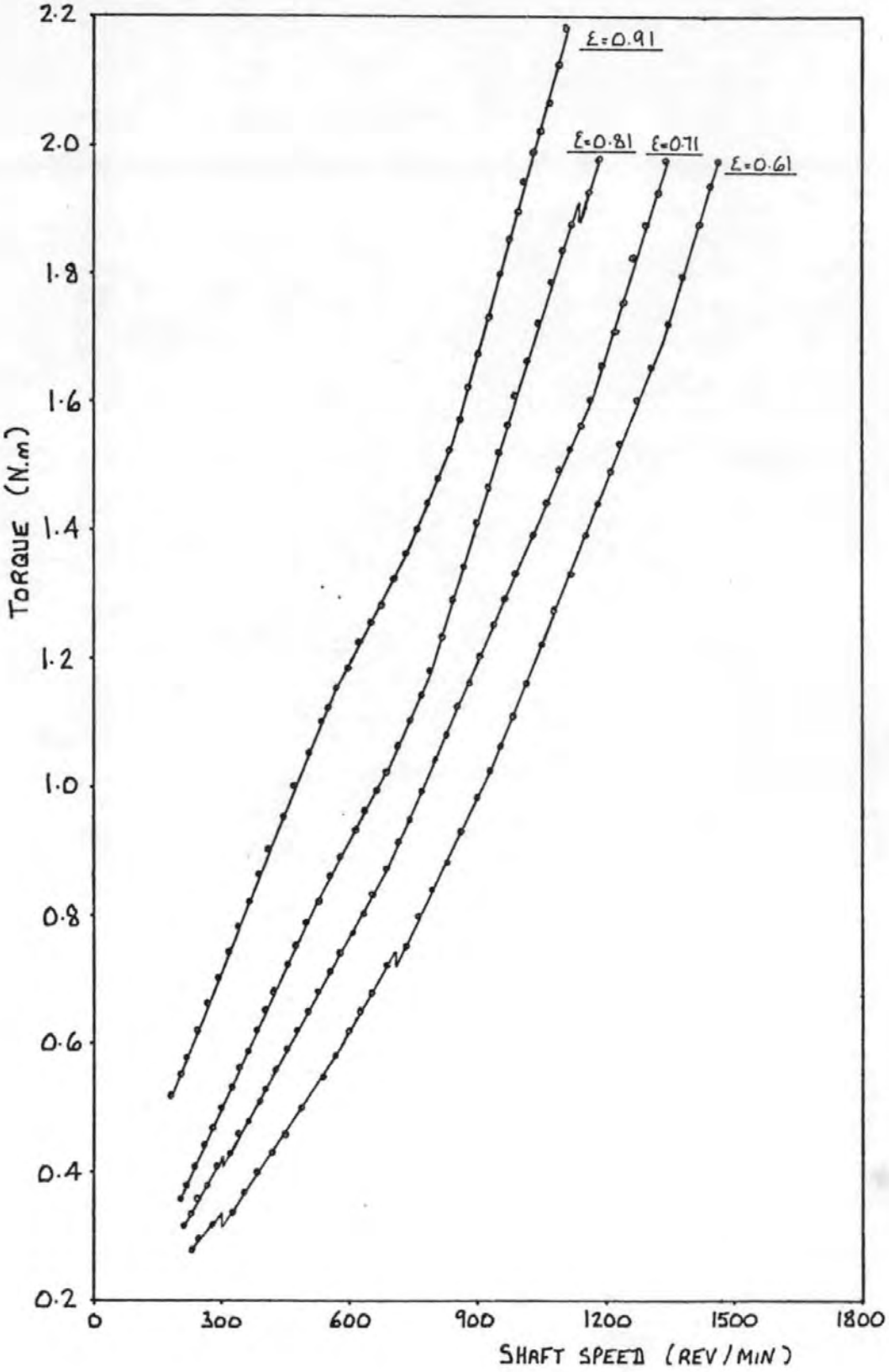

FIG. 103 TORQUE MEASUREMENTS FOR INCREASING SHAFT SPEED: $R_i/R_o = 0.975$, LARNEA 15

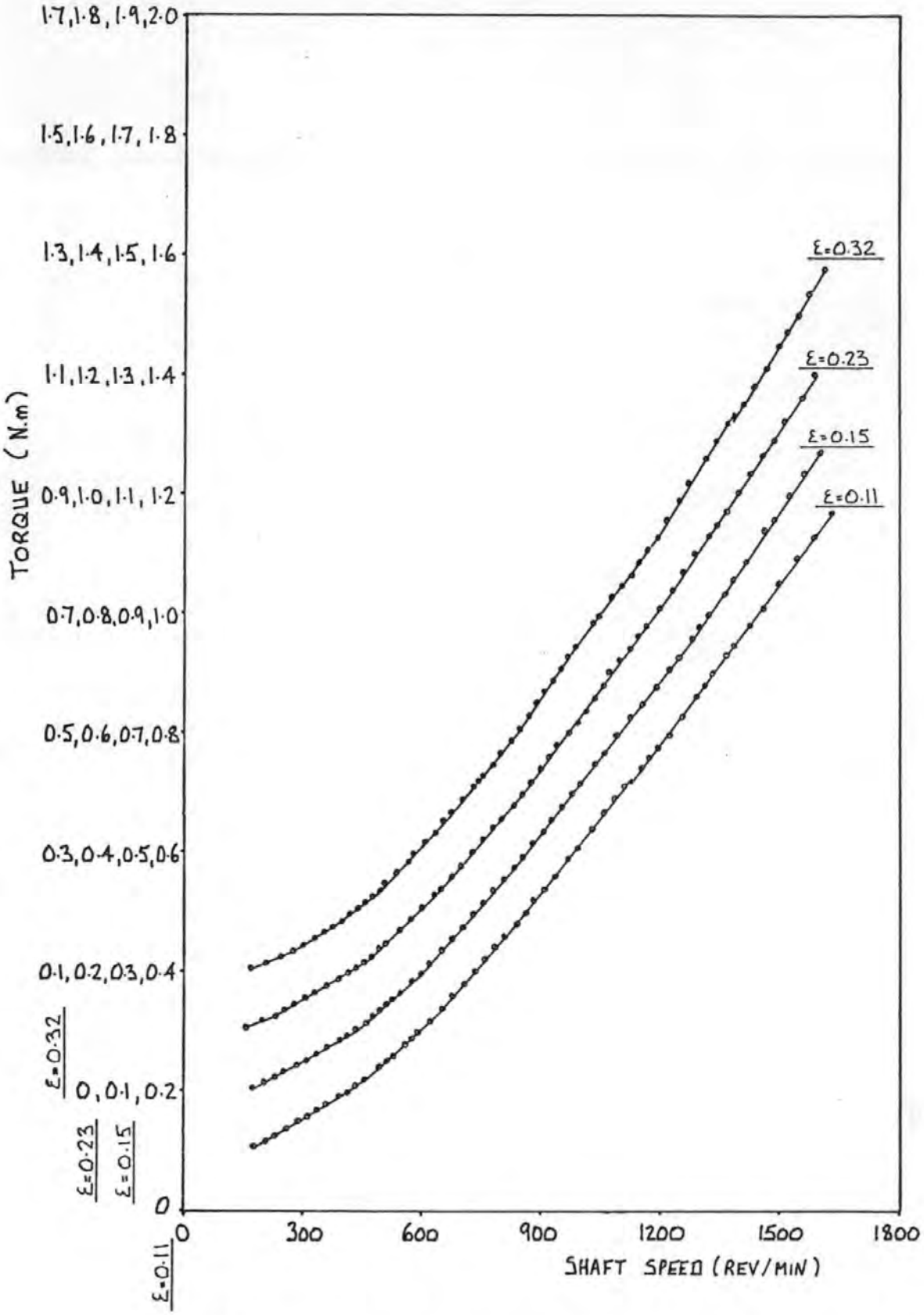

FIG.104 TORQUE MEASUREMENTS FOR INCREASING SHAFT SPEED:
$R_i/R_o = 0.975$, MACRON A

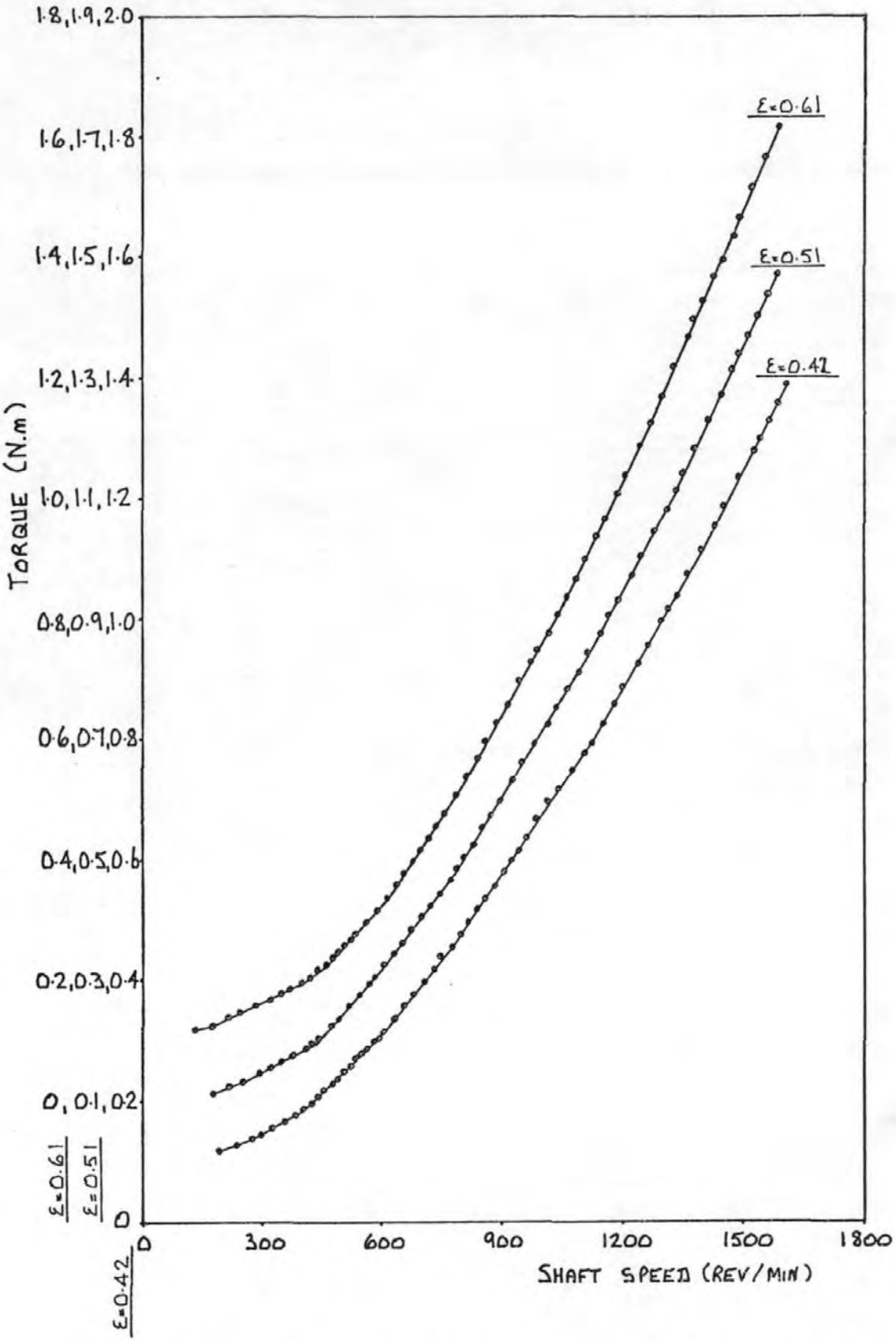

FIG. 105 TORQUE MEASUREMENTS FOR INCREASING SHAFT SPEED: $R_i/R_o = 0.975$, MACRON A

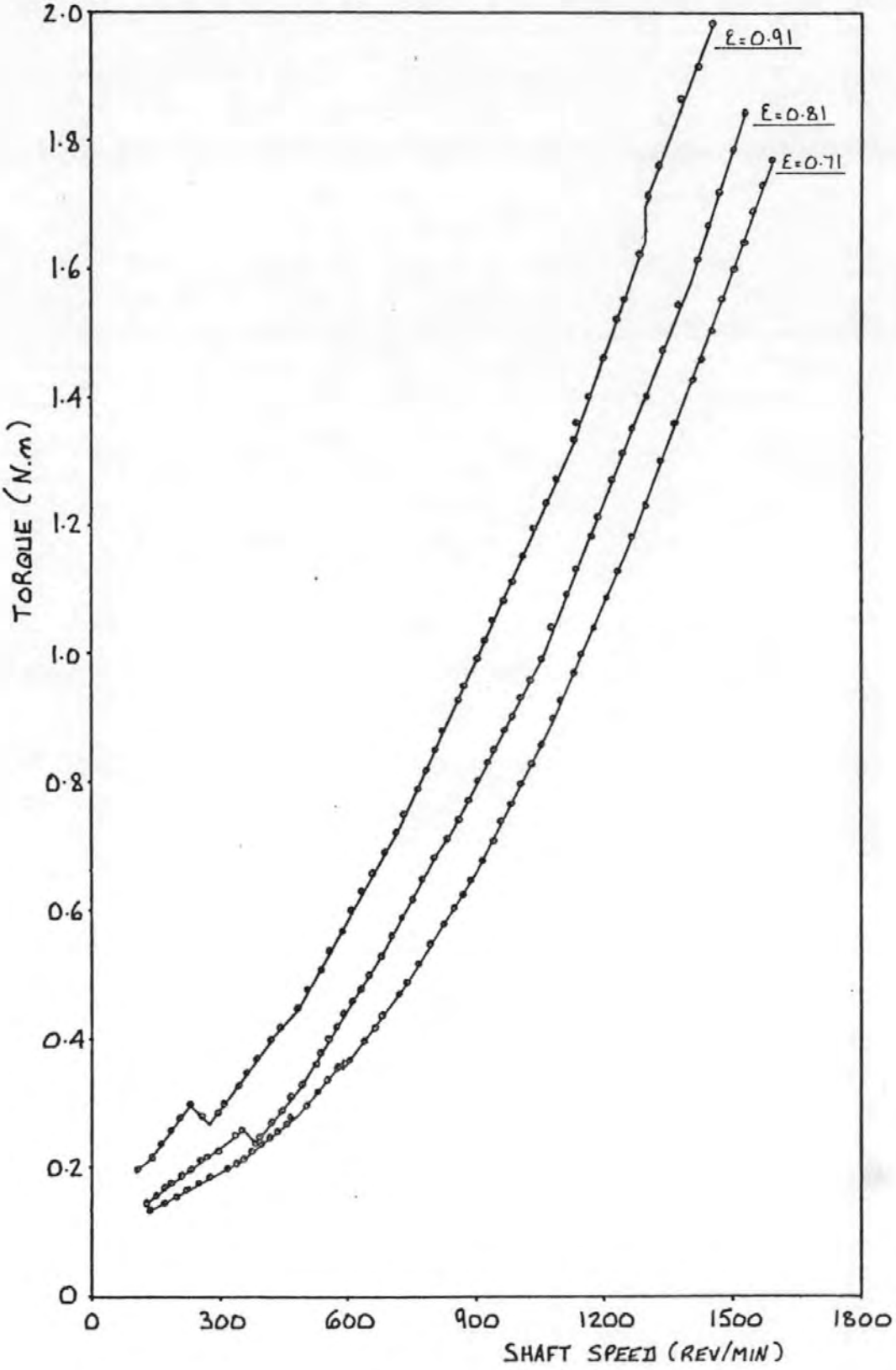

FIG. 106 TORQUE MEASUREMENTS FOR INCREASING SHAFT SPEED: $R_i/R_o = 0.975$, MACRON A

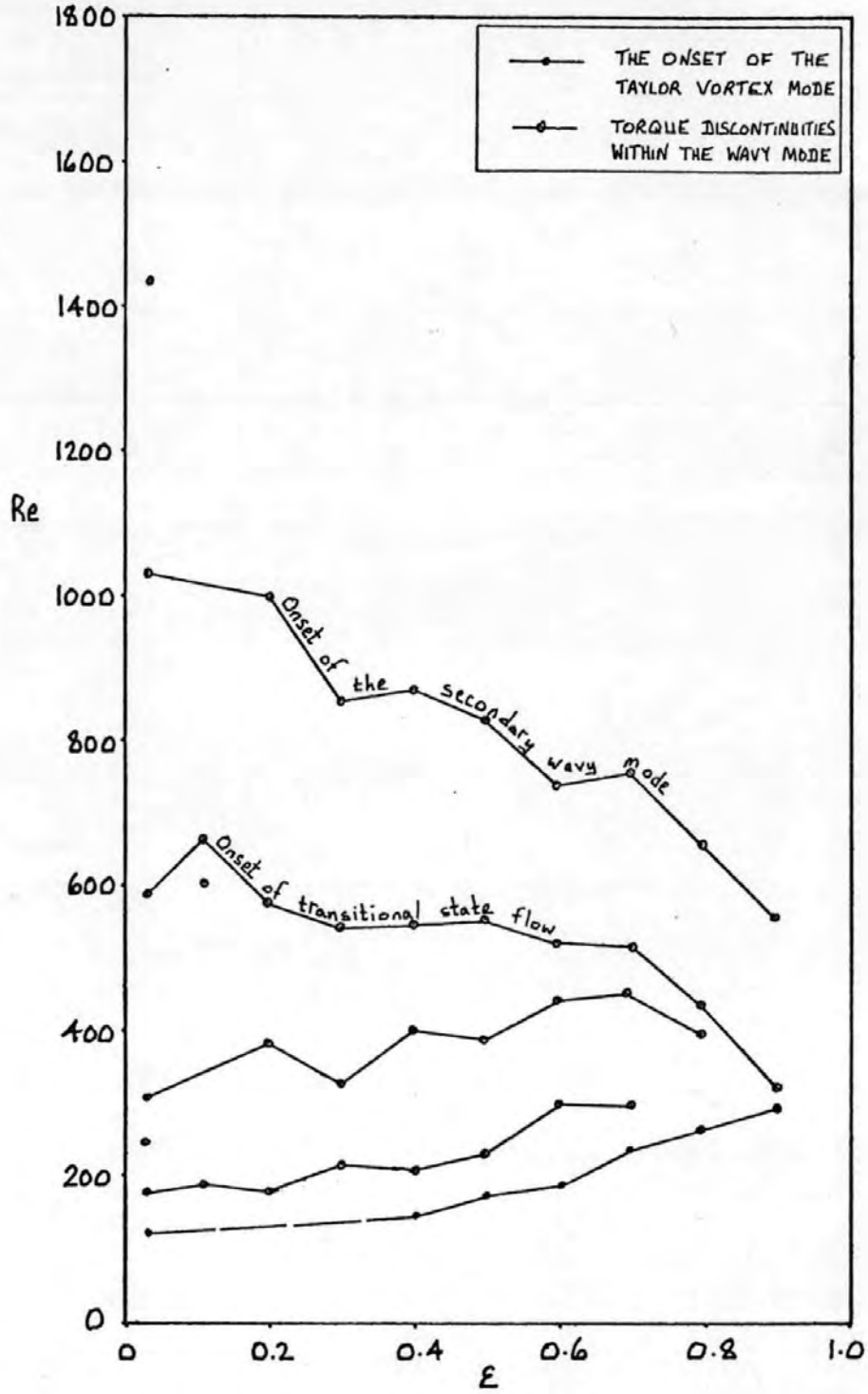

FIG. 107 BOUNDARIES DEFINED BY DISCONTINUITIES IN THE TORQUE MEASUREMENT RESULTS: $R_i/R_o = 0.911$, TELLUS 21

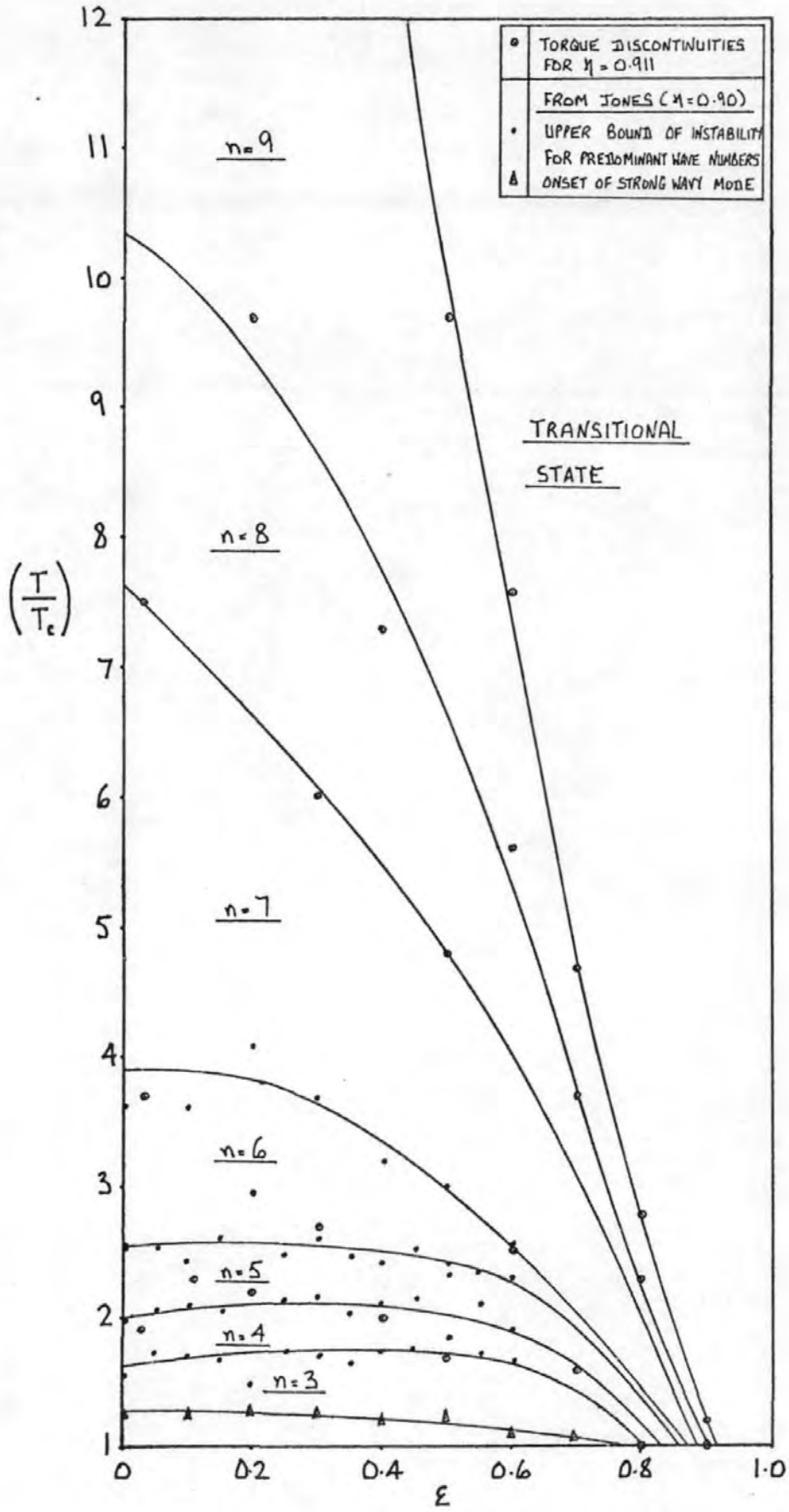

FIG. 108 COMPARISON OF THE RECORDED TORQUE DISCONTINUITIES FOR $R_i/R_o = 0.911$ (TELLUS 21) AND JONES' VISUAL OBSERVATIONS ($\theta = \pi$)

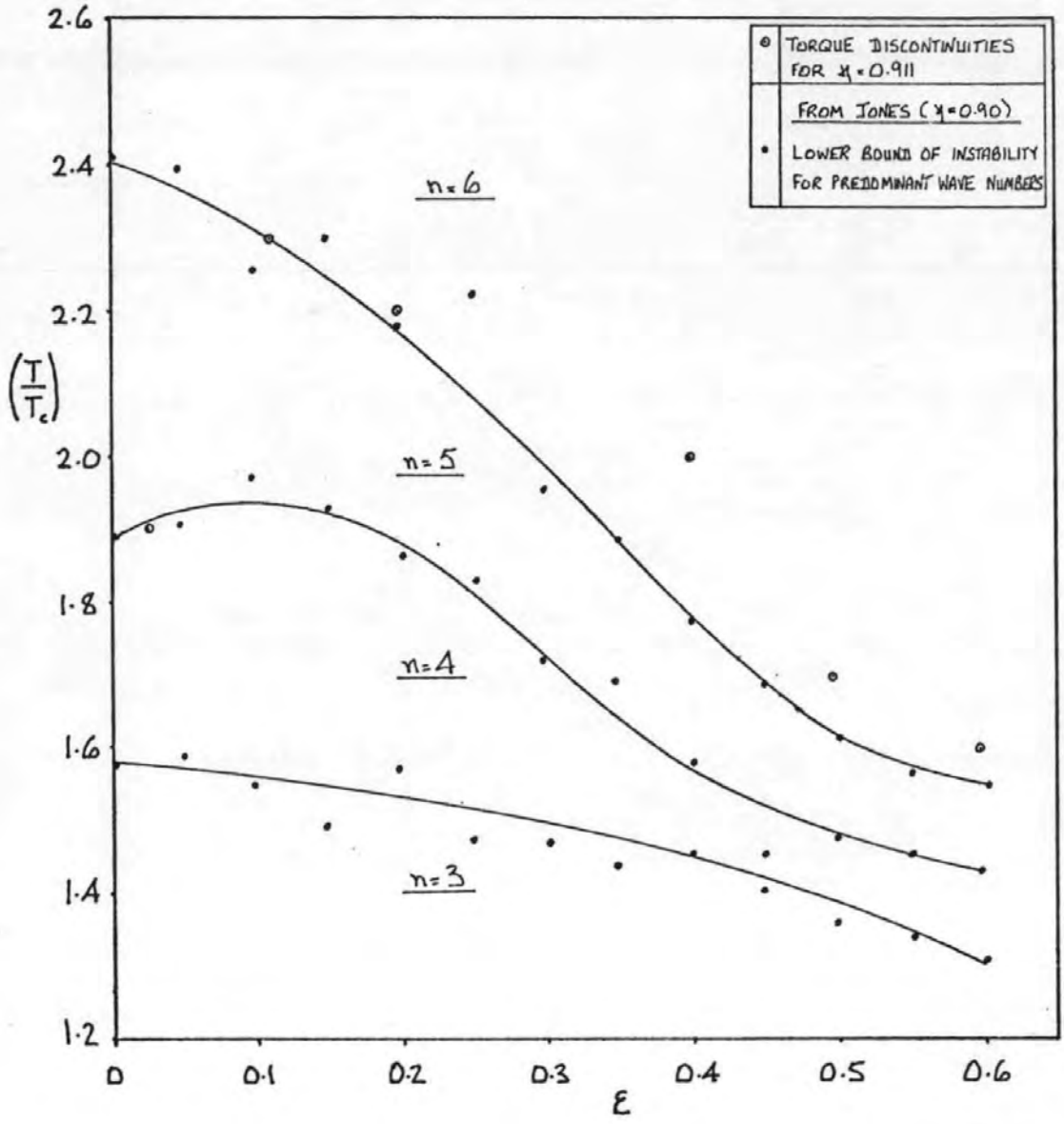

FIG. 109 COMPARISON OF THE RECORDED TORQUE DISCONTINUITIES FOR $R_i/R_o = 0.911$ (TELLUS 21) AND JONES' VISUAL OBSERVATIONS ($\theta = 3\pi/2$)

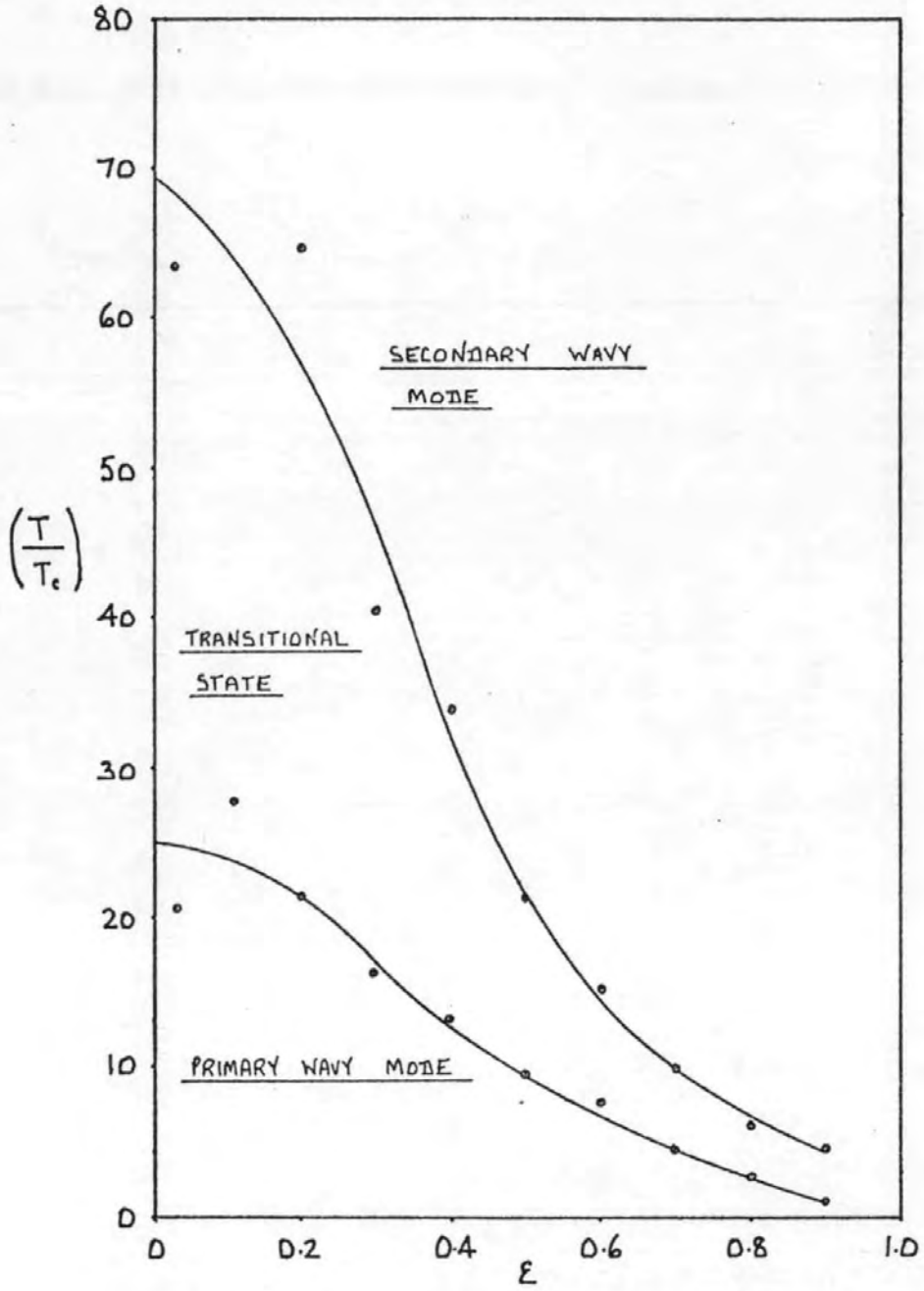

FIG. 110 THE TRANSITIONAL STATE BOUNDARIES DEFINED BY THE TORQUE DISCONTINUITIES FROM A SERIES OF TEST RUNS: $R_i/R_o = 0.911$, TELLUS 21

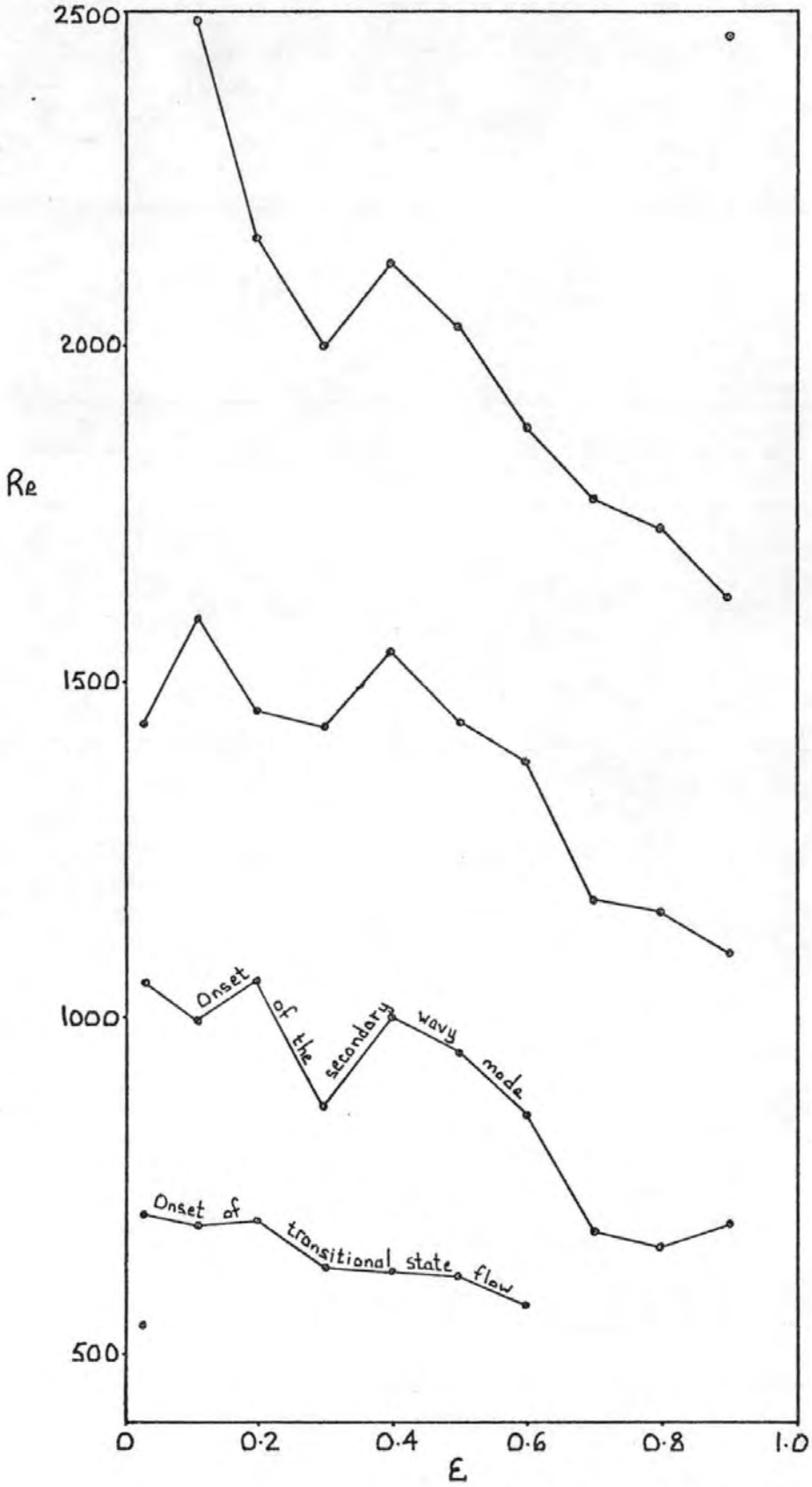

FIG. III BOUNDARIES DEFINED BY DISCONTINUITIES IN THE TORQUE MEASUREMENT RESULTS: $R_i/R_o = 0.911$, CARNEA 15

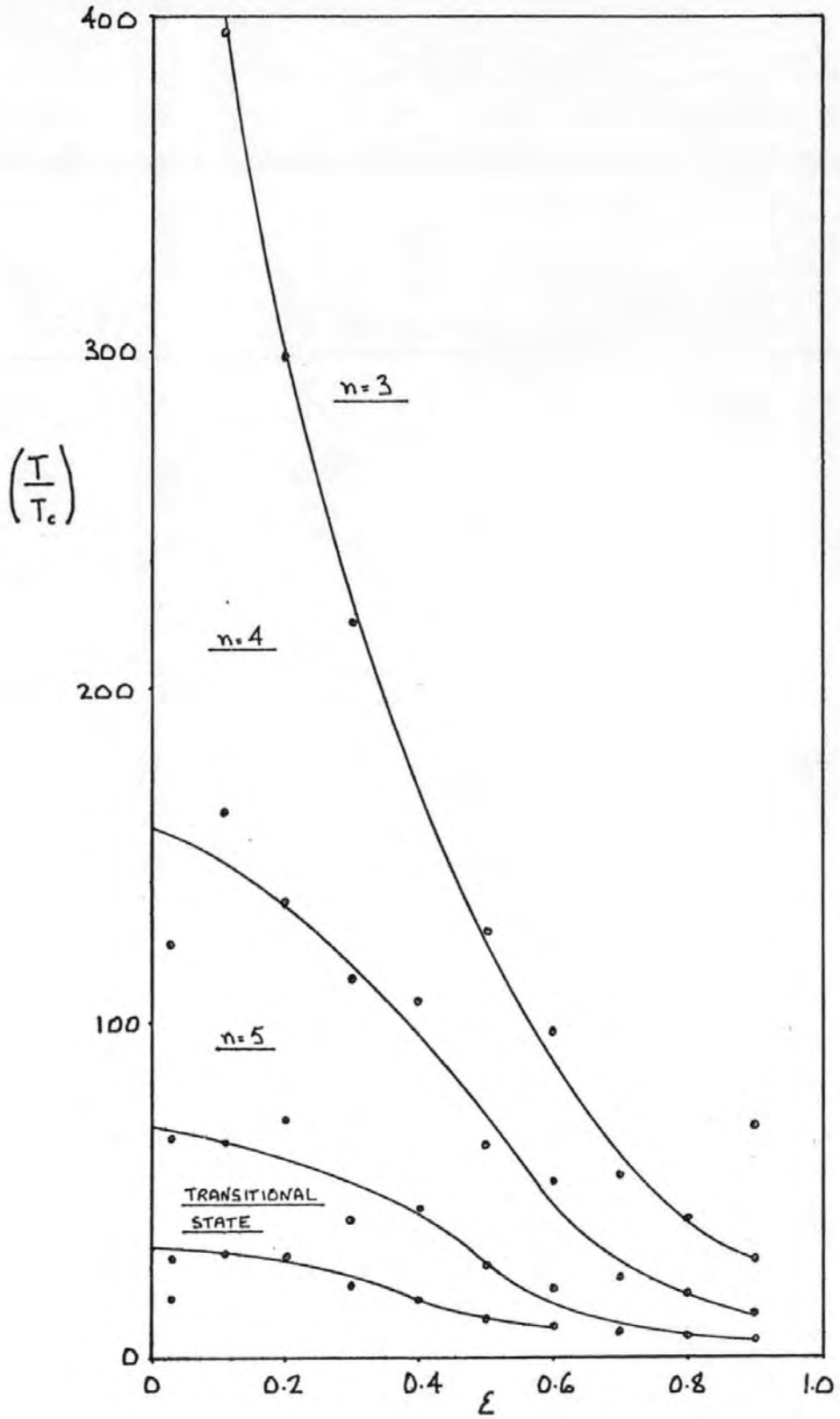

FIG. 112 WAVE NUMBER BOUNDARIES WITHIN THE SECONDARY WAVY MODE DEFINED BY TORQUE DISCONTINUITIES:
$R_i/R_o = 0.911$, CARNEA 15

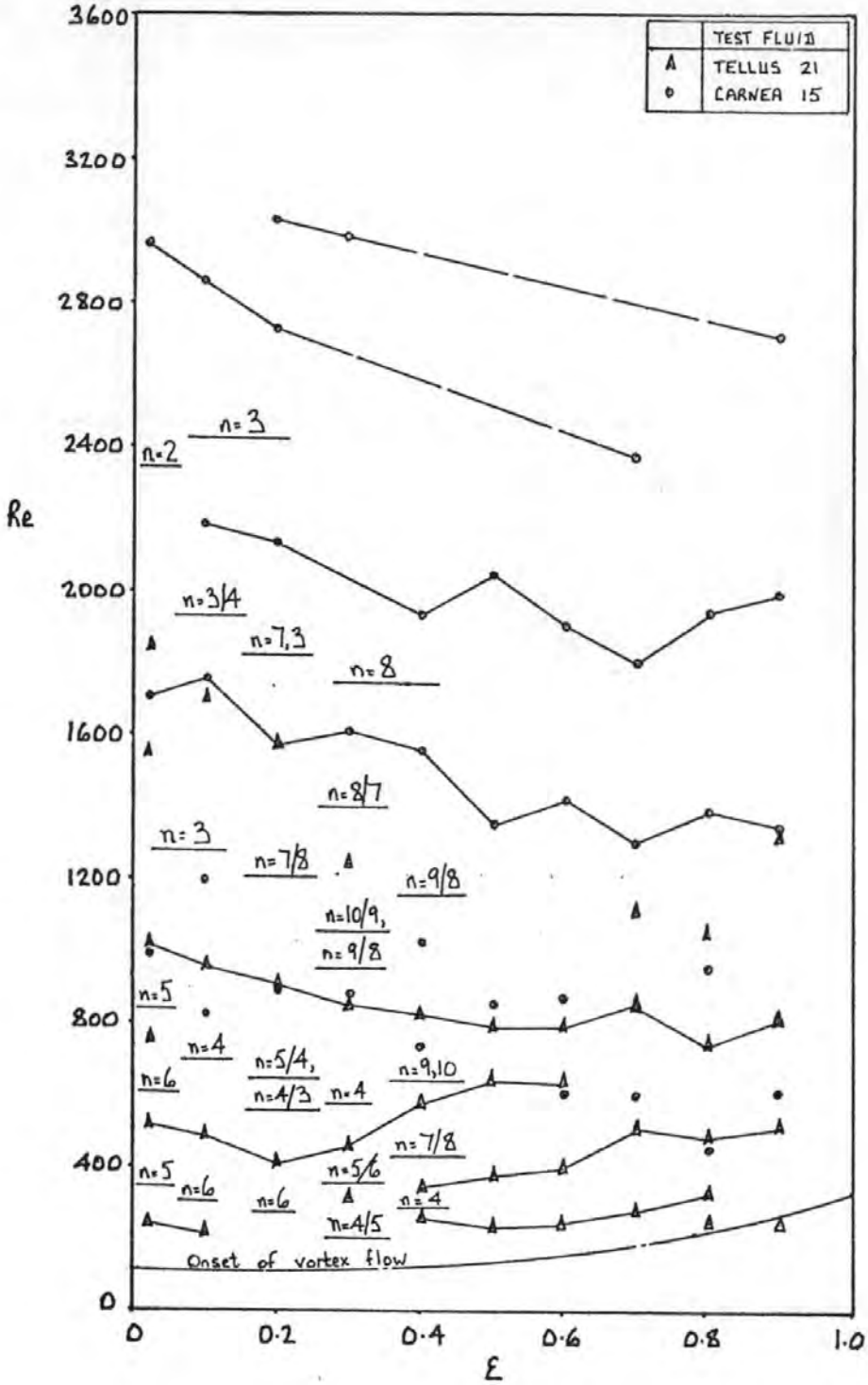

FIG. 113 COMPARISON BETWEEN THE BOUNDARIES DERIVED FROM DISCONTINUITIES IN THE TORQUE MEASUREMENT RESULTS AND WAVE NUMBERS OBSERVED IN THE FLOW VISUALISATION TESTS : $R_i/R_o = 0.874$

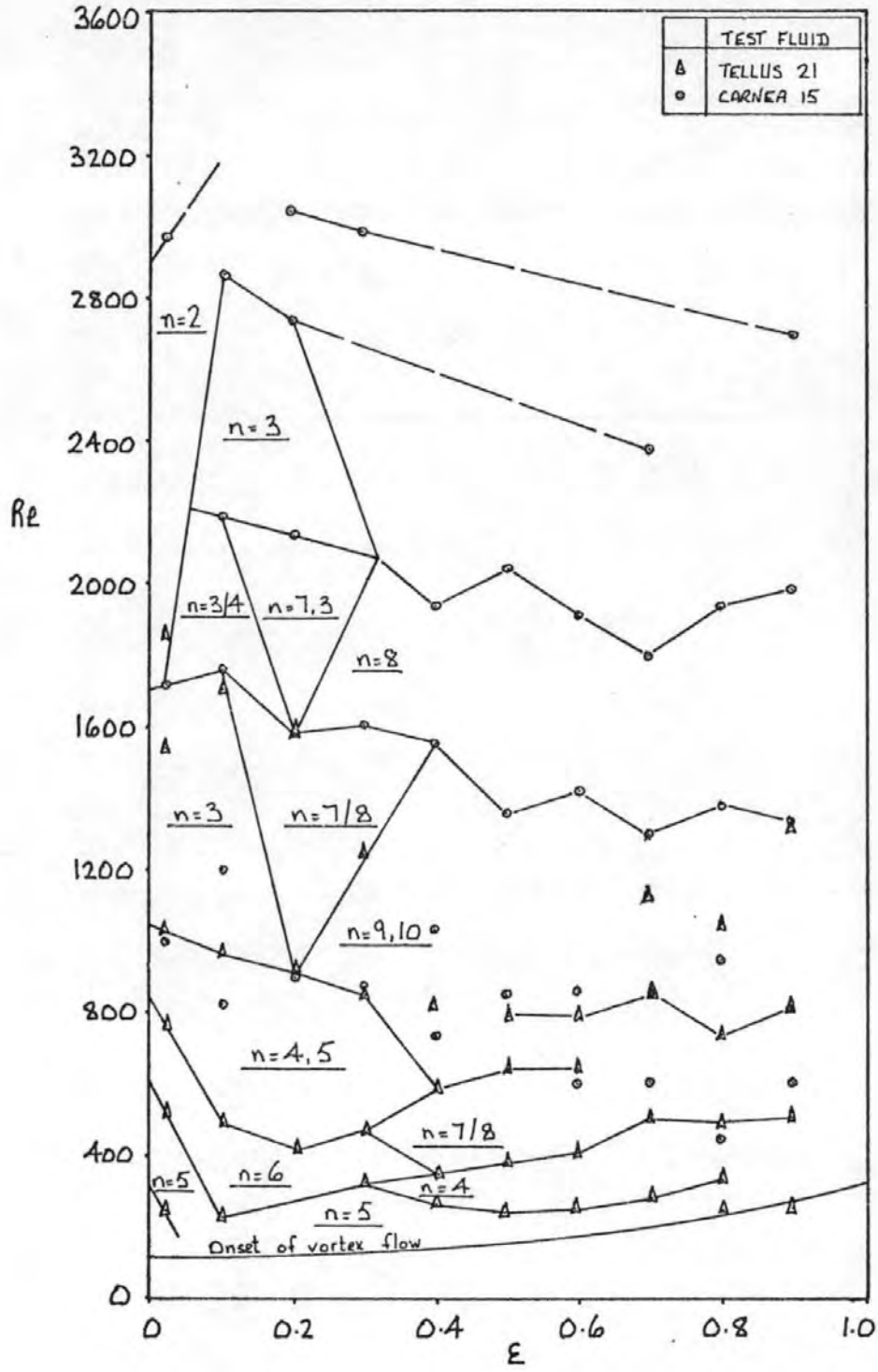

FIG. 114 WAVE NUMBER BOUNDARIES DERIVED FROM THE TORQUE MEASUREMENT AND FLOW VISUALISATION RESULTS: $R_i/R_o = 0.874$

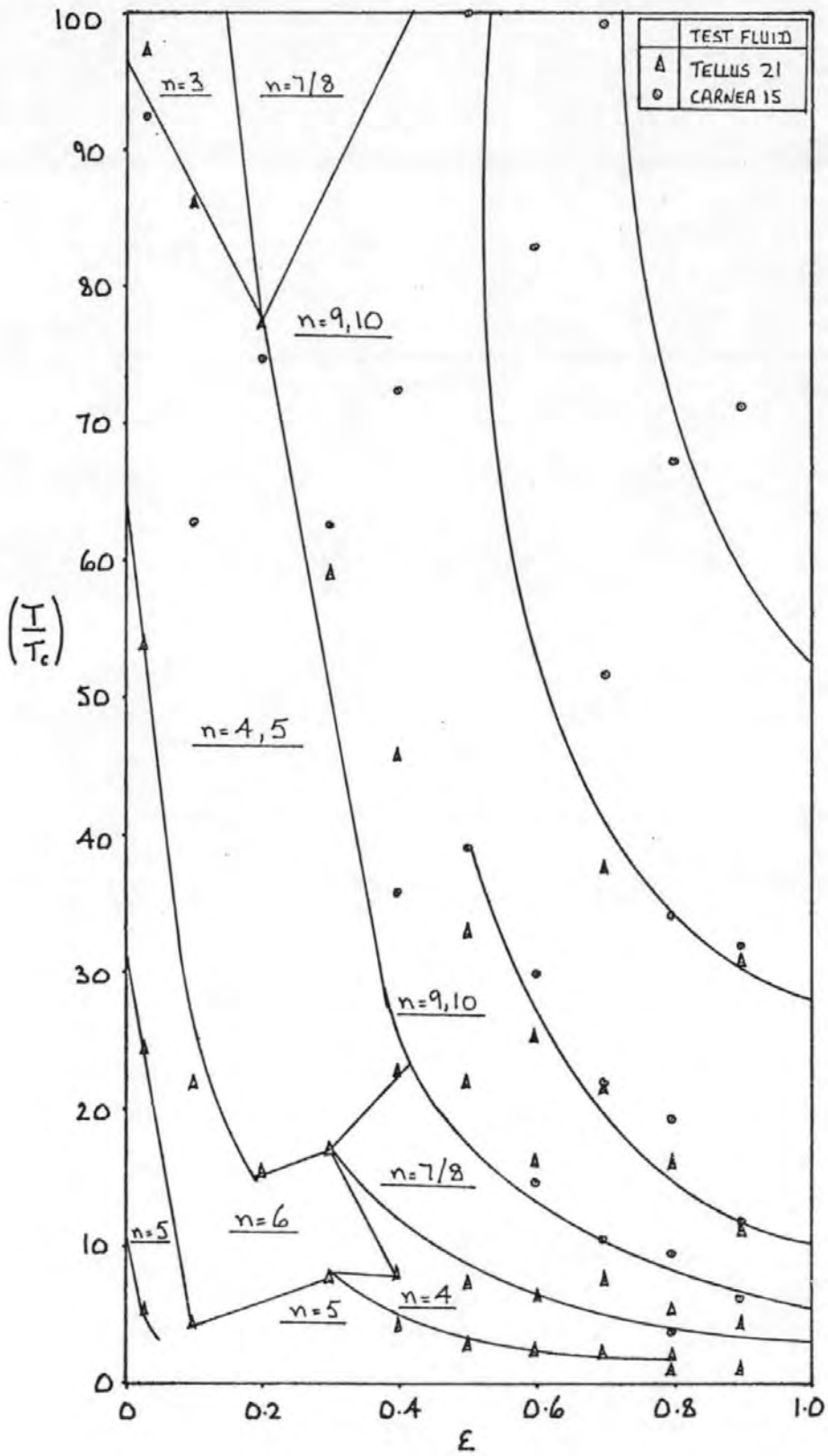

FIG. 115 NORMALISED TAYLOR NUMBERS FOR THE DERIVED WAVE NUMBER BOUNDARIES : $R_i/R_o = 0.874$ (LOW REYNOLDS NUMBER RESULTS)

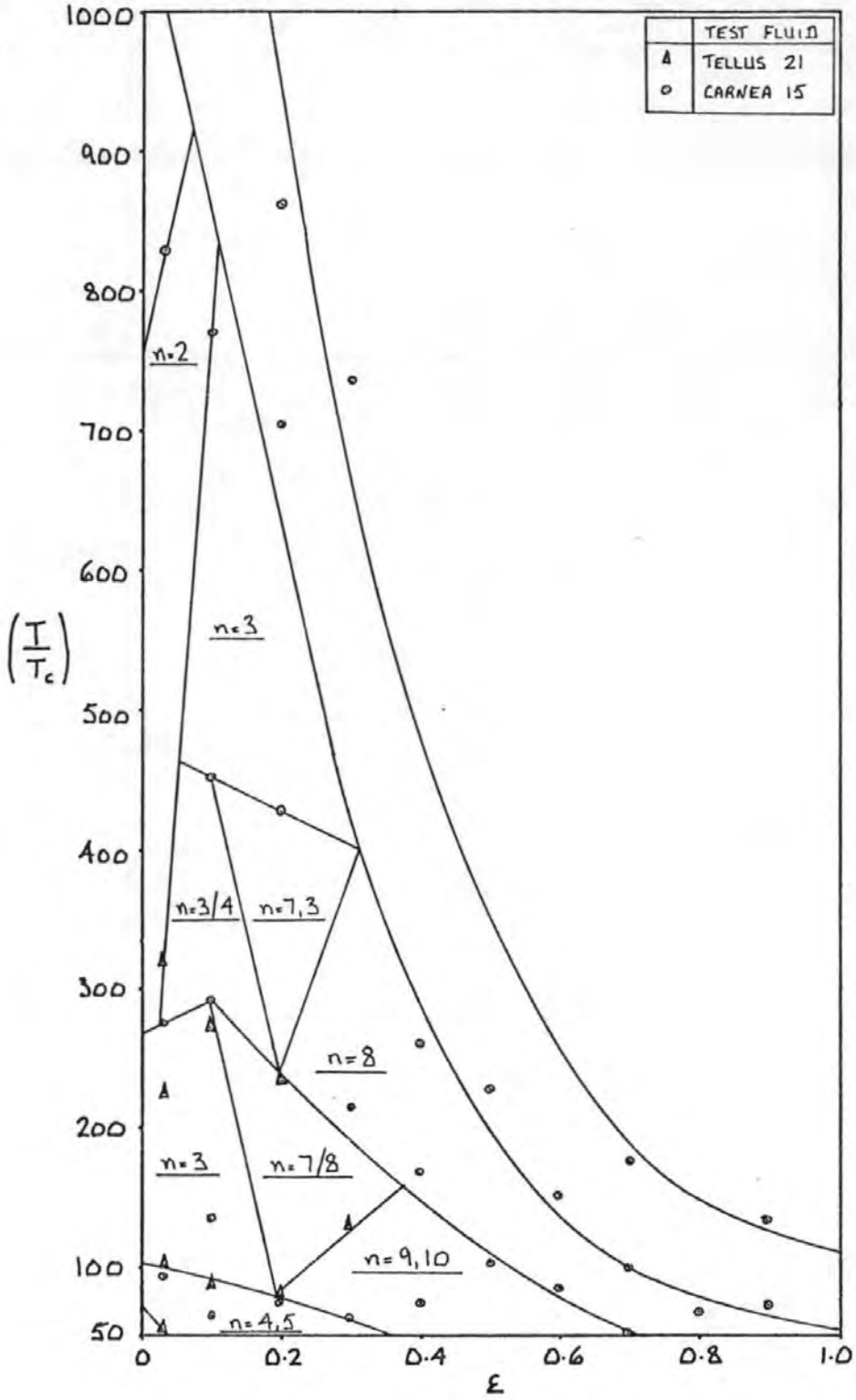

FIG. 116 NORMALISED TAYLOR NUMBERS FOR THE DERIVED WAVE NUMBER BOUNDARIES : $R_i/R_c = 0.874$ (HIGH REYNOLDS NUMBER RESULTS)

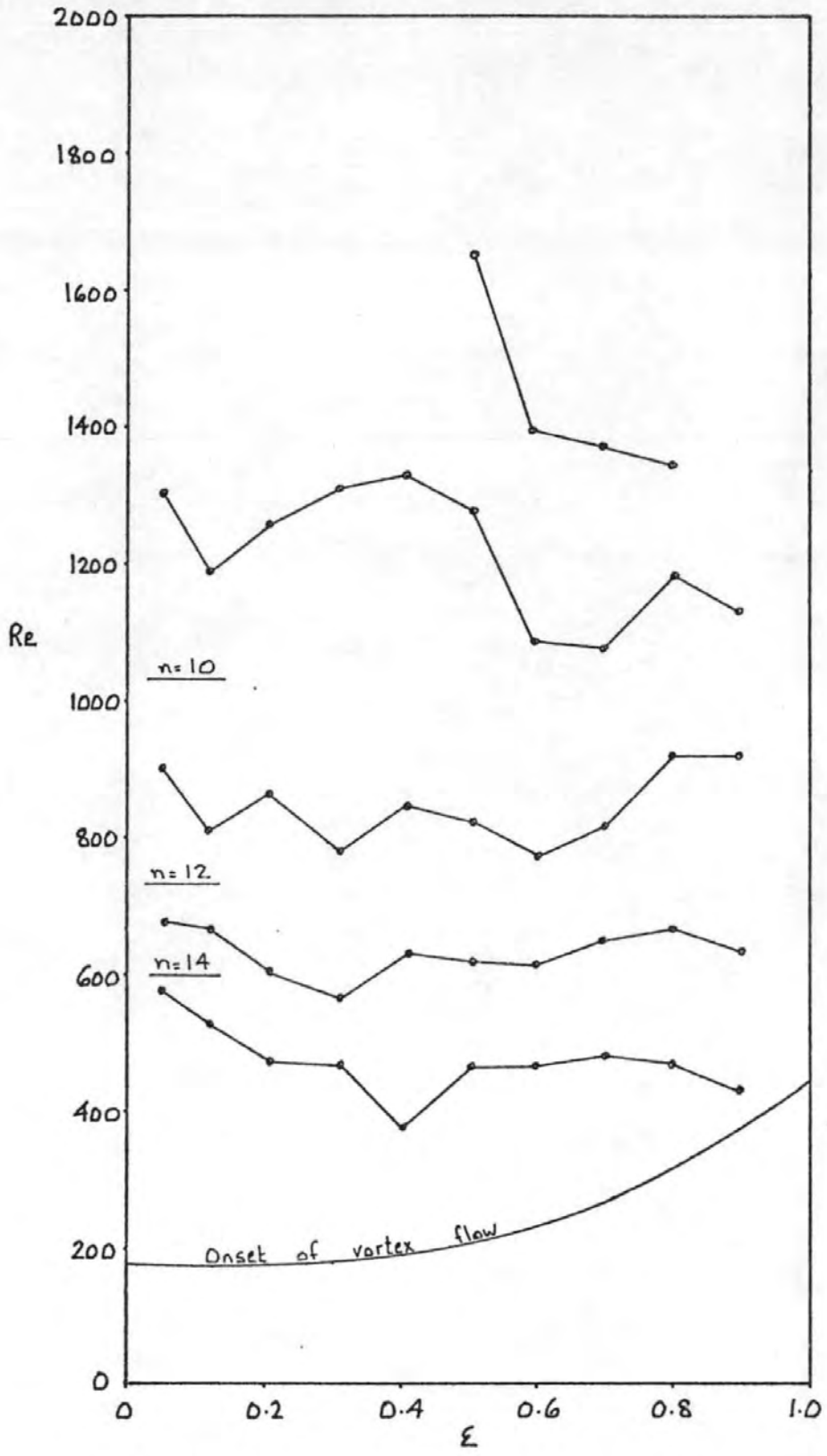

FIG. 117 BOUNDARIES DEFINED BY DISCONTINUITIES IN THE TORQUE MEASUREMENT RESULTS: $R_i/R_o = 0.950$, CARNEA 15

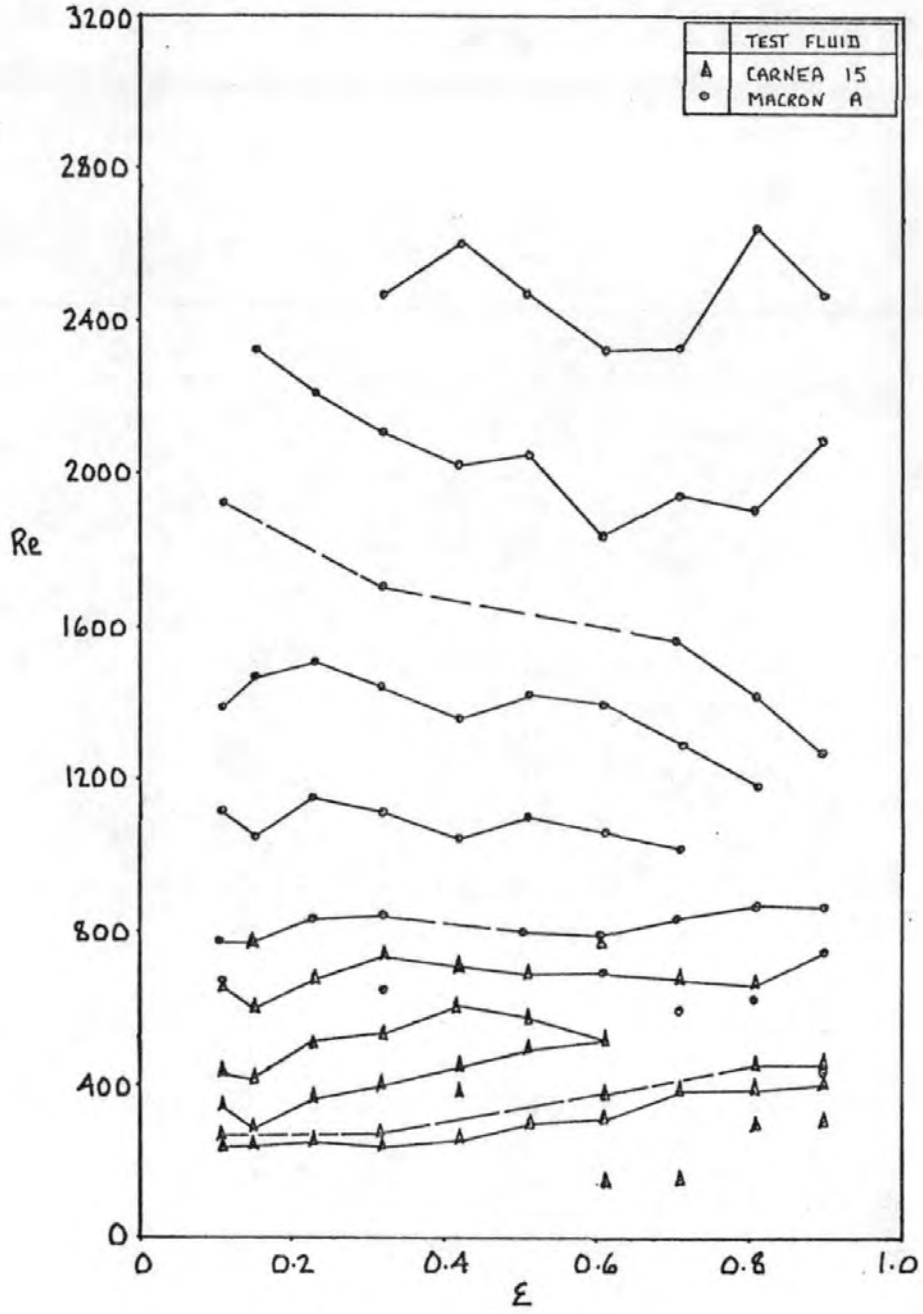

FIG. 118 BOUNDARIES DEFINED BY DISCONTINUITIES IN THE TORQUE MEASUREMENT RESULTS: $R_i/R_o = 0.975$

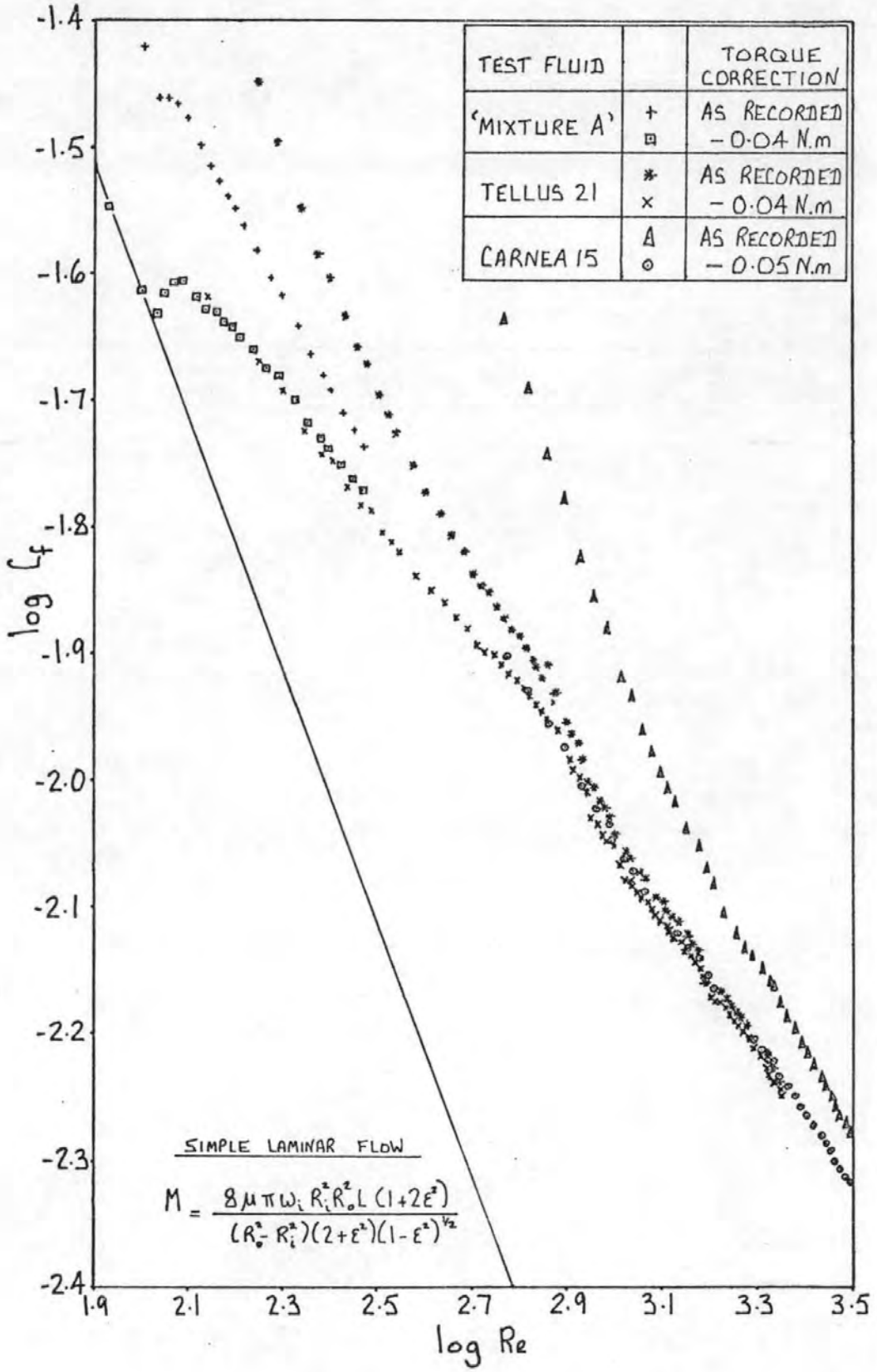

FIG. 119 THE ELIMINATION OF THE EFFECTS OF BEARING FRICTION FROM THE DERIVED FRICTION COEFFICIENT CHARACTERISTICS: $R_i/R_o = 0.874$, $\varepsilon = 0.02$

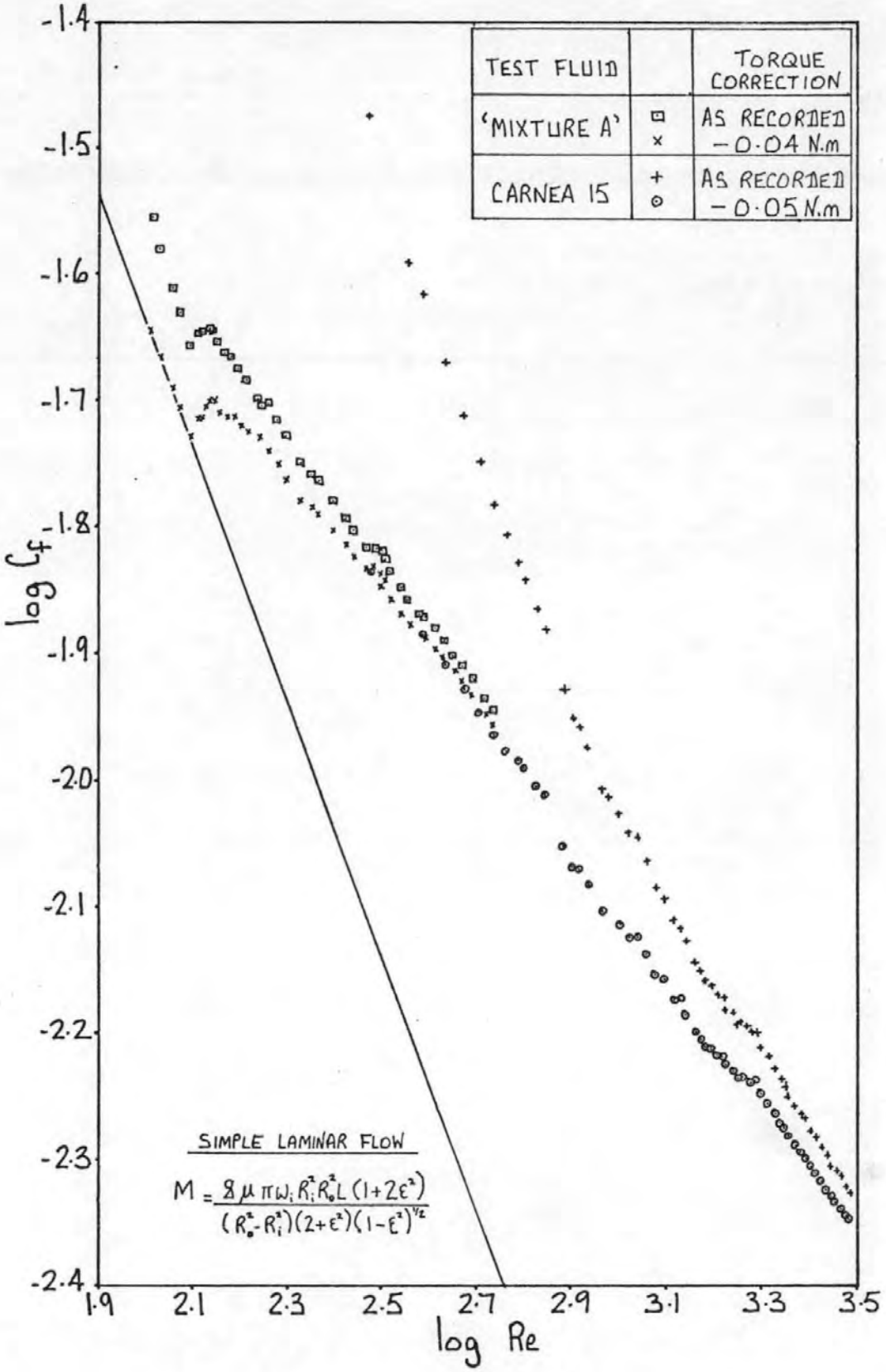

FIG. 120 THE ELIMINATION OF THE EFFECTS OF BEARING FRICTION FROM THE DERIVED FRICTION COEFFICIENT CHARACTERISTICS : $R_i/R_o = 0.911$, $\epsilon = 0.03$

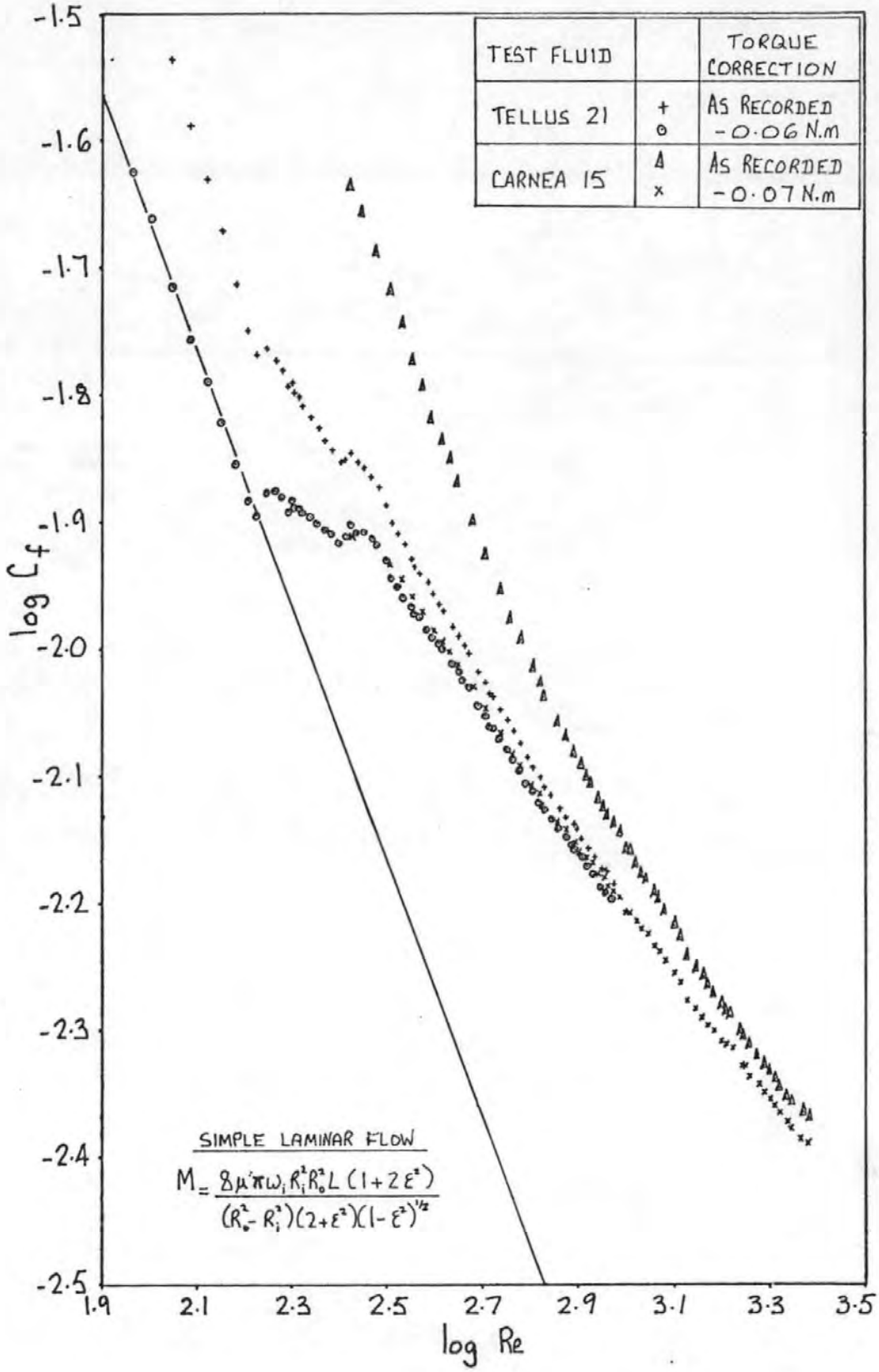

FIG. 121 THE ELIMINATION OF THE EFFECTS OF BEARING FRICTION FROM THE DERIVED FRICTION COEFFICIENT CHARACTERISTICS: $R_i/R_o = 0.950$, $\varepsilon = 0.05$

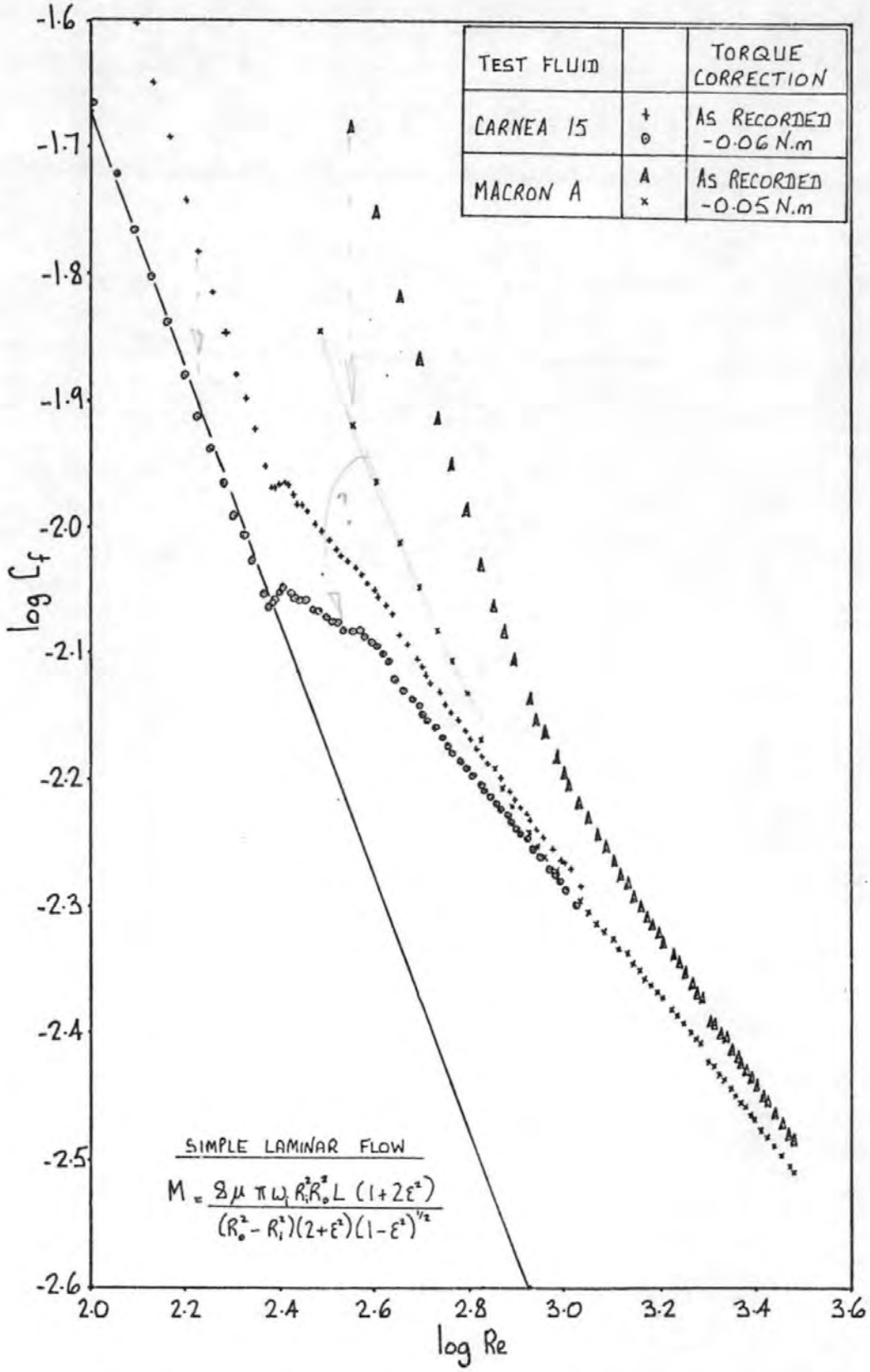

FIG. 122 THE ELIMINATION OF THE EFFECTS OF BEARING FRICTION FROM THE DERIVED FRICTION COEFFICIENT CHARACTERISTICS: $R_i/R_o = 0.975$, $\varepsilon = 0.11$

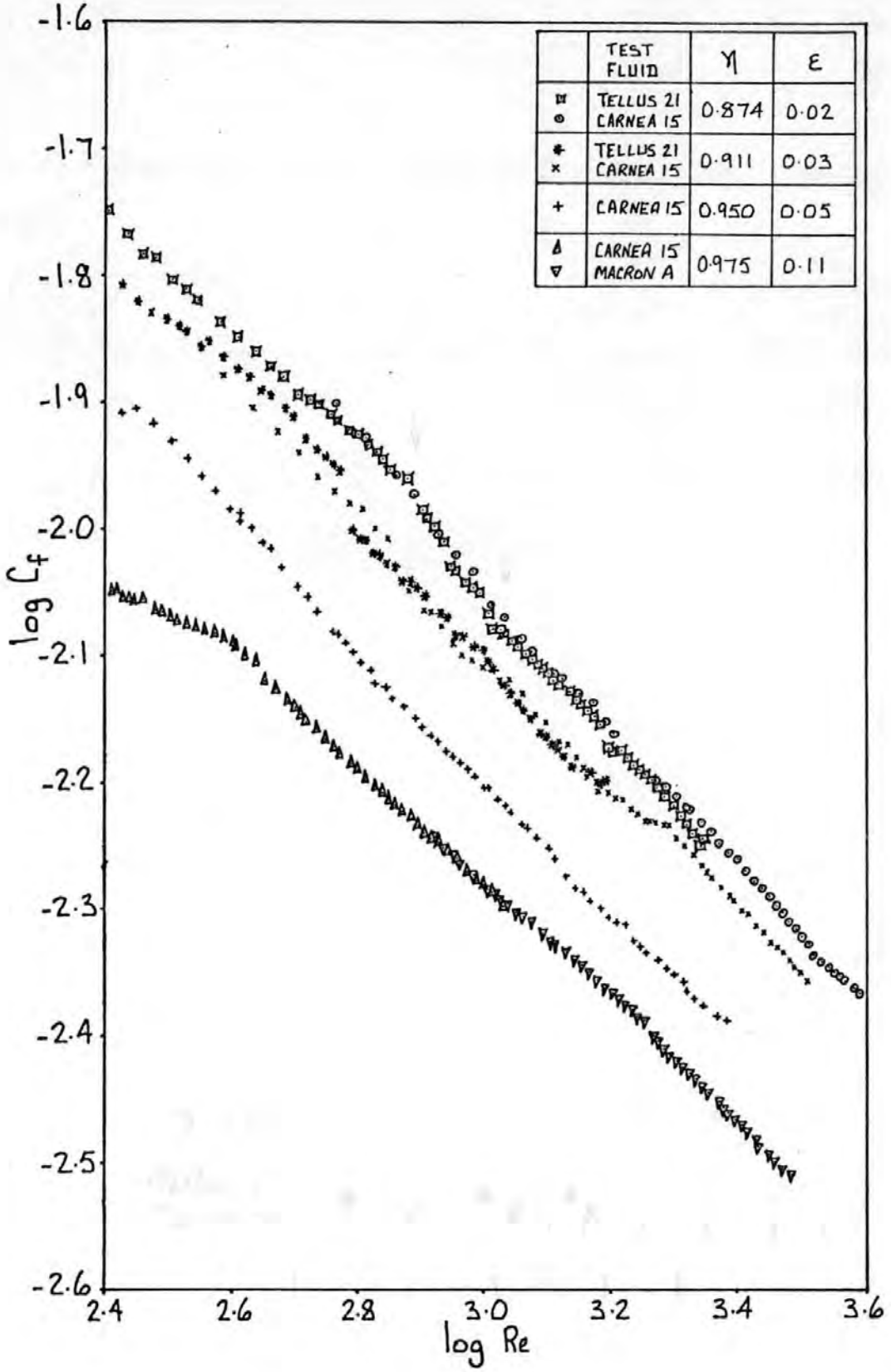

FIG. 123 CORRECTED FRICTION COEFFICIENT CHARACTERISTICS: $\varepsilon_{nom} = 0$

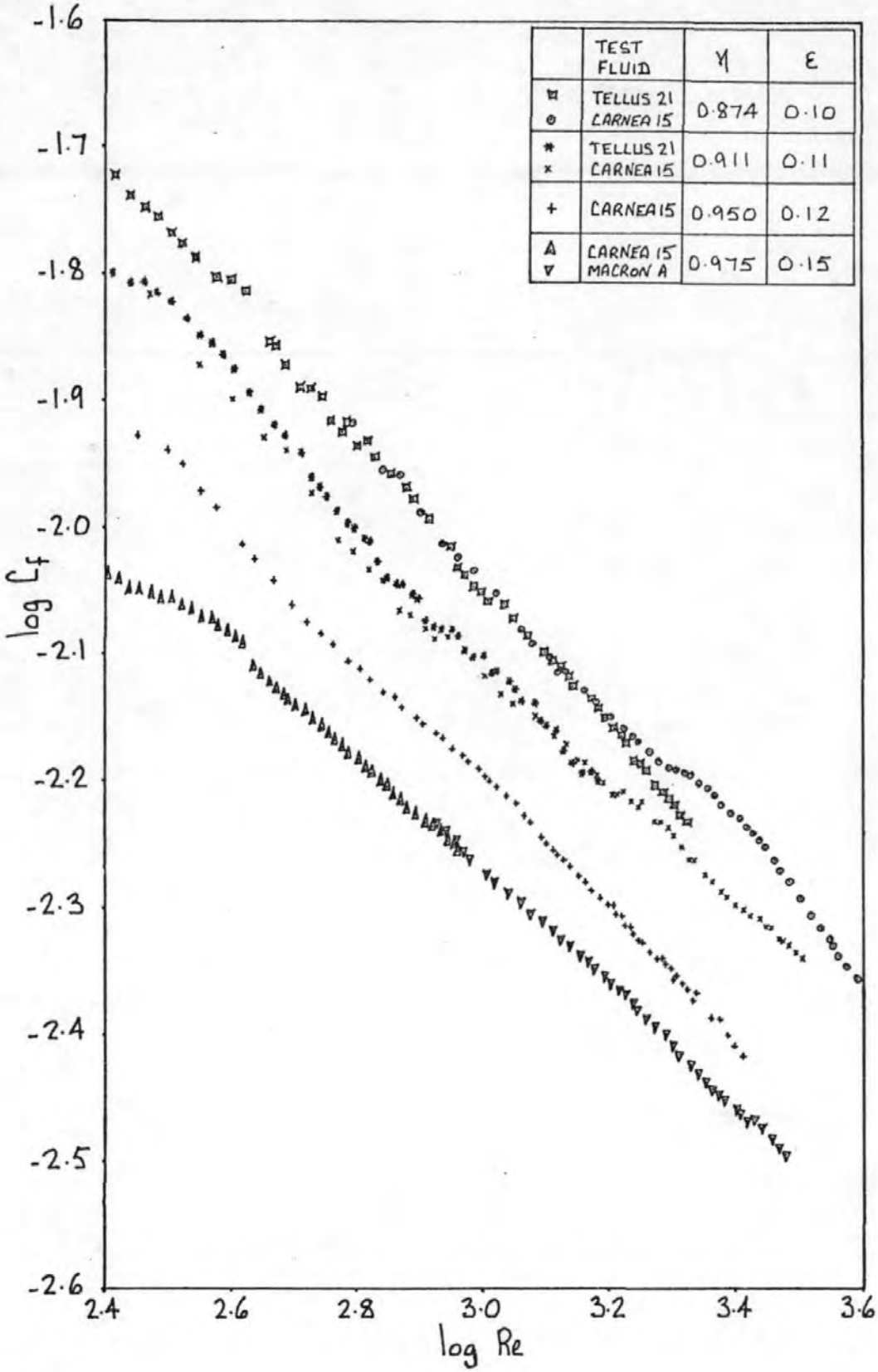

FIG. 124 CORRECTED FRICTION COEFFICIENT CHARACTERISTICS: $\varepsilon_{NOM} = 0.1$

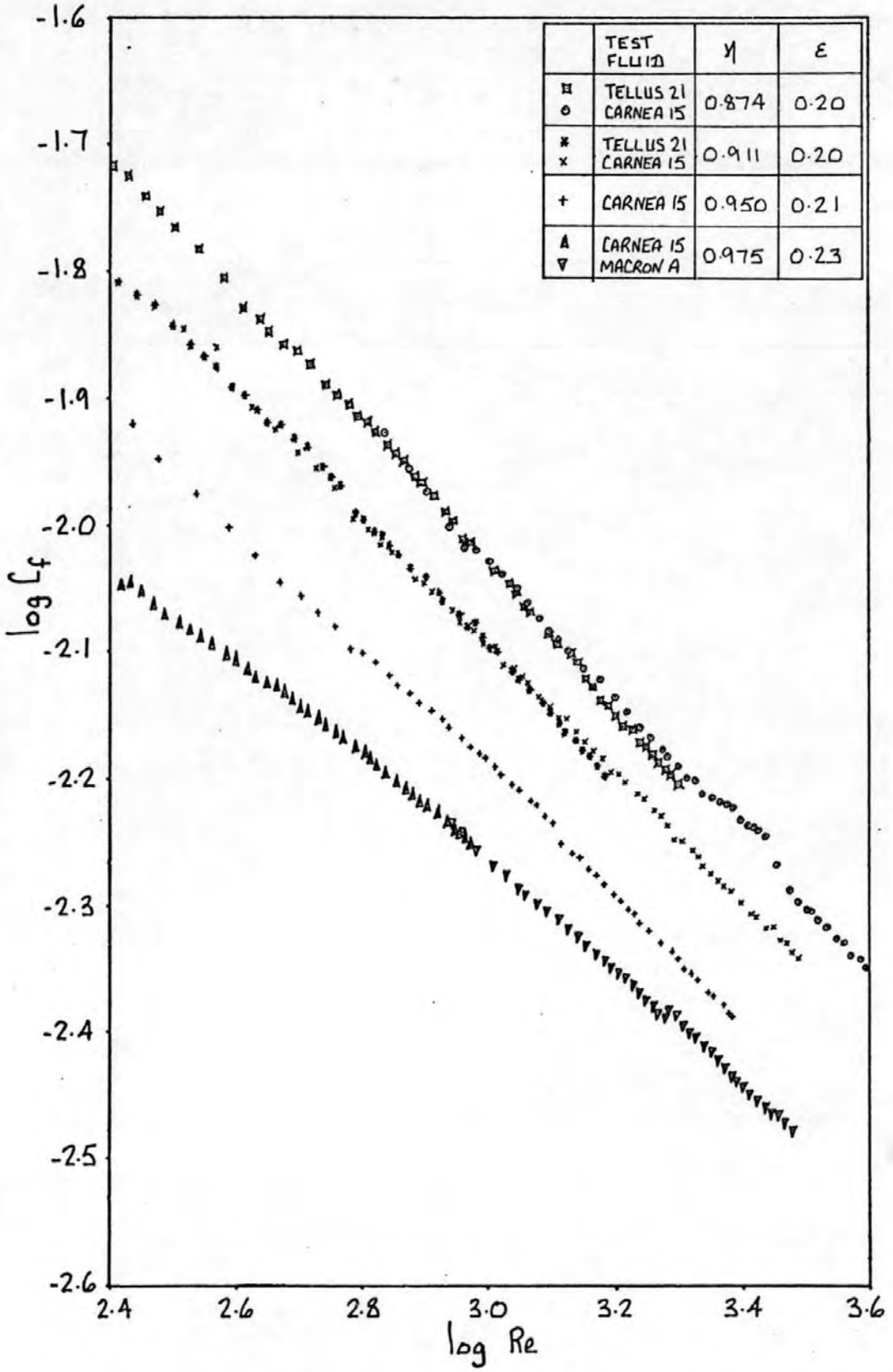

FIG. 125 CORRECTED FRICTION COEFFICIENT CHARACTERISTICS: $\varepsilon_{NOM} = 0.2$

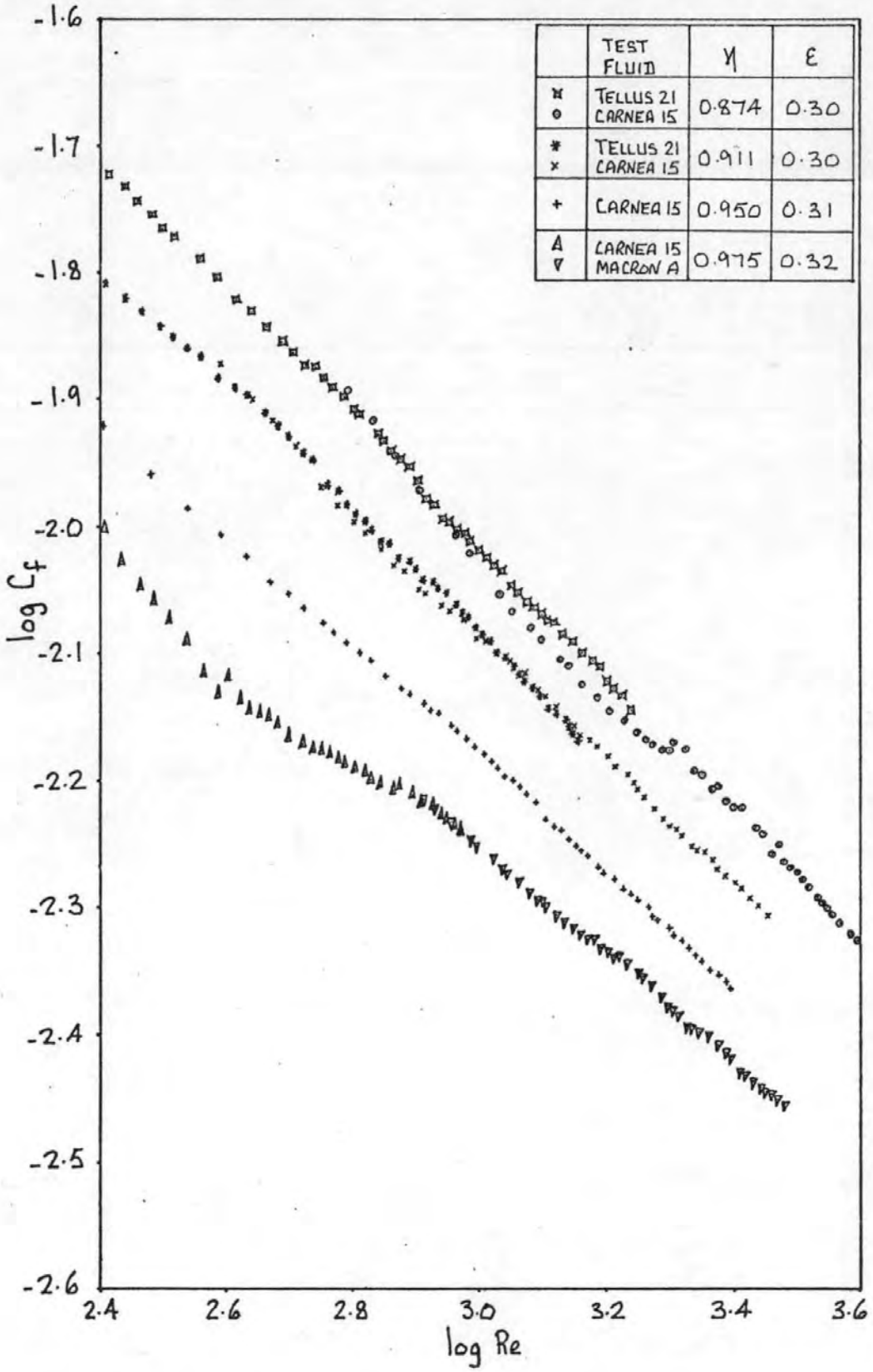

FIG. 126 CORRECTED FRICTION COEFFICIENT CHARACTERISTICS:
$\varepsilon_{NOM} = 0.3$

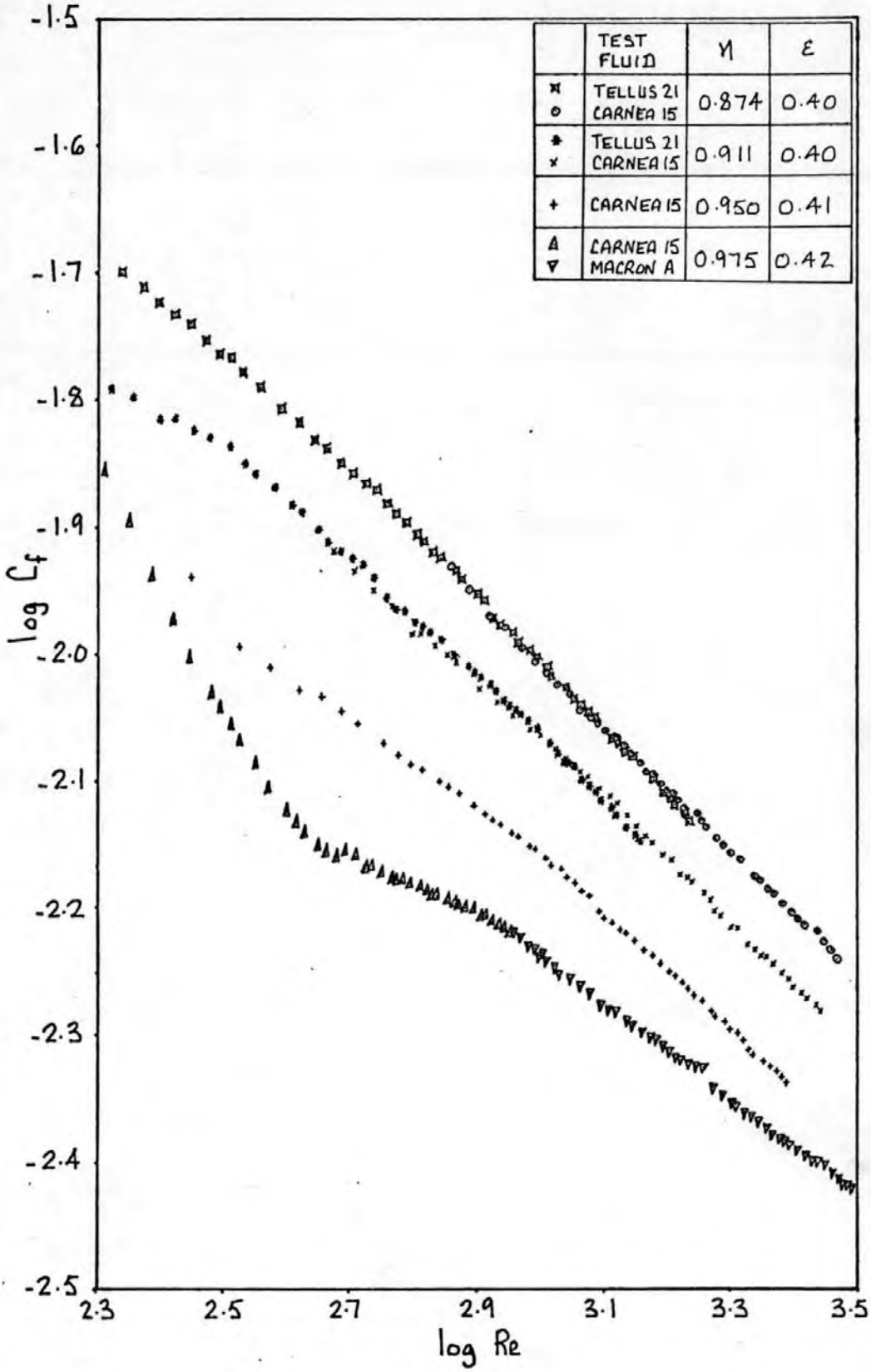

FIG. 127 CORRECTED FRICTION COEFFICIENT CHARACTERISTICS:
$\varepsilon_{NOM} = 0.4$

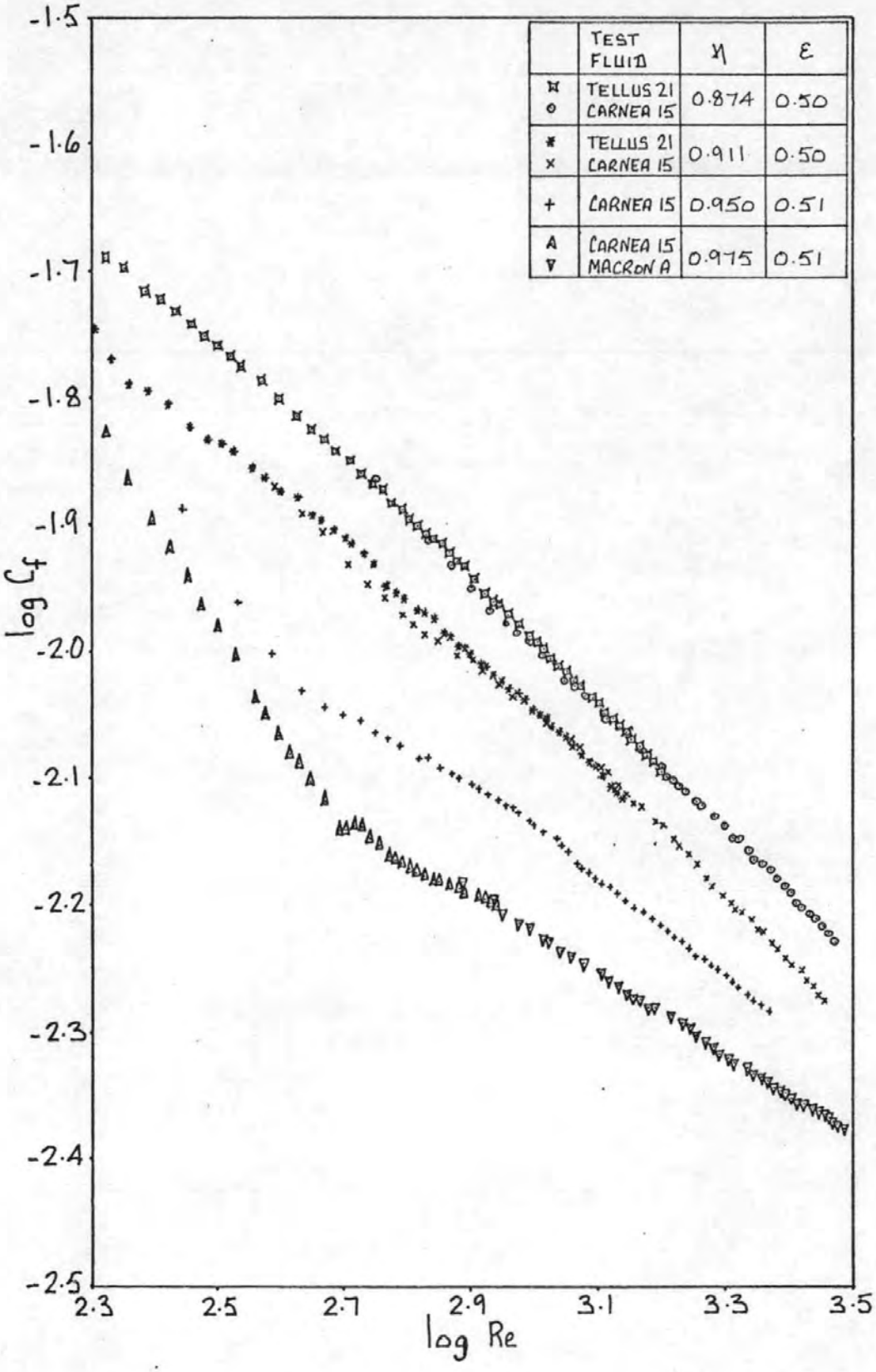

FIG.128 CORRECTED FRICTION COEFFICIENT CHARACTERISTICS: $\varepsilon_{Nom} = 0.5$

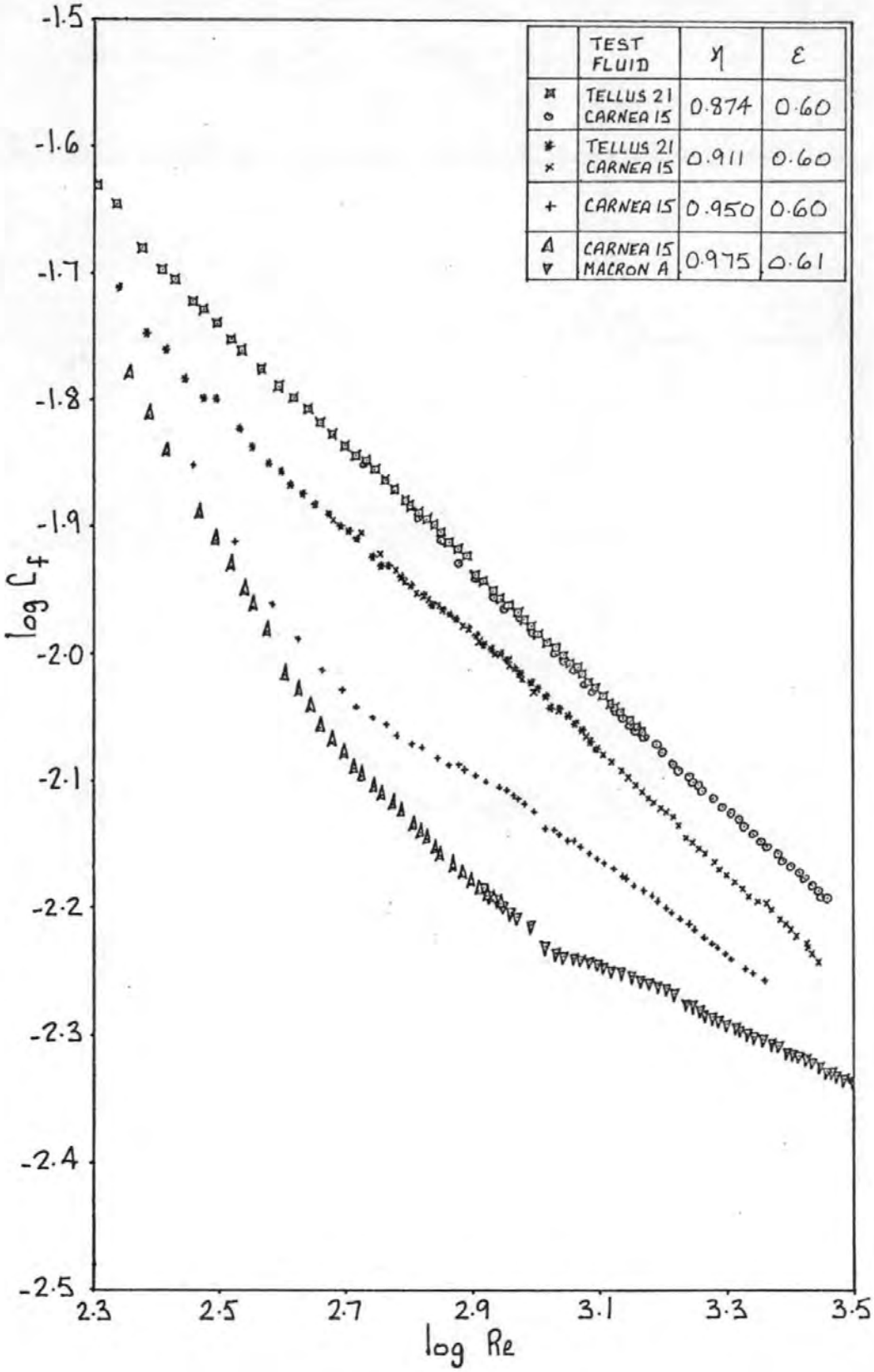

FIG. 129 CORRECTED FRICTION COEFFICIENT CHARACTERISTICS: $\varepsilon_{NOM} = 0.6$

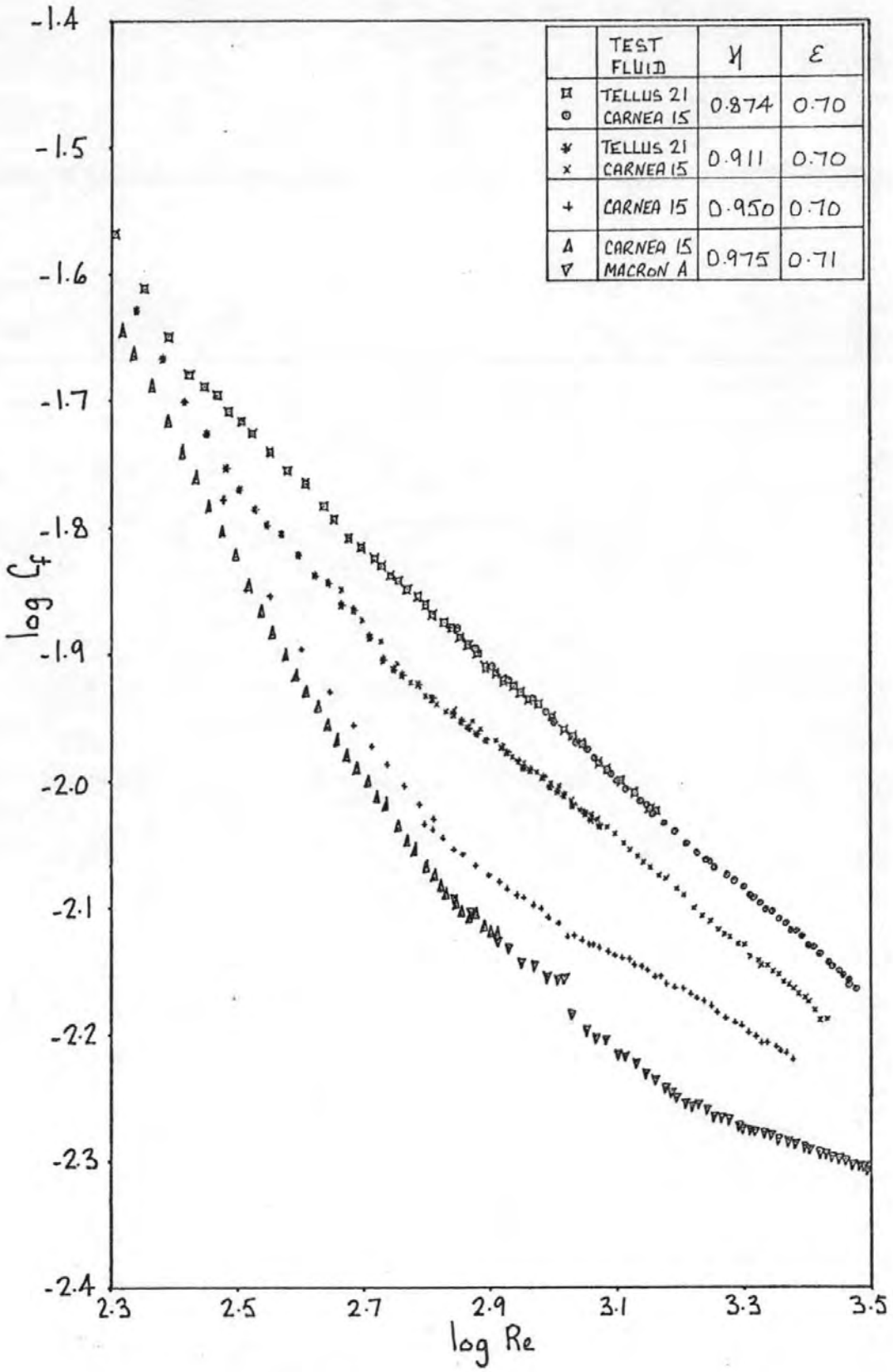

FIG. 13D CORRECTED FRICTION COEFFICIENT CHARACTERISTICS:
$\varepsilon_{NOM} = 0.7$

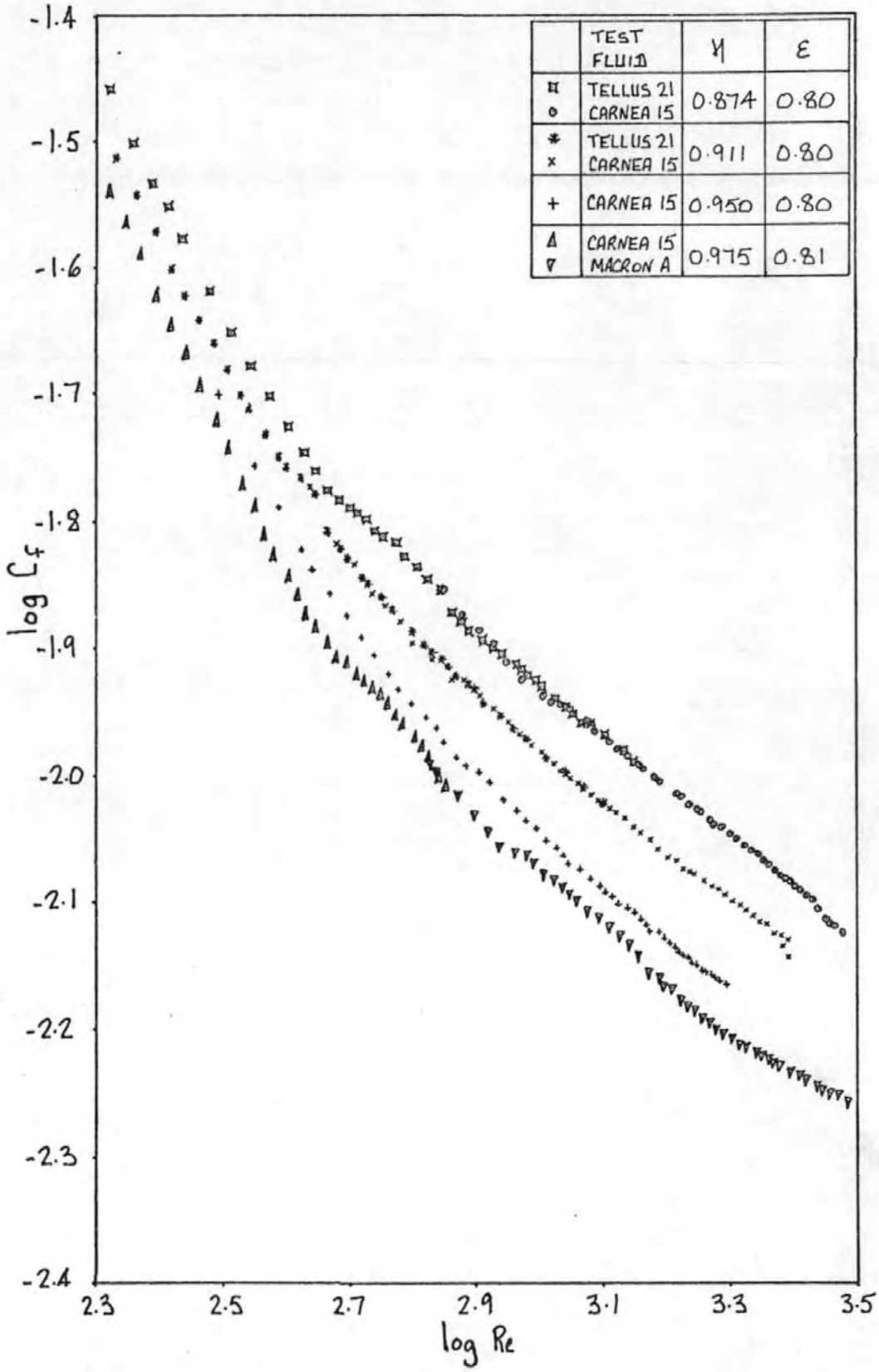

FIG. 131 CORRECTED FRICTION COEFFICIENT CHARACTERISTICS: $\varepsilon_{NOM} = 0.8$

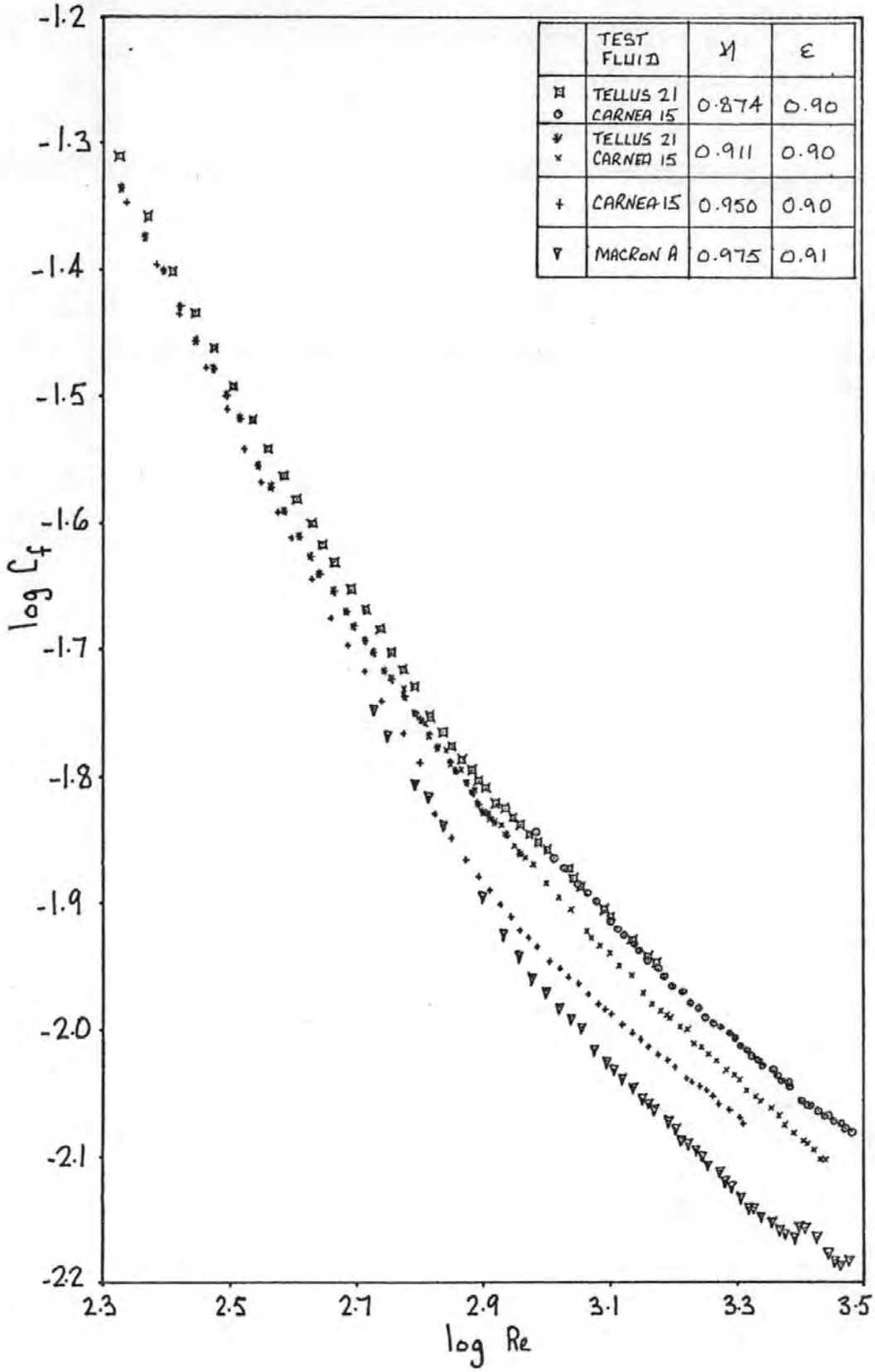

FIG. 132 CORRECTED FRICTION COEFFICIENT CHARACTERISTICS:
$\varepsilon_{NOM} = 0.9$

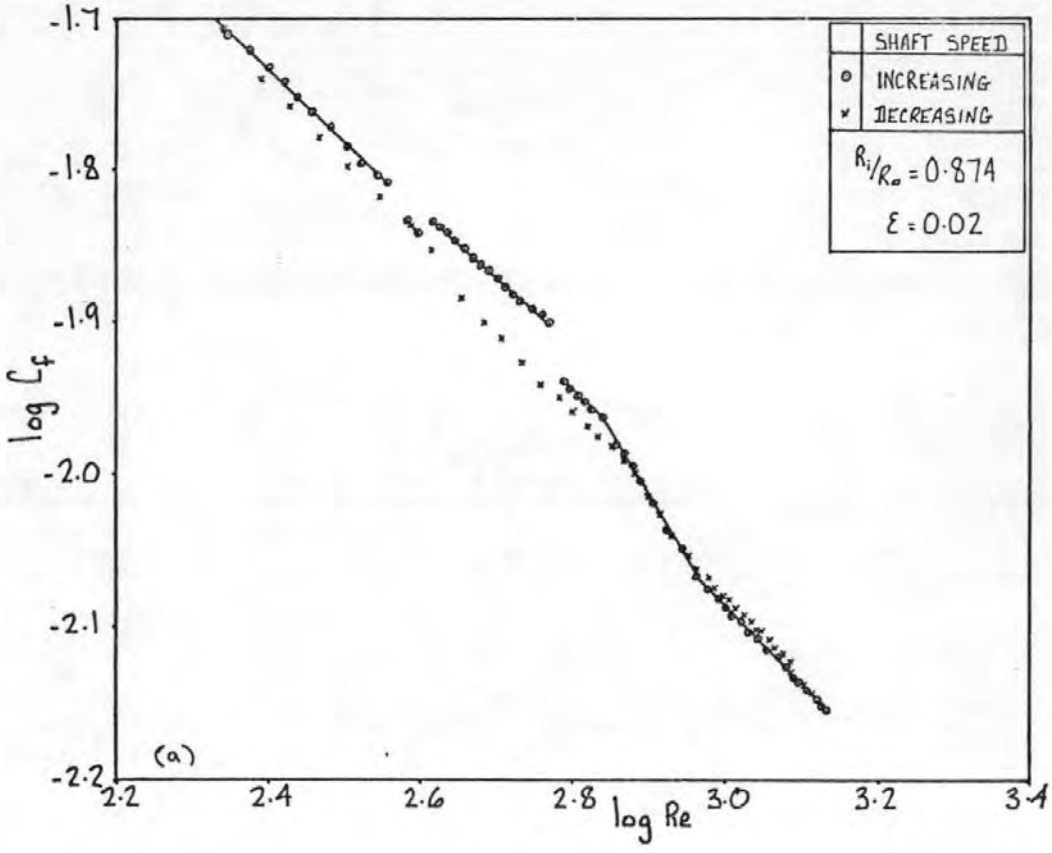

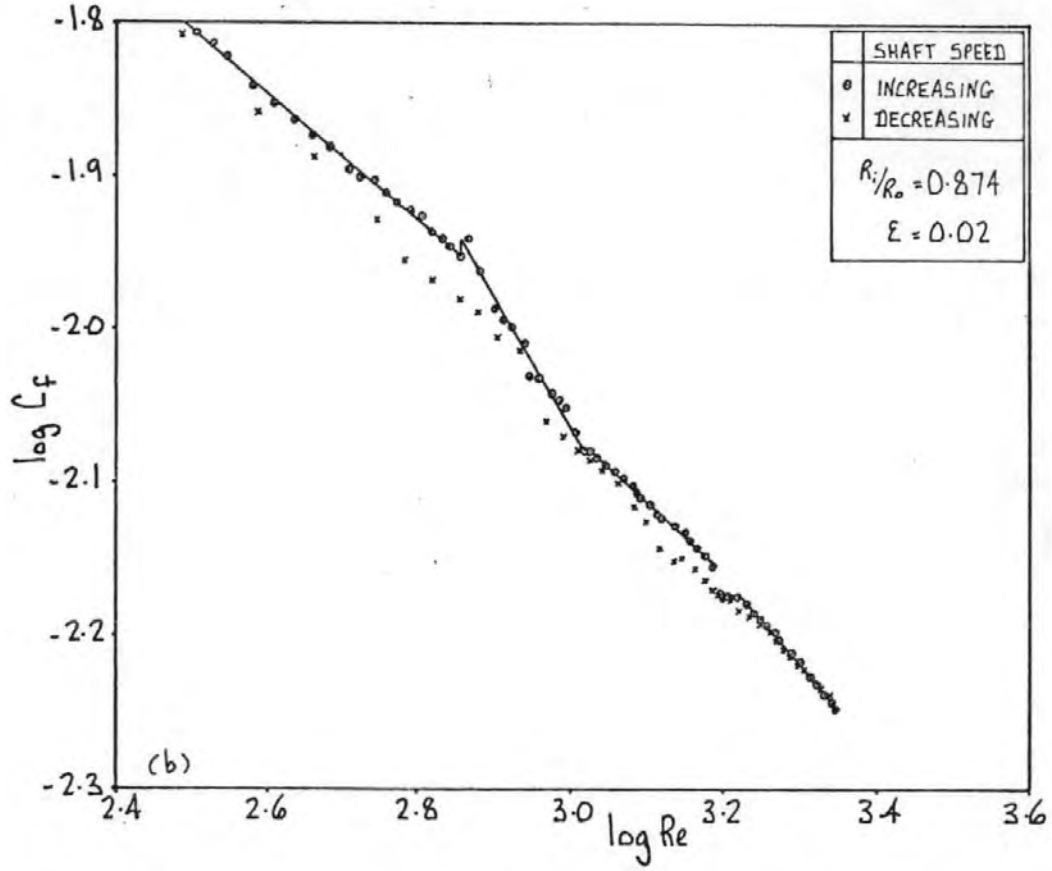

FIG. 133 THE INFLUENCE OF THE VARIATION OF SHAFT SPEED ON THE CORRECTED FRICTION COEFFICIENT CHARACTERISTICS: (a) USING "MIXTURE A", (b) USING TELLUS 21

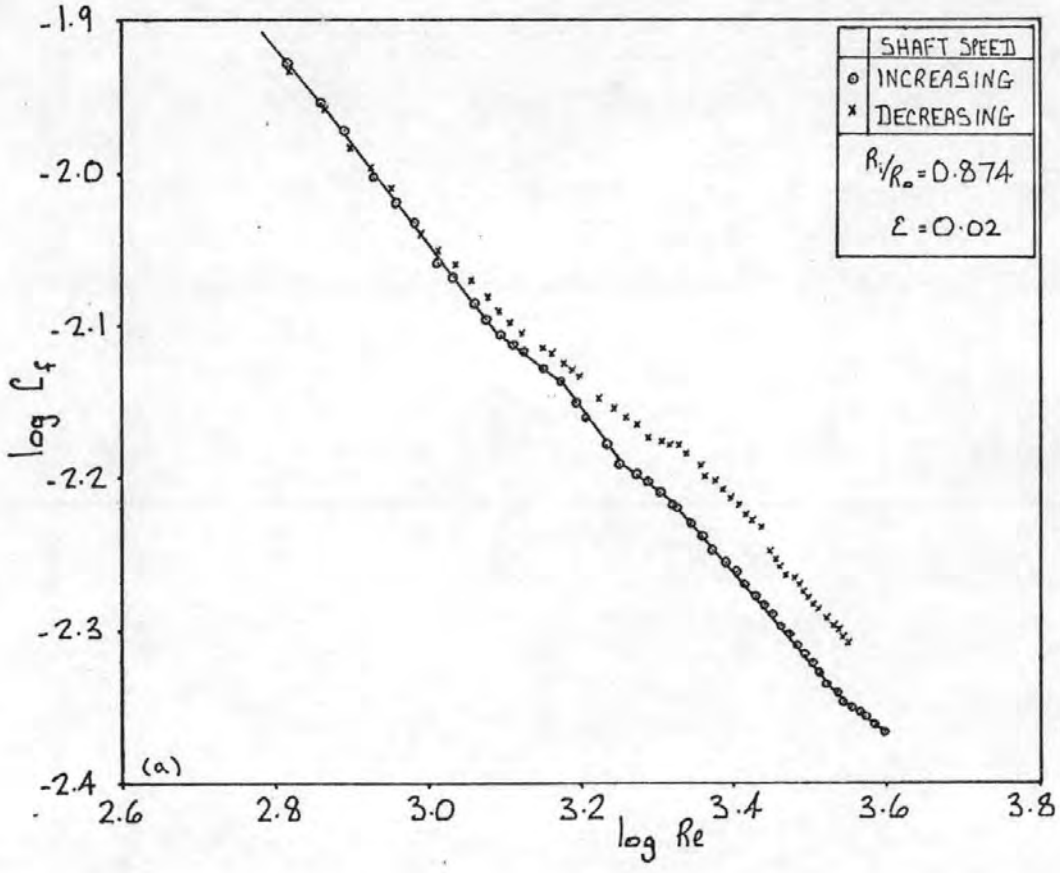

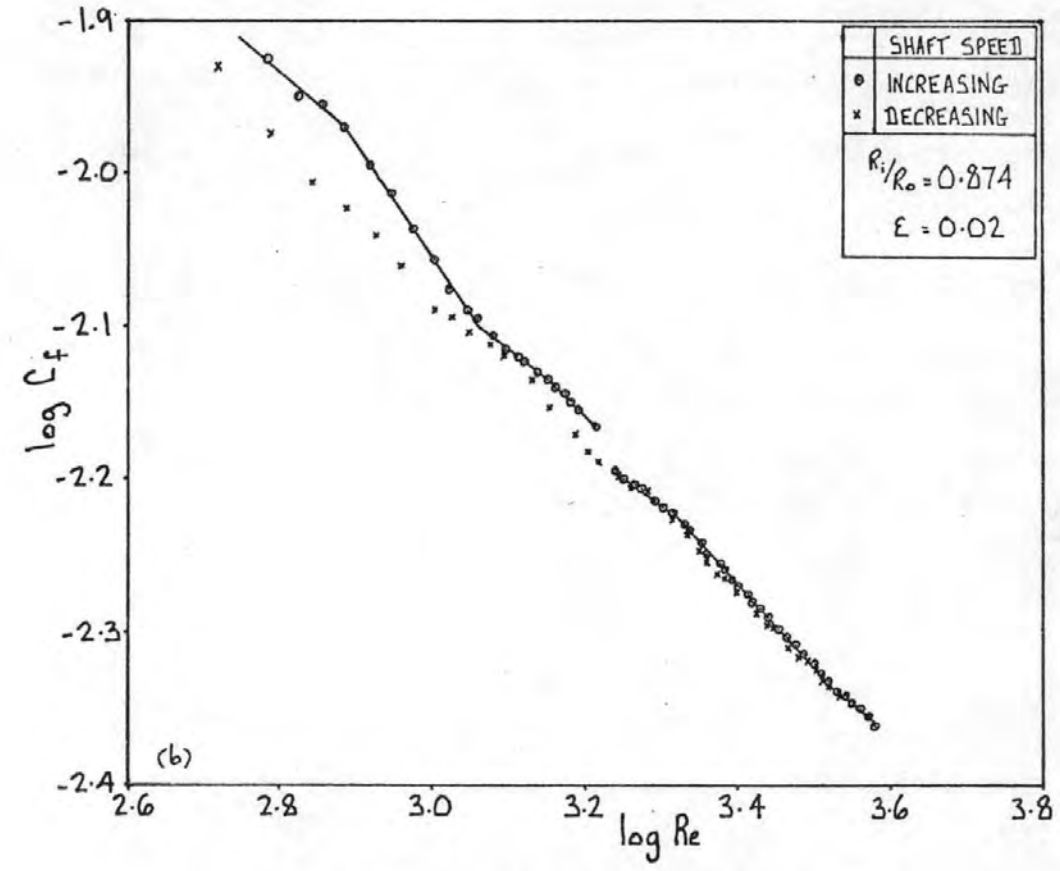

FIG. 134 THE INFLUENCE OF THE VARIATION OF SHAFT SPEED ON THE CORRECTED FRICTION COEFFICIENT CHARACTERISTICS: RESULTS RECORDED USING CARNEA IS AND,
(a) DECREASING THEN INCREASING SHAFT SPEED
(b) INCREASING THEN DECREASING SHAFT SPEED

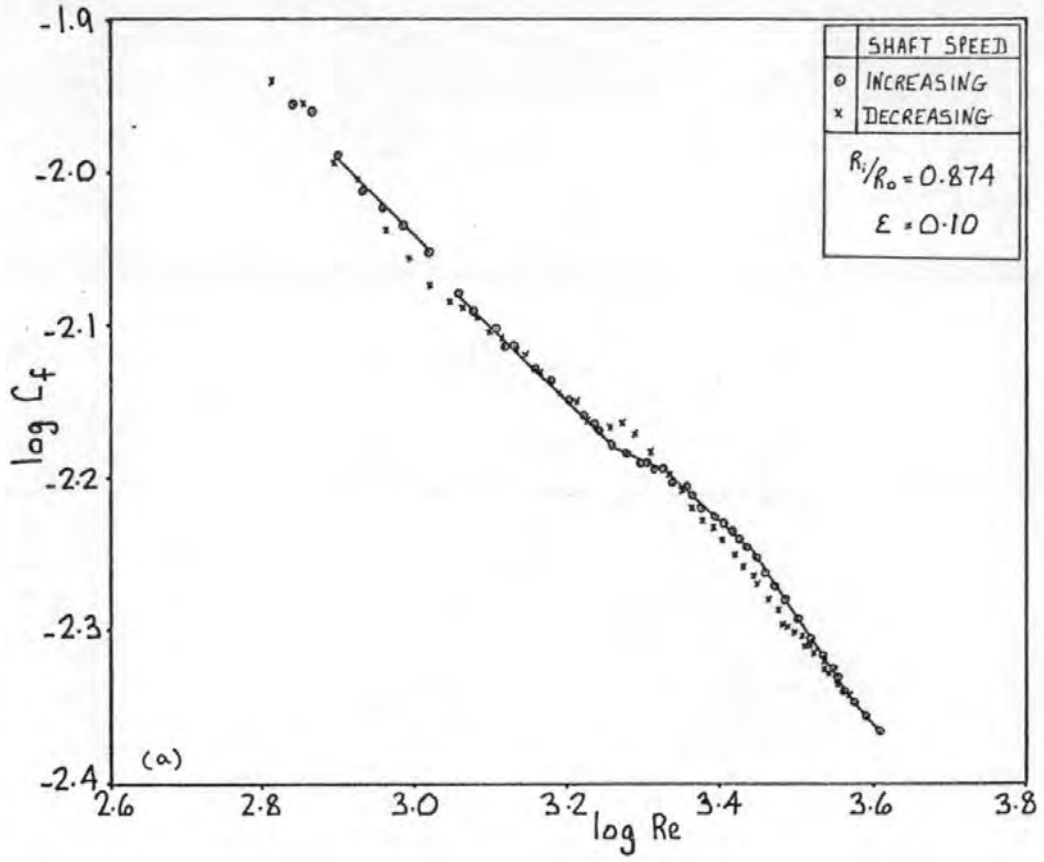

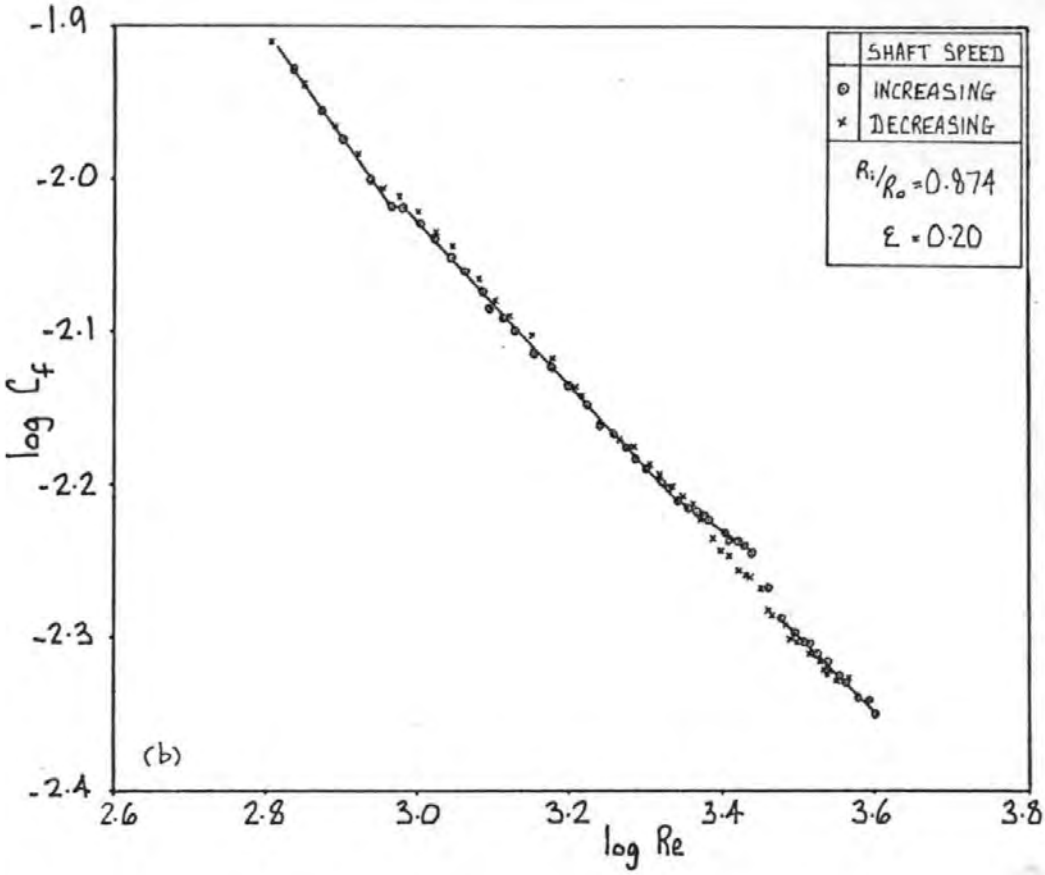

FIG. 135 THE INFLUENCE OF THE VARIATION OF SHAFT SPEED ON THE CORRECTED FRICTION COEFFICIENT CHARACTERISTICS: CARNEA 15

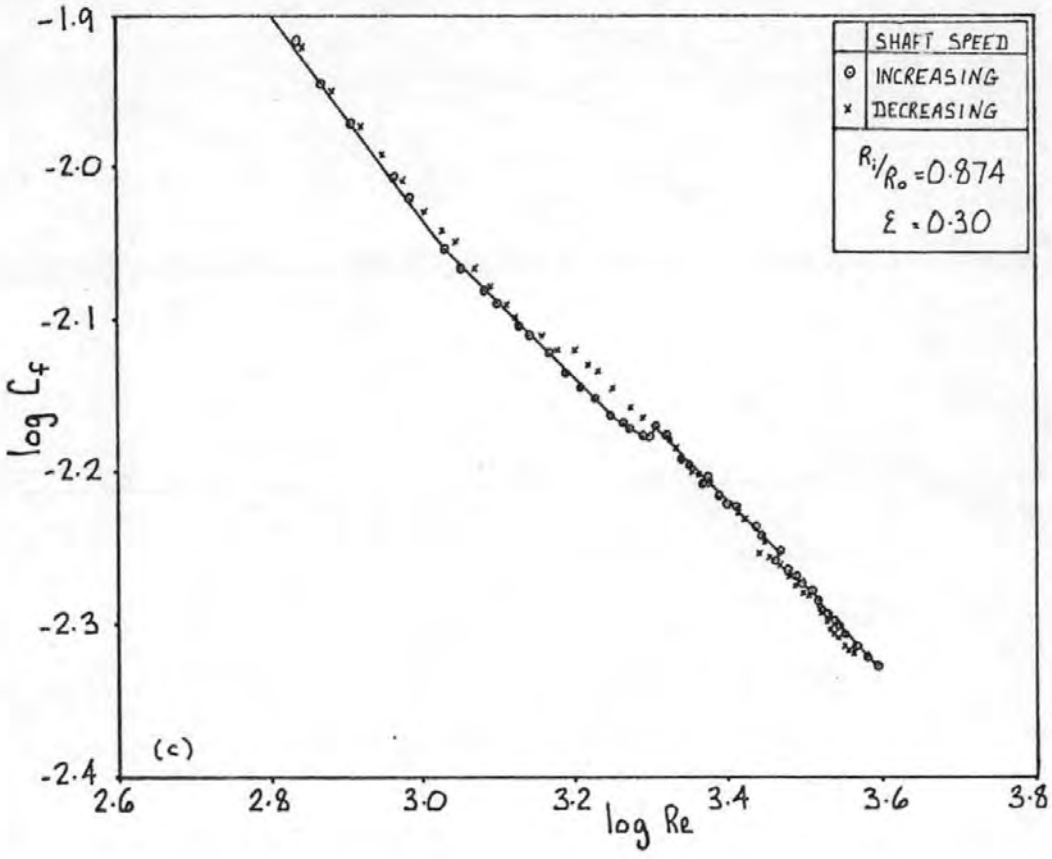

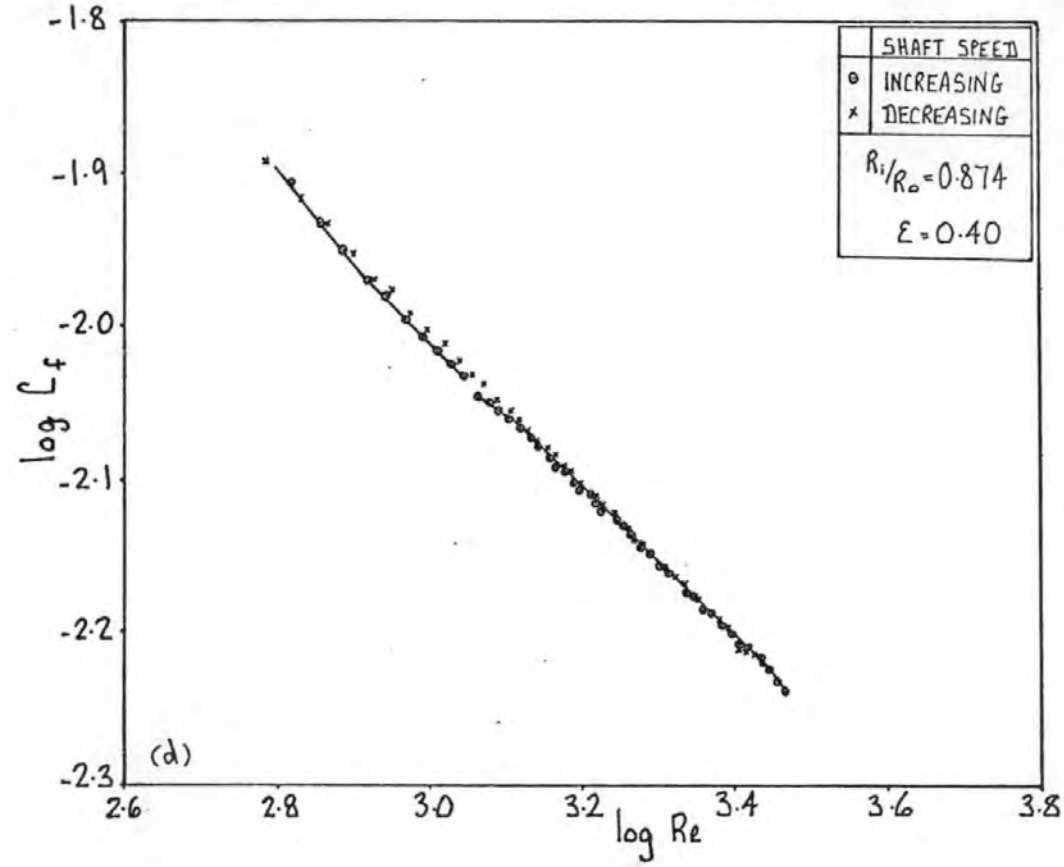

FIG. 135 THE INFLUENCE OF THE VARIATION OF SHAFT SPEED ON THE CORRECTED FRICTION COEFFICIENT CHARACTERISTICS: LARNEA 15

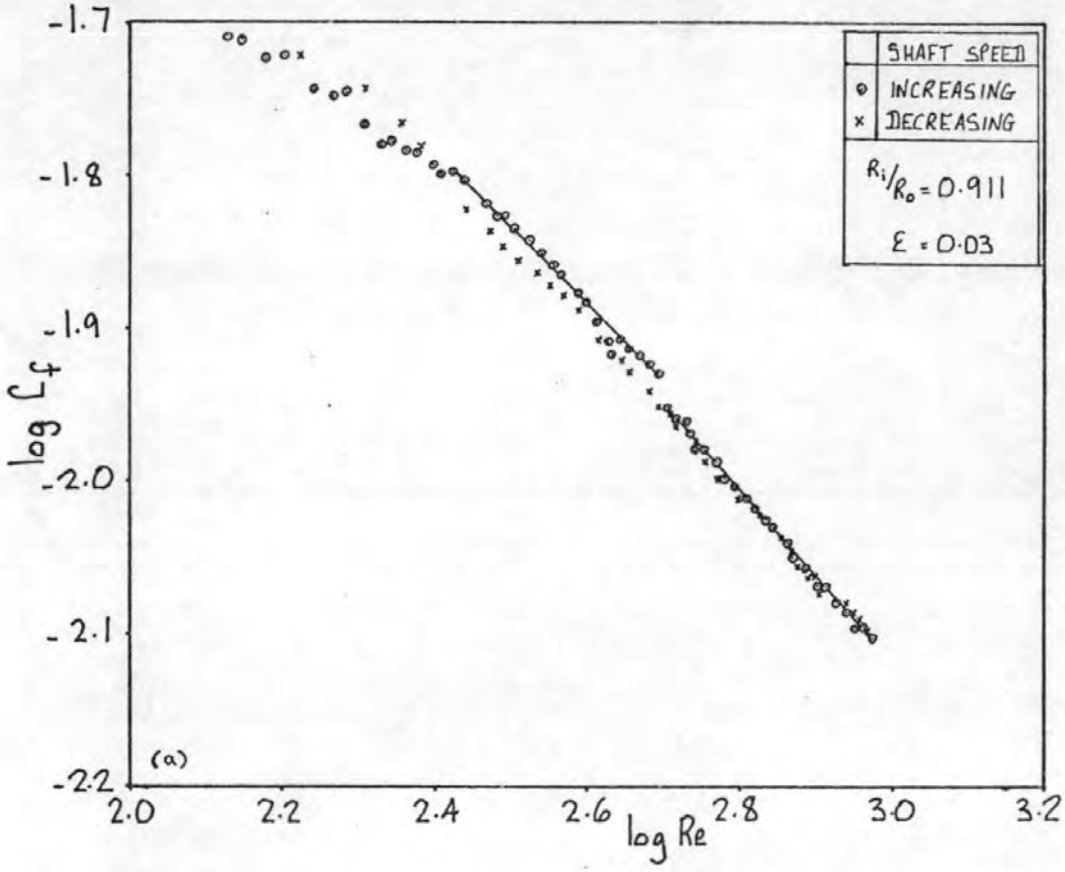

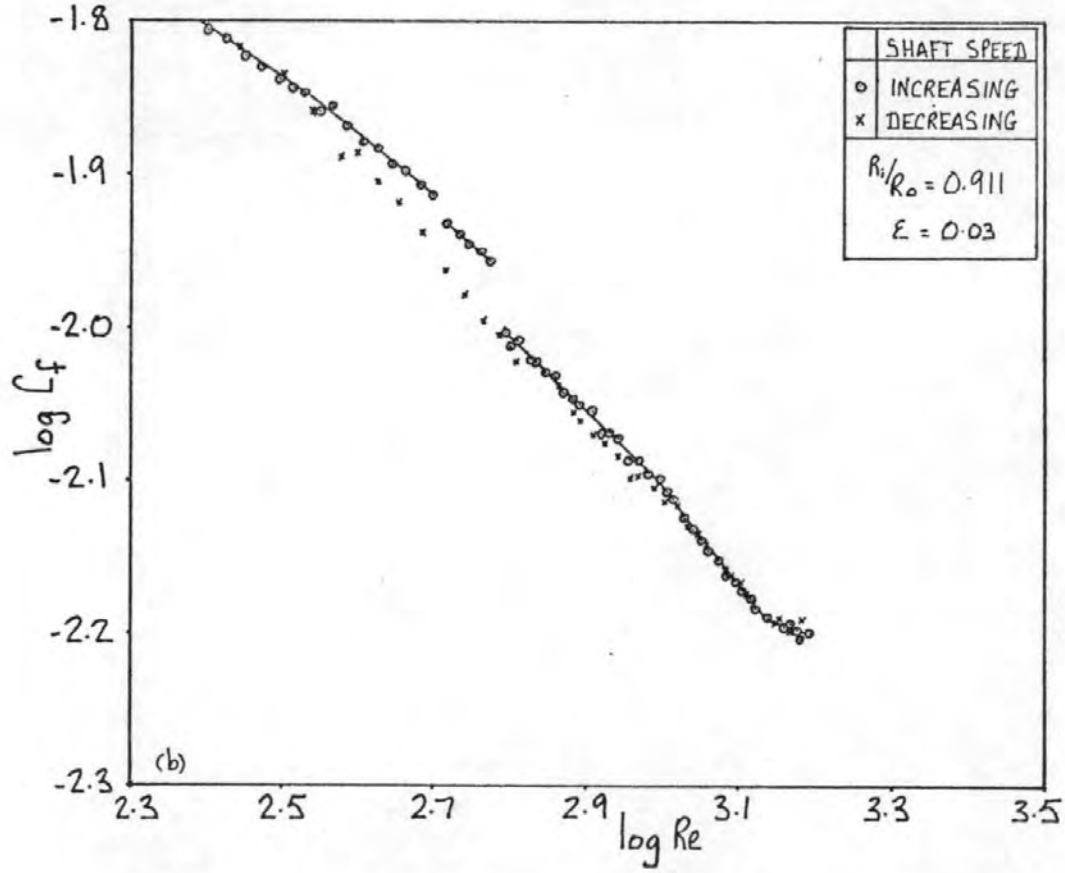

FIG. 136 THE INFLUENCE OF THE VARIATION OF SHAFT SPEED ON THE CORRECTED FRICTION COEFFICIENT CHARACTERISTICS: (a) USING "MIXTURE A", (b) USING TELLUS 21

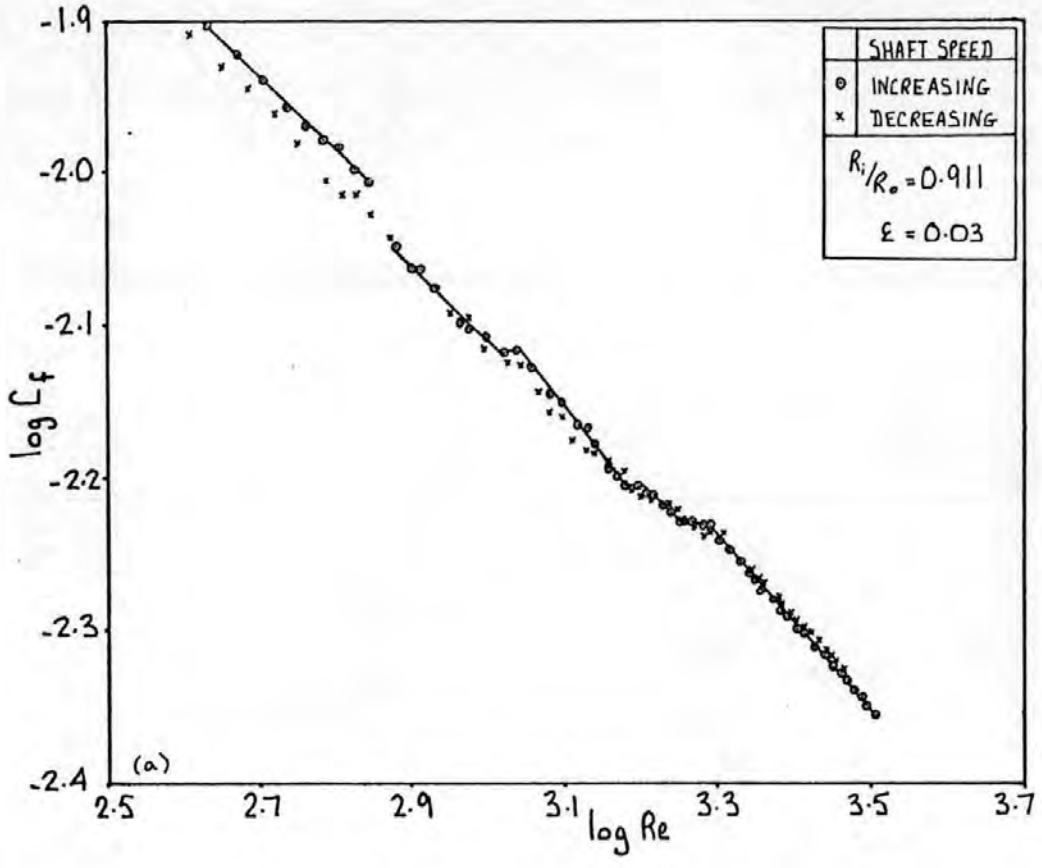

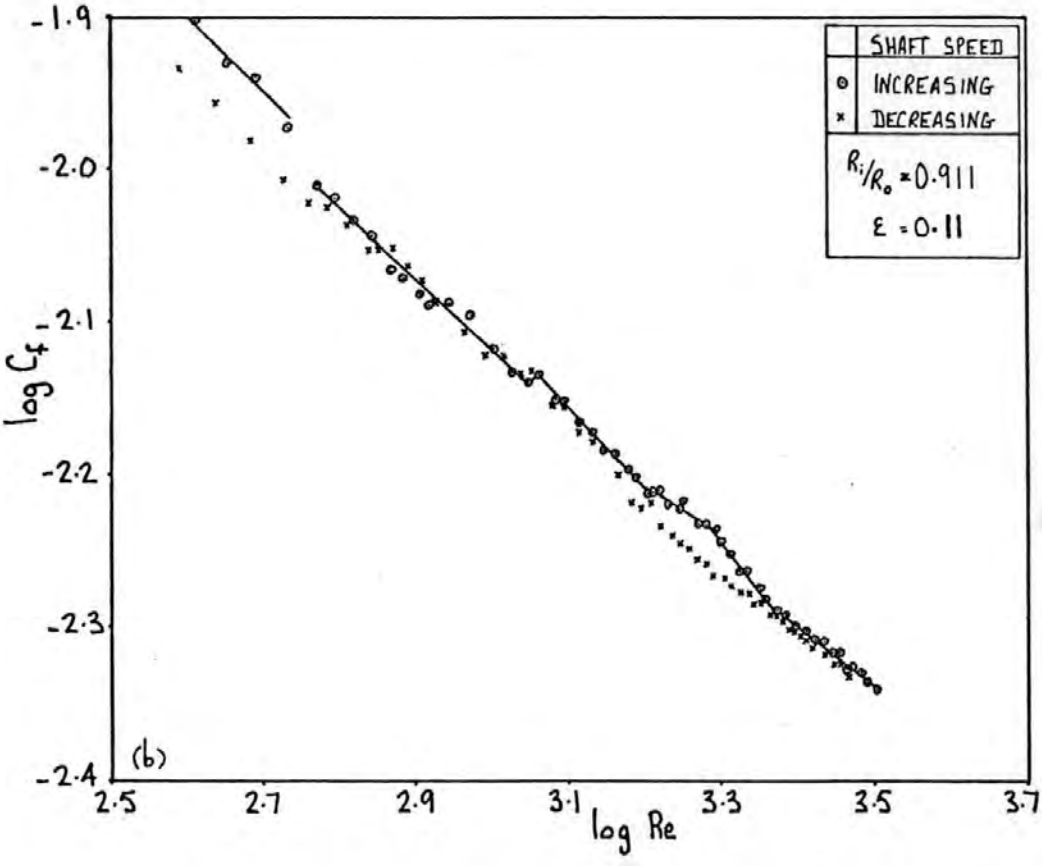

FIG. 137 THE INFLUENCE OF THE VARIATION OF SHAFT SPEED ON THE CORRECTED FRICTION COEFFICIENT CHARACTERISTICS: CARNEA 15

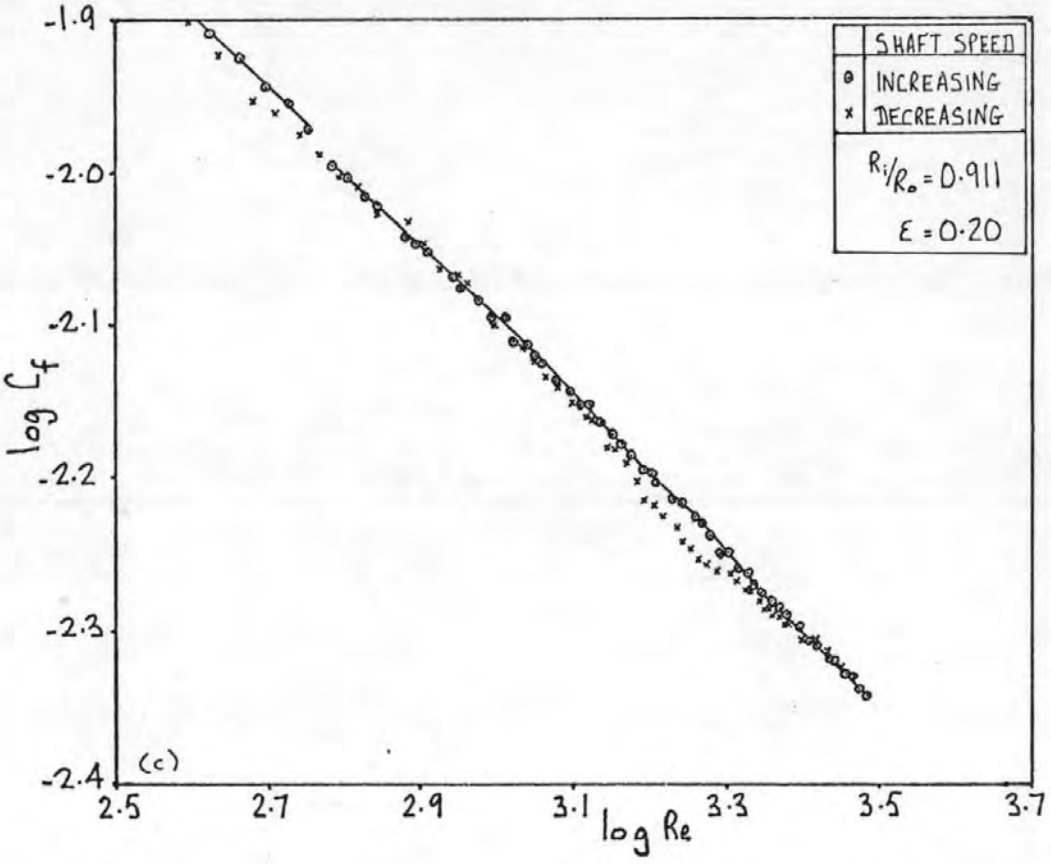

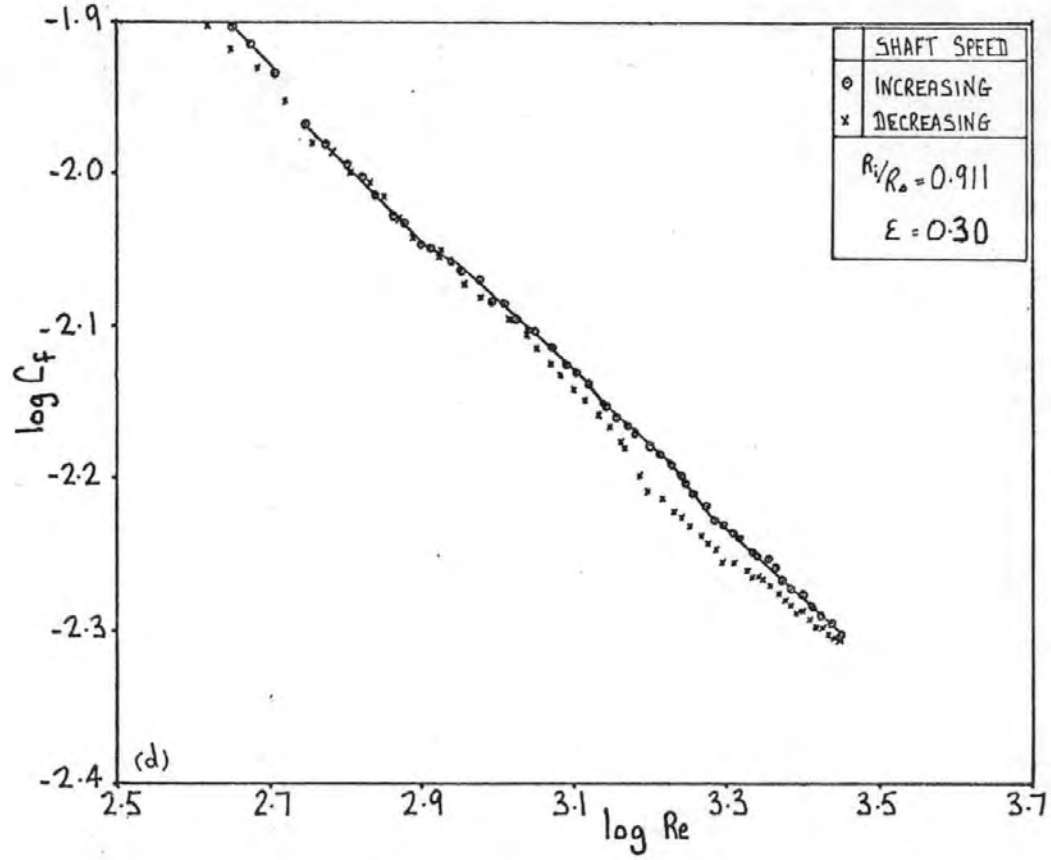

FIG. 137 THE INFLUENCE OF THE VARIATION OF SHAFT SPEED ON THE CORRECTED FRICTION COEFFICIENT CHARACTERISTICS: CARNEA 15

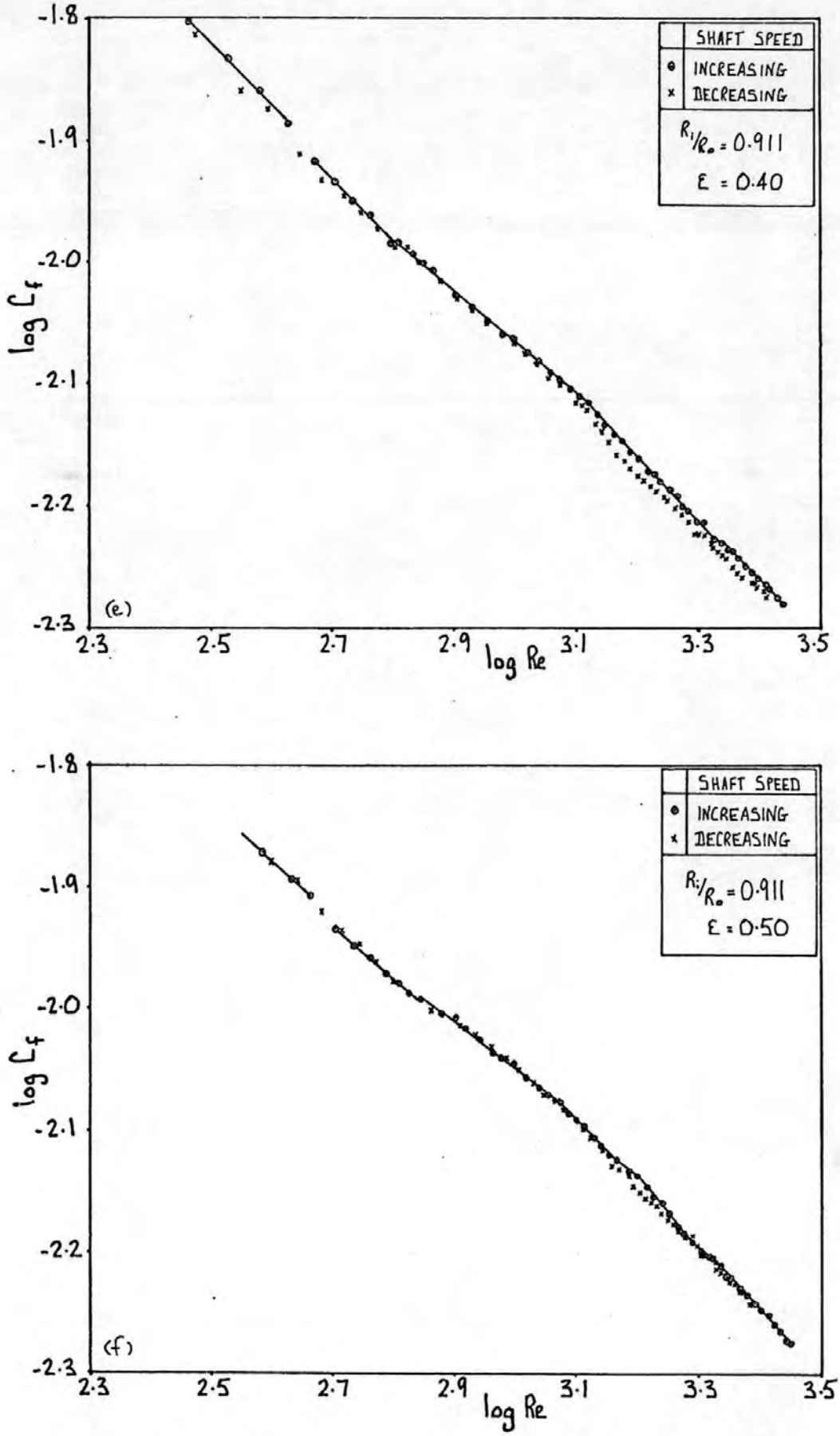

FIG. 137 THE INFLUENCE OF THE VARIATION OF SHAFT SPEED ON THE CORRECTED FRICTION COEFFICIENT CHARACTERISTICS: CARNEA 15

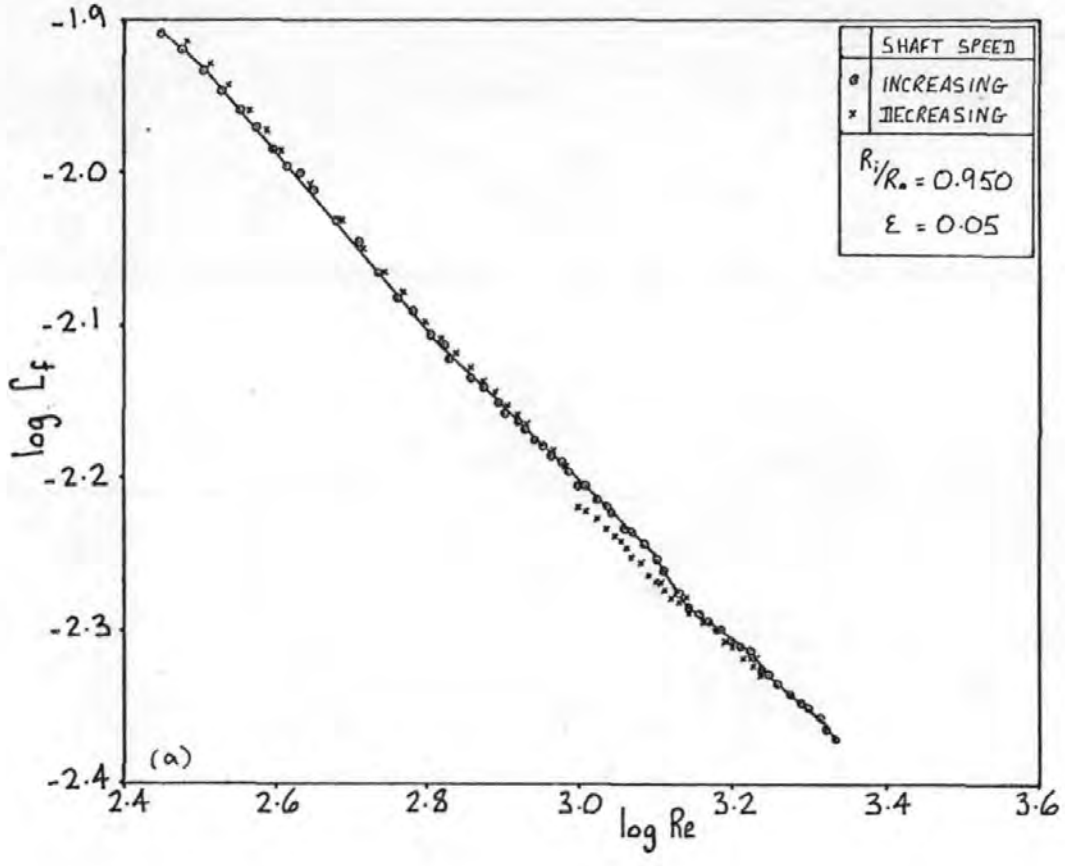

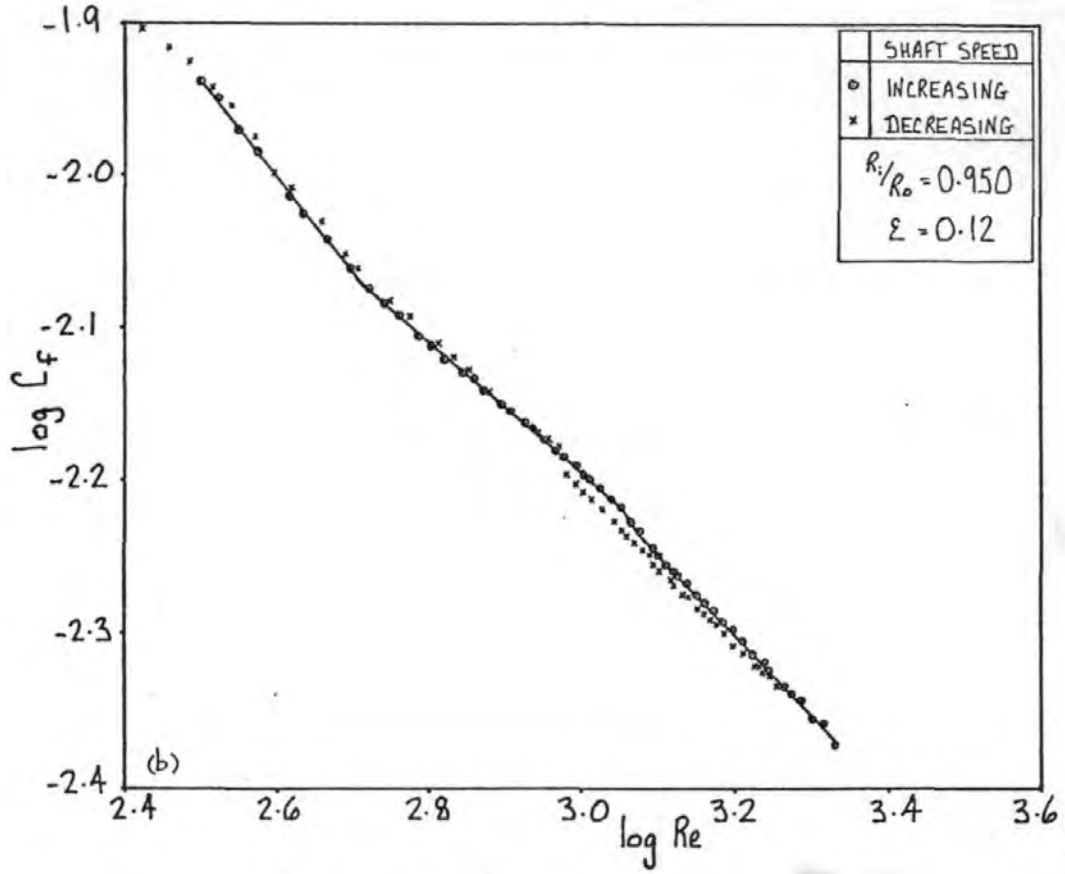

FIG. 138 THE INFLUENCE OF THE VARIATION OF SHAFT SPEED ON THE CORRECTED FRICTION COEFFICIENT CHARACTERISTICS: CARNEA 15

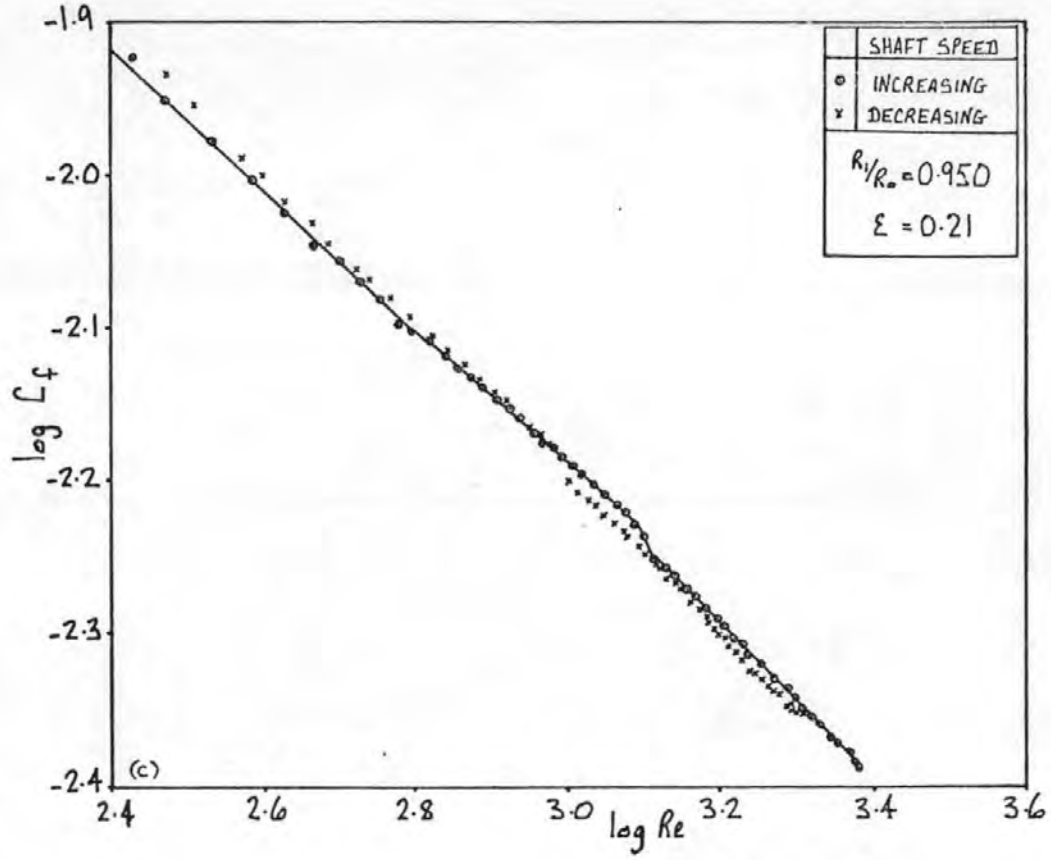

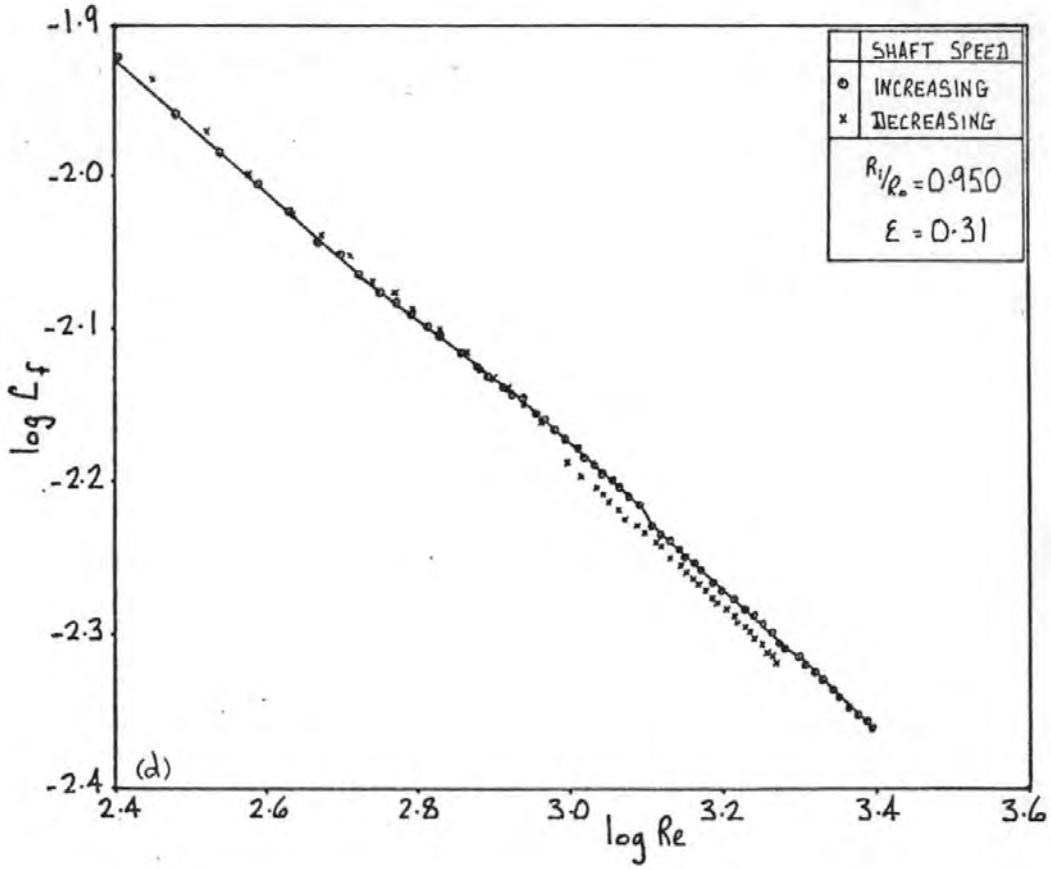

FIG. 138 THE INFLUENCE OF THE VARIATION OF SHAFT SPEED ON THE CORRECTED FRICTION COEFFICIENT CHARACTERISTICS: CARNEA 15

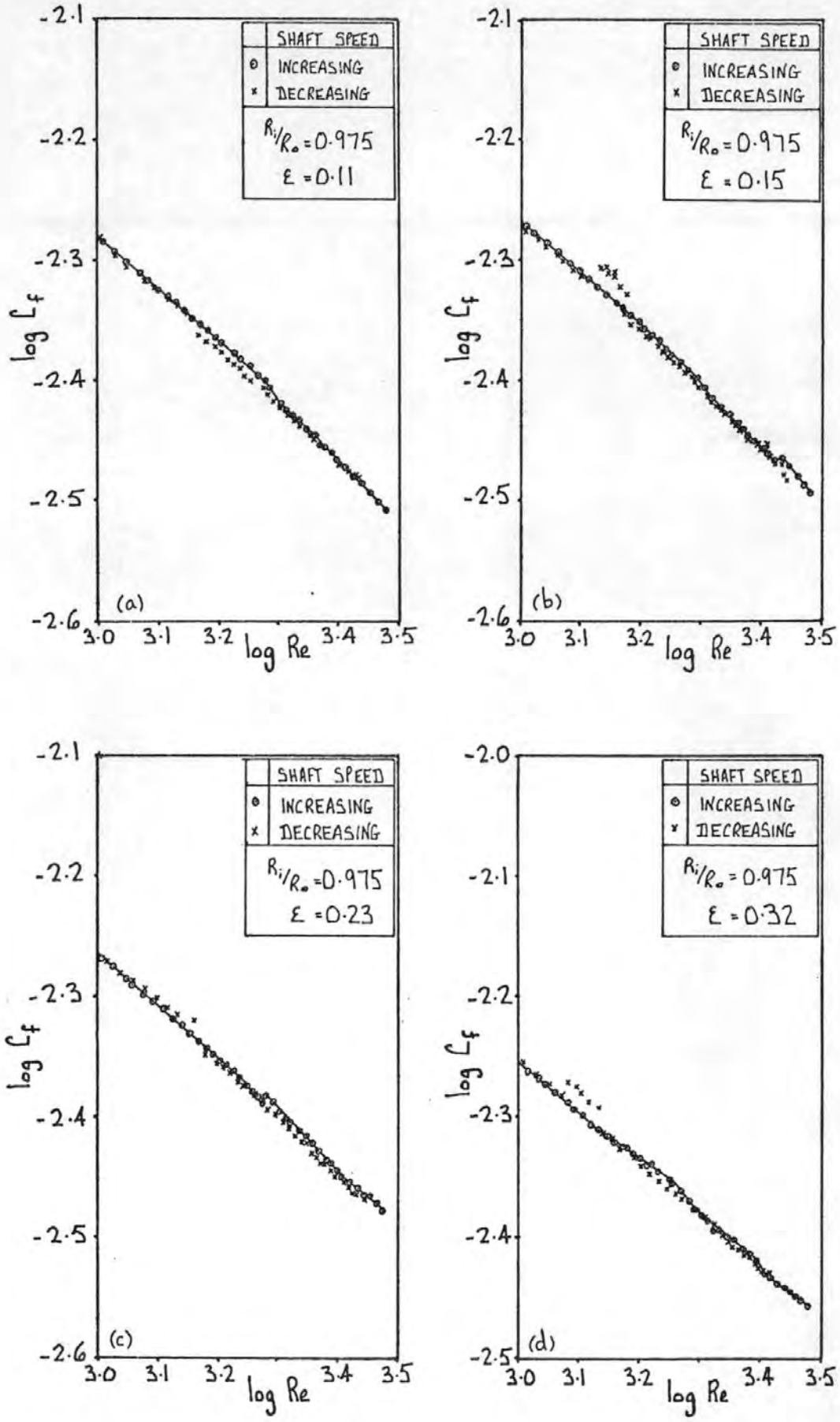

FIG. 139 THE INFLUENCE OF THE VARIATION OF SHAFT SPEED ON THE CORRECTED FRICTION COEFFICIENT CHARACTERISTICS: MACRON A

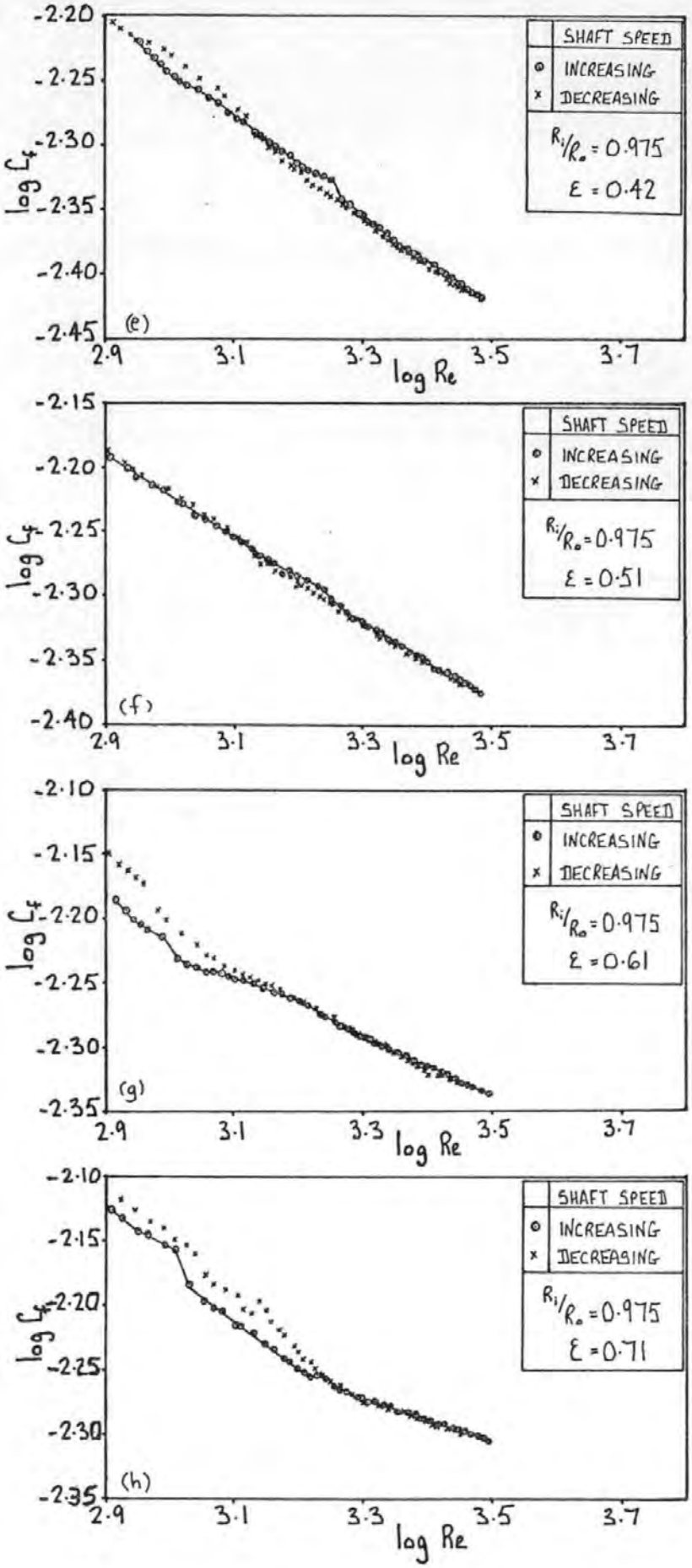

FIG. 139 THE INFLUENCE OF THE VARIATION OF SHAFT SPEED ON THE CORRECTED FRICTION COEFFICIENT CHARACTERISTICS: MACRON A

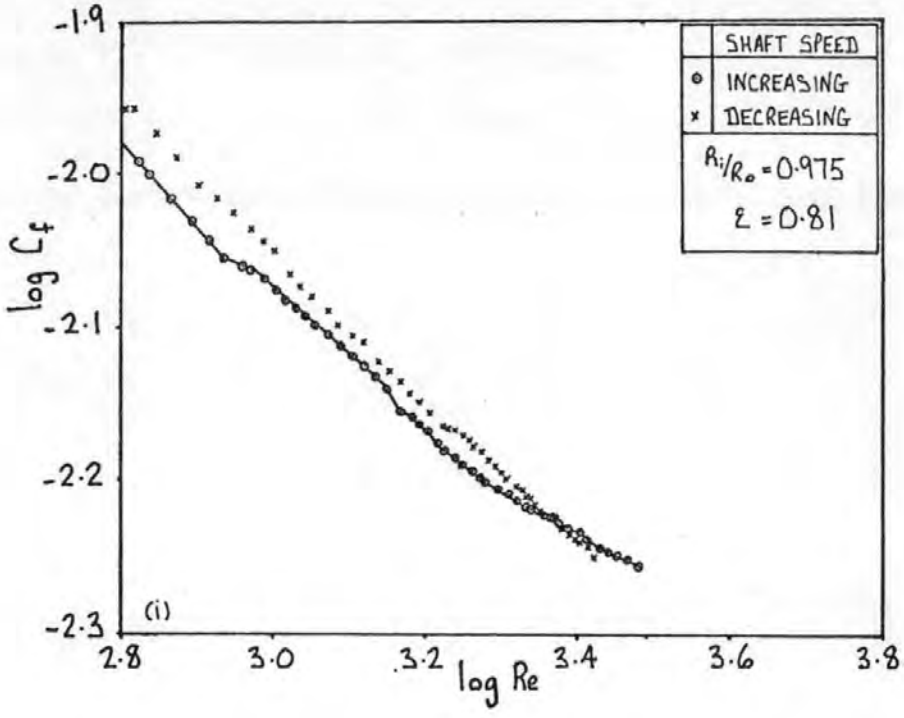

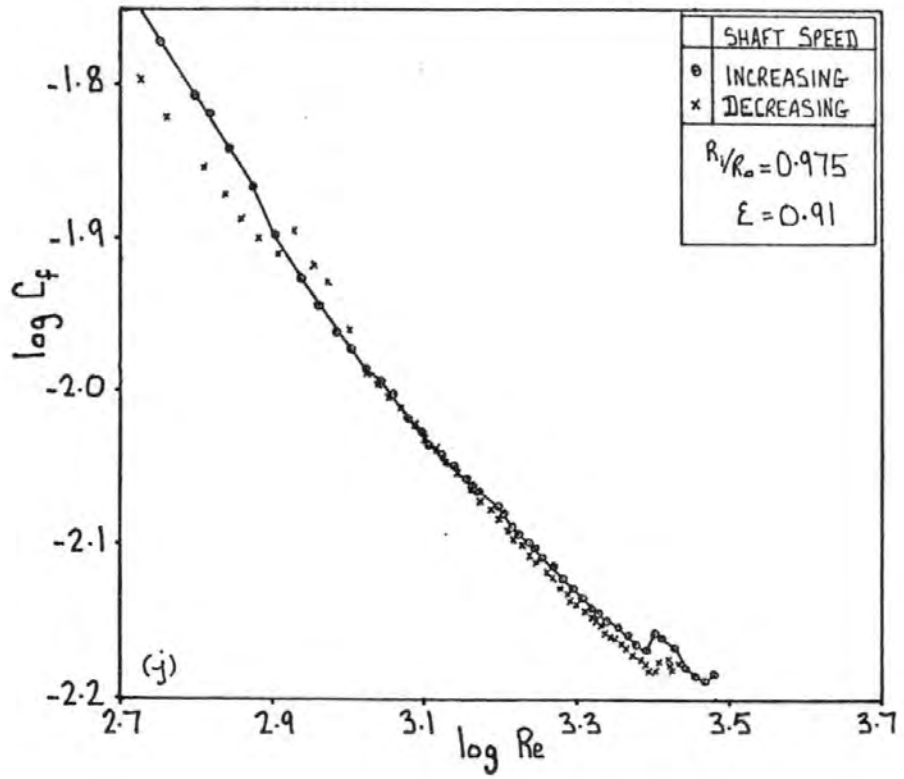

FIG. 139 THE INFLUENCE OF THE VARIATION OF SHAFT SPEED ON THE CORRECTED FRICTION COEFFICIENT CHARACTERISTICS: MACRON A

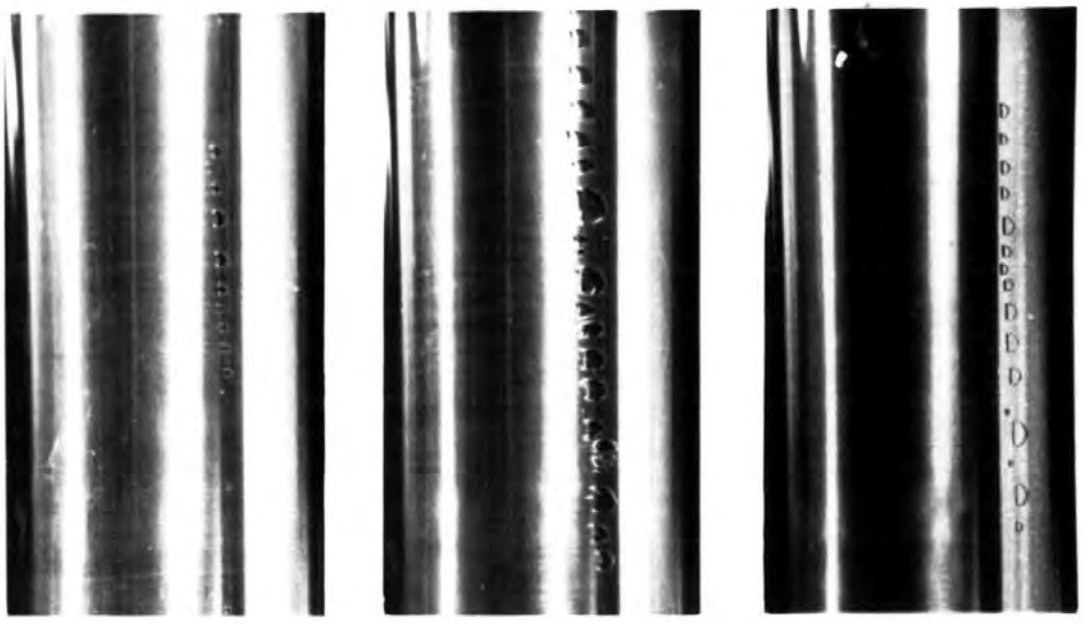

(a) ε = 0.71
Re = 425

(b) ε = 0.71
Re = 495

(c) ε = 0.81
Re = 330

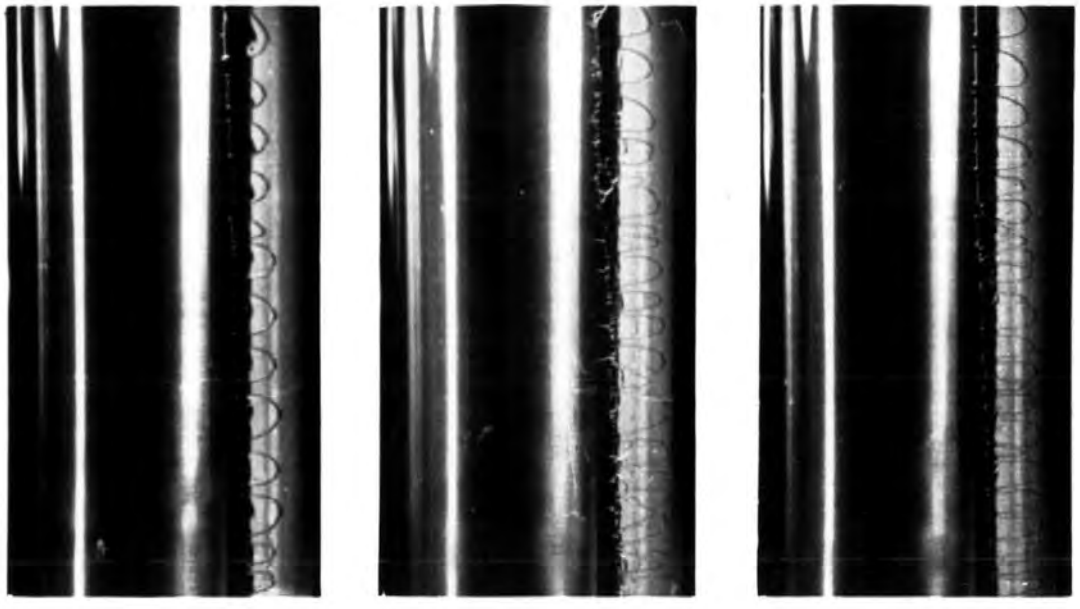

(d) ε = 0.81
Re = 380

(e) ε = 0.91
Re = 170

(f) ε = 0.91
Re = 285

FIG.140 DEVELOPMENT OF CAVITATION USING η = 0.975 AND CARNEA 15

(a) Re = 845

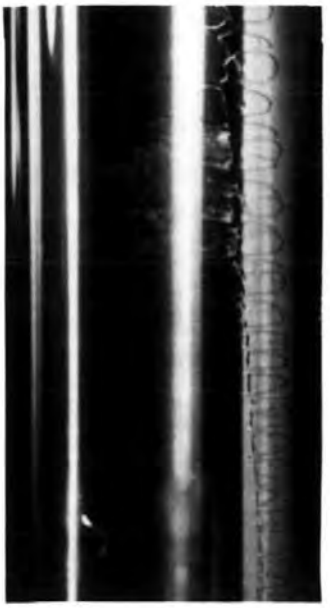

(b) Re = 1275

(c) Re = 1725

(d) Re = 2150

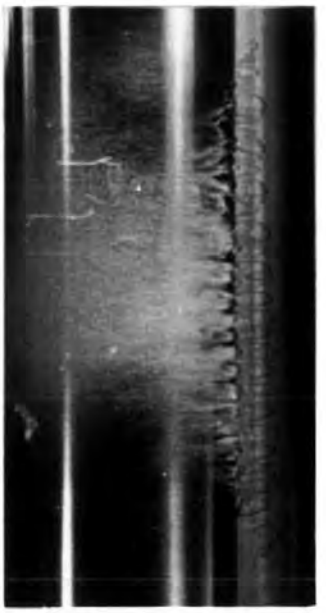

(e) Re = 2695

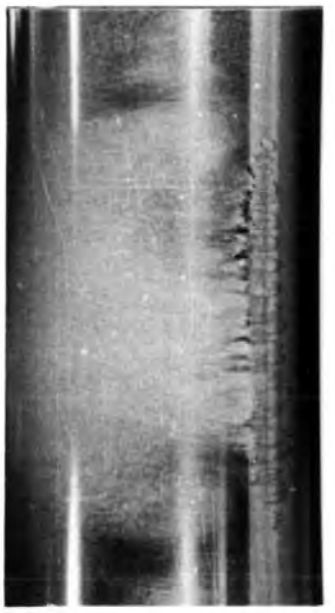

(f) Re = 3055

FIG.141 DEVELOPMENT OF CAVITATION USING η = 0.975 AND MACRON A FOR ε = 0.91

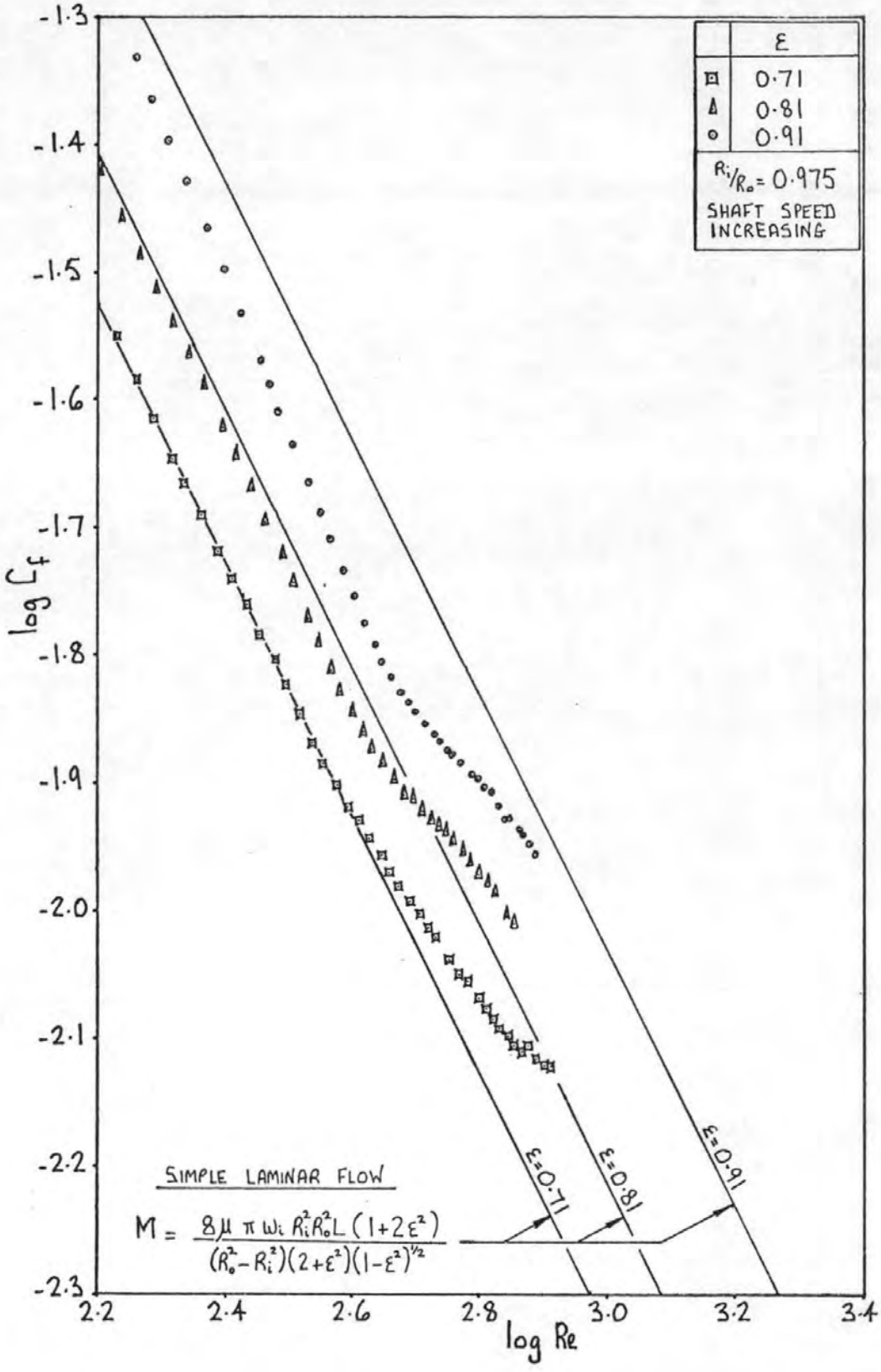

FIG. 142 THE DISAGREEMENT BETWEEN THE CORRECTED TORQUE RESULTS FOR SIMPLE LAMINAR FLOW AND THOSE PREDICTED BY THEORY FOR THE NARROW GAP AND LARGE ECCENTRICITIES

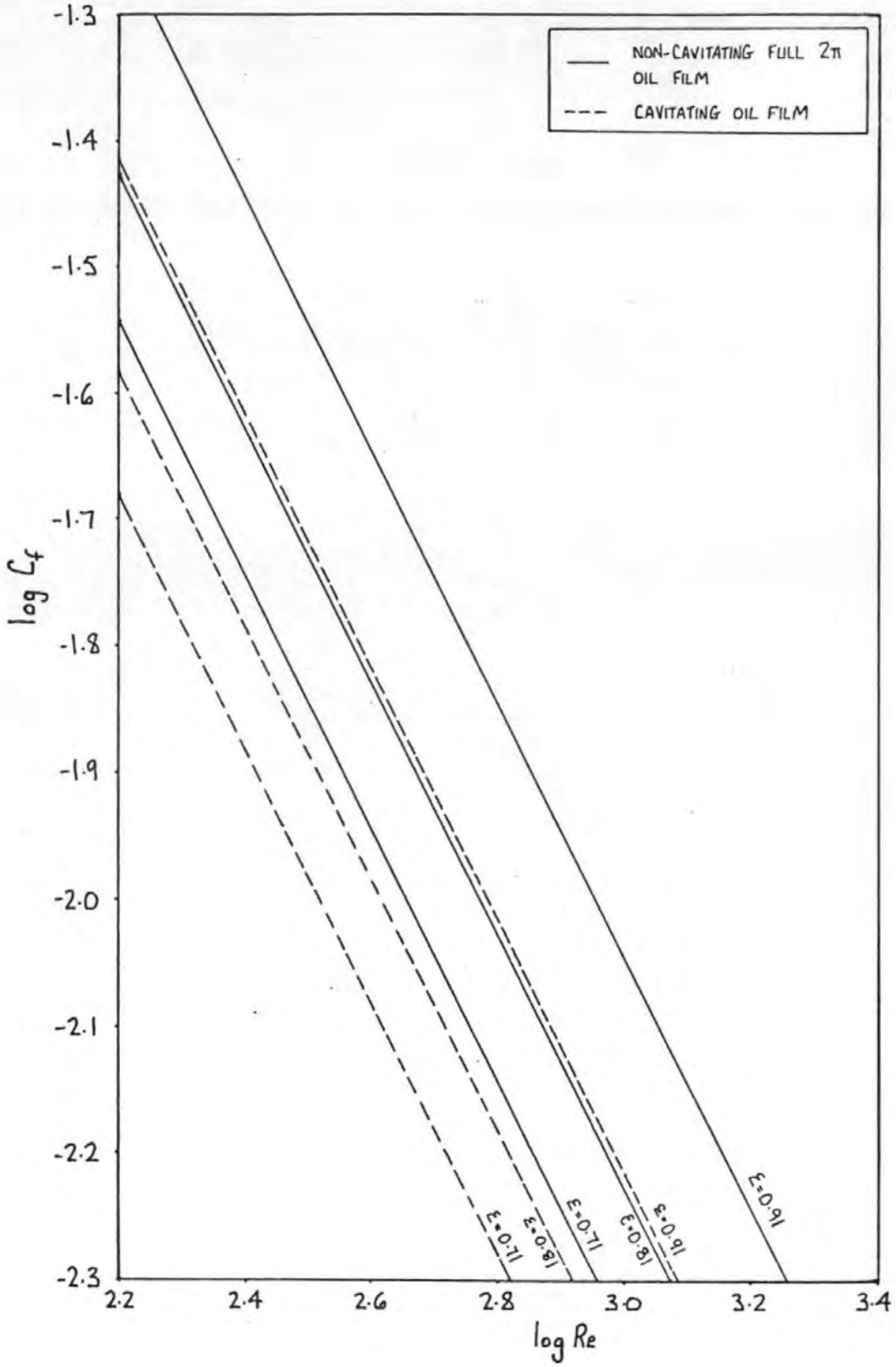

FIG. 143 THE EFFECT OF CAVITATION ON THE THEORETICAL FRICTION COEFFICIENT CHARACTERISTIC FOR SIMPLE LAMINAR FLOW (APPENDIX VI)

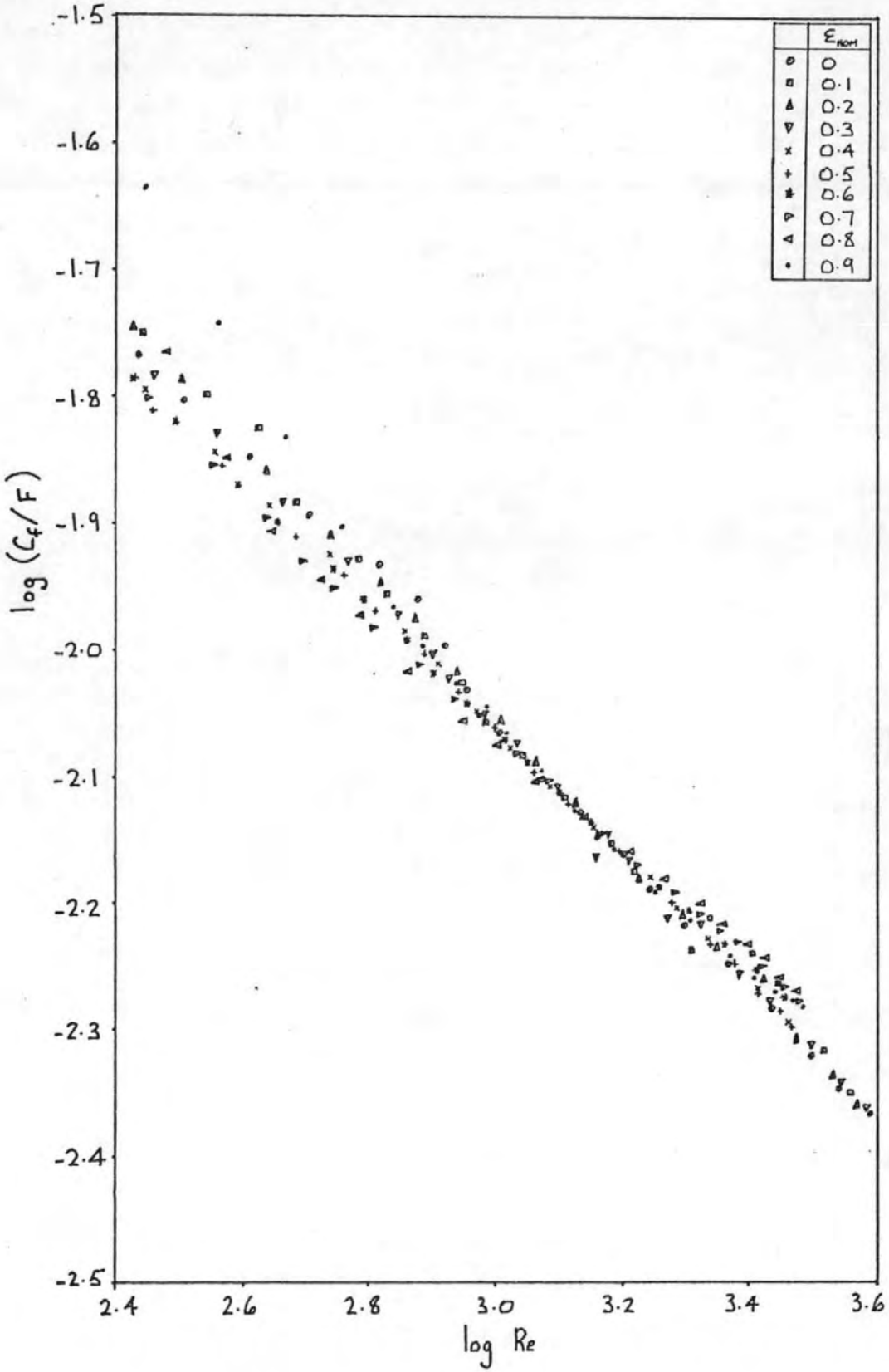

FIG. 144 MODIFIED FRICTION COEFFICIENT CHARACTERISTICS FOR $R_i/R_o = 0.874$

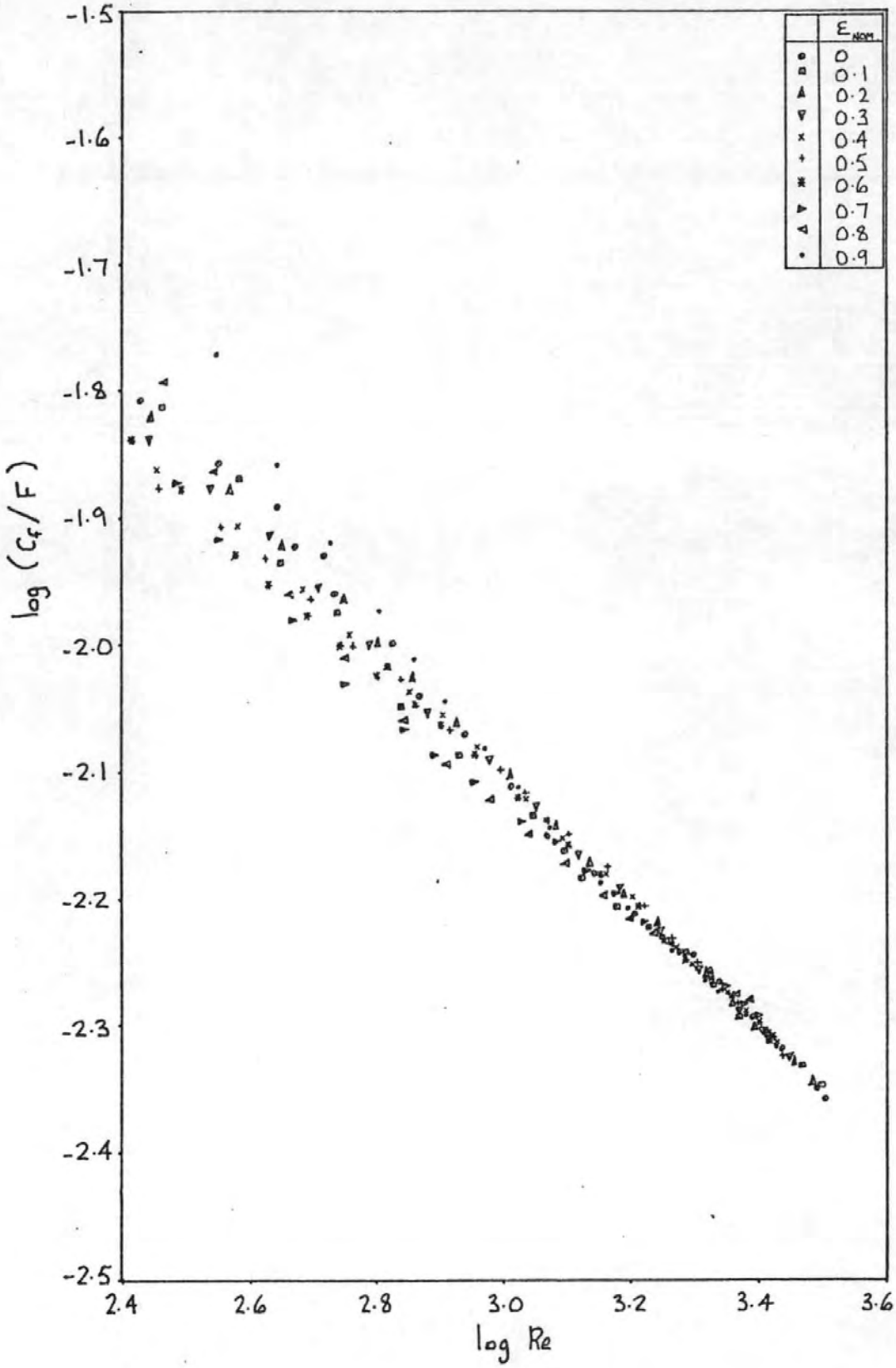

FIG. 145 MODIFIED FRICTION COEFFICIENT CHARACTERISTICS FOR $R_i/R_o = 0.911$

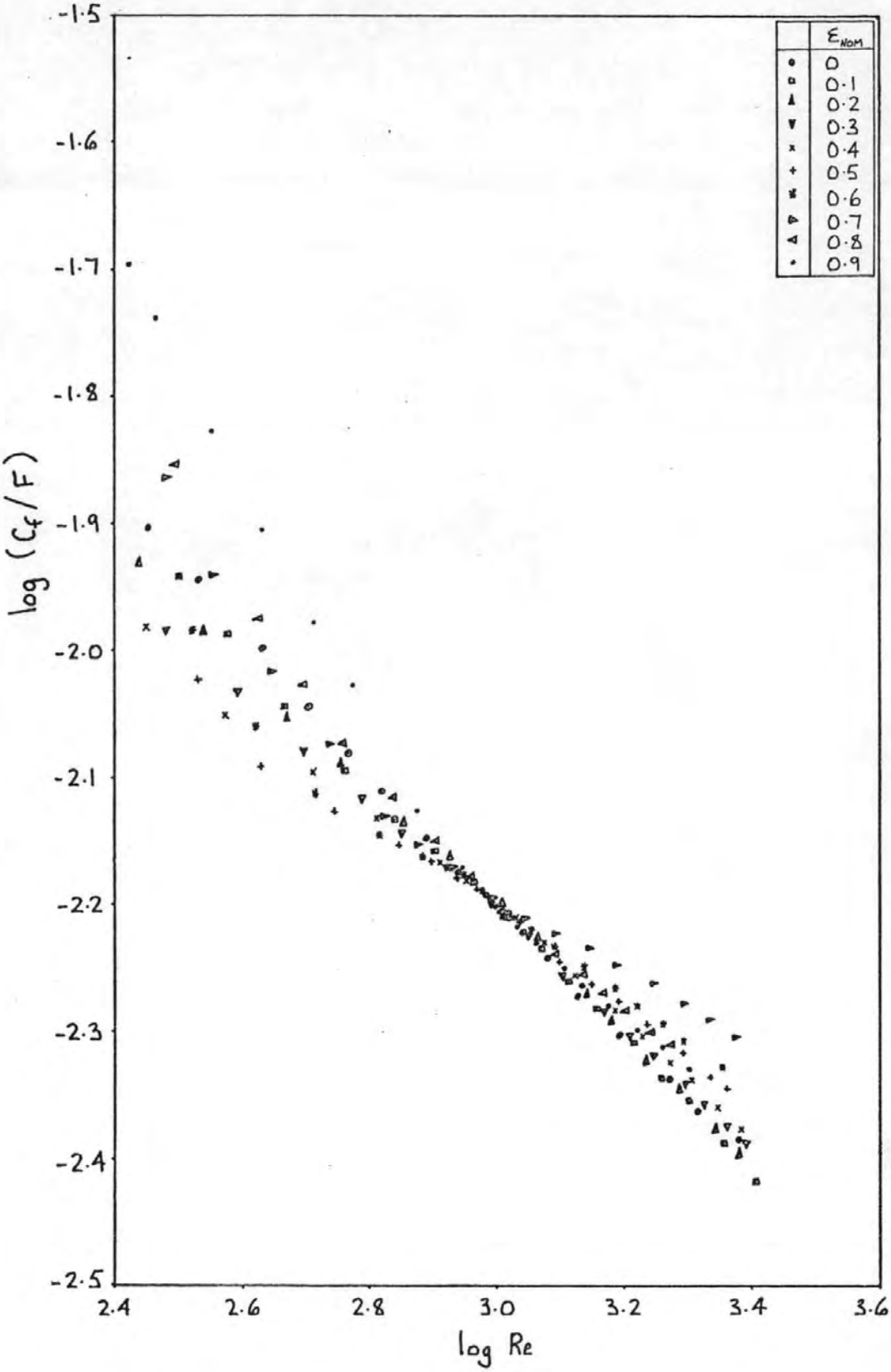

FIG. 146 MODIFIED FRICTION COEFFICIENT CHARACTERISTICS FOR $R_i/R_o = 0.950$

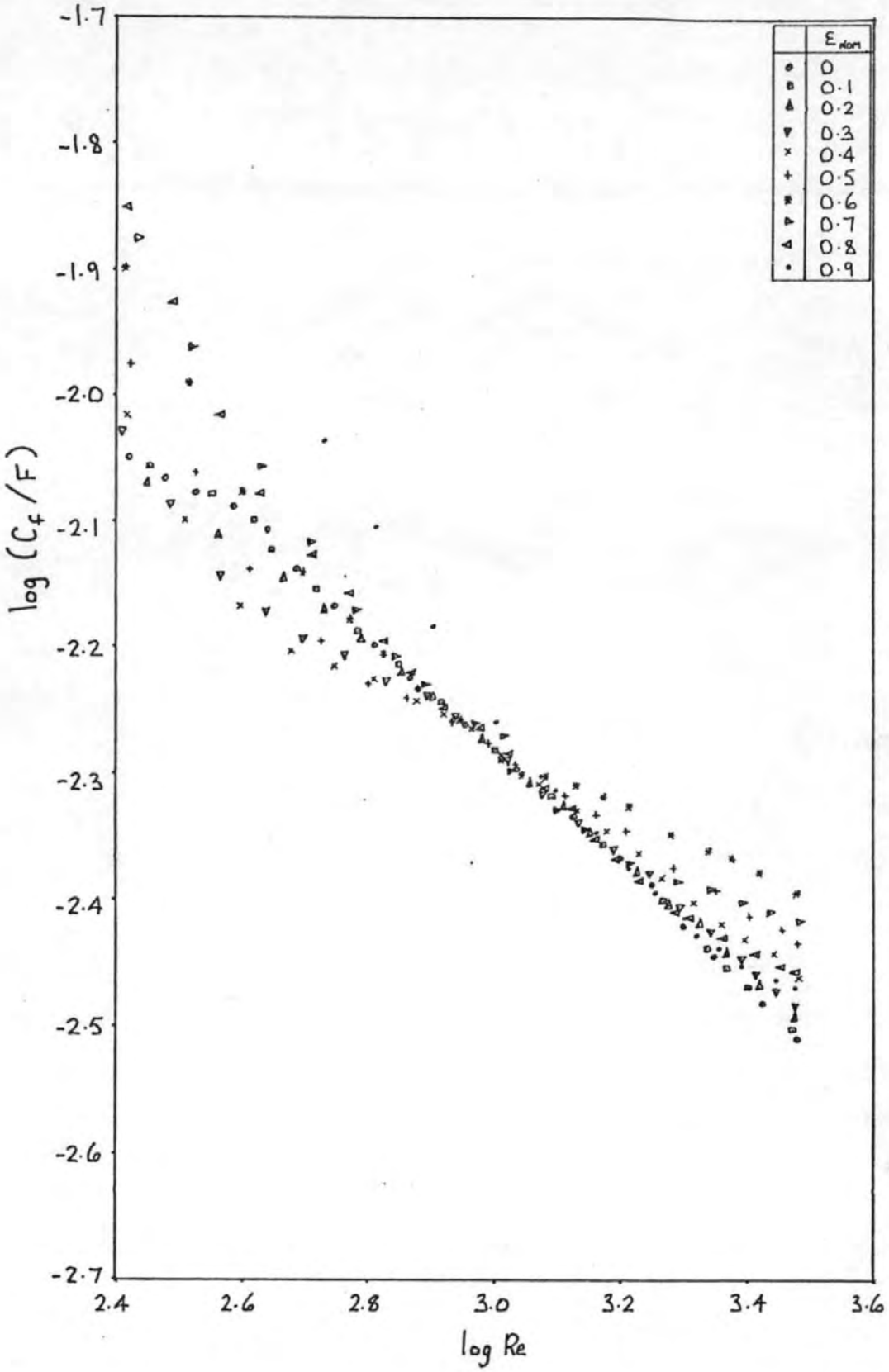

FIG. 147 MODIFIED FRICTION COEFFICIENT CHARACTERISTICS FOR $R_i/R_o = 0.975$

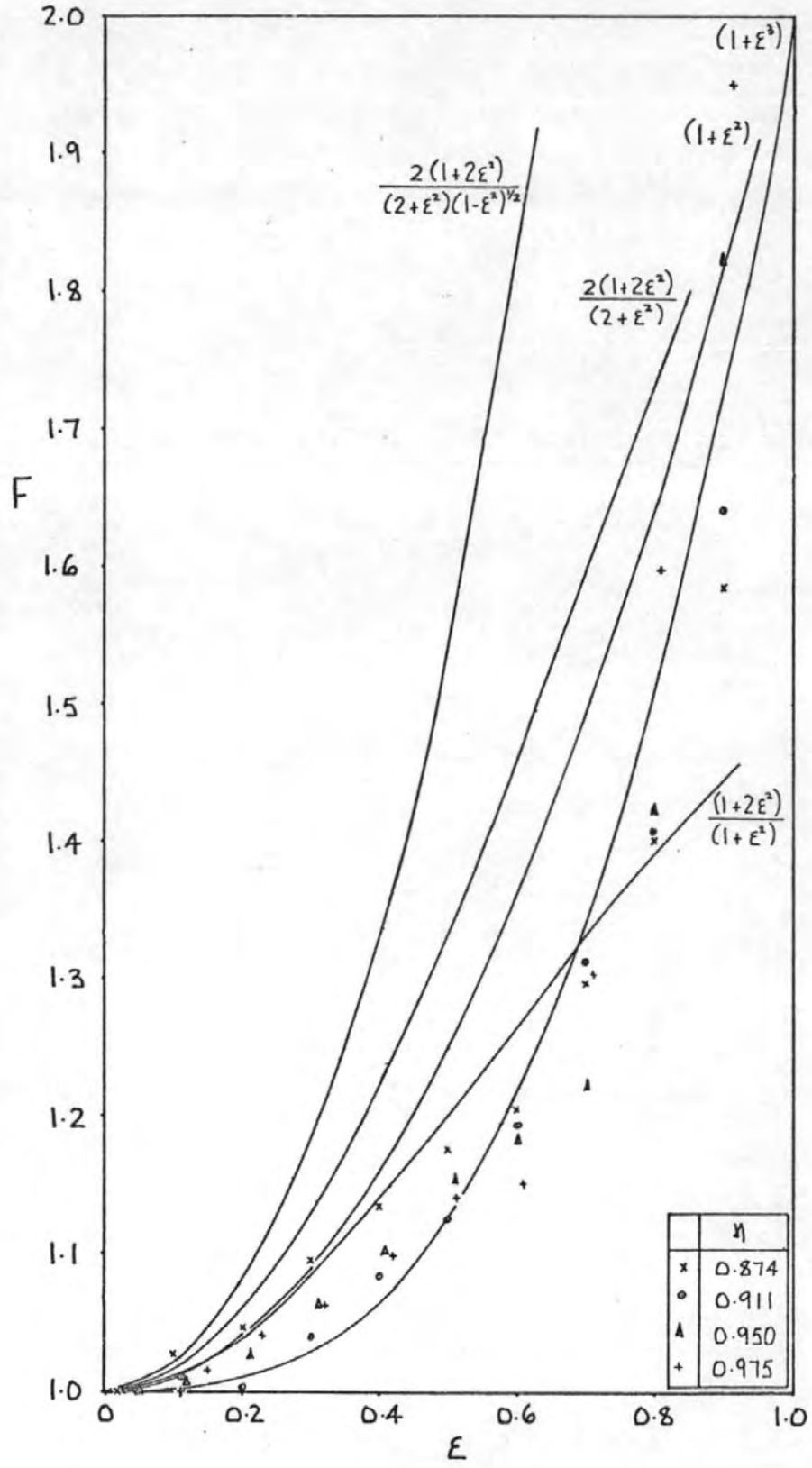

FIG. 148 TRIAL SOLUTIONS FOR THE DERIVED VARIATION OF F WITH ECCENTRICITY

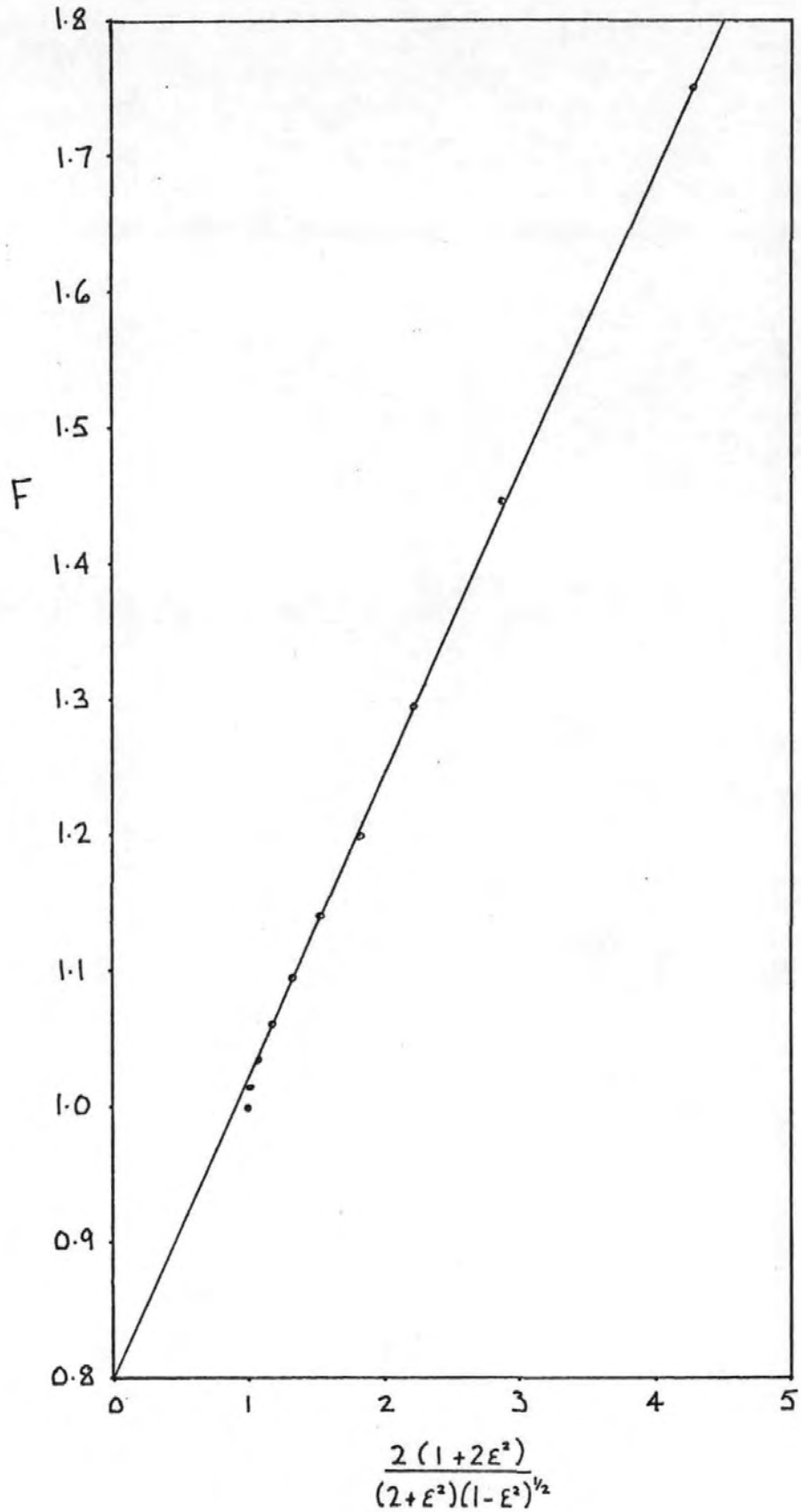

FIG. 149 DERIVED MEAN VALUES OF F FROM TABLE 50

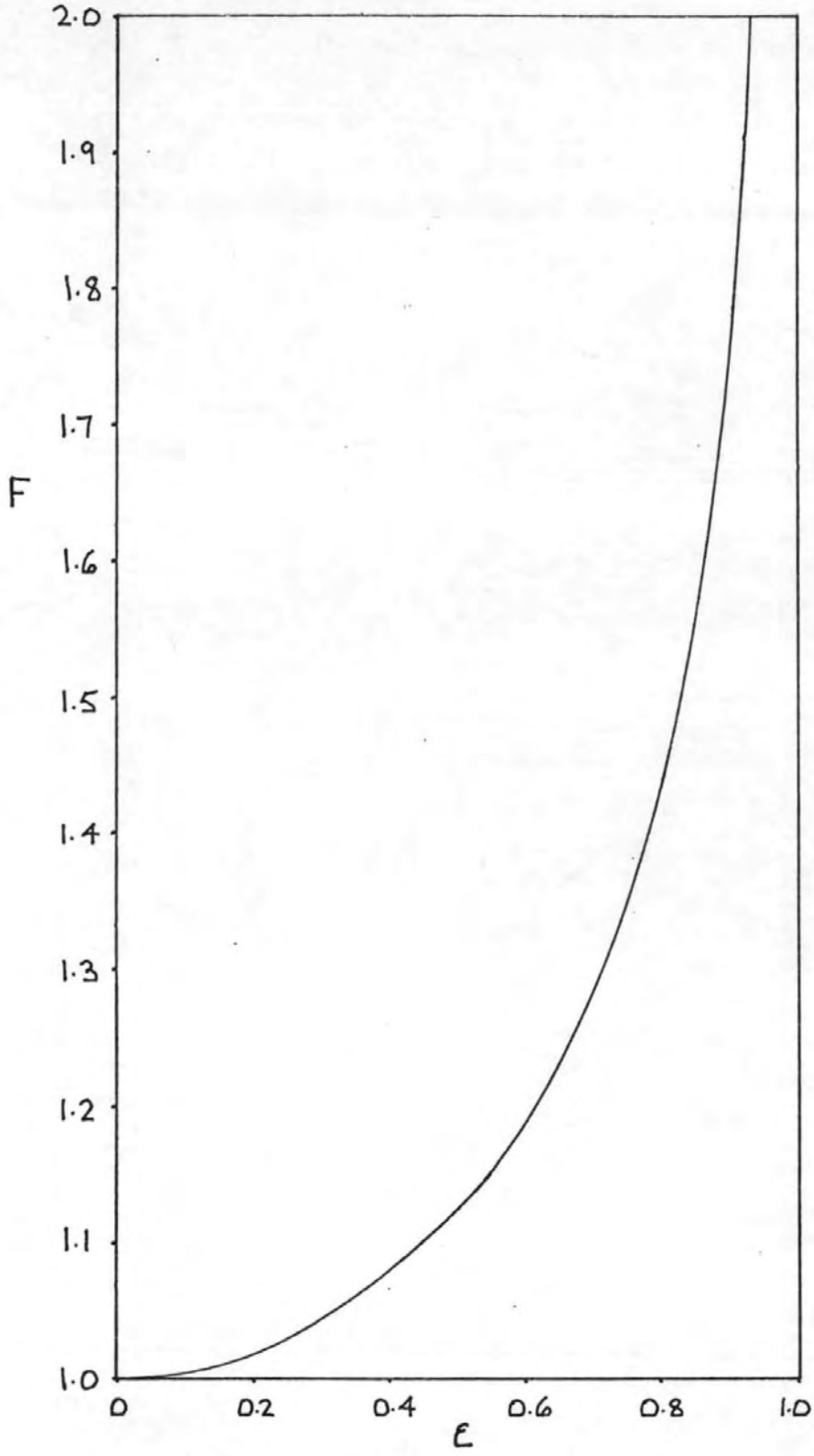

FIG. 150

$$F = 0.23\left[\frac{2(1+2\varepsilon^2)}{(2+\varepsilon^2)(1-\varepsilon^2)^{1/2}}\right] + 0.77$$

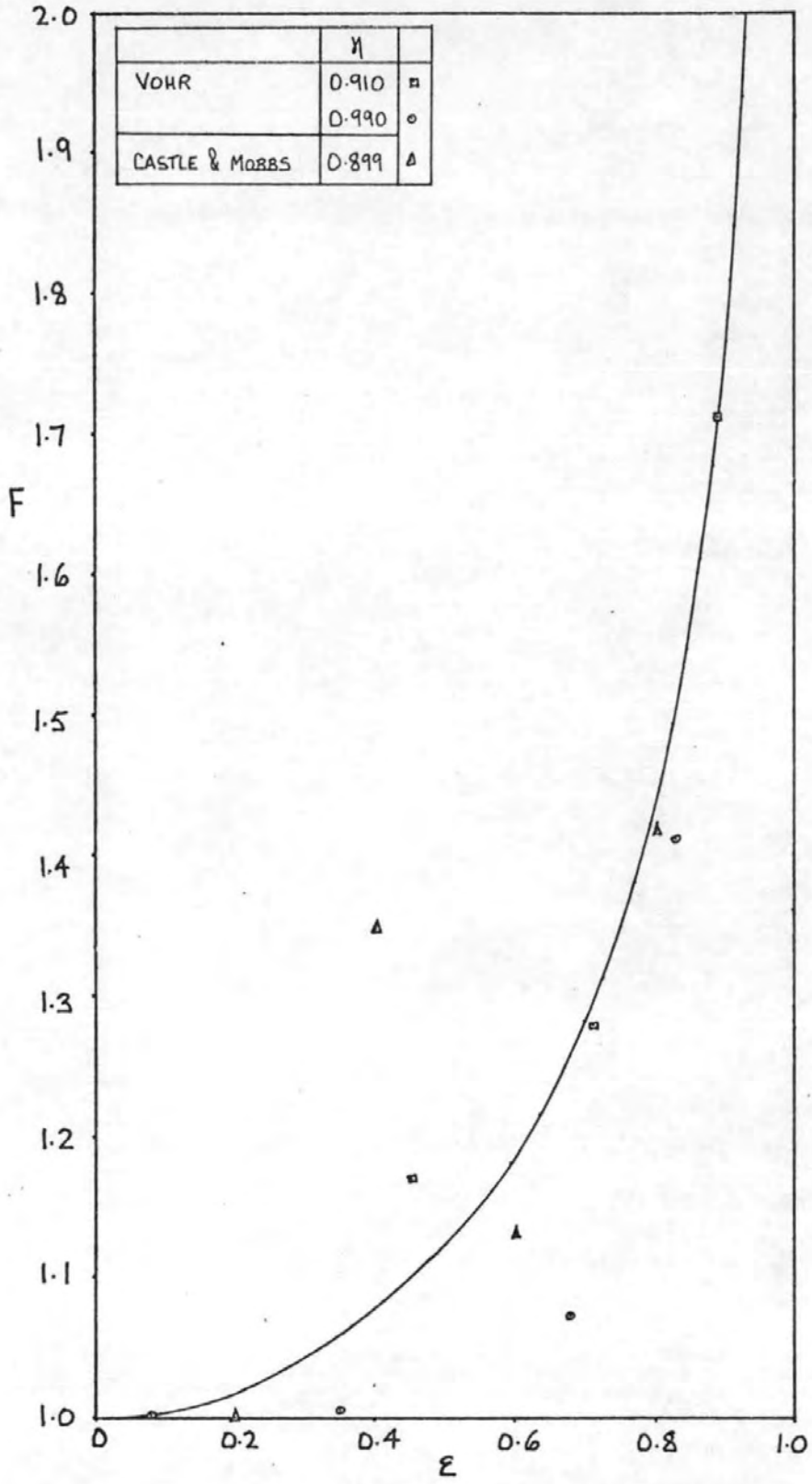

FIG. 151 COMPARISON OF DERIVED RELATIONSHIP FOR F WITH RESULTS FROM PREVIOUS AUTHORS

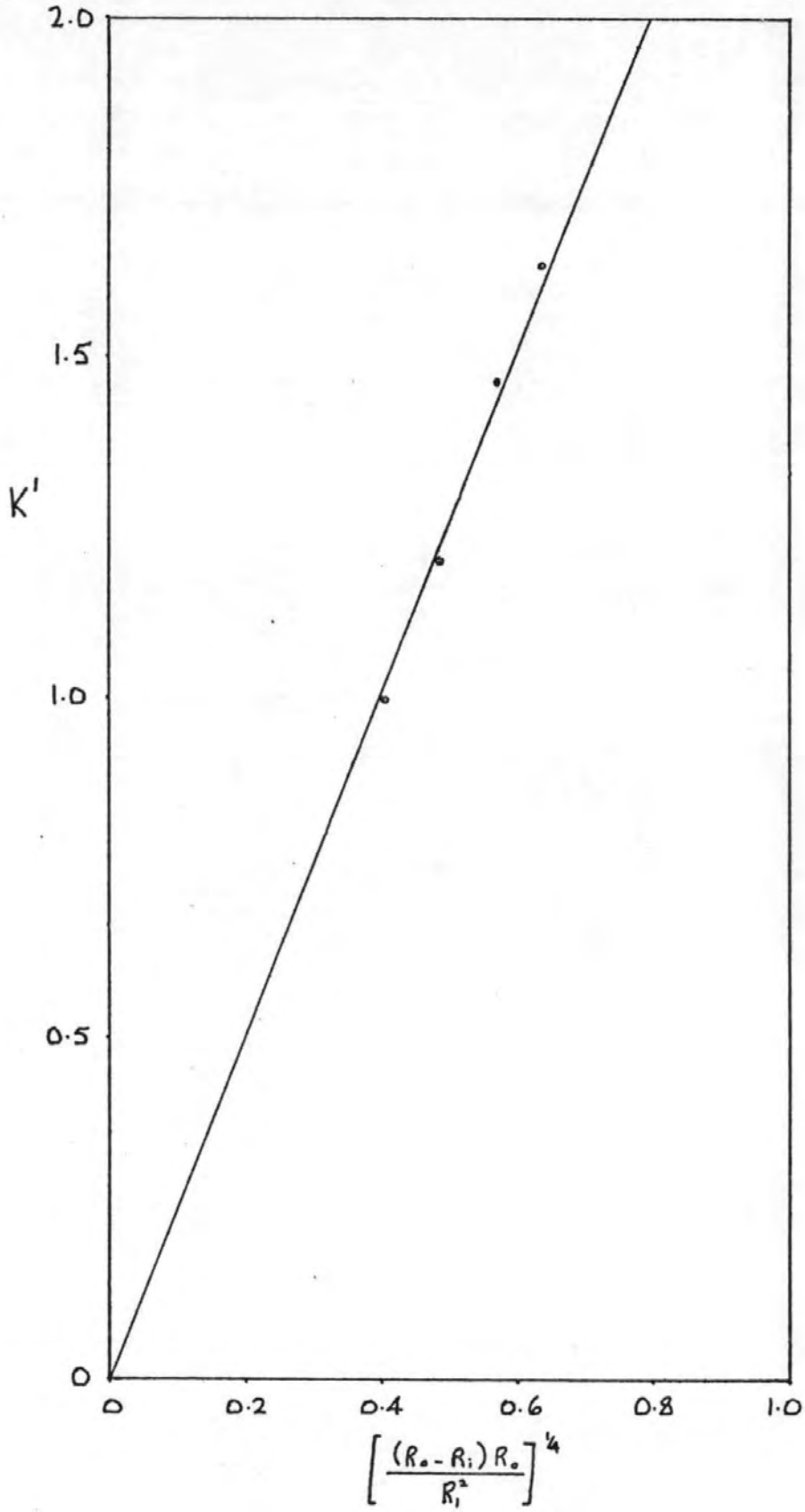

FIG. 152 DEPENDENCE OF DERIVED VALUES OF K' ON TEST RIG GEOMETRY

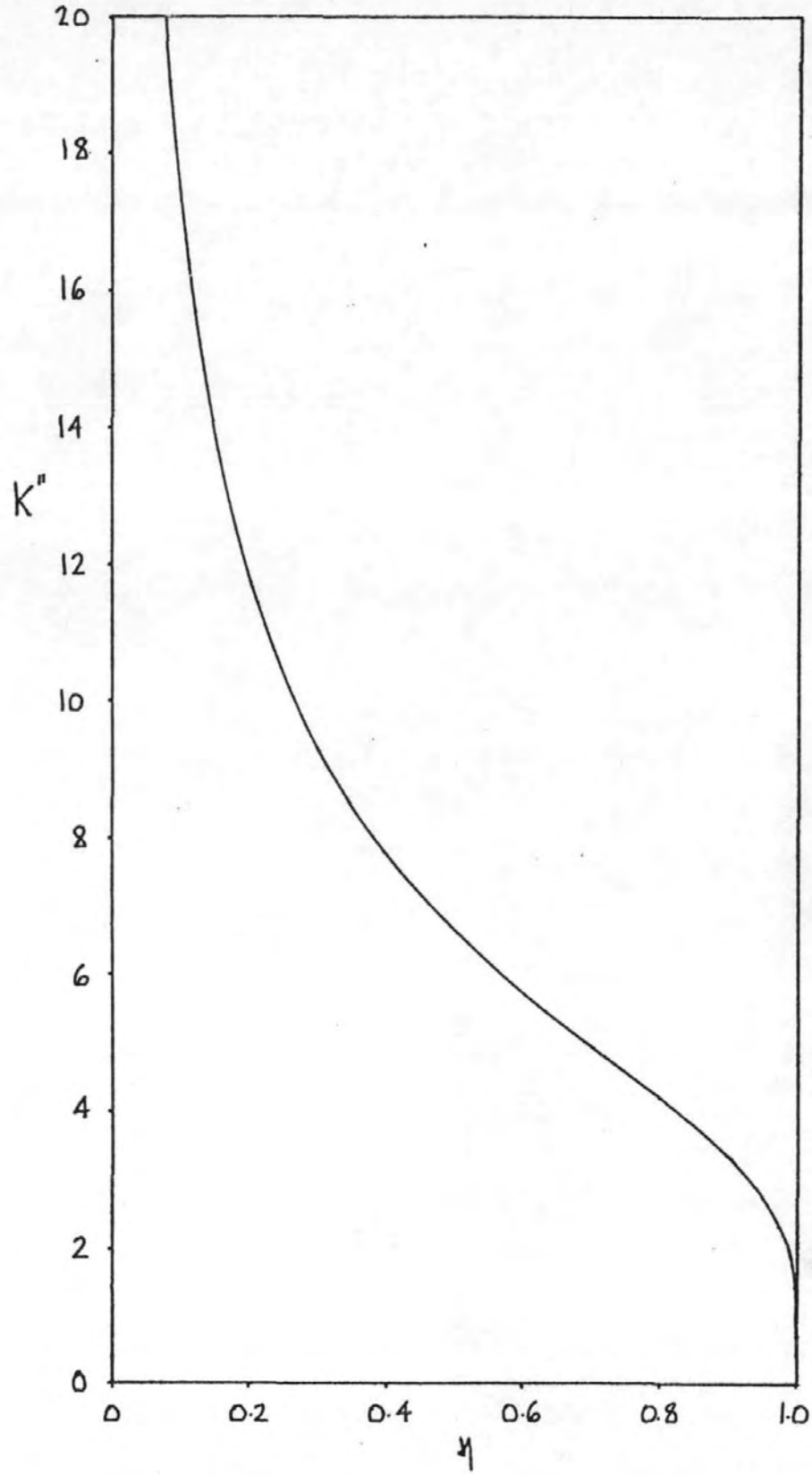

FIG. 153

$$K'' = 5.62 \left[\frac{(R_o - R_i) R_o}{R_i^2} \right]^{1/4}$$

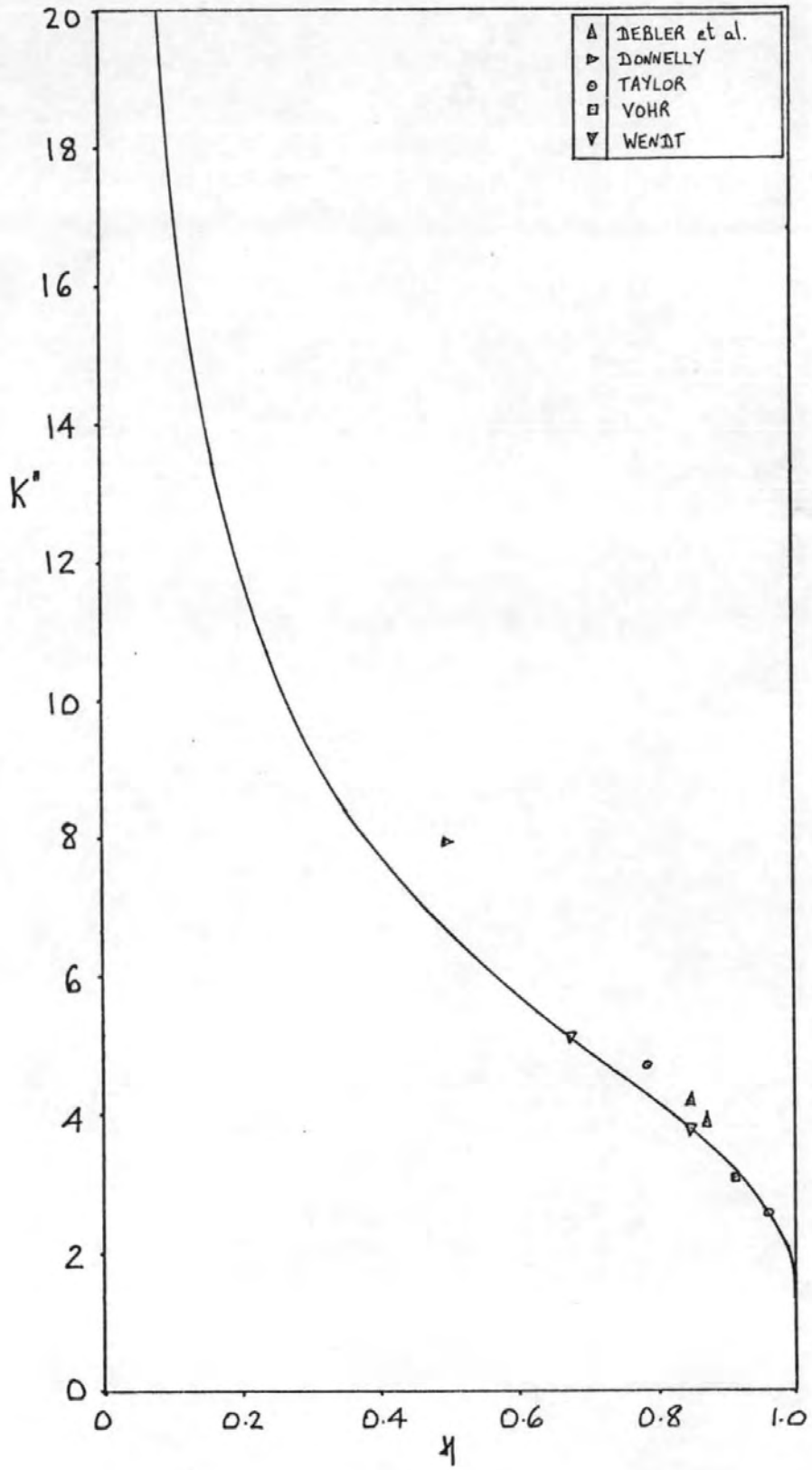

FIG. 154 COMPARISON OF DERIVED RELATIONSHIP FOR K" WITH RESULTS FROM PREVIOUS AUTHORS

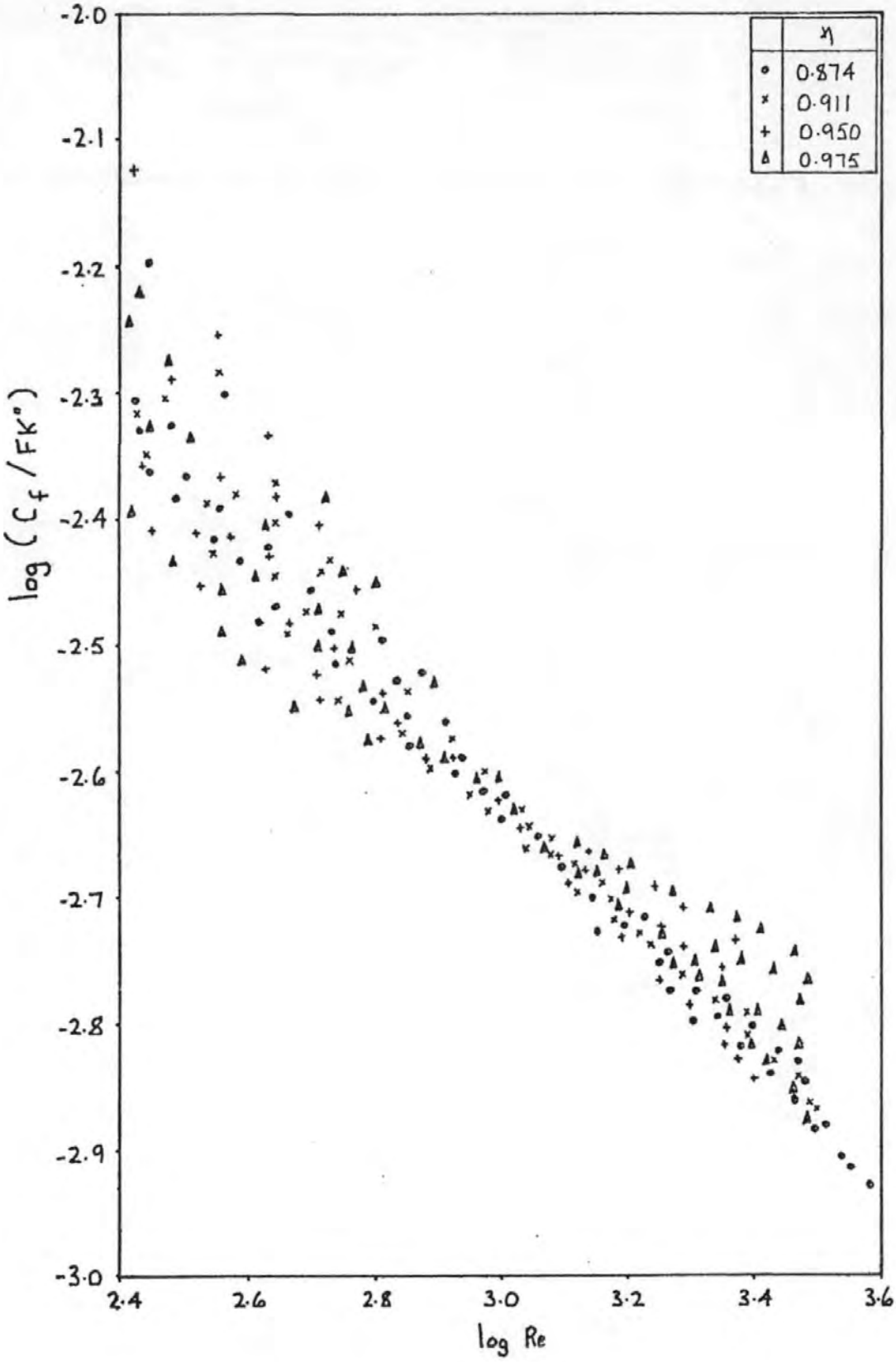

FIG. 155 'CORRECTED' FRICTION COEFFICIENT CHARACTERISTICS FOR THE RANGE OF ECCENTRICITY AND RADIUS RATIO USED IN THE TORQUE MEASUREMENT TESTS

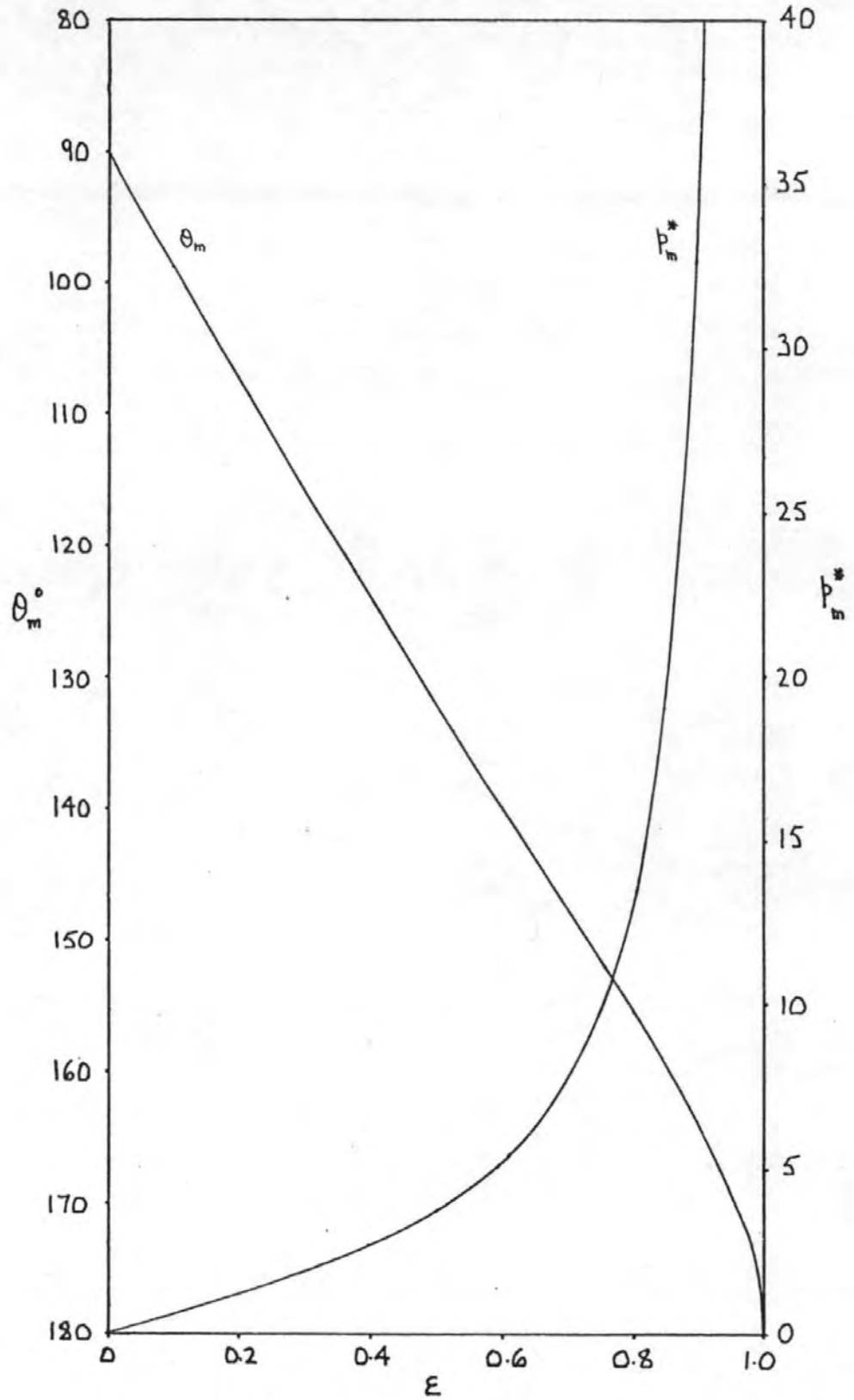

FIG. 156 EFFECT OF ECCENTRICITY ON POSITION AND MAGNITUDE OF SECTION OF MAXIMUM PRESSURE IN AN INFINITELY LONG JOURNAL BEARING RUNNING FULL (APPENDIX V)

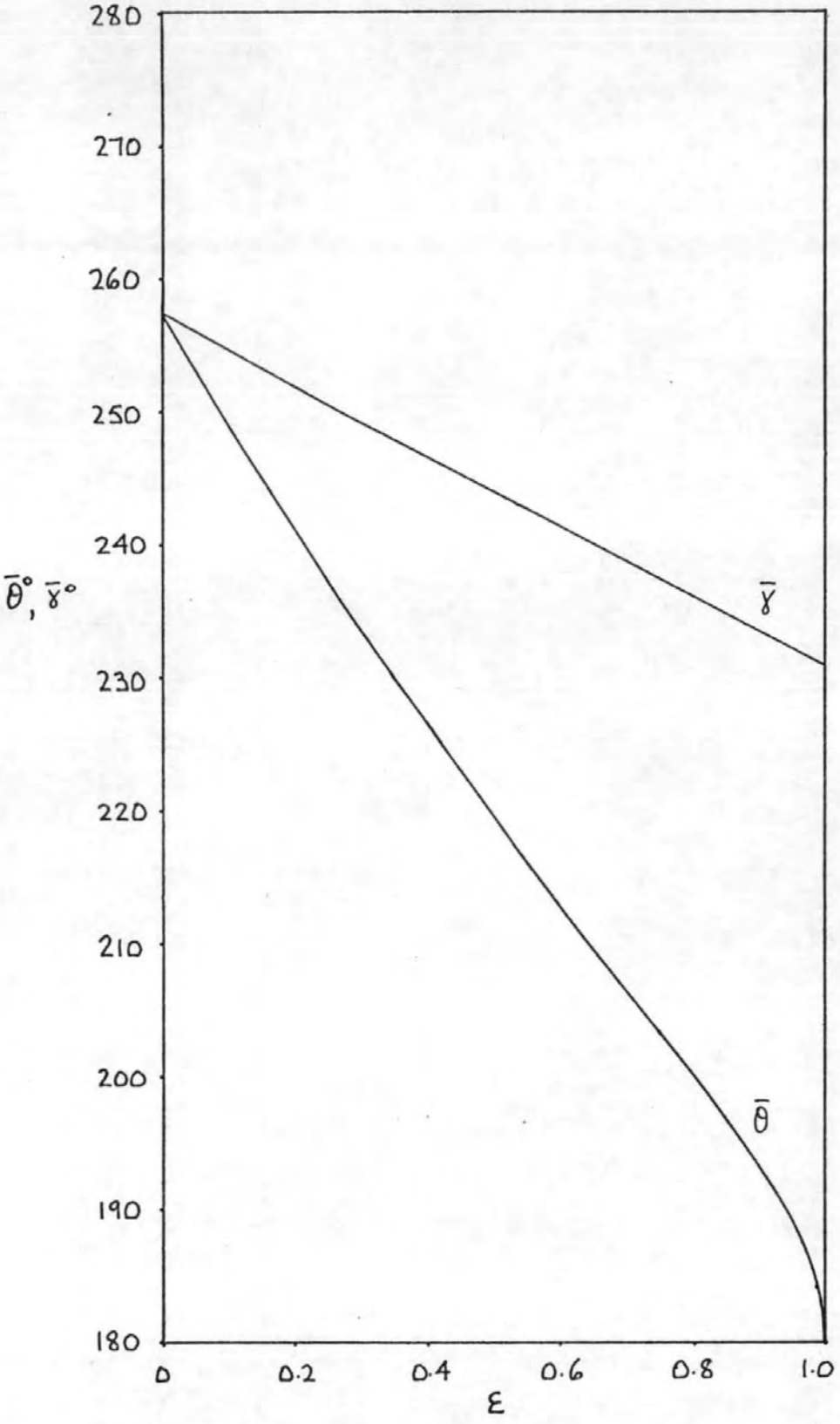

FIG. 157 EFFECT OF ECCENTRICITY ON ASSUMED POINT OF RUPTURE OF JOURNAL BEARING OIL FILM (APPENDIX VI)

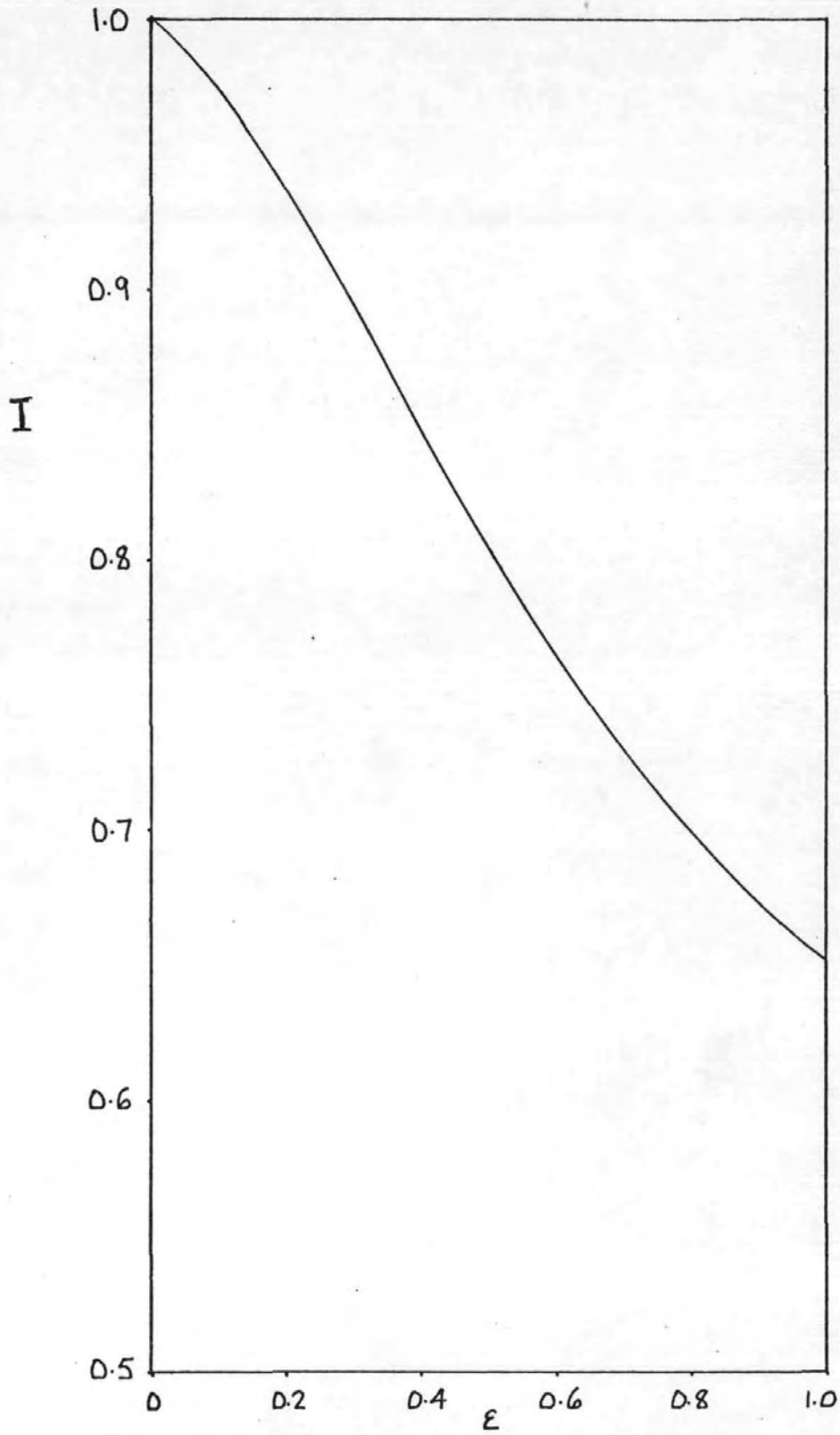

FIG. 158 EFFECT OF ECCENTRICITY ON DERIVED 'CAVITATING FLOW FACTOR' I (APPENDIX VI)